Jean-Michel Lourtioz

Photonic Crystals

Towards Nanoscale Photonic Devices

2nd Edition

Henri Benisty · Vincent Berger
Jean-Michel Gérard · Daniel Maystre
Alexis Tchelnokov

With a contribution by
Dominique Pagnoux

Springer

Photonic Crystals

Jean-Michel Lourtioz · Henri Benisty
Vincent Berger · Jean-Michel Gerard
Daniel Maystre · Alexei Tchelnokov

Photonic Crystals

Towards Nanoscale Photonic Devices

Second Edition

With a contribution by M. Dominique Pagnoux

Translated by M. Pierre de Fornel

Springer

Jean-Michel Lourtioz
Université Paris-Sud
Institut d'Electronique Fondamentale
91405 Orsay Cedex
France

Henri Benisty
Institut d'Optique – Graduate School
Campus Polytechnique, RD 128
91127 Palaiseau Cedex
France

Vincent Berger
Université Paris VII – Denis Diderot
Matériaux et Phenomenes Quantiques
2 place Jussieu
75251 Paris Cedex 05
France

Jean-Michel Gérard
CEA DRFMC
Laboratoire de Nanophysique
et Semiconducteurs
17 rue des Martyrs
38054 Grenoble Cedex 9
France

Daniel Maystre
Faculté des Sciences et Techniques
de Saint Jerome
Institut Fresnel
Ave. Escadrille Normandie-Niemen
13397 Marseille Cedex 20
France

Alexei Tchelnokov
CEA LETI MINATEC
Département d'Optronique
Bâtiment C4
17 rue des Martyrs
38054 Grenoble Cedex 9
France

Dominique Pagnoux
Institut de Recherche XLIM
Faculté des sciences et techniques
de Limoges
123, avenue Albert Thomas
87060 Limoges Cedex
France

ISBN 978-3-540-78346-6 e-ISBN 978-3-540-78347-3

DOI 10.1007/978-3-540-78347-3

Library of Congress Controll Number: 2008921403

© 2008 Springer-Verlag Berlin Heidelberg

This work is subject to copyright. All rights are reserved, whether the whole or part of the material is concerned, specifically the rights of translation, reprinting, reuse of illustrations, recitation, broadcasting, reproduction on microfilm or in any other way, and storage in data banks. Duplication of this publication or parts thereof is permitted only under the provisions of the German Copyright Law of September 9, 1965, in its current version, and permission for use must always be obtained from Springer. Violations are liable to prosecution under the German Copyright Law.

The use of general descriptive names, registered names, trademarks, etc. in this publication does not imply, even in the absence of a specific statement, that such names are exempt from the relevant protective laws and regulations and therefore free for general use.

Coverdesign: deblik, Berlin

Printed on acid-free paper

9 8 7 6 5 4 3 2 1

springer.com

Foreword

The Analogy between Electronic Waves and Electromagnetic Waves

Since the advent of quantum mechanics and the clear demonstration of the existence of 'matter waves', physicists have never failed to take advantage of concepts and theoretical methods developed in the fields of optics and electromagnetism. Thus, a number of phenomena in solid state physics are commonly interpreted by analysing electronic excitations in terms of electronic waves. By contrast, the opposite situation has rarely occurred, and only on a few occasions have optics and electromagnetism borrowed concepts and theoretical methods from solid state physics. From this point of view, the emergence of photonic bandgap materials and photonic crystals at the end of the 1980s can be seen as a revenge to the benefit this time of optics and electromagnetism. In the same way as the periodicity of solid state crystals determines the energy bands and the conduction properties of electrons, the periodical structuring of optical materials at wavelength scales has turned out to be one the most viable approaches towards the control of the energies and of the fluxes of photons occurring in these materials.

The analogy between electronic waves and electromagnetic waves is a mere consequence of the formal relation between the Schrödinger's equation for electronic wavefunctions and Maxwell's equations for electromagnetic waves. Indeed, leaving aside the spins of the particles, a harmonic electromagnetic wave in a dielectric lossless medium satisfies Eq. 1a, which formally is analogous to the equation ruling the wave function for an electron with mass m in a potential V (Eq. 1b):

$$\nabla \times \left[\nabla \times \boldsymbol{E}(\boldsymbol{r})\right] = \frac{\omega^2}{c^2}\, \varepsilon_r(\boldsymbol{r})\ \ \boldsymbol{E}(\boldsymbol{r}) \tag{1a}$$

$$\nabla^2 \Psi(\boldsymbol{r}) = -\frac{2m}{\hbar^2}\left(\mathrm{E} - V(\boldsymbol{r})\right)\ \ \Psi(\boldsymbol{r}) \tag{1b}$$

The spin difference between the photons, which are bosons, and the electrons, which are fermions, results in different statistics for the energy state populations, and also explains that these two equations are of a different nature: the equation for photons is vectorial whereas the equation for electrons is scalar. We shall re-

turn later to the resolution of Eq. 1a, which applies here to the electric field $\boldsymbol{E}$. A brief comparison between this equation and Eq. 1b shows that the relative dielectric permittivity $\varepsilon_r(\boldsymbol{r})$ (the square of the refractive index n) is for photons the analogue of the potential V for electrons. In analogy with the electronic band gaps of semiconductors, it then becomes intuitive that a periodic variation of $\varepsilon_r(\boldsymbol{r})$ may result in the formation of photonic band gaps. In other terms, for a certain range of frequencies, or equivalently of wavelengths, light cannot propagate in the dielectric, whatever its polarization and direction of propagation are. Remaining within the assumption of a lossless dielectric, a light beam incident on this material will be totally reflected.

Of course, the analogy between electronic waves and electromagnetic waves is not restricted to the concept of energy gap. This can be shown by considering the simple system formed by a planar waveguide consisting of a high-permittivity (ε_1) layer, sandwiched between two semi-infinite cladding layers with lower permittivity ($\varepsilon_2 < \varepsilon_1$). Such a system is but the analogue of a potential well V_1 sandwiched between two potential barriers ($V_2 > V_1$). Assuming the propagation constant of light to be larger than ε_2 ω/c in the plane of the waveguide, guided propagation modes occur at discrete frequencies, in much in the same way as electronic levels may exist at discrete energies in the potential well. A transverse distribution of the light intensity ($\alpha|\boldsymbol{E}|^2$) is associated with each guided mode, owing to the fact that the presence of an electron along the transverse axis is characterised by a probability ($\alpha|\psi|^2$).

Photonic Bandgap Materials or Photonic Crystals?

In view of the preceding considerations, the reader might have gathered the impression that ‘photonic bandgap material’ and ‘photonic crystal’ are two terms that can be used indifferently for the same structures. This is not the case however, since the term ‘photonic crystal’ actually applies to any periodic dielectric or metallic structure irrespective of the presence of a photonic band gap in this structure. Further, the very concept of a photonic band gap originally emerged with the desire of achieving a complete control of the spontaneous emission and, ultimately, of designing single-mode microcavities. However, since the pioneering works carried out during the 1990s, the interest in photonic band gaps is no longer restricted to omnidirectional photonic bandgap structures, and the very concept of a photonic crystal has somehow ‘exploded”.

The search for a complete three-dimensional confinement of light is currently a challenging issue. The problem consists in finding the most appropriate cavity structure for solid state microsources with a number of individual emitters as small as possible, possibly a single emitter. Photonic crystal microcavities are promising candidates for addressing this challenge. However, technological difficulties cannot be overlooked, and it is now recognized within the scientific community that there is a long way before the original three-dimensional microwave experiments conducted by E. Yablonovitch *et al* can be reproduced at near-infrared and visible

wavelengths[1]. For this reason, efforts have shifted for the most part from the consideration of three-dimensional photonic crystals to that of two-dimensional photonic crystals, with the underlying idea that two-dimensional photonic band gaps and photonic crystals could develop into a direct continuation of planar integrated optics, with the distinctive advantage however of allowing the realization of optical devices much more compact (wavelength-scaled) than currently existing devices. Fortunately enough, this idea has coincided with the tremendous growth of 1.3-1.5 μm telecommunication systems, which requires the development of an 'optical circuitry' capable of simultaneously analysing an ever increasing number of optical signals, both in fibre and in planar substrate configurations. Indeed, the development of photonic band gaps and photonic crystals in the years extending between the end of the 20th century and the beginning of the 21st century has benefited from the strong demand for innovative devices and systems in optical communications.

In the last decade, considerable advances have been achieved concerning the theoretical understanding, the technical fabrication and the experimental characterisation of photonic crystals. Not only has the concept of a photonic crystal been extended from three-dimensional structures to one and two-dimensional structures, but the guiding, dispersion and refraction properties of periodic structures have also been considered anew in the light of these developments, with the same attention as the properties of photonic band gaps themselves. Giant dispersion effects, including superprism as well as negative refraction and slow-light effects have thus been demonstrated. Periodic metallic structures have also been revisited in the continuity of the pioneering works on artificial dielectrics conducted during the 1950s, revealing new potentialities for microwave antennas, for terahertz circuits and for the control of plasmon waves at optical wavelengths. One of the most striking illustrations of the fruitfulness of research on metallo-dielectric photonic crystals is probably the development of the so-called metamaterials, which are expected to provide a new approach towards negative refraction, through the simultaneous control of the effective permittivity and the effective permeability. Photonic crystals have also made their way into the rich world of nonlinear optics, where they are likely to open new perspectives for frequency conversion, for the generation of harmonic waves and for optical bistability. In this context, we shall see that periodic ensembles of materials for nonlinear optics do not necessarily involve photonic band gap effects.

The study of the physical and optical properties of photonic crystals has generated a burst of new ideas for optical devices and systems. Special mention needs to be made here of photonic crystal silica fibres, which appear as the first application of photonic crystals to the real world of optical communications.

In the field of semiconductors and metals, the fabrication of photonic crystals has represented an important challenge for micro- and nanotechnology. In turn, these technologies have benefited from the validation of processes which has thus

[1] Yablonovitch E., Gmitter T.J., Leung K.M. *Photonic band structures: the face-centered-cubic case employing non-spherical atoms*, *Phys. Rev. Lett*. 67, p. 2295, 1991

been completed. In this respect, the evolution of photonics has paralleled the revolution which has been taking place in the field of electronics with the development of nanotransistors and quantum dot memories. Nanophotonics are now being recognized as a special branch of optics, in much the same way as nanoelectronics form a special branch of electronics. As will be seen in this book, some of the technological problems that had appeared at the time of the first studies on photonic crystals, are currently in the process of being solved. However, it should be stressed that future development and applications of photonic crystals are definitively dependent on the degree of accuracy which can be achieved in the fabrication of micro- and nanostructures, and thus on the overall dimensions of the corresponding devices.

Basic One, Two and Three-Dimensional Structures

In the following chapters, the reader will explore the large variety of photonic structures which have been either imagined or fabricated in the world of photonic crystals. However, some among these structures are quite emblematic, and as such they will be systematically used as references throughout this book. It seems therefore useful to acquire a familiarity with these structures. They are represented here in Fig. 1, where they are ordered from the simplest to the most complex.

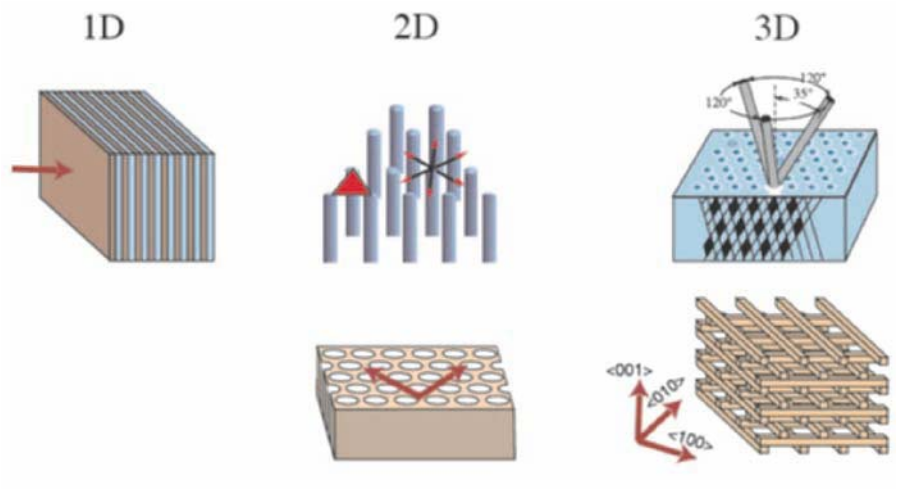

Fig. 1. Emblematic photonic crystals. *From left to right:* One-dimensional structure: Bragg mirror. Two-dimensional structures: hexagonal lattices formed by rods or pores. Three-dimensional structures: 'Yablonovite' and 'woodpile' structures

As is the case in reference textbooks on solid state physics[2], one-dimensional structures are commonly used as reference models, more particularly for understanding the formation of energy band diagrams. In the field of optics, one-dimensional photonic crystals consisting of periodic stacks of thin dielectric layers with a λ/4 optical thickness are actually nothing else than Bragg mirrors (Fig. 1, *left*). Contrary to one-dimensional solid state crystals, these structures are not artificial, and they are actually used in a variety of optical devices. The fabrication of monolithic Bragg mirrors from III-V semiconductors has reached maturity at the end of the 1980s. The first experiments on optoelectronic devices based on the use of planar microcavities were reported at near-infrared wavelengths during the same period. However, the efficiency of Bragg mirrors is strongly dependent on the angle of incidence with respect to the normal to the dielectric layers. When the incidence angle is progressively increased, the reflectivity decreases and the mirror tends to become transparent in the end. Under these conditions, it turns out impossible to achieve an omnidirectional photonic band gap.

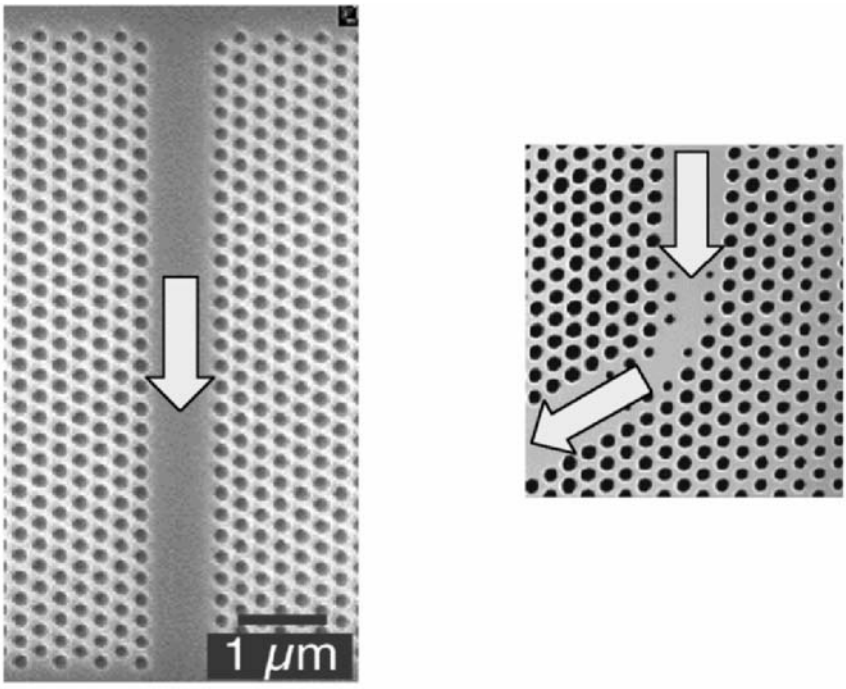

Fig. 2. Channel optical waveguide (*left*) and light bend (*right*) fabricated in a two-dimensional photonic crystal

[2] Kittel C. *Introduction to Solid State Physics,* J. Wiley & Sons, 1971

While two-dimensional photonic crystals are more difficult to fabricate than one-dimensional crystals, they nevertheless remain of a moderate complexity (Fig. 1, *middle*). The strong interest in these structures originates from their potential applications to planar integrated optics and to 'photonic circuitry'. Basically, two different types of such structures exist: the first one consists of disconnected dielectric cylinders (Fig. 1, *middle top*), while the other is formed by air pores drilled in a dielectric matrix (Fig. 1, *middle bottom*). If the in-plane confinement of light could be achieved in a thin slab of such a photonic crystal, then the propagation of light could be totally controlled along two directions. This is illustrated in Fig. 2, which shows how to obtain either a channel waveguide or a light bend by removing a series of patterns from a two-dimensional photonic crystal. This leads to the possibility of envisioning planar photonic circuits that would be analogous to electronic circuits fabricated on silicon wafers. Such circuits would be of particular interest for obviating the shortcomings of the ultraminiature microelectronic chips which are expected to appear in the future. We shall later see that one of the main problems in this context is actually to prevent the light from escaping out of the plane, i.e. out of the dielectric slab. This issue has been addressed in a number of studies. Theoretical investigations often remain complex due to both the finite thickness of the crystal slab and to the local disruptions of the periodicity of the crystal.

Actually, only three-dimensional photonic crystals really allow for omnidirectional photonic band gaps. The last decade has been marked by two main types of structures, represented in the right-hand part of Fig. 1. The so-called Yablonovite Fig. 1, *top right*) was promoted by the famous experiments conducted by Eli Yablonovitch and his group in 1991 (Yablonovitch 1991). Indeed, the fabrication of the first prototype at centimetre scales and the subsequent demonstration of a complete photonic band gap around 12 GHz aroused tremendous interest in photonic crystals within the scientific community. The second emblematic three-dimensional photonic crystal (Fig. 1, *bottom right*), which is referred to either as a ‘woodpile’ or ‘layer-by-layer’ structure, consists of a multilayer stack where each layer is formed by a one-dimensional array of dielectric rods. Existing methods of fabrication, i.e. those used in semiconductor technology, can be applied successfully for the realization of such structures. Actually, both the Yablonovite and the woodpile photonic crystals present the same crystalline structure as diamond or silicon. Indeed, in the first case, the periodic array of pores drilled in the dielectric matrix with an angle of 120° between one another reproduces the empty <110> galleries of the face centred cubic (fcc) lattice with two atoms per cell. In the second case, the intersections between the dielectric rods are organized into two fcc lattices in the same way as carbon atoms are in the diamond crystal.

In practice, the similarity with solid state crystals can be neglected, and photonic structures can be considered as specific instances of two or three-dimensional diffraction gratings. This more traditional optical approach can be quite useful, and therefore it will be adopted at various points in this book.

Objectives of this Book

The growing interest for photonic crystals has generated an extensive literature on this subject. Some websites have tried to maintain an exhaustive bibliography as long as it has been possible, but most of them have given up due to the explosion of the studies on the subject. Contrary to the valuable books which have already been published on this subject, this book does not intend only at describing ideal photonic structures with infinite dimensions in all directions of space, but rather aims at going from photonic crystals to the realization of actual optical devices, and beyond to the development of a photonic circuitry. In this respect, the confinement of light in a 'photonic cage' can be viewed as a first step towards the design of optical devices at the wavelength scale with ultimate properties for storing, filtering, guiding and emitting light. It is also part of a tendency towards the extreme miniaturization of devices and systems, which is made necessary by the manipulation of an ever increasing number of data.

From a more academic point of view, the study of photonic crystals has been, and still remains, a unique opportunity of bringing together a large diversity of skills from such different fields as solid state physics, optics, microwaves and microelectronics. The 'Groupe de Recherche' (GDR) on 'Microcavities and Photonic Crystals' organized by the CNRS in the period from 1996 to 2001 has been the French example of a cooperation between researchers from such different fields. The present book can be seen as the result of this cooperation.

The six authors, coming from different scientific fields, have joined efforts to provide students and researchers with the necessary theoretical background on photonic crystals and their optical properties, while at the same time presenting a large variety of optical and microwave devices to which photonic crystals can be applied.

The book is divided into three parts which can be independently approached. In the first part, the reader will become familiar with photonic band diagrams and theoretical models for both infinite and finite photonic crystals. We address the problem of analysing the presence of local disruptions in the periodicity of photonic crystals, which are also referred to as crystal defects in analogy with solid state physics. We finally consider different issues related to quasi-crystals as well as the main specificities of periodic metallic structures.

The second part of this book is devoted to the specific properties of photonic structures in terms of optical confinement, guiding, refraction and optical nonlinearity. Novel concepts of mirrors, waveguides and optical resonators based on photonic crystals will then be discussed. A particular attention shall be devoted to the problem of a solid state emitter in a microcavity and to the control of its spontaneous emission, which remains one of the major issues in nanophotonics. A detailed bibliography, covering all topics addressed in this book, will allow the reader to delve deeper in the subject, and should provide him with a precise idea of the most recent advances in research.

The last part of the book will be devoted to a review of the potential applications of photonic crystals and of the different methods which have been developed

for their fabrication and their characterization. We shall successively consider semiconductor devices in planar integrated optics, light microsources and photonic crystal fibres. In most cases, photonic crystals will be compared to other technical solutions implemented with existing devices. A specific chapter will be devoted to three-dimensional photonic crystals in optics. Finally, the potential applications of photonic crystals to microwave and THz devices and antennas will also be presented in order to complete this review and to show the many common aspects shared by optics and microwaves.

As can be seen, we have tried throughout this book to capture the strong multidisciplinary character of photonic crystal research, which is an essential part of its appeal to everyone with a broad curiosity.

Orsay, January 2008 Jean-Michel Lourtioz

Table of Contents

Foreword ..... **V**

Part I Theoretical Models for Photonic Crystals **1**

Introduction to Part I **3**

1 Models for Infinite Crystals **5**
1.1 Plane Wave Expansion 5
1.1.1 Maxwell's Equations 5
1.1.2 The Floquet-Bloch Theorem 6
1.1.3 Hermiticity of the Field Operator 10
1.1.4 Simple Examples of Bloch Functions 11
1.1.5 General Plane Wave Method 13
1.2 Other Methods for the Calculation of the Photonic Band Gaps of an Infinite Crystal: the KKR Method 21
1.3 Photonic Band Diagram 21
1.3.1 The Irreducible Brillouin Zone 22
1.3.2 Band Diagrams of One-Dimensional Crystals 25
1.3.3 Band Diagrams of Two-Dimensional Photonic Crystals 33
1.3.4 Off-Axis Propagation in One and Two-Dimensional Photonic Crystals 40
1.3.5 Band Diagrams of Three-Dimensional Photonic Crystals 41
1.4 Infinite Crystals with Defects 43
1.4.1 Point Defects 44
1.4.2 Coupling of Point Defects 50
1.4.3 Supercell Method 52
1.4.4 Methods derived from Tight-Binding Methods in Solid State Physics 53
1.4.5 Extended Defects 54
1.4.6 Semi-Infinite Crystals and Surface Defects 56
1.4.7 Density of States in Photonic Crystals with or without Defects 59

2 Models for Finite Crystals **65**
2.1 Transfer, Reflection and Transmission Matrix Formulations 65
2.1.1 Reflection and Transmission Matrices 66
2.1.2 Pendry Method 72

2.2 Finite Difference in Time Domain (FDTD) Method 80
2.2.1 Numerical Formulation of Maxwell's Equations 80
2.2.2 Case of an Incident Pulse 84
2.2.3 Absorption Region and Boundary Conditions 86
2.2.4 Practical Implementation and Convergence of the FDTD Method 87
2.2.5 Examples of Results obtained for a Point Source with the FDTD Method 89
2.3 Scattering Matrix Method 91
2.4 Other Methods: Integral and Differential Methods, Finite Element Method, Effective Medium Theory 100
2.5 Numerical Codes available for the Modelling of Photonic Crystals 104

3 Quasi-Crystals and Archimedean Tilings 107
3.1 Photonic Quasi-Crystals 108
3.2 Archimedean Tilings 111
3.3 From Photonic Quasi-Crystals to the Localization of Light 115

4 Specific Features of Metallic Structures 121
4.1 Bulk Metals: Drude Model, Skin Effect and Metallic Losses 121
4.1.1 Drude Model 123
4.1.2 Low-Frequency Region: Skin Effect and Metallic Losses 124
4.1.3 From the Infrared to the Visible and UV Regions 125
4.2 Periodic Metallic Structures at Low Frequencies 126
4.2.1 Plasmon-Like Photonic Band Gap 126
4.2.2 Transmission Spectra of Metallic and Dielectric Photonic Crystals 129
4.2.3 Complete Band Gaps in Metallic Photonic Crystals 131
4.2.4 Structures with Continuous Metallic Elements and Structures with Discontinuous Metallic Elements 132
4.3 Periodic Metallic Structures at Optical Frequencies. Idealized Case of a Dispersive Lossless Dielectric 134
4.4 Surface Waves 137
4.4.1 Surface Plasmons at a Metal/Dielectric Plane Interface 137
4.4.2 Propagation of Surface Plasmons along a Periodically Modulated Metal/Dielectric Interface and Local Enhancement of the Field 140
4.4.3 Wood's Anomalies: Phenomenological Theory 144
4.4.4 Photonic Band Gaps for the Propagation of Surface Plasmons at Periodically Modulated Metal/Dielectric Interfaces 148
4.4.5 The Photon Sieve 150
4.4.6 Surface Waves in Metals at Radiofrequencies 151

Part II Optical Properties of Photonic Crystals 157

Introduction to Part II. The 'Many Facets' of Photonic Crystals 159

5 Control of Electromagnetic Waves 163
5.1 The Photonic Crystal Mirror 163

5.1.1 The Semi-Infinite Photonic Crystal: Mirror or Diffraction Grating?. 163
5.1.2 Specular Reflection at a Semi-Infinite Crystal 166
5.1.3 Finite Photonic Crystals as Semi-Transparent Mirrors 167
5.2 Photonic Crystal Waveguides 168
5.2.1 Index Guiding and Photonic Bandgap Guiding 168
5.2.2 Three-Dimensional Photonic Crystal Waveguides 170
5.2.3 Two-Dimensional Photonic Crystal Waveguides 172
5.2.4 Density of States and Multiplicity of Guided Modes 174
5.2.5 Coexistence of Index Guiding and Photonic Bandgap Guiding 178
5.3 Resonators 185
5.3.1 Localized Modes. Origin of Losses 185
5.3.2 Density of States 187
5.3.3 Waveguide formed by Coupled Cavities 188
5.4 Hybrid Structures with Index Guiding. The Light Line 190
5.4.1 Light Cone of a Uniform Waveguide 190
5.4.2 Fictitious Periodicity 191
5.4.3 True One-Dimensional Periodicity 191
5.4.4 Channel Waveguides in Two-Dimensional Photonic Crystals 195

6 Refractive Properties of Photonic Crystals and Metamaterials 197
6.1 Phase Refractive index, Group Refractive Index and Energy Propagation 197
6.1.1 Phase Velocity and Group Velocity 197
6.1.2 Refractive Indexes and Dispersion Diagrams 201
6.1.3 Effective Phase Index and Group Refractive Index 202
6.2 Refraction of Waves at the Interface between a Periodic Medium and a Homogeneous Medium 203
6.2.1 Summary of Refraction Laws in Homogeneous Media 203
6.2.2 Some Well-Known Anisotropic Media: Birefringent Solid-State Crystals 205
6.2.3 Construction of the Waves Transmitted in a Photonic Crystal 206
6.3 Superprism and Negative Refraction Effects 207
6.3.1 Superprism Effect 207
6.3.2 Ultra-Refraction and Negative Refraction 208
6.4 Metamaterials 210
6.4.1 Simultaneous Control of the Dielectric Permittivity and the Magnetic Permeability 210
6.4.2 Negative Refraction in a Slab of Perfect Left-Handed Material 212
6.4.3 Stigmatism of a Slab of Perfect Left-Handed Material 215
6.4.4 Perfect Lens or Superlens? 217
6.4.5 Fabrication of Negative Refractive Index Metamaterials 218
6.4.6 Electromagnetic Cloaking 221

7 Confinement of Light in Zero-Dimensional Microcavities 225
7.1 Microcavity Sources. Principles and Effects 226

7.1.1 A Classical Effect: the Angular Redistribution of the Spontaneous Emission and the Example of Planar Microcavities....226
7.2 Three-Dimensional Optical Confinement in Zero-Dimensional Microcavities....245
7.2.1. Different Types of Zero-Dimensional Microcavities....245
7.2.2 Control of the Spontaneous Emission in Weak Coupling Regime. Some Experimental Results....250
7.2.3 Single-Mode Coupling of the Spontaneous Emission....254
7.2.4 Towards Strong Coupling Regime for Solid State 'Artificial Atoms'....256

8 Nonlinear Optics with Photonic Crystals....261
8.1 The Problem of Phase Matching....262
8.2 $\chi^{(1)}$ Photonic Crystals....265
8.2.1 One-Dimensional $\chi^{(1)}$ Photonic Crystals....265
8.2.2 Two-Dimensional $\chi^{(1)}$ Photonic Crystals....273
8.3. $\chi^{(2)}$ Photonic Crystals....274
8.3.1 One-Dimensional $\chi^{(2)}$ Photonic Crystals....274
8.3.2 Two-Dimensional $\chi^{(2)}$ Photonic Crystals....277
8.4 Photonic Crystals with Third Order Susceptibility....279

Part III Fabrication, Characterization and Applications of Photonic Bandgap Structures....283

Introduction to Part III....285

9 Planar Integrated Optics....287
9.1 Objectives, New Devices and Challenges....287
9.2 Fundamentals of Integrated Optics and Introduction of Photonic Crystals....290
9.2.1 Conventional Waveguides....290
9.2.2 Photonic Crystals in Integrated Optics....295
9.3 Planar Photonic Crystals in the Substrate Approach....306
9.3.1 DFB and DBR Laser Diode Structures....306
9.3.2 Photonic Crystals, a Strong Perturbation for Guided Modes....307
9.3.3 Choice of the Diameter of the Holes and of the Period of the Crystal....309
9.3.4 Specific Parameters for InP- and GaAs-Based Systems....310
9.3.5 Deep Etching....310
9.4 Membrane Waveguide Photonic Crystals....311
9.4.1 Free-Standing Membranes....311
9.4.2 Reported Membranes....314
9.5 Macroporous Silicon Photonic Substrates....314
9.6 Characterization Methods for Photonic Crystals in Integrated Optics....318
9.6.1 Internal Light Source Method....318

9.6.2 End-Fire Method ... 321
9.6.3 Wide-Band Transmission-Reflection Spectroscopy ... 324
9.7 Losses of Photonic Crystal Integrated Optical Devices ... 324
9.7.1 Analysis of Losses in Planar Photonic Crystal Waveguides ... 324
9.7.2 Measurement of Propagation Losses in Straight Photonic Crystal Channel Waveguides ... 326
9.7.3. Losses in the Slow-Light Regime ... 329
9.7.4 Waveguide Bends in Photonic Crystals and Bend Losses ... 329
9.7.5 Photonic Crystal Resonators and Quality Factors ... 330
9.8 Photonic Crystal Devices and Functions : Recent Developments ... 333
9.8.1 Classification of devices ... 333
9.8.2 Coupled Resonators and Waveguides ... 335
9.8.3 Very high-Q cavities ... 337
9.8.4 Other Devices and Optical Functions ... 339

10 Microsources ... 345
10.1 High-Efficiency Light-Emitting Diodes ... 345
10.1.1 Solutions for the Extraction of Light without Confinement ... 345
10.1.2. Enhanced Extraction Efficiency through Planar Confinement ... 347
10.1.3 Increase of the Extraction Efficiency using Two-Dimensional Photonic Crystals ... 350
10.2 Ridge-Type Waveguide Lasers confined by Photonics Crystals ... 352
10.3 Bulk Photonic Crystal Band Edge Lasers ... 355
10.4 Photonic crystal VCSELs ... 358
10.5 Microcavity Lasers ... 360
10.6 Potential Interest of Single-Photon Sources ... 364

11 Photonic Crystal Fibres ... 371
11.1 Another Implementation of Periodic Structures ... 371
11.2 Fabrication of Microstructured Optical Fibres ... 372
11.3 Solid-Core Microstructured Optical Fibres ... 375
11.3.1 Confinement Losses and Second Mode Transition ... 375
11.3.2 Attenuation and Bend Loss ... 378
11.3.3 Chromatic Dispersion Properties ... 378
11.3.4 Main Applications of Solid-Core Microstructured Optical Fibres ... 380
11.4 True Photonic Crystal Fibres (PCF) ... 382
11.4.1 Photonic Bandgap Cladding ... 382
11.4.2 Losses of Photonic Crystal Fibres with Finite Cladding ... 385
11.4.3 Photonic Crystal Fibres with Optimised Structures ... 387
11.4.4 Main Applications of Photonic Crystal Fibres ... 389

12 Three-Dimensional Structures in Optics ... 393
12.1 Geometrical Configurations proposed for Three-Dimensional Structures ... 394
12.1.1 Structures with Omnidirectional Photonic Band Gaps ... 394
12.1.2 Incomplete Band Gap Three-Dimensional Structures ... 397

12.2 Examples of Fabrication Processes and Realizations of Three-Dimensional Photonic Crystals in the Optical Region 399
12.2.1 Complete Band Gap Structures....399
12.3 Metallic Three-Dimensional Photonic Crystals in the Optical Region....410
12.4 Three-Dimensional Photonic Crystals and Light Emitters....412

13 Microwave and Terahertz Antennas and Circuits 413
13.1 Photonic Crystal Antennas 414
13.1.1 Photonic-Crystal Antenna Substrates 415
13.1.2 Photonic-Crystal Antenna Mirrors 418
13.1.3 Photonic Crystal Antenna Radomes or Superstrates....422
13.2 Controllable Structures and Metamaterials....424
13.2.1 Principles and Characteristics of Electrically Controllable Photonic Crystals....424
13.2.2 Electrically Controllable Photonic Crystal Antennas 426
13.2.3 Antennas and Metamaterials....429
13.3 Microwave Circuits and Ultra-Compact Photonic Crystals 430
13.3.1 Ultra-Compact Photonic Crystals 430
13.3.2 Microwave Filters and Waveguides realised from Ultra-Compact Photonic Crystals....433
13.4 From Microwaves to Terahertz Waves 435
13.5 From Microwaves to Optics 436
13.5.1 Impedance Matching of Photonic Waveguides....437
13.5.2 Photonic Crystal THz Imaging System 439
13.5.3 'Microwave Inspired' Nanostructures and Nanodevices 440

Conclusion and Perspectives....443

Appendices 447

Appendix A. Scattering Matrix Method: Determination of the Field for a Finite Two-Dimensional Crystal formed by Dielectric Rods 449
A.1 Incident Field....449
A.2 Field inside the Rods....449
A.3 Field in the Vicinity of a Rod 452

Appendix B. Magneto-Photonic Cystals....459

Appendix C. Stigmatism of a Slab of Perfect Left-Handed Material: Integral for the Total Field. 463

References 467

Index....509

Part I

Theoretical Models for Photonic Crystals

Introduction to Part I

The necessity of developing numerical tools capable of accurately predicting the properties of photonic crystals was recognized very early in the wake of the pioneering studies in this field. There is no doubt that heuristic considerations based on solid state physics have sown the seeds of the concept of a photonic crystal, and that they continue to provide physical interpretations for the basic characteristics of photonic crystals. However, considerations of such a nature cannot provide experimenters with reliable guidelines for the design of actual photonic crystals with certain given properties. Only by combining the use of the fundamental laws of electromagnetism, of mathematics and of sophisticated methods of numerical analysis can such numerical tools be developed.

It might be recalled here that the numerical modelling of scattering from periodic structures had started being investigated much earlier. Since the end of the 1960s, the emergence of powerful computation tools has resulted in spectacular advances in the numerical modelling of scattering and propagation phenomena in the field of electromagnetism. These advances have been particularly rapid and strong for diffraction gratings (Maystre 1993; Moharam 1986; Petit 1980). Nonetheless, the first methods developed for photonic crystals were based on the adaptation to electromagnetism of the modelling of the properties of an electron in a crystal. The chief cause for this state of affairs was the desire of solid state physicists to use simple numerical tools that had already been extensively checked in their field. Unfortunately, the resolution of problems of electromagnetism is in general much more difficult than it is the case for similar problems of electron modelling. The first reason is to be found in the vector character of electromagnetic waves. A second reason lies in the concern of physicists working in the field of electromagnetism to avoid, as much as possible, theoretical approximations.

While simple to implement, the very well-known ‘plane wave method’ rests on certain strong hypotheses. The prerequisite of this method is indeed the assumption that the crystal is infinite along all directions of space. On the other hand, the theory of this method and its numerical implementation are within the reach of a good postgraduate student, even in the case of three-dimensional crystals. This method has played, and it still plays, a vital role in the calculation of photonic band gaps. However, this method suffers from an inherent deficiency. Indeed, actual photonic crystals are always limited in size: as a consequence, inside the photonic band gap, a part of the light illuminating the crystal will be able to propagate through it. The amount of transmitted light can be more or less important, depending on the width of the photonic crystal. In any case, being capable of accurately determining the amount of transmitted light is a crucial issue for most

practical applications of these optical components. As an example, an experimenter will face almost intractable difficulties when designing a laser cavity from a photonic crystal, if he cannot rely on any accurate prediction for the crystal width that would reduce the light losses below a given threshold.

The development of numerical tools that would account for the finite size of actual photonic crystals has thus been recognized as a vital necessity for their investigation. In general, these numerical methods have their origin in the wide array of modern methods developed for electromagnetic modelling. Depending on the degree of realism and sophistication of the model which is adopted, the computation times and memory storage may greatly differ. At the beginning of the 21st century, it should be acknowledged that there still exist serious obstacles on the way to the three-dimensional modelling of finite size photonic crystals with defects. This observation, which will probably remain true well into the next decade, bears important implications for the actual development of device applications.

1 Models for Infinite Crystals

1.1 Plane Wave Expansion

1.1.1 Maxwell's Equations

In this chapter, photonic crystals will be assumed to extend infinitely along all directions of space. A photonic crystal is characterized by a relative dielectric permittivity $\varepsilon_r(x, y, z)$ assumed to be real and periodic along N directions (with $N = 1$, 2 or 3) and invariant along the other 3 - N orthogonal directions. In what follows, the assumption will be made that the photonic crystals considered are made from non-magnetic materials. Let us denote by $\mathbf{a}_i$, where $i \in \{1, ..., N\}$, the vectors describing the elementary cell of the lattice. The system generated by these vectors is neither assumed to be orthogonal nor normed. An elementary cell of the crystal will be obtained from the extremities of the vectors $\mathbf{r}$ defined by the equation:

$$\mathbf{r} = \sum_{i=1,N} p_i \mathbf{a}_i, \qquad p_i \in [0,1] \tag{1.1}$$

The electric and magnetic fields $\mathbf{E}$ and $\mathbf{H}$ satisfy the time-harmonic Maxwell's equations (Born 1965; Kong 2000). Using a time dependence in $\exp(-i\omega t)$ and the standard symbolic notations for the vector operators, these equations can be represented in the following form:

$$\nabla \times \mathbf{E} - i\omega\mu_0 \mathbf{H} = 0 \tag{1.2}$$

$$\nabla \times \mathbf{H} + i\omega\varepsilon_0 \varepsilon_r(x, y, z)\mathbf{E} = 0 \tag{1.3}$$

$$\nabla . [\varepsilon_r(x, y, z)\mathbf{E}] = 0 \tag{1.4}$$

$$\nabla . \mathbf{H} = 0 \tag{1.5}$$

where ε_0 and μ_0 denote the electric permittivity and magnetic permeability of vacuum respectively. In what follows, we shall assume that the fields constitute physically acceptable solutions of Maxwell's equations. This means that these fields should contain a locally bounded electromagnetic energy, which in turn entails that they should be square integrable.

Combining Eqs. 1.2 and 1.3 leads to the following equations:

$$\frac{1}{\varepsilon_r(x,y,z)} \nabla \times [\nabla \times \mathbf{E}] - \frac{\omega^2}{c^2} \mathbf{E} = 0 \tag{1.6a}$$

$$\nabla \times \left[\frac{1}{\varepsilon_r(x,y,z)} \nabla \times \mathbf{H} \right] - \frac{\omega^2}{c^2} \mathbf{H} = 0 \tag{1.7a}$$

with $c = 1/\sqrt{\varepsilon_0 \mu_0}$ and $\frac{\omega}{c} = k_0 = \frac{2\pi}{\lambda_0}$, where c, k_0 and λ_0 represent the speed, the wave number and the wavelength of light in vacuum respectively.

The propagation equations (Eqs. 1.6a and 1.7a) are to be considered in the sense of distributions (Schwartz 1961). This is to say that these equations include boundary conditions at the interfaces of the different materials, and, in the case under consideration, that they include the continuity of the tangential components of the electric and magnetic fields. More generally, and introducing here a symbolic notation, these equations are of the form:

$$O\mathbf{F} = k_0^2 \mathbf{F} \tag{1.8}$$

where **F** stands for one of the fields and O is an operator on the space of the locally square integrable functions **F**. It thus turns out that any arbitrary solution of Maxwell's equations is an eigenfunction of the operator O, and that the eigenvalue corresponding to it is the square of the wave number.

In what follows, we shall first demonstrate that the solutions of the equation of propagation assume the form of Bloch modes. These modes satisfy Maxwell's equations for crystals formed from any type of material. They can be regarded as a form of generalization of the notion of a homogeneous plane wave, which plays an essential role for homogeneous materials, to the more complicated case of a periodically inhomogeneous material.

1.1.2 The Floquet-Bloch Theorem

We shall first define the set of translation operators T in the following way:

$$T[\mathbf{F}(\mathbf{r})] = \mathbf{F}(\mathbf{r} + \sum_{i=1,N} n_i \mathbf{a_i}) \tag{1.9}$$

where the n_i are relative integers.

It can be easily demonstrated that, due to the invariance of the crystal with respect to any translation along an arbitrary vector $\sum_{i=1,N} n_i \mathbf{a_i}$, these operators commute with O (Powell 1965; Cohen-Tannoudji 1973). The possibility therefore exists of finding a common set of eigenvectors for O and T. An eigenvector $\mathbf{u}$ of T satisfies the equation:

$$T[\mathbf{u}] = \rho \mathbf{u} \tag{1.10}$$

In general, the eigenvalues ρ can be expected to be complex. In the present case, however, it is necessary to exclude eigenvalues with a non-unitary modulus, since the corresponding field $\mathbf{u}$ would not in this case remain bounded at infinity and therefore would not contain a locally integrable electromagnetic energy. The demonstration is quite straightforward, and it suffices to apply either T or $(T)^{-1}$ with $|\rho| \neq 1$ an infinite number of times, which of course leads to the divergence of the field. We may therefore restrict ourselves to the consideration of the eigenvectors of O which satisfy Eq. 1.10 with $|\rho| = 1$, which implies that $\rho = \exp(i\varphi)$, where φ is real. These vectors, referred to as 'pseudo-periodic' vectors, would be periodic if ρ were equal to 1.

Further, any translation T can be decomposed onto N translations T_i which correspond to the vectors $\mathbf{a_i}$ of the direct lattice:

$$T = \sum_{i=1,N} n_i T_i \tag{1.11}$$

where the n_i are relative integers.

It therefore turns out that $\varphi = \sum_{i=1,N} n_i \varphi_i$, where φ_i is the phase shift of $\mathbf{u}$ (i.e. the argument of ρ) for a translation along the vector $\mathbf{a_i}$ of the lattice. Introducing a vector $\mathbf{k}$ defined in such a way that $\forall i \quad \mathbf{k}.\mathbf{a_i} = \varphi_i$ with $-\pi < \mathbf{k}.\mathbf{a_i} < +\pi$, the eigenvalue ρ can then be expressed as follows:

$$\rho = \exp\left(i\mathbf{k}. \sum_{i=1,N} n_i \mathbf{a_i} \right) \tag{1.12}$$

Let us now demonstrate that the function $\mathbf{v} = \mathbf{u} \exp(-i\mathbf{k}.\mathbf{r})$ presents the same periodicity as the crystal. For this purpose, it will be enough to show that $\mathbf{v}$ remains invariant under application of the translation operator T. This can be done by using Eq. 1.12 for deriving from Eq. 1.9 that:

$$T[\mathbf{v}] = T\left[\mathbf{u}\ \exp(-i\mathbf{k}.\mathbf{r})\right] = T[\mathbf{u}]\exp\left(-i\mathbf{k}.\left(\mathbf{r} + \sum_{i=1,N} n_i \mathbf{a_i}\right)\right) \tag{1.13}$$

$$= \rho\mathbf{u}\exp\left(-i\mathbf{k}.\sum_{i=1,N} n_i \mathbf{a_i}\right)\exp(-i\mathbf{k}.\mathbf{r})$$

$$= \mathbf{u}\ \exp(-i\mathbf{k}.\mathbf{r}) = \mathbf{v}$$

This crucial result will allow us to express **u** in the form of a series of pseudo-periodic functions. For this purpose, we shall first introduce the reciprocal lattice. The latter has the same dimensions as the physical (direct) lattice and its basis vectors $\mathbf{G_j}$ are defined from the basis vectors $\mathbf{a_i}$ of the direct lattice through the following equation:

$$\mathbf{a_i}.\mathbf{G_j} = 2\pi\delta_{i,j}, \forall i, j \in [1, N] \tag{1.14a}$$

where δ is the Kronecker delta symbol.

An arbitrary spatial vector r can be defined on the basis of Eq. 1.1, under the provision however that the coordinates $\{p_i\}$ should now be allowed to take any value ranging from -∞ to +∞. In this case, Eqs 1.1 and 1.14a lead to the following equation:

$$p_j = \mathbf{r}.\mathbf{G_j}/2\pi \tag{1.14b}$$

The possibility always exists of considering **v** as a periodic function of the variables p_j. As such, this function can be developed into a Fourier series of variables p_j with unit period along each axis of the direct lattice. The elements in this series are given by the expression $\mathbf{V}\exp\left(2\pi i \sum_{j=1,N} n_j p_j\right)$, where the vector **V** depends on the relative integers n_j. From Eq. 1.14b, this term can be rewritten in the form $\mathbf{V}\exp\left(i\,\mathbf{r}.\sum_{j=1,N} n_j \mathbf{G_j}\right) = \mathbf{V}(\mathbf{G})\exp(i\,\mathbf{r}.\mathbf{G})$, where **G** is a linear combination of the vectors of the reciprocal lattice. Denoting by G the entire set of these N vectors, the function **v** can finally be written in the form:

$$\mathbf{v} = \sum_{\mathbf{G}\in G} \mathbf{V}(\mathbf{G})\ \ exp(i\mathbf{G}.\mathbf{r}) \tag{1.15}$$

From the relation between **u** and **v**, it follows that:

$$\mathbf{u} = exp(i\mathbf{k}.\mathbf{r}) \sum_{\mathbf{G}\in G} \mathbf{V}(\mathbf{G})\ exp(i\mathbf{G}.\mathbf{r}) \tag{1.16a}$$

Eq. 1.16a is fundamentally a mere expression of the Floquet-Bloch theorem, which states that the eigenvectors of O and T are characterized by a wave vector **k**, and that they can be expressed in the form of a product of a plane wave expression $\exp(i\,\mathbf{k}.\mathbf{r})$ and a Fourier series. The eigenvector is also referred to as the Bloch mode. The interested reader will find more extensive developments concerning this notion in the textbooks on *Solid State Physics* (Ashcroft 1976; Kittel 1971), where Eq. 1.16a is often presented in the more concise, albeit less precise from a mathematical point of view, form:

$$\mathbf{u} = exp(i\mathbf{k}.\mathbf{r})\sum_{\mathbf{G}} \mathbf{V}(\mathbf{G})exp(i\mathbf{G}.\mathbf{r}) \tag{1.16b}$$

The fact that a solution of the fundamental laws of electromagnetics in a photonic crystal can be expressed in the form of a Bloch mode is itself a crucial result. However, it should be pointed out that the converse proposition does not hold true in general, since the function **u** given by Eq. 1.16a will not in most cases satisfy the equation of propagation (Eq. 1.6a). One can easily convince oneself of the truth of this statement by simply limiting the sum in the right-hand part of Eq. 1.16a to a single term, for example to the term corresponding to $\mathbf{G} = 0$. In this case, the function **u** becomes a homogeneous plane wave with wave number $|\mathbf{k}|$ and since the crystal is inhomogeneous, this plane wave obviously cannot satisfy the equation of propagation at every point of the crystal. This result should not come out as a surprise. Let us indeed recall here that Bloch modes are eigenvectors of the translation operators T. As has been seen, it is possible to find a common system of eigenvectors for O and T, and then to search for eigenvectors of O in the form of Bloch modes. This however does not entail that the expression in the right-hand part of Eq. 1.16a, where arbitrary coefficients $\mathbf{V}(\mathbf{G})$ have been introduced, is an eigenvector of O. In such a case, this expression may well be an eigenvector of T, but not be an eigenvector of O.

An additional remark can be made on the subject of Bloch modes. Since we were considering an infinite space, we have been led to select the eigenvalues ρ of the translation operators with unit modulus in order that the field may contain a locally integrable electromagnetic energy. In practice however, photonic crystals are bounded. Accordingly, the property of pseudo-periodicity fails in such a case, and it is no longer possible to demonstrate that the field can be represented in the form of Bloch modes. While it may seem reasonable at first sight to conjecture that Bloch modes would still represent relatively adequately the field which extends beyond the immediate vicinity of the boundary of the crystal, this conclusion is not justified. Indeed, since the crystal is bounded, there is no reason to exclude non unit values of ρ. In other terms, new Bloch modes presenting an evanescent behaviour must be introduced.

1.1.3 Hermiticity of the Field Operator

We shall now proceed to establish an important property of Bloch modes by demonstrating that the operator O is Hermitian in the space $\mathtt{H}_{\mathbf{k}}$ of the pseudo-periodic functions corresponding to a given value of **k**. For this purpose, we need to show that:

$$\langle O\mathbf{v}, \mathbf{w}\rangle = \langle \mathbf{v}, O\mathbf{w}\rangle \tag{1.17a}$$

where $\mathbf{v} \in \mathtt{H}_{\mathbf{k}}$ and $\mathbf{w} \in \mathtt{H}_{\mathbf{k}}$. Proceeding from Eq. 1.6a, it turns out that:

$$O\mathbf{v} = \frac{1}{\varepsilon_r(x,y,z)} \nabla \times [\nabla \times \mathbf{v}] \tag{1.17b}$$

By definition:

$$\langle \mathbf{u}, \mathbf{v}\rangle = \int_P \varepsilon_r \bar{\mathbf{u}}.\mathbf{v}\, d^N r \tag{1.18}$$

The domain of integration is the elementary cell P of the crystal, as defined by Eq. 1.1. Hence:

$$\langle O\mathbf{v}, \mathbf{w}\rangle = \int_P [\nabla \times (\nabla \times \bar{\mathbf{v}})].\mathbf{w}\, d^N r \tag{1.19a}$$

By applying twice the following identity:

$$\nabla.(\mathbf{a} \times \mathbf{b}) = \mathbf{b}.(\nabla \times \mathbf{a}) - \mathbf{a}.(\nabla \times \mathbf{b}) \tag{1.20}$$

it can be demonstrated that the integrand in Eq. 1.19a can be written in the following form:

$$[\nabla \times (\nabla \times \bar{\mathbf{v}})].\mathbf{w} = \bar{\mathbf{v}}.[\nabla \times (\nabla \times \mathbf{w})] - \nabla.[\bar{\mathbf{v}} \times (\nabla \times \mathbf{w}) + (\nabla \times \bar{\mathbf{v}}) \times \mathbf{w}] \tag{1.21}$$

The problem thus comes down to a difference between two integrals. The second integral, which corresponds to the integration of the second term in the right-hand part of Eq. 1.21, reduces to the flux of a vector (function of **v** and **w)** through the boundary surface of the elementary cell P. However, since we are working in a space of pseudo-periodic functions, and since **v** is conjugated, it turns out that this

vector is periodic and therefore that the integral of the flux is null. We thus obtain the following equation:

$$\langle O\mathbf{v},\mathbf{w}\rangle = \int_P \bar{\mathbf{v}}.\left[\nabla\times\left(\nabla\times\mathbf{w}\right)\right] d^N r = \langle \mathbf{v},O\mathbf{w}\rangle \tag{1.19b}$$

The operator O is therefore an Hermitian operator in the space $\mathtt{H}_{\mathscr{L}}$ of the locally integrable pseudo-periodic functions. The eigenvalues of this operator are real, and its eigenvectors (Bloch modes) form a complete set.

1.1.4 Simple Examples of Bloch Functions

The first example considered here is that of a three-dimensional crystal presenting a simple rectangular parallelepipedic symmetry with periods a_x, a_y and a_z along the *x, y* and *z* axes respectively, as represented in Fig. 1.1. The reciprocal lattice exhibits a rectangular symmetry as well, and is characterized by vectors parallel to the vectors of the direct lattice, with modulus $2\pi/a_x$, $2\pi/a_y$ and $2\pi/a_z$ respectively.

In this case, Eq. 1.16a will assume the following form:

$$\mathbf{E}(x,y,z) = \exp(i\mathbf{k}.\mathbf{r}) \sum_{m=-\infty}^{+\infty}\sum_{n=-\infty}^{+\infty}\sum_{p=-\infty}^{+\infty}\mathbf{E}_{m,n,p}\ \exp\left\{ im\frac{2\pi}{a_x}x + in\frac{2\pi}{a_y}y + ip\frac{2\pi}{a_z}z\right\} \tag{1.22}$$

where *m, n* and *p* are integers.

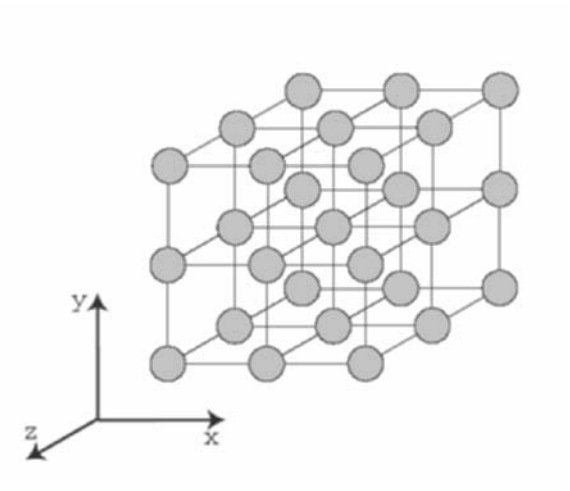

Fig. 1.1. Three-dimensional photonic crystal with a rectangular symmetry

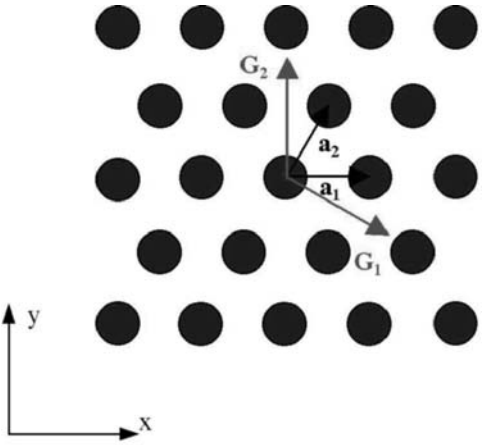

Fig. 1.2. Two-dimensional photonic crystal with a hexagonal symmetry

A more complicated example can be given in the form of a two-dimensional crystal presenting a hexagonal symmetry, with a period a along the x axis and with the same period a along an axis rotated from 60° with respect to the x axis (Fig. 1.2).

In this case, the direct lattice is formed by the vectors $\mathbf{a_1}$ and $\mathbf{a_2}$ with modulus a, as given by the two following equations respectively:

$$\mathbf{a}_1 = a\hat{x} \tag{1.23}$$

$$\mathbf{a_2} = a\left(\frac{\hat{x}}{2} + \frac{\hat{y}\sqrt{3}}{2}\right) \tag{1.24}$$

where $\hat{x}$ and $\hat{y}$ are unit vectors along the x axis and y axis respectively.

From the consideration of the orthogonality relations between the vectors describing the direct and reciprocal lattices, it can be demonstrated that the two vectors $\mathbf{G}_1$ and $\mathbf{G}_2$ of the reciprocal lattice have the same modulus $4\pi / a\sqrt{3}$, and that they are given by the following two equations:

$$\mathbf{G_1} = \frac{4\pi}{a\sqrt{3}}\left(\frac{\hat{x}\sqrt{3}}{2} - \frac{\hat{y}}{2}\right) \tag{1.25}$$

$$\mathbf{G_2} = \frac{4\pi}{a\sqrt{3}}\hat{y} \tag{1.26}$$

In this case, the directions of the reciprocal lattice and of the direct lattice do not coincide. The expansion of the field into Bloch modes will therefore be given by the equation:

$$\mathbf{E}(x,y,z) = \exp(i\mathbf{k}.\mathbf{r}) \sum_{m=-\infty}^{+\infty} \sum_{n=-\infty}^{+\infty} \mathbf{E}_{m,n} \exp\{i(m\mathbf{G_1} + n\mathbf{G_2}).\mathbf{r}\} \tag{1.27}$$

1.1.5 General Plane Wave Method

The plane wave method remains the reference method for the calculation of band gaps in photonic crystals (see Joannopoulos 1995b, and earlier articles published in the special issue of the *Journal of Modern Optics*, vol. 41(2) 1994). Thus, the expression given in the right-hand part of Eq. 1.16a for the field **u**, where **u** may denote either the electric or the magnetic field, is a representation of these fields in terms of plane waves. In fact, two different methods exist, depending on whether the electric or the magnetic field is actually considered. These two methods, respectively referred to as the E and the H methods, will be successively described here. However, the numerical precision of these methods is limited due to truncation problems, and it is often necessary to resort to a third, intermediate method known as the Ho method (Ho 1990).

E Method

This method proceeds by first rewriting Eq. 1.6a in the following form:

$$\nabla \times [\nabla \times \mathbf{E}] = \frac{\omega^2}{c^2} \varepsilon_r(x,y,z)\mathbf{E} \tag{1.6b}$$

The application of Eq 1.16a to the vector $\mathbf{D} = \varepsilon_r(x,y,z)\,\mathbf{E}$ yields:

$$\varepsilon_r(x,y,z)\mathbf{E} = exp(i\mathbf{k}.\mathbf{r}) \sum_{\mathbf{G}\in G} \mathbf{D}(\mathbf{G})\, exp(i\mathbf{G}.\mathbf{r}) \tag{1.16c}$$

Eq. 1.6b can then be rewritten in the form:

$$\nabla \times \left[\nabla \times \frac{1}{\varepsilon_r(\mathbf{r})} (\varepsilon_r(\mathbf{r})\mathbf{E}) \right] = \frac{\omega^2}{c^2} (\varepsilon_r(\mathbf{r})\mathbf{E}) \tag{1.6c}$$

Therefore, by reinserting the right-hand part of Eq. 1.16c into Eq. 1.6c and then by using the periodicity of $\eta(\mathbf{r}) = \dfrac{1}{\varepsilon_r(\mathbf{r})}$ which allows us to write down the following equation:

$$\eta(\mathbf{r}) = \sum_{\mathbf{G}'' \in G} \hat{\eta}(\mathbf{G}'')\, exp(i\mathbf{G}''.\mathbf{r}) \tag{1.28}$$

we finally arrive at the equation:

$$\nabla \times \left[\nabla \times \sum_{\mathbf{G} \in G} \sum_{\mathbf{G}' \in G} \hat{\eta}(\mathbf{G} - \mathbf{G}')\mathbf{D}(\mathbf{G}') \exp(i(\mathbf{k}+\mathbf{G}).\mathbf{r}) \right] = \tag{1.29}$$

$$\frac{\omega^2}{c^2} \sum_{\mathbf{G} \in G} \mathbf{D}(\mathbf{G}) \exp(i(\mathbf{k}+\mathbf{G}).\mathbf{r})$$

where $\mathbf{G} = \mathbf{G}' + \mathbf{G}''$.

By applying twice the generic relation $\nabla \times (\mathbf{V}\,(\exp(i\,\mathbf{u}.\mathbf{r})) = i\mathbf{u} \times \mathbf{V}\,(\exp(i\,\mathbf{u}.\mathbf{r})$, where $\mathbf{u}$ and $\mathbf{V}$ are constants, the following equation can be derived:

$$\sum_{\mathbf{G} \in G} \sum_{\mathbf{G}' \in G} \hat{\eta}(\mathbf{G} - \mathbf{G}')\,(\mathbf{k}+\mathbf{G}) \times \left[(\mathbf{k}+\mathbf{G}) \times \mathbf{D}(\mathbf{G}')\right] \exp(i(\mathbf{k}+\mathbf{G}).\mathbf{r}) = \tag{1.30}$$

$$-\frac{\omega^2}{c^2} \sum_{\mathbf{G} \in G} \mathbf{D}(\mathbf{G}) \exp(i(\mathbf{k}+\mathbf{G}).\mathbf{r})$$

Finally, the projection of the equation onto the basis functions $\exp[i\,(\mathbf{k}+\mathbf{G}).\mathbf{r})]$, where $\mathbf{G} \in G$, leads to the equation:

$$\sum_{\mathbf{G}' \in G} \hat{\eta}(\mathbf{G} - \mathbf{G}')(\mathbf{k}+\mathbf{G}) \times \left[(\mathbf{k}+\mathbf{G}) \times \mathbf{D}(\mathbf{G}')\right] = -\frac{\omega^2}{c^2} \mathbf{D}(\mathbf{G}) \tag{1.31}$$

Maxwell's equation $\nabla.(\varepsilon_r\,\mathbf{E}) = 0$ imposes the transversality of $\mathbf{D}(\mathbf{G})$ with respect to the associated direction of propagation, hence $\forall \mathbf{G}\ \ \mathbf{D}(\mathbf{G}).(\mathbf{k}+\mathbf{G}) = 0$. The vector $\mathbf{D}(\mathbf{G})$ present in Eq. 1.31 can therefore be projected onto two unit and orthogonal vectors $\mathbf{e}_{1,\mathbf{G}}$ and $\mathbf{e}_{2,\mathbf{G}}$ respectively, chosen in such a way as to ensure that $\{\mathbf{e}_{1,\mathbf{G}},\ \mathbf{e}_{2,\mathbf{G}},\ \mathbf{k}+\mathbf{G}\}$ form a direct trihedron. The following relation thus holds true: $\mathbf{k}+\mathbf{G} = \left|\mathbf{k}+\mathbf{G}\right| (\mathbf{e}_{1,\mathbf{G}} \times \mathbf{e}_{2,\mathbf{G}})$.

Using the same notations as above, we may write that:

$$\mathbf{D}(\mathbf{G}) = d_{1,\mathbf{G}}\mathbf{e}_{1,\mathbf{G}} + d_{2,\mathbf{G}}\mathbf{e}_{2,\mathbf{G}} \tag{1.32}$$

where $d_{1,\mathbf{G}}$ and $d_{2,\mathbf{G}}$ denote the components of $\varepsilon_r(x, y, z)\mathbf{E}$ in the coordinate system defined by the orthogonal unit vectors $\{\mathbf{e}_{1,\mathbf{G}}, \mathbf{e}_{2,\mathbf{G}}\}$.

From Eq. 1.32 it follows that Eq. 1.31 can be written in the following form:

$$\sum_{\mathbf{G}' \in G} \hat{\eta}(\mathbf{G}-\mathbf{G}')\left|\mathbf{k}+\mathbf{G}\right|^2 \begin{bmatrix} \mathbf{e}_{1,\mathbf{G}}.\mathbf{e}_{1,\mathbf{G}'} & \mathbf{e}_{1,\mathbf{G}}.\mathbf{e}_{2,\mathbf{G}'} \\ \mathbf{e}_{2,\mathbf{G}}.\mathbf{e}_{1,\mathbf{G}'} & \mathbf{e}_{2,\mathbf{G}}.\mathbf{e}_{2,\mathbf{G}'} \end{bmatrix} \begin{bmatrix} d_{1,\mathbf{G}'} \\ d_{2,\mathbf{G}'} \end{bmatrix} = \frac{\omega^2}{c^2} \begin{bmatrix} d_{1,\mathbf{G}} \\ d_{2,\mathbf{G}} \end{bmatrix} \tag{1.33}$$

Thus, for any given value for **k**, we are led to an infinite eigenvalue problem. If this equation is truncated by restricting G to a set of M vectors **G,** Eq. 1.33 directly shows that the linear system to be inverted is of dimension 2M × 2M, the unknowns being the set formed by the $d_{1,\mathbf{G}}$ and $d_{2,\mathbf{G}}$ components.

The resolution of the eigenvalue problem leads to the possibility of determining the values allowed for ω when a given value for **k** is given, and therefore of establishing their dispersion relations. The validity of the truncation can be verified by using larger values for M. It might be noted here that it is not necessary to determine these relations over the entire range for **k**, and that it suffices to consider only the irreducible Brillouin zone. This subject will be addressed in more detail in Section 1.3.1.

H Method

This method proceeds from the consideration of Eq. 1.7a, which is first rewritten in the form:

$$\nabla \times \left[\eta(x, y, z)\nabla \times \mathbf{H}\right] = \frac{\omega^2}{c^2}\mathbf{H} \tag{1.7b}$$

On the other hand, the application of Eq. 1.16a to the magnetic field yields:

$$\mathbf{H}(\mathbf{r}) = exp(i\mathbf{k}.\mathbf{r}) \sum_{\mathbf{G}\in G} \mathbf{H}(\mathbf{G})\, exp(i\mathbf{G}.\mathbf{r}) = \sum_{\mathbf{G}\in G} \mathbf{H}(\mathbf{G}) exp\left(i(\mathbf{k}+\mathbf{G}).\mathbf{r}\right) \tag{1.16d}$$

By introducing the right-hand part of Eq. 1.16d in Eq. 1.7b, we arrive at the following equation:

$$\sum_{\mathbf{G}\in G}\sum_{\mathbf{G}'\in G}\hat{\eta}(\mathbf{G}-\mathbf{G}')(\mathbf{k}+\mathbf{G})\times\left[(\mathbf{k}+\mathbf{G}')\times\mathbf{H}(\mathbf{G}')\right]exp\left(i(\mathbf{k}+\mathbf{G}).\mathbf{r}\right)= \tag{1.34}$$

$$-\frac{\omega^2}{c^2}\sum_{\mathbf{G}\in G}\mathbf{H}(\mathbf{G})\exp(i(\mathbf{k}+\mathbf{G}).\mathbf{r})$$

Finally, the projection of this equation onto the basis functions exp[i(**k**+**G**).**r**], where $\mathbf{G}\in G$, leads to the equation:

$$\sum_{\mathbf{G}'\in G}\hat{\eta}(\mathbf{G}-\mathbf{G}')(\mathbf{k}+\mathbf{G})\times\left[(\mathbf{k}+\mathbf{G}')\times\mathbf{H}(\mathbf{G}')\right]=-\frac{\omega^2}{c^2}\mathbf{H}(\mathbf{G}) \tag{1.35}$$

Maxwell's equation $\nabla.\mathbf{H} = 0$(Eq. 1.5) imposes the transversality of **H** (**G**) with respect to the associated direction of propagation, hence $\forall\mathbf{G}$ **H**(**G**).(**k**+**G**) = 0. Each vector **H** (**G**) in Eq. 1.16d can therefore be projected onto the unit and orthogonal vectors $\mathbf{e}_{1,\mathbf{G}}$ and $\mathbf{e}_{2,\mathbf{G}}$ defined in Section 1.1.5:

$$\mathbf{H}(\mathbf{r})=\sum_{\mathbf{G}\in G}\left(h_{1,\mathbf{G}}\mathbf{e}_{1,\mathbf{G}}+h_{2,\mathbf{G}}\mathbf{e}_{2,\mathbf{G}}\right)\exp\left(i(\mathbf{k}+\mathbf{G}).\mathbf{r}\right) \tag{1.16e}$$

where $h_{1,\mathbf{G}}$ and $h_{2,\mathbf{G}}$ denote the components of **H**(**G**) in the coordinate system defined by the orthogonal unit vectors $\{\mathbf{e}_{1,\mathbf{G}}, \mathbf{e}_{2,\mathbf{G}}\}$.

Proceeding along the same lines as in Section 1.1.5, i.e. using twice the relation $\nabla\times(\mathbf{V}(\exp(i\,\mathbf{u}.\mathbf{r}))=i\,\mathbf{u}\times\mathbf{V}(\exp(i\,\mathbf{u}.\mathbf{r})$, where **u** and **V** are constants, and then the classical rule on triple vector product, Eq. 1.35 becomes:

$$\sum_{\mathbf{G}'\in G}\hat{\eta}(\mathbf{G}-\mathbf{G}')\left|\mathbf{k}+\mathbf{G}'\right|\left|\mathbf{k}+\mathbf{G}\right|\begin{bmatrix}\mathbf{e}_{2,\mathbf{G}}.\mathbf{e}_{2,\mathbf{G}'} & -\mathbf{e}_{2,\mathbf{G}}.\mathbf{e}_{1,\mathbf{G}'}\\ -\mathbf{e}_{1,\mathbf{G}}.\mathbf{e}_{2,\mathbf{G}'} & \mathbf{e}_{1,\mathbf{G}}.\mathbf{e}_{1,\mathbf{G}'}\end{bmatrix}\begin{bmatrix}h_{1,\mathbf{G}'}\\ h_{2,\mathbf{G}'}\end{bmatrix}= \tag{1.36a}$$

$$\frac{\omega^2}{c^2}\begin{bmatrix}h_{1,\mathbf{G}}\\ h_{2,\mathbf{G}}\end{bmatrix}$$

The truncation of Eq. 1.36a, which can be performed by restricting G to a set of M vectors **G**, directly demonstrates that the eigenvalue problem to be resolved is of dimension 2M × 2M, the unknowns being the set formed by the $h_{1,\mathbf{G}}$ and $h_{2,\mathbf{G}}$ components.

Two-Dimensional Crystals

In the two-dimensional case, all derivatives with respect to the z coordinate vanish when the study is restricted to the propagation along the cross-section plane of the crystal, i.e. along the xy plane. It is a direct consequence of Maxwell's equations (Eq. 1.2) that the transverse components of the electric field, i.e. the components parallel to the xy plane, can be expressed in terms of the longitudinal component H_z of the magnetic field. Likewise, it follows from Eq. 1.3 that the transverse components of the magnetic field can be deduced from the longitudinal component E_z of the electric field. We may therefore limit ourselves to the study of the two longitudinal components E_z and H_z. The projection of the propagation equations (Eqs. 1.6a and 1.7a) onto the three coordinate axes reveals that these two components obey two uncoupled propagation equations:

$$\mathbf{P}_{\mathrm{E}} E_z = \frac{1}{\varepsilon_r(x, y, z)} \nabla^2 E_z = -k_0^2 E_z \tag{1.37}$$

$$\mathbf{P}_{\mathrm{H}} H_z = \nabla . \left(\frac{1}{\varepsilon_r(x,y,z)} \nabla H_z \right) = -k_0^2 H_z \tag{1.38}$$

The propagation equation satisfied by each longitudinal component of the fields thus turns out to be a scalar equation. This crucial property opens the possibility of studying separately the problems corresponding to the two so-called fundamental cases of polarization. These polarization modes will be referred to as TM and TE polarizations depending on whether $E_z \neq 0$ and $H_z = 0$, or $E_z = 0$ and $H_z \neq 0$ respectively. It might be noted here that, in optics, these two polarization modes are classically referred to as the s and p polarizations respectively. For an arbitrary polarization, a general solution to this problem can be readily expressed from the solutions of Eqs. 1.37 and 1.38.

As indicated, we shall now consider Eq. 1. 36a successively for each fundamental polarization mode. Since all the vectors $\mathbf{k} + \mathbf{G}$ are parallel to the xy plane, the vectors $\mathbf{e}_{1,\mathbf{G}}$ can therefore be chosen in such a way as to coincide with the unit vector of the z axis. The vector $\mathbf{e}_{2,\mathbf{G}}$ can then be easily deduced from these two vectors (Fig. 1.3).

TM (or s) Polarization. In this polarization mode, $\mathbf{H}(\mathbf{r})$ is parallel to the xy plane and therefore it has no component along the z axis. Accordingly, $\forall \mathbf{G}\ h_{1,\mathbf{G}} = 0$. On the other hand, $\mathbf{e}_{1,\mathbf{G}'} = \mathbf{e}_{1,\mathbf{G}}$, whence it follows that $\mathbf{e}_{2,\mathbf{G}} . \mathbf{e}_{1,\mathbf{G}'} = 0$. Eq.1.36a thus reduces to the equation:

$$\sum_{\mathbf{G}' \in G} \hat{\eta}(\mathbf{G} - \mathbf{G}') \left| \mathbf{k} + \mathbf{G}' \right| \left| \mathbf{k} + \mathbf{G} \right| h_{2,\mathbf{G}'} = \frac{\omega^2}{c^2} h_{2,\mathbf{G}} \tag{1.36b}$$

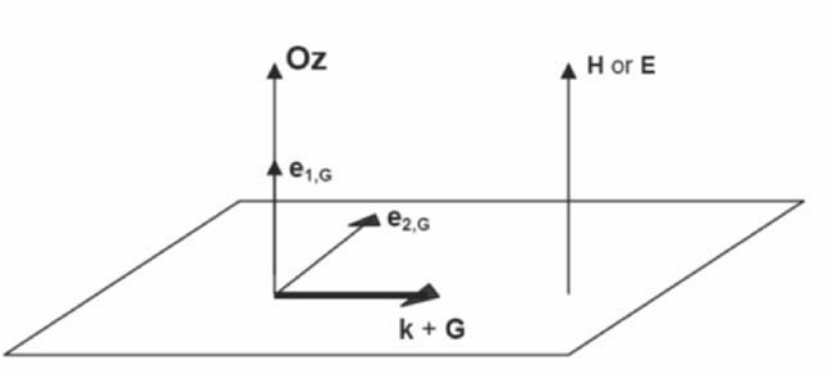

Fig. 1.3. Schematic representation of the vectors in the equations used in the H method applied to a two-dimensional crystal

By limiting G to a set of M vectors **G**, we thus obtain a linear system of M equations, where the **k**-dependent eigenvalue to be determined is represented by ω^2/c^2.

TE (or p) Polarization. In this polarization mode, **H**(**r**) is parallel to the z axis, and therefore $\forall \mathbf{G}\ \ h_{2,\mathbf{G}} = 0$. On the other hand, since $\mathbf{e}_{1,\mathbf{G}} . \mathbf{e}_{2,\mathbf{G}'} = 0$, Eq. 1.36a assumes the following form:

$$\sum_{\mathbf{G}' \in G} \hat{\eta}(\mathbf{G}-\mathbf{G}') \left|\mathbf{k}+\mathbf{G}'\right| \left|\mathbf{k}+\mathbf{G}\right| (\mathbf{e}_{2,\mathbf{G}} . \mathbf{e}_{2,\mathbf{G}'}) h_{1,\mathbf{G}'} = \frac{\omega^2}{c^2} h_{1,\mathbf{G}} \qquad (1.36c)$$

Further, since the angle formed by $\mathbf{e}_{2,\mathbf{G}}$ and $\mathbf{e}_{2,\mathbf{G}'}$ is equal to the angle formed by $\mathbf{k}+\mathbf{G}$ and $\mathbf{k}+\mathbf{G}'$, it follows that $\left|\mathbf{k}+\mathbf{G}\right| \left|\mathbf{k}+\mathbf{G}'\right| (\mathbf{e}_{2,\mathbf{G}} . \mathbf{e}_{2,\mathbf{G}'}) = (\mathbf{k}+\mathbf{G}).(\mathbf{k}+\mathbf{G}')$, and therefore that Eq. 1.36c can be written in the form:

$$\sum_{\mathbf{G}' \in G} \hat{\eta}(\mathbf{G}-\mathbf{G}')(\mathbf{k}+\mathbf{G}')\ (\mathbf{k}+\mathbf{G})\ \ h_{1,\mathbf{G}'} = \frac{\omega^2}{c^2} h_{1,\mathbf{G}} \qquad (1.36d)$$

Determination of the Fourier Transform of η

A prerequisite for the resolution of the linear systems of equations corresponding to the E and H methods is the determination of the Fourier transform of $\eta(\mathbf{r})$. The calculation of the Fourier transform itself does not present any specific problem, but it might be useful to briefly expose the lines along which these calculations are performed in a typical example, that of a two-dimensional crystal consisting of di-

electric rods with relative permittivity ε_a, periodically placed inside a dielectric material with relative permittivity ε_b. This structure can be viewed indifferently either as a lattice of dielectric rods extending in the air, or as a lattice of air holes inside a dielectric. The rods are cylindrical and, for the sake of simplicity, the assumption will be made that they present a circular cross-section with a radius R_c such that $R_c \leq a$, where a is the period of the crystal. It will be further assumed that only a single rod is present inside the elementary cell. The space dependence of the inverse of the permittivity η in this elementary cell can be expressed as follows:

$$\eta(\mathbf{r}) = \eta_b + (\eta_a - \eta_b)\theta(\mathbf{r}) \tag{1.39}$$

where $\theta(\mathbf{r})$ is the Heaviside function, which takes the value 1 in the rod and 0 outside the rod, $\eta_a = 1/\varepsilon_a$, $\eta_b = 1/\varepsilon_b$.

The following equation provides an expression of the Fourier component $\hat{\eta}(\mathbf{G})$ as a function of $\eta(\mathbf{r})$:

$$\hat{\eta}(\mathbf{G}) = \frac{1}{S_{cell}} \int_{S_{cell}} \eta(\mathbf{r}) \exp(-i\mathbf{G}.\mathbf{r}) d^2r \tag{1.40}$$

where S_{cell} is the surface of the elementary cell. By reinserting the right-hand part of Eq. 1.39 in the right-hand part of Eq. 1.40, we finally obtain the following equation for the Fourier transform:

$$\hat{\eta}(\mathbf{G}) = \eta_b \delta_{\mathbf{G},0} + (\eta_a - \eta_b) \frac{1}{S_{cell}} \int_{S_{cell}} \theta(\mathbf{r}) \exp(-i\mathbf{G}.\mathbf{r}) d^2r \tag{1.41a}$$

where $\delta_{\mathbf{G},0} = 1$ if $\mathbf{G} = \mathbf{0}$ and $\delta_{\mathbf{G},0} = 0$ if $\mathbf{G} \neq \mathbf{0}$. The scalar product $\mathbf{G}.\mathbf{r}$ in the right-hand part of Eq. 1.41a can be expressed in the form $|\mathbf{G}|\, r \sin\varphi$, where φ denotes the angle formed by the two vectors $\mathbf{G}$ and $\mathbf{r}$. Taking into account the circular symmetry of the system, Eq. 1.41a can then be written in the form:

$$\hat{\eta}(\mathbf{G}) = \eta_b \delta_{\mathbf{G},0} + (\eta_a - \eta_b) \frac{1}{S_{cell}} \int_{r=0}^{R_c} \int_{\varphi=0}^{2\pi} \exp(i\, |\mathbf{G}|\, r \sin\varphi) dr d\varphi \tag{1.41b}$$

By using the expansion of $\exp(i\xi \sin\varphi)$ into a series of Bessel functions (Abramovitz 1970; Angot 1982) and by integrating in φ, we finally arrive at the following equation:

$$\hat{\eta}(\mathbf{G}) = \eta_b \delta_{\mathbf{G},0} + (\eta_a - \eta_b) \frac{2\pi R_c^2 J_1(|\mathbf{G}|\, R_c)}{S_{cell}\, |\mathbf{G}|\, R_c} \tag{1.42}$$

where $J_1(\xi)$ is a Bessel function of the first kind of first order.

Ho Method

The Ho method (Ho 1990) can be derived from the master field equation used in the E method (Eq. 1.6.b) by developing **E** rather than $\varepsilon_r \mathbf{E}$ into a Bloch series, and by writing down at the same time $\varepsilon_r(\mathbf{r})$ in the form of a Fourier series:

$$\varepsilon(\mathbf{r}) = \sum_{\mathbf{G}'' \in G} \hat{\varepsilon}(\mathbf{G}'') \; exp(i\mathbf{G}''.\mathbf{r}) \tag{1.43}$$

Proceeding along the same lines as in Section 1.1.5, we obtain an equation formally similar to Eq. 1.29, with the difference however that its right-hand part is now the product of a matrix ε with components $\hat{\varepsilon}(\mathbf{G})$ by a column matrix with components $\mathbf{E}(\mathbf{G})$. By multiplying the two sides of this equation by ε^{-1}, inverse of the matrix ε, we obtain the following equation:

$$\sum_{\mathbf{G}} \varepsilon^{-1}(\mathbf{G}'' - \mathbf{G})(\mathbf{k}+\mathbf{G}) \times \left[(\mathbf{k}+\mathbf{G}) \times \mathbf{E}(\mathbf{G})\right] + \frac{\omega^2}{c^2} \mathbf{E}(\mathbf{G}'') = 0 \tag{1.44}$$

For the sake of convenience, let us define $\mathbf{F}(\mathbf{G}) = (\mathbf{k}+\mathbf{G}) \times \mathbf{E}(\mathbf{G})$. The vector product of the two sides of Eq. 1.44 with $\mathbf{k}+\mathbf{G}''$ then yields:

$$(\mathbf{k}+\mathbf{G}') \times \left[\sum_{\mathbf{G}} \varepsilon^{-1}(\mathbf{G}' - \mathbf{G})(\mathbf{k}+\mathbf{G}) \times \mathbf{F}(\mathbf{G})\right] + \frac{\omega^2}{c^2} \mathbf{F}(\mathbf{G}') = 0 \tag{1.45}$$

The resulting equation for the $\mathbf{F}(\mathbf{G})$ vectors is formally similar to the equation for the $\mathbf{H}(\mathbf{G})$ vectors which can be derived from Eqs. 1.7b and 1.16d, with the only difference that $\eta(\mathbf{G} - \mathbf{G}'')$ is replaced by $\varepsilon^{-1}(\mathbf{G} - \mathbf{G}'')$. It might be emphasized that these two matrices are not equal, this being a consequence of the truncation. Indeed, the finite matrix obtained by truncating the inverse of an infinite matrix is not equal to the finite matrix obtained by truncating first the infinite matrix, and then by inverting it. Using the equation $(\mathbf{k}+\mathbf{G}).\mathbf{F}(\mathbf{G}) = 0$, we may proceed along the same lines as in the H method. This finally leads to the resolution of a matrix system of dimension 2M×2M.

The Ho method generally yields more precise results than the H method for the same number of plane waves considered. Comparing the results obtained with either method generally provides a way of evaluating the accuracy of the convergence of the numerical calculations. When the results are very close, it might be admitted that they converge towards the solution of the problem, although a rig-

ourous demonstration would require a convergence test performed by increasing M. It might be noted that, in the case of a three-dimensional photonic crystal with diamond symmetry, 3000 plane waves are required in order to reduce the discrepancy between the results obtained with these two methods to less than 5 percent at the level of the fundamental band gap.

1.2 Other Methods for the Calculation of the Photonic Band Gaps of an Infinite Crystal: the KKR Method

The use of the plane wave method frequently leads to numerical instabilities. This can be explained by the fact that the permittivity of the crystal is discontinuous between two materials, and by the discontinuity of certain components of the electromagnetic field as well. It is well known that the truncation of the Fourier series of such functions leads to a slow convergence of their development (in $1/n$ where n denotes the number of terms in the truncated series) and results, whatever the order of the truncation is, in the occurrence of the Gibbs phenomenon in the vicinity of the discontinuities. These discontinuous functions fail therefore to be adequately represented in the vicinity of the discontinuities, and the numerical instabilities observed are but a consequence of this defect. Other methods, which originate in the analysis of the Schrödinger equation, have been developed for calculating the band diagrams of infinite photonic crystals. From a theoretical point of view, these methods are more complicated than plane wave methods, but they generally provide a much higher degree of stability from a numerical point of view. A description of these methods would be beyond the scope of this book, and the interested reader is referred to (Moroz 1995) where such a detailed description is provided. The best known of these methods is the KKR (Korringa-Kohn-Rostocker) method, which derives from the method initially described by Korringa (Korringa 1947, 1957). This method relies on the use of the scattering matrix of the elementary cell (for a definition of this matrix, see Chap. 2), while the Green function of the periodic structure is developed on the basis of the spherical harmonics in the three-dimensional case (Moroz 1995). One of the most interesting features of the KKR method is that it directly provides the Green function. As will be seen, the density of states and the local density of states, both of which can be easily deduced from the Green function, are important parameters in the study of the physical phenomena associated with photonic crystals.

1.3 Photonic Band Diagram

The photonic band diagram allows the survey of all the dispersion characteristics $\omega(\mathbf{k})$ of the photonic crystal which can be calculated from the plane wave model. In principle, it would be necessary, in order to be exhaustive, to consider all possible directions of propagation in the photonic crystal. Actually however, by relying

on the same considerations as in the field of solid state physics (Kitson 1986), the possibility exists of drawing on the symmetries of the crystal for restricting the calculations to the wave vectors **k** contained in a limited region of the reciprocal space, referred to as the irreducible Brillouin zone. It is quite obvious that the complexity of the diagram depends on the dimensionality of the crystal, which may range from one to three dimensions. In this section, we shall first recall elementary considerations leading to the definition of the irreducible Brillouin zone in some simple cases, before discussing the band diagrams of the main types of photonic crystals with increasing complexity.

1.3.1 The Irreducible Brillouin Zone

The first Brillouin zone can be defined as the region of the reciprocal space formed by the points which are closer to the origin than to any other vertex of the periodical lattice. In Fig. 1.4 are represented various examples of photonic crystals with their corresponding Brillouin zones. As can be seen, the first Brillouin zone is constructed by drawing the perpendicular bisectors (in the one and two-dimensional cases) or the bisecting planes (in the three-dimensional case) of every lattice vector joining the origin to the nearest vertexes of the reciprocal lattice. Each bisector or bisecting plane therefore divides the reciprocal space into two half-spaces, the origin being contained in one these half-spaces. The first Brillouin zone is defined as the intersection of all half-spaces containing the origin. By definition, all the values for **k** which lie outside this zone can be reached from within the zone using the translations of the vectors $\mathbf{G} \in G$. As a consequence, these values are redundant. In other terms, it suffices to consider the variation of **k** within the Brillouin zone for representing the entire set of the dispersion curves of the photonic crystal. The range over which **k** is considered can be further reduced by using the symmetries of the crystal, as is illustrated in the different examples represented in Fig. 1.4.

In the one-dimensional case, and assuming that the elementary cell contains only two layers, the crystal displays obvious symmetries with respect to points located on the plane of symmetry of each layer. Thus, if a wave of vector **k** and frequency ω is found to be a solution to the master equation, then the counterpropagating wave with the same frequency and vector – **k** will be also a solution to this equation. This allows restricting the study to the interval $[0,+\pi/a]$ instead of the entire $[-\pi/a,+\pi/a]$ interval. It is worth noting that this property holds when the elementary cell contains more than two layers. A very simple demonstration of this extension can be obtained by noting that the complex conjugate of the fields, which still satisfies Maxwell's equations in the crystal, propagates in a direction opposite to that of the the initial fields, since $\exp(i\mathbf{kr})$ becomes $\exp(-i\mathbf{kr})$.

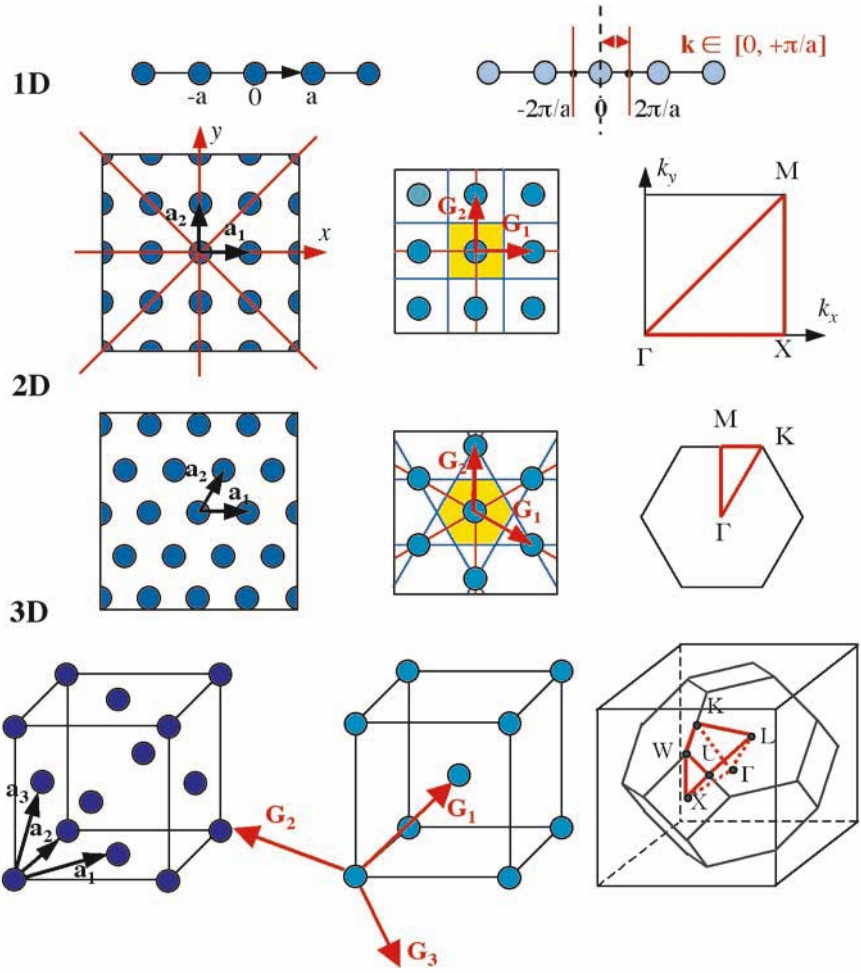

Fig. 1.4. One-, two- and three-dimensional photonic crystals (*left*) with their corresponding Brillouin zones (*middle and right*). For the one-dimensional crystal, the first Brillouin zone and the irreducible Brillouin zone are formed by the intervals $[-\pi/a, +\pi/a]$ and $[0, \pi/a]$ respectively. For two-dimensional crystals, the middle figures represent the first Brillouin zones (*light grey area*) while the right-hand figures show the irreducible Brillouin zones (*thick lines*). For the fcc crystal, the middle figure represents the centred cubic reciprocal lattice and the right-hand figure represents the two Brillouin zones: the first Brillouin zone is a truncated octahedron, while the irreducible Brillouin zone is the polyhedron with apexes Γ Γ, X, U, L, W and K

Let us now consider a two-dimensional crystal with a square symmetry of the same type as the example represented in Fig. 1.4. The assumption is made here that this structure consists of infinite dielectric rods extending in the air and parallel to the z axis. The structure presents four axes of symmetry, represented here by thin lines, which can be deduced from one another through rotations of $\pi/4$. The reciprocal lattice also presents a square symmetry, and the first Brillouin zone will be defined by the following inequalities:

$$-\frac{\pi}{a} < k_x < \frac{\pi}{a} \quad , \quad -\frac{\pi}{a} < k_y < \frac{\pi}{a} \tag{1.46}$$

We are interested here in two-dimensional solutions of the propagation equations, and these solutions are obviously independent from the z coordinate. For the sake of simplicity, we may restrict ourselves to the consideration of a single polarization of the field, for instance, the *s*-polarization. Let us first analyse the consequence of the rotational symmetry of the structure with respect to an axis parallel to Oy. If $E_z(x, y)$ is a solution to the propagation equation (Eq. 1.37) with the wave vector $\mathbf{k}$ of coordinates (k_x, k_y), then the double x-derivative in the Laplacian implies that $E_z(x, y)$ will also be a solution to this equation with, from Eq. 1.16c, the wave vector of coordinates $(-k_x, k_y)$. But since these two solutions correspond to the same frequency ω, it is not necessary to consider both of them in the calculations of the band diagram. It suffices to consider only one of these solutions, and we may therefore restrict ourselves to the half of the Brillouin zone defined by $0 < k_x < \pi/a$, $-\pi/a < k_y < \pi/a$. This result can also be obtained in a more 'mathematical' way. For this purpose, let us define the symmetry operator with respect to Oy in the following way:

$$S_y u(x, y) = u(-x, y) \tag{1.47}$$

It can easily be seen from Eq. 1.37 that S_y commutes with the operator $\mathbf{P}_E$. Hence, if E_z is a proper vector of $\mathbf{P}_E$ with the proper value k_0^2, $S_y E_z$ will also be a proper vector of $\mathbf{P}_E$ with the same proper value k_0^2.

The range over which $\mathbf{k}$ is studied can be further reduced by considering the four other symmetries indicated in Fig. 1.4. It might be noted that only three symmetries need to be considered here, and that the fourth one is but a combination of the first three ones. Accordingly, the range considered for $\mathbf{k}$ simply reduces to an isosceles right triangle with two edges of equal length π/a. The apexes of this triangle are traditionally denoted by Γ, X and M. This triangle, represented here in thick lines in Fig. 1.4 (*right*), constitutes the irreducible Brillouin zone of the square lattice. Actually, as far as band diagram calculations are concerned, it is generally sufficient to let the wave vector $\mathbf{k}$ describe the edge of the irreducible Brillouin zone while ignoring the inner region. Although this simplification does not rely on any rigourous mathematical analysis, it can intuitively be justified from the symmetry of the structure, which entails that the three edges of the trian-

gle represent symmetry axes for the functions $\omega(\mathbf{k})$, solutions to Eq. 1.31. Indeed, assuming that the derivative of $\omega(\mathbf{k})$ is continuous along all directions, the extrema of the function $\omega(\mathbf{k})$ are located along the edges of the triangle. Restricting the study to the three directions ΓX, ΓM and MX therefore comes down to assuming that no other extremum of interest lies inside the irreducible Brillouin zone.

The second example represented in Fig. 1.4 of a two-dimensional lattice is the triangular lattice, which exhibits a hexagonal symmetry. The reciprocal lattice exhibits the same symmetry, while the first Brillouin zone is a hexagon. In this case, six different symmetry axes exist which can be deduced from one another by rotations of $\pi/6$ with an invariance under rotation equal to $\pi/3$. Following a similar line of reasoning than in the case of the square lattice, it can be demonstrated that the irreducible Brillouin zone is the half of an equilateral triangle with apexes Γ, K and M (Fig. 1.4, right). Here again, the assumption is made that it suffices to let the wave vector **k** describe the edge of the irreducible Brillouin zone (along the directions ΓK, ΓM and MK) for reaching the extrema of $\omega(\mathbf{k})$ of interest.

The three-dimensional structure represented in Fig. 1.4 (bottom left) is a face-centred-cubic (fcc) lattice. It might be recalled here that diamond and the main semiconductors (silicon, germanium, gallium arsenide, etc) crystallize in such a lattice, and that the famous 'Yablonovite' itself is but the 'photonic' analogue of the diamond. In more precise terms, the diamond structure consists of two fcc lattices shifted from one another by a quarter of the main diagonal of the cube. In other terms, this structure is a fcc lattice with two atoms per unit cell. The reciprocal lattice is a centred cubic (cc) lattice (Fig. 1.4, *bottom middle*) and, by construction, the first Brillouin zone is a dodecahedron which may also be viewed as a truncated octahedron, as represented in thick lines in Fig. 1.4 (*bottom right*). From symmetry considerations somewhat more elaborated than those previously used in the case of two-dimensional crystals (Kitson 1986), it can be demonstrated that the irreducible Brillouin zone is a four-face polyhedron whose apexes are traditionally denoted by Γ, L, U, X, W and K (Landolt-Börnstein 1982). The main dispersion curves of the band diagram of the fcc lattice will be analysed by having the wave vector **k** describe the edge of the polyhedron.

1.3.2 Band Diagrams of One-Dimensional Crystals

One-dimensional crystals traditionally consist of alternated dielectric layers with different dielectric constants. By analogy with Bragg reflection in solid state crystals, these structures are often referred to as Bragg mirrors or as Bragg multilayer stacks. However, other types of structures, in which the dielectric permittivity varies in a periodical manner, can be devised in the field of 'photonics', for instance structures with a sinusoidal modulation of the dielectric permittivity. Although less widely used, these structures lend themselves to a simpler analytical formulation than Bragg mirrors, which enables an easier insight into their dispersion characteristics. As a first approach, we therefore begin with this simpler case, before recalling the optical properties of classical Bragg mirrors.

Sinusoidal Modulation of the Dielectric Permittivity

Let us assume here that the dielectric permittivity ε_r presents a sinusoidal modulation along the z axis. If the modulation occurs around an average value ε_m with an amplitude ε_d and a period a_z, the equation for ε_r will be simply:

$$\varepsilon_r(z) = \varepsilon_m + \varepsilon_d \sin\left(\frac{2\pi}{a_z} z\right) = \varepsilon_m + \frac{\varepsilon_d}{2i}\left(\exp\left(i\frac{2\pi}{a_z} z\right) - \exp\left(-i\frac{2\pi}{a_z} z\right)\right) \tag{1.48}$$

The basis vector of the reciprocal lattice is $\mathbf{G_1} = 2\pi/a_z \hat{z}$. The other vectors are expressed in the form $\mathbf{G}_p = p\mathbf{G_1}$ where p is a relative integer. From Eq. 1.48, it can be easily demonstrated that the Fourier transform of ε_r possesses only three non-zero components:

$$\varepsilon(\mathbf{0}) = \varepsilon_m \quad ; \quad \varepsilon(\mathbf{G}_1) = \frac{\varepsilon_d}{2i} \quad ; \quad \varepsilon(-\mathbf{G}_1) = -\frac{\varepsilon_d}{2i} \tag{1.49}$$

The transverse electric field of an electromagnetic wave propagating along Oz can be arbitrarily assumed to be parallel to Ox. The plane-wave expansion of this field can therefore be written as follows:

$$E_x = Re\left\{\sum_{p=-\infty}^{+\infty} E_p \exp(i(k + \mathrm{G}_p)z)\right\} \tag{1.50}$$

Using Eqs. 1.49 and 1.50 in the master field equation[1], we arrive at a system of recursive equations, each of which contains three main terms. For instance, the equation of order p is:

$$\left[\left(k + \frac{2\pi}{a_z} p\right)^2 - \varepsilon_m \frac{\omega^2}{c^2}\right] E_p + \frac{\varepsilon_d}{2i}\frac{\omega^2}{c^2} E_{p+1} - \frac{\varepsilon_d}{2i}\frac{\omega^2}{c^2} E_{p-1} = 0 \tag{1.51}$$

---

[1] In the absence of discontinuities in the dielectric function, the electric field **E** can be used in lieu of the displacement vector **D** in the E method described in Sect. 1.1.5. After performing straightforward calculations, we then obtain the following equation in place of Eq. 1.31:

$$(\mathbf{k} + \mathbf{G}) \times \left[(\mathbf{k} + \mathbf{G}) \times \mathbf{E}(\mathbf{G})\right] + \frac{\omega^2}{c^2} \sum_{\mathbf{G}' \in G} \hat{\varepsilon}(\mathbf{G} - \mathbf{G}')\mathbf{E}(\mathbf{G}') = 0$$

Let us first consider a modulation with a zero amplitude ($\varepsilon_d = 0$), and let us restrict ourselves to the consideration of the values of k contained within the first Brillouin zone, i.e. values such that $|k_z| \leq \pi/a_z$. This amounts to considering a homogeneous material (ε_m) with a fictitious period a_z. Under these conditions, Eq. 1.51 has non-zero solutions ($E_p \neq 0$) only in the case where:

$$k = k_p^{\pm} = \pm\sqrt{\varepsilon_m}\,\frac{\omega}{c} - p\frac{2\pi}{a_z} \tag{1.52}$$

where $\omega > 0$.

In the case where $p = 0$, this equation actually reduces to the linear dispersion relation in a homogeneous material $k_0^{\pm} = \pm\sqrt{\varepsilon_m}\,\omega/c$. For $p \neq 0$, the solutions result simply from the folding of the band within the first Brillouin zone. In this case, the band diagram consists of an infinite series of lines which intersect at the values $k = 0$, $k = \pi/a_z$ or $k = -\pi/a_z$, as can be seen in the upper part of Fig. 1.5. For instance, the two lines $k_0^{+}(\omega)$ and $k_{-1}^{-}(\omega)$ intersect at the edge of the zone $k = \pi/a_z$ for the frequency $\omega_0 = \pi c/(a_z\sqrt{\varepsilon_m})$. This specific band diagram is also referred to as the free-photon diagram, which points to the fact that it corresponds to the case of a homogeneous material in the absence of any loss, reflection or diffraction.

Let us now assume a proper sinusoidal modulation ($\varepsilon_d \neq 0$), with only a moderate amplitude ($\varepsilon_d < \varepsilon_m$). The second and third terms in Eq. 1.51 can be regarded as perturbative terms. All the field components E_p are linked to one another. However, within a given range of values for k and ω, the 'perturbed' solutions remain close to the 'unperturbed' solutions obtained for $\varepsilon_d = 0$. For instance, at the edge of the Brillouin zone $k = \pi/a_z$ and at frequencies close to the previously defined frequency ω_0, the field components E_0 and E_{-1} are predominant. We thus need to solve a system of two equations, which for $k = \pi/a_z$ can be written as follows:

$$-\frac{\varepsilon_d}{2i}\frac{\omega^2}{c^2}E_{-1} + \left[\frac{\pi^2}{a_z^2} - \varepsilon_m\frac{\omega^2}{c^2}\right]E_0 = 0 \tag{1.53a}$$

$$\left[\frac{\pi^2}{a_z^2} - \varepsilon_m\frac{\omega^2}{c^2}\right]E_{-1} + \frac{\varepsilon_d}{2i}\frac{\omega^2}{c^2}E_0 = 0 \tag{1.53b}$$

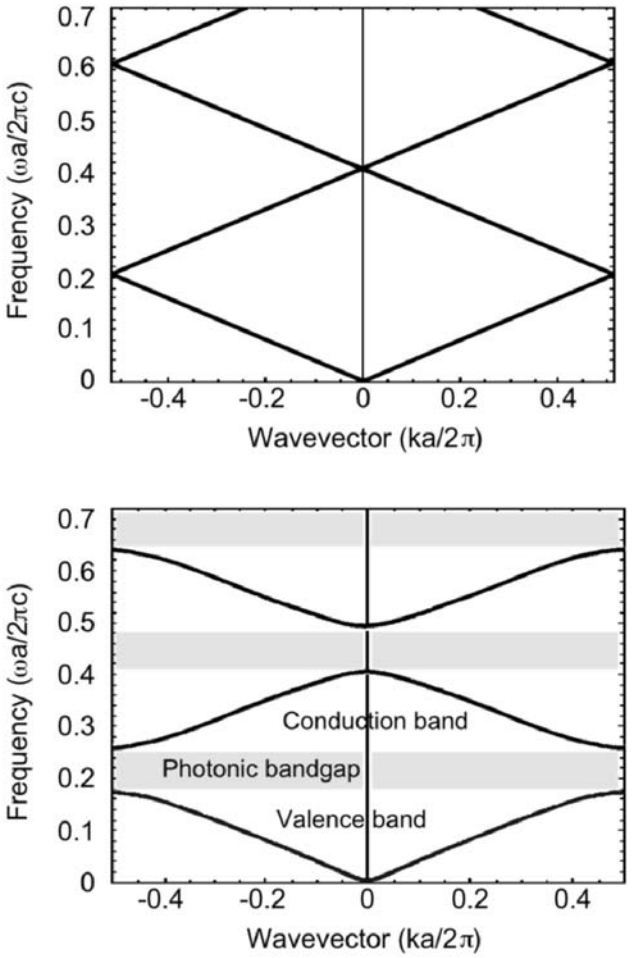

Fig. 1.5. Band diagrams of one-dimensional crystals obtained by the sinusoidal modulation of the dielectric permittivity *Top.* Modulation with a zero amplitude $\varepsilon_d = 0$ ('free photon diagram') *Bottom.* Modulation with a moderate amplitude $\varepsilon_d = 5$. In either cases, the average value for the permittivity is $\varepsilon_m = 6$

The requirement that the solutions should be non-zero results now in two different frequencies instead of a unique frequency ω_0:

$$\frac{\omega^2}{c^2}\left(\varepsilon_m \pm \frac{\varepsilon_d}{2}\right) = \frac{\pi^2}{a_z^2} \tag{1.54}$$

In other terms, there no longer exists any intersection point at ($k = \pi/a_z$, $\omega = \omega_0$) and the dispersion curves separate from one another, leading to the appearance of a photonic band gap. Within the assumption that $\varepsilon_d < \varepsilon_m$, it is quite straightforward to demonstrate from Eq. 1.54 that an approximate expression for the relative width of the gap is given by the equation:

$$\frac{\Delta\omega}{\omega_0} \approx \frac{\varepsilon_d}{2\varepsilon_m} \tag{1.55}$$

As might have been expected, the width of the gap increases with the amplitude of the modulation. The lower part of Fig. 1.5 represents the band diagram calculated for $\varepsilon_d = 5$ and $\varepsilon_m = 6$, which implies that ε_r varies between 1 and 11. The calculations are performed for the first three bands by using only six equations similar to Eq. 1.51. Actually, a pocket calculator would be enough for solving this system of equations. A comparison between this diagram and the 'free-photon diagram' represented in the upper part of Fig. 1.5 clearly evidences the appearance of new band gaps at the harmonic frequencies $2\omega_0$, $3\omega_0$, …and for the wave numbers $k = \pi/a_z$, $-\pi/a_z$ and 0. In the present case where the dielectric permittivity exhibits a sinusoidal modulation, all band gaps are of the same width. The calculated relative width of the gap (~38%) is close to the value determined from the analytical expression given in Eq. 1.55 (~41%).

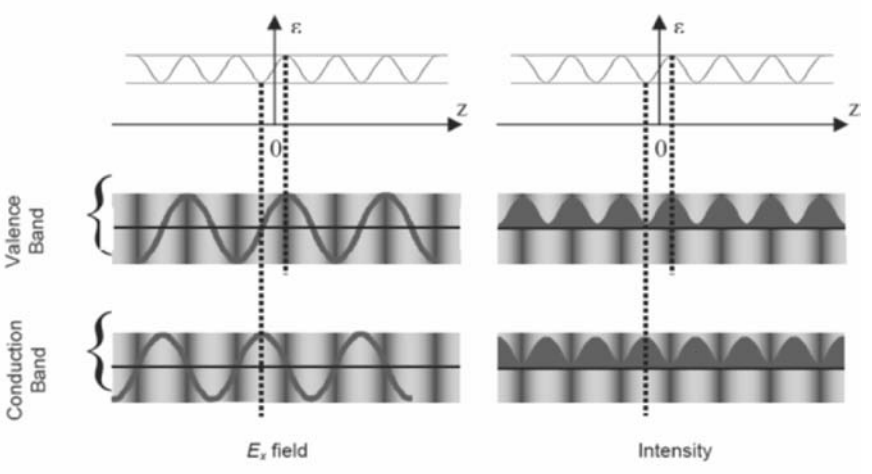

Fig. 1.6. Evolutions of the transverse electric field (*left*) and optical intensity (*right*) along the one-dimensional photonic crystal for frequencies located at the edges of the valence band (*middle*) and conduction band (*bottom*) respectively. The maxima for the field and the intensity are plotted with respect to the minima and maxima of the dielectric permittivity (*upper curves*)

Let us now consider the relationship between the field components E_0 and E_{-1}, expressed by Eqs. 1.53a and 1.53b respectively, for each of the frequencies given by Eq. 1.54. At the lower frequency (i.e at the edge of the valence band, plus sign in Eq. 1.54), the application of Eqs. 1.53a and 1.53b leads to $E_{-1} = iE_0$. Using a plane wave expansion of E_x to the first order (Eq. 1.50), the transverse electric field can then be expressed in the form:

$$E_x \ \alpha \ \cos\left(\frac{\pi}{a_z}z - \frac{\pi}{4}\right) \tag{1.56a}$$

At the higher frequency (i.e. at the edge of the conduction band, minus sign in Eq. 1.54), it now turns out that $E_{-1} = - iE_0$. Using here again a plane wave expansion of E_x to the first order, the equation for the transverse electric field becomes:

$$E_x \ \alpha \ \cos\left(\frac{\pi}{a_z}z + \frac{\pi}{4}\right) \tag{1.56b}$$

The longitudinal evolutions of the electrical field, optical intensity and dielectric permittivity are reported in Fig. 1.6 for the two frequencies considered here. As can be seen from the observation of this figure, the field and intensity maxima coincide at the edge of the valence band with the permittivity maxima. The opposite situation occurs at the edge of the conduction band, where both the amplitude of the field and the optical intensity become zero when the permittivity reaches its maximum value. In the same way as the fundamental level of an electron can be achieved by localizing the wave function of the electron in the region where the potential is the lowest, the electromagnetic mode with lower energy will be obtained by concentrating the electric field, or more precisely the displacement vector, to the region with higher permittivity. A demonstration of the possibility of extending this result to any type of photonic crystal can be found in (Joannopoulos 1995).

Bragg Multilayers

In Fig. 1.7 are displayed the dispersion diagrams of two different Bragg multilayers, represented by solid and dashed curves respectively. In both these two cases, each period consists of a high permittivity layer (ε_1=13) and of an air layer (ε_2 =1). In the diagram represented in solid curves and taken from (Joannopoulos 1995), the widths of the two layers are $d_1 = 0.2a$ and $d_2 = 0.8a$ respectively. These values approximately correspond to the same optical thickness $n_1 d_1 \sim n_2 d_2$, where $n = \sqrt{\varepsilon_r}$ denotes the refractive index. In the diagram represented in dashed curves, the widths of the layers are equal to $d_1 = 0.3a$ and $d_2 = 0.7a$ respectively. This represents a significant difference in terms of optical thickness. It might be noted that the highest (resp. lowest) value ε_1 (resp. ε_2) for the permittivity is about the same

as the maximum (resp. minimum) value $\varepsilon_m + \varepsilon_d = 11$ (resp. $\varepsilon_m - \varepsilon_d = 1$) observed in the case previously considered of a permittivity with sinusoidal modulation (Fig. 1.5). The diagram presented in the lower part of Fig. 1.5 and the diagrams presented in Fig. 1.7 are strikingly similar in this respect. The symmetry with respect to the frequency axis confirms the fact that, for one-dimensional crystals, the study of the dispersion relations can be restricted to the half-side of the Brillouin zone $[0, \pi/a]$. At the lower frequencies, the dispersion is linear and each crystal behaves as a homogeneous material whose permittivity is the average of the permittivity of the crystal in the elementary cell, given respectively by $(d_1\varepsilon_1 + d_2\varepsilon_2)/a$ for Bragg multilayers and by ε_m for the structure with a sinusoidal modulation of the permittivity. Band gaps periodically appear as the frequency increases. The fundamental band gap of Bragg multilayers is centred at $\omega = \pi c/[(d_1 n_1 + d_2 n_2)]$. The latter equation merely expresses the fact that the optical thickness of one bilayer is equal to half the wavelength, which corresponds to the condition of a maximum reflectivity for a Bragg reflector.

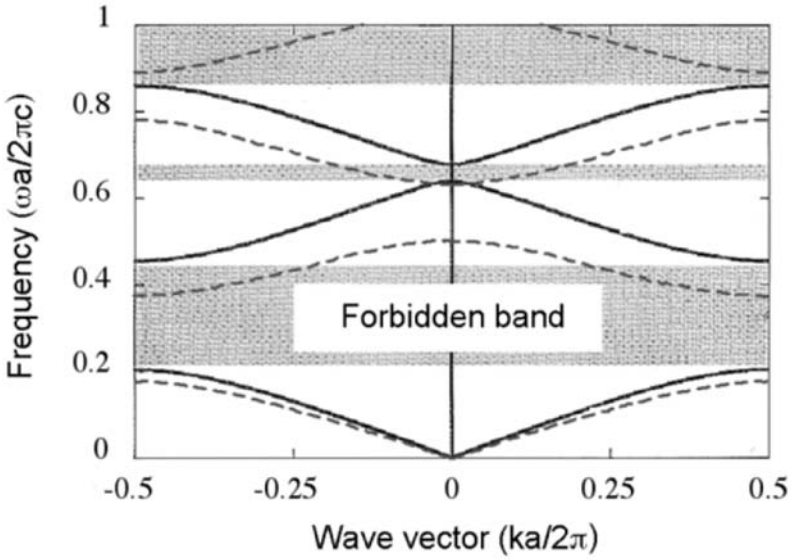

Fig. 1.7. Band diagrams of two one-dimensional photonic crystals in the form of two multilayer films consisting of periodically alternating layers with different widths d_1 and d_2 and different relative permittivities ε_1 and ε_2. In both cases, the relative permittivities of the layers are equal to $\varepsilon_1 = 13$ and $\varepsilon_2 = 1$ respectively. The thick dispersion curves were calculated for $d_1 = 0.2a$ and $d_2 = 0.8a$, where a is the period of the lattice (Joannopoulos 1995), while the dashed curves were calculated for $d_1 = 0.3a$ and $d_2 = 0.7a$

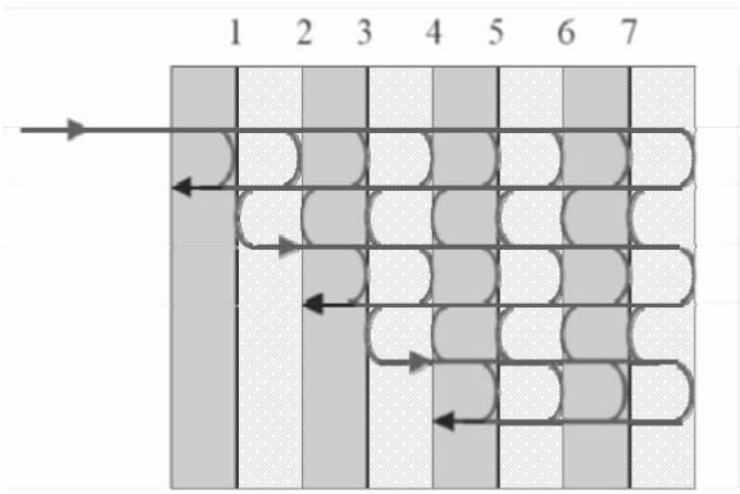

Fig. 1.8. Construction of multiple interferences in the Bragg reflector

Nevertheless, contrary to the structure exhibiting a permittivity with a sinusoidal modulation, Bragg multilayers may present band gaps with different widths at the fundamental and at the different harmonic frequencies ω, 2ω, 3ω, 4ω,.... It emerges that the band gaps at the even harmonic frequencies 2ω, 4ω,... can be much narrower than band gaps at the fundamental and at the odd harmonic frequencies 3ω, 5ω,.... Further, when all the layers of the stacks have the same optical thickness, the band gaps even tend to disappear totally at the even harmonic frequencies 2ω, 4ω. This can be explained from the fact that, at the harmonics 2ω, 4ω, 6ω, each layer constitutes an optical resonator with length $\lambda/2$, λ, $3\lambda/2$, …, in which stationary waves can be contained. It is quite obvious in this case that the existence of stationary waves and resonances is incompatible with the existence of a photonic band gap.

The behaviour of Bragg reflectors can be explained, in a more traditional way, in terms of a construction of multiple interferences inside the periodic stack of layers. As is schematically represented in Fig. 1.8, a wave propagating successively throughout the different layers will undergo multiple reflections at the different interfaces. Each reflection is accompanied by a phase change of π if the wave propagates from the medium with lower index towards the medium with higher index, whereas no phase change occurs in the opposite situation. When the overall width of each bilayer is equal to $\lambda/2$, the wave reflected at the interface (1) is in phase with the waves reflected at the interfaces (3), (5), (7)… As a consequence of these constructive interferences, a phenomenon of total internal reflection occurs: the reflectivity tends towards unity as the number of periods, i.e. of bilayers, increases towards infinity. In other terms, the wave cannot penetrate far into the multilayer stack. Only evanescent waves with an exponential decay may exist in the structure, while the actual propagation of waves is forbidden. Such a

situation actually amounts to the appearance of a photonic band gap. In the specific case where all individual layers present the same optical thickness $\lambda/4$, all the waves reflected at the different interfaces (1), (2), (3), (4) are in phase and, as might easily be imagined, such a situation correspond to the largest band gap. Conversely, at the even harmonic frequencies 2ω, 4ω, 6ω, …, band gaps disappear for the same reasons as mentioned already.

1.3.3 Band Diagrams of Two-Dimensional Photonic Crystals

The analysis developed for one-dimensional photonic crystals has already revealed some of the most fundamental features of photonic structures, which are independent from the dimension of the crystal. However, the very simplicity of the one-dimensional case, in which the propagation of waves is restricted to a single direction, has prevented us from considering issues that become critical at higher dimensions. As an example, the existence of photonic band gaps, as well as their corresponding frequency ranges, might easily have been anticipated by a reader already familiar with Bragg reflectors. By contrast, in the two-dimensional case to be presently considered, not only are there now two main directions of propagation instead of a single one, but the polarization of the wave has a decisive influence which can no longer be ignored. For this reason, the very possibility of achieving a complete photonic band gap for all in-plane directions of propagation and for the two main polarizations (TE and TM) is far from being self-evident. The existence of a complete two-dimensional band gap may not be, as will be seen in the second and third parts of this book, an absolute requirement as far as applications are concerned. However, over the past decade, the search for structures with complete photonic band gaps has been a strong impetus for research, both theoretical and experimental (Cassagne 1996; Gadot 1997; Gérard 1993; Grüning 1996; Joannopoulos 1995a, 1995b, Rowson 1999a). In what follows, we shall discuss the band diagrams of two-dimensional photonic crystals with increasing symmetry (square and hexagonal), and examine how the characteristics of the structure depend on whether the regions with high dielectric permittivity are connected to one another or not.

The Square Lattice

The square lattice has been previously introduced in Section 1.3.1, and a representation is displayed in Fig. 1.4. The irreducible Brillouin zone of this lattice is an isoscele, right-angled triangle (ΓXM) whose hypotenuse ΓM is parallel to the diagonal of each elementary square. In the same way as for one-dimensional photonic crystals (Fig. 1.5, *top*), a first approach to the band diagram consists in arbitrarily assuming that all the components of the square lattice have the same dielectric permittivity ε_m (‘free photon’ diagram, represented in the upper part of Fig. 1.9).

It might be useful here to briefly recall the construction of the ‘free photon’ diagram, which by its very nature is polarization-independent. For instance, let us

follow the ΓX direction in the reciprocal lattice. Proceeding from the origin, the first edge of the Brillouin zone is reached at a point with coordinates (π/a, 0). Proceeding from the vertex ($-2\pi/a$, 0) of the lattice, the edge of the Brillouin zone is reached at a point with coordinates ($-\pi/a$, 0). The length of the path is the same in both cases, and the two points at the edge of the Brillouin zone are strictly equivalent. Bearing in mind that the slope of the dispersion curves is given by the rules on homogenization, it comes out that the corresponding dispersion curves $\omega(\mathbf{k})$ intersect at the frequency $\omega = (1/2)\, 2\pi c/(a\sqrt{\varepsilon_m})$. The 'free photon' diagram is then constructed by following the different directions ΓX, XM, ΓM, starting from vertices of the reciprocal lattice located at increasing distances from the origin. The curvature that can be observed for certain dispersion lines simply results from the fact that the trajectory followed by the extremity of the wave vector **k** does not pass at the origin in the reciprocal lattice. In other terms, the modulus of the wave vector **k** does not follow a linear variation[2].

Fig. 1.9 (*bottom*) represents the band diagram calculated for a square lattice of cylindrical dielectric rods with permittivity $\varepsilon_r = 9$ extending in the air ($\varepsilon_r = 1$). The TM and TE polarizations are represented in this diagram by solid and dashed curves respectively. Here again, one notices the similarity with the 'free photon' diagram represented in the upper part of Fig. 1.9, with the difference however that photonic band gaps now appear in regions where dispersion curves previously intersected in the 'free photon' diagram. The centre frequency of the fundamental TM band gap (X point) is at the normalized frequency $(\omega a/2\pi c) \approx 0.35$. This is in agreement with the value for the frequency observed at the intersection point X in the diagram represented in the upper part of Fig. 1.9. Far from being a fortuitous coincidence, this reflects the fact that the value ε_m used for the dielectric permittivity in the calculation of the 'free photon' diagram is equal to the average permittivity of the square lattice formed by dielectric rods.

One of the most important results presented in Fig.1.9 is the different behaviour in TM and TE polarizations. Thus, band gaps can be seen to be much larger in TM polarization than in TE polarization. Further, contrary to what is the case for TE band gaps, the fundamental TM band gaps tend to overlap along the three main propagation directions, and therefore along any in-plane direction of propagation. The obvious consequence is the absence of a full photonic band gap for the square lattice. It might also be observed that TM band gaps occur at lower photon energies than corresponding TE band gaps. All these differences between TM and TE polarizations can actually be explained from the fact that the dielectric rods are not connected to one another.

---

[2] Trajectories of the wave vector **k** resulting in almost horizontal dispersion curves may also exist (see for instance the dispersion curves originating from the vertices of the lattices (0,1) and (0,–1) in Fig. 1.9). This corresponds to the case where the Bloch waves have a very low group velocity $\mathbf{v_g}$ (see Chapter 6). Actually, the propagating wave can be viewed as the superposition of two waves whose field distributions are symmetrical with respect to the direction of propagation. Under these conditions, the transverse component $\mathbf{v}_{g,\perp}$ becomes zero, while the longitudinal component $\mathbf{v}_{g,//}$ remains non zero.

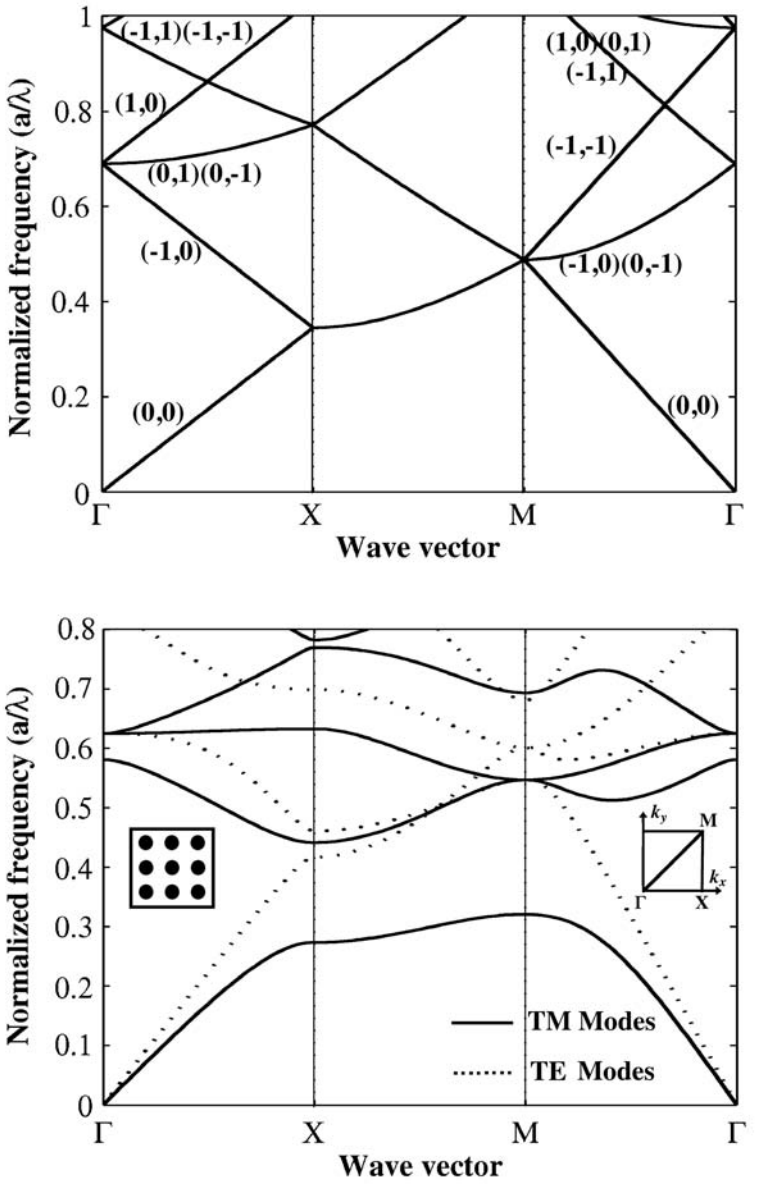

Fig. 1.9. Photonic band diagrams of square lattices. *Top.* 'Free photon' diagram calculated for the dielectric permittivity $\varepsilon_m = 2.1$. *Bottom.* Band diagram calculated for a square lattice of cylindrical dielectric rods ($\varepsilon_r = 9$) in the air ($\varepsilon_r = 1$). The radius of the rods is $r = 0.2a$, where a is the period of the lattice. The average permittivity of the lattice is equal to ε_m

For TM modes, the electric field is parallel to the axes of the cylinders, and remains unchanged when crossing the interface between the dielectric and the air. In this case, the displacement vector $\mathbf{D} = \varepsilon\mathbf{E}$ can be strongly localized within the cylinders, thereby minimizing the energy of the fundamental mode. In contrast, for the first excited mode, the field is for the most part localized inside the air region: its energy is therefore much higher, and a large energy gap separates this mode from the fundamental mode. In TE polarization, the electric field extends within the propagation plane perpendicular to the cylindrical rods. The continuous field lines of the TE modes are therefore forced to penetrate inside the air region if they are to connect the neighbouring rods. This applies not only to the excited modes, but also to the fundamental mode as well. The energy separation between the first excited TE mode and the fundamental mode is therefore reduced, resulting in smaller TE band gaps. On the other hand, TE modes, being more strongly localized inside the air region, generally present higher energies than TM modes of the same order.

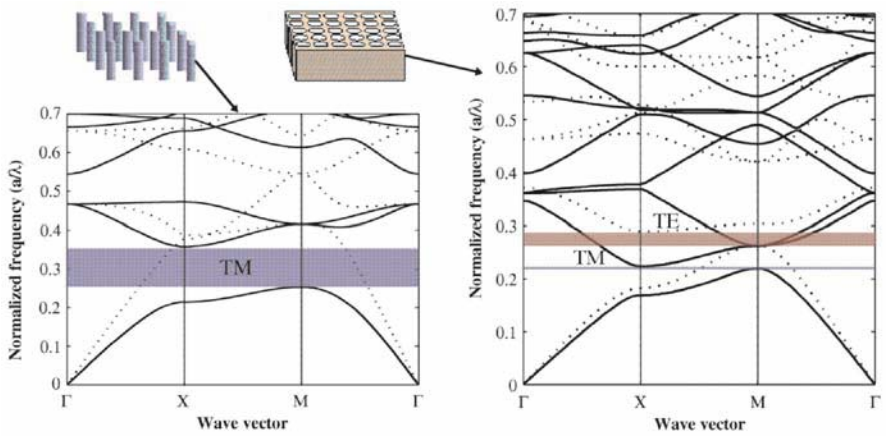

Fig. 1.10. Comparison between the band diagrams calculated for a square lattice of dielectric rods in the air (*left*) and a square lattice of holes drilled in a dielectric substrate (*right*). The square lattice formed by the dielectric rods is slightly different from the lattice represented in Fig. 1.9: the rods have a dielectric permittivity $\varepsilon_r = 11.7$ and a radius $R_c = 0.25a$, where a is the period of the lattice. The lattice of holes is assumed to be fabricated from a dielectric with the same permittivity ($\varepsilon_r = 11.7$) while the radius of the holes is equal to $R_c = 0.4a$. In either case, the dotted curves correspond to TE modes, while the thick curves correspond to TM modes. The fundamental band gaps are indicated in each figure for both TM and TE modes. Contrary to the lattice formed by dielectric rods in the air, the lattice consisting of holes in a dielectric substrate presents the two types of band gaps (TE and TM band gaps). In this case however, the TM band gap is much narrower and it does not overlap with the TE band gap

The opposite situation occurs when the regions of high dielectric permittivity are connected to one another, as is the case for a lattice formed by air columns drilled in a dielectric substrate. Fig. 1.10 presents a direct comparison between the band diagrams of these two types of structures. As can be seen, contrary to the square lattice of dielectric rods in the air (Fig. 1.10, *left*), the square lattice formed by air columns in a dielectric substrate (Fig. 1.10, *right*) exhibits larger photonic band gaps in TE polarization than in TM polarization. Here again, the TM and TE band gaps do not overlap, and a complete photonic band gap cannot be achieved for these two polarizations. A possible solution consists in trying to combine the characteristics of the two types of lattices. As will be described in the next section, a triangular lattice formed by holes with large diameter created in a dielectric substrate offers an interesting compromise in this respect.

The Triangular Lattice

Like the square lattice, the triangular lattice has been introduced already in Sections 1.1.4 and 1.3.1, and it can be seen in Fig. 1.4. If we limit ourselves to the consideration of lattices with a single 'atom' per cell, the triangular lattice is actually the two-dimensional lattice which presents the highest symmetry. The Brillouin zone is a hexagon, with a nearly circular shape. The crystal therefore exhibits a high degree of isotropy, a favourable condition for the appearance of omnidirectional band gaps. In the same way as for the square lattice, the possibility exists of designing either structures formed from disconnected dielectric cylinders or structures where the different dielectric regions are connected to one another. For each of these structures, the same polarization-dependent behaviour reported in the last section can be observed: TM band gaps tend to occur in lattices formed by isolated high-permittivity regions, and TE band gaps in connected lattices. Nevertheless, as a direct consequence of the geometry of triangular lattices, and of their higher degree of compactness, connected lattice tends to combine these two advantages when the diameter of the holes approaches the period of the lattice. In this case, the walls of the pores become indeed so thin that the residual dielectric 'veins' are almost isolated. The fact that such a structure may actually provide a complete two-dimensional band gap has been vindicated by different experiments, conducted first in the mid-infrared region (Grüning 1996), and more recently at telecommunication wavelengths (Rowson 1999a). In Fig. 1.11 is represented the photonic band diagram of a triangular lattice formed by pores created by photochemical etching in a silicon substrate where $\varepsilon_r \approx 11.7$ and the refractive index is ≈ 3.4 (Rowson 1999a). The period of the lattice is equal to 2 μm, while the diameter of the pores is equal to 1.98 μm, which corresponds to an air-filling factor equal to $\approx 72\%$. As can be seen from the consideration of Fig. 1.11, the complete two-dimensional photonic band gap is centred at a wave number equal to ≈ 2100 cm^{-1} i.e. at $\lambda \approx 5$ μm. The relative width of the gap is $\approx 9\%$.

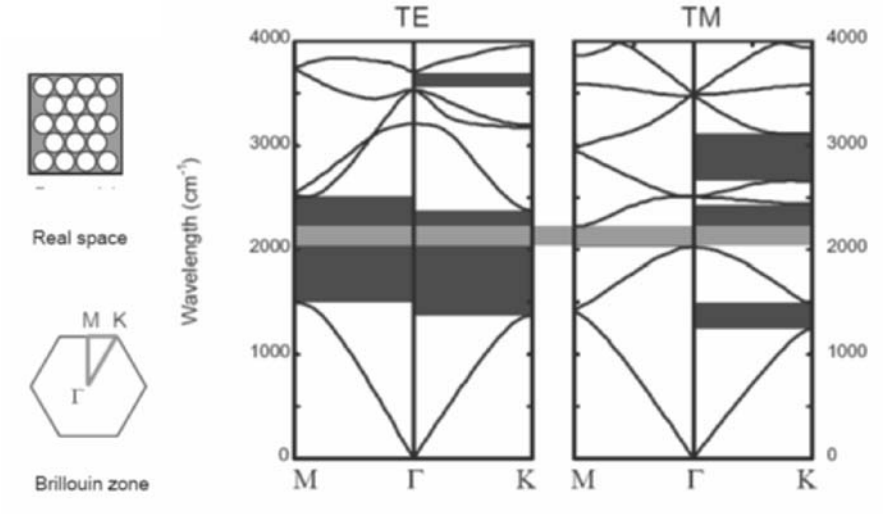

Fig. 1.11. *Left.* Triangular lattice formed by pores created in a dielectric substrate and corresponding Brillouin zone. *Right.* Band diagram calculated for a dielectric substrate with a permittivity $\varepsilon_r = 11.7$ and a period $a = 2$ μm. The radius of the pores is $R_c/a = 0.45$. The band gaps are indicated by grey bands

The Graphite-Type Hexagonal Lattice

To the best of our knowledge, the triangular lattice formed by pores created in a dielectric substrate is the only 'simple' lattice exhibiting a complete two-dimensional photonic band gap between the first transmission bands. Such a situation has never been reproduced for any other two-dimensional lattice, including the dual structure formed by dielectric rods in the air. Only the unrealistic alternative of using dielectric materials with a very high permittivity ($\varepsilon >> 11$) would sufficiently widen the band gaps of any of these other lattices to the point where complete photonic band gaps could appear at lower frequencies. This being said, there do exist certain 'simple' two-dimensional lattices fabricated from standard dielectric materials that may present a complete photonic band gap between high-order bands. The graphite-type hexagonal lattice, also referred to as the honeycomb lattice, is an example of such a lattice. More complex examples of such structures can be found in (Dobson 1999). The graphite-type lattice is represented in Fig. 1.12 (*left*). Contrary to the triangular lattice, this lattice possesses two 'atoms' per unit cell. The reciprocal lattice is also a hexagonal lattice and the corresponding irreducible Brillouin zone is the same as for the triangular lattice. The main directions of propagation are denoted in this figure as ΓK and ΓM. A complete band gap was theoretically predicted for the first time in the case of a structure formed from isolated dielectric cylinders (Cassagne 1996, 1997). These theo-

retical predictions were vindicated the following year in experiments conducted in the millimeter wave region (Gadot 1997). The structure was composed of alumina rods (ε_r = 9) extending in the air. The diameter of the rods was equal to 1.5 mm, while the distance between two neighbouring rods was equal to 2.9 mm. The corresponding band diagram is reported in Fig. 1.12 (*right*). In perfect agreement with the calculations, a complete band gap was experimentally found to occur between the seventh and eighth TM transmission bands and between the fifth and sixth TE transmission bands respectively. The measured values for the centre frequency of the gap and its relative width were found to be equal to 59 GHz and 6%, respectively (Gadot 1997). A similar demonstration of a complete photonic band gap in a graphite-type lattice has also been reported for a structure formed by pores created in a dielectric substrate (Rowson 1998). In the latter case, the photonic crystal was fabricated from silicon by photochemical etching. Experiments conducted in the mid-infrared region revealed the existence of a complete photonic band gap extending in the 5 μm wavelength region.

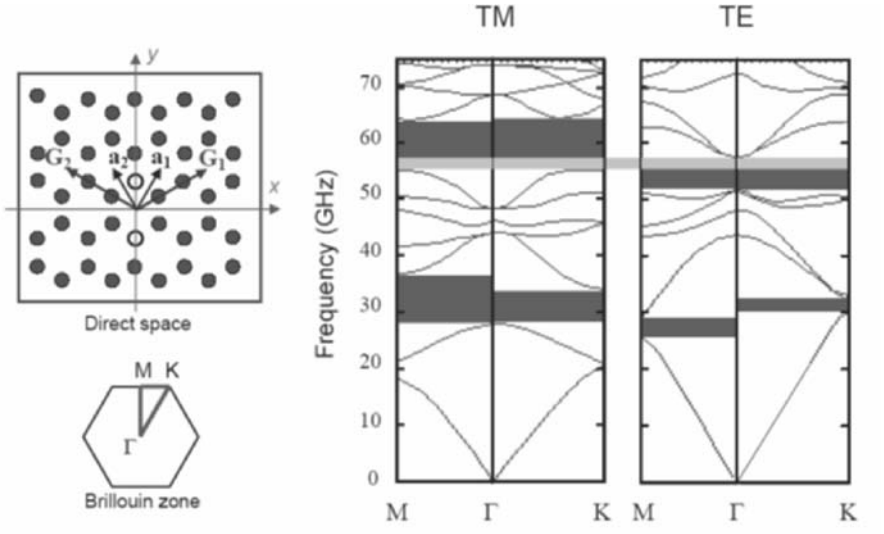

Fig. 1.12. Photonic band diagram of a graphite-type hexagonal lattice. *Left.* Schematic representation of the structure, displaying the basis vectors of the direct and reciprocal lattices (*top*) and its irreducible Brillouin zone (*bottom*). *Right*. Band diagram of a lattice of dielectric rods (ε_r = 9) extending in the air (ε_r = 1). The radius of the rods is equal to $R_c \approx 0.26d$, where d is the distance between two neighbouring rods. The photonic band gaps are represented here in the form of grey bands. The vertical scale for the frequencies is the same as was used for the first demonstration of a complete photonic band gap in such a graphite-type lattice (Gadot 1997)

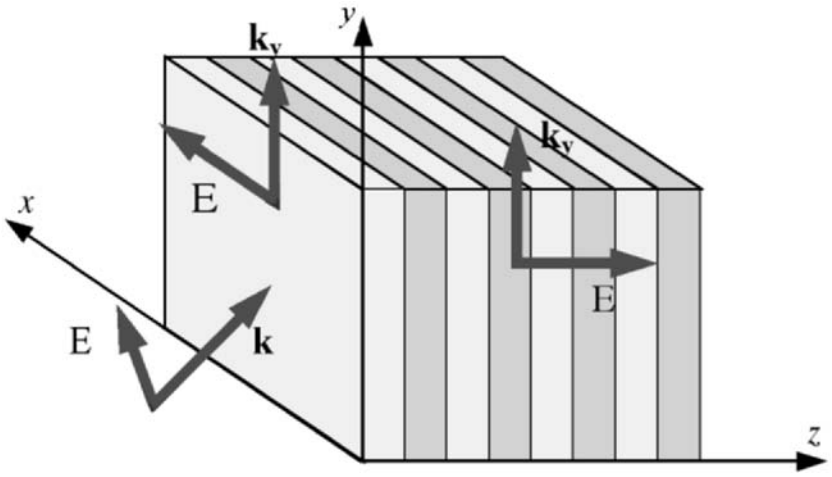

Fig. 1.13. Off-axis propagation in a one-dimensional photonic crystal: general case and limit cases ($k_x = k_z = 0$, $k_y \neq 0$) for two different polarizations of the field

1.3.4 Off-Axis Propagation in One and Two-Dimensional Photonic Crystals

The one and two-dimensional photonic crystals discussed in the preceding sections do not allow the total control of light for all directions of propagation. This can be illustrated by considering for instance the case of a Bragg multilayer stack with an off-axis illumination ($k_x = 0$, $k_y \neq 0$, $k_z \neq 0$), as represented here in Fig. 1.13. No assumption is made on the nature of the medium surrounding the multilayer stack. First, the off-axis propagation of the wave implies that different behaviours will occur depending on the polarization of the field, i.e. depending on whether the electric field is parallel or perpendicular to the incidence plane. Secondly, the band gaps that were achieved in the case of an on-axis propagation along the *Oz* axis tend to become narrower as the incidence angle, i.e. k_y, increases, and they may even vanish for a certain value of the incidence angle.

In order to fully understand the influence exerted by the polarization of the field, let us first recall that the reflection coefficient at each interface, or Fresnel coefficient, comes to depend on the polarization as soon as the incidence is not normal (Born 1965). Further, the variation in the distribution of the displacement vector depending on the polarization of the field must also be accounted for. For the sake of simplicity, we shall consider here the case, represented in Fig. 1.13, where k_y assumes a small value and where $k_z = k_x = 0$. This corresponds to the case of a long wavelength radiation. When the electric field is parallel to the dielectric layers, i.e. along the *Ox* axis, the continuity of the field at the interfaces

tends to cause the displacement vector to be localized in the high-permittivity layers, thereby minimising the electromagnetic energy. When the field is polarized perpendicularly to the dielectric layers, i.e. along the *Oz* axis, the continuity of the displacement vector at the interfaces imposes a uniform distribution of this vector in the whole structure, with the consequence that a higher electromagnetic energy will be contained in the structure. As a result, the dispersion curves of the two polarization modes diverge from the origin.

In order to understand the effects induced by the reduction of the widths of the band gaps in the case of an off-axis propagation, let us consider the limit case where k_y assumes a very high value and where k_z is negligible. This corresponds to the case of a short wavelength radiation. In this case, and whatever the polarization of the field is, the electromagnetic energy tends to concentrate within the regions of higher dielectric permittivity, which actually tend to behave as planar waveguides. In other terms, the wave becomes evanescent in the regions of lower permittivity, while the periodic coupling within the multilayer structure tends to disappear. However, the existence of such a coupling was actually at the origin of the photonic band gaps themselves, and its disappearance causes therefore all these photonic band gaps to vanish. Assuming a continuous variation of the widths of the band gaps, a progressive reduction of these widths occurs in this case for intermediate values of k_y. More precisely, the effect of guiding in the dielectric layers becomes significant as soon as $k_y > \omega/c$, since the wave can no longer escape from these layers.

The effects induced by the reduction of the band gaps in two-dimensional photonic crystals can be explained along the same lines when the light propagates outside the (*xy*) principal plane. In this case, when k_z assumes large values, the electromagnetic energy tends to concentrate within the high-permittivity cylinders which now behave like linear waveguides. However, the propagation of light along the invariant axis may present certain advantages, for instance in the case of microstructured optical fibers, as will be described in Chapter 11.

1.3.5 Band Diagrams of Three-Dimensional Photonic Crystals

The realization of a complete photonic band gap for any direction of propagation and for any polarization of the field can be achieved only with three-dimensional photonic crystals. From the beginnings of research on photonic crystals, numerous attempts were directed toward achieving this objective, and the simplest types of three-dimensional lattices (simple cubic lattice, centred cubic lattice, face centred cubic lattice) were investigated for this purpose. However, most of these attempts failed (Yablonovitch 1994). The structures investigated at this time were often found to behave like semi-metals, where electronic gaps disappear for certain specific directions within the solid state crystal. The decisive breakthrough came with face centred cubic lattices with two ‘atoms’ per unit cell, which reproduce the structure of the most usual semiconductors (silicon, germanium, gallium arsenide, etc) and of diamond (Ho 1990; Yablonovitch 1991a): very large omnidirectional photonic band gaps were then predicted before being reported in the microwave

region. Since these pioneering works, a variety of different technological approaches have been explored in order to reproduce the original experiments at shorter wavelengths, and with other types of materials. In the course of these developments, some of the cubic structures, which had been abandoned after the discovery of the Yablonovite, came to reconsidered. An example is the relatively narrow, albeit quite interesting three-dimensional photonic band gap, which was recently demonstrated in the case of a simple cubic structure (Lin 2001b). Different aspects associated with three-dimensional photonic crystals will be discussed in more detail in Chapter 12.

Fig. 1.14 represents the typical band diagram of a 'Yablonovite' structure. This type of structure was first suggested by E. Yablonovitch, and since then its characteristics have been validated by numerous studies (Yablonovitch 1991a). These structures are formed by drilling holes in a dielectric substrate along three directions. This reproduces the <110> galleries of the diamond crystal, as can be seen from the consideration of Fig. 1 in the preface to this book. In the example represented in Fig. 1.14, the dielectric substrate is assumed to have a permittivity $\varepsilon_r = 13$, and the ratio between the radius of the holes and the period of the lattice is such that the air-filling factor is equal to 57% after drilling the holes. The Brillouin zone of a Yablonovite is simply that of the fcc lattice, i.e. a truncated octahedron with a nearly spherical shape. The high degree of isotropy presented by such a structure obviously increases the probability for omnidirectional band gaps to appear. The band diagram represented in Fig. 1.14 was calculated along the (X, U_3, W, K_3, L_3, Γ, L_1, K_1, W, U_1, X,) path joining the main apexes of the irreducible Brillouin zone. In the present case, calculations were limited to the first six bands of lower energy. As can be seen, a complete photonic band gap with a relative width $\Delta\omega/\omega$ equal to 15 percent appears for any direction of propagation and any polarization of the field between the second and the third transmission bands. Of all the parameters of the structure, the air-filling factor and the permittivity (or refractive index) contrast have the main influence on the width of the gap. Accordingly, high values for the air-filling factor and the index contrast tend to result in larger bad gaps. The systematic study on this influence has shown that, for an air-filling factor equal to ~60%, a complete band gap appears if and only if the dielectric permittivity is higher than ~ 6, or equivalently if the refractive index is higher than ~ 2.5.

It is quite obvious that calculations of band diagrams for three-dimensional photonic crystals will be more difficult and time-consuming than for one-dimensional and two-dimensional photonic crystals. While a decomposition of the field using a basis consisting of a thousand plane waves is generally sufficient for describing the photonic band structure associated with two-dimensional crystals, the accuracy of the results obtained with this method when applied to three-dimensional crystals is less certain, and convergence tests are required before the results can be validated (see Section 1.5 in this chapter).

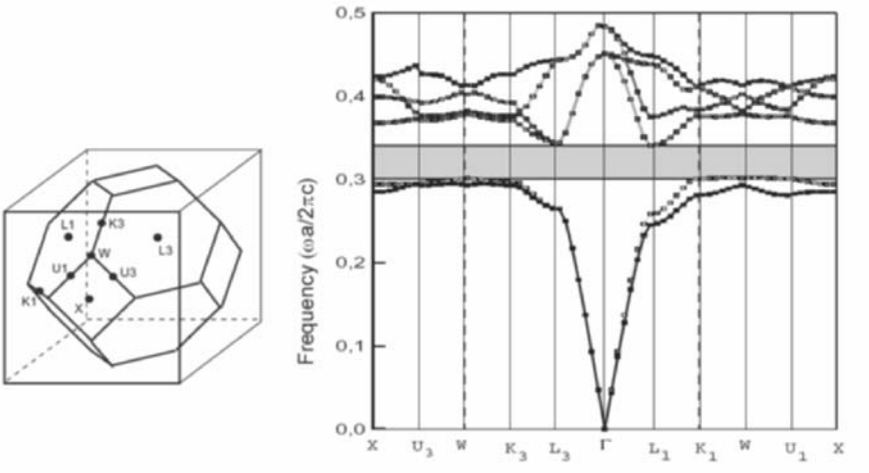

Fig. 1.14. Brillouin zone of the fcc lattice and band diagram of the Yablonovite structure calculated for the first six bands. The permittivity of the dielectric is $\varepsilon_r = 13$, while the ratio between the radius of the holes and the period of the crystal is such that the air-filling factor is equal to 57% after drilling the holes (David 2003)

1.4 Infinite Crystals with Defects

Throughout the preceding sections, photonic crystals have been assumed to be perfectly periodic systems. Nevertheless, much in the same way as the doping of semiconductor crystals is essential for the realization of actual electronic devices, the implementation of specific optical functions with photonic crystals generally requires the insertion of defects, either localized or extended, which causes a disruption in the periodicity of the crystal. Specific issues associated with the implementation of optical functions and the realization of optical devices will be addressed in the second and third parts of this book. In this section, we describe the modifications induced by the presence of defects on the band diagram of photonic structures, as well as the appropriate methods of calculation, which are based on expansions of the fields in terms of Bloch modes (see Section 1.1.2 in this chapter). In the strict sense of the term, the translational symmetry of the crystal disappears as soon as the periodicity is disrupted due to the insertion of defects, with the consequence that Bloch modes are no longer solutions of Maxwell's equations. In order to remain within this framework, it is therefore necessary to introduce approximations. As in the case of perfectly periodic crystals, the band diagram provides a synthetic view of the spectral properties of doped crystals, even if it is at the price of approximations. In the final analysis, one cannot dispense with the rigorous analysis of the influence exerted by defects, which requires the introduc-

tion of electromagnetic models of the same type as for photonic crystals with finite size. These models will be described later in Chapter 2.

In the same way as for solid state crystals, two main types of defects exist: point defects and extended defects. Point defects are associated to very local disruptions in the periodicity of the crystal, and their presence is revealed by the appearance of electromagnetic modes at discrete frequencies, which can be viewed as the analogues of isolated electronic states. In the same manner, extended defects can be seen as analogous to the dislocations of a solid state crystal, and they may result in the appearance of transmission bands in spectral regions where a photonic band gap previously existed in the case of a perfectly periodic crystal. In what follows, we shall successively illustrate these two types of defects by using different examples with increasing complexity, ranging from one to three dimensions. We shall then discuss the effects of coupling phenomena between point defects. This in turn will allow us to introduce the 'supercell' method used for the calculations of band diagrams. Other methods of calculations, for instance methods relying on the Wannier functions introduced in solid-state physics (Wannier 1937) will also be discussed in the course of this section. Finally, in order for this survey to be as complete as possible, we consider the case of semi-infinite crystals, where electromagnetic modes can be localized at the surface of the crystals. This description will serve as a transition with the finite crystal models discussed in Chapter 2.

1.4.1 Point Defects

Points Defects in One-Dimensional Photonic Crystals

Point defects in a one-dimensional crystal can be obtained by modifying either the refractive index or the thickness of one of the crystal layers. It is quite obvious that such defects are equivalent to Fabry-Perot cavities. Electromagnetic modes may therefore occur at discrete frequencies within the different photonic band gaps, depending on the modifications of the refractive index thus induced, or on the length of the optical cavity. The upper part of Fig. 1.15 shows the changes arising in the band diagram of Fig. 1.7 when the thickness of one of the high-index layers is increased by a factor of 2.2, i.e. when $d_1' = 0.44a$ instead of $d_1 = 0.2a$. In this case, discrete energy levels are found to occur in each of the three first photonic band gaps. The electric field distributions calculated with the help of a multilayer model (Born 1965), and represented in the lower part of Fig. 1.15, show that the electromagnetic modes corresponding to these band gaps exhibit respectively one, two and three oscillations within the central layer forming the cavity. This demonstrates that these modes are actually but the first three modes of a planar cavity bounded on either side by semi-infinite Bragg reflectors. Due to the infinite number of alternations from one Bragg layer to the other, the reflection coefficient of each Bragg reflector has an amplitude equal to unity, but it may exhibit a non-zero

phase $\varphi(\omega)$, which is dependent on the frequency. For a cavity with a length L, the resonance condition can be expressed for each mode in the simple following form:

$$\frac{2\pi L\omega}{n_1 c} + 2\varphi(\omega) = 2p\pi \tag{1.57}$$

where p is an integer and $n_1 = \sqrt{\varepsilon_1}$ is the refractive index of the dielectric layer formed by the cavity.

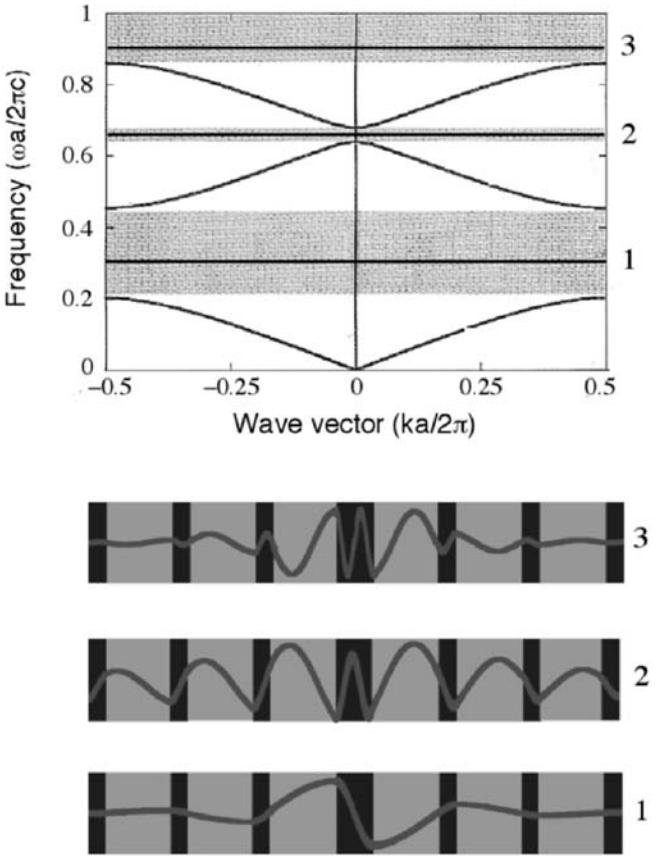

Fig. 1.15. Defect modes created in the one-dimensional crystal shown in Fig. 1.7 ($d_1 = 0.2a$, $d_2 = 0.8a$). The thickness of one of the high-index layers is increased here by a factor of 2.2. *Top.* Discrete energy levels occurring within photonic band gaps. *Bottom.* Distributions of the electric field calculated for the first three defect modes. The high-index layers are represented here in black, while the low-index layers are represented in grey

In fact, the situation observed in Fig. 1.15 does not represent the general case, and the insertion of point defects does not systematically lead to the existence of discrete energy levels within all photonic gaps. This specific result is due to the choice of both the length of the cavity and the dielectric layers forming the Bragg reflectors. As has already been mentioned in Section 1.3.2, the fact that the optical thickness of the high-index layers ($0.2\ a\sqrt{\varepsilon_1} \sim 0.72\ a$) is slightly different from the optical thickness of the low-index layers ($0.8a\sqrt{\varepsilon_2} = 0.8\ a$) causes band gaps to appear for all harmonics of the fundamental frequency ω_0 of the gap. The properties of Bragg mirrors depend on the harmonic parity: thus, the band gaps at even harmonics are narrower than band gaps at odd harmonics. The efficiency of the Bragg mirror is therefore lower for even-order band gaps, resulting in this case in a lower confinement of the electric field within the cavity, as can be seen in Fig. 1.15. Further, the phase $\varphi(\omega_0)$ of the reflection coefficient significantly deviates from zero in this case, while it remains almost zero for resonances in the odd-order band gaps (odd multiples of ω_0). The resonance condition expressed by Eq. 1.57 implies in this case that the frequency difference between the successive resonant modes will not be constant. This phenomenon can be observed in the upper part of Fig. 1.15. When the length of the cavity is modified, resonant modes of odd order sweep across their respective band gaps, while resonant modes of even order may suddenly disappear.

Point Defects in Two and Three-Dimensional Photonic Crystals

Most of the observations made for one-dimensional photonic crystals actually apply to two and three-dimensional photonic crystals as well. In these crystals, point defects can be created by locally modifying the refractive index, by changing the size of the patterns (substitution defect), by displacing one of the periodic patterns (interstitial defect) or by inserting a different pattern (dopant). Here again, the presence of a point defect may lead to discrete energy levels within the photonic gaps. However, contrary to what was the case for one-dimensional photonic crystals, these levels correspond to localized electromagnetic modes only in the case where the band gaps are omnidirectional, even if they exhibit this characteristic only for a certain polarization. If this condition is fulfilled, the electromagnetic field will actually be found to be concentrated in the region of the defect, and to be evanescent in the surrounding regions. By contrast, in the case where the band gap is not omnidirectional, a fraction of the electromagnetic energy will constantly leak away from the region of the defect towards directions along which propagation is allowed. In this case, the presence of a point defect essentially leads to a peak in the density of electromagnetic states (see Section 1.4.7 below). It is quite obvious that the consideration of two or three-dimensional crystals reveals a higher degree of complexity in terms of field distributions than was previously the case. Further, the symmetries of the crystal may result in the degeneracy of the defect modes

Fig. 1.16 represents the field distribution (displacement vector) calculated for a defect created in a two-dimensional square lattice formed by dielectric cylinders

($\varepsilon_r = 9$, $n \approx 3$) in the air. The defect was created by removing one cylinder, i.e. by introducing a vacancy in the lattice. The incident wave is assumed to be TM polarized, a condition under which an omnidirectional photonic band gap appears between the first two transmission bands (Fig. 1.9). The defect mode represented in Fig. 1.16 appears near the edge of the conduction band. The field distribution presents characteristics similar to those of the Bloch mode associated with the conduction band. As can be seen, two field extrema with opposite signs exist within all dielectric cylinders adjacent to the defect, which means that the field nodes are aligned along the diameter of each such cylinder. Actually, by replacing the lacking cylinder with a dielectric cylinder with variable permittivity, the frequency of the defect can be made to range quasi-continuously from the top of the valence band to the bottom of the conduction band (Joannopoulos 1995; Mc Call 1991; Meade 1993). The frequency of the defect mode increases as the dielectric permittivity of the cylinder forming the defect decreases. This phenomenon merely reflects the reduction of the effective optical diameter $n_{eff}\,\Phi$ of the cavity associated with the defect.

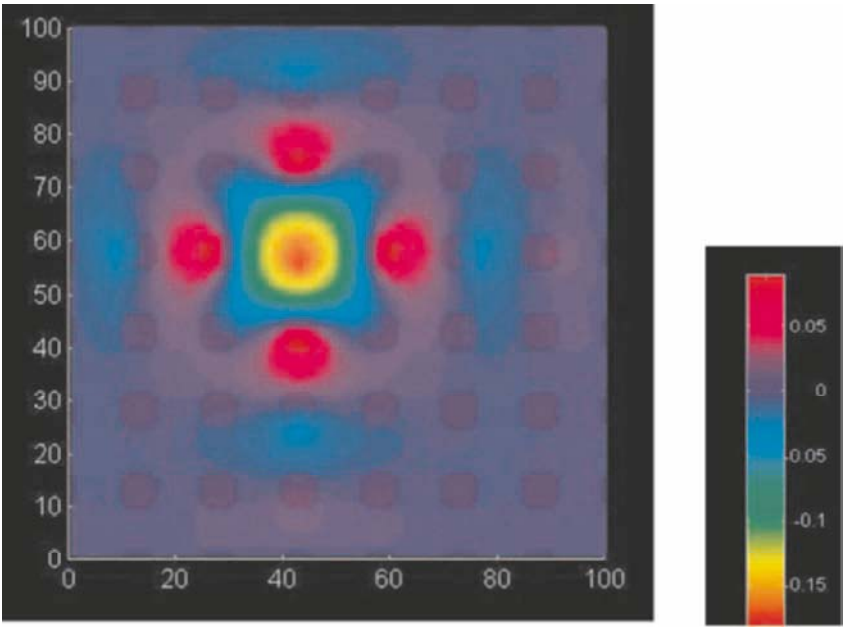

Fig. 1.16. Field distribution (displacement vector) associated with a point defect mode in a two-dimensional square lattice formed of dielectric cylinders ($\varepsilon_r = 9$) extending in the air (Gadot 1998). The radius of the cylinders is equal to $0.25a$, where a is the period of the lattice. The defect, constituted by a single missing cylinder, is equivalent to a vacancy in the lattice. The different colours, ranging from red to purple, correspond to different amplitudes of the field

The defects represented in Figs. 1.15 and 1.16 can be said to be point defects only in the sense that the space is voluntarily limited to one and two dimensions respectively. In the actual space, which by essence is three-dimensional, modifying a whole cylinder is actually equivalent to inserting an infinite linear defect, since the field in this case is localized in the whole region extending along the modified cylinder. Likewise, the modification of the thickness of a layer in a one-dimensional photonic crystal is equivalent to the insertion of a planar defect. The concept of a point defect really becomes meaningful when considering three-dimensional photonic crystals. Indeed, in this case, creating such a defect amounts to creating a three-dimensional microcavity, whose dimensions may be sufficiently small as to allow the existence of only a limited number of electromagnetic modes, and even a single mode, within a given frequency region. We shall return later in Chapters 7 and 10 to the possibility of such a total control of electromagnetic waves.

A different example of a point defect in a three-dimensional photonic crystal is represented in the upper part of Fig. 1.17. In this example, taken from (Chelnokov 1997, 1998), the three-dimensional photonic crystal is of the 'woodpile' type (Ho 1994), and consists of periodic arrays of dielectric (silicon) rods ($\varepsilon_r \sim 13$) vertically stacked on top of one another. The rods of two successive arrays are oriented along two perpendicular directions and form a half-period of the crystal along the vertical direction (<001> direction in figure 1.17). Further, each half-period is shifted from the preceding one by half a square diagonal in the horizontal plane (<100> direction in Fig. 1.17). Four arrays of rods are therefore necessary for forming one period of the crystal along the vertical direction. The fcc structure thus created is analogous to the diamond structure, and as such it exhibits a complete photonic band gap.

In the experiments corresponding to this example (Chelnokov 1997), the existence of a complete photonic gap was demonstrated at frequencies close to 1 THz (Fig. 1.17, *bottom*) using a structure with an appropriate size. Four point defects, consisting of square parallelepipeds made of silicon, i.e. with the same material as the rods themselves, and acting therefore as dopants, were inserted in four different empty regions of the crystal, as can be seen in the upper part of Fig. 1.17. The creation of these defects resulted in the appearance of resonance peaks, which can be observed at the low-frequency side of the complete photonic band gap (Fig. 1.17, *bottom*). According to the conventional terminology used in (Joannopoulos 1995b), these defects can be described as dielectric defects, i.e. defects with field characteristics similar to those of the Bloch modes associated to the valence band. In the experimental demonstration reported in Fig. 1.17, the low value measured for the transmission at the resonance peak frequency (-27 dB) may seem surprising, since in this case a transmission close to unity, as in a lossless Fabry-Perot cavity, might have been expected. This low value was first explained by the residual absorption of silicon in the experiments (Chelnokov 1998), but it later appeared that its chief cause is actually the weak coupling between the incident plane wave and the localized defect mode. Indeed, a large fraction of the incident energy is not coupled with the defects, and is either reflected or diffracted along the allowed directions. While it was originally thought that the insertion of four

defects instead of a single defect would compensate for the weak coupling between the plane wave and the defect mode, the small distance between the defects actually tends to create a coupling between these defects. As a consequence, the resonance peak broadens, but it remains nonetheless of a limited amplitude. The coupling of defects in photonic crystals will be addressed in more detail in the following section.

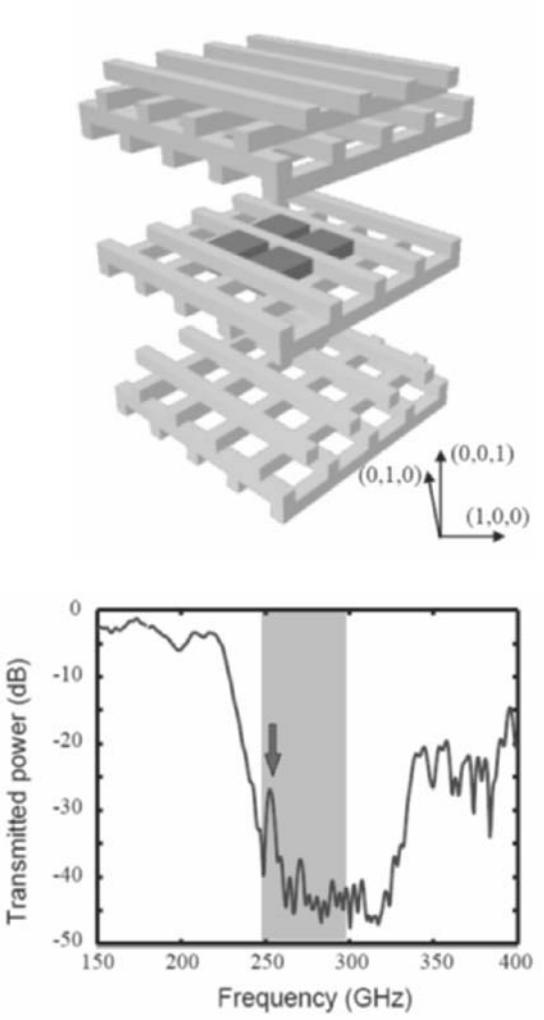

Fig. 1.17. *Top.* Exploded view of a three-dimensional photonic crystal of the 'woodpile' type formed from silicon. Four point defects consisting of square silicon parallelepipeds (represented in black) are inserted in the middle of the crystal. *Bottom.* Transmission spectrum of the crystal with defects measured along the (001) direction. The shaded area in this figure corresponds to the complete photonic band gap (Chelnokov 1998)

Experiments similar to those reported in Fig. 1.17 have been carried out in the infrared region (Lin 1999). The photonic crystal used for these experiments was also of the woodpile type, with the difference however that the defects were obtained by removing parts of certain dielectric rods, i.e. by creating vacancies rather than by inserting dielectric elements. Some of the rods were thus discontinuous. The dimensions of the defects created in these experiments and the volumes of the corresponding electromagnetic modes ($0.06\lambda^3$) are not very far from the ultimate values predicted in the case of a three-dimensional crystal ($\sim \lambda^3/4n^3$, which corresponds to $\sim 0.007\lambda^3$ for a material with a refractive index $n = 3.3$). A resonance peak, whose relative amplitude is comparable to the amplitude reported in Fig. 1.17, was measured around the centre of the photonic band gap.

1.4.2 Coupling of Point Defects

When several point defects of the same nature are present in a photonic crystal, the mutual influence between these defects can be neglected insofar as the distance between them is large enough,. In this case, everything happens as if an energy degeneracy of the system was occurring several times. Indeed, while the electromagnetic modes associated to the different defects are localized in different regions of the crystal, their field distributions are identical. By contrast, when the distance between the defects decreases, the coupling between these defects leads to the formation of electromagnetic modes with different field distributions: in this case, the energy degeneracy is lifted. Fig. 1.18 illustrates the effects induced by such a coupling through spectral measurements performed for a two-dimensional photonic crystal with a square symmetry (Lourtioz 1997). This photonic crystal, of finite size, is similar to the crystal represented in Fig. 1.16. Two vacancies were introduced by removing dielectric rods. The transmission spectrum of the crystal was then measured for two different distances between the defects. As a consequence of the centimeter size of the crystal, the measured frequencies are in the microwave region.

When the two defects are distant from one another, as is the case in the upper part of Fig. 1.16, a single transmission peak is observed at the high-frequency side of the TM band gap. This corresponds to an air defect, according to the terminology used in (Joannopoulos 1995b). When the defects are at a close distance from one another, the transmission maximum splits into two peaks, thereby revealing the existence of two different electromagnetic modes. Assuming the origin to be at the centre of the structure, the low-frequency mode presents a symmetric field distribution, while the high-frequency mode presents an anti-symmetric field distribution. This phenomenon is quite analogous to the situation occurring when a particle is released in a quantum well (Cohen-Tannoudji 1973): the wave function of the fundamental state is symmetric, whereas the wave function of the first excited state is anti-symmetric.

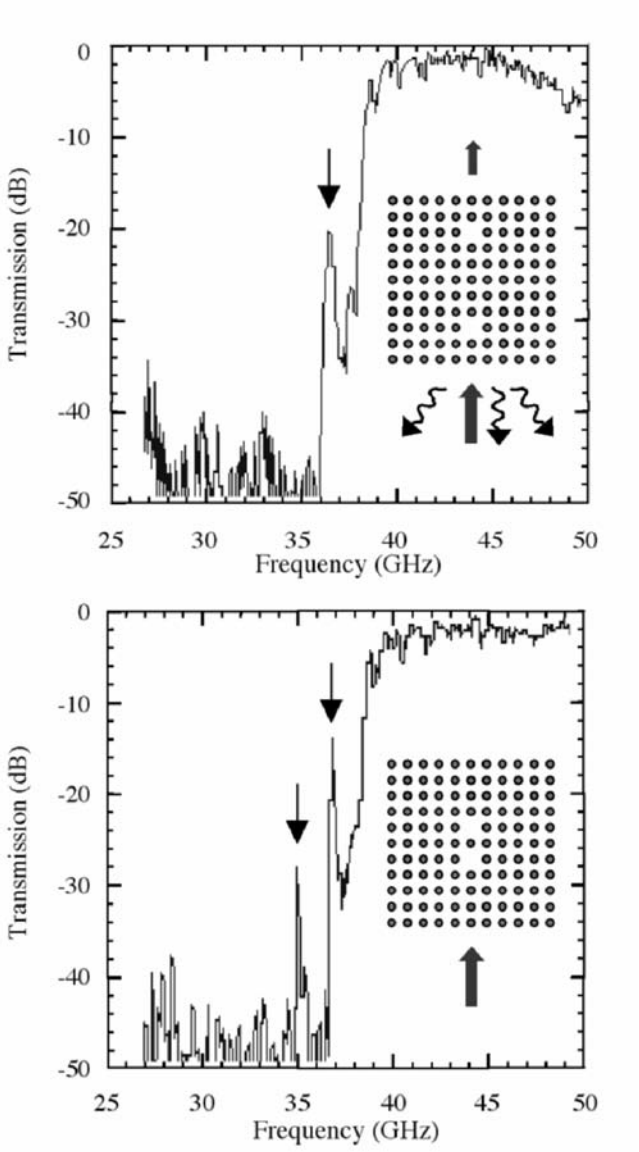

Fig. 1.18. Coupling between two point defects in a two-dimensional photonic crystal with square symmetry (Gadot 1998). The crystal here is formed by a lattice of alumina rods ($\varepsilon_r = 9$) extending in the air. *Top*. Transmission spectrum measured in weak coupling regime. *Bottom.* Transmission spectrum measured in strong coupling regime

1.4.3 Supercell Method

A necessary requirement for using the plane wave method in the calculation of a defect mode is that the periodicity disrupted by the defect should be artificially re-introduced. To this purpose, the defect is considered as the centre of a new unit cell formed by several successive rows of patterns. The construction of this *supercell* is then repeated along the different spatial directions along which the original photonic crystal is periodically organized. The artificial structure thus defined consists of periodic defects separated by regions of perfect photonic crystal. From the discussion in Section 1.4.2, the spectral properties of this new arrangement can be expected to be quite similar to the properties of the original arrangement, under the condition however that the distance between the periodic defects is large enough, which entails that the dimensions of supercell should be sufficiently large. Two examples of supercells are represented here in Fig. 1.19. The first example corresponds to the square lattice formed by dielectric rods in the air, which has already been introduced in Section 1.4.2. Here the defect is associated to a rod with a lower permittivity, or even to a missing rod. The supercell presents itself in the form of a square pattern consisting of 5×5 rods, having as its centre the rod with lower permittivity.

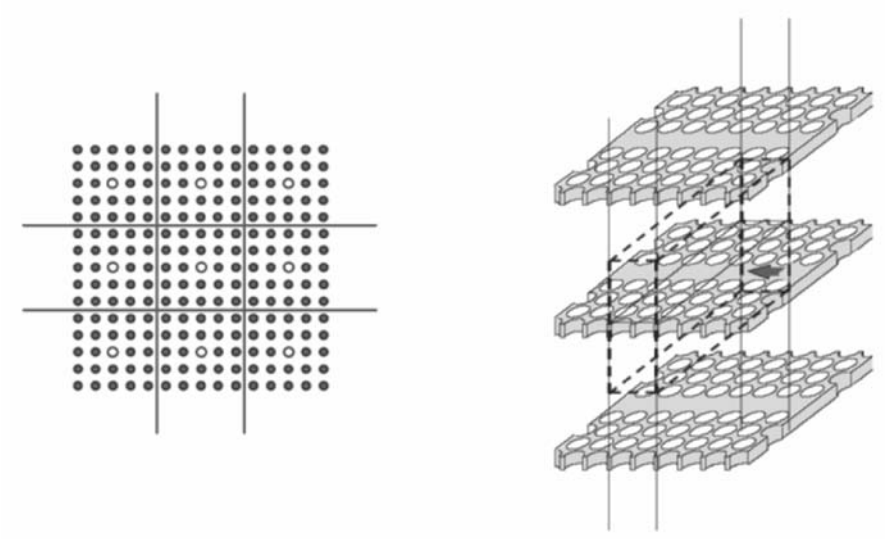

Fig. 1.19. Examples of supercells used for calculating the band diagrams of photonic crystals with defects. *Left.* Two-dimensional lattice of dielectric rods where a zero-dimensional defect was created by modifying the dielectric permittivity of a single rod. *Right.* Two-dimensional lattice of holes in a thin film, where a one-dimensional defect is associated with a row of missing holes. The finite thickness of the film imposes that three-dimensional calculations be performed. The supercell is represented here by the parallelepiped in dashed lines

The second example corresponds to a hexagonal lattice formed by holes created in a semiconductor film with a small thickness. A one-dimensional defect is associated here with a row of missing holes, which amounts to creating a linear waveguide. A first difficulty presents itself due to the finite thickness of the two-dimensional crystal. The solution adopted here consists in replacing the single film with a periodic stack of films placed at a very large distance from one another. In the artificial three-dimensional periodic structure thus created, the defect is now 'periodized', and it can be described using a supercell with a parallelepiped shape. This method allows the correct description of the dispersion curves associated with the guided modes, but it should be handled cautiously when considering leaky modes which may propagate away from the film (Le Vassor d'Yerville 2002). We shall return to the consideration of these issues in Chapter 5 of this book.

1.4.4 Methods derived from Tight-Binding Methods in Solid State Physics

The method based on the 'linear combination of atomic orbitals', or LCAO method, is among the most currently used methods for calculating electronic band structures and impurity levels in solid state crystals. Originally developed by F. Bloch in 1928 (Bloch 1928), this method resorts to a basis of elementary wave functions for electrons, localized around the individual atoms of the crystalline lattice. The atomic interactions are arbitrarily restricted to the interactions arising between neighbouring atoms, while the overlaps between neighbouring orbitals are considered as perturbations. A multiplying factor $\exp(i\mathbf{k}.\mathbf{r})$ is then applied to all basic wave functions in order to account for the periodicity of the crystalline lattice. The calculations of the band diagram then proceed by solving a matrix system of equations, analogous to the system obtained with the plane wave method (see Section 1.1.5 in this chapter). However, the use of localized wave functions allows more direct calculations of impurity levels in the crystal.

The extension of the LCAO method to photonic crystals is far from being obvious, and adapting this method has required considerable effort. The major difficulty stems from the absence of localized functions for the electromagnetic field in photonic crystals. Among the most recent methods developed to overcome this problem, we shall describe more specifically the method reported in (Albert 2000; Monge 2000) and based on the use of Wannier functions (Wannier 1937). This method proceeds in three successive stages and can be summarized as follows. The first stage consists in predefining localized functions reproducing the main symmetries of the field distributions. These functions are separately calculated using the plane wave method. In general, the analysis can be restricted to *s*- and *p*-type symmetries, in direct analogy with atomic orbitals. After introducing the periodicity of the crystal through the multiplying factor $\exp(i\mathbf{k}.\mathbf{r})$ and after determining the number of 'atomic' sites in interaction, the field can be developed in the form of a linear combination of Bloch functions corresponding to different sym-

metries and different atomic sites. The eigenvalue equations of the type $O\mathbf{F} = k_0^2 \mathbf{F}$ (Eq. 1.8) can then be solved. The parameters involved in these equations are simultaneously adjusted in order to reproduce the band diagram of the perfect crystal, calculated by using the plane wave method. Actually, obtaining the matrix elements of the operator O does not necessarily require a precise definition of the initial basis functions. The second stage consists in calculating the Wannier functions using a Fourier transformation of the Bloch functions. Contrary to Bloch functions, Wannier functions are not associated with a specific wave vector **k** in the Brillouin zone, but with a unit cell of the crystal. These functions are well suited to the description of localized defect states. Finally, in the third stage, the Wannier functions are used for determining the eigenvalues of the matrix equations corresponding to the case of a photonic crystal with defects. The deviation from the ideal case of a periodic crystal is introduced in the equation through an additional perturbation operator V.

1.4.5 Extended Defects

Extended defects, with one, two, or three dimensions, can be created only in photonic crystals of higher or equal dimension. Among all extended defects, one-dimensional defects have undoubtedly been the most intensively studied, this being due to the fact that these defects can be used as waveguides in photonic crystals. In this respect, it can be noted that the possibility exists of imagining two or three-dimensional defects formed by a succession of one-dimensional waveguides connected end-to-end to one another and oriented along different directions, thereby allowing the propagation of light along any path inside the crystal. In this section however, we shall consider exclusively one-dimensional defects, and issues related to the guiding of light will be more specifically addressed in Chapters 5 and 9.

The basic example of a one-dimensional defect is that of a linear waveguide inside a two-dimensional crystal. A method for realizing such a waveguide consists in aligning identical point defects, regularly spaced along the desired direction. Each point defect constitutes an optical resonator. If the distance between two defects is small enough, as is the case in the example presented in Fig. 1.18, a coupling between these defects arises, resulting in the formation of two defect modes. It is therefore quite apparent that the coupling between an infinite number of identical resonators might lead to the formation of a transmission band consisting of an infinite number of coupled modes. Such a waveguide, based on coupled resonators, was first suggested in 1999 (Yariv 1999). However, the most generally used method for creating a linear waveguide in a two-dimensional crystal consists simply in removing or modifying one or several rows of patterns along one of the directions of the crystal. The band diagram is then calculated using the supercell method introduced in Section 1.4.3.

In the left-hand part of Fig. 1.20 are shown the results of calculations conducted along these lines for a triangular lattice of holes where a row of patterns had been removed along the ΓK direction. The supercell used for the calculations is similar

to the supercell represented in Fig. 1.19 (*right*), but in the pure two-dimensional case of a film with infinite thickness. The dielectric permittivity of the substrate is equal to $\varepsilon_r = 13$, while the radius of the holes is $R_c = 0.4a$, where a is the period of the lattice. For the sake of simplicity, the band diagram is presented here only in the case corresponding to a ΓK direction and a TE polarization. The shaded areas in Fig. 1.20 correspond to transmission band regions for a perfect crystal without defect: in this case, a band gap appears between the two normalized frequencies $(\omega a/2\pi c) = 0.24$ and $(\omega a/2\pi c) = 0.39$. When the waveguide is taken into account in the calculations, thick dispersion curves are superimposed over the shaded areas representing the transmission bands. These curves actually correspond to guided modes which can be distinguished according to their parity: the field distribution of even modes is symmetric with respect to the axis of the waveguide, while the field distribution of the odd modes is anti-symmetric (see Fig. 1.20, *middle*). The relatively high number of dispersion curves in the band diagram is due both to the influence of band folding effects and to the existence of high-order guided modes. The band diagram of the structure is further complicated by the presence of anticrossing phenomena. As can be observed in this figure, the waveguide is single-mode only over narrow frequency bands.

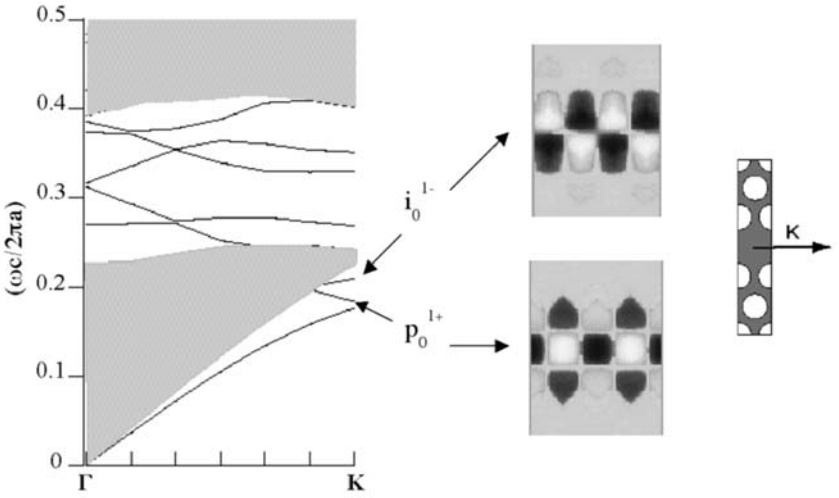

Fig. 1.20. *Left.* Band diagram of a triangular lattice of holes created inside a dielectric substrate ($\varepsilon_r = 13$) where a linear waveguide formed by one row of missing holes along the ΓK direction has been inserted. The diagram is presented here only for TE polarization and along the ΓK direction. *Middle.* Field distributions associated with the even mode p_0^{1+} and with the odd mode i_0^{1-} respectively. The index 0 corresponds to the mode order while the exponent 1+ and 1– correspond respectively to the higher and lower branches of the first band folding. *Right.* Supercell used for the calculations

Fig. 1.20 corresponds to the ideal situation where the photonic crystal is perfectly two-dimensional. In practice, and as will be described in the second part of this book, it is necessary to account for the influence of the finite thickness of actual structures. This is all the more true for photonic crystal waveguides fabricated from thin films, but it also applies to photonic crystal buried waveguides fabricated from bulk substrates. In such cases, three-dimensional calculations need to be performed, for instance by using three-dimensional supercells similar to the example represented in the right-hand part of Fig. 1.19. More elaborate calculations, based on the scattering matrix method, allow the determination of the losses induced by the leaky guided modes which may propagate away from the plane of the waveguide (Le Vassor d'Yerville 2002).

1.4.6 Semi-Infinite Crystals and Surface Defects

To this point, only defects embedded in photonic crystals have been considered. This restriction was quite natural, as photonic crystals have been assumed thus far to be infinite. We did, however, mention at various places in this chapter that the finite size of actual structures may result in significant changes in the properties of photonic crystals (see Sections 1.4.3 and 1.4.5). In this respect, the supercell method has proven to be a powerful theoretical method for approaching this problem from the band diagram of infinite structures. The properties of a photonic crystal with a finite size are strongly dependent on the surface bounding such a crystal. Thus, local disruptions in the periodicity of this surface may result in the appearance of specific electromagnetic modes, known as surface modes.

This can be demonstrated by considering the simplest case of a semi-infinite Bragg layer stack where the thickness of the upper layer is either larger or smaller than that of the internal layers with the same dielectric permittivity. Under these conditions, the upper layer forms an asymmetric Fabry-Perot cavity bounded by air on one side and by the rest of the Bragg mirror on the other side. Stationary waves may be present in this cavity, with the consequence that the electromagnetic field will be evanescent both in the air and in the Bragg mirror. In other terms, one is presented here with a resonant mode trapped at the surface of a one-dimensional crystal.

For crystals of a higher dimension, the situation becomes obviously more complex. For the sake of simplicity, we shall restrict ourselves here again to the consideration of semi-infinite two or three-dimensional photonic crystals with a plane interface. The properties of such crystals depend not only on the orientation of the plane of the surface with respect to the planes of the crystal, but also on the surface termination, i.e. on the way this plane intersects with the periodic patterns of the crystal. As an example, the upper part of Fig. 1.21 represents a Yablonovite crystal whose upper interface corresponds to a (111) fcc crystal plane. The lattice of holes defined by the surface termination is a triangular lattice. It is quite apparent that a different orientation of the surface would have resulted in a lattice of a different nature, and even possibly in an aperiodic lattice. Similarly, if the surface had cut the lattice with the same orientation of the surface, i.e parallel to the (111)

plane, but at a different depth inside the crystal, the resulting patterns may not be have been perfectly circular holes.

For a semi-infinite crystal of the same type as the crystal represented in Fig. 1.21, four main types of electromagnetic modes can be distinguished:

1. modes propagating in the air, but evanescent in the crystal (PE),
2. modes propagating in the crystal, but evanescent in the air (EP),
3. modes propagating in the air as well as in the crystal (PP)
4. modes evanescent in the air as well as in the crystal, but propagating at the surface of the crystal (EE).

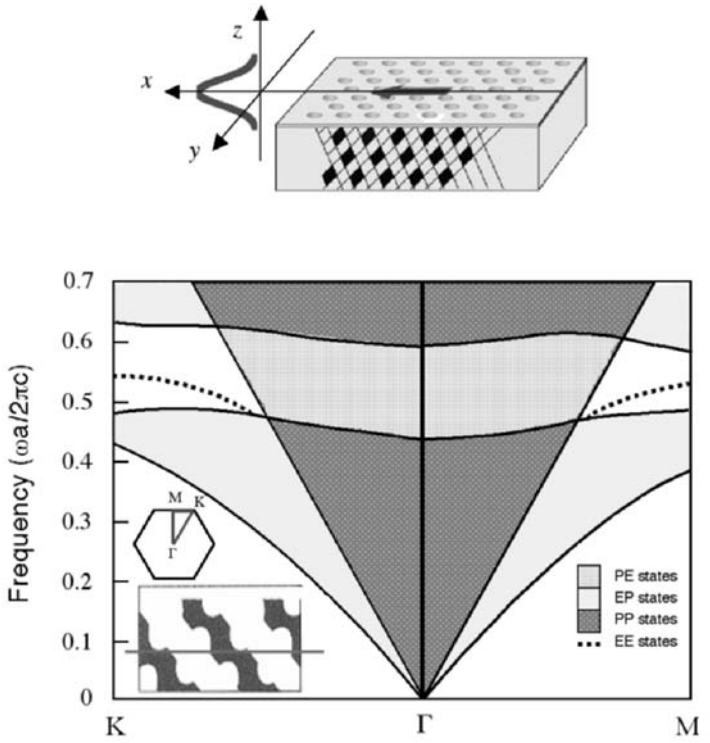

Fig. 1.21. *Top.* Schematic representation of a surface mode propagating at the surface of semi-infinite Yablonovite crystal. *Bottom*. Band diagram of the (111) crystal surface, revealing a triangular lattice of holes (Joannopoulos 1995). The different regions correspond to the different electromagnetic modes which may exist in this structure, while the thick dashed lines in the gap correspond to surface modes. The position of the surface plane is indicated by the thin solid line. The insert in the bottom left corner of the figure represents the cross-section of a Yablonovite crystal

In the example represented in Fig. 1.21, the plane of the interface is parallel to the *xy* plane, and the wave vectors of the surface modes are therefore parallel to this plane ($\mathbf{k} = \mathbf{k}_{//}$, $k_z = 0$). Since the translational symmetry is disrupted along the *z* direction, $\mathbf{k}_{//}$ is actually the only vector defined for an eigenmode of the crystal. On the other hand, for a wave propagating from the air towards the crystal or from the crystal towards the air, $\mathbf{k}_{//}$ will be the only vector to be conserved. It is therefore useful to introduce separate band structures for the air and for the three-dimensional crystal projected onto the *xy* plane, as represented in the lower part of Fig. 1.21. For this purpose, we consider the variation of the vector $\mathbf{k}_{//}$ along the main directions of the surface lattice, which in this case is a triangular lattice of holes, and we calculate all solutions allowed for k_z in the three-dimensional crystal for each (ω, $\mathbf{k}_{//}$) couple. The set of solutions determines the domains of the modes that may propagate in the crystal (EP and PP). It then suffices to search for solutions allowed for k_z in the air. For vectors $\mathbf{k}_{//}$ such that $|\mathbf{k}_{//}| \geq \omega/c$, it is apparent that no solution exists. The 'light line' $|\mathbf{k}_{//}| = \omega/c$ divides therefore the (ω, $\mathbf{k}_{//}$) plane into two regions, a region where modes propagate in the air (PE and PP) and a region where they are evanescent in the air (EP and EE). By combining the two separate diagrams, a region EE where surface modes are to be found can now be delimited. This region is represented in Fig. 1.21 by a white area. Finally, by performing three-dimensional calculations with the help of the supercell method, described in Section 1.4.3 in this chapter, allows the exact determination of the dispersion curves $\mathbf{k}_{//}(\omega)$ of these modes. The dispersion curves are represented in thick dashed lines in Fig. 1.21.

The diagram represented in Fig. 1.21 was actually obtained for a specific surface termination of the crystal, and the insert in this figure represents a cross-section view of the Yablonovite. The position of the surface plane chosen in this example is indicated here by a thin solid line. The question then arises whether, for a given three-dimensional photonic crystal, surface modes may always exist. For this purpose, let us consider here a continuous displacement of the plane of the crystal surface over a period of the crystal along the z direction: one bulk unit cell is thus added per surface unit cell to the semi-infinite crystal. This leads to increasing the total number of allowed states (modes) in the valence band by two (one state per polarization). As the surface termination changes, the frequencies of the two modes necessarily decrease from the bottom of the conduction band to the top of the valence band, and they sweep across the band gap in much the same way as a point defect mode does when the relative permittivity of a pattern of the crystal increases continuously from unity to the value corresponding to the dielectric from which the crystal is formed (see Section 1.4.1). Since the electromagnetic modes within the band gap are actually defect modes and, in the present case, surface modes, it thus turns out that, for any photonic crystal, surface terminations allowing the existence of localized surface modes can be found.

1.4.7 Density of States in Photonic Crystals with or without Defects

In the same way as the electronic density of states in a semiconductor undergoes significant modifications when materials are structured at nanometer scales, the periodic modulation of the dielectric permittivity at the scale of optical wavelengths results in a density of photonic states (or of electromagnetic modes) which can be dramatically different from the density of states in free space. Let us recall here that the photonic density of states (DOS) is defined as the number of electromagnetic modes allowed per frequency unit. When the photonic density of states is modified in a certain region of space, the radiative lifetime of any light emitter present in this region is modified in turn. In the upper part of Fig. 1.22 is presented a schematic comparison between the photonic density of states in free space and in a photonic crystal.

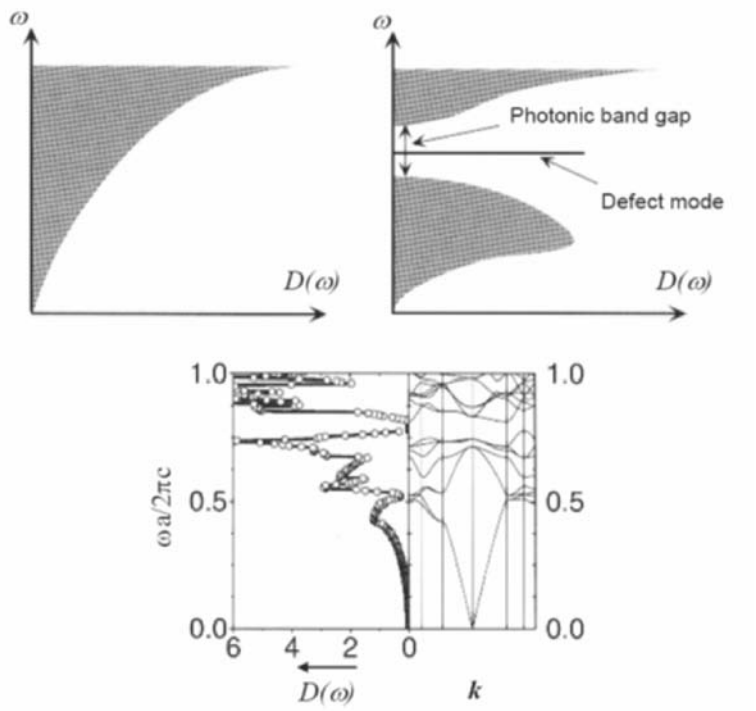

Fig. 1.22. *Top.* Schematic comparison between the photonic densities of states $D(\omega)$ in free space *(left)* and in a photonic crystal *(right)*. *Bottom.* Photonic density of states of an fcc inverse opal formed by air in a dielectric substrate ($\varepsilon_r = 11.9$), calculated as a function of the normalized frequency $\omega a/2\pi c$ (Kœnderick 2003). The right-hand part of this figure displays the complex dispersion diagram corresponding to wave vectors between the high-symmetry points X, U, L, Γ, X, W, and K, represented here by vertical lines. The photonic density of states in the complete photonic band gap is zero around the frequency $\omega a/2\pi c = 0.8$

In free space, the density of states $D(\omega)$ is proportional to ω^2, and can be expressed, for a volume V, by the following equation:

$$D(\omega) = \frac{\omega^2 V}{\pi^2 c^3} \tag{1.58}$$

Eq. 1.58 still applies to the case of a homogeneous material with a refractive index n assumed to be frequency-independent, i.e. to the case of a non-dispersive material, provided however that c be replaced with the speed of light in the material v = c/n. By contrast, this equation is no longer valid for photonic crystals, this being a consequence of the dispersion characteristics $\omega(\mathbf{k})$ of the crystal. Assuming these characteristics to be known, the density of states is calculated by counting all allowed states with a given frequency ω, i.e. as an integral of a Dirac δ function over the first Brillouin zone with a summation over all transmission bands:

$$D(\omega) = \sum_i d^3\mathbf{k}\,\delta\big(\omega - \omega_i(\mathbf{k})\big) \tag{1.59}$$

As can be seen in Fig. 1. 22, the typical density of states in a three-dimensional photonic crystal presents a significant deviation from the density of states in free space. It becomes zero at frequencies located in the omnidirectional band gap and exhibits maxima near the edges of this gap. In the case of an ideally isotropic crystal (flat bands), the maxima would be located exactly at the band edges, and their values would be infinite. In general, secondary maxima may occur each time the dispersion curves of the crystal present a tangent parallel to the axis of the wave vector ($d\omega/dk = 0$). This phenomenon is also known in solid state physics, where it is referred to as the van Hove singularity. Such domains of singular dispersion, where the group velocity of light $d\omega/dk$ is close to zero, are of particular significance not only as regards the absorption or the emission of light, but also as regards frequency conversion and other non-linear optical effects. The group velocity is defined as the speed at which the energy of the electromagnetic field propagates in matter. Thus, when the group velocity decreases, the interaction between the electromagnetic wave and matter tends to be reinforced. The presence of defects in the photonic crystals may also lead to DOS singularities. In particular, for zero-dimensional point defects, Dirac peaks occur in complete photonic band gaps, as can be seen in the upper part of Fig. 1.22 (*right*).

An example of a DOS calculated in the realistic case of an inverse three-dimensional opal formed by air in a dielectric (fcc lattice) is represented here in the lower part of Fig. 1.22 (Kœnderick 2003). The main characteristics of the photonic density of states that were discussed in the above can be observed in this figure. Note that it has been experimentally demonstrated that changes in the local DOS may significantly affect the power radiated by emitters embedded in such opals. However, for applications to quantum optical experiments in photonic crystals, it is necessary to consider not only the total availability of modes with a fre-

quency ω, but also the local coupling arising between an excited atom emitting a photon at the frequency ω and the electromagnetic environment created by the photonic crystal in the region where the atom is located. In other terms, the overlap occurring between the matrix element of the dipolar moment of the atom on the one hand, and the electric field of the electromagnetic mode(s) on the other hand, is the determining factor for such quantum optical characteristics as the radiative lifetime of the atom. This overlap can be clearly discerned from the local photonic density of states $D(\mathbf{r},\omega)$, defined as follows:

$$D(\mathbf{r},\omega) = \sum_i d^3\mathbf{k}\left|\mathbf{E}_{ik}(\mathbf{r})\right|^2 \delta\left(\omega - \omega_i(\mathbf{k})\right) \tag{1.60}$$

As far as practical calculations are concerned, the (ω, $\mathbf{k}$) space needs to be discretized in order to calculate the summations involved in Eqs. 1.59 and 1.60. In most cases, very dense meshes need to be used over the whole Brillouin zone, with the result that the noise-free determination of the density of states requires very lengthy calculations. Nevertheless, rapid insight into the main features of the density of states can be gained by counting only states located along the contour of the irreducible Brillouin zone instead of summing Eq. 1.59 over the whole zone. To the extent that band extrema can be assumed to be located along the contour, the results of the calculations provide valuable information on photonic gaps and DOS maxima.

The benefits of this simplifying approach are illustrated in Fig. 1.23, which shows the evolution of the TE and TM gaps of a triangular array of air holes ($n = 1$) in a dielectric matrix ($n = 2.8$, $\varepsilon_r = 7.84$), when varying the diameter of the holes, i.e. when varying the air-filling factor of the structure. The construction method can be described as follows. The band structure is computed for each value of the air-filling factor using a regular k-spacing along the ΓMKΓ contour defined by the irreducible Brillouin zone of the triangular lattice (see Fig.1.11). The number of photonic states is then counted for each frequency interval $\Delta\omega$. The map is finally constructed by plotting the results versus the filling factor and by associating colours, from dark blue to bright red, to densities of states with increasing values.

The summation of Eq. 1.59 remains zero within the gap regions and gaps appear as expected in the form of black areas (Fig. 1.23*a* and *b*). For this reason, the term ‘gap map’ has been applied to figures such as Figs. 1.23*a* and *b*. Gap maps provide additional information beside information on the gaps themselves, in particular on the nearby bands and their band edges. An example in Fig.1.23*a* is the bright line located below the main TE gap, which corresponds to the DOS maximum near the upper edge of the first transmission band along the ΓM direction (see Fig.1.11). Similarly, observation of the air band extending above the main TE gap reveals a faint, bright line associated with another DOS maximum near the lower edge of the second transmission band along the ΓK direction (see Fig.1.11).

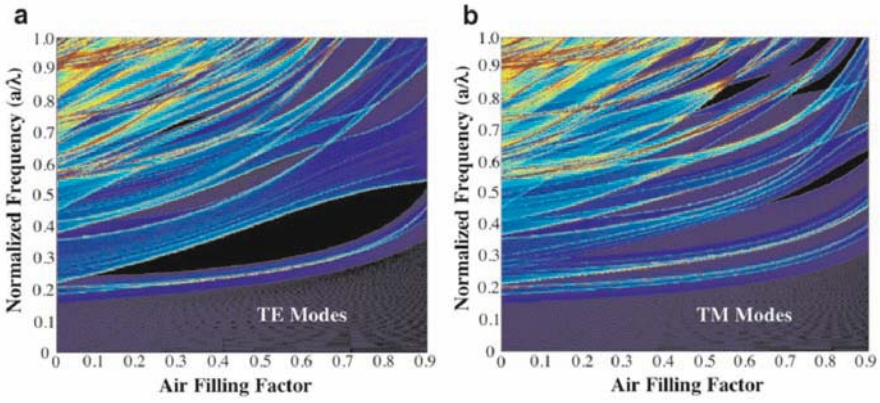

Fig. 1.23. Gap maps of a two-dimensional triangular photonic crystal of air holes ($n = 1$) in a dielectric matrix with index $n = 2.8$ ($\varepsilon_r = 7.84$) *a*. 'H' or 'TE' polarization with the magnetic field parallel to the axis of the holes, *b*. 'E' or 'TM' polarization with the electric field parallel to the axis of the holes. The construction method consists in computing the band structure for each value of the air-filling factor using a regular *k*-spacing along the ΓMKΓ contour in the reciprocal space (see Fig. 1.11). The number of photonic states is then counted for each frequency interval $\Delta\omega$. The dark regions on the map correspond to low densities of states, while brighter regions are associated with high densities. Gaps appear therefore on the map in the form of black areas, while DOS extrema at the K, M or Γ points appear as bright veins. Note that the TE and TM gaps overlap only for air-filling factors with values between 0.7 and 0.8 (*courtesy of L. Rutemöller*)

A few additional comments on Figs. 1.23*a* and *b* should finally be made:

- the overlap between the TM and TE gaps can be seen to reduce to a very small region corresponding to air-filling factors around 0.7-0.8. This confirms the drastic conditions required for obtaining a complete two-dimensional gap, i.e. a large air-filling factor and a high index contrast (see Section 1.3.3). The limited overlap between the TM and TE gaps in Figs. 1.23*a* and *b* is explained at the present time by the moderate index contrast chosen for the calculations (1÷ 2.8 instead of 1÷ 3.4 in Fig. 1.11).
- the main gap regions, and especially the TE gap at lowest frequencies, appear 'whale shaped', a characteristic related to the very nature of Bloch modes. At small air-filling factors, the field minima of modes below the gap tend to be located in the holes. The frequencies of these modes are therefore relatively insensitive to the size of the holes, which explains the relatively slow evolution of the lower gap edge in Fig. 1.23*a*. By contrast, a rapid evolution can be observed for modes extending near the upper edge of the gap, whose field maxima are located in the air holes. At large air-filling factors, the situation is reversed for each type of modes. Since the residual fraction of dielectric material in the crystal is small, any additional removal of dielectric material will

strongly affect modes extending below the gap, whose field maxima are located in the dielectric. Conversely, the removal of dielectric material has but a limited influence on modes extending above the gap, due to the fact that the thin dielectric shell causes the electromagnetic field to remain pinned inside the air holes.

2 Models for Finite Crystals

Theoretical models for photonic crystals with a finite size fall broadly into two categories. The first class of models includes methods used for the determination of the reflection and transmission properties of the diffraction grating formed by a layer of a photonic crystal. With the exception of certain theories based on the finite element method, these calculation methods generally rely on formulations in terms of transfer, reflection and transmission matrices.

These models apply for instance to the case where the size of the crystal is assumed to be finite along the vertical direction and infinite along the horizontal directions. This assumption allows taking full advantage of the pseudo-periodicity properties of the fields along the horizontal directions, which leads to the possibility of significantly reducing computation times. However, when analysing periodicity defects, it is necessary to turn to the supercell method, already introduced in Section 1.4.3 of Chapter 1.

The second class of models includes methods which apply to crystals with a finite size along any direction of periodicity. This actually amounts to the consideration of a scattering problem, in which the periodicity of the crystal is never taken into account, since in the mathematical sense of the term a periodic structure is necessarily infinite. The development and implementation of such complex methods generally requires a significant effort in terms of numerical analysis and programming. However, the results are worth the effort, as evidenced by the development of numerical codes allowing the resolution of most of the problems that may arise in this field, which have become indispensable tools for the investigation of photonic crystals.

2.1 Transfer, Reflection and Transmission Matrix Formulations

In this section, we shall consider theories based on the notions of transfer, reflection and transmission matrices. These notions appear under various forms in a large variety of methods used in the fields of electromagnetism and acoustics. Therefore, it seemed necessary to present these notions first in a simple case before using them in the description of more complex theoretical methods.

2.1.1 Reflection and Transmission Matrices

For the sake of simplicity, the notions of reflection and transmission matrices will be described here for a two-dimensional crystal presenting a square symmetry. As represented in Fig. 2.1, the crystal is assumed here to be finite along the y direction, but to remain infinite along the x and z directions. The crystal thus defined is but a diffraction grating consisting of a stack of N grids infinite along the x axis, which themselves are formed by infinite rods parallel to the z axis. The assumption is made here that the crystal is illuminated by a monochromatic plane wave whose wavelength, polarization and incidence angle are fixed.

One of the most interesting features of the model based on the diffraction grating model is the possibility of using the numerous studies conducted since the 1970s on diffraction gratings. These theoretical studies have been largely vindicated by experimental results for all wavelength ranges, from X rays to microwaves, and for all types of diffraction gratings. In terms of implementation, not only are these models extremely reliable and versatile, but they have also demonstrated low computation times (Petit 1980; Moharam 1986; Maystre 1993).

A second reason for the interest in the diffraction grating model lies in its capability of predicting phenomena occurring at the interface between the crystal and the air, or the attenuation of the field propagating in the crystal. For instance, in the case of the crystal represented in Fig. 2.1 and for a given band gap, this method can be used for determining the decrease of the transmission as a function of the number N of grids. Numerous examples of such calculations can be found in (Maystre 1994a).

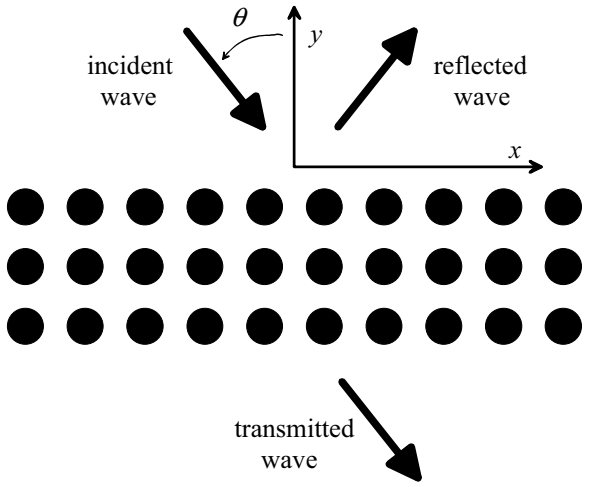

Fig. 2.1. Model of a photonic crystal considered as a diffraction grating

Here again, the mathematical problem to be solved is defined by the two Eqs. 1.2 and 1.3, with the difference however that the permittivity $\varepsilon_r(x,y)$ is no longer periodic along y. In addition to these equations, two supplementary conditions, referred to as the radiation conditions at infinity or as the outgoing waves conditions need to be introduced. The physical meaning of these two conditions is quite obvious:

1. the field reflected above the crystal, and defined as the difference between the total and incident fields, propagates away from the crystal, hence towards $y = +\infty$,
2. the total field transmitted under the crystal propagates away from it, hence towards $y = -\infty$.

By using the concept of a transfer matrix, this problem can be restricted to a single grid. This can be evidenced by considering in Fig. 2.2 the case of one of the grids (numbered $N - 1$) represented in Fig. 2.1, with $a_x = a_y = a$ being the periods along x and y respectively. When the crystal represented in Fig. 2.1 is illuminated by an incident monochromatic plane wave in s (or TM) polarization, it can be demonstrated that the field in the two homogeneous regions R^+ and R^- extending above and beneath the grid can be expressed in the form of plane wave expansions, also known as Rayleigh expansions (Maystre 1993). The two regions are said to be homogeneous in the sense that no straight line parallel to the x axis may cross the rods of the grid in these regions. Accordingly, the plane wave expansions to be considered here are quite different from the expansions that were previously obtained with the plane wave method.

Let us now demonstrate the validity of the plane wave expansion for the simple case where the incidence angle θ is equal to zero. It is known that the polarization of the total field remains the same (either s ou p) as the polarization of the incident field. The total electric field therefore reduces in s-polarization to its component E_z along the z axis. This component, denoted by E in the following, satisfies Eq. 1.37. Further, since the grid is periodic with a period a along the x axis, the total field can be written in the form of a Fourier series, as it would be the case for a Bloch mode not propagating along the x axis, with $k_x = 0$ as $\theta = 0$:

$$E(x,y) = \sum_{n=-\infty}^{+\infty} E_n(y)\exp(i\alpha_n x) \tag{2.1}$$

where:

$$\alpha_n = n\frac{2\pi}{a} \tag{2.2}$$

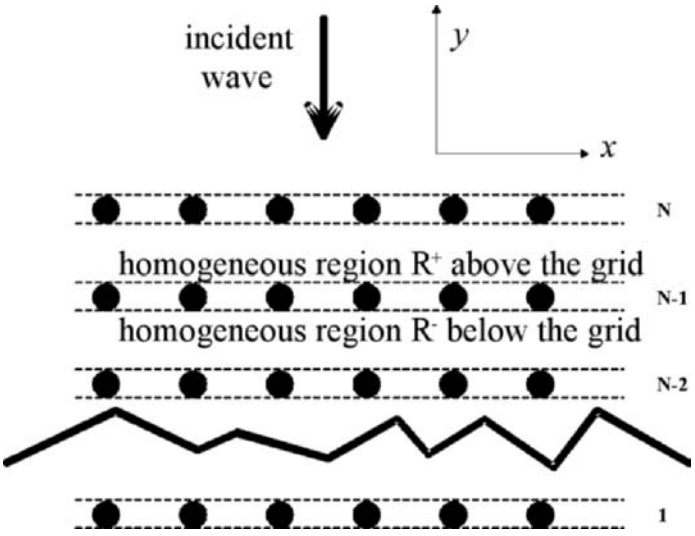

Fig. 2.2. Plane wave expansions in the two homogeneous regions extending along both sides of an arbitrary grid, and numbering scheme for the grids used in Eqs. 2.11 and 2.12

The relative permittivity $\varepsilon_{r,ext}$ is constant in the regions $R^{\pm}$. Therefore, it follows from Eq. 1.37 that the field satisfies the Helmholtz equation:

$$\nabla^2 E + k_0^2 \varepsilon_{r,ext} E = 0 \tag{2.3}$$

Introducing the Fourier expansion of Eq. 2.1 into Eq. 2.3, we are thus presented, in the regions $R^{\pm}$, with solutions of the form:

$$E_n(y) = A_n^{\pm} \exp(-i\beta_n y) + B_n^{\pm} \exp(+i\beta_n y) \tag{2.4}$$

where:

$$\beta_n = \sqrt{k_0^2 \varepsilon_{r,ext} - \alpha_n^2} \quad or \quad i\sqrt{\alpha_n^2 - k_0^2 \varepsilon_{r,ext}} \tag{2.5}$$

The field in the regions $R^{\pm}$ can therefore be written as follows:

$$E(x,y) = \sum_{n=-\infty}^{+\infty} A_n^{\pm} exp\left(i\alpha_n x - i\beta_n y\right) + \sum_{n=-\infty}^{+\infty} B_n^{\pm} exp\left(i\alpha_n x + i\beta_n y\right) \tag{2.6}$$

The expression for the field given by Eq. 2.6 remains valid in the general case where the incidence angle θ is not null, provided however that Eq. 2.2 be replaced with the following equation:

$$\alpha_n = k_0 n_{ext} \sin(\theta) + n\frac{2\pi}{a} \tag{2.7}$$

where n_{ext} denotes the optical index in the regions $R^{\pm}$, as given by the equation:

$$n_{ext} = \sqrt{\varepsilon_{r,ext}} \tag{2.8}$$

It may be noted that, as a consequence of Eq. 2.5, the number of real-valued β_n is finite, and therefore only a finite number of homogeneous plane waves can be retained in the field expansion given in Eq. 2.4. All other plane waves present either an increasing or a decreasing exponential behaviour along the y axis. The first summation represents either homogeneous plane waves propagating towards $y = -\infty$ or evanescent waves exponentially decreasing when y tends towards $-\infty$. Conversely, the second summation represents either homogeneous plane waves propagating towards $y = +\infty$ or evanescent waves exponentially decreasing when y tends towards $+\infty$.

The transfer matrix of the grid expresses the linear relation between the set of coefficients A_n^+ and B_n^+ on the one hand, and the set of coefficients A_n^- and B_n^- on the other hand:

$$\begin{pmatrix} A^+ \\ B^+ \end{pmatrix} = \begin{pmatrix} T_1 & T_2 \\ T_3 & T_4 \end{pmatrix} \begin{pmatrix} A^- \\ B^- \end{pmatrix} \tag{2.9}$$

The column matrices $A^{\pm}$ and $B^{\pm}$ are of infinite order and contain the different coefficients $A_n^{\pm}$ and $B_n^{\pm}$. The four square matrices T_i are therefore also of an infinite order.

An alternative approach would consist in defining scattering matrices rather than transfer matrices. The scattering matrices thus defined link the amplitudes of the waves B^+ and A^- scattered on both sides of the grid in Fig. 2.2, i.e. waves propagating away from the grid or exponentially decreasing with the distance to the grid on the one hand, to the amplitudes of the incident waves A^+ and B^-, i.e. waves propagating towards the grid or exponentially increasing with the distance to the grid on the other hand. In other terms, the scattering matrices express the column matrices B^+ and A^- in terms of the column matrices A^+ and B^-:

$$\begin{pmatrix} B^+ \\ A^- \end{pmatrix} = \begin{pmatrix} S_1 & S_2 \\ S_3 & S_4 \end{pmatrix} \begin{pmatrix} A^+ \\ B^- \end{pmatrix} \tag{2.10}$$

For obvious reasons, the two scattering matrices S_1 and S_4 are referred to as reflection matrices, while the scattering matrices S_2 and S_3 are referred to as transmission matrices.

The equations defining the scattering matrices are direct consequences of the linearity of Maxwell's equations combined with causality relations. The field scattered by a grid, i.e. the field which propagates away from the grid or decreases exponentially with the distance to the grid, can be linearly expressed in terms of the field which generates it, i.e. the field which propagates towards the grid or increases with the distance from the grid. By contrast, demonstrating the existence of transfer matrices is more difficult, since, while linearity is preserved, the causality relation disappears in this case.

The presence, in the definition of the notions of transfer and scattering matrices, of waves whose amplitude increases exponentially with the distance to the grid may seem surprising. It is quite apparent that such waves cannot exist in the case where the grid is not surrounded by other grids. Indeed, the existence of waves with an infinite amplitude at infinity cannot be admitted, since $R^{\pm}$ would also in this case extend at infinity. However, when $R^{\pm}$ is limited in space, there is nothing to prevent such 'anti-evanescent waves' from existing. It suffices to note here that an anti-evanescent wave in the region R^+ is actually an evanescent wave in the upper grid. Accordingly, rejecting the existence of these anti-evanescent waves would amount to denying the existence of evanescent waves.

The transfer and scattering matrices thus defined are identical for all grids, and this is where their primary significance lies. The calculation of these matrices can thus be realized in a single step, irrespective of the actual number of grids in the crystal. It might be emphasized here that the notion of transfer matrix, and more generally of scattering, reflection or transmission matrices, is of central importance in the fields of electromagnetism and acoustics, and that it essentially comes down to the more general notion of invariant in physics. Assuming the crystal to be illuminated by an incident wave, this can be explained in more precise terms by observing that, while the amplitudes of the waves propagating in the regions $R^{\pm}$ are dependent on the number $N^{\pm}$ of grids extending above R^+ and below R^-, the matrices defined above are not. The problem considered here can therefore be decomposed into two successive stages. First, the scattering matrices are calculated for a single grid. The field reflected and transmitted by the entire stack of grids are then determined through basic operations of addition, multiplication and inversion on the matrices thus calculated. The first step can be achieved by using one of the numerical methods described in this chapter (Sections 2.1.2, 2.1.3 and 2.1.4), or some of the methods elaborated within the framework of the theory of diffraction gratings (Petit 1980; Moharam 1986; Maystre 1993). Let us now describe in more detail the second step in the calculations. For this purpose, let us denote by $A_n^{(0)}$ and $B_n^{(0)}$ respectively the coefficients corresponding to the field in the region lo-

cated below the lower grid of the photonic crystal represented in Fig. 2.2. The radiation condition imposes that $\forall n,\ B_n^{(0)} = 0$. Using the matrix relation given by Eq. 2.9 and thus replacing A^+, B^+, A^- and B^- in this equation by $A^{(1)}$, $B^{(1)}$, $A^{(0)}$ and 0 respectively, the column matrices $A^{(1)}$ and $B^{(1)}$ characterizing the field above the lower grid can be expressed in terms only of the column matrix $A^{(0)}$. Further, Eq. 2.9 allows to successively pass through all the grids by simple matrix multiplications. It thus turns out that the two column matrices $A^{(N)}$ and $B^{(N)}$ characterizing the field above the upper grid of the crystal can be expressed in the form of linear combinations of the matrix $A^{(0)}$:

$$A^{(N)} = M_a A^{(0)} \tag{2.11}$$

$$B^{(N)} = M_b A^{(0)} \tag{2.12}$$

$A^{(N)}$ is known from the radiation condition at infinity, due to the fact that the field above the upper grid cannot contain anti-evanescent waves, i.e. waves increasing exponentially when $y \to \infty$. Moreover, the only homogeneous plane wave that may propagate towards the grid is the incident wave. Accordingly, in the column matrix $A^{(N)}$, only the central coefficient $A_0^{(N)}$ remains nonzero, and its amplitude is equal to the amplitude of the incident wave, which itself is known. Therefore, inverting the matrix M_a after having proceeded to its truncation allows the determination, using Eq. 2.11, of the field transmitted by the crystal. This field is defined by the column matrix $A^{(0)}$. Further, Eq. 2.12 yields the field reflected by the crystal and defined by the column matrix $B^{(N)}$. The truncation is realized by restricting all coefficients $A_i^{(n)}$ and $B_i^{(n)}$ in all column matrices $A^{(n)}$ and $B^{(n)}$, where $n \in (0, N)$, to coefficients with index i ranging from $-P$ to $+P$.

Actually, scattering matrices can be used instead of the transfer matrices. In this case, it can be easily demonstrated that, proceeding from the lowest to the upper grid, the reflected and transmitted fields can be obtained through matrix multiplications and inversions. From a numerical point of view, it should be pointed out that, due to the larger number of grids present in the stack, scattering matrix formulations present a higher degree of stability than transfer matrix formulations, and therefore they should be preferred over the latter. Finally, it might be noted that, in contrast to the structure represented in Fig. 2.1, certain photonic crystals do not present any homogeneous region, since the upper part of a grid may overhang over the lower part of the grid extending above. An example would be the case of a two-dimensional photonic crystal with a hexagonal symmetry, where the ratio of the diameter of the rods over the period is larger than a certain critical value. In such a case, the method described here becomes inapplicable. However, as will be discussed in the following section, this method can be extended to apply to such situations.

2.1.2 Pendry Method

Like the method described in the preceding section, the Pendry method will be presented in the specific case of an *s*-polarized plane wave incident onto a two-dimensional crystal with a square symmetry. Accordingly, all derivatives with respect to *z* will be zero. The Pendry method (Pendry 1994) is essentially numerical in nature, in the sense that it uses Maxwell's equations in a very direct way, without requiring a complex preliminary mathematical apparatus.

In the case where the incident angle is zero, Eqs. 1.2 and 1.3 become in *s*-polarization:

$$\frac{1}{i\omega\mu_0}\frac{\partial E_z}{\partial y} = H_x \tag{2.13}$$

$$-\frac{1}{i\omega\mu_0}\frac{\partial E_z}{\partial x} = H_y \tag{2.14}$$

$$\frac{1}{-i\omega\varepsilon_0\varepsilon_r}\left(\frac{\partial H_y}{\partial x} - \frac{\partial H_x}{\partial y}\right) = E_z \tag{2.15}$$

Eq. 2.13 entails that the *y*-derivative of the field E_z can be expressed in terms of the component H_x of the magnetic field:

$$\frac{\partial E_z}{\partial y} = i\omega\mu_0 H_x \tag{2.16}$$

Likewise, it is be easily demonstrated that the *y*-derivative of H_x can be expressed from the component E_z of the electric field and from its *x*-derivatives. To this purpose, it suffices to introduce the expression for H_y given by Eq. 2.14 in Eq. 2.15. This leads to the following equation:

$$\frac{\partial H_x}{\partial y} = i\omega\varepsilon_0\varepsilon_r E_z - \frac{i}{\omega\mu_0}\frac{\partial^2 E_z}{\partial x^2} \tag{2.17}$$

The (x,y) space is discretized by using elementary meshes with widths χ along *x* and τ along *y* respectively. The discretization thus performed allows us to use the classical formulas for the approximation of derivatives:

$$\frac{\partial H_x}{\partial y} \cong \frac{H_x(x, y+\tau) - H_x(x, y)}{\tau} \tag{2.18}$$

$$\frac{\partial E_z}{\partial y} \cong \frac{E_z(x, y+\tau) - E_z(x, y)}{\tau} \tag{2.19}$$

$$\frac{\partial^2 E_z}{\partial x^2} \cong \frac{E_z(x+\chi, y) + E_z(x-\chi, y) - 2E_z(x, y)}{\chi^2} \tag{2.20}$$

Introducing approximations of the derivatives in Eqs. 2.16 and 2.17, the values of the field at the ordinate $y + \tau$ can then be deduced from its values at the ordinate y :

$$E_z(x, y+\tau) \cong E_z(x, y) + i\omega\mu_0\tau H_x(x, y) \tag{2.21}$$

$$H_x(x, y+\tau) \cong H_x(x, y) + i\frac{\tau}{\omega\mu_0\chi^2}\left[E_z(x+\chi, y) + E_z(x-\chi, y) + \left(k_0^2\varepsilon_r\chi^2 - 2\right)E_z(x, y)\right] \tag{2.22}$$

Determination of the Dispersion Relations in a Periodic Crystal

In this section, we shall first demonstrate that, in the simple case of an infinite crystal with a square symmetry, Eqs. 2.21 and 2.22 allow the determination of the dispersion relations. For this purpose, the values for the widths of the elementary meshes used in the discretization of space will be set to $\tau = \chi = a/M$, where a is the period of the crystal and M is the number of points at each side of the elementary mesh. Fig. 2.3 provides a schematic representation of the discretization thus defined.

The origin of the axes is located at the bottom-left corner of the cell. We assume here that the values for the fields E_z and H_x at the M points P_m ($m \in (1, M)$) with coordinates $\{y = 0, x = (m-1)\tau\}$ are already known, and we proceed by introducing, in the two column matrices $\mathbf{E}_z(0)$ and $\mathbf{H}_x(0)$ respectively, the M values for $E_z(x, 0)$ and $H_x(x, 0)$ at the points P_m.

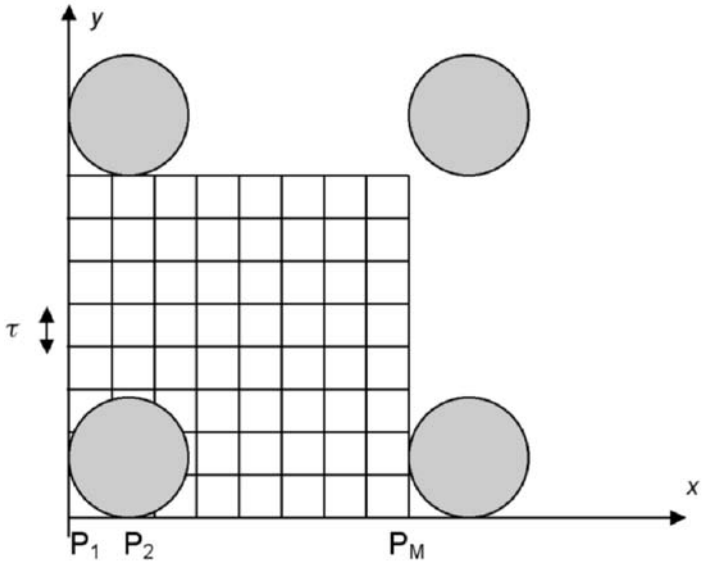

Fig. 2.3. Discretization of the elementary mesh of a two-dimensional photonic crystal with a square symmetry

The problem then consists in searching for pseudo-periodic solutions satisfying equations analogous to Eq. 1.22. In turn, this will allow us to determine, from the components $\mathbf{E}_z(0)$ and $\mathbf{H}_x(0)$, the values of the components E_z and H_x at any point with coordinates $\{y = 0, x = (m - 1)\tau\}$, where m is now an arbitrary relative number. Consequently, the values of the field will be known at any discretization point located along the y axis. As an example, the following equation yields the value of $E_z(a, 0)$:

$$E_z(a,0) = E_z(0,0)\,exp(ik_x a) \tag{2.23}$$

Eqs. 2.21 and 2.22 therefore allow us to express the field at any discretization point along the line $y = \tau$ as a linear combination of the M components of $\mathbf{E}_z(0)$ and $\mathbf{H}_x(0)$, which amounts to saying that $\mathbf{E}_z(\tau)$ and $\mathbf{H}_x(\tau)$ can be expressed in terms of a linear combination of $\mathbf{E}_z(0)$ and $\mathbf{H}_x(0)$. Thus, by proceeding step by step along the y axis, $\mathbf{E}_z(a)$ and $\mathbf{H}_x(a)$ can be expressed in the form of linear combinations of the matrices $\mathbf{E}_z(0)$ and $\mathbf{H}_x(0)$:

$$\mathbf{E}_z(a) = O\mathbf{E}_z(0) + P\mathbf{H}_x(0) \tag{2.24}$$

$$\mathbf{H}_x(a) = Q\mathbf{E}_z(0) + R\mathbf{H}_x(0) \tag{2.25}$$

where O, P, Q and R are square matrices of size $M \times M$.

Further, the relation of pseudo-periodicity given by Eq. 1.22 provides yet another way of expressing $\mathbf{E}_z$(a) in terms of $\mathbf{E}_z(0)$. Indeed, the following equation holds:

$$E_z(x,a) = E_z(x,0)\exp\left(ik_y a\right) \tag{2.26}$$

The same applies to the component H_x. This leads to the following two equations:

$$\mathbf{E}_z(a) = L\mathbf{E}_z(0) \tag{2.27}$$

$$\mathbf{H}_x(a) = L\mathbf{H}_x(0) \tag{2.28}$$

where L is a diagonal square matrix of size $M \times M$, whose diagonal terms are equal to $\exp(ik_y a)$. It is therefore quite straightforward to deduce from Eqs. 2.24, 2.25, 2.27 and 2.28 that:

$$(O - L)\mathbf{E}_z(0) + P\mathbf{H}_x(0) = 0 \tag{2.29}$$

$$Q\mathbf{E}_z(0) + (R - L)\mathbf{H}_x(0) = 0 \tag{2.30}$$

These two equations can be rewritten in the form of a linear system of $2M$ equations with $2M$ unknowns:

$$U\mathbf{F}(0) = 0 \tag{2.31}$$

The column matrix $\mathbf{F}(0)$ of size $2M$ in this system contains successively the two column matrices $\mathbf{E}_z(0)$ and $\mathbf{H}_x(0)$, while the square matrix U of size $2M \times 2M$ is given by the equation:

$$U = \begin{pmatrix} O - L & P \\ Q & R - L \end{pmatrix} \tag{2.32}$$

The homogeneous linear system represented by Eq. 2.31 admits a non-null solution only in the case where the determinant of U is zero. Therefore, for a given

value ω of the frequency, the characteristics of the Bloch waves associated with the infinite crystal will be obtained by determining the values of k_x and k_y at which the determinant of U becomes zero:

$$\det\left[U(k_x, k_y)\right] = 0 \tag{2.33}$$

Application to Finite Crystals

We shall now consider the case of a photonic crystal with a finite width, i.e. a photonic crystal consisting of a finite number of grids assumed to be infinite along the horizontal directions, as represented in Fig. 2.1. The discretization used here is the same as in Fig. 2.3, with the difference however that the origin is now located at the bottom of the lowest grid, while the discretization process is continued along the y axis in such a way that the upper part of the mesh at $y = h$ will be located over the upper grid (Fig. 2.4). Applying the same method as in the case of an infinite photonic crystal, the column matrices $\mathbf{E}_z(h)$ and $\mathbf{H}_x(h)$ can be expressed through a linear combination of matrices $\mathbf{E}_z(0)$ and $\mathbf{H}_x(0)$:

$$\mathbf{E}_z(h) = O'\mathbf{E}_z(0) + P'\mathbf{H}_x(0) \tag{2.34}$$

$$\mathbf{H}_x(h) = Q'\mathbf{E}_z(0) + R'\mathbf{H}_x(0) \tag{2.35}$$

In normal incidence, it is necessary for this purpose to replace equations like Eq. 1.22, which express the pseudo-periodicity of the Bloch waves, with equations expressing the periodicity of the fields along the x axis. In the case of a non-normal incidence, another pseudo-periodicity equation can be readily derived from Eqs 2.6 and 2.7:

$$E_z(x + a, y) = exp\left(ik_0\sqrt{\varepsilon_{r,ext}}\, a\, sin(\theta)\right)E_z(x, y) \tag{2.36}$$

Eqs. 2.34 and 2.35 form two matrix equations linking the four column matrices $\mathbf{E}_z(0)$, $\mathbf{H}_x(0)$, $\mathbf{E}_z(h)$ and $\mathbf{H}_x(h)$. The two other equations can be determined using the radiation conditions. A simple way of deducing these equations is by demonstrating that the four column matrices can be expressed as a linear combination of two new column matrices. These two matrices can then be calculated from Eqs. 2.34 and 2.35 alone.

Let us now describe this method in more precise terms. The radiation condition imposes that the field in the region below the crystal propagates away from the crystal, hence towards $y = -\infty$. As a consequence, the coefficients B_n^- in the ex-

pression of the field given by Eq. 2.6 become zero. Therefore, if $y < 0$, then the field beneath the crystal can be written in the form:

$$E_z(x,y) = \sum_{n=-\infty}^{+\infty} A_n^- \, exp\left(i\alpha_n x - i\beta_n y\right) \tag{2.37}$$

Likewise, above the crystal, the amplitudes of the plane waves propagating towards the crystal become zero, the only exception being the amplitude of the incident wave. Therefore, if $y > h$, the field above the crystal can be expressed in the following form:

$$E_z(x,y) = A_0^+ \, exp\left(i\alpha_0 x - i\beta_0 y\right) + \sum_{n=-\infty}^{+\infty} B_n^+ \, exp\left(i\alpha_n x + i\beta_n y\right) \tag{2.38}$$

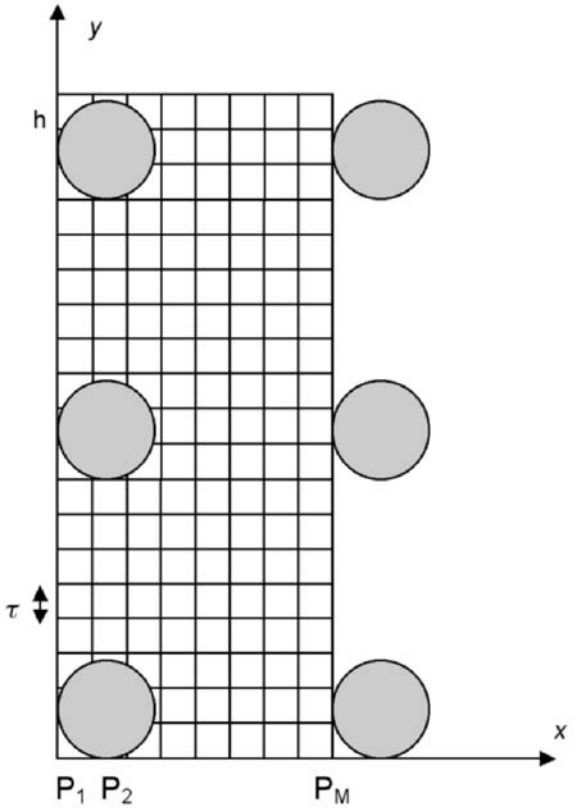

Fig. 2.4. Spatial discretization for a crystal with finite width

Eq. 2.13 allows deriving an expression for H_x from Eqs. 2.37 and 2.38:

– if $y < 0$:

$$H_x(x,y) = \frac{-1}{\omega\mu_0} \sum_{n=-\infty}^{+\infty} \beta_n A_n^- \exp\left(i\alpha_n x - i\beta_n y\right) \tag{2.39}$$

– if $y > h$:

$$H_x(x,y) = \frac{1}{\omega\mu_0}\left(-\beta_0 A_0^+ \exp\left(i\alpha_0 x - i\beta_0 y\right) + \sum_{n=-\infty}^{+\infty} \beta_n B_n^+ \exp\left(i\alpha_n x + i\beta_n y\right)\right) \tag{2.40}$$

For the purpose of expressing Eqs. 2.37 to 2.40 in matrix form, let us define two column matrices $\mathbf{A}^-$ and $\mathbf{B}^+$ of odd order $2P + 1$, where P is a positive integer, containing the amplitudes A_n^-, $n \in [-P,+P]$ and B_n^+, $n \in [-P,+P]$. The assumption will me made from this point onwards that the number M of discretization points along x in the elementary mesh is odd as well, and that this number is equal to $2P + 1$. Assuming for the sake of simplicity that the amplitude A_0^+ of the incident plane wave is equal to unity, elementary calculations allow us to reach the conclusion that Eqs. 2.37 to 2.40 can be written in the form of the following matrix equations:

$$\mathbf{E}_z(0) = \Gamma_E^- \mathbf{A}^- \tag{2.41}$$

$$\mathbf{H}_x(0) = \Gamma_H^- \mathbf{A}^- \tag{2.42}$$

$$\mathbf{E}_z(h) = \mathbf{E}_z^0 + \Gamma_E^+ \mathbf{B}^+ \tag{2.43}$$

$$\mathbf{H}_x(h) = \mathbf{H}_x^0 + \Gamma_H^+ \mathbf{B}^+ \tag{2.44}$$

where $\mathbf{E}_z^0$ and $\mathbf{H}_x^0$ are two column matrices defined by the equations:

$$\left(\mathbf{E}_z^0\right)_m = \exp\left(i\alpha_0 x_m - i\beta_0 h\right) \tag{2.45}$$

$$\left(\mathbf{H}_x^0\right)_m = \frac{-\beta_0}{\omega\mu_0} \exp\left(i\alpha_0 x_m - i\beta_0 h\right) \tag{2.46}$$

while Γ_E^-, Γ_H^-, Γ_E^+ and Γ_H^+ are square matrices respectively defined as follows :

$$\left(\Gamma_E^-\right)_{m,n} = exp\left(i\alpha_n x_m\right) \tag{2.47}$$

$$\left(\Gamma_H^-\right)_{m,n} = \frac{-\beta_0}{\omega\mu_0} exp\left(i\alpha_n x_m\right) \tag{2.48}$$

$$\left(\Gamma_E^+\right)_{m,n} = exp\left(i\alpha_n x_m + i\beta_n h\right) \tag{2.49}$$

$$\left(\Gamma_H^+\right)_{m,n} = \frac{\beta_0}{\omega\mu_0} exp\left(i\alpha_n x_m + i\beta_n h\right) \tag{2.50}$$

The values of x_i are the abscissas of the discretization points along the x direction in the elementary mesh:

$$x_m = (m-1)\frac{a}{M} \tag{2.51}$$

Introducing in Eqs. 2.34 and 2.35 the expressions given by Eqs. 2.41 to 2.44 respectively of the four column matrices $\mathbf{E}_z(0)$ $\mathbf{H}_x(0)$ $\mathbf{E}_z(h)$ and $\mathbf{H}_x(h)$, it turns out, after proceeding to tedious, albeit elementary, calculations that:

$$\mathsf{V}\mathbf{F}(0) = \mathbf{S} \tag{2.52}$$

where V is a square matrix of size $2M = 4P + 2$, defined in the following way:

$$\mathsf{V} = \begin{pmatrix} -\Gamma_E^+ & O'\Gamma_E^- + P'\Gamma_H^- \\ -\Gamma_H^+ & Q'\Gamma_E^- + R'\Gamma_H^- \end{pmatrix} \tag{2.53}$$

while $\mathbf{S}$ and $\mathbf{F}(0)$ are column matrices of size $2M$, defined by the two following equations respectively:

$$\mathbf{S} = \begin{pmatrix} \mathbf{E_z^0} \\ \mathbf{H_x^0} \end{pmatrix} \tag{2.54}$$

$$\mathbf{F}(0) = \begin{pmatrix} \mathbf{E}_z(0) \\ \mathbf{H}_x(0) \end{pmatrix}$$

The inversion of the linear system in Eq. 2.52 permits the direct calculation of the reflected and transmitted amplitudes. The efficiencies ρ_n and τ_n, i.e. the ratios of the reflected or transmitted energies respectively over the incident energy in the different orders of the grating, are given by (Maystre 1993):

$$\rho_n = \frac{\beta_n}{\beta_0}\left|B_n^+\right|^2 \tag{2.55}$$

$$\tau_n = \frac{\beta_n}{\beta_0}\left|A_n^-\right|^2 \tag{2.56}$$

The Pendry method is thus particularly simple as regards both its theoretical development and its numerical implementation. The precision of the results could actually be improved by using a slightly more complicated meshing process, where the discretization points along y for H_x would be shifted from half an interval $a/2M$ with respect to the discretization points for E_z. This applies more specifically to Eqs. 2.16 and 2.17, as will be described in the next section.

2.2 Finite Difference in Time Domain (FDTD) Method

2.2.1 Numerical Formulation of Maxwell's Equations

In contrast to the Pendry method, the FDTD method can be listed among the general numerical methods in electromagnetism. Its originality lies in the preliminary resolution of a scattering problem in the time domain rather than in the frequency domain. The harmonic solutions are obtained in a second stage by a Fourier transformation in time. As will be seen, one of the main advantages of this method lies in the fact that it does not require any matrix inversion. Of course, an exhaustive description of the different existing versions of this method would be largely beyond the scope of this book, and the interested reader is referred for a more extensive presentation, to the original article by K S. Yee (Yee 1966) or to the book by A. Taflove (Taflove 1995). Descriptions of this method more specifically adapted to the case of photonic crystals can be found in (Joannopoulos 1995b; Reineix 1996).

Since we consider in this section non-harmonic time-dependent fields, we shall be led for the time being to abandon the notion of the complex amplitude of the fields. Accordingly, the problem to be addressed will be the determination of the total field at any time t and at any point of space when a time-dependent field strikes a photonic crystal with finite size. For the sake of simplicity, we retain the model of a two-dimensional photonic crystal illuminated by an *s*-polarized incident wave. Let us now consider the component $E_z\ (x, y, t)$ of the electric field

along the z axis. Like the magnetic field $\mathbf{H}(x, y, t)$, this component must satisfy the time-dependent Maxwell's equations. For non-dispersive materials, these equations assume the following form:

$$\nabla \times E\hat{\mathbf{z}} = -\mu_0 \frac{\partial \mathbf{H}}{\partial t} \tag{2.57}$$

$$\nabla \times \mathbf{H} = \varepsilon_0 \varepsilon_r \frac{\partial E}{\partial t} \hat{\mathbf{z}} \tag{2.58}$$

As an example, in the case of a Gaussian pulse with a plane wave front, the component E^i along z of the time-dependent incident field is given by:

$$E^i = exp\left[-\left(t - t_0 - \frac{\mathbf{u.r}}{\mathrm{v}} \right)^2 \Big/ \Delta t^2 \right] \tag{2.59}$$

where v denotes the velocity of the pulse, $\mathbf{u}$ is a unit vector oriented along the direction of propagation, t_0 is the reference time and Δt is the width of the pulse. By contrast, in the case of a sinusoidal wave with a plane wavefront reaching the origin at time $t = t_0$, the equation for the incident field assumes the following form:

$$E^i = sin\left[\omega\left(t - \frac{\mathbf{u.r}}{\mathrm{v}} \right) \right] \times \theta\left(t - t_0 - \frac{\mathbf{u.r}}{\mathrm{v}} \right) \tag{2.60}$$

where $\theta(t)$ is the Heaviside function which takes the value 0 for $t < 0$ and is equal to unity for $t > 0$. The assumption is made here that at $t < 0$, the incident field is zero in the region surrounding the crystal. This region will be defined in more precise terms for $t < 0$ in the course of this section.

In the same way as in the Pendry method, Maxwell's equations are first projected onto the axes, before being discretized along x, y and t. The projection of Eqs. 2.57 and 2.58 onto the axes yields the following equations:

$$\frac{\partial E_z}{\partial y} = -\mu_0 \frac{\partial H_x}{\partial t} \tag{2.61}$$

$$\frac{\partial E_z}{\partial x} = \mu_0 \frac{\partial H_y}{\partial t} \tag{2.62}$$

$$\frac{\partial H_y}{\partial x} - \frac{\partial H_x}{\partial y} = \varepsilon_0 \varepsilon_r \frac{\partial E_z}{\partial t} \tag{2.63}$$

In order to proceed to the discretization of these equations, we adopt here the two following rules. First, the component E_z of the electric field will be calculated at the times $t = n\Delta t$, where n is a positive or null integer, while the two components of the magnetic field will be calculated at the times $t = (n + 1/2)\Delta t$. Secondly, the three components of the field will be calculated at precise locations in space, represented in Fig. 2.5 and defined as follows :

- for E_z, [$x = i\Delta x$ and $y = j\Delta y$], where i and j are integers,
- for H_x, [$x = i\Delta x$ and $y = (j + 1/2)\Delta y$],
- for H_y, [$x = (i + 1/2)\Delta x$ and $y = j\Delta y$].

The theoretical justification for this discretization, which originates in the integral form of Ampere's and Faraday's laws (Taflove 1995), will not be discussed here. It suffices to observe that this discretization allows rewriting Maxwell's equations by replacing the space and time derivatives with centred finite differences. The term 'centred finite difference' is used here to refer to the following approximation of the derivative:

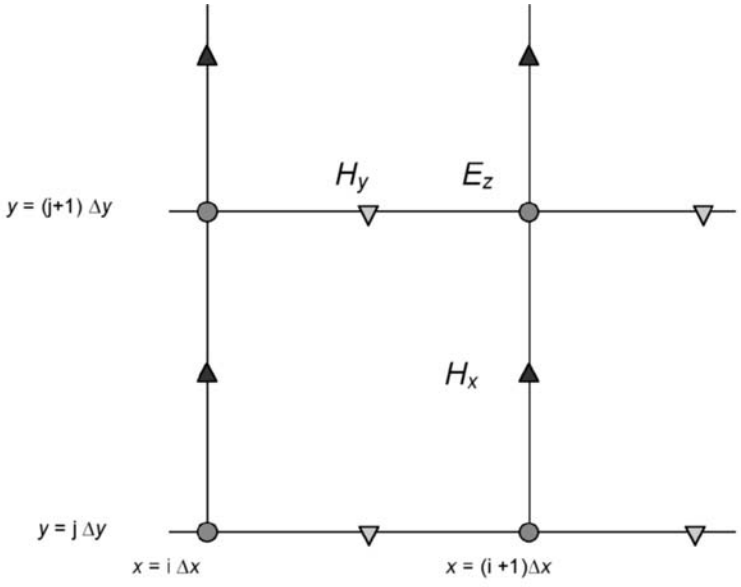

Fig. 2.5. Spatial discretization used in the FDTD method: the circles, triangles and inverted triangles represent the discretization points used for E_z, H_x and H_y respectively

$$\frac{df}{du}(u_0) \cong \frac{f(u_0 + \Delta u) - f(u_0 - \Delta u)}{2\Delta u} \tag{2.64}$$

This approximation leads to an error of the second order in Δu. It might be noted in this respect that non-centred finite differences of the type used in the Pendry method (Eqs. 2.18 and 2.19) lead to an error of the first order.

For the purpose of presenting the finite difference equations in a form as convenient as possible, we shall adopt here the conventions introduced by A. Taflove, which consists in representing the value of any arbitrary component $U(\psi\Delta x, \zeta\Delta y, \xi\Delta t)$ of the fields in the form $U\Big|_{\psi,\zeta}^{\xi}$. As an example, the value $E_z(i\Delta x, j\Delta y, n\Delta t)$ of the electric field at the point located in the bottom-left corner of Fig. 2.5 ($x = i\Delta x$, $y = j\Delta y$) and at a time $t = n\Delta t$, will be written in the form $E_z\Big|_{i,j}^{n}$.

Eqs. 2.61, 2.62 and 2.63 thus become:

$$E_z\Big|_{i,j}^{n} = E_z\Big|_{i,j}^{n-1} + \frac{\Delta t}{\Delta y \varepsilon_0 \varepsilon_r\Big|_{i,j}} \times \tag{2.65a}$$

$$\left(\frac{H_y\Big|_{i+\frac{1}{2},j}^{n-\frac{1}{2}} - H_y\Big|_{i-\frac{1}{2},j}^{n-\frac{1}{2}}}{\Delta x} - \frac{H_x\Big|_{i,j+\frac{1}{2}}^{n-\frac{1}{2}} - H_x\Big|_{i,j-\frac{1}{2}}^{n-\frac{1}{2}}}{\Delta y} \right)$$

$$H_x\Big|_{i,j+\frac{1}{2}}^{n+\frac{1}{2}} = H_x\Big|_{i,j+\frac{1}{2}}^{n-\frac{1}{2}} - \frac{\Delta t}{\Delta y \mu_0} \times \left(E_z\Big|_{i,j+1}^{n} - E_z\Big|_{i,j}^{n} \right) \tag{2.66a}$$

$$H_y\Big|_{i+\frac{1}{2},j}^{n+\frac{1}{2}} = H_y\Big|_{i+\frac{1}{2},j}^{n-\frac{1}{2}} + \frac{\Delta t}{\Delta x \mu_0} \times \left(E_z\Big|_{i+1,j}^{n} - E_z\Big|_{i,j}^{n} \right) \tag{2.67a}$$

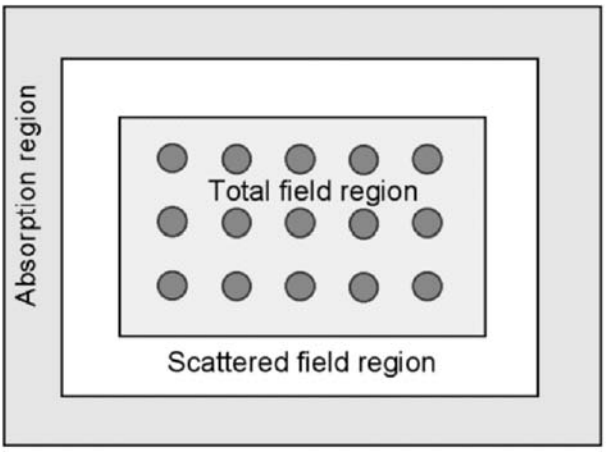

Fig. 2.6. Discretization realized by decomposing the region of space considered into a total field region and a scattered field region. The latter includes an absorption region

These three equations will be alternately used for calculating the time variations of the components of the electric and magnetic fields. Indeed, these equations allow the determination of the components of the field at time t from the values of the same components at times $(t - \Delta t)$ and $(t - \Delta t/2)$. Since the incident field, and, consequently, the total field for reasons pertaining to causality, are zero in the discretized domain when $t \leq 0$, Eqs. 2.66a and 2.67a can be used for determining the two components of the magnetic field at time $\Delta t/2$. The value of the electric field at time Δt, can then be determined from Eq. 2.65a, and so forth. However, it should be pointed out that, since Eqs. 2.66a and 2.67a as they stand now are homogeneous, this process obviously leads to values of the fields equal to zero at any time. This actually is not surprising in view of the fact that the existence of an incident field has not been taken into account yet in these equations. As will be described hereafter in Section 2.2.2, the existence of this incident field entails the necessity of introducing complementary terms in the equations. As a result, these equations will no longer remain homogeneous. The case of an incident pulse will be discussed first, before turning to the consideration of a point source emitting in the vicinity of the crystal.

2.2.2 Case of an Incident Pulse

The approach described in this section is based on the 'total field - scattered field' formulation. In this theory, the discretization proceeds by dividing the region of space considered into two subregions: a total field region extending from the centre and a scattered field region surrounding the first region (Fig. 2.6).

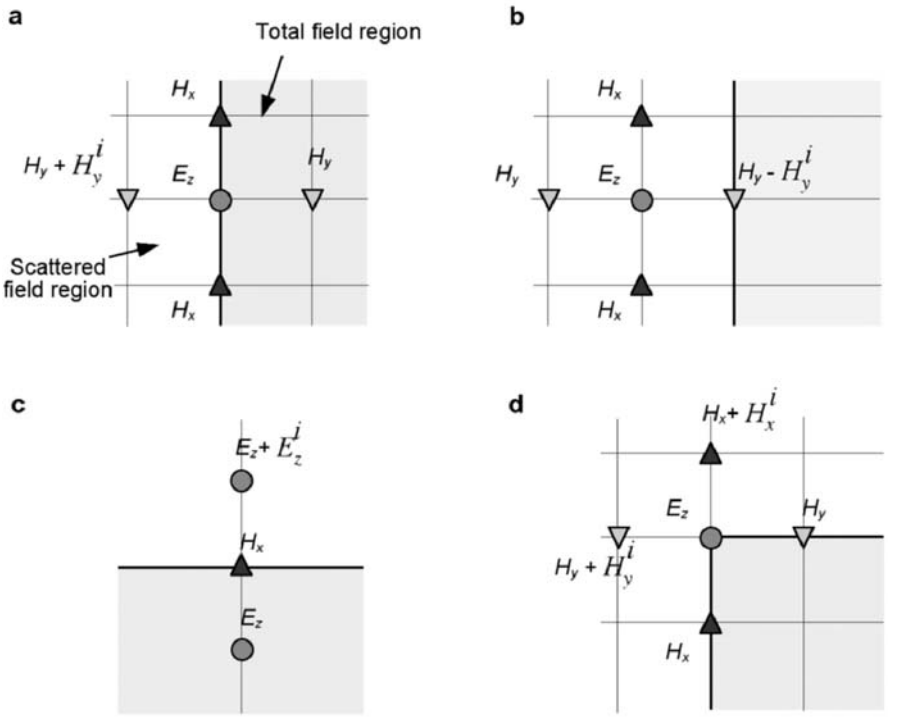

Fig. 2.7. Schematic illustration of the rules used for introducing the incident field at the boundary between the total field region and the scattered field region. In each case, the boundary between these two regions is represented by a thick line, while the meshes used in the numerical calculations are represented by thin lines. E_z^i, H_x^i and H_y^i denote the components of the incident field, while the discretization points for E_z, H_x and H_y are denoted by the same symbols as in Fig. 2.5. The examples represented in the figure are: *a.* Eq. 2.65a, calculation of E_z at the boundary *b*. Eq. 2.65a, calculation of E_z near the boundary in the scattered field region *c.* Eq. 2.66a, calculation of H_x at the boundary *d.* Eq. 2.65a, calculation of E_z at one of the corners of the rectangle delimiting the boundary (Fig. 2.6)

The scattered field region must be homogeneous, which is to say that it must extend outside the region containing the photonic crystal. The scattered field in this region is classically defined as the difference between the total and incident field. The components of the field involved in Eqs. 2.65a, 2.66a and 2.67a will be either identical with the components of the scattered field in the scattered field region, or equal to the total field in the total field region. The boundary between these two regions forms a rectangle whose sides include the points represented in Fig. 2.5. This boundary is considered as belonging to the total field region.

Of course, it would be incorrect to introduce the scattered field at some points in the mesh, and the total field at some other points, while leaving unchanged Eqs.

2.65a, 2.66a and 2.67a. A correct description requires that, when the equations simultaneously contain discretization points in the two separate regions, the incident field should be either added, for points in the scattered field region, or subtracted, for points in the total field region. The first or the second rule is used depending on whether the discretization point corresponding to the left-hand side of the equation is located in the total field region or in the scattered field region, respectively. Fig. 2.7 illustrates the application of these rules in some examples.

2.2.3 Absorption Region and Boundary Conditions

At first sight, the scattering problem may appear to have been solved entirely. Indeed, the use of Eqs 2.65a, 2.66a and 2.67a allows the determination of the time-dependence of the total field in the total field region and of the scattered field in the scattered field region, provided that the simple rules previously described are followed when introducing the incident field. However, it should be noted here that the scattered field region cannot extend at infinity in space. Therefore, for discretization points associated with the left-hand side of Eqs. 2.65a, 2.66a and 2.67a located at the external boundary of this region, certain discretization points associated with the right-hand side of this equation will inevitably be located outside this region. A seemingly simple method for overcoming this problem would consist in merely ignoring the corresponding points, i.e. in truncating Eqs. 2.65a, 2.66a and 2.67a in such a way as to retain only terms associated with points located in the scattered field region. However, it is quite clear that this approach results in dramatic consequences for the calculation of the field. Indeed, arbitrarily cancelling the terms corresponding to the points located outside the scattered field region amounts to assuming that the scattered field is actually zero outside this region. The boundary condition artificially introduced is therefore incorrect, as it fails to satisfy the rigorous boundary value problem defined by the elementary laws of electromagnetism, which states that the scattered field does not vanish outside the discretized domain. By causality, since the scattered field is continuous at the boundary of this region, it satisfies a radiation condition at infinity, whence it follows that it propagates away from the crystal. It thus turns out that this approach introduces parasitic and artificial reflection phenomena at the boundary, and therefore it must be abandoned.

Since the scattered field region cannot extend at infinity, an alternative approach consists in including an absorption region extending around the external boundary of the scattered field region. This region should be defined in such a way as to progressively absorb the scattered field without generating any artificial reflection phenomena. If such a region can be realized, then the field scattered outside the discretized domain might be assumed to be zero. Indeed, since the scattered field will be almost zero beyond the absorption region, this assumption does not entail any noticeable consequence as regards the validity of the calculations. Further, since this absorption region does not generate any artificial reflection of the scattered field, the radiation condition is satisfied. Interestingly enough, this approach reproduces at a theoretical level the experimental arrangement adopted

for microwave measurements in anechoic chambers, where in order not to perturb the measurement of the field scattered by an object located at the centre of the chamber, an absorbing material is used for covering the walls and thus for preventing any reflection from occurring.

The research of efficient absorbing conditions is probably the issue related to the FDTD method which has led to the most subtle investigations. The interested reader will find a more detailed exposition of these studies in (Taflove 1995). Roughly speaking, the absorption region is realized by introducing lossy materials with a conductivity different from zero. This can be attempted for instance by giving ε_r a complex value in this region. This solution presents the advantage that Eqs. 2.65a, 2.66a and 2.67a will remain almost the same save for the change in the permittivity of the absorption region. However, it is obvious that such an approach is too simplistic. Finding a material that would totally absorb a scattered field without generating any reflection is far from being a trivial task. Indeed, this condition implies, that, whatever the angle of incidence is, an incident plane wave arriving at the interface of such a material will not generate any reflection. Without going into detail here, the most efficient method to date appears to be the method developed by JP Bérenger (Bérenger 1994). The perfectly matched layer (PML) formulation suggested by this author takes a step beyond the introduction in Maxwell's equations of the complex permittivity and permeability, by splitting E_z into two parts with different electromagnetic constants. This method is remarkably efficient since the width of the absorption region can generally be limited to a number of elementary meshes of the order of five.

2.2.4 Practical Implementation and Convergence of the FDTD Method

The implementation of the FDTD method can be separated into three stages. In the first stage, which might be referred to as the null-field stage, the wavefront of the incident field has not reached the discretized domain yet. Eqs. 2.65a, 2.66a and 2.67a are homogeneous and the total field is zero at any point. In the second step, referred to as the illumination stage, the incident field has now reached the discretized domain. It must therefore be introduced in the equations at the boundary between the scattered field region and the total field region, or immediately outside this boundary, as represented in Fig. 2.7. Accordingly, the total field is no longer zero. Finally, in the third stage, referred to as the relaxation stage, the incident field has moved beyond the discretized domain and therefore it tends towards zero in this domain. In this case, no correction is needed in Eqs. 2.65a, 2.66a and 2.67a for introducing the incident field, and the equations return to being homogeneous. In contrast to the first situation, the field is not at the beginning of the relaxation stage immediately zero, but it is expected that it will tend towards zero at the end of this stage, since the radiation losses of the scattered field are not compensated by any incident field.

It is obvious that the third stage will assume quite a different form if the incident field is a sinusoidal wave of the form given by Eq. 2.60 rather than an electromagnetic pulse of the type described by Eq. 2.59. In such a case, the incident

field remains non-zero and the relaxation step actually becomes a stabilization step, at which the field tends towards a time-harmonic behaviour.

In terms of calculations, the process described above represents an ideal case. However, things may turn out quite differently in practice. In particular, calculations may diverge when time increases, for instance at the third step in the calculations. The possibility that such a divergence may occur can be explained in the following terms. Let us first represent Eqs. 2.65a, 2.66a and 2.67a using an operator notation. At any given time, all the values of the discretized field are ordered in column matrices. Thus, $E_z(n)$ will represent the set of values $E_z\Big|_{i,j}^{n}$ for all i and j, while $H_x(n - 1/2)$ and $H_y(n - 1/2)$ will represent the sets of values $H_x\Big|_{i,j+\frac{1}{2}}^{n-\frac{1}{2}}$ and $H_y\Big|_{i+\frac{1}{2},j}^{n-\frac{1}{2}}$ respectively. Using this symbolic notation, Eqs 2.65a to 2.67a now assume the following form:

$$E_z(n+1) = E_z(n) + O_1 H_x(n+1/2) + O_2 H_y(n+1/2) \tag{2.65b}$$

$$H_x(n+1/2) = H_x(n-1/2) + O_3 E_z(n) \tag{2.66b}$$

$$H_y(n+1/2) = H_y(n-1/2) + O_4 E_z(n) \tag{2.67b}$$

where the operators O_i can easily be deduced from Eqs. 2.65a to 2.67a.

Introducing the right-hand sides of Eqs. 2.66b and 2.67b into Eq. 2.65b, we arrive at the following equation:

$$\begin{aligned} E_z(n+1) &= E_z(n) + O_1\left(H_x(n-1/2) + O_3 E_z(n)\right) + O_2\left(H_y(n-1/2) + O_4 E_z(n)\right) \\ &= O_5 E_z(n) + O_6 H_x(n-1/2) + O_7 H_y(n-1/2) \end{aligned} \tag{2.65c}$$

Further, by converting the three column matrices $E_z(n)$, $H_x(n - 1/2)$ and $H_y(n - 1/2)$ into a unique column matrix $F(n)$, the equation system formed by Eqs. 2.65b, 2.66b and 2.67b can be written in the following symbolic form:

$$F(n+1) = OF(n) \tag{2.68}$$

The latter equation entails that the values of the electric field at time $(n + 1)\Delta t$ and the values of the magnetic field at time $(n + 1/2)\Delta t$ can be derived from their values at times $n\Delta t$ and $(n - 1/2)\Delta t$ respectively by applying the operator O. This operator is successively applied to each discretization point in time, from the beginning to the end of the scattering process. It is well known that such a process is numerically stable only if no eigenvalue of O has a modulus greater than the unity. If this criterion is not satisfied, the numerical calculations may diverge exponentially with time, and this divergence will be all the more noticeable that the calculations are carried out over a longer period. Let us for instance consider here the case of a microcavity embedded in a photonic crystal with a complete band gap. If the incident pulse causes a resonant oscillation of the field located in the microcavity, the oscillation thus induced may persist for a long time due to the fact that the radiation losses are small. When the calculations should be continued until the end of the relaxation or the stabilization stage is reached, such a behaviour is likely to have dramatic consequences. Indeed, it should be borne in mind that the harmonic response of the crystal is calculated by performing either a Fourier transformation in time of this response, in the case of an incident pulse, or a direct calculation until stabilization of the response, in the case of a sinusoidal wave front. When precision as well as stability requirements are to be simultaneously satisfied, the algorithm used in the implementation of the FDTD method should be selected very carefully, for instance, by using more accurate values for the centred finite differences than those given in Eq. 2.64.

Let us finally observe that the method described in Sections 2.2.2, 2.2.3 and 2.2.4 of this chapter does not allow the calculations of the scattered field at infinity. The latter problem can be resolved through the use of methods known as near field/far field transformation techniques. These methods are based on the fact that the value of the field scattered outside a well chosen surface surrounding the photonic crystal can be determined from the field at this surface by simple integral calculations. This result will not come as a surprise for a reader already acquainted with the mathematical form of Huygens' principle (Born 1965).

2.2.5 Examples of Results obtained for a Point Source with the FDTD Method

When considering a point source introduced in the crystal itself rather than an incident wave arriving from an external region, certain changes are required in the implementation of the FDTD method. These changes, which are necessary only to the extent that the field is singular at the point source, will not be described in this section. Fig. 2.8 represents an example where the FDTD method was used for determining the field generated in an angled photonic crystal waveguide by a point source located at the entrance of the waveguide shown in the upper region of the figure. The crystal is a two-dimensional crystal with a finite size and with a square symmetry. Each segment of the waveguide is obtained by removing one line of rods. The field is s (or TM) polarized, while the frequency is in the first band gap of the crystal. It can be seen that the wave follows the 90 degree bends without

any noticeable loss and that the penetration of the field in the walls of the waveguide is limited. By contrast, and as can be observed in the lower section of the figure, a strong divergence of the field arises at the extremity of the waveguide. This divergence can be explained by the fact that the width of the waveguide is of the same order of magnitude as the wavelength of light.

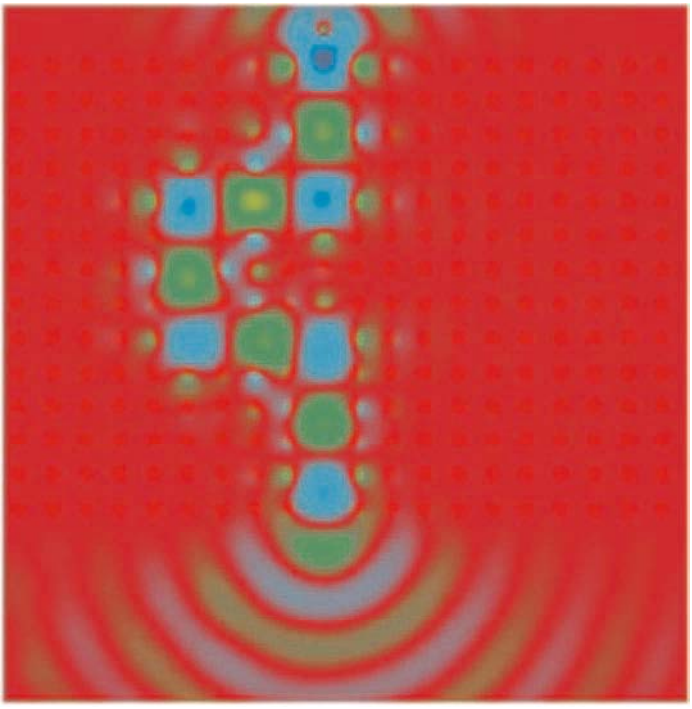

Fig. 2.8. Results of calculations performed using the FDTD method: propagation of the field generated by a point source located inside a photonic crystal angled waveguide. The two-dimensional photonic crystal consists of a square lattice formed by dielectric rods ($\varepsilon_r = 9$) in the air. The ratio of the radius of the rods to the period of the lattice is $r/a = 0.25$, while the wavelength used in the calculations is $\lambda/a = 0.3$ in normalized units. The red regions in this figure correspond to fields with very small amplitude, while the purple and blue regions correspond to the highest values of the field modulus. The phase shift in complex amplitude between the latter two regions is equal to π

2.3 Scattering Matrix Method

The scattering matrix method, also known as the multipole method, or as the modal method**,** has proved to be particularly efficient for the resolution of scattering problems involving a large, albeit finite, number of objects. This method, which can be presented in a rigorous mathematical form, rests on a very intuitive approach, from a physical point of view, to the problem of scattering by a set of objects. In addition, the mathematical development of this theory is accessible to postgraduate students and its numerical implementation does not present any major difficulty. In marked contrast to the methods previously discussed, the implementation of this method is much simpler for two-dimensional photonic crystals with circular rods, or for three-dimensional photonic crystals formed by spherical inclusions. This method is of particular interest for the study of crystals with a finite size, irrespective of whether they exhibit periodicity defects or not. It has also demonstrated a remarkable potential for the analysis of the propagation of light in microstructured optical fibres.

The pioneering role in the development of the modal method should be attributed to Lord Rayleigh, who first elaborated it in the electrostatic case (Rayleigh 1892). However, the development of this method in its electromagnetic form dates only from the 1980s, when it was independently developed in various forms by different groups (Chew 1992; Defos du Rau 1997; Elsherbeni 1992; Felbacq 1994a, 1994b; Nicorovici 1995; Vlassis 1996; Youssif 1988). As a survey of the studies published on this topic would reveal, the application range of this method is quite large: it may apply to two-dimensional as well as to three-dimensional objects, to dielectric, to metallic or to perfectly conducting objects, and to periodical as well as to random arrangements of objects in space. In all these cases however, the principles of this method remain the same.

While this method can be applied to objects with arbitrary shapes and with different electromagnetic parameters, we shall limit ourselves here, within the framework adopted for the study of photonic crystals, to a set of identical objects. For the sake of simplicity, we shall consider here, as in the previous methods, the case of two-dimensional photonic crystals formed by identical circular rods and illuminated under *s*-polarized light. Fig. 2.9 provides a schematic representation of the physical problem to be considered: an incident monochromatic plane wave with a wavelength $\lambda_0 = 2\pi/k_0$ in vacuum, propagating in an homogeneous material with a relative permittivity $\varepsilon_{r,ext}$, illuminates in *s*-polarization and with an angle of incidence Θ^{inc} a set of N identical dielectric rods with a radius R and a relative permittivity $\varepsilon_{r,int}$. We denote by $n_{ext} = \sqrt{\varepsilon_{r,ext}}$ and $n_{int} = \sqrt{\varepsilon_{r,int}}$ respectively the optical indices of the materials outside and inside the rods.

The complex amplitude of the incident electric field is given by the following equation:

$$\mathbf{E}^i = E_z^i \hat{z} \tag{2.69}$$

where:

$$E_z^i = exp\left(ik_0 n_{ext}(x\,sin\Theta^{inc} - y\,cos\Theta^{inc})\right) \tag{2.70}$$

From Eq. 1.37, the total electric field satisfies the Helmholtz equation in the sense of distributions:

$$\nabla^2 E_z + k_0^2 \varepsilon_r(x,y) E_z = 0 \tag{2.71}$$

where:

$$\varepsilon_r(x,y) = \begin{cases} \varepsilon_{r,ext} \text{ outside the rods} \\ \varepsilon_{r,\text{int}} \text{ inside the rods} \end{cases} \tag{2.72}$$

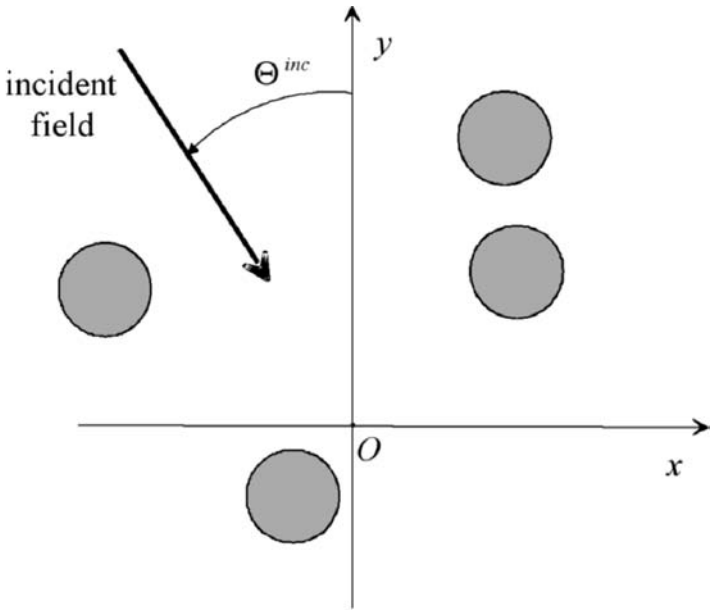

Fig. 2.9. Schematic representation of the scattering problem considered here: *N* rods are illuminated in *s*-polarization by an incident plane wave. In this example, *N* = 4

The theoretical justification of the method used for the resolution of Eq. 2. 71 is developed at greater length in Appendix A, and only a brief outline of the formalism will be presented here. This method proceeds in three steps. The first step consists in demonstrating that the total field in certain regions of space can be expressed in the form of Fourier-Bessel series. This fundamental property can be demonstrated by using for each individual rod a local system of polar coordinates (r_j, θ_j) whose origin is located at the centre of the rod, as is represented in Fig. 2.10. Although we limit ourselves here to systems with a circular symmetry, the property to be demonstrated here can be extended to non-circular rods as well. In this case however, the domain of validity of the Fourier-Bessel series does not extend over the entire section of the rod.

For any given value of r_j, it is plain that the electric field is a periodic function of θ_j with a period 2π. Accordingly, this field can be represented in the form of a Fourier series:

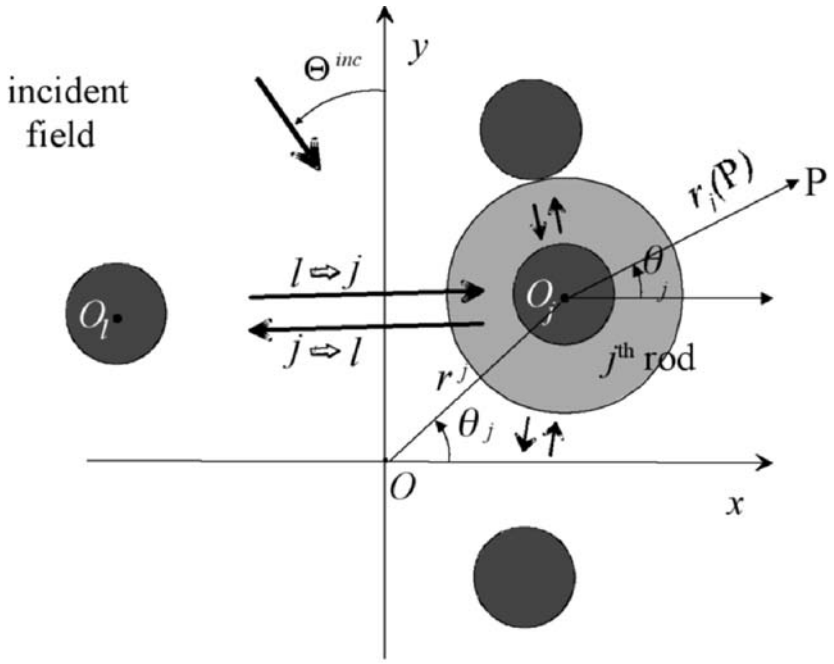

Fig. 2.10. Domains of validity of the Fourier-Bessel series. The dark grey area represents the domains of validity for the expansion of the field into Fourier-Bessel series inside the rods (with Bessel functions of the first kind), while the light grey area represents the domain of validity for this expansion around the j^{th} rod (with Hankel functions). The two arrows $l \rightarrow j$ and $j \rightarrow l$ point to the fields scattered by the l^{th} and j^{th} rods respectively, which propagate in or out of the latter region

$$E_z\left(r_j, \theta_j\right) = \sum_{m=-\infty,+\infty} E_{z,m}\left(r_j\right) exp\left(im\theta_j\right) \tag{2.73}$$

More precisely, it can be demonstrated (see Appendix A for more detail on this demonstration) that the field in each rod can be expressed, for $r_j < R$, by the following equation:

$$E_z\left(r_j, \theta_j\right) = \sum_{m=-\infty,+\infty} c_{j,m} J_m\left(k_0 n_{int} r_j\right) exp\left(im\theta_j\right) \tag{2.74}$$

where J_m is the Bessel function of the first kind of order m.

Therefore, the problem of determining the field in the rods comes down to the calculation of the coefficients $c_{j,m}$ of the Fourier-Bessel series in the right-hand side of Eq. 2.74.

Let us now consider the ring surrounding the j^{th} rod and extending to the nearest point of the immediately neighbouring rod. This region is represented in Fig. 2.10 by a light grey area, and it can be demonstrated that the field in this region assumes the form of a different type of Fourier-Bessel series:

$$E_z\left(r_j, \theta_j\right) = \sum_{m=-\infty,+\infty} a_{j,m} J_m\left(k_0 n_{ext} r_j\right) exp\left(im\theta_j\right) \tag{2.75}$$

$$+ \sum_{m=-\infty,+\infty} b_{j,m} H_m^{(1)}\left(k_0 n_{ext} r_j\right) exp\left(im\theta_j\right)$$

where $H_m^{(1)}$ is the Hankel function of the first kind of order m. It is convenient to note that the right-hand side of Eq. 2.75 now contains two Fourier-Bessel series with coefficients $a_{j,m}$ and $b_{j,m}$. On the other hand, the field represented by the summation of these two series can be decomposed into three distinct components having different physical meanings:

1. the incident plane wave, i.e. the source, given by Eq. 2.70,
2. the fields scattered by all other rods in the direction of the j^{th} rod: these fields behave with respect to this rod as any other incident wave,
3. the field scattered by the j^{th} rod which, according to the radiation condition, must propagate away from the rod.

Various physical considerations allow us to reach the conclusion that the first two types of incident fields cannot present any singularity in the light grey region and in the dark grey region corresponding to the j^{th} rod. These fields are therefore represented by the first series in the right-hand side of Eq. 2.75, which will be referred to as the local incident field at the j^{th} rod. The second series corresponds to the third field, i.e. to the field scattered by the j^{th} rod. It presents a singularity at

the origin (see Appendix A). As a consequence, each coefficient $a_{j,m}$ can be decomposed into two coefficients which correspond respectively to the first two fields:

$$a_{j,m} = a_{j,m}^{source} + a_{j,m}^{rods} \tag{2.76}$$

Using the decomposition of a plane wave into Fourier-Bessel series (see Appendix A for more detail), the coefficients $a_{j,m}^{source}$ turn out to be analytic. These coefficients are given by the equation:

$$a_{j,m}^{source} = (-1)^m \, exp\left(ik_0 n_{ext} r^j \, sin\left(\Theta^{inc} - \theta^j\right) - im\Theta^{inc}\right) \tag{2.77}$$

where r^j and θ^j are the coordinates of O_j in the general coordinate system represented in Fig. 2.10.

The second step in the method can be understood by considering the following physical interpretation. It has been seen that the local incident field contains two components: the term representing the source, which is known, and the field scattered by the other rods towards the j^{th} rod, which is not. The latter component, represented by the coefficient $a_{j,m}^{rods}$, is nothing other than a sum of terms with the same physical origin as the second series in Eq. 2.75, the summation being carried out over all the rods save the j^{th} one. This means, in other words, that the coefficients $a_{j,m}^{rods}$ can be expressed in terms of the set of $(N-1)$ series of coefficients $b_{l,m}$ with $l \neq j$. The assumption is made here that the expression of the field scattered by one rod, i.e. the right-hand side of Eq. 2.75, remains valid outside the light grey ring represented in Fig. 2.10 (Maystre 2002). Under this assumption, and proceeding once more to coordinate transformations, it turns out after a few calculations that the field scattered along the direction of the j^{th} rod by the ensemble formed by all other rods can be written in the following form (see Appendix A for more detail):

$$a_{j,m}^{rods} = \sum_{l \neq j} \sum_{q=-\infty,+\infty} b_{l,q} \exp\left(i(q-m)\theta_j^l\right) H_{m-q}^{(1)}\left(k_0 n_{r,ext} r_j^l\right) \tag{2.78}$$

where r_j^l and θ_j^l are the coordinates of O_l in the system of polar coordinates system associated with the j^{th} rod (see Fig. A.1 in Appendix A). Adding the coefficient $a_{j,m}^{source}$ of the incident source field (Eq. 2.77) to the coefficient $a_{j,m}^{rods}$, it finally appears that the coefficient of the total incident field can be expressed in terms of the coefficients of the field scattered by the other rods:

$$a_{j,m} = (-1)^m \exp\left(ik_0 n_{ext} r^j \sin\left(\Theta^{inc} - \theta^j\right) - im\Theta^{inc}\right) + \sum_{l \neq j} \sum_{q=-\infty,+\infty} b_{l,q} \exp\left(i(q-m)\theta_j^l\right) H_{m-q}^{(1)}\left(k_0 n_{ext} r_j^l\right) \tag{2.79}$$

The last step in the calculations consists in rewriting first Eq. 2.79 in matrix form. A second matrix equation is then obtained by applying the boundary conditions of the field on both sides of each rod. For the purpose of representing Eq. 2.79 in a matrix form, we introduce a set of column matrices $\boldsymbol{a_j}$ and $\boldsymbol{b_j}$ with components $a_{j,m}$ and $b_{j,m}$, which yields:

$$\boldsymbol{a}_j = \boldsymbol{Q}_j + \sum_{l \neq j} \boldsymbol{T}_{j,l}\, \boldsymbol{b}_l \tag{2.80}$$

where $\boldsymbol{Q_j}$ is a column matrix whose m^{th} component $Q_{j,m}$ is given by the following equation:

$$Q_{j,m} = (-1)^m \exp\left(ik_0 n_{ext} r^j \sin\left(\Theta^{inc} - \theta^j\right) - im\Theta^{inc}\right) \tag{2.81}$$

while $\boldsymbol{T_{j,l}}$ is a square matrix whose $(m, q)^{th}$ component $T_{j,l,m,q}$ is given by the equation:

$$T_{j,l,m,q} = \exp\left(i(q-m)\theta_j^l\right) H_{m-q}^{(1)}\left(k_0 n_{ext} r_j^l\right) \tag{2.82}$$

Eq. 2.80 is a system of N matrix equations formed by the $2N$ column matrices $\boldsymbol{a_j}$ and $\boldsymbol{b_j}$. The notion of a scattering matrix is then used in order to obtain a second system of N equations. It has been seen that the expression, given in Eq. 2.75, for the field around a given rod contains two sums, which represent the total incident field and the field scattered by the rod respectively. Further, it has already been demonstrated in Section 2.1 that a causal relation exists between these two fields, and this relation can be expressed in a mathematical form through the use of a scattering matrix defined as follows:

$$\boldsymbol{b}_j = \boldsymbol{S}_j \boldsymbol{a}_j \tag{2.83}$$

where $\boldsymbol{S_j}$ is a square matrix of infinite order.

In the particular case where the rods are circular, the scattering matrix can be readily derived from the boundary conditions at the surface of a rod. Since Eq. 2.71 is valid in the sense of distributions, the electric field and its normal derivative are continuous across this surface. This property can also be established by

considering the continuity of the tangential components of the electric and magnetic fields. By using the expansions of the field given by Eqs. 2.74 and 2.75 inside and outside the rod, and then by identifying the Fourier coefficients on both sides, it can be deduced that:

$$a_{j,m} J_m\left(k_0 n_{ext} R\right) + b_{j,m} H_m^{(1)}\left(k_0 n_{ext} R\right) = c_{j,m} J_m\left(k_0 n_{int} R\right) \tag{2.84}$$

$$a_{j,m} \left.\frac{dJ_m\left(k_0 n_{r,ext} r_j\right)}{dr_j}\right|_{r_j = R} + b_{j,m} \left.\frac{dH_m^{(1)}\left(k_0 n_{r,ext} r_j\right)}{dr_j}\right|_{r_j = R} = c_{j,m} \left.\frac{dJ_m\left(k_0 n_{r,\mathrm{int}} r_j\right)}{dr_j}\right|_{r_j = R} \tag{2.85}$$

By eliminating the coefficients $c_{j,m}$ between Eqs. 2.84 and 2.85, the following equation is finally deduced:

$$b_{j,m} = -\frac{J_m\left(k_0 n_{ext} R\right) \left.\frac{dJ_m\left(k_0 n_{int} r_j\right)}{dr_j}\right|_{r_j = R} - J_m\left(k_0 n_{int} R\right) \left.\frac{dJ_m\left(k_0 n_{ext} r_j\right)}{dr_j}\right|_{r_j = R}}{H_m^{(1)}\left(k_0 n_{ext} R\right) \left.\frac{dJ_m\left(k_0 n_{int} r_j\right)}{dr_j}\right|_{r_j = R} - J_m\left(k_0 n_{int} R\right) \left.\frac{dH_m^{(1)}\left(k_0 n_{ext} r_j\right)}{dr_j}\right|_{r_j = R}} a_{j,m} \tag{2.86}$$

It might be noted that the variable r_j in this equation can be replaced by a variable r independent from the rod, which demonstrates that this causal relation does not depend on the rod. All matrices $\boldsymbol{S}_l$ defined by Eq. 2.83 are therefore diagonal and equal to the matrix $\boldsymbol{S}$ defined by:

$$S_{m,m} = -\frac{J_m\left(k_0 n_{ext} R\right) \left.\frac{dJ_m\left(k_0 n_{int} r_j\right)}{dr_j}\right|_{r_j = R} - J_m\left(k_0 n_{int} R\right) \left.\frac{dJ_m\left(k_0 n_{ext} r_j\right)}{dr_j}\right|_{r_j = R}}{H_m^{(1)}\left(k_0 n_{ext} R\right) \left.\frac{dJ_m\left(k_0 n_{int} r_j\right)}{dr_j}\right|_{r_j = R} - J_m\left(k_0 n_{int} R\right) \left.\frac{dH_m^{(1)}\left(k_0 n_{ext} r_j\right)}{dr_j}\right|_{r_j = R}} \tag{2.87}$$

and, if $n \neq m$:

$$S_{n,m} = 0 \tag{2.88}$$

It should be pointed out that the determination of the scattering matrix for non-circular cylinders is much more complex. It requires that the scattering matrix of a single cylinder should be first calculated, for instance by using the FDTD method. While these calculations will not be analytic as was previously the case, the application here of the FDTD method presents the advantage of being restricted to a single rod, in contrast with the FDTD calculations presented in Section 2.2, where the problem of the scattering by N rods had to be resolved. Likewise, it might be noted that, in the case where the rods are not of the same radius or of the same permittivity, the scattering matrices are no longer identical, but that they remain diagonal in the case where the rods are circular.

In order to obtain a single matrix equation, we need only to multiply both sides of Eq. 2.80 by $\boldsymbol{S}_l = \boldsymbol{S}$, while Eq. 2.83 is used for simplifying its left-hand side. This leads to the following equation:

$$\boldsymbol{b}_j - \sum_{l \neq j} \boldsymbol{S}\boldsymbol{T}_{j,l}\, \boldsymbol{b}_l = \boldsymbol{S}\boldsymbol{Q}_j \tag{2.89}$$

which can be written in the more explicit form:

$$\begin{vmatrix} \boldsymbol{I} & -\boldsymbol{S}\boldsymbol{T}_{1,2} & -\boldsymbol{S}\boldsymbol{T}_{1,3} & \cdots & \cdots \\ -\boldsymbol{S}\boldsymbol{T}_{2,1} & \boldsymbol{I} & -\boldsymbol{S}\boldsymbol{T}_{2,3} & \cdots & \cdots \\ -\boldsymbol{S}\boldsymbol{T}_{3,1} & -\boldsymbol{S}\boldsymbol{T}_{3,2} & \boldsymbol{I} & \cdots & \cdots \\ \cdots & \cdots & \cdots & \cdots & \cdots \\ \cdots & \cdots & \cdots & \cdots & \cdots \end{vmatrix} \begin{vmatrix} \boldsymbol{b}_1 \\ \boldsymbol{b}_2 \\ \boldsymbol{b}_3 \\ \cdots \\ \cdots \end{vmatrix} = \begin{vmatrix} \boldsymbol{S}\boldsymbol{Q}_1 \\ \boldsymbol{S}\boldsymbol{Q}_2 \\ \boldsymbol{S}\boldsymbol{Q}_3 \\ \cdots \\ \cdots \end{vmatrix} \tag{2.90}$$

We thus arrive at an infinite linear system of equations, with $\boldsymbol{I}$ as its infinite unit matrix. In order to reduce the size of the system size, the matrices $\boldsymbol{S}$, $\boldsymbol{T}_{j,l}$, $\boldsymbol{Q}_j$ and $\boldsymbol{b}_l$ are truncated by limiting m and q to values ranging from $-M$ to $+M$. The system of equations to be inverted is therefore of size $N(2M+1)$.

Finally, the field at infinity can be easily calculated from the column matrices $\boldsymbol{b}_l$. For this purpose, we use the expression of the field scattered outside each cylinder (right-hand side of Eq. 2.75) after transforming it to the xy coordinate system. The transition from the local coordinate system associated with a rod to the unique xy coordinate system can be achieved by using Graf's formula (Abramovitz 1970). Thus, if $r \geq r^j$:

$$H_m^{(1)}\left(k_0 n_{ext} r_j(P)\right) exp\left(im\theta_j(P)\right) \tag{2.91}$$
$$= \sum_{q=-\infty,+\infty} exp\left(i(m-q)\theta^j\right) J_{q-m}\left(k_0 n_{ext} r^j\right) H_q^{(1)}\left(k_0 n_{ext} r\right) exp(iq\theta)$$

where r and θ are the polar coordinates of a point P of space in the xy coordinates system. At a large distance from the rods, it turns out that:

$$E^d(P) = \sum_{q=-\infty,+\infty} b_q H_q^{(1)}\left(k_0 n_{ext} r\right) exp(iq\theta) \tag{2.92}$$

where:

$$b_q = \sum_{j=1,N} \sum_{m=-\infty}^{+\infty} b_{j,m}\, exp\left(i(m-q)\theta^j\right) J_{q-m}\left(k_0 n_{ext} r^j\right) \tag{2.93}$$

The expression of the field at infinity is obtained by using the asymptotic form at infinity of the Hankel function, which is described in Appendix A. Eq. 2.92 thus becomes:

$$E^d(P) = g(\theta)\frac{exp(ikr)}{\sqrt{r}} \tag{2.94}$$

where:

$$g(\theta) = \sqrt{\frac{2}{\pi k_0 n_{ext}}}\; exp\left(-i\frac{\pi}{4}\right) \sum_{q=-\infty,+\infty} b_q\, exp\left(-iq\frac{\pi}{2}\right) exp(iq\theta) \tag{2.95}$$

The intensity of the field at infinity, also referred to as the bistatic differential cross-section in the field of radar detection, is given by the equation:

$$D(\theta) = 2\pi\left|g(\theta)\right|^2 \tag{2.96}$$

In the case where all materials, i.e. both the rods and the external medium, are lossless, the energy balance equation assumes the following form:

$$\int_0^{2\pi} \left|g(\theta)\right|^2 d\theta \;+\; 2\sqrt{\frac{2\pi}{k_0 n_{ext}}}\, Re\left[\, exp\left(i\frac{\pi}{4}\right)\; g\left(\Theta^{inc}+\pi\right)\right] = 0 \tag{2.97}$$

This equation is of course very useful for testing the validity of a numerical code. However, it only provides a sanity check of results, and it should not be regarded as a formal demonstration of their validity.

2.4 Other Methods: Integral and Differential Methods, Finite Element Method, Effective Medium Theory

Integral and finite element methods are probably the two most extensively used methods in electromagnetism, in particular for the resolution of the time-harmonic Maxwell's equations. As a general rule, integral methods allow the reduction of a scattering problem to the resolution of an integral equation, or to a system of coupled integral equations.

An integral equation is an equation in which the unknown function appears under an integral sign, with possible occurrences outside this integral sign.

As an example, $\varphi(l) = \varphi_0(l) + \int_D K(l,l')\varphi(l')dl'$ is an integral equation where φ is the unknown function, K is the kernel, i.e. a known function of two variables, and φ_0 is a known function. In electromagnetism, the unknown function is often related to the value of the electric or magnetic field, while l generally is a spatial variable. Boundary integral equations need to be distinguished from volume integral equations. In the latter case, the unknown function is defined over the whole space, and the number of spatial variables of integration is therefore equal to the dimension of the scattering problem, for instance to three if the problem at hand is three-dimensional. By contrast, in a boundary integral equation, the unknown function is defined at the boundaries of the scattering objects. The number of spatial variables of integration is therefore reduced by one with respect to the dimension of the scattering problem. Thus, in a three-dimensional problem, the number of variables reduces to only a couple of variables.

Let us consider for instance a two-dimensional photonic crystal with a finite size, illuminated by an incident wave. In such a case, the unknown function in a boundary integral equation will depend on the value of the fields at the boundaries of the entire set of rods of the crystal, with the variable l ranging over the points at these boundaries. The latter are formed by N circular lines, where N denotes the number of rods. By contrast, a volume integral equation must be defined for each point of the two-dimensional space, with the consequence that the integral becomes a double integral.

The classical method for deriving an integral equation relies on the use of the theory of Green's functions and, in more complicated cases, on the theory of dyadic Green's functions. In our opinion however, the most elegant and rigorous way to derive such an equation is to employ the theory of distributions. In this respect, it suffices to observe that the very definition of a Green's function refers to the Dirac function, which itself is but a distribution. The integral equation is an exact representation of the scattering problem. Therefore, once this equation has been solved, the field can be very easily determined at any point of space.

From a numerical point of view, a large variety of methods exist for the resolution of integral equations. One of the most commonly used methods is the finite element method (Bossavit 1989; Silberstein 2001). This method can be briefly described in the following terms:

– the unknown function is first represented in the form of a sum of finite elements in the variable l. For instance, in the example previously given of an integral equation, this sum will be equal to:

$$\varphi(l) = \sum_{j=1}^{Q} \varphi_j w_j(l)$$

Each finite element $w_j(l)$ is zero everywhere save in an elementary interval of the range of integration. A special form of the finite element method is the so-called Galerkin method, which can be illustrated by considering a boundary integral equation in the very simple case of a two-dimensional crystal reduced to a unique circular rod with a radius R. Let us define a basis of finite elements $w_j(l),\ j \in (1,Q), l \in (0,2\pi R)$, where Q is a natural integer, l is the curvilinear abscissa of a point at the boundary of the rod and j is the index of the finite element w_j. The latter may assume for instance the form of a rectangle function:

$$\forall j \in (1,Q) \quad w_j(l) = \begin{cases} 1 & \text{if } l \in (l_j, l_{j+1}) \\ 0 & \text{if } l \notin (l_j, l_{j+1}) \end{cases}$$

where $l_j = (j-1)\dfrac{2\pi R}{Q}$

– the integral equation is then projected onto the same basis, leading therefore to a system of Q linear equations containing Q unknown φ_j. The validity of the numerical results thus obtained can be tested from the convergence of the function $\varphi(l)$ when Q increases.

Boundary integral equations (Maystre 1994) present the obvious advantage over volume space integral equations that, since the unknown functions and the ranges of integration are limited to the boundaries of the scattering objects, the size Q of the linear system to be solved is much lower than it would have been the case for volume space integral equations. In the latter case indeed, the entire space, or at least the interior of all scattering objects, must be discretized. Further, as soon as the integral equation contains more than one variable of integration, it becomes necessary to use finite elements of several variables, which leads to a meshing of a two-dimensional or three-dimensional space (Guenneau 2001). Very efficient meshing algorithms currently exist, but most of the time they need to be adapted to the specific scattering object considered. In addition, when the integral equation extends to the entire space rather than to the interior of the scattering ob-

jects, the range of integration needs to be truncated with the help of absorbing boundary conditions, as in the FDTD method.

The differential method, as well as the rigorous coupled wave method which belongs to the same class of methods, draw their inspiration from an opposite approach. These methods are characterized by their simplicity as regards both their theoretical development and their numerical implementation. Instead of reducing the scattering problem to an integral equation, as in the integral method, by resorting to non-trivial mathematical notions like Green's functions or distributions, the differential method uses Maxwell's equations almost in a direct way. In its present stage of development, this method cannot apply to photonic crystals with a finite size along all directions and in principle its use is restricted to crystals with an infinite size along the transverse directions, i.e. in the *xz* plane. Some methods of overcoming these limitations exist nonetheless (Silberstein 2001).

Let us consider the case of a two-dimensional crystal created by superposing a finite number of infinite dielectric grids, as represented in Fig. 2.1, and let us further assume for the sake of simplicity that this structure is illuminated under normal incidence. Assuming the *x* axis to be perpendicular to the axis of the rods in the plane of the grids, the differential method is based on the expansion of the fields into Fourier series of the variable *x*. Since the *y* axis is perpendicular to the grids, the Fourier series thus obtained are functions of *y*. These series are then introduced into Maxwell's equations, and it can be very easily demonstrated that the Fourier coefficients of these series satisfy a system of coupled differential equations. The resolution of such a system is a most classical problem of numerical analysis, which of course requires that the infinite system be truncated. The differential and coupled wave methods diverge at this point. While the first method directly proceeds to the resolution of the differential system (Popov 2001a), the latter method replaces the rods by a stair-like structure, after having cut the rods by drawing equidistant lines parallel to the *x* axis onto them (Moharam 1986). The differential method and the rigorous coupled wave method have proven to be very efficient for the analysis of dielectric structures. The only exception to this rule is the case of metallic structures in the visible, infrared and microwave regions, where the conductivity of the metal becomes very high. In this case, strong numerical instabilities may arise when implementing these methods, even though it must be said that remarkable advances have taken place recently in this field. For more information on these recent developments, the reader is referred to (Li 1996; Lalanne 1996; Granet 1996; Popov 2001b) and to (Silberstein 2001), where crystals with finite size are more specifically considered.

Although of quite a different nature than the methods described above, the effective medium theory, also known as the homogenization method (Dautray 1984), cannot be ignored. Indeed, in certain specific cases, this method allows to simplify the scattering problem to such an extent that its resolution will be considerably simpler than the original problem. The effective medium theory draws its inspiration from a very evident observation: the properties of a periodic material like a photonic crystal tend to approach the properties of a homogeneous material when the wavelength of the light illuminating it tends towards infinity. This is perhaps best illustrated by the fact that solid state crystals, for instance diamonds

or semiconductors, can be perfectly described by an optical index in the optical region, where the corresponding wavelengths are much larger than the elementary cell of the crystal. This being said, two different problems now arise, concerning on the one hand the calculation of the electromagnetic characteristics of the homogeneous material associated with a given photonic crystal, and on the other hand the limits on the validity of the homogenization process. Indeed, while the elementary cell of solid state crystals is much smaller than optical wavelengths, this is not true of photonic crystals, since the periods currently available for the latter are of the same order of magnitude as optical wavelengths. It should be emphasized that the stakes are high, as the homogenization process is directed at transforming a very difficult problem, in which light illuminates a large number of scattering objects periodically arranged in space, into a very simple problem involving a unique, homogeneous scattering object.

The effective medium theory relies on very sophisticated mathematical methods known under the name of limit analysis. A description of these methods would lead us beyond the scope of this chapter, but it can be noted nonetheless that that limit analysis methods have been developed along two different approaches. In the first approach, the photonic crystal is assumed to extend at infinity along all directions, before considering the limits of the characteristics of the material when the wavelength tends to infinity. The second method, on the other hand, is based on the consideration of a model of a crystal with a fixed finite size illuminated at a fixed wavelength, while the size of the elementary crystal cell tends towards zero, which implies that the number of elementary cells tends towards infinity (Felbacq 1998; Guenneau 2000). The second type of analysis presents a higher degree of complexity than the first one, but it offers the advantage of accounting for phenomena occurring at the boundary of the crystal, some of which are very important. This observation can be illustrated by considering a photonic crystal with a finite size, illuminated by a point source placed in the air and in the vicinity of the crystal. This point source generates a field in the direction of the crystal. A part of this field consists of evanescent waves whose amplitude exponentially decreases with the distance to the point source. However, since the point source is located at a very short distance from the crystal, the amplitude of these waves may remain significantly high at the boundary of the crystal. Further, these evanescent waves propagate along a direction parallel to the boundary of the crystal, and their transverse wavelength, i.e. the period of the evanescent wave along the direction of propagation, can be much smaller than the actual wavelength of light in vacuum. This transverse wavelength is the decisive element in the validity of the homogenization process, since it actually represents the true period of the field of the evanescent waves. This is a well-known phenomenon in near field optics, where surface features much smaller than the wavelength of light in vacuum can be detected thanks to the small transverse wavelength of the evanescent part of the field generated by an optical antenna located at a very short distance from the surface. This demonstrates that the notion of homogenization initially used, where the finite size of the actual crystal is neglected and only the ratio between the wavelength and the size of the elementary cell is considered, is insufficient and may lead to erroneous results.

length and the size of the elementary cell is considered, is insufficient and may lead to erroneous results.

The mathematical study of homogenization processes is of such a degree of complexity that not all types of photonic crystals can be analysed with this method. However, some extremely valuable results have been reached. In particular, crystals realized from perfectly conducting metals have been demonstrated to be equivalent to dielectric materials (Pendry 1996b; Felbacq 1997).

2.5 Numerical Codes available for the Modelling of Photonic Crystals

The electromagnetic modelling of photonic crystals is a time-consuming activity, which in addition requires a high level of competence. The efficient and fine modelling of the most complex structures, for instance three-dimensional structures, cannot be achieved save through the combination of expertises in such diverse fields as applied mathematics, electromagnetism, numerical analysis and programming. As a consequence, a research group can be uncertain as to whether it should engage in such a project, especially in view of the availability of free and commercial electromagnetic simulation software for the modelling of photonic crystals.

Of course, a numerical code developed internally by a research group will always provide greater guarantees in terms of reliability and security, as a personal understanding of the theoretical and numerical foundations is key to avoiding errors. A numerical code is not by any means a 'black box' that would provide an accurate answer to any possible question. Not only is the author of a numerical code able to avoid most of the pitfalls that a less informed user might experience, but he generally is in a position of adapting the code to new situations and circumstances. This is a crucial advantage in a field where structures are evolving at an extremely rapid pace.

Nevertheless, it should be acknowledged that commercial codes may provide valuable services for many users. It is not the purpose of this section to provide an exhaustive review of these numerical programs, and the interested reader is referred to websites such as http://www.pbglink.com/software.html for specific resources on photonic crystals or http://emlib.jpl.nasa.gov for more general resources on electromagnetic modelling. Most of these codes are based on the general methods of electromagnetism, for instance on the finite element method, the FDTD method or the integral methods: thus, the famous 'High Frequency Sequence Simulator'(HFSS) code is based on the finite element method and relies on a meshing which is automatically refined until the convergence of the result is reached. Of course, the introduction of convergence tests reduces possible errors. As a general rule, classical physical criteria like the energy balance equation or the reciprocity theorem provide sanity checks for evaluating the validity of the results. For instance, in the case of a photonic crystal consisting of a finite stack of infinite and lossless dielectric grids, the sum of the transmitted and reflected energies

should be equal to the incident energy. By way of conclusion, it should be stressed that beginners need to be extremely cautious before admitting the validity of numerical results, especially when they do not know the theoretical and numerical foundations of the code used for obtaining these results.

3 Quasi-Crystals and Archimedean Tilings

The consideration of photonic crystals with defects or photonic crystals with finite sizes has already led us to move beyond crystalline periodicity in the stricter sense of the term. The photonic quasi-crystals that will be described in this chapter can be regarded as yet another form of deviation from the ideal case of a periodic photonic crystal. It will be seen that some of the numerical models discussed in the previous chapters can be applied to certain of these non-periodic structures.

The *International Union of Crystallography* (IUC) now defines the term 'crystal' as 'any solid having an essentially discrete diffraction diagram' (IUC 1992). The large family of solid state crystals thus defined can then be divided into two classes:

1. periodic crystals exhibiting a perfectly periodic structure at the atomic scale: photonic crystals are the 'photonic' analogues of these crystals,
2. aperiodic crystals

Microscopic periodicity thus turns out to be a sufficient, albeit not necessary, condition for the existence of a crystalline state. Actually, the definition developed by the IUC rests on the properties of lattices in the reciprocal (or Fourier) space. A diffraction diagram, for instance the X-ray diffraction diagram, can indeed be seen as the Fourier transform of the 'atomic distribution' of the crystal in the real space. The reciprocal lattice can be defined as the set of all combinations of wave vectors corresponding to peaks in the diffraction diagram. According to this definition, even wave vectors corresponding to the less intense diffraction peaks belong to the reciprocal lattice.

A crystal is said to be periodic if and only if the minimal number of vectors necessary for generating it is equal to the dimensionality of the crystal: for instance, if the crystal is two-dimensional, then this minimal number must be equal to 2. In such a case, the diffraction diagram corresponds to the reciprocal lattice of the crystal, with which we are already familiar.

Nevertheless, other situations may exist where several low intensity peaks appear between the main peaks in the diffraction diagram. The number of these secondary peaks is generally found to increase with the resolution of the Fourier transform. In such a case, the reciprocal lattice is said to be 'dense' in the mathematical sense of the term: there is no condition imposing a minimal distance between two wave vectors associated with diffraction peaks. The lattice of the crystal is therefore quasi-periodic. It is precisely the absence of a condition imposing a

minimal distance between the vectors of the reciprocal lattice which allows quasi-periodic crystals to exhibit symmetries that could not be achieved in periodic crystals, for instance a rotational invariance of order $N = 5$ or $N > 6$.

3.1 Photonic Quasi-Crystals

A very simple method for constructing quasi-crystals is represented in Fig. 3.1. This method consists in projecting a structure exhibiting a periodicity in an N-dimensional space onto a space of lower dimensionality. The structure considered here is a grid G with a square symmetry. A one-dimensional quasi-crystal can be derived from the grid G by considering all intersections of this grid with a straight line Δ of irrational slope. The intersection points thus generated are indeed distributed according to a quasi-periodic pattern. In practice, a photonic quasi-crystal can be constructed by alternately stacking dielectric layers with permittivities ε_1 and ε_2 respectively, in such a way that the thickness of the layers will vary with the distance between the successive intersection points represented in Fig. 3.1.

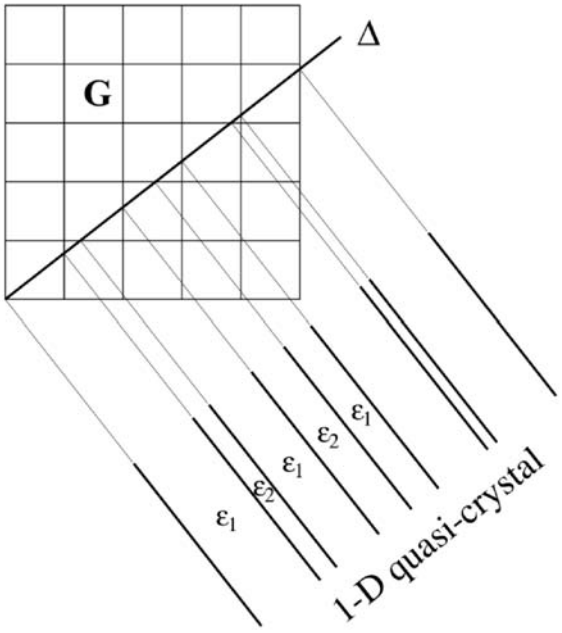

Fig. 3.1. Construction of a one-dimensional photonic quasi-crystal through the projection of a two-dimensional square grid onto a straight line with irrational slope

Quasi-crystals like the example described above are deterministic, perfectly ordered structures that do not present any translational symmetry. As has already been mentioned, two-dimensional quasi-crystals may exhibit a rotational symmetry of unusual order, for instance $N = 5$ or $N > 6$. Solid-state quasi-crystals were discovered in 1984 (Shechtman 1984), and their electrical, thermal and mechanical properties have turned out to be very different from the properties of 'traditional' crystals (Hippert 1994). More than a decade after the first studies conducted on solid-state quasi-crystals, and at a time when the study of photonic crystals was gaining momentum, the question whether quasi-periodic electromagnetic (EM) structures might present any unexpected or interesting specific properties became the subject of considerable interest. Since quasi-crystals may exhibit a high-order rotational symmetry ($N = 8$, 10, 12, to be compared with the maximal order $N = 6$ for Bravais lattices), these structures were expected to better approach the absolute isotropy than Bravais lattices. These expectations led to proposals for photonic quasi-crystals with an order of rotational symmetry as high as $N = 18$. The authors proceeded from the image of diffraction patterns with the desired symmetry, before using Fourier transformation and filtering for the purpose of retrieving the actual structures (Lee 2005).

Another interesting feature that these structures were originally thought to exhibit was the existence of omnidirectional photonic band gaps in two-dimensional photonic quasi-crystals with a low refractive index contrast, in the form ideally of photonic crystals constituted by air and silica (Zoorob 2000). Unfortunately, this claim was later demonstrated to be unfounded (Zhao 2001).

The theoretical investigation of photonic quasi-crystals really began during the mid-nineties. From a methodological point of view, photonic quasi-crystals present the same difficulties as solid quasi-crystals. Thus, as a consequence of the lack of periodicity of photonic quasi-crystals, calculation methods available in the reciprocal space (expansion of the field into a limited number of plane waves) cannot be directly applied to quasi-crystals. A possible method for overcoming this limitation consists in using a finite truncation of the infinite quasi-crystal and in periodically repeating this truncation. The properties of the periodic structure thus constructed, also referred to as an 'approximant' can therefore be expected to approximate the properties of the original quasi-crystal. However, in the case of solid state quasi-crystals, it has been demonstrated that the properties of approximants do not systematically converge, even when the size of the cells of the structure is increased.

An alternative method for approximating the properties of electromagnetic (EM) quasi-crystals relies on the simulation of the propagation of the EM wave in the real space, for instance by using finite difference in time domain (FDTD) methods (see Chapter 2). Here again, one is presented with a finite structure, i.e., with the truncation of a quasi-crystal. In this respect, it is not without interest to mention that, prior to the proposal of the concept of a photonic crystal, metal patch antennas based on fractal or self-similar shapes had been already investigated independently by different authors. The interested reader is referred to (Baliarda 2000), where further references are also presented. It has thus been demonstrated that the specific EM properties of these antennas, for instance their operation in

several spectral bands or in a single extremely large band, are directly associated with the fractal nature of the patterns.

The two approaches outlined above have been used by several research groups worldwide for investigating the optical properties of photonic quasi-crystals. An extensive series of simulation results have thus been reported for two-dimensional photonic quasi-crystals with rotational symmetry of order $N = 8$, 10 and 12 (Chan 1998; Chelnokov 1999; Zoorob 2000). By performing calculations both in the real and in the reciprocal space, it was demonstrated that these structures possess almost perfectly isotropic band gaps. However, the prediction of band gaps at very low frequencies and the claim that complete band gaps could be achieved in structures with a low index contrast ($\Delta n \leq 1.5$) were invalidated. In many respects, albeit not in all, photonic quasi-crystals behave like periodic structures. The lasing characteristics of quasi-periodic photonic crystal microcavities are similar to those of photonic crystal microcavities (Lee 2006; Nozaki 2006). By contrast, while band-edge lasers based on conventional crystals emit on extended modes (see Chapter 10 for more detail), band-edge lasers based on photonic quasi-crystals tend to emit on a series of localized modes (Wang 2006; Della Villa 2006).

The density of states of photonic quasi-crystals is still a much debated question. The first studies investigating this subject were conducted for the simplest type of photonic quasi-crystals, i.e. for one-dimensional photonic quasi-crystals consisting of multilayer structures. Some authors have reached the conclusion that the transmission spectra of a generalized Fibonacci multilayer structure exhibit a fractal behaviour (Dulea 1990; Zoll 1998). In other terms, the transmission bands consist of several transmission peaks densely distributed at the scale of the wavelength and separated by narrow reflection peaks. Under certain specific conditions, Fibonacci multilayer structures may also present stop-bands, whose existence is strongly dependent on the exact sequence of the layers. However, all the one-dimensional structures considered were of finite size, and the calculations were performed only in a single dimension. For this reason, the EM simulations provided precise information only on the propagation of light perpendicularly to the multilayers, and not on the total density of radiative states in the structure. In order to determine the total density of states, it would have been necessary to consider all directions in the real space.

The case of two-dimensional and three-dimensional photonic quasi-crystals is even more complex. Certain studies have revealed the existence of proper stop-bands in such structures (Zhang 2001), and these results are actually supported by the exponential dependence of the transmission on the thickness of the crystal. The reported stop-bands were bordered by relatively ‘smooth’ transmission bands. At the same time however, transmission spectra consisting of numerous individual peaks were reported by other studies. The discrepancy between these two series of results can be explained by drawing on similar studies devoted to solid state quasi-crystals based on Penrose icosahedrical lattices (Zijstra 2000). The electronic density of states in these lattices was calculated with the ‘maximal possible precision’. The spectral distribution of the density of states in two-dimensional tilings turned out not to be smooth, even if it was not possible to derive any conclusion regarding its fractal character. On the contrary, the spectral distribution of the density of

states in three-dimensional quasi-periodic structures was found to be smooth, and therefore not to exhibit any fractal feature. The authors also observed that, for three-dimensional structures, sharp peaks appear in the spectral distribution of the density of states when too small an approximant is chosen or when the precision of the calculations is insufficient. As in the very early days of three-dimensional photonic crystals, microwave transmission experiments provide a useful means of validating numerical predictions on three-dimensional quasi-crystals (Man 2005).

As can be seen, the absence of a translational invariance in quasi-periodic structures results in a higher degree of complexity in the calculations. Further, since each site in such a crystal is different, the properties of the interfaces of the defects or of the guiding structures tend to be dependent on the exact location of the defects or of the waveguides themselves.

The possibility however exists of resorting to the now well-established fact that the properties of quasi-periodic photonic systems with high index contrast, for instance structures consisting of air holes drilled in a semiconductor matrix, can be reproduced almost exactly with specific strictly periodic structures. The Archimedean tilings that will be discussed in the next section are actually examples of such specific structures.

3.2 Archimedean Tilings

Archimedean tilings are periodic two-dimensional structures whose properties have turned out to be quite similar to those of photonic quasi–crystals. These tilings are constructed from regular convex polygons of one or several types. The plane is tessellated by these polygons, without any interval or overlap between the polygons. All vertices are therefore strictly identical. The ‘atoms’ of the structure are located at these vertices. Eleven different Archimedean tilings exist, including the traditional Bravais lattice (Senechal 1995). The number of possible tilings can be increased by allowing certain specific arrangements of ‘atoms’ around some of the vertices of the lattice. The tilings thus defined are referred to as semi-regular or Archimedean-like tilings. Fig. 3.2 represents the three most elementary Archimedean-like tilings, where the arrangement of the polygons around one of the vertices differs from the arrangements around all other vertices.

Since these structures are strictly periodic, an elementary cell and an associated Brillouin zone can be defined. This leads to the possibility of applying the plane wave method for investigating the properties of these crystals. The structures displayed in Fig. 3.2*b* and 3.2*c* present a rotational symmetry of 12^{th} order, while the structure represented in Fig. 3.2*a* closely ‘approaches’ the same order of symmetry. The symmetry of the structure is clearly revealed in the diffraction diagrams presented in Fig. 3.3.

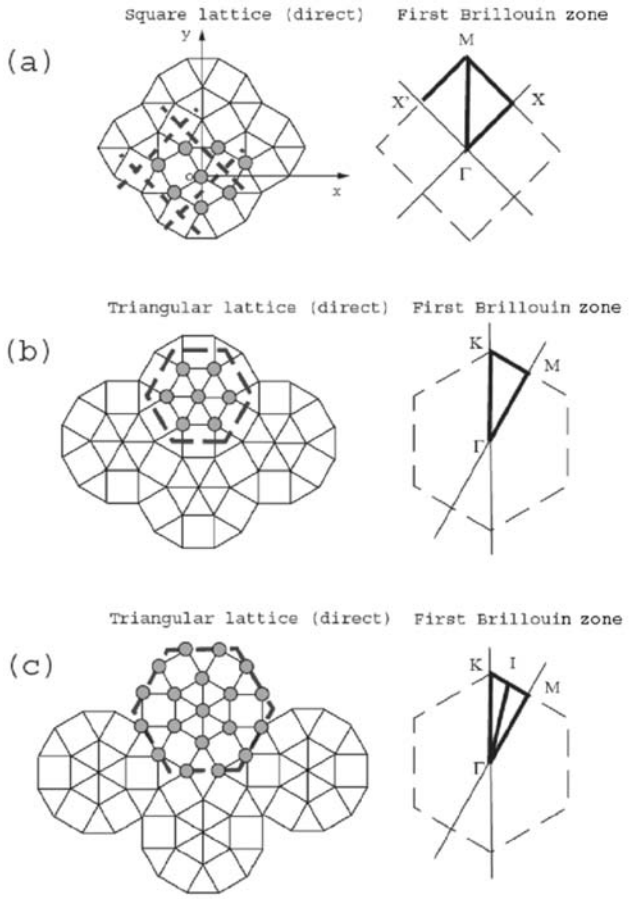

Fig. 3.2. *Left.* Semi-regular photonic crystals constructed from Archimedean tilings. *Right.* Brillouin zones associated with: *a.* a square lattice with a 4-atom unit cell, *b.* a triangular lattice with a 7-atom unit cell, *c.* a triangular lattice with a 13-atom unit cell. For each direct lattice represented in the left-hand part of the figure, the elementary cell is represented in thick dashed lines, while the bonds connecting the 'atoms' are represented in thin solid lines. The thick lines in the reciprocal lattices (*right*) correspond to the directions used for the calculation of the band diagrams (Fig. 3.4)

In all these cases, the distance between an 'atom' and its nearest neighbours remains constant, while the number of nearest neighbours is the same either for all 'atoms' (Fig. 3.2*a*) or for all the atoms save one (Figs. 3.2*b* and 3.2*c*). As can be seen in Fig. 3.4, the isotropy of the structures is further vindicated by the results of the band diagram calculations. These results were obtained using the plane wave method under the assumption that the lattices consisted of air cylinders ($n = 1$) extending in a semiconductor ($n = 3.5$) (David 2000, 2001). The existence of

photonic band gaps, which were found to be quasi-independent on the direction of propagation, has also been confirmed by numerical simulations performed using the finite element method.

The isotropy of Archimedean-like lattices improves when the number of 'atoms' contained in the elementary cells of the lattice increases, whereas the location and the width of the band gaps vary only slightly with the size of the cells. This actually results from the fact that the frequency of the main band gap does not depend on the size of the cells, but is imposed by the distance between two neighbouring 'atoms'.

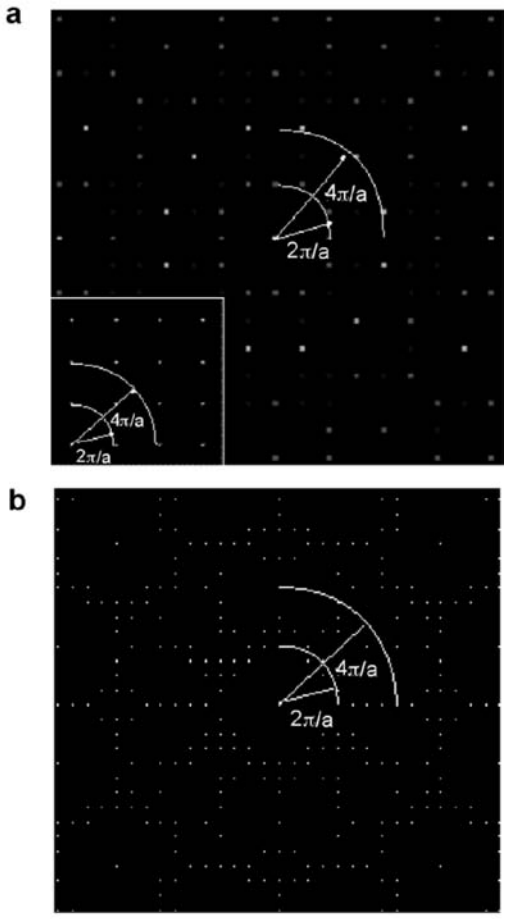

Fig. 3.3. Diffraction patterns calculated for the Archimedean tilings represented in Figs. 3.2*a* and 3.2*b*. The circles of radius $n\pi/a$, where n is an integer and a is the distance between a given atom and its nearest neighbours offer an insight in the relative isotropy of the two lattices

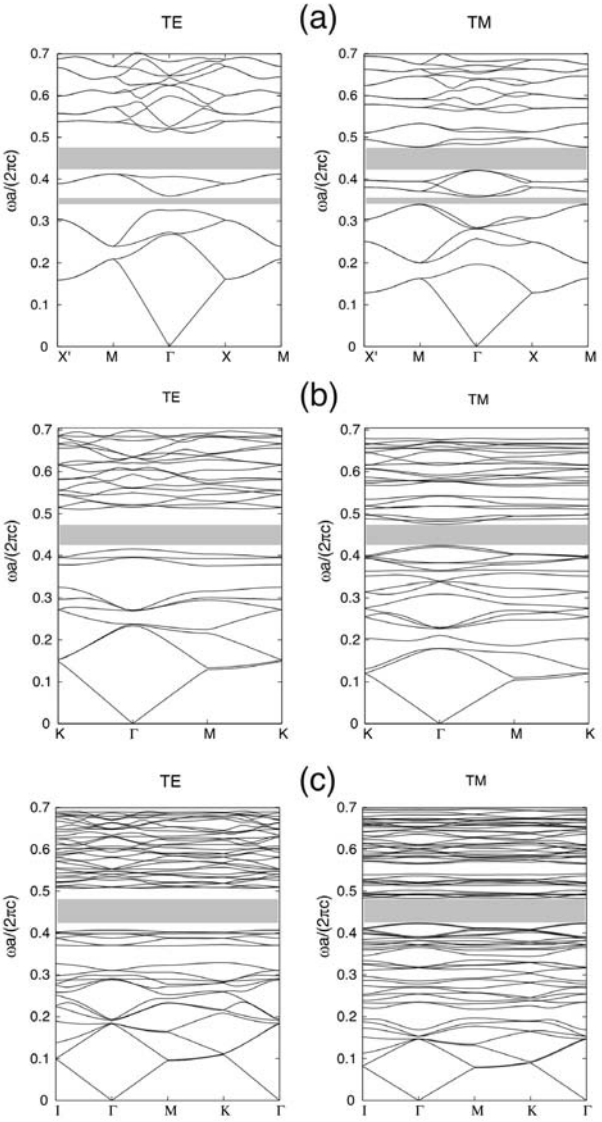

Fig. 3.4. Band diagrams calculated for the Archimedean-like tilings represented in Fig. 3.2. The calculations were performed for both TE and TM polarizations. *a.* Square lattice with a 4-atom unit cell, *b*. Triangular lattice with a 7-atom unit cell, *c.* Triangular lattice with a 13-atom unit cell. The photonic structures consist of periodic pores ($\varepsilon = 1$) in a dielectric material with a high permittivity ($\varepsilon = 12$). In all three cases, the air-filling factor is equal to 75 %. The grey bands correspond to the complete two-dimensional band gaps

A most surprising result is that the structure with the smallest elementary cell, consisting of only four atoms, represented in Fig. 3.2*a*, still exhibits properties very close to those of quasi-crystals, not only in terms of isotropy, but also as regards the position and width of the band gaps. This similarity can be observed in particular in the case of crystals with a high index contrast, where the interaction between an EM wave and the 'atoms' of the lattice is strong enough. The properties of the structure are therefore defined by the local order at a small scale, i.e. by the distance between the nearest neighbours and by the number of the nearest neighbours for each atom. Let us here recall that in photonic crystals with a high refractive index contrast, only a few lattice periods are necessary for obtaining stop-band reflectivity approaching 100 percent. The fact that the local order is the main factor determining the properties of these structures opens the way to the possibility of composite structures combining different types of lattices. These structures can be thought of as the photonic analogues of semiconductor heterostructures and superlattices.

3.3 From Photonic Quasi-Crystals to the Localization of Light

Extending the line of reasoning developed above with respect to composite photonic crystals, the question may arise whether the spatial symmetry of the lattice is really a necessary requirement for forbidding the propagation of light and ultimately for controlling it.

The localization of electromagnetic waves in a completely random diffusive medium was first predicted back in the 1980s (Anderson 1985; John 1984), and an experimental demonstration in the infrared wavelength range was first reported in 1997 (Wiersma 1997). A cloud is actually an example of such a random medium. The light emitted by the Sun propagates through the cloud following a randomly ordered path, with the consequence that only a fraction of the light reaches the ground. The attenuation of light induced by the cloud can be defined as the ratio of the thickness of the cloud to the mean free path of the light wave, the mean free path being defined itself as the distance that the light wave needs to travel between two successive scatterers in the cloud. The light not transmitted across the cloud is reflected, with the consequence that the cloud seems to be white when observed in the direction of the Sun.

The situation changes dramatically when the diffusion of light becomes strong, and when the mean free path reaches an order comparable to the wavelength. In this case, two different types of light localization are to be distinguished:

1. weak localization, which cause the phenomenon of enhanced backscattering,
2. strong localization, also referred to as Anderson localization.

These two types of localization can be generated either by a set of randomly distributed diffusing particles, or by randomly rough surfaces, i.e. surfaces with

randomly distributed corrugations. The roughness of such a surface can be described using such statistical parameters as the average height of the corrugations or the average distance between two neighbouring corrugations. A review of the different studies devoted to this subject can be found in (Maystre 1991).

When an ensemble of particles is illuminated by a light beam, as represented in Fig. 3.5, the existence of a backscattering effect is revealed by the appearance of a peak in the angular distribution of the scattered field. This peak is directed along the direction opposite to the incident beam, as can be seen in Fig. 3.6. It can be experimentally observed, and theoretically demonstrated, that the amplitude of the peak can be twice as high as that of the pedestal.

A heuristic explanation of this phenomenon is presented in Fig. 3.5. Let us here consider an incident wave represented by two incident rays, appearing in the figure in the form of a dark grey line and of a light grey line respectively. In the first case (Fig. 3.5*a*), the dark grey ray is successively scattered by the particles 1, 2, 3 and 4, before emerging outside the randomly diffusing medium, with a direction different from the direction of incidence. A second path, represented by the light grey line, is then associated to this first path. The ray corresponding to this path is scattered successively by the same particles as the first one, but in the inverse order (4, 3, 2, and 1).

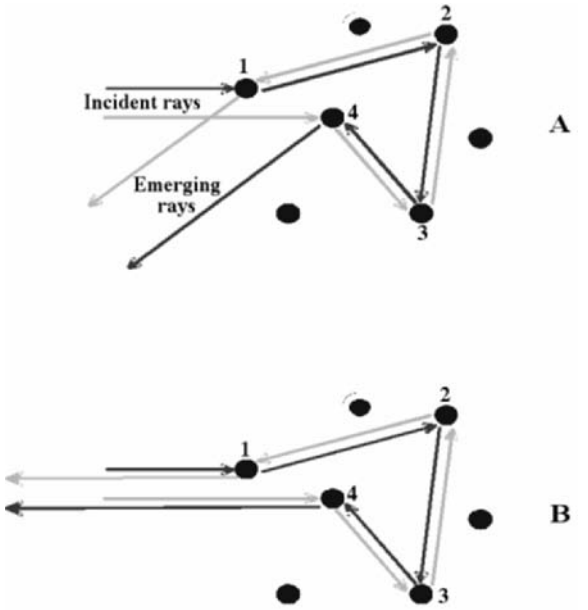

Fig. 3.5. Scattering of light by an ensemble of particles *a.* The rays emerging along any arbitrary direction with respect to that of the incident light are not in phase *b.* The rays emerging along the direction opposite to that of the incident rays are in phase (backscattering phenomenon)

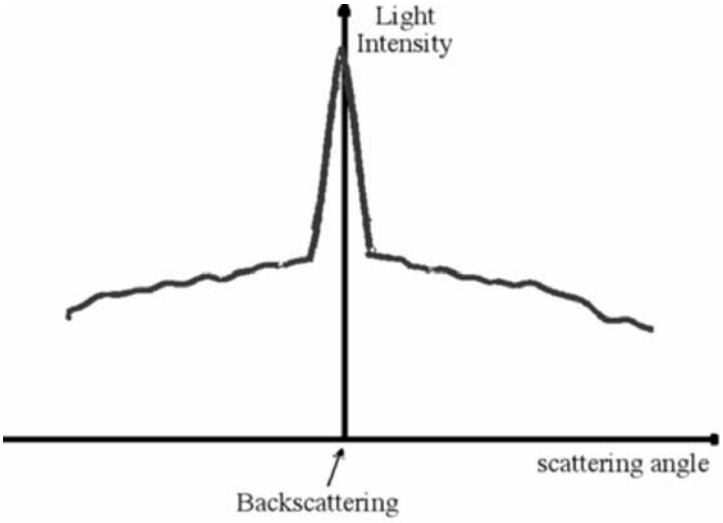

Fig. 3.6. Peak associated with an enhanced backscattering effect

In the second case (Fig. 3.5*b*), the spatial distribution of the particles is the same, but the direction of propagation of the rays emerging from the medium is now directly opposed to the direction of the incident rays. The two incident rays are part of the same beam and are therefore in phase. Since the dark grey and light grey rays follow the same paths along opposite directions, the principle of reciprocity entails in this case that the emerging backscattered rays will be in phase as well. This case thus turns out to be quite different from the situation depicted in Fig. 3.5*a*, where the phase was not conserved. The rays propagating along the backscattering direction can be grouped into couples consisting of two perfectly coherent rays. This is not the case for any other direction, and rays propagating along these directions are perfectly incoherent. A peak corresponding to the direction of the backscattered light can therefore be expected to appear in the angular distribution of the scattered light.

The same type of intuitive explanation can be provided for the situation created when a light beam is incident onto a randomly rough surface. Experimental and numerical illustration of the phenomenon can be found in (Greffet 1991; Kim 1990; Maradudin 1990; Maystre 1994b; O'Donnel 1987; Soto-Crespo 1989). It might be noted that phenomena of enhanced backscattering of light can be observed in everyday life, for instance when an airplane flies over a cloud layer. In this case, a passenger looking outside the window will see not only the shadow projected by the plane onto the cloud layer, but also a luminous halo extending around this shadow. The appearance of such a halo, also known as a 'glory', results from the fact that, in such an optical configuration, the eyes of the passenger receive the light backscattered by the cloud.

The phenomenon of strong localization of light presents itself in a very different way. When particles form a very dense random structure, the effects induced by the interferences become extremely strong, and the propagation of light becomes almost impossible. Let d be the thickness of the layer where the diffusive particles are contained. In the strong localization case, the amplitude of the field decreases exponentially with d (in $e^{-\alpha d}$), which contrasts with the case previously considered of a weakly diffusing medium, where the decrease of the field followed a $1/d^2$ dependence.

These mathematical laws are actually of a statistical nature. In other terms, these evolutions are measured only over statistical averages of the fields, by considering multiple successive realizations with the same statistical characteristics of a given set of particles. The term 'realization' is used here to denote any arrangement of a set of N particles randomly distributed inside a given volume. The notion of a realization can be explained for instance by considering an instantaneous arrangement of micrometer-sized latex spheres agitated inside a liquid. After a time sufficiently long, the spheres will be ordered in a completely different arrangement, but the statistical parameters remain the same. This second arrangement is said to represent a different realization of the same system.

In practice, when considering the instantaneous field for a given realization, i.e. for a particular observation, a very strong inhomogeneity in the distribution of the field can be observed. The electromagnetic field is granular, with very bright regions separated by dark regions. These localized modes can be interpreted in terms of resonant modes, quite in the same way as if they were inside a resonant cavity. The theory of Anderson localization for photons is quite complex, and it resorts to specialized mathematical theorems associated with stochastic processes. This theory will not be described here.

It might be noted, however, that a slightly perturbed photonic crystal creates conditions which are particularly favourable to the strong localization of light at frequencies near the edge of the band gap (Felbacq 1995). Such a perturbation can be achieved for instance through the random displacement of each 'atom' of the crystal. In view of the preceding considerations, this is not actually surprising. Let us consider indeed a photonic crystal illuminated by an electromagnetic wave at a wavelength located in the band gap, but near its edge. If all the 'atoms' of the crystal are randomly displaced, for instance by translating the 'atoms' over the same distance, but along random arbitrary directions, it is quite plain that the average distance between atoms will be reduced in certain regions of the crystal, while being increased in other regions. The band edges of certain regions of the photonic crystal will therefore shift outside the band gap of the original crystal, with the result that these regions become transparency regions inside which the field can propagate. These regions are surrounded by 'reflecting' areas, where propagation is forbidden and where the amplitude of the field decreases exponentially. To some extent, the perturbation thus induced can be seen as creating a series of microcavities embedded in the original photonic crystal. If the resonance wavelength of one of these microcavities lies within the band gap, then the electromagnetic field will resonate in the cavity and form a localized mode with a low amount of loss. The fact that light propagates with difficulty between two such 'light grains'

explains that statistically the field may exponentially decrease in such a random medium with a strong localization.

A different example of a material allowing the strong localization of light can be considered in the form of a more or less monodisperse semiconductor powder, i.e. a perfectly disordered material (Wiersma 1997). However, even if the propagation of light can be totally forbidden in such materials, the corresponding band gaps do not present any clearly defined edge as was the case with photonic crystals.

As has been previously mentioned, strong localization phenomena may sometimes occur over randomly rough surfaces. For instance, in the visible wavelengths range, the propagation of a plasmon wave along a rough metallic surface may result in the formation of high-intensity regions separated by dark regions. These bright regions are sometimes referred to as 'localitons', from the contraction of the terms 'localisation' and 'plasmons' (Maystre 1994b).

By way of conclusion, the interaction of light with a medium containing scattering centres may lead to a variety of different situations, ranging from the 'ideal' photonic crystals or the photonic quasi-crystals to randomly disordered media, where light can be localized, and to structures intermediary between periodic and random structures. Drawing a clear boundary between these different configurations is not necessarily simple. For instance, at what point does a photonic crystal turn into a randomly diffusing structure when it is submitted to increasingly strong perturbations? Likewise, to which extent do electromagnetic quasi-crystals, which are a combination of square and triangular lattices, differ from more 'traditional' photonic crystals? These are but two of the several questions raised by these issues.

4 Specific Features of Metallic Structures

In the preceding chapters, photonic crystals have been essentially considered as (quasi) periodic ensembles of dielectric elements, which allow the control of the propagation of light through the effects of photonic band gaps and transmission bands. It might be pointed out, however, that the first periodic (one, two and three-dimensional) ensembles of materials had been historically fabricated from metals rather than from dielectrics (Harvey 1963; Marconi 1919). The use of periodic metallic grids for filtering radiofrequency waves with different polarizations can thus be traced back to the beginnings of the 20th century (Marconi 1919). The idea that any dielectric function could be artificially 'realized' through the use of metals led to the concept of 'artificial dielectrics' developed in the 1950s (Harvey 1959, 1963). In either case, these periodic filters and artificial dielectrics were fundamentally photonic crystals, even though realizations at this time were restricted as regards their applications to wavelengths much larger than wavelengths in the optical region. As this brief survey indicates, the concept of photonic crystal can be extended, in quite a natural way, to metallic as well as to metallodielectric periodic structures.

Standard metals present electromagnetic properties which are fundamentally different from those of dielectrics. For this reason, the first part of this chapter will be devoted to reviewing the effects associated with free-charge carriers in metals. We shall then successively consider different types of periodic structures, depending on whether they are adapted to long wavelengths (ranging from microwaves to the far infrared region) or to short wavelengths (extending from the infrared to the visible regions). Finally, we shall discuss the specific effects induced by surface waves for all metallic structures.

4.1 Bulk Metals: Drude Model, Skin Effect and Metallic Losses

In the case of metallic media, Maxwell's equations contain an additional term associated to the current density $\mathbf{j} = \sigma\mathbf{E}$. In the harmonic regime, these equations can be written as follows:

$$\nabla \times \mathbf{E} - i\omega\mu\mathbf{H} = 0 \tag{1.2b}$$

$$\nabla \times \mathbf{H} + i\omega\varepsilon\mathbf{E} - \mathbf{j} = \nabla \times \mathbf{H} + i\omega\left(\varepsilon + i\frac{\sigma}{\omega}\right)\mathbf{E} = 0 \qquad (1.3b)$$

In the following, we shall confine ourselves to the consideration of non-magnetic metals[1], where $\mu = \mu_0$. Under this condition, Eq. 1.2b turns out to be identical with Eq. 1.2. Further, Eq. 1.3b can be rewritten in the form of Eq. 1.3 if an effective dielectric permittivity $\tilde{\varepsilon}$ is introduced instead of $\varepsilon_0 \varepsilon_r(x,y,z)$ in order to account for the free-charge carrier effects associated with the conductivity term σ:

$$\tilde{\varepsilon} = \varepsilon + i\frac{\sigma}{\omega} \qquad (4.1)$$

Let us recall that the 'true' dielectric constant ε accounts for dipolar interactions involving bound electrons contained inside the metal. These interactions can often be neglected at low frequencies, when $\varepsilon \approx \varepsilon_0$. Further, the condition of a local electric neutrality of the metal[2] imposes that:

$$\nabla.(\tilde{\varepsilon}\mathbf{E}) = 0 \qquad (1.4b)$$

This result can also be obtained by considering the divergence of the two members of Eq. 1.3.

In the case of homogeneous metals, $\tilde{\varepsilon}$ is constant and independent of the direction in space, whence it follows that $\nabla.\mathbf{E} = 0$. Using Eq. 1.4b, the combination of Eqs. 1.2 and 1.3b then leads to the familiar Helmholtz equation:

$$\nabla^2\mathbf{E} + \frac{\omega^2}{c^2}\tilde{\varepsilon}_r\mathbf{E} = 0 \qquad (4.2)$$

where:

$$\tilde{\varepsilon}_r = \tilde{\varepsilon}/\varepsilon_0$$

[1] The incorporation of magnetic materials inside photonic crystals of finite size opens the possibility of exploiting certain non-reciprocal effects in the propagation of light. More detailed information on this subject can be found in Appendix B and in the various studies devoted to some of these effects (Belotelov 2007; Chul-Sick 2000; Figotin 2001; Inoue 1997; Kato 2003; Nishizawa 1997; Sigalas 1997a; Wang 2005).

[2] The electric neutrality can be locally perturbed as a result of local modifications of the charge density. However, the recovery time for metals is typically of the order of 10^{-18} s.

In a homogeneous metal, the simplest solution for this equation is here again a plane wave. However, contrary to the case of the dielectric media that were previously considered, a complex wave number is now associated with the wave:

$$\mathbf{E} = \mathbf{E}_0 \, exp\, i(\mathbf{k}.\mathbf{r} - \omega t)$$

where:

$$k^2 = \frac{\omega^2}{c^2}\tilde{\varepsilon}_r \tag{4.3}$$

4.1.1 Drude Model

The conductivity of the metal is in general dependent on the frequency. This dependence can be satisfactorily approximated by using the Drude model (Born 1965; Drude 1890). In this model, the motion of a single electron in a metal submitted to an electric field is assumed to be resulting from two opposite forces: the force $e\mathbf{E}$ associated with the electric field itself and a damping force $-m\,\mathbf{v}/\tau$ associated with the collisions occurring between the electron and the atoms of the metallic lattice. The damping time τ is typically of the order of 10^{-14} s. The equation for the motion of the electron thus assumes the following form:

$$m\frac{d\mathbf{v}}{dt} + m\frac{\mathbf{v}}{\tau} = -e\mathbf{E}(\mathrm{t}) \tag{4.4}$$

where m and e are the mass and the charge of the electron respectively and $\mathbf{E}(\mathrm{t})$ is the real, time-dependent electric field. Denoting as N the electron density in the metal, the instantaneous current density can be expressed in the form $\mathbf{j} = -Ne\,\mathbf{v}$. In the harmonic regime, Eq. 4.4 thus leads to the following relations:

$$\mathbf{j}(\omega) = \sigma(\omega)\mathbf{E} = \frac{Ne^2}{m\left(1/\tau - i\omega\right)}\mathbf{E} = \frac{Ne^2\left(1/\tau + i\omega\right)}{m\left(1/\tau + \omega^2\right)}\mathbf{E} \tag{4.5}$$

Using the expression for the conductivity $\sigma(\omega)$ given in Eq. 4.1 with $\varepsilon \approx \varepsilon_0$, the following equation yields the effective dielectric permittivity of the metal:

$$\tilde{\varepsilon} = \varepsilon_0\left[1 - \frac{\omega_p^2\left(1 - i/\omega\tau\right)}{\left(1/\tau^2 + \omega^2\right)}\right] \tag{4.6}$$

where ω_p represents the plasma frequency of the electron gas, as given by the equation:

$$\omega_p^2 = \frac{Ne^2}{m\varepsilon_0} \tag{4.7}$$

It can be readily verified that the plasma frequency ω_p lies in the ultraviolet region for typical electron densities between 10^{22} and 10^{23} cm^{-3}. As an example, the photon energy corresponding to ω_p is approximately equal to 15 eV for aluminium and to 3.8 eV ($\lambda \sim 328$ nm) for silver. A consequence is that the inequality $\omega_p >> 1/\tau$ is generally satisfied in most cases. By contrast, different situations need to be considered depending on the frequency region that is under consideration.

4.1.2 Low-Frequency Region: Skin Effect and Metallic Losses

In the low-frequency region, which extends from radiofrequencies to the far infrared region, the following relations hold true: $\omega_p >> 1/\tau >> \omega$. In such a case, the conductivity and permittivity of the metal, expressed by Eqs. 4.5 and 4.6 respectively, can be approximated as follows:

$$\sigma \approx \frac{Ne^2\tau}{m} = \varepsilon_0 \omega_p^2 \tau \tag{4.8}$$

$$\tilde{\varepsilon} \approx \varepsilon_0 \left[1 + i\frac{\omega_p^2 \tau}{\omega} \right] \approx i\frac{\varepsilon_0 \omega_p^2 \tau}{\omega} \tag{4.9}$$

The permittivity of the metal is very close to a purely imaginary number, while its conductivity is associated with a real number. In the case of a plane wave with frequency ω, propagating inside the medium, the corresponding wave number deduced from Eq. 4.3 is therefore a complex number k given by the equation:

$$k \approx \frac{1+i}{c}\sqrt{\frac{\sigma\omega}{2\varepsilon_0}} = (1+i)\sqrt{\frac{\sigma\omega\mu_0}{2}} \tag{4.10}$$

The imaginary part of k corresponds to the attenuation that the wave undergoes in the metal. More precisely, an electromagnetic wave penetrating inside the metal will be attenuated by a factor equal to $1/e$ over the distance $\delta = \sqrt{2/\sigma\omega\mu_0}$, referred to as the skin depth of the metal. The higher the frequency, the higher is the conductivity, and correlatively the smaller is the skin depth. For instance, at the 10GHz frequency, the skin depth of a copper conductor ($\sigma \sim 5 \times 10^7$ $\Omega^{-1}m^{-1}$) is lower than 1 μm. In other words, the electromagnetic energy tends to be expelled outside the metallic conductor and to be reflected by it. In the case of a wave impinging upon a metallic surface, the intensity reflection coefficient is given by the following equation (Born 1965):

$$R = \left| \frac{\tilde{n} - 1}{\tilde{n} + 1} \right|^2 \tag{4.11}$$

where:

$$\tilde{n} = \sqrt{\tilde{\varepsilon} / \varepsilon_0} \approx (1 + i)\sqrt{\sigma / 2\varepsilon_0 \omega}$$

Since the amplitude of $\tilde{n}$ is much larger than unity, the reflection coefficient is close to 100 percent. The lower the frequency, the closer to unity the reflection coefficient R is. As a consequence, in the low-frequency region ranging from radiofrequency waves to the infrared, the amount of metallic losses is very low, and metals thus tend to behave like perfect reflectors.

4.1.3 From the Infrared to the Visible and UV Regions

In the optical region of high frequencies, ranging from the near-infrared to the visible and near UV, the parameters ω_p, $1/\tau$ and ω are ordered in a different manner, and the following relations typically hold true: $\omega_p \sim \omega > 1/\tau$. Arbitrarily assuming that $\varepsilon \approx \varepsilon_0$, the effective dielectric permittivity of the metal expressed by Eq. 4.6 can be approximated as follows:

$$\tilde{\varepsilon} = \varepsilon_0 \left[1 - \frac{\omega_p^2}{\omega^2} + i \frac{\omega_p^2}{\omega^3 \tau} \right] \tag{4.12}$$

The real part in the right-hand side of Eq. 4.12, which is often referred to as the 'Drude dielectric function', clearly evidences the role of the plasma resonance in bulk metals. From this point onwards, two different situations must be separately considered.

In the infrared and visible regions, the optical frequency tends generally to be significantly lower than the plasma frequency. Since the $-(\omega_p/\omega)^2$ term is predominant in the right-hand side of Eq. 4.12, the permittivity of the metal is very close to a negative real number with a large modulus compared to unity. Correspondingly, the refractive index $\tilde{n} = \sqrt{\tilde{\varepsilon} / \varepsilon_0}$ will be associated to a purely imaginary number of large amplitude. In other terms, metals remain good reflectors in these regions.

In the deep ultraviolet region, the optical frequency finally reaches an order higher than the plasma frequency, and therefore $\omega > \omega_p > 1/\tau$. Accordingly, the permittivity of the metal will be represented by a real positive number smaller than unity. The metal thus tends to behave as a weakly absorbing dielectric and to exhibit a permittivity smaller than the permittivity of vacuum. Actually, a metal

may also exhibit in this frequency region optical resonances associated with bound electrons, and in general its optical response cannot be described simply as the optical response of a free electron gas.

4.2 Periodic Metallic Structures at Low Frequencies

The radiofrequency and microwave regions remain privileged areas for metals. This results from the fact, described in Section 4.1.2, that perfectly conductive materials are also perfect reflectors. For this reason, it is in these regions that metallic photonic crystals have attracted the greatest interest, and most studies concerned with the applications of these structures are conducted in these frequency ranges. The EM properties of periodic metallic structures can be determined by using some of the numerical codes developed for dielectric structures and presented in Chapters 1 and 2. A requirement is that the most adequate formula for the dielectric permittivity should be used (see Section 4.1). To this end, an even more precise solution consists in using the numerical or analytical values given in reference textbooks. It is not entirely surprising that the concept of photonic band gap might still apply to the case of periodic metallic structures. However, as will be described here, the behaviour of periodic metallic structure may significantly differ from that of periodic dielectric structures.

4.2.1 Plasmon-Like Photonic Band Gap

One of the most important features of metallic photonic crystals results from the existence of a photonic band gap extending from the zero-frequency onwards. In direct analogy with the plasma resonance which can be observed for bulk metals at optical frequencies and which has been described in Sections 4.1.1 and 4.1.2, this photonic band gap is generally referred to as a plasmon photonic band gap. This analogy was first suggested by J. Pendry in the specific case of photonic crystals consisting of metallic wires with very small diameter compared to both the period of the crystal and the wavelength (Pendry 1996, 1998). The argument developed in general terms by J. Pendry will be briefly exposed here. It should be mentioned that rigorous demonstrations were developed at around the same time by D. Felbacq *et al* on the basis of electromagnetic studies where wires were assumed to be perfectly conductive (Felbacq 1994a, 1994b, 1997).

Let us here consider briefly a two-dimensional lattice of metallic wires assumed to be parallel to the z axis and with an infinite length, as represented in Fig. 4.1. For the sake of simplicity, the lattice in Fig. 4.1 has been chosen with a square symmetry. This particular choice however is of no consequence for the demonstration. An incident wave may efficiently interact with the crystal and thus induce an elementary current I in each wire, provided that this incident wave is TM polarized, i.e. that the electric field $\mathbf{E}$ is parallel to Oz. As a consequence, the magnetic field radiated by a single wire extends within the Oxy plane. At a distance r from

the origin much smaller than the wavelength, this magnetic field is proportional to the Hankel function $H_1^{(1)}(k_0 r)$, solution to the Helmholtz equation, which exhibits a $1/r$ asymptotic behaviour (Abramovitz 1970). The amplitude of the magnetic field can thus be expressed in the form:

$$\mathrm{H(r)} = \frac{I}{2\pi r} = \frac{\pi r_c^2 Nev}{2\pi r} \tag{4.13}$$

where I is dependent on the electron charge density N in the wire, on the velocity of the charges v and on the cross-section πr_c^2 of the conducting wire. On the other hand, the vector potential **A** can be introduced according to its standard definition:

$$\mathbf{H}(\mathbf{r}) = \mu_0^{-1} \nabla \times \mathbf{A} \tag{4.14}$$

Although the formulation presented above is not in general univocal, the ambiguity can be lifted in the present case owing to the periodicity of the structure. It can readily be verified that **A** is parallel to the z axis. It can also be demonstrated that, in the vicinity of the origin, its amplitude is satisfactorily approximated by the following formula (Pendry 1998):

$$\mathrm{A}(r) = \frac{\mu_0 \pi r_c^2 Nev}{2\pi} \ln(a/r) \tag{4.15}$$

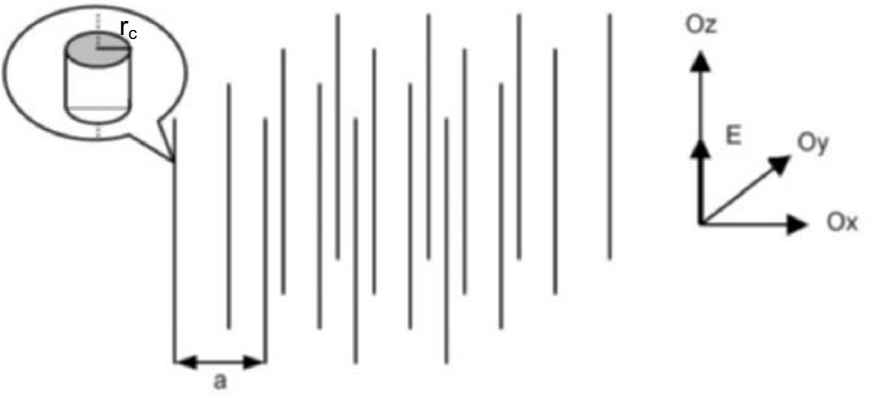

Fig. 1.1 Square array of very thin metallic wires ($r_c << a$) parallel to Oz. At low frequencies, the electromagnetic properties of such an array are similar to those of a bulk metal around the plasma resonance

It is known from quantum mechanics that the presence of a magnetic field results in an additional contribution $e\mathbf{A}$ to the velocity of the electron charges. In the present case, this contribution is even predominant by comparison with the $m\mathbf{v}$ term, and this leads to the possibility of introducing an effective electron mass m_{eff}. This effective mass can then be approximated by the equation $m_{\text{eff}}\mathrm{v} \approx e\mathrm{A}$. In order actually to demonstrate the analogy existing between an array of wires and a bulk metal, it is necessary to average the carrier density and the effective mass over the entire space, i.e. to proceed to a homogenization of the medium. The homogenization thus performed leads to the following equations for N_{eff} and m_{eff} respectively (Pendry 1996, 1998):

$$N_{\text{eff}} = N\frac{\pi r_{\text{c}}^2}{a^2} \tag{4.16a}$$

$$m_{\text{eff}} = \frac{\mu_0 \pi r_{\text{c}}^2 N e^2}{2\pi}\ln(a/2r_{\text{c}}) \tag{4.16b}$$

Using Eqs. 4.16a and 4.16b into Eq. 4.7 leads to the definition of a plasma frequency below which the homogenized medium totally reflects external waves:

$$\omega_{\text{p,eff}}^2 = \frac{2\pi c^2}{a^2\ln(a/2r_{\text{c}})} \tag{4.17}$$

It is apparent from Eq. 4.17 that, contrary to what was the case for bulk metals, the plasma frequency depends on the structural parameters of a lattice and not on some intrinsic parameters of the material. For lattices with a millimetre period and wires with a diameter of a few microns, the plasma frequency typically lies in the domain of gigahertz frequencies. This demonstrates that a 'pseudo-metal', where in principle the cutoff plasma frequency could be controlled, has been created.

The previously mentioned studies on the homogenization of metallic photonic crystals (Felbacq 1994a, 1994b, 1997; Guida 1998) have also permitted to vindicate in a more precise and accurate way the theoretical approach first suggested by J. Pendry. Indeed, at low frequencies, the asymptotic behaviour of a photonic crystal consisting of continuous metallic elements is the same than the behaviour of a lossless (i.e. such that ε is a real number) homogeneous dielectric medium exhibiting a plasma resonance. In particular, Eq. 4.17 remains a satisfactory approximation, even in the case where the diameter of the wire is relatively large compared to the period of the lattice (Guida 1998). Actually, the fact that photonic crystals consisting of continuous metallic elements present a low-frequency cutoff in all cases is far from being surprising. It suffices here to recall that, contrary to dielectric waveguides, a hollow waveguide with metallic walls also exhibits such a low-frequency cutoff.

4.2.2 Transmission Spectra of Metallic and Dielectric Photonic Crystals

The differences between the behaviours of metallic and dielectric photonic crystals can be illustrated through the consideration of their calculated and measured transmission spectra. Fig. 4.2 displays a comparison between the transmission spectra of two-dimensional lattices with a similar geometry: the upper part of the figure corresponds to the dielectric case while the lower part corresponds to the metallic case. In either case, the lattice presents a square symmetry and is composed of rods extending in the air, while the incident wave is TM polarized. The dielectric lattice consists of eleven rows of 18 alumina rods ($\varepsilon_r \sim 9$) with a diameter $d = 1.5$ mm and a length $L = 100$ mm. The period a of the lattice is equal to 3 mm. The metallic lattice consists of seven rows of 18 copper rods with the same diameter ($d = 1.5$ mm) but with a length L equal to 50 mm. The period a of the lattice in this case is equal to 6 mm. For the sake of calculations, the metal will be assumed to be perfectly conductive. The calculated spectra, represented by black curves, were obtained using a FDTD model (see Chapter 2), in which rods were assumed to be of an infinite length. The measured spectra, represented by grey curves, were obtained by means of a microwave network analyser.

As has been described already in Chapter 1, dielectric photonic crystals always present a transmission band at low frequencies (Fig. 4.2*, upper part*). The first band gap is associated with the Bragg condition $\lambda/2 \sim a$, where λ represents the wavelength in the crystal. In other words, the centre frequency of the band gap is approximately given by the equation $\nu \approx c/(2n_{eff}a)$, where $n_{eff} = \sqrt{\varepsilon_{eff}}$ is the effective refractive index at low frequencies, $\varepsilon_{eff} = (1 - f) + f\varepsilon_r$ is the averaged dielectric permittivity and f is the filling factor of the dielectric. In the present case where $f \approx 0.2$, the value for the centre frequency determined from the formula above is equal to 31.5 GHz. This is consistent both with the experimentally measured value and the value deduced from the numerical FDTD model. Beyond the first band gap, the transmission spectrum presents a succession of transmission bands and band gaps with a progressive decrease of their respective contrasts.

As can be seen from the observation of the lower figure, the spectrum of the metallic photonic crystal presents the same alternation of transmission bands and band gaps with the same progressive decrease of the transmission contrast. However, the low-frequency region of the spectrum exhibits a fundamentally different aspect. Starting from the zero-frequency, a strong attenuation of the crystal, associated with the plasmon-like photonic band, can thus be observed in this region. The cutoff frequency numerically calculated from the FDTD model (~ 22 GHz) is close to the value estimated on the basis of the approximate formula given in Eq. 4.17 (~ 16.5 GHz). The plasmon photonic band gap is then followed by a first transmission band whose centre frequency (~ 27 GHz) corresponds to $\lambda/2 \sim a$. The situation turns out to be reversed compared to the case of dielectric photonic crystals, where the same exact relation corresponds to the first band gap. In the first transmission window, the metallic photonic crystal behaves as an ensemble of Fabry-Perot cavities coupled to one another along the propagation direction. In the

case under consideration, there are six cavities, which correspond to the seven rows of metallic rods, and six resonance peaks can indeed be observed in the transmission spectrum. As an aside, it can be noted that an excellent agreement between experimental measurements and numerical values calculated with the FDTD model has been achieved. The shift in amplitude arises simply from the fact that the measurement system was limited to transmission amplitudes higher than – 45 dB.

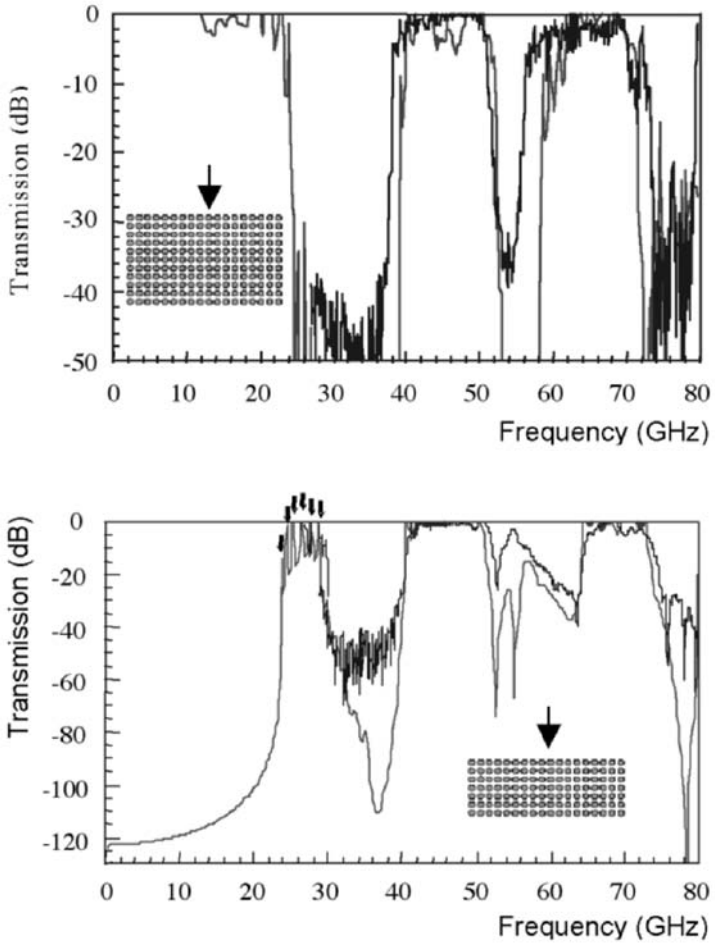

Fig. 4.2. Transmission spectra of square lattices of rods extending in the air for a normal incidence in TM polarization. The black curves correspond to the calculated spectra, while the grey curves correspond to experimental measurements. *Top.* Dielectric lattice consisting of eleven rows of 18 alumina rods ($\varepsilon_r \sim 9$) with a diameter $d = 1.5$mm and a length $L = 100$ mm. The period of the lattice is $a = 3$ mm. *Bottom.* Metallic lattice consisting of seven rows of 18 copper rods with a diameter $d = 1.5$ mm and a length $L = 50$ mm. The period a of the lattice is equal to 6 mm (Gadot 1998)

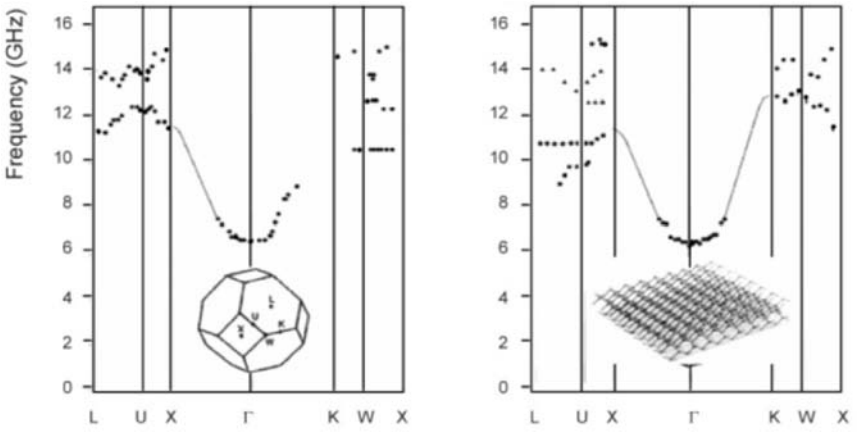

Fig. 4.3. Band diagram of a lattice of connected metallic wires arranged into a diamond structure. Each wire has a one centimeter length, corresponding to the distance between atoms inside the simulated diamond crystal (Sievenpiper 1996). *Left*. Measured diagram for an *s*-polarized wave incident onto a <100> crystal plane. *Right*. Measured diagram for a *p*-polarized wave incident onto the same crystal plane. The insert in the left-hand figure represents the Brillouin zone of the diamond crystal, while the insert in the right-hand figure represents a partial view of the metallic structure

4.2.3 Complete Band Gaps in Metallic Photonic Crystals

As has been previously emphasized in Section 1.3.3, two-dimensional lattices of disconnected rods exhibit much smaller band gaps in TE polarization than in TM polarization. This behaviour can be verified for lattices of dielectric rods as well as for lattices of metallic rods. The difference between the two polarizations is even more marked in the latter case. Indeed, while the transmission spectrum in TE polarization exhibits only limited amplitude variations, a very strong attenuation can be observed in TM polarization, at least for the first band gaps, as can be seen from the consideration of the lower part of Fig. 4.2. As a result of the strong TM efficiency of two-dimensional lattices formed by metallic rods or wires, a complete photonic band gap can be easily achieved for all propagation directions and all polarizations using a simple cubic lattice formed by metallic rods or wires. A cubic lattice can indeed be viewed as a superposition of three two-dimensional square lattices whose rods (or wires) are aligned along the three directions *Ox*, *Oy* and *Oz* respectively. Each of these lattices then presents a plasmon-like band gap for a certain polarization of the field and for the directions of propagation normal to the rows of rods or wires. When a wave propagates along a direction other than

the three main directions, several two-dimensional lattices will simultaneously interact with this wave, but a band gap extending from the zero-frequency will nonetheless remain present in all cases. Therefore, the possibility of achieving a complete photonic band gap does not require a metallic structure as elaborate as the 'Yablonovite'. The diamond-like cubic structure with two 'atoms' per unit cell has also been reproduced from a lattice of interconnected metallic wires. In this case, the 'atoms' in the diamond structure were simulated by the intersections of the wires (Sievenpiper 1996). A complete plasmon-like photonic band gap was thus experimentally demonstrated before being vindicated by a theoretical modelling (Fig. 4.3). The detailed study of this structure also revealed the existence of longitudinal electromagnetic modes.

4.2.4 Structures with Continuous Metallic Elements and Structures with Discontinuous Metallic Elements

Thus far, metallic photonic crystals have always been assumed to consist of continuous metallic rods or wires. However, it is apparent that the theoretical approach to the plasmon-like band gap presented in Section 4.2.1 is no longer valid when the continuous wires are replaced by discontinuous wires. In the very low frequency region where metallic elements can be considered as localized elements, the introduction of discontinuities between these elements amounts to inducing capacitive effects which combine to the self-inductances induced by the circulating currents. This results in the generation of an impedance of the type $(LC\omega^2 - 1)/C\omega$ instead of the inductive short-circuits $L\omega$ that existed for continuous wires (Bridges 1970; Ulrich 1963, 1967). As a consequence, the metallic photonic crystal will exhibit a transmission band instead of a band gap, as is the case at very low frequencies. A general and more detailed explanation will be developed along these lines in Section 4.4.6 when addressing the subject of surface waves in more detail. This explanation will allow us to understand why photonic crystals formed by discontinuous metallic wires are actually closer to dielectric photonic crystals than to the purely metallic photonic crystals that were previously considered.

Fig. 4.4 allows a more precise comparison between the transmission spectra of a two-dimensional lattice of continuous metallic rods (upper part of the figure) and the transmission of a two-dimensional lattice of discontinuous metallic rods (lower part of the figure). The parameters are the same as those that were used in the lower part of Fig. 4.2: the lattice has a square symmetry and a period equal to 6 mm, while the diameter d of the rods is equal to 1.5 mm. In the case of seven rows of continuous rods, represented by the dashed curves in the upper part of Fig. 4.4, the same transmission spectrum as in Fig. 4.2 can be observed. For a smaller number of continuous rows ($n = 2$), represented by the solid curves in the upper part of Fig. 4.4, the band gaps are less marked, but the transmission within the 'plasmon photonic band gap' falls down to -50 dB, while this band extends to frequencies approaching 20 GHz.

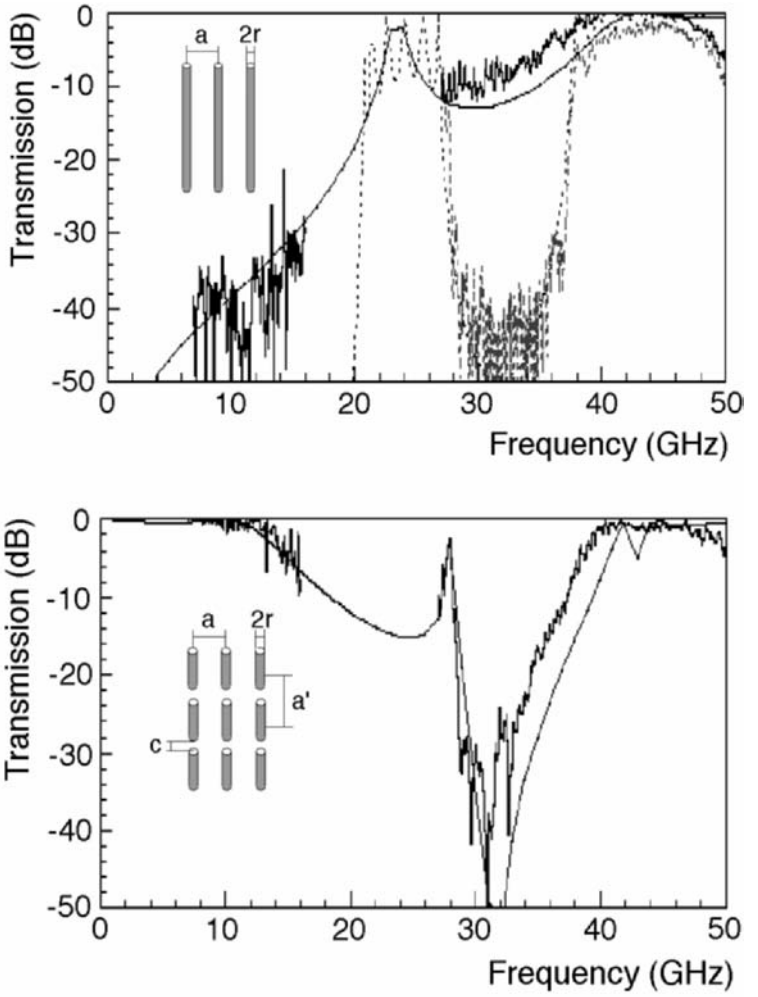

Fig. 4.4. Transmission spectra of square lattices formed by continuous metallic rods (*top*) and by discontinuous metallic rods (*bottom*). The incident wave here is a TM polarized wave. The thick curves correspond to experimental measurements, while the thin curves correspond to numerical calculations carried out using a finite element model (HFSS software from Hewlett Packard). Lattices with seven rows (*dashed curves*) and with two rows (*solid curves*) of continuous rods are simultaneously considered, while only a lattice with two rows of discontinuous rods is considered. In all three cases, the period of the lattice is equal to 6 mm and the diameter of the rods to 1.5 mm. The discontinuities are formed by air gaps with a 1.5 mm length, periodically distributed along the rods with a period equal to 6.5 mm (Lourtioz 1999)

The comparison with the lattice of discontinuous rods is carried out for this small number of rows. Discontinuities are introduced in the form of air 'gaps' with a length equal to 1.5 mm, periodically distributed along each metallic rod with a period of 6.5 mm. As can be seen in the lower part of Fig. 4.4, the transmission spectrum of the lattice of discontinuous rods is fundamentally different from the transmission spectrum of the lattice of continuous rods. Not only does a transmission band appear instead of the 'plasmon photonic band gap', but an attenuation of 15 dB, corresponding to the first transmission band in the upper part of Fig. 4.4, also appears within a frequency region extending around 25 GHz. Further, the existence of a narrow, albeit very pronounced, attenuation peak corresponding to the second band gap around 32 GHz, can be noted. The attenuation due to two rows of discontinuous rods is as strong (- 50 dB) as the attenuation due to seven rows of continuous rods.

As will be described in Section 13.2, the various behaviours observed in Fig. 4.4 can be exploited for the design of switchable microwave filters. Fig. 4.4 also demonstrates that the numerical results calculated from a finite element model are consistent with the results of experimental measurements. Returning to the consideration of the simple LC model introduced above, the relevant capacitor with respect to the discontinuous rods is simply the capacitor associated with each individual air gap. In the example presented in Fig. 4.4, the capacitor was estimated to be equal to 10 fF. Numerical simulations similar to those reported in Fig. 4.4 were repeated for different gap lengths, i.e. for capacitors with different values (Lourtioz 1999). As predicted by the LC model, the frequency at the edge of the first transmission band was found to be in inverse ratio to the square root of the value of the capacitor.

4.3 Periodic Metallic Structures at Optical Frequencies. Idealized Case of a Dispersive Lossless Dielectric

As has been mentioned already, the reflectivity of a metal is lower at optical wavelengths than at centimeter or millimeter wavelengths, and metallic losses, even when they are low, can never be completely neglected. This phenomenon, combined with the difficulty of realizing patterns with a micron or a submicron size, explains that there is currently a relative paucity of studies on metallic photonic crystals in the infrared and visible regions. Thus far, researches in this field have been for the most part directed at the realization of three-dimensional lattices of small metallic spheres (Moroz 1999; Pendry 1994; Zhang 2000), which can be relatively easily fabricated from colloidal solutions containing spheres in suspension (Astratov 1995; Lawendy 1988).

From an historical point of view, the optical properties of (non necessarily periodic) ensembles of metallic spheres with sizes close to the optical wavelength, released in a dielectric medium, were first studied at the beginnings of the twentieth century (Maxwell Garnett 1904, 1906; Mie 1908). In particular, Maxwell Garnett

demonstrated the possibility of assimilating such ensembles to a medium with a complex refractive index $n = n'(1 + i\kappa')$, and introduced analytical expressions for n' and κ' (Maxwell Garnett 1904, 1906). A few years after, Mie developed a rigorous theory for the diffraction of plane waves by a single sphere, which applies to any sphere whatever its composition and size are, irrespective of the nature of the surrounding medium (Mie 1908). In the context of this book, the possibility always exists of using one of the models developed in Chapters 1 and 2 for determining the band diagram of a periodic ensemble of spheres, provided however that the model thus employed accounts for the dispersion of the metal. To a first approximation, the permittivity of a metal around the plasma frequency ω_p can be represented by the real part of the Drude expression (Eq. 4.12). This approximation is well suited to silver in the visible and near UV regions, especially in the wavelength region extending from 310 to 520 nm where silver is only weakly absorbing. In the more general case however, the Drude expression fails to take into account the resonant absorption of metals and the absorption effects due to surface plasmons (Bohren 1984). The issue of surface plasmons will be briefly discussed in the next section (Section 4.4).

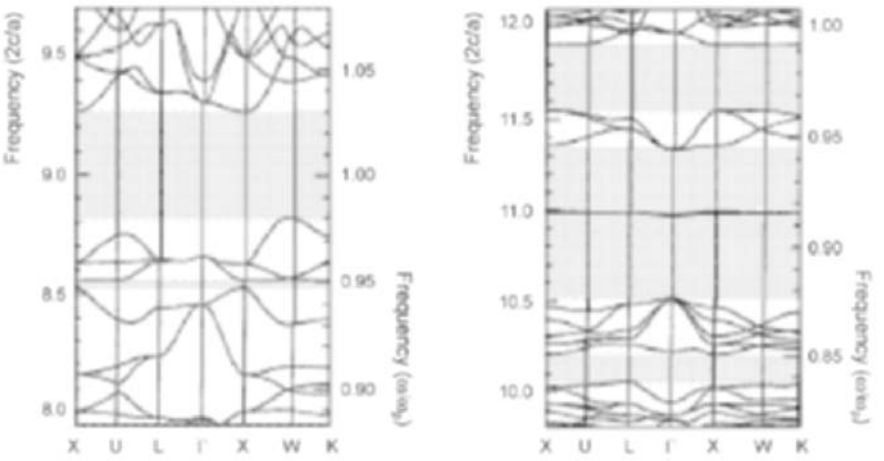

Fig. 4.5 Band diagrams of face-centred cubic lattices consisting of metallic spheres extending in the air (Moroz 1999). The side of the unit cell is denoted as $a = 2r$, where r is the radius of the spheres. The wave frequency ($\omega / 2\pi$, vertical axis) is expressed either in normalized frequency units ($2c / a$) or in plasma frequency units (ω_p) *Left.* Band diagram calculated for $r/\lambda_p = 1.013$, where $\lambda_p = 2\pi c/\omega_p$ is the plasma wavelength *Right.* Band diagram calculated for $r/\lambda_p = 1.35$

Fig. 4.5 represents the band diagrams of face-centred cubic lattices of metallic spheres extending in the air, calculated by approximating the permittivity of the metal with the real part of the Drude expression in Eq. 4.12 (Moroz 1999). Since the imaginary part of ε is neglected, this is obviously an idealization. Calculations were performed using the KKR model, while the spheres were assumed to be in direct contact to one another. The two diagrams presented in Fig. 4.5 correspond to two arbitrarily chosen values for the frequency (or the wavelength) of the plasma respectively: in the first case, displayed on the left, the ratio of the radius of the sphere to the wavelength of the plasma is equal to 1.013, while in the second case, displayed on the right, this ratio is equal to 1.35. As can be seen, these diagrams are to some extent similar to those obtained for dielectric photonic crystals. However, in spite of the fact that the crystal has a simple face-centred structure, the existence of complete band gaps with a large width ($\Delta\omega / \omega \sim 10\%$) can nonetheless be observed. This phenomenon can be explained by the very high index contrast existing between the air and the metallic spheres for wavelengths close to the plasma wavelength ($\varepsilon \to 0$). Actually, the structure is almost equivalent to a cubic lattice of air spheres inside a dielectric with a very high permittivity. The widest gap is obtained around the plasma frequency itself, where the wavelength of the plasma reaches an order comparable to the radius of the sphere. When the wavelength of the plasma is lower than the radius of the sphere, several gaps of larger width appear for frequencies below the plasma frequency. In this case, represented in the right-hand side of Fig. 4.5, the existence of transmission bands with a very small curvature, i.e. with a very low dispersion, may also be noted. These transmission bands correspond to group velocities of light which can be estimated to be less than $\sim c / 200$, where c is the speed of light in vacuum.

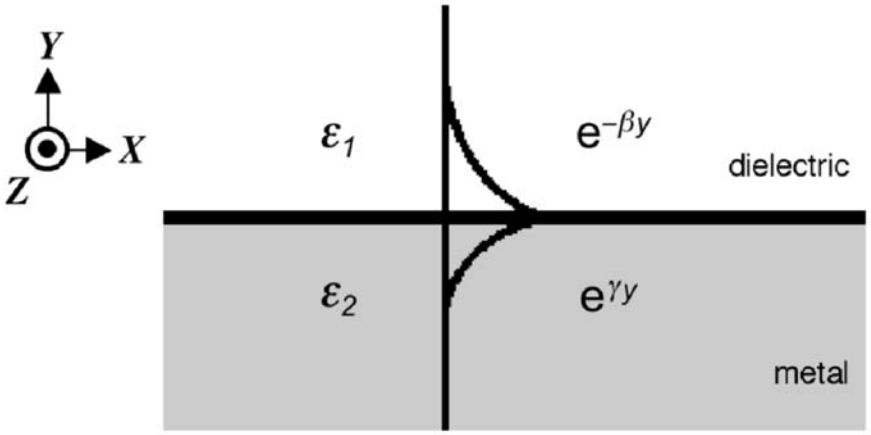

Fig. 4.6. Schematic description of a wave propagating at the interface between a dielectric (ε_1) and a metal (ε_2). The wave decays exponentially on either side of the interface

4.4 Surface Waves

A property of metals is that they may allow the propagation of surface waves, i.e. electromagnetic waves that remain localized at the interface between the metal and the air or between the metal and any other surrounding dielectric (Fig. 4.6). In the radiofrequency and microwave regions, surface waves are more often referred to as surface currents. This points to the fact that these electromagnetic waves may actually extend over distances equal to several thousands of wavelengths in the air or in a dielectric. By contrast, in the optical region, surface waves are well localized at the interface. In this context, these waves are also referred to as surface plasmons (or polaritons), since their generation and propagation involve resonant oscillations of the surface charges (Raether 1988).

Nevertheless, the existence of surface waves in either of these wavelength regions results from the fact that the real part of the dielectric permittivity of metals is negative. In this section, we shall first recall the general properties of surface waves for metals with a plane interface. We shall then discuss the influence of the periodic corrugation of the surface of the metal in these two wavelength regions. Finally, different possible applications of such periodic structures will be briefly considered near the end of the chapter.

4.4.1 Surface Plasmons at a Metal/Dielectric Plane Interface

Let us here consider a TM wave propagating along the x direction in the plane interface (Oxz) between two materials with relative permittivity ε_1 and ε_2 respectively (Fig. 4.6). The first medium of permittivity ε_1 is dielectric while the second medium of permittivity ε_2 is metallic. The problem to be addressed is therefore to determine the conditions allowing the propagation of surface waves, whose amplitude decreases exponentially on both sides of the interface. In TM polarization[3], the component E_z of the electric field is zero, while the magnetic field has a single non-zero component H_z. Let us denote here by α_{pl} the propagation constant associated with the plasmon wave along the Ox axis. Using Eqs. 1.37 and 1.38 for the propagation in two homogeneous materials, combined with the condition that the amplitude of the surface wave should decrease when $y \to \pm\infty$, the magnetic field can be as expressed in the form:

[3] In this section, we shall adopt the standard conventions used for electromagnetic waveguides. Surface plasmon modes propagate in the x direction. The magnetic field of TM modes is therefore normal to Ox and parallel to Oz. This implies that when the plane interface is replaced with a grating with grooves parallel to Oz (Section 4.4.2), the definition of the TM modes will be different from the definition adopted in the discussion of two-dimensional photonic crystals in Chapter 1 of this book (Section 1.1.5), where TM modes were defined in such a way that the electric field rather than the magnetic field was parallel to the cylinder axis (in this case the groove axis). The same remark applies to TE modes.

$$H_z = A_{pl}\, exp\left(i\alpha_{pl}x - \beta_{pl}y\right) \quad if \quad y > 0 \tag{4.18}$$

$$H_z = B_{pl}\, exp\left(i\alpha_{pl}x + \gamma_{pl}y\right) \quad if \quad y < 0 \tag{4.19}$$

with:

$$\left(\alpha_{pl}\right)^2 - \left(\beta_{pl}\right)^2 = k_0^2\varepsilon_1 \quad \text{and} \quad \left(\alpha_{pl}\right)^2 - \left(\gamma_{pl}\right)^2 = k_0^2\varepsilon_2 \tag{4.20}$$

where A_{pl} and B_{pl} are scalar, and where the real parts of β_{pl} and γ_{pl} must be positive in order to ensure that the amplitude of the field given by Eqs. 4.18 and 4.19 is continuously decreasing as the distance to the interface increases. Finally, one must account for the boundary conditions at $y = 0$. The continuity of the tangential component of the magnetic field at the interface imposes that:

$$A_{pl} = B_{pl} \tag{4.21a}$$

Likewise, the continuity of the tangential component E_x of the electric field at the interface implies from Maxwell's equation (Eq. 1.3) that $(1/\varepsilon_i)(\partial H_z/\partial y)$ should be a continuous function of the variable y:

$$\frac{\beta_{pl}}{\varepsilon_1} A_{pl} = -\frac{\gamma_{pl}}{\varepsilon_2} B_{pl} \tag{4.21b}$$

Eq. 4.21a must be consistent with Eq. 4.21b, which leads to:

$$\frac{\beta_{pl}}{\varepsilon_1} = -\frac{\gamma_{pl}}{\varepsilon_2} \tag{4.21c}$$

Using Eq. 4.21c with Eq. 4.20 and taking the square roots of α_{pl} , β_{pl} and γ_{pl} respectively, the following expressions can finally be derived:

$$\alpha_{pl} = \sqrt{\frac{\varepsilon_1\varepsilon_2}{\varepsilon_1+\varepsilon_2}}k_0 \ , \quad \beta_{pl} = \frac{i\varepsilon_1}{\sqrt{\varepsilon_1+\varepsilon_2}}k_0 \ , \quad \gamma_{pl} = \frac{-i\varepsilon_2}{\sqrt{\varepsilon_1+\varepsilon_2}}k_0 \tag{4.22}$$

The effective decay of the fields which occurs as $y \to \pm\infty$ can be observed when the square roots in the relations presented in Eq. 4.22 lie within the upper region of the complex plane. It is immediately apparent from the equations for β_{pl} and γ_{pl} that surface waves cannot exist when ε_1 and ε_2 are both positive, i.e. when the materials on each side of the interface are standard dielectrics. Indeed, if such were the case, β_{pl} and γ_{pl} would be purely imaginary numbers and the boundary

conditions for $y \rightarrow \pm\infty$ would not be satisfied. The same remark applies to weakly absorbing dielectrics.

The previous analysis can be reproduced in TE polarization, save for one decisive change. Since the two materials are now assumed to be non-magnetic ($\mu = \mu_0$), the continuity of the H_x component of the magnetic field at the interface reduces now to a simple condition concerning the continuity of the y-derivative of the electric field $\partial E_z/\partial y$. Accordingly Eqs. 4.21b and 4.21c now lead to $\beta_{pl} = -\gamma_{pl}$, which from Eq. 4.20 imposes in turn that $\varepsilon_1 = \varepsilon_2$. This result is obviously inconsistent with the very existence of an interface. The propagation of a TE polarized surface wave is therefore forbidden for a plane metal/dielectric interface. Note however that it may become allowed if the interface exhibits pronounced corrugations or irregularities. In this case, the surface wave results from the coupling between the corrugations, which act like open cavities.

Let us here consider a plane interface between the air and aluminium, with a refractive index equal to $0.82 + i\,5.99$ at the wavelength $\lambda = 546$ nm. The propagation constant α_{pl} determined from Eq. 4.22 then turns out to be equal to $(1.013 + i\,3.8\,10^{-3})k_0$. As has been seen, the imaginary part of α_{pl} is very low while its real part is slightly larger than k_0. This result actually applies to any metal which, like for instance gold or silver, is highly conductive in the infrared and visible regions. Since $\Re e\{\alpha_{pl}\}$ is larger than the amplitude of the wave vector in free space, a surface plasmon wave cannot be excited by an incident plane wave nor by an incident beam, since the projection of their wave vector onto the x axis would necessarily be smaller than k_0. From the consideration of dispersion diagram, this amounts to saying that no solution $\omega(k)$ exists within the light cone for a surface plasmon propagating along a perfect metallic plane. At optical frequencies, it may be convenient to use the approximated expression for the permittivity of the metal given by the Drude formula (Eq. 4.12). Then, provided that metallic losses can be neglected and that the metal can be assumed to be surrounded with air ($\varepsilon_1 = 1$), the equation for the dispersion of a plasmon wave can be deduced from the first equation in Eq. 4.22:

$$\alpha_{pl} = \sqrt{\frac{\omega_p^2 - \omega^2}{\omega_p^2 - 2\omega^2}}\, k_0 \tag{4.23}$$

A graphical representation of Eq. 4.23 is displayed in Fig. 4.7. The cutoff frequency for plasmon waves is equal to $\omega_p/\sqrt{2}$: in the vicinity of this frequency, the wave vector of the surface wave reaches a very high amplitude compared to k_0. As can be seen from the observation of this figure, the entire dispersion curve lies below the light line, which confirms that plasmon waves cannot in principle be coupled to free-space waves. Actually, in the optical region, the residual roughness of dielectric/metal interfaces is always high enough to allow the weak coupling of plasmon waves and free-space-waves. Further, the use of a dielectric prism in direct contact with the surface is a well-known classical arrangement for optimizing such a coupling via an evanescent wave (Kretschmann 1971).

4.4.2 Propagation of Surface Plasmons along a Periodically Modulated Metal/Dielectric Interface and Local Enhancement of the Field

The possibility for a plasmon wave to propagate along the plane interface between a metal and a dielectric has been demonstrated in the preceding section. However, it has also been shown that, in principle, such a wave cannot be excited by using an incident light beam. In the present section, we shall see that the excitation of the surface plasmon by an external light beam becomes possible when the interface is periodically modulated. The phenomenon can be intuitively explained in the following terms: a periodically modulated surface, i.e. a diffraction grating of the kind represented in Fig. 4.8, induces a coupling between waves whose respective propagation constants at the surface differ by an integer, which is a multiple of the spatial frequency $2\pi / d$, where d is the period of the grating. Although the plasmon dispersion curve lies below the light line in the case, represented in Fig. 4.7, of a perfect plane, the band-folding effects associated with spatial periodicity cause the dispersion curves of certain propagation modes to extend beyond the light line, with the consequence that surface plasmon waves can now be excited. A more mathematical description of this phenomenon will be presented in the following pages. This will allow us to explain the increase in the absorption of light by metals under certain conditions, as well as the strong local enhancement of the electromagnetic field at the surface.

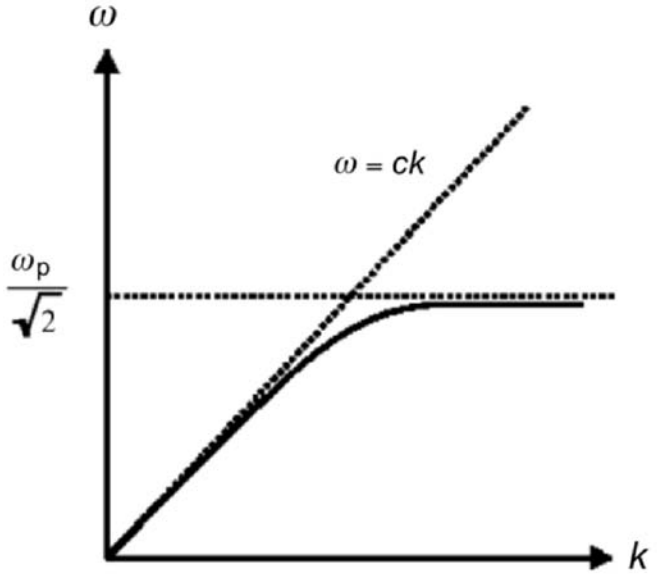

Fig. 4.7. Dispersion of surface plasmons propagating along a metallic plane

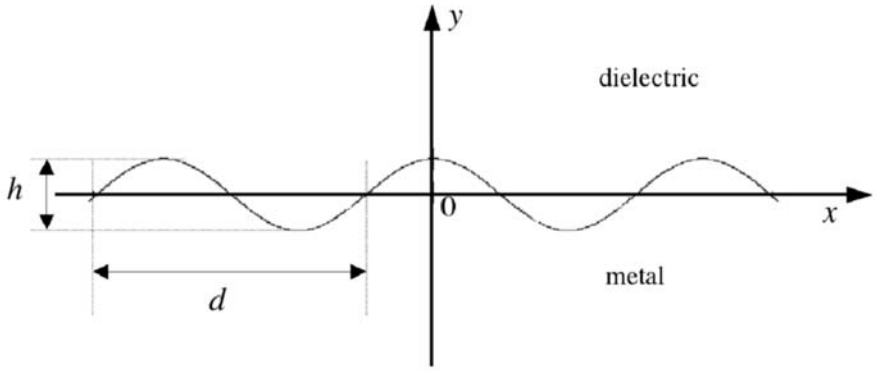

Fig. 4.8. Diffraction grating and conventions used for its description

Let us consider here the metallic diffraction grating represented in Fig. 4.8. The metal has a permittivity ε_2 and is assumed to be bounded by a dielectric with a permittivity ε_1. For the sake of simplicity, it will be further assumed here that the surface of the grating presents a sinusoidal modulation. The period of the grating and the groove depth will be referred to as d and h, respectively.

In this respect, the question arises whether a surface wave can propagate along the x direction. The answer to this question, at least in the case of TM polarization, is positive. In this specific case, the grating can be derived from the plane interface considered in Section 4.4.1 through a continuous, mechanical deformation. Bloch's theorem allows us to expand the EM field into a series of x-dependent Bloch waves, as follows:

$$H_z = \sum_{n=-\infty}^{+\infty} f_n(y) exp\left(i\alpha_{pl,n}(h)x\right) \tag{4.24}$$

$$\alpha_{pl,n}(h) = \alpha_{pl,0}(h) + nK, \tag{4.25}$$

where $K = \frac{2\pi}{d}$.

Using the Helmholtz equation for the EM field in each medium (see Section 2.1.1), it can be demonstrated that the functions $f_n(y)$ are exponential functions of y on both sides of the inhomogeneous region ($-h/2 < y < h/2$):

$$H_z = \sum_{n=-\infty}^{+\infty} A_{pl,n}(h) exp\left(i\alpha_{pl,n}(h)x - \beta_{pl,n}(h)y\right), \text{ if } y > h/2 \tag{4.26}$$

$$H_z = \sum_{n=-\infty}^{+\infty} B_{pl,n}(h) exp\left(i\alpha_{pl,n}(h)x + \gamma_{pl,n}(h)y\right), \text{ if } y < -h/2 \tag{4.27}$$

where:

$$\left(\beta_{pl,n}\right)^2 = \left(\alpha_{pl,n}\right)^2 - k_0^2\varepsilon_1 \quad \text{and} \quad \left(\gamma_{pl,n}\right)^2 = \left(\alpha_{pl,n}\right)^2 - k_0^2\varepsilon_2 \tag{4.28}$$

The real parts of $\beta_{pl,n}$ and $\gamma_{pl,n}$ in Eq. 4.28 must be positive in order to ensure the decay of the field for each side of the interface.

When the groove depth h of the grating tends towards 0, the equations for the field given in Eqs. 4.26 and 4.27 ought to tend towards the expressions given in Eqs. 4.18 and 4.19 for a plane interface. This entails that one of the terms of the series in Eq. 4.26 must correspond to the right-hand part of Eq. 4.18 and, likewise, that one of the terms of the series in Eq. 4.27 must correspond to the right-hand part of Eq. 4.19. Since the indices for the terms are arbitrary, we may for instance decide that the non-zero terms for $h = 0$ are the same as those associated with $n = 0$. Hence,

$$\alpha_{pl,0} = \alpha_{pl} \tag{4.29}$$

$$A_{pl,n}(0) = B_{pl,n}(0) = 0 \quad \text{if } n \neq 0 \tag{4.30}$$

$$\frac{A_{pl,0}(0)}{A_{pl}} = \frac{B_{pl,0}(0)}{B_{pl}} \tag{4.31}$$

It is apparent that, for small values of h, $\alpha_{pl,0}(h)$ remains close to α_{pl}. Further, if the grating has such a period that:

$$-k_0\sqrt{\varepsilon_1} < Re\left\{\alpha_{pl} - K\right\} < k_0\sqrt{\varepsilon_1} \tag{4.32}$$

then the dispersion curve of the mode of propagation constant $\alpha_{pl,-1}(h)$ is contained inside the light cone. This might be true as well for other modes associated with different constants $\alpha_{pl,n}(h)$. Under such conditions, the imaginary part of $\alpha_{pl,n}(h)$ is small, and therefore each corresponding $(\beta_{pl,n})^2$ number in Eq. 4.28 tends towards a negative real number. This obviously entails that the $\beta_{pl,n}$ solution which has a negative imaginary part should be chosen. In this case, the wave associated to $\alpha_{pl,-1}(h)$ and $\beta_{pl,-1}(h)$ in Eq. 4.26 is very close to a plane wave propagating away from the grating surface with an inclination angle θ_{-1} with respect to the y axis:

$$\sin(\theta_{-1}) = \frac{\mathrm{Re}\left\{\alpha_{pl,-1}(h)\right\}}{k_0\sqrt{\varepsilon_1}} \tag{4.33}$$

More generally, the waves associated with the different terms in Eq. 4.26 are very close to diffracted waves propagating towards $y = +\infty$ or to evanescent waves, depending on whether the mode with propagation constant $\alpha_{pl,n}(h)$ lies inside or outside the light cone ($- k_0\sqrt{\varepsilon_1} < Re\{\alpha_{pl,n}(h)\} < k_0\sqrt{\varepsilon_1}$). Contrary to the case of a plane interface case, the existence of a finite number of leaky waves

propagating away from the surface can now be observed, with the result that radiation losses occur in addition to the metallic losses induced by plasmon surface waves, i.e. by a Joule heating effect. A relative increase of the imaginary part of $\alpha_{pl,n}(h)$ is therefore to be expected.

If the imaginary part of $\alpha_{pl,-1}(h)$ were zero for any value of n, the field represented by Eqs. 4.26, 4.31 and 4.32 would propagate exactly along the same directions as the field diffracted by the grating in the case of an incident wave with an incidence angle $-\theta_{-1}$ with respect to the y axis. A most surprising conclusion can therefore be drawn: the surface plasmon can be considered as being generated from an incident plane wave with a complex propagation constant $\alpha_{pl,-1}(h)$ along the x axis, notwithstanding the fact this incident wave has a zero-amplitude and therefore that it is only virtual. The idea that a diffracted wave may exist in the absence of an incident wave may come as a shock. However, it should be borne in mind that we are concerned here with homogeneous solutions of Maxwell's equations. The fundamental laws of physics are not violated. Indeed, since the propagation constant has an imaginary part, the amplitude of the surface plasmon decreases as it propagates, for the very reason that the energy carried by an incident wave cannot compensate for the absorption and radiation losses. However, it would not be correct to assert that the surface plasmon does not receive any energy. Quite on the contrary, the fact that its amplitude tends towards infinity along the direction opposed to the propagation suggests the presence of an energy source at $x = -\infty$. This source cannot obviously be an incident wave. In practice, this energy can be due to the bombardment of the surface of the metal by a beam of electrons with an adequate energy. Such a technique was used actually for the generation of surface plasmons. In any case, the above discussion emphasizes the main differences between the present equations and the homogeneous equations used for instance in Section 1.1.5 for the determination of the eigenmodes in a dielectric photonic crystal. In the latter case indeed, the dielectric constants are real numbers, and the field operators are Hermitian, thereby resulting in real-valued propagation constants.

The existence of surface plasmons as homogeneous solutions of Maxwell equations has important consequences as regards the diffraction properties of metallic gratings. While surface plasmons may exist in the absence of an incident wave, the presence of an incident wave with a propagation constant approaching $\alpha_{pl,-1}(h)$ may excite inside the metal a large-amplitude wave close to a surface plasmon. This phenomenon is analogous to the oscillations of a damped pendulum, which can be characterized by a complex oscillation frequency. In this case, when the real-valued excitation frequency tends to approach the complex-valued free oscillation frequency, forced oscillations with large amplitude are generated, and this is all the more true when the imaginary part of the free oscillation frequency is small. In analogy with the forced oscillations of a pendulum, the excitation of surface plasmons can therefore be described in terms of a classical resonance effect. This observation, first noted by A. Hessel *et al* (Hessel 1965), is at the origin of the modern theory of surface plasmons on gratings, and has made possible the interpretation of Wood's anomalies, as will be briefly described in the following section.

4.4.3 Wood's Anomalies: Phenomenological Theory

At the beginnings of the twentieth century, the American astronomer R.W. Wood reported the surprising phenomenon that under certain circumstances, waves diffracted by metallic gratings could exhibit extremely abrupt variations of their amplitude while at the same time undergoing only very limited variations of either the incidence angle or the wavelength (Wood 1902). This phenomenon, known as 'Wood's anomalies', has fascinated researchers in optics for nearly a century. A few years after the discovery of Wood's anomalies, Lord Rayleigh observed that this phenomenon always occurred in the neighbourhood of a transition from an evanescent wave to a propagating plane wave, i.e. propagating in the y-direction, or conversely, and this observation led him to attribute Wood's anomalies to such a transition. Only half a century later was this simple explanation recognized to be false. Hessel and Oliner were the first to correctly explain Wood's anomalies in terms of the excitation of surface plasmons (Hessel 1965). Since the real part $\alpha_{pl,0}(h)$ of the propagation constant associated with the surface plasmon is close to k_0, the phenomenon does indeed occur in the neighbourhood of a transition from an evanescent wave to a propagating plane wave or conversely, but it should not, however, be confused with the transition itself. The excitation of surface plasmons leads to a strong increase in the amplitude of the field in the vicinity of the grating surface, up to two orders of magnitude. The absorption in the metal is therefore dramatically reinforced, while the amplitudes of the diffracted waves undergo abrupt variations. The phenomenological theory of Wood's anomalies has led to the mathematical expression of formerly intuitive insights, in particular through the use of pology, i.e. through the study of the properties of functions of complex variables.

We present here only a brief outline of this theory (Maystre 1976, 1977, 1982; Nevière 1980) in the specific case where the dispersion curve of the mode with propagation constant $\alpha_{pl,-1}(h)$ is contained within the light cone. Let us consider the case of an incident wave with amplitude A' and incidence angle θ, as represented in Fig. 4.9 (*right*). Using the classical analysis of the diffraction by a grating (see Section 2.1.1), we may define as A_n and B_n respectively the amplitudes of the diffracted waves in the dielectric and in the metal. Although normalized amplitudes such as $\tilde{A}_n = A_n/A'$ are generally defined for real values of the incidence angle and propagation constant $\alpha = k_0\sqrt{\varepsilon_1}\,\sin\theta$ along the x direction, this analysis can be mathematically extended to the case where α is a complex variable, with the $\tilde{A}_n(\alpha)$ functions remaining defined as functions of real variables. The analytical extension of the functions $\tilde{A}_n(\alpha)$ to the complex plane is univocal, and the pology consists in determining the poles and the zeros of these functions. In the case under consideration here, one of the poles seems to be obvious. Indeed, when α reaches $\alpha_{pl,-1}(h)$ in the complex plane, the amplitudes A_n and B_n can be non-zero even if the amplitude A' of the incident wave is zero (see Section 4.4.2.). In this case, all normalized amplitudes $\tilde{A}_n(\alpha)$ are infinite. This can be analytically expressed in the following form:

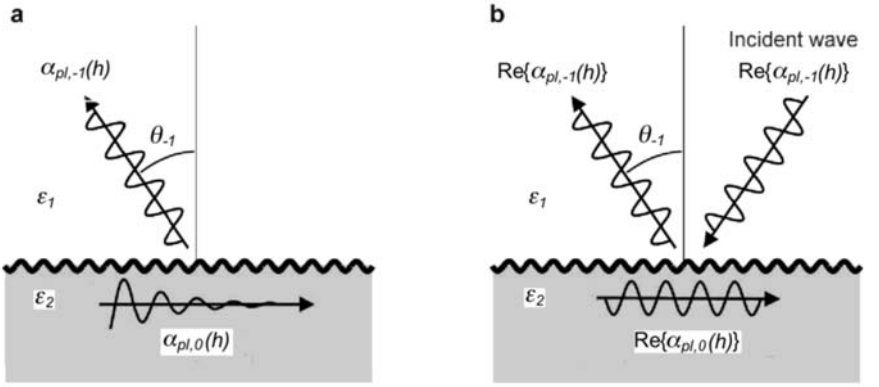

Fig. 4.9. *Left.* Homogeneous solutions including plasmon waves *Right.* Resonant excitation of homogeneous solutions by an incident plane wave

$$\tilde{A}_n = \frac{P_n(\alpha, h)}{\alpha - \alpha_{pl,-1}(h)} \tag{4.34a}$$

where $P_n(\alpha,\ h) \neq 0$ for $\alpha = \alpha_{pl,-1}(h)$. It might be observed that, from Eq. 4.25, the imaginary parts of $\alpha_{pl,0}(h)$ and $\alpha_{pl,-1}(h)$ are identical and, from Section 4.4.1, that the modulus of the imaginary part of $\alpha_{pl,0}(0) = \alpha_{pl}$ is close to $3.8 \times 10^{-3} k_0 \sqrt{\varepsilon_1}$ for aluminium. Hence, it follows that the amplitudes $\tilde{A}_n$ will undergo a strong variation if an incident plane wave with a propagation constant in the vicinity of $\alpha = k_0 \sqrt{\varepsilon_1}\ \sin\theta_{-1}$ (see Eq. 4.33) strikes the grating. Let us indeed assume here that $\alpha_{pl,-1}(h)$ varies slowly in proportion to h. It therefore follows from Eqs. 4.25 and 4.33 that $\alpha_{pl,-1}(h) \approx \alpha_{pl,0}(0) - K = k_0 \sqrt{\varepsilon_1} \sin\theta_{-1} + i\, 3.8 \times 10^{-3} k_0 \sqrt{\varepsilon_1}$. Accordingly, under these conditions, a small variation $\delta\theta$ of the incidence angle such that $\delta\alpha = k_0 \sqrt{\varepsilon_1} \cos\theta_{-1}\, \delta\theta = 3.8 \times 10^{-3} k_0 \sqrt{\varepsilon_1}$ will be sufficient for causing the denominator of $\left|\tilde{A}_n(\alpha)\right|$ to increase by a factor of $\sqrt{2}$. Therefore, since the electromagnetic energy itself is in proportion to the square $\left|\tilde{A}_n(\alpha)\right|$, it will decrease from a factor of 2. It might be noted that the variation considered here for θ is only of a few tenths of degree. Indeed, a variation ten times larger would lead to a decrease of the electromagnetic energy from a factor of one hundred. This demonstrates the presence here of a resonance phenomenon, which manifests itself in the excitation of surface plasmons.

A prerequisite for the validity of the previous results is that the numerator in $\tilde{A}_n(\alpha)$ should not present any significant variation in the neighbourhood of $\alpha = Re\{\alpha_{pl,-1}(h)\}$. However, this approximation is to be rejected for all propagating modes whose dispersion curve is contained inside the light cone, since the conservation of energy must be accounted for. In the case under consideration where only the dispersion curve of the mode with propagation constant $\alpha_{pl,-1}(h)$ is contained inside the light cone, the only wave diffracted by the grating is the re-

flected wave. Assuming the metal to be a good conductor, it might reasonably be expected that this wave should present an amplitude of the same order as the reflection coefficient of a standard metallic reflector. On the other hand, the law of energy conservation imposes that $|\tilde{A}_n(\alpha)|$ be smaller than unity. This seems to be inconsistent with the variations from two orders of magnitude that were previously mentioned. However, this apparent contradiction can be resolved, provided that, in the neighbourhood of $\alpha = Re\{\alpha_{pl,-1}(h)\}$, the behaviour of the numerator of $\tilde{A}_1(\alpha)$ is similar to the behaviour of its denominator. In other terms, $P_{-1}(\alpha)$ must possess a zero within the complex plane in the neighbourhood of $\alpha_{pl,-1}(h)$.

As a conclusion, Eq. 4.34a is valid only for evanescent modes whose dispersion curve lies outside the light cone. For $n = -1$, Eq. 4.34a assumes the following form:

$$\tilde{A}_{-1} = Q(\alpha, h)\frac{\alpha - \alpha_z(h)}{\alpha - \alpha_{pl,-1}(h)} \tag{4.34b}$$

If $h = 0$, the surface plasmon cannot be excited. From Eqs. 4.25 and 4.29, it can therefore be deduced that:

$$\alpha_z(0) = \alpha_{pl,-1}(0) = \alpha_{pl} - K \tag{4.35}$$

$$Q(\alpha, 0) = r(\alpha) \tag{4.36}$$

Under these conditions, when the groove depth is cancelled out, both the zero and the pole of $\tilde{A}_{-1}(\alpha)$ tend towards the same value $\alpha_{pl,-1}(0)$, which results in the mutual annihilation of their influences. As a consequence, $\tilde{A}_{-1}(\alpha)$ simply identifies to the reflection coefficient of the plane mirror $r(\alpha)$. The resonance must disappear for evanescent waves as well, which in turn imposes that:

$$P_n(\alpha, 0) = 0 \tag{4.37}$$

As the height h increases, evanescent waves undergo a phenomenon of resonance in the neighbourhood of $\alpha = Re\{\alpha_{pl,-1}(h)\}$, leading to a local increase of the electromagnetic field in the vicinity of the grating surface. This phenomenon is obviously accompanied by metallic losses due to Joule heating. As has been previously mentioned, the radiative losses occurring in the reflection order –1 cause the pole to move away from the real axis. The rigorous calculations thus performed demonstrate in turn that the zero generally tends towards the real axis, and that it intersects it for a certain value $h = h_a$, as represented in Fig. 4.10. If the incidence angle for this specific value of the groove depth is determined in such a way that $\alpha = \alpha_z(h_a)$, then the application of Eq. 4.34b shows that the normalized amplitude of the wave reflected at the grating is strictly zero. Since all the other

waves are evanescent waves, we reach the most surprising conclusion that all the incident energy is absorbed by the grating.

The total absorption of a wave by a grating was first theoretically predicted (Maystre 1976) before being experimentally verified shortly afterwards in the visible region using a holographic grating coated with gold and illuminated with a krypton laser beam working at the 647 nm wavelength (Hutley 1976). The measured reflectivity was found to be as low as 0.3 percent, and the angular peak width to be equal to 1.3 degrees. This absorption phenomenon was all the more surprising that the groove depth was no higher than one tenth of the period of the grating. The surface of the grating presented a sinusoidal undulation with a period equal to 555 nm and an amplitude $h = 37$ nm. Thus, a very low degree of undulation at the surface of a mirror may cause a decrease in the experimentally measured reflectivity of the mirror, from more than 90 percent to less than 1 percent.

This demonstrates the importance of the resonance phenomena induced by surface plasmons. All these phenomena generally lead to the strong exaltation of evanescent waves, and sometimes to an abrupt decrease of the reflected waves, which in certain specific cases may even totally vanish. From a theoretical point of view, this example also illustrates the potential of phenomenological theories based on pology.

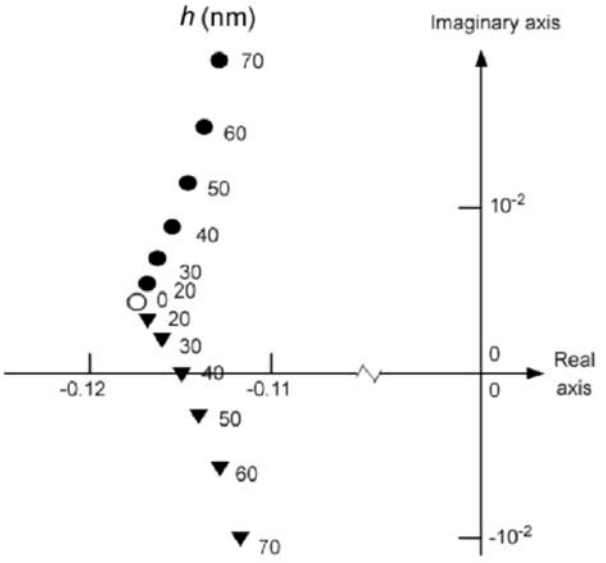

Fig. 4.10. Evolution of the pole (*solid circles*) and zero (*solid triangles*) of $\tilde{A}_{-1}(\alpha)$ represented as functions of the modulation height h. The grating here is assumed to be coated with gold and to have a period $d = 555$ nm. The incident wavelength λ is equal to 647 nm (Hutley 1976)

4.4.4 Photonic Band Gaps for the Propagation of Surface Plasmons at Periodically Modulated Metal/Dielectric Interfaces

In light of the possibility of creating photonic band gaps in periodic dielectric structures, it might be inquired whether the periodicity of a grating could likewise allow the creation of photonic band gaps for the propagation of surface plasmons. This question is of practical interest for several different reasons. Two examples will be considered here.

As a first example, we may consider the dramatic consequences of absorption phenomena induced by surface plasmons on the diffraction gratings used in spectroscopic studies. For instance, the diffraction gratings mounted at the rear of telescopes are designed for analysing the spectral composition of the light emitted by distant celestial objects, often with a very low intensity. If Wood's anomalies cause one or several wavelengths in the spectrum to be occulted, the analysis may be significantly perturbed. In this respect, preventing the propagation of surface plasmons can be an elegant way of answering this problem.

On the other hand, the local enhancement of the field in the vicinity of a grating surface can be used in a positive fashion, for instance for enhancing either the Raman scattering or the light emission of dye molecules deposited over a grating. The creation of photonic band gaps for the propagation of surface plasmons can therefore allow the control of such phenomena (Barnes 1996, 1997; Kitson 1996).

A method for creating a surface-plasmon photonic band gap relies on the coupling of two surface plasmons propagating along opposite directions. This requires that the spatial frequency of the grating satisfies the equation:

$$K = 2\,Re\left\{\alpha_{pl}\right\} \tag{4.38}$$

The modulation of the grating results in a folding of the dispersion curves (represented by dashed curves in Fig. 4.11) that were originally located just below the light line (solid curves in Fig. 4.7). The coupling between the two plasmons induces a frequency gap whose width increases with the groove depth h. The resulting dispersion curves are the dotted curves represented in Fig. 4.11. However, the frequency gap obtained in this case presents a limited interest since it occurs below the light line, i.e. in a region where the different waves cannot be excited by means of an incident beam.

A simple geometrical solution to this problem exists. For a gap to be created inside the light cone, the dispersion curves in Fig. 4.11 have to be shifted by a distance equal to $K/2$. This can be achieved by superimposing a second modulation with a spatial frequency $K/2$, i.e. with a period $2d$, over the original modulation with spatial frequency K, i.e. with period d. As a result, the grating possesses simultaneously two different modulations with periods $2d$ and d respectively. The first modulation is used for inducing a coupling between the two surface plasmons propagating along opposite directions, while the second modulation is used for positioning a gap within the light cone. As can be seen in Fig. 4.12, this results in the appearance of a gap whose centre lies along the axis of the light cone.

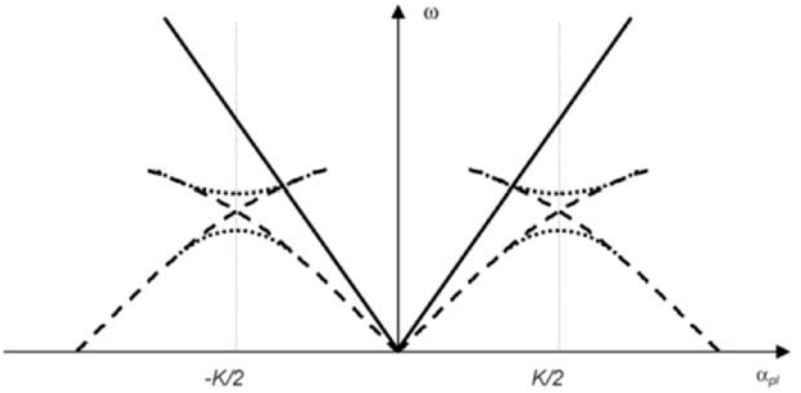

Fig. 4.11. Dispersion curves of two plasmons coupled through the modulation of a grating with a spatial frequency satisfying Eq. 4.38

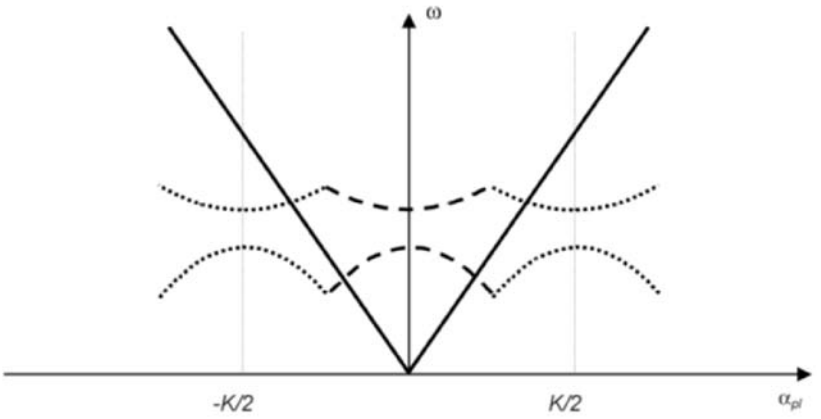

Fig. 4.12. Dispersion curves of a double-modulation grating with a fundamental period 2*d* and a first harmonic period *d*

It might be pointed out that other solutions for positioning the gap within the light cone exist. For instance, when a metal layer is deposited over a substrate, a solution consists in using a prism placed on the side of the substrate. The light cone associated with the prism thus presents a larger angle of aperture than the light cone associated with vacuum, and therefore it partially contains gaps similar to those represented in Fig. 4.11.

Different methods for creating surface-plasmon photonic band gaps have been described here. However, these methods apply to the propagation of surface plasmons along the direction normal to the grooves of a one-dimensional grating,

whereas for most applications the problem to be addressed is actually the creation of a band gap for all directions of propagation along the *xOz* plane. To this end, a two-dimensional grating must be used in place of a one-dimensional grating. An universal gap has thus been actually demonstrated using such a grating fabricated by etching holes inside a metal in order to create a hole lattice with an hexagonal symmetry (Kitson 1996).

4.4.5 The Photon Sieve

The resonant phenomena associated with the excitation of surface plasmons may also offer an explanation for the extraordinary light transmission achieved through a thick metallic grid containing holes with a sub-wavelength diameter (Ebbesen 1998). The fact that a metallic grid formed from a perfectly conductive metal behaves like a high-pass filter is a well-known phenomenon, and a rigorous numerical study of this behaviour can be found in (Mc Phedran 1977). The behaviour of the high-pass filter is actually quite intuitive. Let us here for instance consider the microwave regime. Basically, a hole drilled inside a thick metal plate is but a truncated waveguide. As such, it possesses a cutoff frequency below which, or equivalently a cutoff wavelength above which no propagation is allowed, except for exponentially decreasing modes. The cutoff wavelength is equal to $3.5R$, where R represents the radius of the hole. In the wavelength region extending above the cutoff wavelength, an exponential decrease in the transmission of light can thus be observed.

However, in the visible range, T.W. Ebbesen was able to demonstrate experimentally the existence of transmission peaks in this long-wavelength region (Ebbesen 1998). This phenomenon can be explained in terms of the excitation of surface plasmons, which occurs at the surface of the two-dimensional grating, and more specifically in the region of the geometrical shadow of the incident beam. Surface plasmons do not exist in the microwave region. By contrast, the resonant excitation of surface plasmons allows the propagation of photons through the holes at certain specific incident wavelengths in the visible region. For this reason, the transmission spectrum exhibits several transmission peaks. A detailed numerical and analytical study of the phenomenon can be found in (Enoch 2002c). The optical properties of surface plasmons may find a practical application, both for the miniaturization of optical circuits and for the characterization of biological structures.

To some extent, an analogy may be drawn between the resonant excitation of surface plasmons and the resonant effects which occur in a microcavity embedded inside a photonic crystal of finite size. When the wavelength of the incident beam coincides with a resonance wavelength of the microcavity, photons may propagate through the whole crystal in spite of the presence of a photonic band gap. The first photons thus accumulate inside the microcavity, with the result that the EM field in the microcavity becomes extremely intense.

4.4.6 Surface Waves in Metals at Radiofrequencies

Plane Metallic Surfaces and Concept of Surface Impedance

Let us here consider an interface between a metal and the air. The permittivity ε_1 of the air is equal to 1 and, as has been described in Section 4.1, the permittivity of the metal in the radiofrequency region can be adequately approximated by a purely imaginary number with a large modulus compared to unity. Hence, $\varepsilon_2 \approx 1 + i\sigma / \varepsilon_0\omega \approx i\sigma /\varepsilon_0\omega$. Under these conditions, the formulas given in Eq. 4.22 for α, β and γ can be rewritten as follows:

$$\alpha \approx \frac{\omega}{c}, \quad \beta \approx \sqrt{\frac{-1}{\varepsilon_2}}\frac{\omega}{c} = \sqrt{\frac{\omega\varepsilon_0}{2\sigma}}\frac{\omega(1+i)}{c} \quad \text{and} \tag{4.39}$$

$$\gamma \approx \sqrt{-\varepsilon_2}\frac{\omega}{c} \approx \sqrt{\frac{i\sigma}{\omega\varepsilon_0}}\frac{\omega}{c} = \frac{1-i}{\delta}$$

where δ represents the skin depth of the metal (see Section 4.1.2) The surface wave thus propagates at approximately the same speed as light in vacuum. Since the attenuation coefficient $\mathrm{Im}\{\beta\}$ is very small, the wave extends largely inside the surrounding medium, in this case in the air. Conversely, since γ is large, the penetration of the surface wave inside the metal is limited, and the surface waves are actually in this case surface currents. The existence of these surface currents allows us to introduce the concept of surface impedance in an appropriate manner. The surface impedance is defined as the ratio E/H, where E and H respectively denote the electric field and the magnetic field components in the plane of propagation.

In the case of a TM polarized wave, the relevant field components are E_x and H_z respectively. Proceeding from the expression for H_z given in Eq. 4.18, an expression for E_x can be derived using Maxwell's equations (Eqs. 1.2 and 1.3). The ratio $-E_x/H_z$ can finally be written in the form:

$$Z_s(\mathrm{TM}) = -\frac{E_x}{H_z} = -\frac{i\beta}{\omega\varepsilon_0} \tag{4.40}$$

The presence of a negative sign in front of E_z/H_x ensures that the surface wave will be absorbed and not amplified. Let us here recall that the time dependence of the fields is of the form $\exp(-i\omega t)$. The expression for Z_s in Eq. 4.40 therefore corresponds to an inductance $(-iL)$. In other terms, a TM polarized wave will propagate only if the surface impedance is inductive. The equation for the dispersion $\alpha(\omega)$ of the TM wave can thus be easily deduced from the expressions given for α and β in Eq. 4.22 and from the expression given for Z_s in Eq. 4.40:

$$\alpha = \frac{\omega}{c}\sqrt{1 - \frac{Z_s^2(TM)}{\eta^2}} \tag{4.41}$$

where η is the impedance of vacuum, whose value is given by:

$$\eta = \sqrt{\frac{\mu_0}{\varepsilon_0}} = 377\ \Omega$$

In the case of a TE polarized surface wave whose propagation is actually restricted to corrugated metallic surfaces, the relevant field components are E_z and H_x, respectively. Using an expression for the E_z component similar to the expression given in Eq. 4.18 for the H_z component, this allows the derivation from Maxwell's equations (Eqs. 1.2 and 1.3) of an expression for H_x, and then of an equation for the surface impedance. The latter equation assumes the following form:

$$Z_s(\mathrm{TE}) = \frac{E_z}{H_x} = \frac{i\omega\mu_0}{\beta} \tag{4.42}$$

Here again, the presence in front of E_z/H_x of a positive sign ensures that the surface wave will be absorbed rather than amplified. Since the time dependence of the fields is of the form $\exp(-i\omega t)$, the expression for Z_s now corresponds to a capacitance (i/C). In other terms, a TE polarized wave will propagate only if the surface impedance is capacitive. The equation for the dispersion $\alpha(\omega)$ of such a wave can then be deduced from Eqs. 4.22 and 4.42:

$$\alpha = \frac{\omega}{c}\sqrt{1 - \frac{\eta^2}{Z_s^2(TE)}} \tag{4.43}$$

Periodically Structured Metallic Surfaces

In the last decades, a number of studies have been devoted to the propagation of radiofrequency waves in periodic metallic structures. The reader is referred among others to (Bozzi 2000; Chan 1995; Elahi 1976; Harvey 1959; Kruusing 2001). In the case of metallic surfaces, the term 'corrugated surfaces' or the term 'frequency selective surfaces' (FSS) will be employed, depending on whether the corrugation depth or the choice of the surface patterns is the determining factor in the behaviour of the structure. In the context of photonic crystals, we shall focus here on the possibility of creating photonic gaps for the propagation of surface waves. More precisely, we shall consider periodically structured metallic surfaces with patterns much smaller than the wavelengths of interest. Under these conditions, the structure can be adequately described by using an effective medium model, while its

properties can be analysed in terms of the notion of surface impedance introduced above.

In Fig. 4.13 is represented the cross-section view of the high-impedance surface developed by D. Sievenpiper *et al* (Sievenpiper 1999a, 1999b). The upper surface of the structure consists of metallic patches periodically organized into a square lattice. Each patch is shorted to the metallic ground plane with a via. The whole structure either extends in the air or is embedded inside a dielectric. The enlarged view presented in Fig. 4.13 (*right*) shows that an elementary pattern of the structure can be reduced to a parallel resonant circuit consisting of a capacitor and a self-inductor. The use of an effective circuit model is justified here insofar as the size of the patterns is small with respect to the wavelength. This structure can therefore be assimilated to a surface with an impedance $Z = -iL\omega / (1 - LC\omega^2)$. Actually, the adequate parameters to be used in this model are not the capacitance and inductance of the individual elements, but rather the sheet capacitance and sheet inductance, both of which are dependent on the value of each individual element and on their arrangement.

When the frequency is lower than the resonance frequency $\omega_0 = 1\sqrt{LC}$, the impedance reduces to an inductance, and only TM polarized surface waves may propagate, as in the case of a metallic plane. As ω tends towards ω_0, the surface impedance $Z = E/H$ dramatically increases, while the electric field simultaneously tends to reach its maximum amplitude at the upper surface of the metallic structure. The situation is to some extent reversed compared to the classical case of a metallic plane, where the amplitude of the electric field is generally zero. This property is of prime importance since it entails that an external incident wave might be reflected at the high-impedance surface without any phase shift. For frequencies larger than the resonance frequency, the surface impedance reduces to a capacitance, and only TE polarized surface waves may propagate in this case.

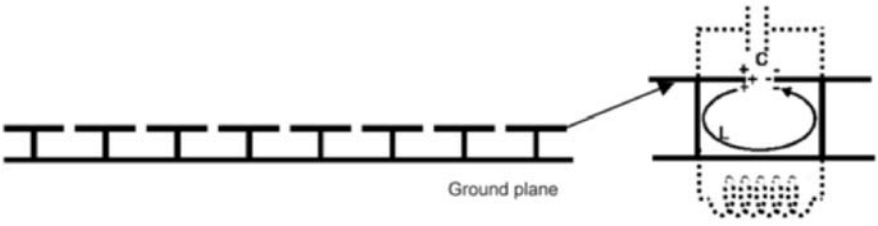

Fig. 4.13. *Left.* Cross-section view of the high-impedance surface developed by D. Sievenpiper *et al* (Sievenpiper 1999a, 1999b). *Right.* Enlarged view of an elementary pattern of the structure

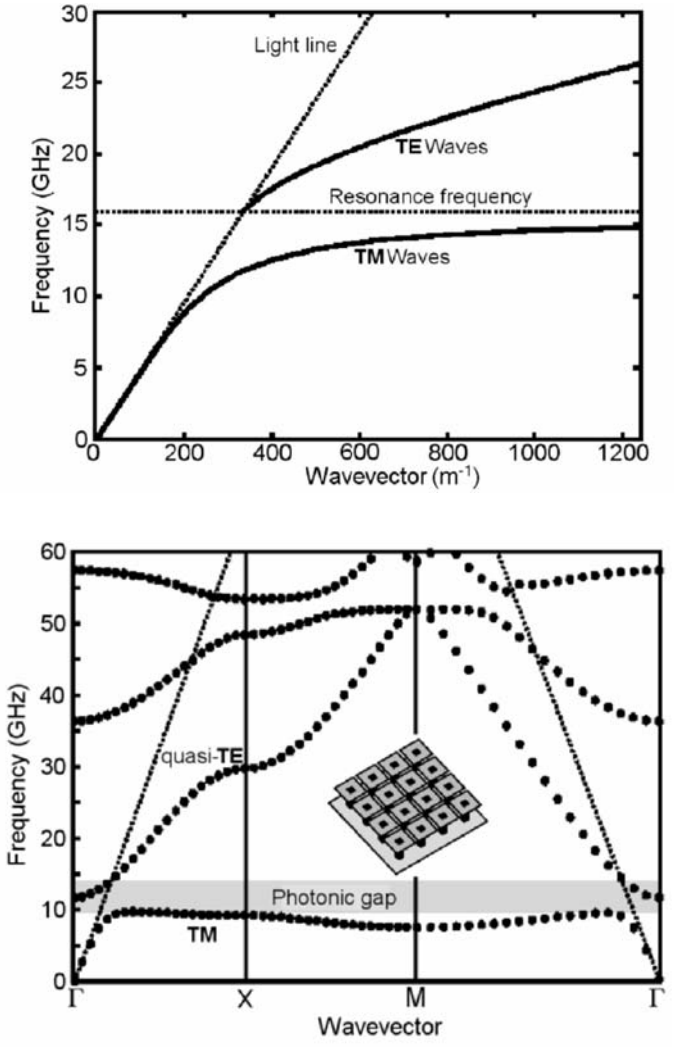

Fig. 4.14. *Top.* Dispersion diagram of a high-impedance surface analytically determined from Eqs. 4.41 and 4.43 (Sievenpiper 1999b). *Bottom.* Band diagram of a similar structure calculated from a finite element model (Quian 1999; Sievenpiper 1999b). The structure represented in the insert consists of a square lattice of metallic patches embedded inside a dielectric and shorted to the metallic ground plane with vias

The dispersion relations of the structure can be determined from Eqs. 4.41 and 4.42 respectively, depending on the respective values for ω and ω_0. Fig. 4.14 (*top*) represents a dispersion diagram calculated along these lines, in the case of a square lattice formed by metallic patches (Sievenpiper 1999b). The period of the

lattice is equal to 2.4 mm, the spacing between the patches to 0.15 mm, the height of the vias to 1.6 mm and their width to 0.36 mm. The surrounding dielectric is made from epoxy of the kind used in printed boards, and has a permittivity $\varepsilon = 2.2$. Although the dispersion diagram presented in the upper part of Fig. 4.14 does not reveal any band gap, a clear discontinuity occurs at the resonance frequency around 16 GHz, corresponding to the transition from the TM to the TE mode. It can be noted that the two dispersion curves both lie below the light line $\omega = ck$. Accordingly, Eqs. 4.41 and 4.43 only account for modes bound to the surface without radiative losses. An exhaustive analysis of the modes, including leaky modes, necessarily requires the use of more elaborated models, an example of which is employed in the lower part of Fig. 4.14.

The band diagram of a high-impedance surface represented in the lower part of Fig. 4.14 was calculated by using a finite element model (Quian 1999; Sievenpiper 1999b). The structure displayed in the insert is similar to the structure considered in the upper figure. However, it might be pointed out that numerical calculations now allow predicting the existence of a complete band gap at a frequency close to the resonance frequency estimated in the analytical model. For the frequency region extending up to 30 GHz below the light line and along the ΓX and ΓM direction, a relative agreement can also be observed between the analytical and the numerical results. By contrast, the finite element model further accounts for the leaky modes located above the light line, and it also provides a complete description of the band diagram for all directions of propagation and all polarizations of the field. In any case, the essential result to be noted here is the demonstration of the existence of a complete photonic gap. As will be described in the third part of this book, the suppression, and even better, the control of surface waves are of the highest interest for microwave antennas.

Part II

Optical Properties of Photonic Crystals

Introduction to Part II. The Many 'Facets' of Photonic Crystals

The first part of this book has been devoted to a survey of the theoretical models used for the description of photonic structures, and more generally of periodic structures. To a large extent, we have restricted ourselves to a conception of photonic crystals as the optical analogues of solid state crystals. However, when considering the optical properties of photonic crystals that can be exploited in optics, it becomes necessary to adopt a much broader perspective. Accordingly, the second part of this book will be devoted to the description of the main properties of photonic crystals which have led to devising various forms of control of electromagnetic waves, and beyond that, to the perspective of devising wavelength-scale devices and components. For the sake of simplicity, two different types of optical properties can be distinguished depending on whether photonic crystals are illuminated externally by one or several incident electromagnetic waves, or internally by one or several miniature sources, which can be formed simply by elementary oscillating dipoles. The now classical image of the excited atom immersed in a photonic crystal, which corresponds to the second situation, is precisely the intuition which led E. Yablonovitch to his first proposal of photonic band gap structures as optical systems for achieving a complete control of the spontaneous emission.

Likewise, the classification of the properties of photonic crystals into two categories, i.e. depending on whether the crystal is seen from outside or from inside, is an oversimplification, which tends to reach certain limits. Actually, the concept of optical confinement is the most suited for analysing all the intermediate cases that may arise, for instance the optical guiding of waves propagating between two photonic crystal mirrors. Chapter 5 will thus proceed from the situation of an external illumination to that of internal illumination, by successively considering different levels of optical confinement. For an electromagnetic wave arriving from a semi-infinite medium and impinging on a photonic crystal, the latter will be seen either as a particular mirror or more generally as a diffracting object (Section 5.1). In the case of a wave confined in a homogeneous medium between two photonic crystal mirrors, different ways of investigating the photonic crystal guiding will be described (Section 5.2.) Planar and linear waveguides realized in two and three-dimensional structures will be considered in this context. Finally, Section 5.3 will address the case of resonators, where the optical confinement is expected to occur along all possible directions, i.e. in all three directions and in two dimensions if the space is arbitrarily limited to two dimensions.

The idea of a ‘control of electromagnetic waves’ suggests the existence of a unifying concept behind the different optical components mentioned above. Indeed, due to their property of acting as 'optical insulators', photonic band gap structures offer the opportunity of achieving a more complete optical confinement than was the case with the previous generation of optical devices. For the most part, the latter devices were based on the refractive index confinement which occurs as a plane wave impinges on a plane boundary between two media at an incident angle higher than the critical angle. This form of optical confinement reaches its limits as soon as one moves to micrometric optical devices. For sizes approaching the optical wavelength, an electromagnetic mode can no longer be approximated in a simple way by a unique plane wave. Retaining the notion of incident angle, the waves to be controlled are actually combinations of multiple plane waves impinging on the plane interface at all possible angles of incidence, and it is quite obvious that some of these angles are larger than the critical angle.

In this context, however, no reason opposes the possibility of combining these two types of confinement, for instance a refractive index confinement along one dimension and a photonic band gap confinement in the two other directions. Such a scheme is being currently investigated in relation to the development of applications of photonic crystals to integrated optics and optoelectronics. It will be presented in Section 4 of Chapter 5, where the concept of ‘light line’ will be also discussed in more detail. This concept, which has already been mentioned in the first part of this book, is useful in the sense that it provides an insight into the limitations imposed by the choice of a refractive index confinement, which is often dictated by technological constraints.

The transmission bands of a photonic crystal rather than its photonic band gaps can also be exploited for the propagation of waves extending in the periodically structured medium formed by this crystal, i.e. for the propagation of the Bloch waves introduced in the first part of this book. One of the most interesting features of photonic crystals is the possibility of achieving very small group velocities associated with the flattest bands. This property, as well as other unusual refractive properties like the ultra-refraction and ‘superprism’ effects, will be discussed in Chapter 6. In particular, negative index refraction opens the way to the design of new types of optical lenses based either on photonic crystals or on metamaterials. The correct exploitation of all these effects rests on a large extent on the choice of the interface between the crystal and the external medium, where the usual types of waves (plane, Gaussian, etc) are converted into Bloch waves, while the reverse conversion takes place at the output of the photonic crystal.

The last two chapters of this second part will be devoted to certain issues related to the combination of active media with photonic crystals. Thus, Chapter 7 will address the problem of optical emitters in photonic crystal microcavities. This is one of the major problems in this field, be it only for the reason that it was at the very origin of the concept of a photonic crystal. In this chapter, simple notions like that of the spontaneous emission factor of emitters will first be introduced as a first approach towards reaching a better understanding of the utility of photonic systems with highly confined modes, even in the absence of strong singularities in the density of states. We shall then in a second step enter the physics of micro-

sources, which exhibit a very singular density of photonic states. It will be seen in this case that the lifetimes of electromagnetic modes can be dramatically 'reduced' (Purcell effect), and that different quantum electrodynamic effects may also appear. Finally, the performances of standard microcavities with 'shape resonances' (microspheres, microdisks) will be compared to those of photonic crystal microcavities.

Chapter 8 will be devoted to the subject of nonlinear optics in photonic crystals. This rapidly expanding field is very promising in terms of applications. Various nonlinear effects will be successively discussed, depending on the optical waves involved in these effects, namely the fundamental wave, its harmonics or the waves at difference or sum frequencies. Correspondingly, different orders of electrical susceptibility are associated with these effects: the first-order susceptibility ($\chi^{(1)} = \varepsilon_r - 1$), the second-order susceptibility $\chi^{(2)}$, etc. While second-order effects in photonic crystals are of particular interest for frequency conversion and light generation at new frequencies, third-order nonlinearities in photonic crystals pave the way to the development of miniature all-optical switches with ultimate performances.

5 Control of Electromagnetic Waves

5.1 The Photonic Crystal Mirror

What happens when a wave propagating in an isotropic, linear and homogeneous medium with index *n* illuminates a photonic crystal? This question will be addressed first in the case of a semi-infinite crystal, beginning with the general consideration of the problem in Section 5.1, before limiting ourselves to the case of specular reflection in Section 5.2. Finally, we consider in Section 5.3 the case of a finite crystal, which can be viewed as a semi-transparent mirror.

5.1.1 The Semi-Infinite Photonic Crystal: Mirror or Diffraction Grating?

Let us consider here a semi-infinite photonic crystal with an omnidirectional band gap. The energy flux at frequencies within the band gap cannot penetrate far in the crystal, and therefore it will be reflected in the general sense of the term. However, since the object illuminated in this case by the wave exhibits a periodic structure, the wave must necessarily satisfy the usual laws of diffraction gratings, which apply to any interface presenting two basic lattice vectors $\mathbf{R_1}$ and $\mathbf{R_2}$:

$$\mathbf{k}_{\text{refl},\,//} - \mathbf{k}_{\text{inc},\,//} = m_1\,\mathbf{G}_1 + m_2\,\mathbf{G}_2 \tag{5.1}$$

where $\mathbf{k}_{\text{inc},\,//}$ denotes the projection of the incident wave vector onto the plane of the interface and $\mathbf{k}_{\text{refl},\,//}$ is the projection of the wave vector associated with a wave diffracted or reflected by the same plane, while $\mathbf{G}_1$ and $\mathbf{G}_2$ are the reciprocal wave vectors of the direct lattice and m_1 and m_2 are two integers. This result is actually a direct consequence of the global invariance of the system with respect to translations of the real lattice, and of the application of the Bloch theorem to the total field, which includes the incident field as well as the diffracted or reflected fields:

$$\mathbf{E}(\mathbf{r},\omega) = \mathbf{E}_{\text{inc}} + \mathbf{E}_{\text{refl}} \tag{5.2}$$

In order to obtain the usual expression of the grating formula with the angle of incidence, it suffices to take into account the requirement of frequency conservation. The latter states that, for all the elementary waves which compose the incident and diffracted waves (in general, a single incident wave and several diffracted waves exist), the corresponding wave vectors must have the same modulus $n\omega/c$. The allowed diffracted orders are therefore obtained by considering the intersections of the vertical lines drawn through the nodes of the two-dimensional reciprocal lattice with the hemisphere of radius $n\omega/c$, as represented here in Figs. 5.1*a* and *b*. For Eq. 5.1 to be satisfied, the origin of the reciprocal lattice must be located at the extremity of $\mathbf{k}_{\text{inc},//}$, the projection of $\mathbf{k}_{\text{inc}}$ onto the plane of the interface.

The periodicity of the plane of the interface is an implicit assumption in the considerations above. From a mathematical point of view however, it should be emphasized that the existence of such a periodicity is the less frequent case, as has already been explained in Chapter 3 when considering quasi-crystal structures, i.e. structures that can be obtained by cutting periodic crystals along planes with non-rational indices (Miller indices). Nevertheless, a periodic approximation, even if it may present a very large period compared to the original lattice, still provides a very good compromise for the description of actual electromagnetic phenomena. We shall assume throughout this chapter that we are dealing with such a periodic interface.

As desirable as it would be to have a general rule for the number of allowed diffraction orders and for its dependence on whether the operating frequency lies inside or outside a photonic band gap, no overall statement can be made. Photonic crystal structures have periods of the order of λ and the frequency cutoff of diffracted orders is never very far from the frequencies in the band gaps. We shall here consider two typical configurations for an incident wave whose frequency lies within the band gap. These two configurations will be encountered later when studying two-dimensional photonic crystals. First, let us consider the case where a wave impinges from a high-index homogeneous dielectric medium onto a crystal formed by air columns drilled inside the same medium, with a relatively large air-filling factor. In such a case, the frequency of the band gap is relatively high, as can be seen in Fig. 5.1*a*, and the radius $n\omega/c$ of the hemisphere is therefore large. Accordingly, even if the interface is formed by a dense surface of the crystal, i.e. if it is associated with the largest possible vectors $\mathbf{G}_1$ and $\mathbf{G}_2$, diffraction will be allowed at least in one nonspecular order (m_1 or $m_2 \neq 0$).

Conversely, let us consider a crystal formed by dielectric rods placed in the air. The hemisphere with radius ω/c is now comparatively small. In addition, if the vectors $\mathbf{G}_1$ and $\mathbf{G}_2$ are as large as possible, the construction will yield a single point of intersection, as can be seen in Fig. 5.1*b*. In such a case, reflection remains specular for most incidence angles, i.e. for all values accessible for $\mathbf{k}_{\text{inc},//}$, while the incident energy is entirely reflected in the specular beam, $m_1 = m_2 = 0$.

Figs. 5*c* and *d* show the construction of diffracted waves in the case of a simpler, more familiar photonic crystal consisting of a two-dimensional periodic array of holes in a dielectric. The crystal is assumed to be operated at a frequency slightly above the gap frequency, so that that the incident wave is also partially

transmitted and diffracted at the output of the crystal. This case is actually closer to that of standard ruled diffraction gratings.

Once the allowed diffracted orders have been determined, we need to address the problem of the determination of their respective intensities. This actually requires the use of more advanced modelling methods of the kind described in Section 2.1 of Chapter 2, for instance the scattering matrix method, which is a generalisation of the classical models for diffraction gratings, or the Sakoda method (Sakoda 1995), based on the plane wave expansion with indirect inclusion of boundary conditions.

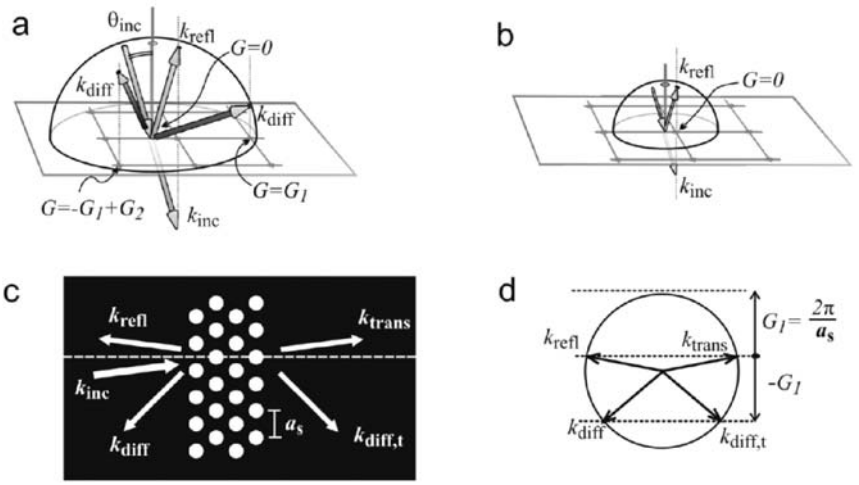

Fig. 5.1. Grating formula in the reciprocal space. The reciprocal lattice of the surface is represented with its origin located at the projection in the horizontal plane of the incident wave vector $\mathbf{k}_{inc}$ *a.* The allowed orders are therefore to be found at the intersection between the vertical lines drawn through the nodes of the two-dimensional reciprocal lattice, on the one hand, and the hemisphere where the modes of the semi-infinite medium are located at the frequency under consideration, on the other hand. In addition to the specular reflection $\mathbf{G} = \mathbf{0}$ (wave denoted by $\mathbf{k}_{refl}$), only two particular diffracted waves are represented here in order not to overload the figure: (i) $\mathbf{G} = \mathbf{G}_1$, which is similar to the usual grating formula with the plane of incidence normal to the grooves of the lattice, (ii) more general case where $\mathbf{G} = -\mathbf{G}_1 + \mathbf{G}_2$ *b.* For a surrounding medium with lower index, like the air, or for lattices with a small period, the only remaining intersection is $\mathbf{G} = \mathbf{0}$. In other terms, only specular reflection occurs *c.* Two-dimensional geometry with boundary period a_s *d.* Relation in the reciprocal space of the wave vectors k and G in the two-dimensional case

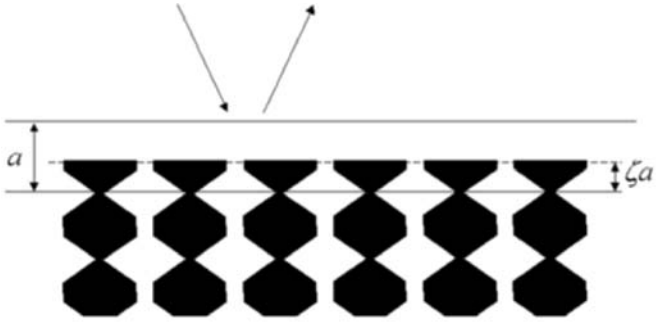

Fig. 5.2. Reflection of a beam on a photonic crystal cut at a fraction ζ in the last layer of a dense array of unit cells. The reflection phase is not a linear function of ζ

5.1.2 Specular Reflection at a Semi-Infinite Crystal

From all the diffraction/reflection configurations for a wave incident on a semi-infinite photonic crystal, the simplest is specular reflection, where only one reflected order exists, while all other orders are of an evanescent rather than a propagating nature. As we shall see later in Section 13.1.2 of Chapter 13, this is an interesting case for shaping the radiation of antennas. The specific interest of this configuration lies in its reflection phase and amplitude, which can be significantly different from those of the metallic ground plane used in the area of microwaves. This can be illustrated by considering the schematic example of the two-dimensional photonic crystal represented in Fig. 5.2. The cutting plane can be continuously translated until an extra unit cell is added. This assumption amounts to letting the parameter ζ continuously vary from 0 to 1.

It is obvious that, in most cases, the periodical pattern in the plane of the interface will evolve in a complex manner. There is therefore no reason for the reflection phase to be a linear function of the variable ζ. For the same physical reason, in the case where the value for ζ is fixed, there is no simple rule for the dependence of the reflection phase on the angle of incidence θ or on the frequency ω. For instance, one may go from a band gap to a transmission band by tuning the frequency or by changing the direction of propagation. As a consequence, the conceptions developed in the context of plane interfaces should be entirely revised. Experiments and calculations conducted on two and three-dimensional crystals used as reflective planes for antennas (Kesler 1996) have demonstrated that, for a given frequency and angle of incidence, the behaviour of these crystals is comparable to that of a perfectly conducting metallic plane, but would have been buried at a distance $d(\theta, \omega)$ beneath the surface. The precise analysis of $d(\theta, \omega)$ retrieves the emission diagram of an antenna located in front of the photonic crystal and also helps to explain such features as the narrowing of the emission lobes at specific frequencies. In addition to these beam-shaping effects, photonic crystals used

as reflective planes can be expected to exhibit an almost constant phase in a certain frequency range, a quite desirable feature.

However, research on this subject has been thus far limited to studies concerned with specific examples. Contrary to the one-dimensional case, where the phase evolution is well-known, there are, to the best of our knowledge, no simple rules that would allow predicting the behaviour of a given two or three-dimensional photonic crystal. As an example, for traditional Bragg mirrors, the phase presents a lower slope in the band gap and an abrupt transition at the edges of the gap. For two and three-dimensional structures, the situation is considerably more complex. In the cases where diffraction can be neglected, it seems intuitively sound to consider that, at a certain incidence, only one periodicity of the crystal is really involved in the reflection. The behaviour of the structure can therefore be expected to be similar to that of the one-dimensional stack realized by an adequate averaging along this direction. However, it remains difficult to predict the behaviour of these structures in more complex situations, for instance for directions at the intersection of two reciprocal planes, where two different periods of the crystal may act simultaneously. Among these complex cases, mention should be made of the 'anticrossing' effects observed in studies on the reflective properties of opals at angles very oblique with respect to the (111) growth axis of the opal (van Driel 2002; Vos 2001).

5.1.3 Finite Photonic Crystals as Semi-Transparent Mirrors

We shall end our review of mirrors with the consideration of photonic crystals with a finite thickness. These structures may act as semi-transparent mirrors. Here again, we shall assume that the crystals are infinite in the plane of the interface, and correspondingly we remain within the assumption of an infinite plane wave. In the absence of this assumption, focalization or collimation phenomena would indeed occur. The latter phenomena will be addressed in Chapter 6 of this book. For a uniform plane wave propagating at a frequency within the photonic band gap, the transmission of N 'atomic' planes of the crystal assumes the form $T_0 \exp(-AN)$, where A and T_0 are constant parameters. The transmitted wave may also emerge in several diffracted orders as it is the case for reflection. The fact that the crystal presents an omnidirectional band gap ensures that all orders will follow the exponential decreasing behaviour of the kind previously described, but with factors A and T_0 depending on the diffraction order.

The physical analysis becomes complex as soon as photonic crystals are considered in a frequency range where transmission bands coexist with directional band gaps. In terms of wave vectors, each order has a specific constraint associated to it and will therefore undergo a different fate. Thus, while some orders can be associated with gaps and therefore give rise to an exponentially decaying evolution, other orders can be associated with Bloch waves. These waves propagate without undergoing any attenuation, but their relative intensities, as well as the coupling factors between these waves and external plane waves, either incident or transmitted, can take any arbitrary value. An apparent behaviour of negative re-

fraction may occur in this context (Lombardet 2005), as will be seen in Chapter 6. Further, for a very thin slab of only a few periods, it is no longer possible to neglect the power transmission occurring from one interface to the other, due to the partial overlap of the tails of waves associated to evanescent orders in the semi-infinite situation.

5.2 Photonic Crystal Waveguides

5.2.1 Index Guiding and Photonic Bandgap Guiding

The principles of classical guiding, or index guiding, are represented here in Fig. 5.3*a*. This guiding mechanism is based on the total internal reflection of light at the interface between a high-index medium *H* and a medium *L* with lower index: these two media are referred to as the core and the cladding of the waveguide respectively. More detail on this subject, concerning for instance the number of modes allowed by these waveguides or the mathematical expression of their mode profile, will be provided in Chapter 9, devoted to planar waveguides. By contrast, Fig. 5.3*b* illustrates the principles of photonic bandgap guiding, where the confinement of light is achieved by exploiting the photonic band gap of a periodic medium. By analogy with index guiding and with optical fibres, the term 'cladding' will be used here for describing this medium.

It is known that within a given band gap, even a directional band gap, the reflectivity of a photonic crystal rapidly approaches unity as the number of rows increases, and that this behaviour is all the more pronounced that the index contrast is high. In other words, even in the case where the cladding is finite, a wave may undergo a large number of successive reflections without any noticeable attenuation. If the classical zigzag ray model representing the propagation of rays between two parallel mirrors is used here for the description of guidance, this situation turns out to be simply the general case of a classical Fabry-Perot resonator at arbitrary incidence angles. When the multiple interferences of all these rays are in phase, i.e. when each ray is actually a wave with an infinite extent along the waveguide axis, a resonance condition is achieved. Correspondingly, the energy stored in the resonator, i.e. in this case in the waveguide, reaches its maximum value. This phase-matching condition, or optical path length condition, establishes a relation between the frequency and the wave vector. This expression can be generically expressed in the form $f(\omega, k) = 0$, but it can also be written in terms of a dispersion relation $\omega = \omega(\mathbf{k})$, possibly with multiple branches.

Having retrieved the dispersion relation of the guided mode, we should note, however, that k itself has an unequivocal meaning only in the case where the structure presents a complete translational invariance along the axis of the waveguide. In the case of periodic structures like photonic crystals, periodicity along the direction of the waveguide implies that infinitely many equivalent val-

ues for k exist, all of which are multiple of the fundamental spatial frequency of the photonic crystal waveguide.

Returning to the Fabry-Perot model, we shall denote by R_1 and R_2 respectively the reflection coefficients at the two walls of the waveguide, while L_{opt} will denote the optical path between two successive reflections. The lifetime of a photon in the waveguide will be given by the equation $\tau \sim L_{opt}/[c\mathrm{Ln}(1/R_1R_2)]$, since a number $N \sim 1/\mathrm{Ln}(1/R_1R_2) \sim 1/(1 - R_1R_2)$ of reflections is necessary before the guided wave may undergo any noticeable attenuation. This means that attention should be paid not only to the value for k, but also to the frequency as well, since the finite lifetime τ induces a corresponding broadening $\Delta\omega \sim 1/\tau$ of the resonances associated with the guided modes. Only in the case of an ideal Fabry-Perot with an infinite τ would the Airy function tend towards a set of zero-width Dirac functions. This reveals a similarity between the physics of Fabry-Perot resonators and the physics of a waveguide formed by two photonic crystals. This similarity even turns to be an identity for planar multilayer systems, i.e. when k is unambiguous: in this case, one simply deals with a one-dimensional photonic crystal with a defect (see Section 1.4.1 in Chapter 1), or in other terms, with a planar microcavity confined by Bragg mirrors.

Planar microcavities based on semiconductors have been most intensively studied since 1988, first with the primary intent of realizing vertical-cavity surface-emitting lasers (VCSELs) and later for the investigation of such fundamental phenomena as the strong coupling between a confined wave and excitons in semiconductors (see Chapter 7). Interest in these structures was also prompted by the development of very high efficiency light-emitting diodes (David 2006, 2007; Delbeke 2002; Rattier 2002).

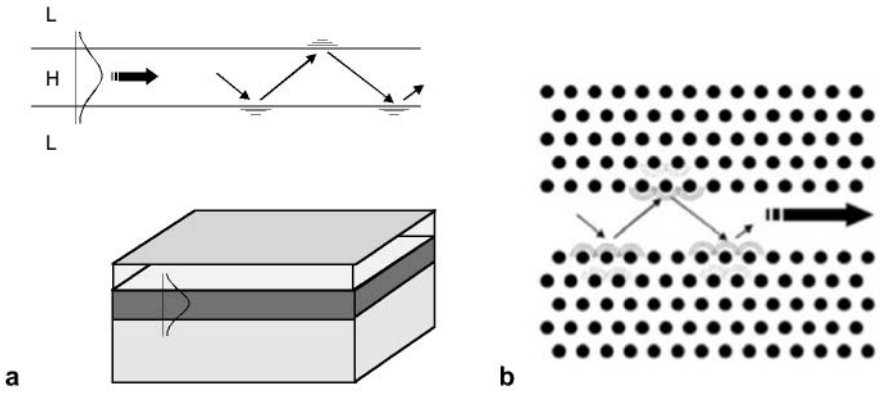

Fig. 5.3. *a.* Index guiding: the upper part of the figure is a cross-section view representing the field profile and the zigzag ray model with total internal reflections and evanescent waves. The lower part of the figure represents the usual planar guiding *b.* Photonic bandgap guiding: the successive reflections are 'created' by the entire set of interferences generated by all atoms of the crystal, both along and normally to the axis

The limitations presented by these planar multilayer systems are exactly the same as those that originally led to the research on photonic crystals: the band gap is only directional. Going back to the zigzag ray model, this implies that, as soon as the incidence angle lies outside a certain limited range, a large leakage flow of light is bound to occur through the walls of the waveguide, with the consequence that confinement will cease to be effective. An optimally designed waveguide therefore requires that a three-dimensional structure with an omnidirectional band gap be used in order to prevent leakage along the two other directions.

5.2.2 Three-Dimensional Photonic Crystal Waveguides

The guiding of light in a three-dimensional photonic crystal raises the same issues that were discussed in Section 5.2.1. In addition, as illustrated in Fig. 5.4, it is necessary to specify the geometry used for the guiding, and for instance to determine whether light will be confined along one dimension or along two dimensions, with propagation along the two or one other dimension(s) respectively remaining free. These two configurations correspond to a planar and to a channel waveguide respectively. Accordingly, it is legitimate to define a one or two-dimensional wave vector that will be associated with the guided wave in each of these situations. A large variety of methods may be devised for designing a planar or a channel waveguide in a three-dimensional photonic crystal. As an example, let us here consider first the case of a planar waveguide created inside an inverse opal structure. This structure is face-centred cubic (fcc, see Section 12.2.2 in Chapter 12) with a stacking order ABCABC…. Possible geometries for creating a waveguide in such a structure include:

- the introduction of a spacing between two perfect semi-infinite crystals, as represented here in Fig. 5.4*a*,
- the introduction of a single stacking fault among the crystalline planes of the crystal, for instance a missing C plane ABCABCABABCABC,
- the removal of a crystalline plane,
- the removal in a two-dimensional periodic fashion of certain ‘atoms’ inside a crystalline plane of the crystal,
- the periodic modification of a series of atoms (or cells) inside a crystalline plane, with respect to their size, index or shape.

This enumeration is by no means exhaustive. It is of course quite obvious that, when the propagation is free along the two in-plane dimensions, i.e. when $\omega = \omega(k_x, k_y)$, the presence of the underlying crystal lattice may result in the appearance of guided modes exhibiting a series of specific features. In this case, the in-plane azimuthal orientation becomes a crucial parameter, as can be seen in Fig 5.4*d* for a different type of lattice. At the very least, a significant anisotropy along the different crystallographic directions of the walls of the waveguide can be expected to occur.

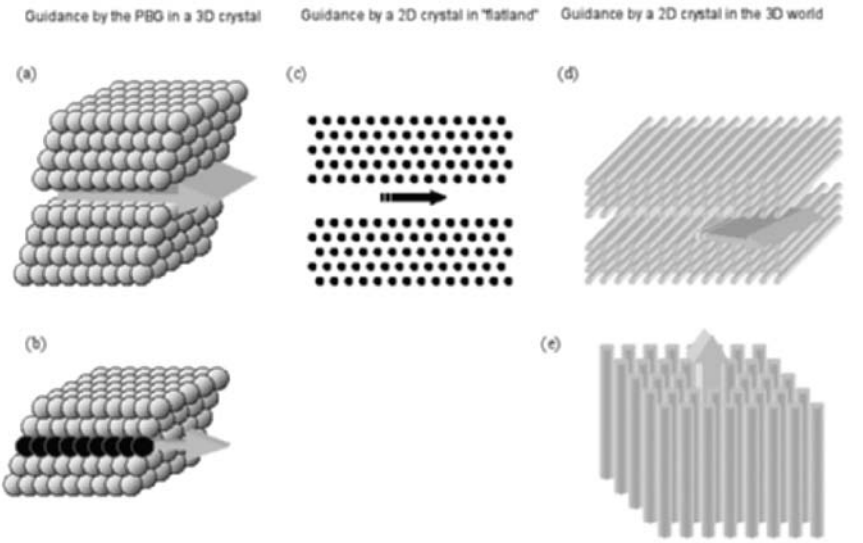

Fig. 5.4. Waveguides in two and three-dimensional photonic crystals. *a.* and *b.* Guiding in a three-dimensional crystal in the cases of a planar and of a linear defect respectively *c.* Linear guiding in a two-dimensional crystal, represented in a purely two-dimensional way, as it would be seen in 'Flatland' (Abbott 1992) *d.* and *e.* Guiding along two or one dimensions respectively in a two-dimensional crystal, with a three-dimensional representation of the system

Similarly, examples of methods for creating a channel waveguide in a three-dimensional crystal include:

- the removal of a row of atoms, as in the case represented in Fig. 5.4*b*, or of several adjacent such rows,
- the removal of a periodic series of atoms inside a given row,
- the modification of a series of atoms inside a given row, with respect to their size, index or shape.

Here again, this enumeration is not exhaustive. For a further insight into the very large variety of possible combinations, the interested reader is referred among others to (Noda 2002b), where they are investigated in the context of three-dimensional deterministic structures.

These channel waveguides can be expected to exhibit specific features as regards their dispersion relation. Since the situation now is comparable to the propagation in a one-dimensional periodic medium, the dispersion relation $\omega = \omega(k_x)$ is likely to be strongly affected by the periodicity induced on the channel. Contrary to what was the case in a planar waveguide, the appearance of band gaps at wave vectors multiple of (π/period) may now correspond to a region with a true zero-

density of states, i.e. to a region where no states are allowed, provided that no other branch exists at this gap frequency. In the planar case, there is no reason for omnidirectional gaps to be present in the dispersion diagram.

In the specific case of the fundamental band gap associated with the one-dimensional periodicity of such a channel waveguide (the gap at $k_x = \pi$/period), there is no obvious reason why it should lie inside the omnidirectional band gap of the surrounding three-dimensional crystal. This fundamental band gap can be below, inside or above the omnidirectional band gap. For very large periods, associated with the so-called 'vicinal' directions of the three-dimensional crystal, i.e. with small angles with respect to the direction of a dense row, this fundamental band gap is associated to low spatial frequencies, quite below the three-dimensional band gap. It is most likely that only certain higher-order guided modes will be located within the three-dimensional band gap.

5.2.3 Two-Dimensional Photonic Crystal Waveguides

An arbitrary limitation to a purely two-dimensional world amounts to considering that propagation occurs along a single direction within the *(x,y)* plane in a system assumed to be perfectly invariant and infinite along *z*. This is an idealized vision of planar integrated optics (see Chapter 9), where the third degree of freedom is totally 'frozen'. Examples of photonic band gap structures of this type can be found in the form of dielectric columns in the air or of infinite air holes in a dielectric matrix. Taking a three-dimensional view of these two-dimensional structures, it can be seen that the only remaining canonical geometry for the guiding is of a planar type, as in the example represented in Fig. 5.4*c*, where it was created by removing a row of columns. In the case where $k_z = 0$, the guiding can be described by a vector **k** with a single component, for instance k_x. The dispersion relation for the guided modes will therefore reduce to $\omega = \omega(k_x)$. In view of the complete invariance of the system along *z,* including the field, it becomes perfectly legitimate to describe this case as a channel guiding in the *xy* plane.

The question arises however of the behaviour of such a two-dimensional system when the restriction to $k_z = 0$ is removed and when all other possible directions of propagation are allowed. Such a 'mixed' geometry calls for a specific analysis, since the wave may not be guided at all for certain values of k_z at which the cladding does not exhibit a two-dimensional band gap. According to this more general view, two different types of waveguides may be distinguished, depending on the nature of the defects created in a two-dimensional crystal:

- two-dimensional defects, described earlier in this chapter. Such defects are formed by a plane of missing atoms along *Oxz* between two semi-infinite two-dimensional crystals with the same axis *z* (Fig. 5.4*d*). Thus far, this geometry remains of a purely academic interest.
- one-dimensional defects, formed for instance by a missing dielectric column or by a missing air hole in two-dimensional crystals respectively formed by dielectric columns in air or by air holes inside a dielectric. This case is repre-

sented in Fig. 5.4*e*, and corresponds exactly to the geometry of photonic crystal fibres, or microstructured fibres. These fibres will be discussed later in Chapter 11. The most studied situation in the literature is the case where guiding is achieved only for large values for k_z with respect to the transverse components k_x and k_y. The physics of such a waveguide is therefore substantially different from what has been seen so far, since there is no longer any necessity for the period of the crystal to be of the order of the half-wavelength. The possibility for the period to be much larger than this value leads to a simplification of the fabrication process and to a substantially relaxation of requirements on index contrast, which enables silica (SiO_2, n ~1.46) and glass to be effectively used.

The physics of a waveguide created by a one-dimensional defect can be summarized as follows. Since the main component of the wave vector lies along an invariant direction of the system, the value of this component may approach the order of $n\omega/c$, where n is the index of the 'waveguide' (with $n = 1$ in the case of a missing column). Therefore, by limiting ourselves to small angles with respect to the Oz direction, the photonic band gap phenomenon comes into play only along the xy coordinates, i.e. with respect to transverse propagation (Fig. 5.5) . Patterns with a large period are sufficient due to the fact that the transverse components k_x and k_y remain small. This is comparable to what occurs in a number of optics experiments described in textbooks, where large, widely spaced fringes are associated with extremely small angles with respect to the axis. Let us consider here the case of an air/glass system, where the index contrast is 1 :1.5, and let us go from $k_z = 0$ to the largest values for k_z. In the case of air holes in glass, which is of practical interest for fibres, it is known from Section 1.3.3 in Chapter 1 that the low index contrast prevents the appearance of a two-dimensional omnidirectional band gap for $k_z = 0$. In this case, transmission bands, separated by thin directional band gaps appear instead in the band diagram (see Section 11.1 in Chapter 11). When oblique directions of propagation are allowed, i.e. when $k_z \neq 0$, the introduction of k_z will result in an increase in the frequency of the partial band gaps for a given period a of the lattice. In other terms, a/λ increases. The same effect can be observed for one-dimensional structures, where it is a well-known fact that, for low index contrasts, a blue-shift occurs in the spectral features depending on the $\cos\theta$ factor, where θ is an average angle in the stack. Since 1996 and the researches conducted by P. St-John Russel *et al*, it is recognized that, for certain specific two-dimensional structures, two-dimensional omnidirectional band gap can be created for large values of k_z. The interested reader will find more detail on this subject in (Knight 2003; Ortigosa-Blanch 2000; Russel 2003). In this case, a defect formed by a single missing 'atom' may allow the guiding of light, with a dispersion relation of the form $\omega = \omega(k_z)$. For the reader familiar with localized defects in two-dimensional photonic crystals, this dispersion relation can be interpreted in the following terms: for each value of k_z, at least within a certain range, a guided mode corresponding to this frequency exists with a well-defined field pattern in the Oxy plane. The dispersion relation $\omega = \omega(k_z)$ thus represents in a sense a concatenation of these modes. This shall be discussed in more detail in Chapter 11, devoted specifically to the issue of photonic crystal fibres.

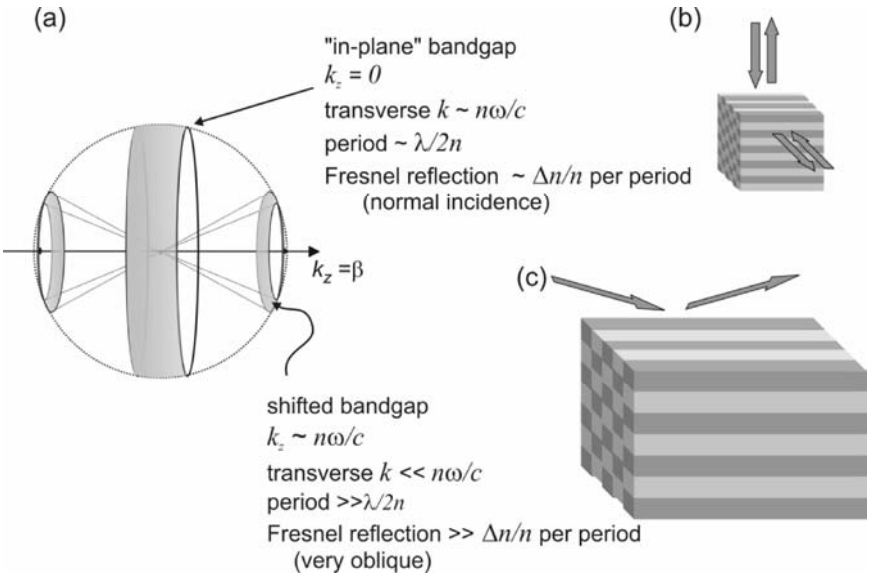

Fig. 5.5. Evolution of the basic quantities in a two-dimensional crystal, depending on the direction of propagation of the waves. *a.* Position of the related waves in the *k*-space, represented on a sphere with radius $k = n\omega/c$ *b.* Real-space configuration for waves propagating normally to the direction of invariance of the photonic crystal (in-plane band gap, $k_z = 0$) *c.* Real-space configuration for waves propagating along a direction close to the invariance axis ($k_z \sim k$), as in the case of photonic crystal fibres

5.2.4 Density of States and Multiplicity of Guided Modes

A photonic crystal waveguide can be generically described as a medium *2*, in the form either of an homogeneous ordinary medium or of any photonic crystal, surrounded by a medium *1* with a photonic band gap ensuring the confinement of electromagnetic wave. The density of states of a one-dimensional channel is defined as the ratio $dN/d\omega\, dl$ calculated per unit length of the channel, while in the case of a two-dimensional planar waveguide the density of states is the ratio $dN/d\omega\, dS$ calculated per unit area of the waveguide. The presence of a waveguide results in the formation of nonzero density of states in the band gap of the confining material, i.e. in the cladding.

Let us first consider the case of a channel waveguide along *Ox*. Dispersion branches of the form $\omega = \omega_i(k_x)$ associated with the guided modes appear in the band gap. Each of these branches contributes to a number of states which is in proportion to the length of the waveguide. The associated density of states can be formally written in the form:

$$D(\omega) = \int_{BZ} dk_x \delta(\omega - \omega_i(k_x)) \propto (d\omega_j / dk_x)^{-1} \tag{5.3}$$

The number of guided modes at a given frequency and their dispersion (group velocity) determine the total density of states. As is the case for conventional index guiding (see Chapter 9), the dispersion branches cover only a limited frequency range: each mode has one or several cutoff frequencies. The dispersion curve often tends to flatten when reaching a cutoff frequency ($d\omega_j/dk_x = 0$), while the density of states either diverges or presents singularities ($dk/d\omega \to \infty$) (Kleppner 1981), a phenomenon which corresponds to van Hove singularities in solid state physics (Ziman 1992) .

Only in the case of waveguides exhibiting relatively large transverse dimensions, formed from an homogeneous material with index n, can some simple predictions be made. Within the limits just indicated, the number of modes per unit volume of the waveguide tends asymptotically towards that of a bulk system formed by the homogeneous material filling the whole space. Assuming that the density of states in such a medium is, for either of the two polarizations:

$$D_2(\omega) = \frac{1}{V}\frac{dN}{d\omega} = \frac{1}{V}\frac{dN}{dk}\frac{dk}{d\omega} = \frac{1}{8\pi^3} 4\pi k^2 \frac{n}{c} = \frac{1}{2\pi^2}\frac{n^3\omega^2}{c^3} \tag{5.4}$$

and that the section of the waveguide is equal to $S = L_y L_z$, where L_y and L_z are large with respect to λ/n, then the linear density of states of the waveguide should be of the order:

$$\frac{dN}{dx d\omega} = SD_2(\omega) = \frac{S}{2\pi^3}\frac{n^3\omega^2}{c^3} \tag{5.5}$$

Different examples of dispersion diagrams and density of states calculated for three different waveguides realized in a photonic crystal formed by a triangular lattice of air holes in a dielectric medium are presented here in Fig. 5.6. Each waveguide corresponds to a given number of missing rows of holes along a dense direction of the crystal. In the purely two-dimensional examples considered in this figure, this number is equal to 5, 3 or 1, hence the naming of these waveguides as W5, W3 or W1. Each diagram is calculated using the supercell method described in Section 1.4.3 in Chapter 1. The grey areas here correspond to the multiple transmission bands of the bulk crystal surrounding the waveguides. When going from the broad waveguide represented in Fig. 5.6a to the narrow waveguide represented in Fig. 5.6*c*, it can be seen in the assembled graphs shown in Fig. 6*d* that the density of states evolves from a continuum $D(\omega) \propto \omega$ interspersed with multiple superimposed singularities associated with flat bands, towards a more structured form displaying more prominent gaps and singularities. We shall return later in Section 5.2.5 to the issue of some of these internal gaps.

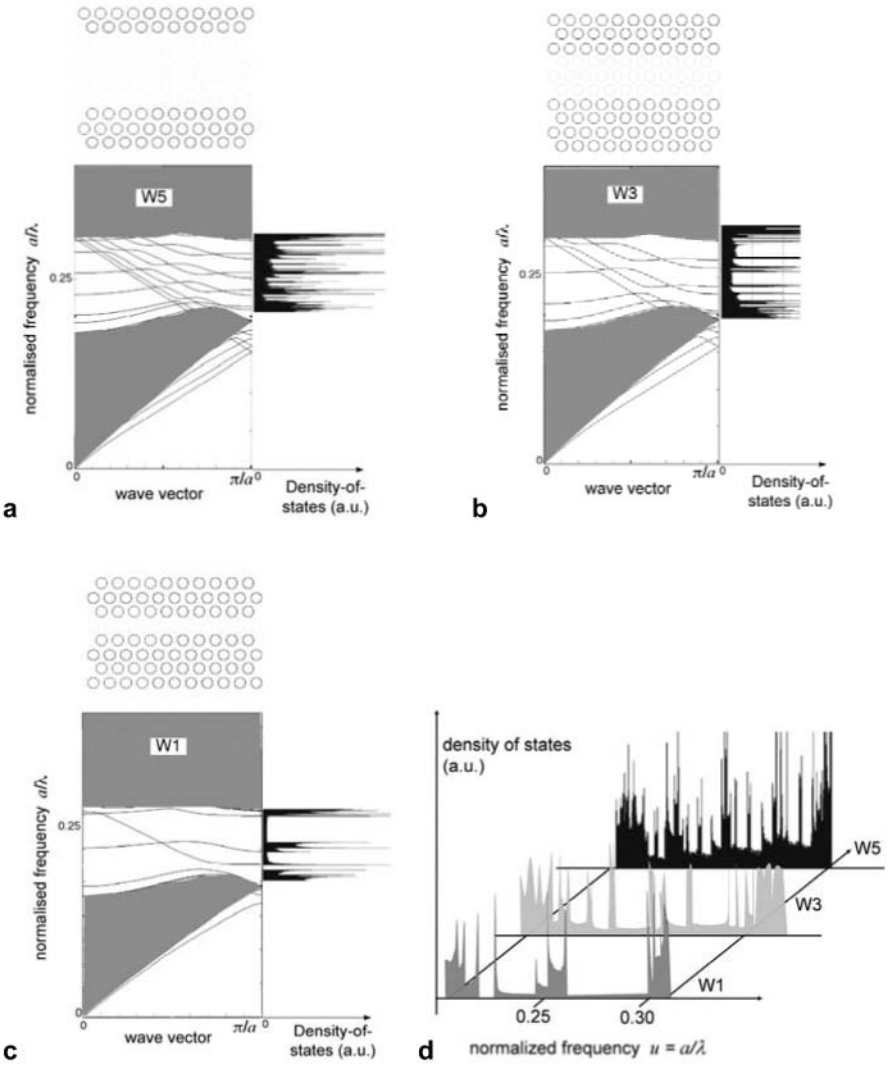

Fig. 5.6. Dispersion diagrams and corresponding density of states, represented on the right of the diagrams, for waveguides with: *a.* five missing rows of holes (W5), *b.* three missing rows of holes (W3), *c.* one missing row of holes (W1). In all three cases, the waveguide is schematically represented above the corresponding diagram. The photonic crystal is formed by air holes in a dielectric matrix ($\varepsilon = 11$, $f = 0.37$). The grey areas in the diagrams represent the projections of the transmission bands of the bulk crystal without defects. The diverging singularities in the density of state (peaks in the dispersion diagrams) are bounded due to the discretization of the calculations over a finite, albeit large, number of values for k *d.* Assembled graphs of the density of states of the three waveguides, showing the slow evolution toward a continuum at large widths

In the case where the guiding medium itself is structured, we return to original line of argument by explicitly writing that the number of states is equal to the number of values for k allowed by boundary conditions of the Born-von Karman type common in solid-state physics (Ziman 1992). This amounts to considering the waveguide as being approximately a very elongated rod with a section $S = L_y L_z$. The density of states per unit volume $D^s(\omega)$ of such a structured medium is obtained by integration over the elements dS_ω of the iso-frequency surfaces S_ω in the k-space. For a frequency interval $d\omega$, the thickness in the k-space of the shell containing the relevant dN states reads as $dk = v_g d\omega$. This generic density of states can be expressed in the form of a summation over the elementary volumes $dS_\omega dk$, and more specifically in the form:

$$D^s(\omega) = \frac{1}{V}\frac{dN}{d\omega} = \frac{1}{8\pi^3}\int_{S_\omega} dS_\omega v_g d\omega \tag{5.6}$$

In the case under consideration of a channel waveguide with a section S, and remaining within the assumption, to be verified afterwards, that the number of branches is relatively large, the density of states per unit length is approximately:

$$D^s_{lin}(\omega) = SD^s(\omega) \tag{5.7}$$

The planar version of this equation can be readily obtained by replacing S with the thickness of the waveguide, which will be denoted here by L_y. While the above equations are somewhat trivial, it should be noted that photonic crystals may exhibit less common volume densities of states $D^s(\omega)$, for instance a very low density of states over a large frequency interval. Such a material can thus be used in the form of relatively thick guiding layers. In spite of their thickness, these layers may indeed allow the propagation of only a relatively small number of modes, down to a single mode.

Let us now return to the examples represented in Fig. 5.6. When the width of a waveguide decreases, the number of allowed states decreases as well, and the mode cutoffs associated with regions where the group velocity is zero give rise to the appearance of more pronounced singularities in the density of states. However, the description of these singularities, which depend on the finer structure of the Brillouin zone, is more complex in the two-dimensional case (planar waveguides) than it was in the one-dimensional case. Here again, it might be emphasized that, in general, there is no isotropy between the x and y directions of an arbitrary planar waveguide defined in a photonic crystal.

When the width of a waveguide further decreases, only one or two dispersion branches remain, in the channel as well as in the planar case. These dispersion branches may not extend over the entire band gap of the cladding, and therefore they may leave frequency ranges with a true zero-density of states. For extremely thin waveguides, the remaining modes typically extend only over a very small band near one of the edges of the band gap. For this reason, these modes can be

compared to shallow defects, created for instance by dopants, in semiconductors. For the simplest types of structures, the high-frequency band located just above the band gap is an air band, whereas the low-frequency band below the same gap is a dielectric band (see Chapter 1). The introduction of an ultrathin waveguide proceeds either by adding or by removing dielectric. The corresponding guided mode then presents essentially the same characteristics as the associated band, save for a small frequency shift towards the centre of the gap. In particular, the electromagnetic field of the mode extends mainly in the cladding, where the defect formed by the waveguide 'anchors' this mode, much in the same way as shallow dopants or defects do in semiconductors. A strong similarity also exists with the surface modes described in Section 1.4.6 of Chapter 1.

5.2.5 Coexistence of Index Guiding and Photonic Bandgap Guiding

Nature of the Defect Mode

Index guiding and photonic bandgap guiding should not be seen as exclusive of each other. As has just been recalled in the preceding section, the introduction of a defect in a bulk crystal creates a mode whose characteristics are essentially the same as those of the air band (at high frequency) or those of the dielectric band (at low frequency), depending on whether the defect was formed by adding or removing some material. For instance, creating an 'air' defect amounts to separating two semi-infinite photonic crystals in such a way as to form an air layer between these two crystals. This approach is frequently used when dealing with dielectric columns. By contrast, the method generally favoured for forming a waveguide in an array of holes consists in suppressing some of these holes, i.e. in filling them.

In the case of an 'air' defect, no index guiding occurs, since the effective phase index of the mode, i.e. the ratio kc/ω, is not high enough compared to that of the cladding. Indeed, if the cladding exhibits transmission bands, then the effective index of these bands must be higher than unity. For all values of k along the dispersion branch, the confinement of the guided wave involves multiple reflections on the photonic band gap material. A genuine 'photonic bandgap guiding' can thus be achieved. The general idea of such a system can be traced back to the pioneering work by Yeh and Yariv (Yeh 1976). However, the exploitation of a high index contrast and of the entire frequency range of the band gap makes for a much powerful approach than the scheme originally proposed by Yariv, since the latter relied on the use of one-dimensional structures with relatively limited operating ranges.

In the case of a dielectric defect, the situation is quite different. At the lowest values for k along the dispersion branches in the band gap, the physical mechanism still involves multiple reflections at the cladding formed by a photonic crystal material. If this crystal were to be replaced with a cladding formed by a homogeneous material with a low index, then the guided modes would turn into a series of weak resonances. This is quite different from the situation occurring at higher values for k. Indeed, in the latter case, the guiding mechanism would be essentially

the same if the photonic crystal were to be replaced with a homogeneous material with an average index of the same order of magnitude. In other terms, the physics of this phenomenon are in most respects the same as the physics of index guiding.

Thus, index guiding occurs for dielectric defects on a part of the dispersion branch of each mode. Let us consider here again the case, represented in Fig. 5.7, of a dielectric matrix, where a waveguide has been created in a triangular lattice of round air holes by omitting to drill a few rows. At $k_x = 0$, the 'guided' mode will be analogous to the mode of a Fabry-Perot resonator formed by two perfect mirrors ($R \sim 1$), as represented in Fig. 5.7*a*.

In spite of a certain penetration of the field in the photonic crystal, leakage is formally prevented by the fact that the cladding of the photonic crystal waveguide is assumed to be infinitely thick. This remains true for non-zero, albeit relatively small, angles of incidence ($k_x \neq 0$), whereas for larger angles, index guiding will occur. In order to remain within the band gap of the cladding, we assume that we move to lower branches when k_x and the frequency increase. However, as has been discussed in Section 2.3 of this chapter, index guiding may well subsist even in the absence of an omnidirectional band gap. Finally, for the largest values of k, the field of the fundamental mode does not penetrate far in the cladding, whose effective index is low enough for enforcing index guiding and the exponential decay of the field, as can be seen in Fig. 5.7*b*. This is all the more true when we travel along the dispersion branches down to the fundamental guided mode. This effect will be met again in Chapter 11 when studying microstructured fibres.

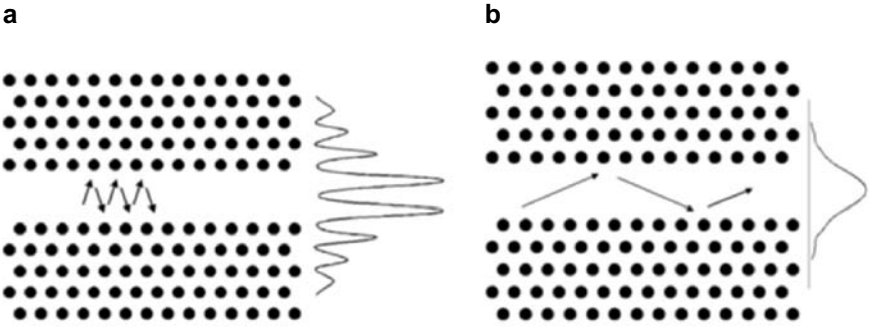

Fig. 5.7. Waveguide created in a triangular array of holes by omitting to drill a few rows *a.* Propagation (represented by arrows) and schematic intensity profile of a Fabry-Perot type mode close to the normal incidence *b.* Propagation and schematic intensity profile for a mode in the case where index guiding is the main guiding mechanism

These considerations, based solely on the band structure $\omega(k_x)$, need however to be carefully assessed. As can be seen for instance in Fig. 5.8, band folding also causes an 'ordinary' index confined branch to move back to $k_x = 0$. Therefore, an apparent contradiction arises: while the mode is of an index guided nature, it exhibits a very low value for k_x, just as a Bragg confined mode would do. This situation points to an intrinsic difficulty in the Bloch theorem, which states, among other things, that k_x can be restricted to the first Brillouin zone irrespective of the nature of the mode. Actually, the predominant nature of the mode can be determined from the consideration of its actual content in terms of spatial harmonics. When using the folded picture, it should be borne in mind that the main k-component of the folded modes around $k_x = 0$ is actually $k_x = \pm 2\pi/a$ (Lombardet 2005). The group velocity and its evolution in the vicinity of the region under consideration also provide precious indications as to the actual nature of the mode. Thus, a large group velocity ($\sim c/n$) is not compatible with a Fabry-Perot type behaviour and with its associated Bragg guiding mechanism.

Effects of Periodicity on Photonic Bandgap Waveguides

Index guiding is the main guiding mechanism for waveguides formed by photonic crystals where a dielectric defect has been created. However, these waveguides present a marked periodicity, which must be accounted for. Its basic effects will be discussed from a perturbative approach by considering the only type of waveguide which can easily be modelled, the perfect waveguide confined by ideal metallic planes. Additionally, we shall restrict ourselves here to a two-dimensional analysis and to a scalar approach.

This restriction can be justified by the fact that, even in the case of simple slab waveguides, no analytical expression of the dispersion relation exists (see Chapter 9). The idealized waveguide represented in Fig. 5.8*a* has a width L along y and allows the propagation of modes with a scalar field of the form:

$$E = E_0 \sin\left(k_y y\right) exp\left(ik_x x\right) exp\left(-i\omega t\right) \tag{5.8}$$

with $k_y = m\pi/L$, where m is an integer. The latter condition ensures that the boundary conditions calling for a zero field at the walls of the waveguide are satisfied (Fig. 5.8*a*). Denoting by n the refractive index of the waveguide, the dispersion relations assume the following form:

$$\omega_m = \frac{c}{n}\sqrt{k_x^2 + \left(m\frac{\pi}{L}\right)^2} \tag{5.9}$$

while the corresponding dispersion curves are hyperbolic branches, as can be seen in Fig. 5.8*b*. Similar hyperbolic branches can be observed around $k_x = 0$ in the diagrams represented in Fig. 5.8*b*. This is a clear indication of the relevance of this model.

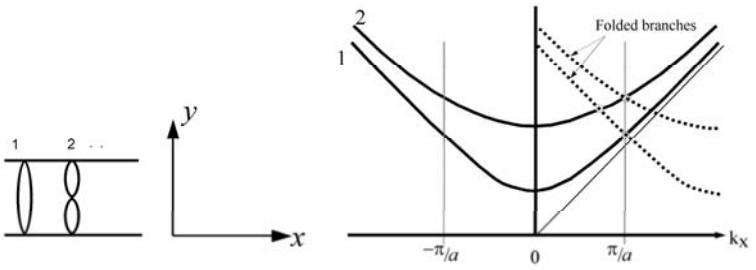

Fig. 5.8. Effects induced by periodicity. *a.* Ideal waveguide with a cladding formed by perfectly conducting metals *b.* Dispersion diagrams (*solid lines*) and effects induced by periodicity on an 'empty lattice' (*dotted lines*). Duplication at a $2\pi/a$ interval creates the impression of a folding of the dispersion branches

Let us now introduce a fictitious period a, corresponding to what is referred to as the 'empty lattice' in crystallography. In this case, everything will occur as if k_x were defined modulo $2\pi/a$, which results in the appearance of a 'folding' in the dispersion diagram at the edge of the Brillouin zone $k_x = \pi/a$. Actually, a $2p\pi/a$ shift is indeed required in order to bring all dispersion branches back into the first Brillouin zone $[-\pi/a, \pi/a]$. However, since $\omega(-k_x) = \omega(k_x)$, the impression created is exactly that of a folding at the edge of the zone. In the example considered here of a metallic waveguide, such a periodicity could be introduced in the form of a corrugation with a period a along the metallic walls of the waveguide. The Fourier components of the permittivity would then be non-zero at all multiples of $2\pi/a$, and in particular they would be so at $2\pi/a$ itself.

Such a folding of the dispersion branches may induce dramatic effects on guided waves. This is especially true when two branches tend to cross one another, i.e. when two of the ideally guided modes in Fig. 5.8*b* interact due to the $2\pi/a$ wave-vector difference between them.

At the edges of the zone, i.e. in this case at $-\pi/a$, 0 or at π/a, photonic gaps similar to those described in Section 1.3.2 of Chapter 1 appear. Fig. 5.8*b* presents examples of such phenomena, more particularly for the lowest branches at π/a. The equivalent coupling at zone edge also exists for semiconductor channel waveguides with corrugated boundary. For instance, distributed feedback (DFB) and distributed Bragg reflector (DBR) lasers are familiar devices in the field of optoelectronics. These structures were proposed around 1970 for the purpose of providing optical feedback in the fundamental lasing mode. In practice, DFB and DBR lasers are operated with a low feedback per unit length, or in other words, with a minute relative modulation of the effective index, of the order or 10^{-3} or less. A significant reflectivity can thus be provided with only a few hundred μm. While these structures are not in the strong-index-contrast regime, they are nonetheless conceptually relevant to the picture of the waveguide mode interaction presented here. The same applies to fibre Bragg gratings, which usually are centime-

tre-long systems. In view of the limited index contrast involved in these systems, the coupled mode theory (Kogelnik 1972) remains well suited to accurately describe the slowly varying field envelopes without resorting to photonic bandgap theory.

The most original effect occurs when a crossing takes place outside the edges of the zone. In this case, two dispersion branches, associated with modes of a different nature, are necessarily involved. The coupling between modes induced by periodicity allows energy transfers from one mode to the other, provided that symmetry rules are satisfied, as will be seen later. According to a microscopic and unfolded view, the polarization induced by one of the two modes presents a small spatial component at the spatial frequency of the other mode. This simply results from the multiple Fourier components of the dielectric constant which are seen by the two modes. Accordingly, the interaction between the two modes results in a lifting of the degeneracy at the crossing point and in an anticrossing of the dispersion curves. In other terms, it leads to the appearance of a band gap between the two modes. This phenomenon can be observed in several of the examples presented in Fig. 5.8*b*. Indeed, when considering the propagation of the fundamental mode at variable frequencies, a significant attenuation can be observed in the spectral region where the anticrossing occurs. This phenomenon has been termed by some authors as a 'mini-stopband' in order to distinguish it from the usual stop band (Olivier 2001b). In reality, this phenomenon is not a photonic band gap in the stricter sense of the term, since the cancellation of the photonic density of states can be prevented by the contribution of other modes that, although not being involved at all in the process discussed here, may exist with the same frequency. For instance, if a large number of guided modes exist in the spectral region where the anticrossing of two modes occurs, no significant change will arise in the density of states at the corresponding frequencies inside the minigap, although a very strong attenuation of the fundamental mode will be measured in practice.

An interpretation of this phenomenon in terms of a diffraction by a grating can also be attempted. Indeed, the law of diffraction by a grating, expressed in terms of wave vectors, comes down simply to $\Delta k = 2p\pi/a$. Accordingly, and going back to the representation of guided modes as a superposition of two oblique plane waves (represented by zigzag rays in Figs. 5.3 and 5.7), these plane waves can be diffracted by the grating formed by the walls of the waveguide themselves. For the sake of simplicity, we shall assume here that the corrugation of the wall of the waveguide is reasonably 'flat', and therefore that plane waves will arrive with the same well-defined incidence at all points of the wall. Likewise, the diffracted plane waves will undergo the same multiple reflection processes at the walls as the waves from which they were originally generated. However, since the diffracted waves propagate with a different angle, these multiple reflection processes will generally lead in this case to destructive interferences, with the consequence that almost no energy will be taken out of the original guided mode. By contrast, in the specific situation where the phase-matching condition is achieved for the multiple reflections of the diffracted waves, another eigenmode (guided mode) of the structure can be excited from the original guided mode. In other terms, the phase matching resulting from the periodicity of the waveguide may lead to a coupling

between two different modes. The general ideas of coupled mode theory are relevant in this context, and the reader is referred for instance to the work by H. Kogelnik in (Tamir 1990). As for the one-dimensional photonic band gaps discussed in Section 1.3.2 of Chapter 1, the spectral width allowed around resonant transfer, i.e. in this case the spectral width of the anticrossing, is directly dependent on the amplitude of the Fourier component of the dielectric constant, involved in either of the two coupled modes.

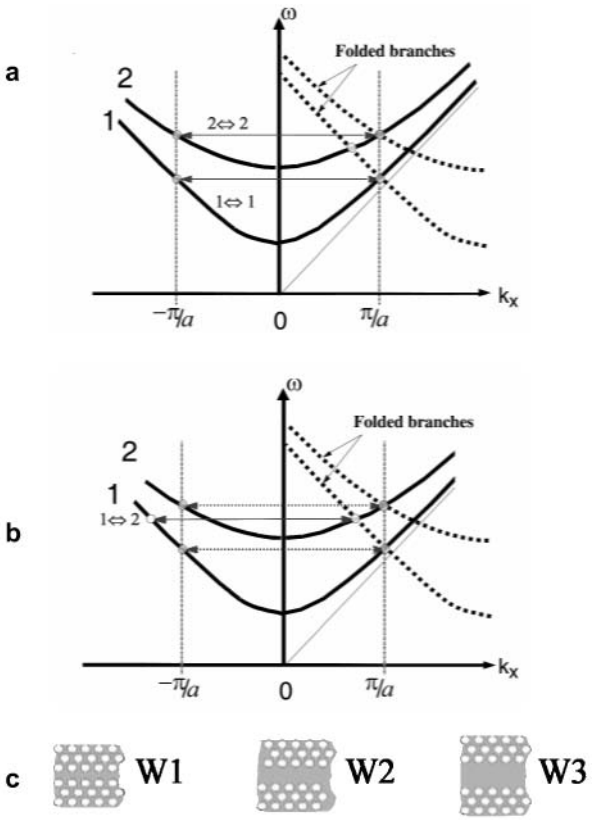

Fig. 5.9. Effects induced by periodicity (*continued*). *a.* 'Diagonal' coupling with a band gap at the edge of the Brillouin zone *b.* Coupling between different modes and gap in the middle of the Brillouin zone, *c.* Schematic representation of a waveguide created in a triangular lattice with 1, 2 and 3 missing rows: the spectral interval between the dispersion branches decreases when the number of missing rows increases. The symmetry alternates: W1 and W3 have a symmetry plane along the axis of the waveguide, and only branches with the same parity are coupled. In particular, the 1⇔2 coupling is forbidden. Conversely, W2 requires a glide operation (shift of a half period + symmetry) in order to remain invariant and only branches with opposite parities are coupled

When the periodicity of the two walls of the waveguide is symmetric with respect to the axis of the waveguide, which is the case for all the examples represented in Fig. 5.7, coupling phenomena occur only between modes with the same parity. Conversely, for modes with opposite parities, the overlap integral between the fields of the modes and the periodic 'potential' is zero. This is similar to what occurs in quantum mechanics, where the selection rules stem from the cancellation of the matrix elements.

As will be seen in the third part of this book, triangular lattice of holes of the type represented in Fig. 5.9 are generally preferred over other structures in the field of guided optics. In the examples shown in this figure, the periodic structures on each side of the waveguide are symmetric with respect to the axis of the latter if an odd number of rows is omitted along dense directions of the crystal. Conversely, for an even number of missing rows, the holes alternate, with a shift of a half-period being required in addition to the symmetry operation for retrieving the original structure. In the latter case, only modes with opposite parities will be coupled. It can easily be seen that, in the real space, the contributions of modes with the same parity will be in phase opposition (with respect to the spatial period a) at the two walls of the waveguide. This amounts to introducing in the reciprocal space a structure factor $\exp(-i\pi) = -1$, hence a mutual cancellation of these contributions, which are dependent on the optical polarization $\mathbf{E}\delta\varepsilon(\mathbf{r})$. The considerations developed above suggest that, at frequencies where such crossings occur, an original method exists for controlling the interaction between two guided modes through the control of the relative spatial phase of the two walls of the waveguide.

At this point, it might be emphasized that the irregularities of the photonic crystal waveguide resulting from an imperfect fabrication, for instance irregularities in the shape of the holes at the edges of the waveguide, may actually induce parasitic mode coupling effects. These irregularities induce irreproducible, albeit non-zero Fourier components and therefore non-zero couplings in a system where the different effects must exactly compensate for one another. The risk therefore exists here that any crossing will result in a coupling and in an energy transfer, even if it can be expected that this phenomenon will remain of a much lower order of magnitude than the structural coupling previously described.

Before concluding these remarks on the subject of irregularities, it seems intuitively sound that, when there are either one too many or one too few entire patterns, significant perturbations might occur in a photonic crystal waveguide. In this respect, it might be noted that the insertion or removal of such a pattern brings us close to resonators, which will be discussed in the following section. From a practical point of view, 'deterministic' fabrication processes only induce more or less important irregularities between the patterns. By contrast, photonic crystals created by self-organization (see Section 12.2.2 in Chapter 12) may precisely present defects of the kind discussed here, in the form for instance of a missing sphere in an opal. When defining a waveguide in such a structure, it is therefore essential of course to carefully avoid such 'native' defects.

It is quite clear that the mode coupling phenomena discussed here cannot occur in the case where the waveguide is by construction single-mode. We shall later

discuss in the third part of this book the conditions required for achieving such a single-mode regime.

5.3 Resonators

5.3.1 Localized Modes. Origin of Losses

The introduction in an infinite crystal of a point defect, for instance through the modification or the removal of some pattern, leads to the appearance of at least one localized mode within the photonic band gap. Assuming an infinite lossless crystal with an internal excitation of such a localized mode, then the energy stored in the mode would never decrease. In reality, however, a crystal is necessarily finite, and the electromagnetic field of the localized mode, even if it decreases exponentially with the distance from the defect, will couple at some point with radiation modes outside the crystal. In practice, two limit situations may arise. First, in the case where a relatively large number of crystal rows or planes exist around the defect, the leakage due to radiation modes is negligible compared to other energy decay mechanisms such as the residual absorption or the imperfections of the structure. This applies to any type of photonic crystal, irrespective of whether it is a self-assembled or a deterministic structure. By contrast, the second limit case occurs when the number of planes or of rows is limited, and typically when it is lower than five, along one or several direction(s) of space (see Fig. 5.10, and Section 1.4.2 in Chapter 1). In this case, the main energy decay mechanism is the coupling of the defect mode to the radiation modes of the surrounding medium, which occurs through the limited number of planes or rows.

It is convenient to quantify each loss channel with a quality factor in inverse proportion to the resulting photon flux. In the following, Q_{sys} will denote the quality factor associated with the absorption and imperfections of the crystal, while Q_{PBG} will denote the quality factor associated with the field leakage and with the subsequent radiation losses resulting from the finite size of the crystal. Denoting by N the number of layers around the defect, then Q_{PBG} can be found to increase exponentially with N. The overall quality factor Q, which describes the number of periods of the oscillating electric field after which the energy of the localized mode has decreased by $1/e^2$, and the amplitude of the field by $1/e$, is then simply given by the equation:

$$Q = (Q_{sys}^{-1} + Q_{PBG}^{-1})^{-1} \tag{5.10}$$

Losses can be further distinguished according to whether they result from microscopic, fluctuating and irreproducible imperfections of the crystal, or whether they are associated with some intrinsic geometrical feature of the system under consideration.

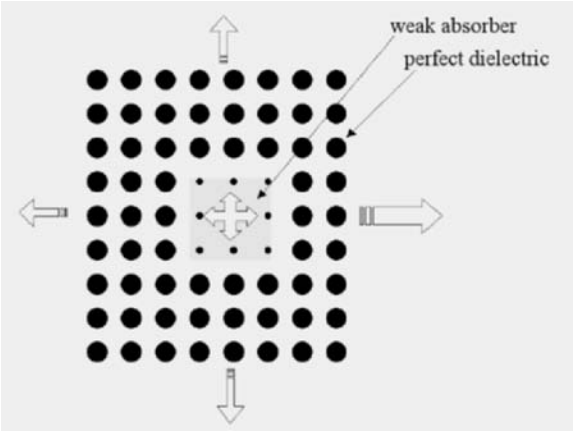

Fig. 5.10. Localized mode in a defect formed by one missing atom and eight smaller ones, with some internal dissipation (*grey absorbing zone*), and radiation losses due to the leakage occurring through the photonic crystal (*outgoing arrows*)

Losses of the first type are at the origin of Rayleigh scattering phenomena (Born 1965) in strongly textured environments, and more particularly in three-dimensional crystals. Examples of losses of the second type include etching defects, for instance the frequent narrowing from top to bottom of the holes in two-dimensional arrays of holes. In two-dimensional systems where in-plane confinement is generally accompanied by an index confinement along the vertical direction (see Section 5.4 in this chapter and Chapter 9), radiation losses may also occur in the substrate or superstrate layers of the cladding, which add to radiation losses due to the finite size of the crystal (Q_{PBG}). Indeed, as has been discussed earlier in Section 5.1, index guiding is significantly less efficient than photonic bandgap guiding as regards the suppression of radiations along all directions. The problem of radiation losses will be further discussed in Section 5.4 of this chapter and will be addressed in more general terms in Chapter 9 in the context of planar integrated optics. We shall see in Section 9.8.3 that, following the so-called membrane approach, the thorough analysis of the various radiation mechanisms allows the design of 'ultra-high Q' cavities with very small mode volume. These cavities are created in thin two-dimensional photonic crystal slabs suspended in the air .

For Fabry-Perot cavities defined by two semi-reflecting mirrors with modal reflectivities r_1 and r_2, separated by an optical path nL, the Q factor is usually expressed in the form $Q_{FP} = m\mathrm{F} = m\pi (r_1 r_2)^{1/2}/(1 - r_1 r_2)$, where F is the cavity finesse and m is related to the mode order, $m = nL/(\lambda/2)$. The very application of the notions of cavity length and mirror reflectivity to the case of an arbitrary defect microcavity in a photonic crystal can be considered questionable, in light of the lack

of clear separation between the photonic crystal 'mirrors' and of the strong dependence of the effective reflectivity of the photonic crystal surrounding the cavity on the localized cavity mode itself. Nevertheless, a general trend can be observed indicating that the Q factor tends to increase with the size of the defect in the same proportion as Q_{FP} increases with L. This simply reflects the fact that light can spend more time in the mode of a larger defect. Some subtleties may arise however. For example, a small defect can give rise to an extended mode in the photonic crystal, in particular when the defect is a weak perturbation of the lattice, analogous to a shallow impurity in a semiconductor.

5.3.2 Density of States

Since the modes of a localized defect are discrete, the density of states turns out to be a series of Dirac peaks (see Section 1.4.7 in Chapter 1), whose amplitude in the sense of distributions reflects the possible degeneracies of the modes. These degeneracies are in general associated with certain geometrical invariances. The presence of leakage mechanisms transforms the density of states into a series of Lorentzian peaks with a finite width. If these Lorentzian peaks were to significantly overlap, then the description in terms of localized modes would cease to be adequate.

The number of modes associated with a defect follows the general laws applying to waveguides which have been described in Section 5.2.4 of this chapter. If the defect consists of a volume of some homogeneous material, then, for large volumes, the number of modes per unit frequency tends asymptotically towards the value associated with this bulk material $V \times D_2(\omega)$. Therefore, for a three-dimensional system, $D(\omega)$ will be in proportion to $n^3\,\omega^2$ (see Section 1.4.7).

The different localized modes of a given defect may exhibit very different loss characteristics, and therefore different quality factors. The problem of losses in this context presents much the same issues as for the photonic crystal mirrors discussed in Section 5.1. Evanescent waves generated in the vicinity of the defect will exhibit different characteristics along the different directions of the crystal. In general, evanescent waves propagating along different directions have different spatial decay constants (imaginary part of k). However, all the modes localized in the band gap have an evanescent part in the crystal, which actually is a superposition of such evanescent waves, with coefficients depending in a nontrivial way on the shape and index structure of the defect. As a consequence, the determination of the quality factors will also be nontrivial. This contrasts with the case of standard Fabry-Perot cavities briefly mentioned in Section 5.3.1. In most studies, modes are first classified according to their spatial field pattern and symmetry, as for instance the whispering-gallery modes of microspheres and microdisks. The characteristics of the modes in terms of frequency and losses are then investigated with respect to some variable parameter, for instance the air-filling factor of the surrounding crystal, or the shape of the defect or cavity. Finally, the results thus obtained are used for quantitatively verifying that the mechanisms heuristically inferred are actually present (Vuckovic 2002a).

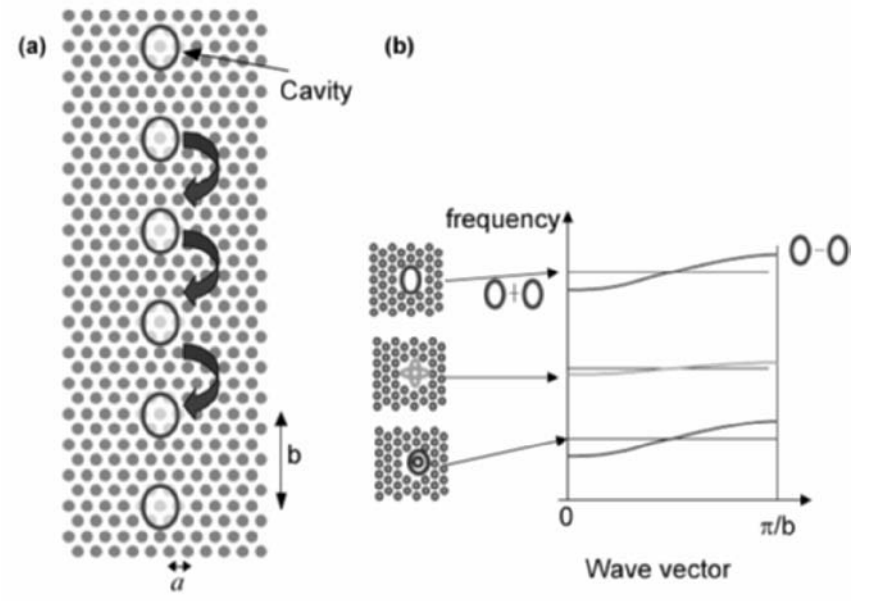

Fig. 5.11. *a.* Example of a coupled cavity waveguide, formed in a triangular lattice of holes by cavities of seven missing holes each. The ovals in the figure represent isolated cavity modes *b.* Formation of narrow bands around each frequency of an isolated cavity mode, for frequencies within the photonic band gap. Note the transition along each branch from a totally symmetric global mode at low frequency ($k_x = 0$) to an anti-symmetric global mode at the edge of the zone ($k_x = \pi/b$)

As an example, when photonic crystal microcavities are used as filters between two access waveguides, the central issue will be the coupling with external waves, and in the present case, with guided waves. If the coupling is intrinsically weak, then the maximum transmission of the microcavity will remain low, even in the case where the quality factor Q of the excited mode is high. In such a situation, there is simply no point in increasing the number of rows or planes of crystal isolating the cavity from the waveguides. This is only one aspect of the broader issue of the coupling between a waveguide and a cavity, which still remains an open field for research.

5.3.3 Waveguide formed by Coupled Cavities

While the coupling between a waveguide and a photonic crystal microcavity is of a great importance for a number of applications, the possibility also exists of devising applications that would be based on a coupling between such microcavities. This insight led N. Stefanou in 1998 (Stefanou 1998) and A. Yariv, in a more pedagogical exposition in 1999 (Yariv 1999), to propose the concept of a coupled

resonator optical waveguide (CROW) or chain of coupled resonators. The underlying idea is to create a waveguide by approaching isolated cavities from one another, and to form in the end a periodic chain of such cavities The principles of this waveguide are schematically represented in Fig. 5.11.

Readers familiar with solid state physics will immediately recognize here the tight-binding approach, wherein an electron is strongly bound to an ion even though its wave function only marginally overlaps neighbouring ions. For the description of the electromagnetic field and for the dispersion relations, we shall remain here within the formal framework introduced earlier in Section 5.2. The interest of the coupled cavity waveguide is that it leads to dispersion relations for the guided modes which are at once simple and quite remarkable. These relations simply results from the fact that each band is centred in frequency around the eigenmodes of a single cavity. Thus, the dispersion relation is of the form:

$$\omega(k_x) = \omega_0 + \Delta\omega \cos(k_x b) \tag{5.11}$$

where ω_0 has about the same value as the frequency of an isolated cavity eigenmode, b is the spatial period of the cavity in the chain and $\Delta\omega$ is the spectral width which depends on the strength of the coupling between the cavities, and therefore on the number of crystal rows separating any two cavities. $\Delta\omega$ also depends on the value of the quality factor Q_{PBG} introduced in Section 5.3.1, which represents the total intrinsic radiation loss associated with a given cavity.

Slightly increasing the number of rows between the cavities, hence the value for b, causes the spectral width $\Delta\omega$ to decrease and therefore the group velocity to decrease as well. As can be seen in the band diagram represented in Fig. 5.11*b*, the guided branches become narrow bands, each of which is almost centred on a mode of the isolated cavity.

The main argument in favour of coupled cavity waveguides is their conceptual simplicity. In standard photonic crystal waveguides, almost no simple guidelines exist for the resolution of certain inverse problems, for instance the problem of finding shapes and frequencies that would minimize the group velocity of propagating waves.

From a practical point of view, it is quite obvious that the individual cavities of the CROW should not present too high a level of losses, since such losses would cause most of the energy to dissipate before even reaching the next cavity. In other terms, propagation in such a case would be achieved only at the price of unacceptable attenuation losses.

By way of conclusion, it has been seen in Sections 5.1, 5.2 and 5.3 that a confinement of the electromagnetic energy by photonic band gap crystals can always be achieved. However, due to the complexity of the interactions between light and photonic crystals, this confinement may assume a large variety of forms. The fundamental phenomenon, which is without equivalent in perfectly metallic waveguides, is simply the diffraction induced by the periodicity. When considering this effect in the context of guiding, a further degree of complexity arises due to the interplay between diffraction, which leads to certain values for Δk being

privileged, and confinement, which imposes that a phase-matching condition be satisfied between the two walls of the waveguide. The guiding mechanism in such waveguides can be, in part, an index guiding. Systems based on the combination of waveguides and resonators are a very promising branch of research on photonic crystals, provided however that a satisfactory mode engineering be developed. In the following section, we shall see that for actual two-dimensional structures, which are more easily realizable in practice, an additional level of complexity arises.

5.4 Hybrid Structures with Index Guiding. The Light Line

The higher degree of maturity of two-dimensional systems, compared to three-dimensional systems, is the main incentive for attempting to achieve a control of light in these two-dimensional systems, while at the same time implementing a 'partial' confinement along the third direction. The latter objective can be achieved by using an index contrast, i.e. by resorting to a phenomenon of total internal reflection. Since we are no longer dealing with simple planar interfaces, the confinement of light by a homogeneous medium of lower index along the third direction will necessarily be partial. For this reason, the concept of total internal reflection must be either abandoned or, at the very least, significantly revised in this case. An understanding of the specific features displayed by these hybrid structures is therefore necessary. As will be seen in Chapter 9, these structures have offered a strategy which has led to striking developments in the realm of photonic crystal integrated optics.

5.4.1 Light Cone of a Uniform Waveguide

Let us first recall the concept of 'light cone' in the simple case of an optical slab with finite thickness and index n_{core}, clad by media with index n_{clad}. In such a slab, the guided modes of such a slab have a propagation constant $\beta = k_{//}$, necessarily larger than $n_{clad}\omega/c$.

The dispersion curves of the guided modes lie outside the cone $|k_{//}| = n_{clad}\omega/c$, referred to as the light cone. In the example represented in Fig. 5.12*a*, $\mathbf{k}_{//}$ is a two-dimensional vector, while the line(s) $k_{//} = n_{clad}\omega/c$ describe a cone in the (k_x, k_y, ω) space. Any mode in the light cone is said to be a 'radiation' mode. Such a mode is a wave impinging at a certain incidence angle from one of the claddings, which undergoes multiple reflections at the two interfaces of the core as it travels through it before propagating at infinity in the other cladding. Unlike guided modes, these modes form a continuum with a variable density of states, which exhibits, however, a singularity just at the surface of the light cone. This density of states will turn out to be a crucial parameter when the coupling of localized modes to the continuum will be analysed in terms of a perturbation. According to this view, the proper guiding of the wave in the core is ensured by the fact that no

mode with a value for $k_{//}$ high enough exists in the cladding, thereby preventing the coupling to the continuum formed by radiation modes. This description is strictly equivalent to the argument that $\sin\theta < 1$ in the account of total internal reflection given by Snell's law.

5.4.2 Fictitious Periodicity

Proceeding along the same lines as in Section 5.2.5, we shall now introduce a one-dimensional fictitious periodicity in the core of the planar waveguide. It should be borne in mind however that the core of the waveguide actually remains fully invariant. The period and the periodic axis will be denoted by a and x respectively. Any guided mode can then be decomposed into Bloch modes. In other terms, the guided modes can be described in terms of a multiplicity of wave vectors $k_{//}$ defined modulo $2\pi/a$ and associated each with a given dispersion branch. This leads to indefinitely duplicating the initial dispersion diagram by $2\pi/a$ shifts. The result is identical with the 'folding' of the dispersion branches observed earlier. Here again, branches with opposite group velocities tend to meet at $k_{//} = \pm \pi/a$, as can be observed in Fig. 5.12*b*.

Strikingly enough, this implies that branches that previously were outside the light cone may now partly or completely lie inside it. At this stage, the folding expresses the fact that the periodic part of the Bloch wave can be developed into a Fourier series whose successive orders are multiple of $K = 2\pi/a$. According to the Bloch theorem, the coefficients of these different components are generally non-zero. However, since periodicity in this case is fictitious, only the fundamental Fourier component associated with the dispersion relation represented in Fig. 5.12*a* actually exists. The introduction of a fictitious period has therefore led to introducing harmonics of this wave, albeit harmonics with rigorously zero coefficients. For this very reason, and in spite of the presence of branches in the light cone, no leakage whatsoever occurs in the continuum of modes.

5.4.3 True One-Dimensional Periodicity

Let us now turn to the consideration of a true periodicity rather than a fictitious periodicity (Figs. 5.12*c* and 5.13). In this case, the Bloch wave now actually contains several components with non-zero coefficients. Another effect induced by true periodicity is to cause couplings, either between counterpropagating modes at the edges of the Brillouin zone, or between modes of a different nature inside this zone (see Section 5.2.5). In particular, band gaps appear for dispersion branches located near the edge of the Brillouin zone at $k_{//} = \pm \pi/a$.

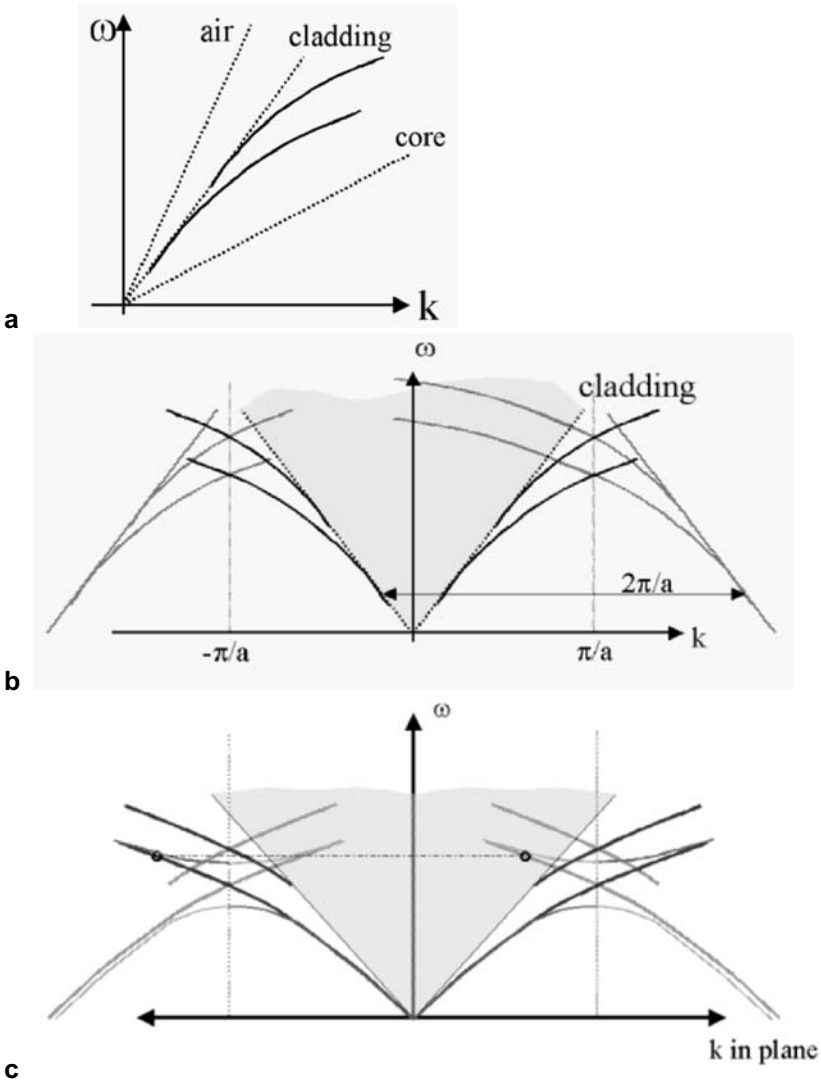

Fig. 5.12. The light line (or light cone). *a.* Case of a uniform slab *b.* Waveguide with a fictitious periodicity, where a folding phenomenon occurs *c.* Waveguide with a true periodicity: band gaps appear but contrary to *b* the modes above the light line present proper non-zero coefficients for the corresponding Fourier components, resulting in the possibility of leakage and radiation loss in the cladding

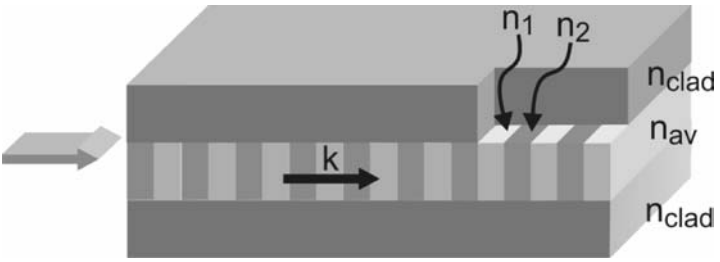

Fig. 5.13. Waveguide with true one-dimensional periodicity (in this case a variation in the refractive index of the core)

From the observation of the band diagram represented in Fig. 5.12*c*, two possible situations may be distinguished. These two situations will be extended to waveguides with a core formed by a two-dimensional photonic crystal, where the concept of light cone should be preferred over the concept of light line[1]. These two situations correspond respectively to:

- lossless modes, which can be defined as modes lying outside the light cone in the folded band diagram, i.e. in the diagram restricted to $[-\pi/a, \pi/a]$ according to the one-dimensional approach, and without any harmonics inside the light cone, since all these harmonics are outside the Brillouin zone.
- 'resonant' modes, also referred to as 'leaky' or as 'lossy' modes. These modes can be defined as modes extending inside the light cone in the first Brillouin zone. The case may arise where there is only one component in the light cone, for instance the zero-order component identified in a perturbative approach, while all other components are outside the line cone. Nevertheless, this will suffice to induce a leakage, and therefore radiation losses. The strength of the coupling to the continuum modes depends on the value of this non-zero coefficient. Conversely, light impinging from outside can be substantially transformed into guided energy when the (ω, k_x) parameters of the incident beam satisfy the dispersion relation of the waveguide. When seen from outside, this will give rise to narrow resonances.

[1] In the case where not only the core, but the cladding as well are formed from a periodically structured material, the concept of light cone can still be used provided that the modified photon dispersion relation of the cladding is taken into account. This obviously leads to a distortion of the straight cone displayed in Fig. 5.12. However, a first approximation consists in modelling the cladding as a homogeneous material with an average index

In relation with Fig. 5.13, it might be useful to discuss the properties of DBR and DFB laser structures introduced in Section 5.2.5, and familiar to practitioners in the field of optoelectronics. Periodicity in these structures is frequently achieved by corrugating the interface between the cladding and the core layers rather than by alternating materials in the core layer itself. As a consequence, the index of the cladding is only slightly below the index of the core. However, the result is the same in either case. For a first-order DFB ($K \sim 2\, k_x$, where k_x is a guided wave vector), the feedback regime takes place slightly outside the light cone, due to the fact that the effective indices of the interacting modes are larger than the index of the cladding. By contrast, second-order DFB lasers ($K \sim k_x$) are in general leaky structures, where light can leak almost normally to the device. This results from the fact that the diffracted wave vector component satisfies $(k_x - K) << K$.

Fig. 5.14 illustrates, for a waveguide with a true one-dimensional periodicity, the three cases of a pure guided mode (Fig. 5.14*a*), of a pure 'radiation' mode (Fig. 5.14*b*) and of a 'resonant' mode lying above the light line (Fig. 5.14*c*) respectively. The wave vectors associated with these different modes are also presented in these figures.

As far as 'resonant' modes are concerned, the existence of a coupling of these modes to a continuum prevents them from being described as modes in the strict sense of the term. Even in the case of lossless materials, the lifetime τ of a photon in the state considered is finite. The spectrum of the mode can no longer be represented by a Dirac peak as was possible for discrete modes. It now exhibits a Lorentzian profile, whose width at half the maximum is inversely proportional to the lifetime of a photon. Accordingly, the mode may only propagate over a finite distance. In terms of wave vectors, the resonance has a width Δk which is inversely proportional to the propagation length.

The use of the term 'resonance' can be justified as follows: if a wave propagates from the cladding with appropriate values for $\mathbf{k}_{//}$ and ω, its energy will be concentrated in the waveguide during a time τ, just as it would be the case in a Fabry-Perot resonance. A description in terms of modes can therefore be restored, but only at a high price since the whole universe is now to be considered for all modes, while the 'resonances' will be denoted by the relative concentration of energy in the waveguide.

An elegant mathematical description of such a resonance consists in using the complex poles ($\mathbf{k}_{//}$, ω) in the scattering matrix, following an approach similar to the method described in Section 2.1.1 in Chapter 2, but adapted to structures with a finite height (Le Vassor d'Yerville 2002; Tikhodeev 2002; Whittaker 1999). From an experimental point of view, these resonances are revealed by the presence of singularities in the reflectivity curves when the system is illuminated from the cladding at variable angles and frequencies (Astratov 2000; Patrini 2002). Anomalous reflection by gratings and its modelling are still being intensively studied in the field of electromagnetism, in particular for narrow-band filtering applications, and these researches are likely to benefit also to the study of photonic crystals. This method provides an access in the band structure of quasi two-dimensional systems, at least for the part which lies in the light cone.

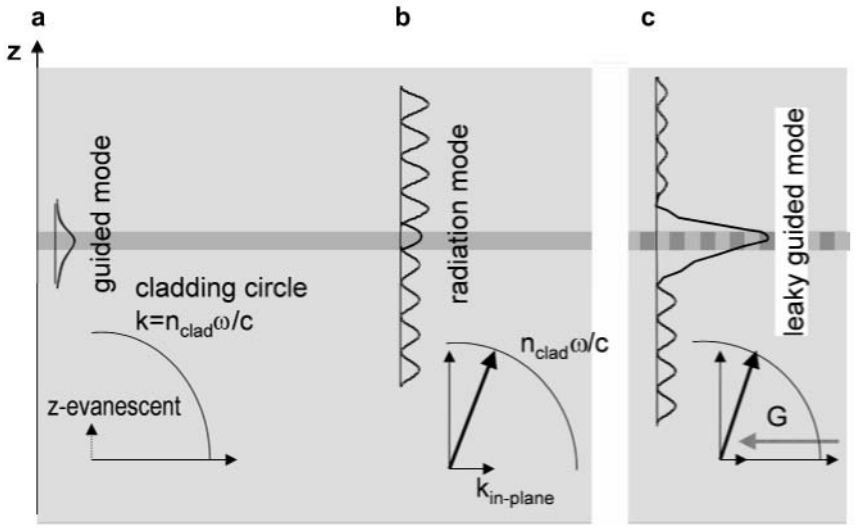

Fig. 5.14. *a.* Uniform waveguide and profile of a guided mode *b.* The same waveguide with the profile of a radiation mode *c.* Corrugated waveguide and profile of a resonant mode. The relevant components of the wave vector in each case are schematically represented below these figures, in particular the in-plane component $k_{//}$. This component is larger than the radius $n_{clad}\omega/c$ for the guided mode represented in *a* and smaller than $n_{clad}\omega/c$ for the pure radiation mode represented in *b*. For the resonant mode represented in *c.* the periodic modulation (G) couples the two types of modes. The resulting hybrid mode presents Fourier components which are related both to the guided and to the radiation cases

5.4.4 Channel Waveguides in Two-Dimensional Photonic Crystals

When a channel waveguide is created by omitting one or several rows of elements in a two-dimensional photonic crystal, defined in a planar waveguide itself, the situation is in most respects the same as in Section 5.4.3. These waveguides will be discussed in more detail in Chapter 9. The essential modification is that consideration must now be given to modes that are confined both laterally by the photonic band gap effect and vertically by an index contrast. Of course, the problem of the confinement of modes propagating at the frequency of the band gap did not occur in the case of a two-dimensional crystal without defects.

In light of the preceding discussion, the guided modes of a channel waveguide created in a two-dimensional photonic crystal can be expected to be either lossless modes or 'resonant' lossy modes. This is a crucial issue in the applications of these waveguides.

It might be appropriate at this point to provide a few indications on the subject of two-dimensional cavities in the context of a vertical index guiding. In the case of a localized mode, defining a wave vector is not of course possible, and the very

concept of light cone is no longer valid. A coupling necessarily occurs between the cavity modes and the radiation modes, which in turn leads to a reduction of their quality factor. Hence, while lossless modes may theoretically exist for waveguides formed from a two-dimensional photonic crystal slab waveguide, the cavity modes created in the same structure will necessarily be leaky. Nevertheless, from an experimental point of view the possibility exists of designing intermediate systems where potentially lossless waveguides and very low loss cavities would be combined. For instance, let us here consider an elongated waveguide closed at both ends. Actually, such a waveguide is but a very elongated cavity. While light may propagate without undergoing any loss along the waveguide, a leakage is bound to occur due to the reflection of light at the closed ends. Whatever the length of the waveguide is, the situation is locally the same at both ends (at least asymptotically, since radiation losses occurring at one end should not be seen at the other). For the sake of analysis, such an elongated cavity can therefore be considered as a cavity with localized losses. This is clearly at variance with the usual analysis of microcavities, where losses are generally considered as a whole.

In this section, we have described in formal terms the physical aspects of systems where a double optical confinement is achieved, i.e. where both a photonic bandgap guiding and an index guiding are involved. These aspects will be of particular importance for applications of these systems. In this respect, a most important problem is that of quantitatively determining the losses of ‘resonant modes’. In view of both the complexity of the underlying electromagnetic problems and the relatively recent development of theoretical tools for their resolution, an exhaustive analysis of this subject would be beyond the scope of this book. Nevertheless, this question will be discussed in the third part of this book in relation to certain specific examples which have now become well-known.

6 Refractive Properties of Photonic Crystals and Metamaterials

Photonic crystals can be used, either as mirrors or as reflective walls in waveguides, at wavelengths corresponding to band gaps. However, the possibility also exists of using them at wavelengths corresponding to their transmission bands, where these structures exhibit very particular refractive and dispersive properties. As has already been seen, the periodic structuring of a material profoundly modifies its optical properties, by generating anisotropy and dispersion effects. In turn, these effects induce dramatic changes in the refractive properties of such material, which will be specifically considered in the present chapter.

In order to correctly analyse the modifications induced on the refractive behaviour of a material, we shall first recall the essential differences between the phase refractive index and the group refractive index. The necessary approximation of the effective refractive index will be also briefly discussed.

6.1 Phase Refractive index, Group Refractive Index and Energy Propagation

6.1.1 Phase Velocity and Group Velocity

The propagation of a monochromatic wave in a linear, isotropic and homogeneous medium can be described by the wave equation (Eqs. 1.6a and 1.7 in Section 1.1.1 of Chapter 1). Monochromatic plane waves are the most elementary solutions to this equation. The real fields associated to such waves have a sinusoidal dependence in both space and time. The propagation speed of these fields is referred to as the 'phase velocity' since this speed is but the displacement speed of a point in space, associated with a given value of the phase.

As an example, let us consider a monochromatic plane wave propagating at frequency $\omega = \omega_0$ along the x axis towards $x = +\infty$. One of the components of the electric or magnetic field can be expressed in the form:

$$U(x) = g_0 \exp(ik_0 x), \quad g_0 \text{ a complex number} \tag{6.1}$$

It should be borne in mind that this equation represents the complex amplitude of the field. The associated time-dependent field can be written in the form:

$$u(x,t) = \mathrm{Re}\{U(x)\exp(-i\omega_0 t)\} = \mathrm{Re}\{g_0 \exp(ik_0 x - i\omega_0 t)\} \tag{6.2}$$

The phase $\varphi(x,t)$ of the field is equal to $k_0 x - \omega_0 t + \arg(g_0)$. The phase velocity can thus be obtained by writing that the phase remains constant, which yields:

$$v_\varphi = dx/dt = \omega_0 / k_0 \tag{6.3}$$

Monochromatic waves, being perfectly periodic in time and space, cannot transmit information. Indeed, such waves fill the whole space from $x = -\infty$ to $x = +\infty$, and they extend from $t = -\infty$ to $t = +\infty$. Since these waves do not actually exist in reality, information has to be introduced through a modulation in the amplitude or the phase of the wave. Conversely, real waves do not have a sinusoidal behaviour in time, and neither are they harmonic. However, the non-harmonic fields considered by practitioners in optics and electromagnetics are in general very close to harmonic fields. As an example, one of the parameters of a femtosecond laser is its frequency, which actually identifies to the central frequency of the light pulse. Such a wave can be easily expressed by summing the harmonic fields given in Eq. 6.2 over a small range of frequencies:

$$u(x,t) = \mathrm{Re}\left\{\int_{-\infty}^{\infty} g(k)\exp\left(ik_0 x - i\omega(k)t\right)dk\right\} \tag{6.4}$$

The right-hand members of Eqs. 6.3 and 6.4 obviously tend toward each other when $g(k) = g_0\delta(k - k_0)$. A simple method for representing a non-harmonic field close to the one expressed in Eq. 6.2 consists therefore in introducing in the right-hand member of Eq. 6.4 a real function $g(k)$ which tends rapidly towards zero as $|k - k_0|$ is increased. In other words, $g(k)$ must be a real function centred at $k = k_0$, with a half width δk satisfying $\delta k << k_0$. A typical example of such a function is given by the real Gaussian function $\exp[-(k - k_0)^2/\delta k^2]$. The associated time-dependent field is nothing other than a wave packet, i.e. a group of waves with a k-distribution centred at k_0. In the simple case of a non-dispersive medium, the equation $\omega(k)/k = \omega_0/k_0$ is verified for any ω. Hence,

$$\begin{aligned} u(x,t) &= \mathrm{Re}\left\{\int_{-\infty}^{\infty} g(k)\exp\left(ik\left(x - \frac{\omega_0}{k_0}t\right)\right)dk\right\} \\ &= \mathrm{Re}\left\{\hat{g}\left(x - \frac{\omega_0}{k_0}t\right)\right\} \end{aligned} \tag{6.5}$$

where $\hat{g}$ is the Fourier transform of g:

$$\hat{g}(x) = \int_{-\infty}^{\infty} g(k) \exp(ikx) dk \tag{6.6}$$

Since $g(k)$ is a real function centred at $k = k_0$ symmetrical with respect to $k = k_0$, which tends rapidly toward zero as $|k - k_0|$ increases, it is straightforward to show from elementary rules on Fourier transforms that $\hat{g}(x)$ can be expressed in the form:

$$\hat{g}(x) = \exp(ik_0 x)\hat{\gamma}(x) \tag{6.7}$$

where $\hat{\gamma}(x)$ is the Fourier transform of $g(k - k_0)$, i.e. the function deduced from $g(k)$ by a translation along the x axis and centred at the origin:

$$\hat{\gamma}(x) = \int_{-\infty}^{\infty} g(k - k_0) \exp(ikx) dk \tag{6.8}$$

Function $\hat{\gamma}(x)$ is real and centred at the origin. It tends toward zero for $k \to \pm\infty$ and has a very large half-width with respect to $\lambda_0 = 2\pi/k_0$. It can be readily verified that the Gaussian function satisfies these properties, since its Fourier transform has a half-width $2/\delta k >> \lambda_0/\pi$. Eqs. 6.5 and 6.7 thus yield:

$$u(x,t) = \mathrm{Re}\left\{ \exp\left[ik_0\left(x - \frac{\omega_0}{k_0} t \right)\right] \hat{\gamma}\left(x - \frac{\omega_0}{k_0} t \right)\right\} \tag{6.9}$$

The field is therefore a wave packet propagating along the x axis with a phase velocity equal to ω_0/k_0 due to the phase term $\exp\left[ik_0\left(x - \frac{\omega_0}{k_0} t \right)\right]$, and a group velocity equal to ω_0/k_0 and associated to the real part of $\hat{\gamma}\left(x - \frac{\omega_0}{k_0} t \right)$:

$$\mathrm{v}_g = \mathrm{v}_\varphi = \omega_0 / k_0 \tag{6.10}$$

Thus, in a non-dispersive medium, both the group and phase velocities identify to the phase velocity of the plane wave at frequency ω_0.

In a dispersive medium, the phase and group velocities are derived from Eq. 6.4 by recalling that $g(k)$ is a function centred at $|k - k_0|$ which rapidly tends toward

zero as $|k - k_0|$ increases. Accordingly, $\omega(k)$ can be expanded at the first order around $k = k_0$:

$$\omega = \omega_0 + (k - k_0)\left(\frac{\partial\omega}{\partial k}\right)_{k=k_0} \tag{6.11}$$

Introducing this expression in Eq. 6.4 yields:

$$u(x,t) \approx \mathrm{Re}\left\{\exp(ik_0x - i\omega_0 t)\hat{\gamma}\left(x - \left(\frac{\partial\omega}{\partial k}\right)_{k=k_0} \times t\right)\right\} \tag{6.12}$$

Thus, while the phase velocity is still $v_\varphi = \omega_0/k_0$, the wave packet (i.e. the signal and the energy) propagates at the group velocity defined by:

$$v_g = \left(\frac{\partial\omega}{\partial k}\right)_{k=k_0} \tag{6.13}$$

The analytical expressions for v_g and v_φ can actually be extended to the whole k-space without referring to any specific value for k (in this case $k = k_0$). The group velocity $v_g = \partial\omega/\partial k$ can therefore be expressed in terms of the phase velocity $v_\varphi = \omega/k$, as follows:

$$v_g = \partial\omega/\partial k = \partial(v_\varphi k)/\partial k = v_\varphi + k\,\partial v_\varphi/\partial k. \tag{6.14}$$

Introducing $\lambda = 2\pi/k$ then leads to Rayleigh's equation:

$$v_g = v_\varphi - \lambda\frac{\partial v_\varphi}{\partial\lambda} \tag{6.15}$$

In a medium with reasonably low dispersion, the wave packet travels as a whole, without undergoing any significant 'diffusion' nor spreading. Under these conditions, the group velocity describing the propagation speed of the wave packet also represents the speed at which energy propagates (Born 1965). As can be seen from Eq. 6.15, the group velocity can be either positive or negative, while its modulus can be either larger or smaller than the phase velocity. The notion of negative group velocity is not an abstraction. This phenomenon is exploited for instance in vacuum tubes known as 'carcinotrons' or as backward wave tubes, used for the generation of millimeter electromagnetic waves.

Nevertheless, certain situations exist where the group velocity does not correctly describe the propagation of energy. This is the case for instance near strong absorption peaks in media with a strong anomalous dispersion. In such cases, the Poynting vector should be used instead of the group velocity vector. The notion of 'ray velocity' which derives from the Poynting vector is sometimes used when studying the optical properties of anisotropic crystals (Born 1965).

6.1.2 Refractive Indexes and Dispersion Diagrams

The phase and group refractive indexes can be deduced from the phase and group velocities respectively by using the following simple equations:

$$n_\varphi = c / \mathrm{v}_\varphi \tag{6.16}$$

$$n_g = c / \mathrm{v}_g \quad \approx \quad n_\varphi - \lambda \frac{\partial n_\varphi}{\partial \lambda}$$

Since the dispersion diagrams (band structures) yield the relations $\omega(\mathbf{k})$ in the different directions of propagation in the crystal, the phase and group refractive indexes can be quite readily obtained from these diagrams using Eqs. 6.1, 6.13 and 6.16. Fig. 6.1 illustrates graphically how the phase and group velocities can be deduced from the dispersion diagrams. For a wave packet with frequency ω propagating along a given direction, one or more solutions for k may exist depending on the shape of the dispersion curves. The phase velocity is defined as the ratio ω / k at the corresponding points of the dispersion diagram (Fig. 6.1, *left*). The group velocity is deduced from the slope of the curve at the same points (Fig. 6.1, *right*). Depending on the exact location of the points in the dispersion curve, one may find different values, either positive or negative, for the group velocity.

Actually, the simple construction presented in Fig. 6.1 is valid only for one-dimensional crystals and for a direction of propagation perpendicular to the layers of the crystal. In the more general case of two- and three-dimensional photonic crystals, the phase and group velocities become vectors. While the phase velocity $\mathbf{v}_\varphi = \omega_0 \mathbf{k}_0 / |\mathbf{k}_0|^2$ still has a modulus $\omega_0 / |\mathbf{k}_0|$, there is no reason for the group velocity of the wave packet centred at ω_0 and $\mathbf{k}_0$ to necessarily lie in the same plane as the phase velocity. In such a case, the algebraic formulation given by Eq. 6.13 for the group velocity should be replaced by the following vector equation:

$$\mathbf{v}_g = \nabla_{\mathbf{k}=\mathbf{k}_0} \left(\omega(\mathbf{k}) \right) \tag{6.17}$$

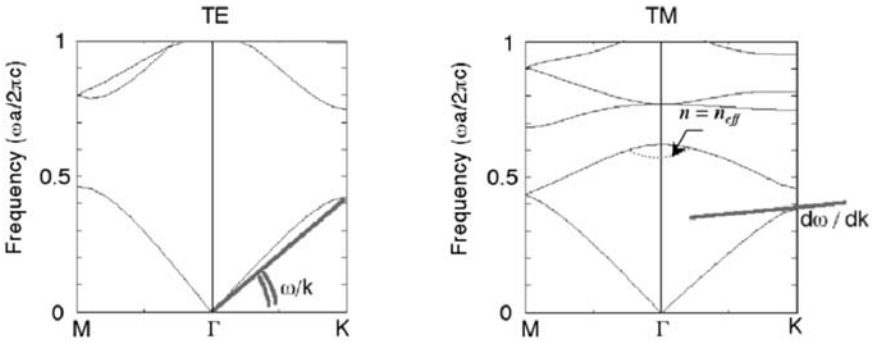

Fig. 6.1. Dispersion curves of a two-dimensional photonic crystal and graphical representations of the phase and group velocities. At the apex of the second photonic transmission band, indicated by the point Γ in the right-hand side of the figure, the isofrequency curve tends towards a circular shape, with the consequence that a negative refractive index can be assigned to the photonic crystal

The group velocity is therefore defined by the normal to the isofrequency surface ($\omega(\mathbf{k}) = \omega_0$) at point ($k_x$, k_y, k_z). The expression for the group refractive index is the same as in Eq. 6.9, with the provision, however, that v_φ, v_g, n_φ and n_g now stand for the modulus of $\mathbf{v}_\varphi$, $\mathbf{v}_g$, n_φ and n_g respectively. The sign of v_g, and hence of n_g, will be positive or negative depending on whether $\mathbf{v}_g$ is directed toward the exterior or the interior of the isofrequency contour respectively. It can easily be seen that the anisotropy of the photonic crystal frequently imposes different directions for the group and phase velocities. We shall comment later on this point in Section 6.2.2.

6.1.3 Effective Phase Index and Group Refractive Index

In light of the preceding discussion of the anisotropy of two and three-dimensional photonic crystals, the question may arise whether the notion of effective refractive index should be retained for describing these structures. In the long wavelength region, i.e. at low frequencies, the approximation of the crystal as a homogeneous material does not create any particular difficulty. Mathematicians have indeed developed homogenization techniques based on limit analysis (see Section 2.4 in Chapter 2). In this approach, the effective refractive index is an asymptotic notion, which becomes rigorous for wavelengths infinitely long with respect to the size of the elementary cell of the crystal (Felbacq 1997). Analytical formulas exist for describing such a situation (Bao 2000).

For wavelengths of an order comparable to the period of the structure, the situation becomes more complex. Nevertheless, numerical simulations of the propagation of the field as well as experimental evidence have revealed that, under certain

conditions, a periodic or a quasi-periodic structure may behave like a bulk homogeneous material, except at the interfaces of the structure at which scattering effects may always occur. In particular, these conditions are approached for a two-dimensional (respectively three-dimensional) photonic crystal when the isofrequency curve or surface tends towards a circle or a sphere respectively. This occurs, for instance, at frequencies near the Γ point in the conduction band of a hexagonal photonic crystal (Fig. 6.1, *right*). Under these circumstances, it seems that we are entitled to define an effective refractive index, even though its mathematical justification has not been clearly established yet. If the group velocity is negative (negative slope in the right-hand part of Fig. 6.1), then the effective refractive index will be negative as well (Gralak 2000). Assigning an effective refractive index to the photonic crystal simplifies the description of the propagation of waves in such a structure.

6.2 Refraction of Waves at the Interface between a Periodic Medium and a Homogeneous Medium

6.2.1 Summary of Refraction Laws in Homogeneous Media

As has been emphasized already in Section 6.1, and leaving aside some very specific cases that will not be addressed here, the direction of propagation of a light beam in any medium is defined by the group velocity vector. This direction is indeed the same as the direction of the Poynting vector ($\sim \mathbf{E} \times \mathbf{H}$), or the time averaged energy flux. In a homogeneous isotropic medium, the group velocity vector is collinear with the wave vector. Assuming the medium to be non-dispersive, which amounts to considering a spectral region sufficiently distant from the resonances and to restricting ourselves to a relatively narrow spectral range, the phase and group refractive indexes are also identical. We may therefore adopt the simple account given by geometrical optics of this phenomenon, where the propagation of the electromagnetic energy is represented by light rays associated to the wave vectors **k** and propagating in a medium with a unique index n. The transition from a homogeneous medium with index n_1 to a second medium with index n_2 depends on the incident angle of the ray with respect to the interface. The excitation of the transmitted wave entails that the component of the wave vector parallel to the interface will be conserved during transition at the interface. In other terms, the projections of the incident and transmitted wave vectors onto the plane of the interface are equal. The latter condition leads to the formulation of Snell's law $n_1 \sin\theta_1 = n_2 \sin\theta_2$. The refracted ray can also be determined using Ewald spheres, as can be seen in Fig. 6.2 (*upper right*). For each of the media represented in this figure, the isofrequency curve is a circle with a radius defined by the absolute value of the wave vector in the medium ($n\omega/c$).

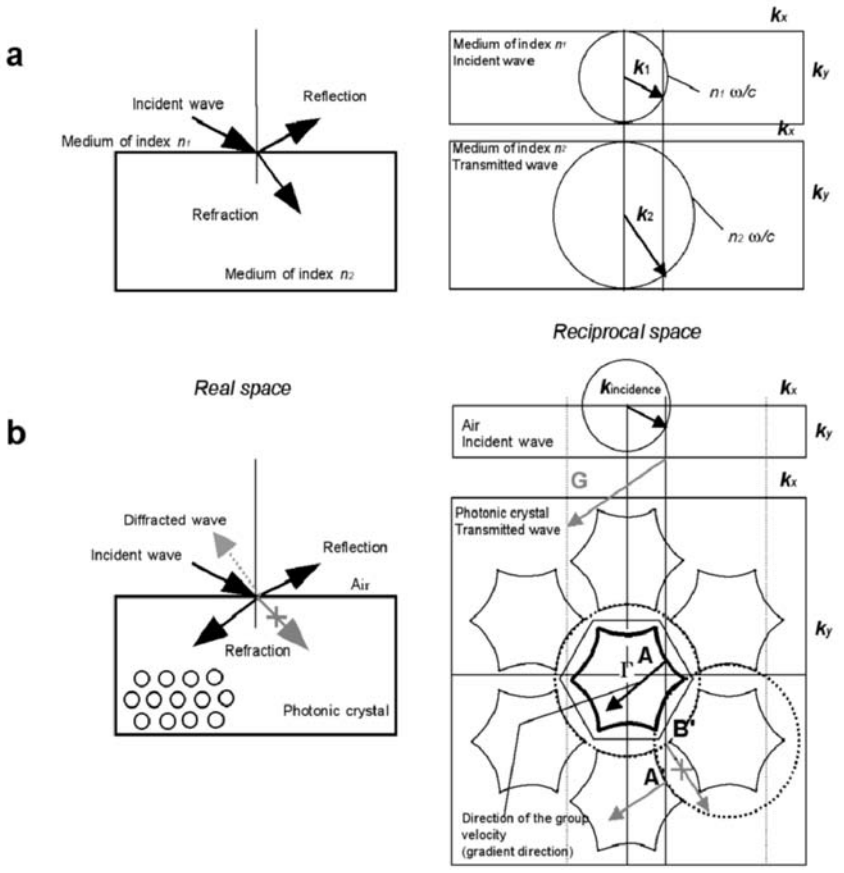

Fig. 6.2. *a.* Refraction at the interface between two homogeneous media with positive effective refractive indexes *b.* Refraction at the interface between the air and a two-dimensional photonic crystal with a hexagonal symmetry. It is assumed here that the photonic crystal has a negative effective refractive index. The left-hand figures show the trajectories of the light rays in the real space, while the right-hand figures represent the construction of the transmitted wave vectors in the reciprocal space. In the latter figures, the isofrequency curves can be seen to be circles (Ewald circles) in case *a* and to assume a more complex shape with a hexagonal symmetry in case *b*. The crossed arrows indicate the trajectories of the ordinary refracted rays that are being suppressed due to the presence of a photonic gap, as described in Section 6.2.3. Note in the bottom right figure that the vertical line passing through point A has a second intersection point with the isofrequency dispersion curve (*bold curve*). The choice of point A is imposed by the fact that the group velocity must be directed towards the lower hemisphere due to causality

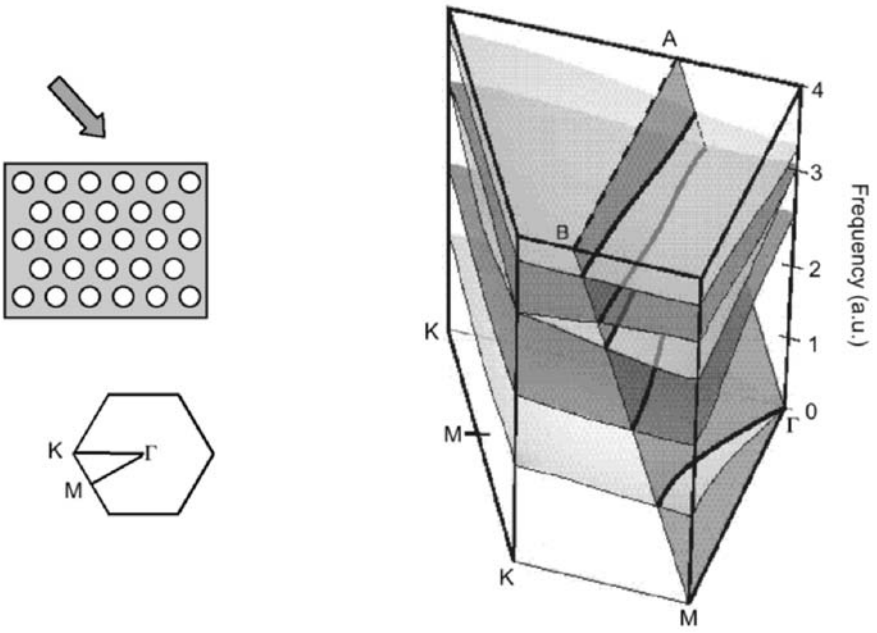

Fig. 6.3. *Right.* Three-dimensional representation of the band diagram of a two-dimensional photonic crystal with a hexagonal symmetry. The horizontal axes correspond to the ΓK and ΓM directions respectively, while the vertical axis corresponds to the frequency ω. *Left.* Photonic crystal with a finite size illuminated from the air. The interface of the crystal is parallel to the ΓK direction. The transmitted wave vector(s) is or are obtained from the intersections of the dispersion surfaces with a plane $\omega/k_{\Gamma K}$= constant

6.2.2 Some Well-Known Anisotropic Media: Birefringent Solid-State Crystals

The phenomenon of refraction is substantially modified as soon as one of the media on either side of the interface is anisotropic. Two and three-dimensional photonic crystals are by construction anisotropic, but a number of solid state crystals that are both transparent and anisotropic also exist in nature. The optical anisotropy of these crystals manifests itself in the form of a birefringence, which merely expresses the dependence of the refractive index on the direction of propagation and on the polarization of light. The fundamental principles of the optics of anisotropic crystals were established by A. Fresnel in 1820, long before the development of the electromagnetic theory. The reader will find a more detailed introduction to the optical properties of anisotropic crystals in the reference works (Born 1965; Landau 1969). In general, the angular dependence of the phase refractive index in such solid state crystals can be described by an index ellipsoid, which

allows an analytical formulation for the refraction of light in birefringent crystals. Compared to solid state crystals, photonic crystals present dispersion curves with a much more complex shape, as can be seen in Fig. 6.3. The spatial profiles of the index n (k_x, k_y, k_z) at a given frequency in the reciprocal space, or in other terms, the isofrequency curves or surfaces (Notomi 2000a) are therefore very far from being ellipsoidal.

In the two-dimensional case represented in Fig. 6.3, the isofrequency profiles are obtained by horizontally cutting the dispersion surfaces separately calculated by means of a plane wave model. Fig. 6.2 (*lower right*) presents an idealized example of an isofrequency curve for the same two-dimensional triangular crystal with hexagonal symmetry. The value selected for the frequency is slightly higher than the frequency of the fundamental band gap. The group velocity vector is directed here towards the interior of the contour, which corresponds to a negative group refractive index. The isofrequency surfaces of photonic crystals are actually a direct analogue to Fermi surfaces for solid state crystals (Kittel 1971).

6.2.3 Construction of the Waves Transmitted in a Photonic Crystal

Both the phase and the group velocities, or equivalently the phase and group refractive indexes, are involved in the refraction of a ray at an interface between a homogeneous medium and a photonic crystal. The relation between the phase refractive indexes of the two media determines the transition at the interface (conservation of the component of the wave vectors parallel to the interface), while the group velocity determines the subsequent propagation of the beam and that of the electromagnetic energy in the crystal.

Fig. 6.2 (*lower right*) shows how the wave(s) transmitted inside a photonic crystal with a triangular symmetry can be constructed for an incident wave arriving from a homogeneous medium. The vertical line which passes through the extremity of the incident wave vector corresponds to the component k_x that will be conserved in this case. Each intersection of this line with the star-shaped isofrequency curve defines the extremity of a Bloch vector of the field transmitted in the crystal, or coupled with it. The periodicity of photonic crystals implies that multiple intersections are possible. Due to causality, we need to consider only transmitted waves whose group velocity vector is directed towards the lower hemisphere, i.e. towards the interior of the photonic crystal. However, there also exist reflected waves that will be redirected back into the homogeneous medium, as can be seen in Fig. 6.2.

In the case under consideration, only one direction of propagation is allowed in the crystal (intersection point *A*). The group velocity vector, normal to the isofrequency curve, is directed towards the interior of the curve, with the consequence that the crystal seems to behave like a material with a negative refractive index. It might be noted that using the same geometrical parameters but with an infinitely small index contrast, the isofrequency curves tend towards a circular shape, as can be seen in Fig. 6.2. At certain frequencies, the vertical straight line can be seen to intersect twice the isofrequency curves (intersection points A' and B), which cor-

responds to the existence of two transmitted waves. The conclusion must therefore be drawn that the increase in the index contrast and the subsequent appearance of the band gap prevents 'ordinary' refraction from occurring (Notomi 2000a).

Let us now consider frequencies in the second transmission band (see the band diagram represented in Fig. 6.1). The representative points (ω, k) will now be located in the vicinity of the point Γ of the Brillouin zone. If a high index contrast exists, the shapes of the isofrequency curves will tend towards circles with, however, a smaller radius than was previously the case. The photonic crystal thus behaves like a homogeneous medium with an 'average' refractive index. This 'average' refractive index can be negative, provided that the normals to the dispersion curves are directed towards the negative part of the frequency axis (Section 6.1.3 in this chapter).

6.3 Superprism and Negative Refraction Effects

6.3.1 Superprism Effect

The strong chromatic dispersion of photonic crystals was first demonstrated by SY Lin *et al* (Lin 1996) in experiments where a 20% variation of the effective (isotropic) refractive index was obtained for a relative change in frequency equal to 30%. These first results were followed by a series of theoretical and experimental studies (Enoch 1999; Gralak 2000; Kosaka 1998, 1999; Notomi 2000a; Wu 2002). In particular, H. Kosaka *et al* have reported a spectacular superprism effect with an angular deviation of 50° for a relative variation of the wavelength equal to 1%, which indicates that an angular dispersion equal to 5°/nm has been achieved, as can be seen in Fig. 6.4. Unlike the first experiments performed by SY Lin *et al*, the experiments conducted by H. Kosaka *et al* are based on exploitation of both the anisotropy of the crystal and negative refraction index effects. Experimental conditions were chosen in such a way as to exploit the isofrequency surfaces in the regions where deformation is the most intense (the branches of the stars in Fig. 6.2). As a consequence, even a slight variation in the wavelength was sufficient to induce dramatic changes in the direction of the group velocity. The superprisms used in these experiments consisted of photonic crystals with a triangular symmetry, and fabricated with the autocloning method. The fabrication of these crystals will be described in more detail in Chapter 12, devoted to three-dimensional photonic crystals (see Fig. 12.11).

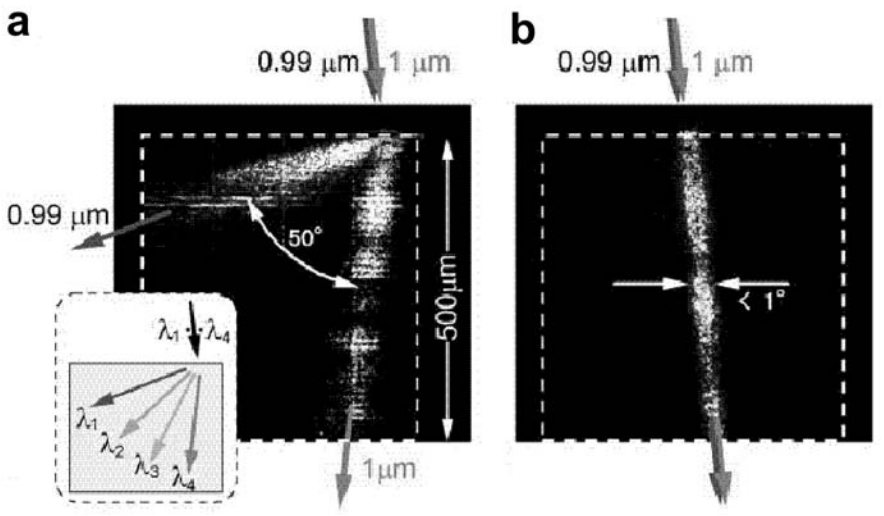

Fig. 6.4. Photographs showing the trajectories followed by light rays. *a.* In a photonic crystal *b.* In a silica layer. Two incident laser beams at two different wavelengths equal to 0.99 and 1.0 μm respectively were used in these experiments (Kosaka 1999). The TM polarized laser beams become visible due to the light scattering which occurs outside the plane of the crystal or of the silica layer. The two-dimensional crystal has a triangular symmetry and its lateral dimensions are $500 \times 500\ \mu m^2$. The edge of the crystal is oriented along the ΓK direction. The incidence angle with respect to facet of the crystal is equal to 15°

6.3.2 Ultra-Refraction and Negative Refraction

Ultra- and negative refraction effects are not fundamentally different from superprism effects, in the sense that all these phenomena are ultimately related to the dispersion properties of photonic crystals. The term 'ultra-refraction' specifically refers to the situation where an effective refractive index less than unity can be assigned to the photonic crystal, whereas the term 'negative refraction' is used when the crystal is assigned a negative index. In such cases, the photonic crystal is assumed to behave as an isotropic dielectric medium, in which refraction can be described by Snell's law. A typical situation is that of a two-dimensional crystal for frequencies within the second transmission band and near the centre Γ of the Brillouin zone. In this case, the shape of the isofrequency curve is very close to a circle. Likewise, for a three-dimensional crystal, the isofrequency curve would be close to a sphere. It has also been numerically demonstrated that a negative refractive index could be obtained in all directions at frequencies corresponding to the fundamental transmission band near the extremity of the Brillouin zone rather than at its centre (Luo 2002).

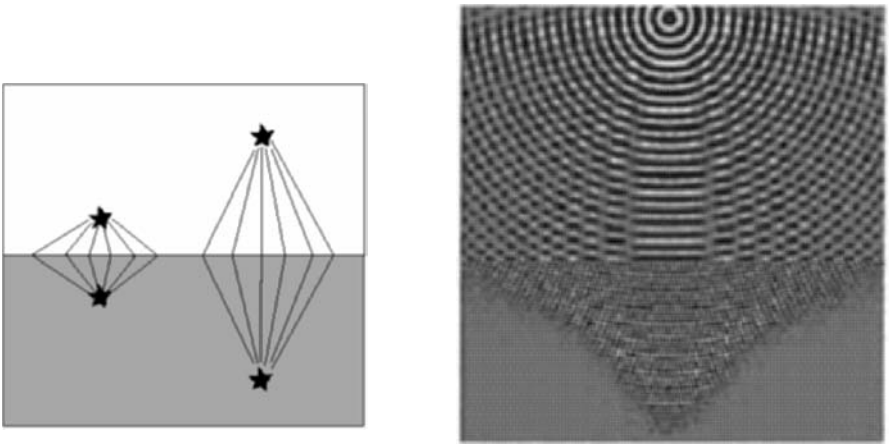

Fig. 6.5. *Left.* Schematic construction of the light rays refracted by a photonic crystal with a negative effective index (in this example, $n_{eff} = -1$). The surface of the crystal behaves like a mirror lens. *Right.* Numerical simulation of the distribution of the field in an ultra-refractive photonic crystal illuminated by an external point source (Notomi 2000a)

An analogy can be drawn between the effective index of photonic crystals and the effective mass of charge carriers in semiconductors. In semiconductors, the electronic states associated with negative effective masses are simply the empty states of the valence band. The existence of effective masses with opposite signs merely reflects the difference in the curvature of the electronic band on the two opposite sides of the gap (Kittel 1971).

The phenomenon of 'negative refraction' is schematically illustrated in the left-hand part of Fig. 6.5, while the right-hand part of this figure represents the corresponding field distribution in the crystal when the latter is illuminated by an external point source (Notomi 2000a).

It can be observed that a material with a negative refractive index can focus light beams in a very specific fashion, and that it actually behaves like a 'slab lens' or like a 'mirror lens'. While a conventional lens possesses a focal plane and produces images in a two-dimensional plane at a short distance from its focal plane, a negative refractive index lens produces three-dimensional images through a spatial inversion process similar to that of a mirror: $(x, y, z) \rightarrow (x, y, -\beta z)$, where $\beta = |n_{eff}/n_0|$. The lens thus realized has no principal axis, but exhibits on the contrary a translational symmetry in the plane of the interface.

6.4 Metamaterials

The approach to negative refraction described in the above is essentially based on the periodicity of dielectric structures. However, a different approach has been developed towards this phenomenon. This approach is based on the concept of a metamaterial, and it finds its origin in a series of experiments conducted on artificial dielectrics during the 1950s and 1960s. These experiments demonstrated that a composite material may exhibit a very different electromagnetic response from those of 'natural' materials used in its composition. However, most of these results remained confined to the radar science community, without reaching at this time a wider audience.

The concept of a metamaterial is that of a composite material created by combining different types of structures or materials, including metals, and allowing the simultaneous control of both the effective permittivity ε_{eff} and the effective permeability μ_{eff} for addressing specific requirements of certain applications. As regards more specifically negative diffraction, the aim is to create a metamaterial, possibly periodic, that would exhibit a negative refractive index at frequencies much lower than the frequencies of the band gap.

It should be emphasized at this point that the full electromagnetic description of refraction at a plane interface between two materials cannot be achieved from the knowledge of the index alone. As will be seen in Sections 6.4.2, 6.4.3 and 6.4.4, calculating the reflected and transmitted fields from Maxwell's equations is actually essential for a comprehensive analysis of the 'perfect lens' based on negative-refraction metamaterials.

Maxwell's equations (Eqs. 1.2 to 5) were given in Chapter 1 for non-magnetic materials, in which relative permittivity is the only electromagnetic parameter. In general, whilst the constituents of a metamaterial are non-magnetic, the effective relative permeability of such a metamaterial can be very different from one. Maxwell's equations must therefore explicitly account for both the dielectric permittivity and the magnetic permeability if we are to study the properties of reflection and transmission at the boundary between the metamaterial, considered as a homogeneous medium, and a background medium. This leads to a new set of Maxwell's equations, where $\mathbf{H}$ in Eqs. 1.2 and 1.5 is replaced by $\mu_r\mathbf{H}$, while Eqs. 1.3 and 1.4 remain unchanged. Similarly, the determination of the electromagnetic properties of a metamaterial placed in an external medium requires knowledge of ε and μ instead of just $n = (\varepsilon\mu)^{1/2}$.

6.4.1 Simultaneous Control of the Dielectric Permittivity and the Magnetic Permeability

Transparent materials of the most usual types typically present positive values for the dielectric permittivity ε and for the magnetic permeability μ. However, certain materials can also be found where either ε or μ is negative, although these two conditions are never simultaneously satisfied in a given material. For instance, a

neutral non-collisional plasma presents a negative permittivity at frequencies lower than the plasma oscillation frequency. Likewise, certain metals and semiconductors may exhibit the same type of response under specific conditions and for a limited range of frequencies. As has been described in Section 4.1 of Chapter 4, the condition $\varepsilon < 0$ necessarily entails that the material is opaque and reflective, at least in the case where μ remains positive.

If magnetic charges, i.e. Dirac's monopoles existed, then a gas formed from such charges would present a magnetic permeability similar to the dielectric permittivity $\mu = \mu_0(1 - \omega_m^2/\omega^2)$ of the plasma mentioned above. However, since magnetic charges do not exist in nature, only antiferromagnetic systems may exhibit a negative permeability $\mu < 0$ at frequencies near the resonances. However, these materials are also strongly anisotropic.

V. Veselago was probably the first author to consider in 1964 the possibility of creating an artificial material with negative values for both ε and μ (Veselago 1964, 1968). After theoretically investigating the properties of such materials using Maxwell's equations, he concluded that the refractive index of such a material would be negative and that it would present very unusual optical properties. Thus, the sign of the Doppler effect would be reversed, so that the apparent frequency of a source approaching from a detector would actually be lower than the frequency measured for the same source when it propagates away from this detector. Likewise, the Vavilov-Cherenkov effect would be reversed in such a material. The electromagnetic wave emitted by a charged particle propagating at the speed $v > c/n$ in a medium with negative refractive index would propagate along a direction opposite to the direction of the movement of this particle. Finally, the optical law of refraction would be modified much in the same way as they are for photonic crystals with a negative refractive index, or with a 'negative photonic mass' (Fig. 6.5). As has already been mentioned in Section 6.3.2, a plane layer formed by a negative-refraction material would act as a lens. The complete electromagnetic description of reflection and transmission phenomena between the air and a negative-refraction metamaterial actually reveals an even more surprising imaging effect in the case where both the relative permittivity ε_r and the relative permeability μ_r are equal to -1. From a theoretical point of view at least (see Section 6.4.2), a lens satisfying these conditions would be perfect, stigmatic, and would concentrate all the energy emitted by the point source onto the point image.

For a monochromatic plane wave propagating in a medium characterized by its average permittivity and permeability, the two following equations are valid:

$$\mathbf{k} \times \mathbf{E} = \frac{\omega}{c} \mu \mathbf{H} \tag{6.18}$$

$$\mathbf{k} \times \mathbf{H} = -\frac{\omega}{c} \varepsilon \mathbf{E} \tag{6.19}$$

It can be seen from these equations that vectors **E**, **H** and **k** form a right-handed basis if $\varepsilon > 0$ and $\mu > 0$. This basis becomes left-handed in the case where $\varepsilon < 0$ and $\mu < 0$ simultaneously hold. For this reason, materials with this property are often referred to as 'left-handed materials' (LHM). In order to avoid confusion with chiral materials, where left-handed as well as right-handed helical structures exist, other terms have been suggested for use, including those of negative refractive material, negative index material, backward medium, double negative medium, negative phase velocity medium, etc. All these different terms point to the fact that the direction of the wave vector **k** is opposed to the direction of the energy flux, or Poynting vector, $\mathbf{S} \sim \mathbf{E} \times \mathbf{H}$.

It should be noted that values for ε and μ can be simultaneously negative only in the presence of dispersion. Indeed, in the absence of dispersion phenomena, the total energy of the electromagnetic field in this medium is:

$$W = \varepsilon E^2 + \mu H^2 \tag{6.20}$$

The total energy would therefore always be negative. In the presence of dispersion, the electromagnetic energy satisfies the following equation (Veselago 1968):

$$W = \frac{\partial(\varepsilon\omega)}{\partial\omega} E^2 + \frac{\partial(\mu\omega)}{\partial\omega} H^2 \tag{6.21}$$

For the energy to be positive, the following conditions must be fulfilled:

$$\frac{\partial(\varepsilon\omega)}{\partial\omega} > 0 \quad \text{and} \quad \frac{\partial(\mu\omega)}{\partial\omega} > 0 \tag{6.22}$$

Thus, only in a limited frequency range can the desired properties, i.e. $\varepsilon < 0$ and $\mu < 0$, actually be created.

6.4.2 Negative Refraction in a Slab of Perfect Left-Handed Material

Let us consider a slab of a left-handed material with a relative permittivity and a relative permeability equal to –1 at frequency ω. This material will be referred to as a 'perfect left-handed' (PLH) material in the following. The slab has a width equal to e, and is illuminated at an angle of incidence θ by an *s*-polarized plane wave with unit amplitude and wavelength $\lambda_0 = 2\pi/k_0$. Using a Cartesian coordinate system *xyz*, the incident and total electric field are assumed to be parallel to the *z* axis, while the upper interface extends along the *xz* plane, as represented in Fig. 6.6.

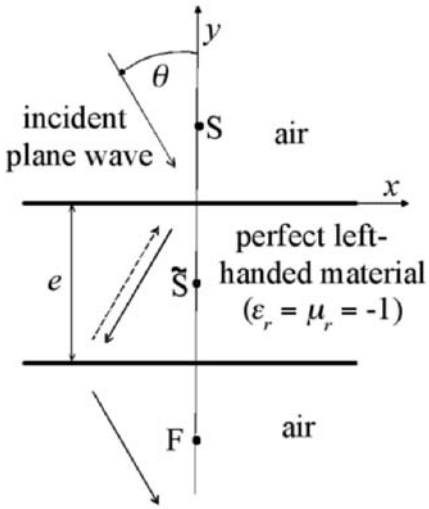

Fig. 6.6. Negative refraction and perfect lens using a slab of perfect left-handed material

Defining $\alpha = k_0 \sin(\theta)$ and $\beta(\alpha) = \sqrt{k_0^2 - \alpha^2} = k_0 \cos(\theta)$, the projection E^i of the incident electric field onto the z axis can be expressed in the form:

$$E^i = \exp\left(i\alpha x - i\beta(\alpha) y\right) \tag{6.23}$$

As has been seen in Chapter 2, due to invariance by translation along the x axis of the slab, the independence with respect to x of $E^i(x, y)\ \exp(-i\alpha x)$ implies that function $E(x,y)\exp\left(-i\alpha x\right)$, where E is the z-component of the total field, is independent on x as well. The total field can therefore be written as follows:

$$E(x,y) = \exp\left(i\alpha x\right)\tilde{E}(y) \tag{6.24}$$

Further, bearing in mind that the product of the relative permittivity by the relative permeability is equal to 1 in all three regions of space, the total field in each region satisfies Helmholtz equation $\nabla^2 E + k_0^2 E = 0$. Introducing the right-hand member of Eq. 6.24 in Helmholtz equation shows that, in each of these three regions, $\tilde{E}(y)$ is a linear combination of an $\exp(-i\beta(\alpha)y)$ term propagating downward and of an $\exp(i\beta(\alpha)y)$ term propagating upward. In the upper region, the $\exp(-i\beta(\alpha)y)$ term corresponds to the incident wave and has a unit amplitude, while in the lower region, the $\exp(i\beta(\alpha)y)$ term vanishes due to the radiation condition, since it would otherwise correspond to an incident wave propagating from

the bottom side of the device. The field in each of the three regions can therefore be expressed by the equations:

$$\text{if } y > 0,\ \ E = \exp\left(i\alpha x - i\beta(\alpha)y\right) + r(\alpha)\exp\left(i\alpha x + i\beta(\alpha)y\right) \tag{6.25}$$

$$\text{if } -e < y < 0,\ \ E = a(\alpha)\exp\left(i\alpha x - i\beta(\alpha)y\right) + b(\alpha)\exp\left(i\alpha x + i\beta(\alpha)y\right) \tag{6.26}$$

$$\text{if } y < -e,\ \ E = t(\alpha)\exp\left(i\alpha x - i\beta(\alpha)y\right) \tag{6.27}$$

In order to calculate the $a(\alpha)$, $b(\alpha)$, $r(\alpha)$ and $t(\alpha)$ coefficients, we need to express the boundary conditions at each of the two interfaces of the slab. From the continuity of E at each interface, it turns out that:

$$1 + r(\alpha) = a(\alpha) + b(\alpha) \tag{6.28}$$

$$a(\alpha)\exp(i\beta(\alpha)e) + b(\alpha)\exp(-i\beta(\alpha)e) = t(\alpha)\exp(i\beta(\alpha)e) \tag{6.29}$$

From Maxwell's equations, the continuity of the tangential x-component of the magnetic field reduces to the continuity of $\frac{1}{\mu_r}\frac{\partial E}{\partial y}$. Hence:

$$-1 + r(\alpha) = -(-a(\alpha) + b(\alpha)) = a(\alpha) - b(\alpha) \tag{6.30}$$

$$\begin{aligned} -a(\alpha)\exp(i\beta(\alpha)e) + b(\alpha)\exp(-i\beta(\alpha)e) = \\ -(-t(\alpha)\exp(i\beta(\alpha)e)) = t(\alpha)\exp(i\beta(\alpha)e) \end{aligned} \tag{6.31}$$

Straightforward calculations allow us to deduce from Eqs. 6.28 to 6.31 that:

$$r(\alpha) = a(\alpha) = 0, \quad b(\alpha) = 1, \quad t(\alpha) = \exp(-2i\beta(\alpha)e) \tag{6.32}$$

It thus turns out that the reflected wave has zero amplitude. Further, since $a(\alpha) = 0$, the field inside the slab (represented in Fig. 6.6 by a dashed vector) propagates toward the upper interface. This property may seem unphysical at first glance, since the field propagating upward in the slab results from the reflection at the lower interface of the field propagating downward. However, it should be recalled that, for a monochromatic plane wave propagating in a left-handed material, vectors **k, E**, **H** obey the left-hand rule. This property entails the strong consequence that the energy inside the slab, hence the group velocity, is directed downwards (solid vector in Fig. 6.6), which satisfies causality. Fig. 6.6 clearly shows the phenomenon of negative refraction, and explains why Snell's law still holds true in the case of a PLH material with a refractive index equal to -1.

6.4.3 Stigmatism of a Slab of Perfect Left-Handed Material

It has been shown in Section 6.3.2 that a slab of photonic crystal with index equal to -1 can be used as a lens. However, not only did the demonstration rely on the notion of ray, but we were unable to evaluate the intensity ratio between the image and the object. The case of a slab of PLH material (PLHM) will provide us with the opportunity to calculate precisely all features of the imaging process.

We shall consider here the field emitted by the point source S of ordinate y_S located above the slab, as described in Fig. 6.6. In order to preserve the two-dimensional character of the problem, we assume the monochromatic light to be emitted from a luminous wire parallel to the z axis. The field radiated by the source at a point M located above the slab can be expressed in the form of a sum of plane waves (Morse 1953). Eqs. 6. 25 to 6.32 apply to any of these waves, and none of them are reflected at the interface between the PLHM and the air. From straightforward calculations (see Appendix C), it turns out that below the ordinate $y = y_S - 2e$ the field transmitted by the slab identifies with the field that would be radiated by a point source located at point F with coordinates $x = 0$, $y = y_S - 2e$ (Fig. 6.6). In other words, the image of the point source S at point F is stigmatic and has the same intensity as S (Pendry, 2000).

Similarly, the consideration of the field extending in the slab shows the existence of another stigmatic image of S located at point $\tilde{S}$ and symmetrical to S with respect to the upper interface of the slab. From Eqs. 6.25 to 6.27 and Eq. 6.32, it can easily be verified that the field in the region $-y_S < y < 0$ of the slab is symmetrical with respect to the ($y = 0$) plane to the field in the region $0 < y < y_S$ above the slab, and that the same property holds for the fields in the regions $-e < y < -y_S$ and $y_S - 2e < y < -e$, symmetrical with respect to the ($y = -e$) plane. In simpler words, an arbitrary incident field impinging on an interface between air and a PLH material generates at the other side of the interface a second field symmetrical with respect to the interface (Maystre 2004).

This simple rule also suggests a strong analogy between the field transmitted through an air/PLHM interface and the virtual field generated by a perfectly-plane, perfectly-reflecting mirror surface, since the latter field is symmetrical to the incident field with respect to the mirror surface. As is well known, a perfect mirror is a stigmatic instrument, but the image of a point source is merely virtual. PLH materials can therefore be seen as a means to bring into real space the virtual image of a point source generated by a plane mirror. This in a sense turns into reality the adventures of Alice told in *Through the Looking Glass.* In this famous book, published in 1872 by the English writer and mathematician Charles Lutwidge Dogson better-known by his pen name Lewis Carroll, Alice enters a parallel world by stepping through a mirror (Carroll 1872).

The first theoretical investigations of PHL materials and the subsequent experimental studies caused a controversy in the scientific community (Garcia 2002b; 't Hooft GW 2001; Maystre 2004; Pendry 2001a, 2001b; Valenju 2002; Williams 2001; Ziolkovski 2001, Pendry 2001b). In particular, it has been pointed out (Garcia 2002b; Maystre 2004) that the integral representing the field below the

slab diverges in the region between the lower PLHM/air interface and point F, i.e. when $-e < y < y_S - 2e$ (see Appendix C). The same divergence was also observed in the region between point $\tilde{S}$ and the lower PLHM/air interface. This divergence is the consequence of the asymptotic behaviour of the following term in the integral for $|\alpha| \to \infty$:

$$\exp\left(i\alpha x - i\beta(\alpha)\left[y - y_S + 2e\right]\right) = \exp\left(i\alpha x + \chi(\alpha)\left[y - y_S + 2e\right]\right) \tag{6.33}$$

$$\text{with } \chi(\alpha) = \sqrt{\alpha^2 - k_0^2} \to |\alpha| \quad \text{when} \quad |\alpha| \to \infty \tag{6.34}$$

Since $y - y_S + 2e > 0$ in the region between the lower PLHM/air interface and point F ($y_S - 2e < y < -e$), the modulus of the integrand in the right-hand member of Eq. 6.32 increases exponentially at infinity. On the other hand, for $y < y_S - 2e$, i.e. below point F, the integrand decreases exponentially at infinity, with the consequence that the field is well-defined.

This divergence is actually related to the behaviour of the field in the slab, and to the fact that all incident plane waves in this field are evanescent. It can be readily derived from Eqs. 6.26 and 6.32 that the field generated by these incident evanescent waves inside the slab do not decay away exponentially from the upper interface, but increases exponentially as y decreases. Another approach towards understanding this behaviour consists in recalling that the field below the upper interface between the air and the PLH material is symmetrical to the incident field with respect to this interface. Thus, proceeding downward from the point source S, each component of the incident field corresponding to an evanescent incident wave decreases exponentially as long as we stay above the slab, before increasing exponentially in the slab. Accordingly, the amplitude takes, at a point $\tilde{S}$, the same value as at point S. Conversely, the amplitude first increases exponentially below $\tilde{S}$ until the lower interface between the slab and the air is reached, before decreasing exponentially below the slab. Thus, it takes, at a point F, the same value as at points $\tilde{S}$ and S. These evolutions explain the formation of the two perfectly stigmatic images $\tilde{S}$ and F.

An important remark concerning this physical interpretation is that the amplitude of each evanescent plane wave in the region between $\tilde{S}$ and S is greater than at the point source. This actually is the reason for the divergence of the integral expression of the total field. The increase in the amplitude of each evanescent plane wave in the slab may seem quite unphysical at first sight, since it could be interpreted as an amplification process, a plain impossibility in a passive material. However, the exponential increase of amplitude in the slab actually occurs along the y direction, whereas the evanescent wave propagates along the orthogonal x direction. There is therefore no physical contradiction involved in this increase of amplitude, and only improperly can it be described as an amplification process.

This interpretation also shows the vital role played by evanescent waves in achieving the property of stigmatism. In this respect, it should be noted that a conventional optical instrument such as a lens cannot increase the amplitude of eva-

nescent waves while simultaneously preserving their contribution in the field at the image plane. Accordingly, the evanescent waves contained in the field emitted by the point source become negligible when they reach the point image. Even in the case where the classical lens is perfect, i.e. where it totally transmits all the homogeneous plane waves contained in the field emitted by the point source, these waves correspond to the finite range $\alpha \in [-k_0, +k_0]$. As a consequence, the integral representing the total field (see Eq. C.2b in Appendix C) is actually restricted to this interval. The field in the image plane is therefore the Fourier transform of a function with bounded support. This integral can be calculated in closed form, leading to the result that the width of the image is of the order of half the wavelength. This constitutes the Rayleigh resolution limit for classical optical instruments. It should be noted that this limitation does not hold for the slab of PLH material, due to the fact that this structure preserves at the point image the amplitudes of the evanescent waves generated by the point source.

6.4.4 Perfect Lens or Superlens?

The divergence, in a region of space, of the integral representing the field raises a consistency problem which affects the very notion of a PLH material. According to Garcia *et al*, this integral 'cannot represent any physically realizable wave field' (Garcia 2002b). Should we conclude from this that the very concept of a perfect lens fails? The fact that the demonstration presented by Pendry contains a divergent integral is certainly no proof that his conclusion is erroneous. Mathematicians are able to give a sense to integrals that are obviously divergent from the point of view of physicists. Further, experimental and numerical investigations have actually proved the existence of negative refraction, as well as the possibility of near-field imaging using slabs of left-handed materials and photonic crystals.

It can be rigorously demonstrated that the perfect lens does not exist, and the interested reader will find a mathematical proof in (Maystre 2004). Nonetheless, it can also be shown that a slab of metamaterial may act as a 'superlens', i.e. as a lens with resolution smaller than the Rayleigh criterion. For this purpose, let us first recall that a left-handed material is not a strictly homogeneous material, but an artificial material with a spatial period p assumed to be much smaller than the wavelength of light. This period being finite, the integration range in the integral representing the field at any point of space actually reduces to a finite integration range. Indeed, the integrand contains the term $\exp(i\alpha x)$, which is but the expression of a plane wave, either homogeneous or evanescent, propagating along the x axis. The phase velocity of this wave is equal to α, and the corresponding wavelength, referred to as the transverse wavelength in the following, is therefore equal to $\lambda_T = 2\pi/\alpha$. As $|\alpha|$ tends toward infinity, the transverse wavelength tends towards 0. Bearing in mind that waves become evanescent as soon as $|\alpha| > k_0$, we are thus led to the conclusion that a point source can generate a near field containing evanescent waves with a transverse wavelength very close to 0, and hence much smaller than the actual wavelength λ_0 of light. It is obvious that homogenization rules no longer apply when the transverse wavelength becomes close to or smaller

than the period of the material. For this reason, it would be quite erroneous to allege that the relative permittivity and the relative permeability of the material can be considered equal to -1. In practice, this only means that the corresponding waves do not contribute to the imaging process and therefore that they should be removed from the integral.

The vital influence of evanescent waves on the imaging process is very well known in near-field microscopy. The use of optical antennas positioned at a very short distance from a rough surface allows specialists in this technique to generate incident fields at this surface that contain evanescent waves with significant amplitudes. The corresponding transverse wavelengths can be very small with respect to the actual wavelength of the light source, with the consequence that details of the rough surface more than a hundred times smaller than the wavelength can be visualized (Pohl 1993). This demonstrates that the scattering phenomenon generated by such incident waves on a rough surface is strongly influenced by the asperities, even though the latter are of an order of magnitude much smaller than the wavelength. In the case under consideration, the period of the metamaterial plays the same role as the size of the asperities.

A mathematical form to the limitation of the integration range in the field integral can be given by recalling that, roughly speaking, usual homogenization rules (Felbacq 1997) apply as long as the wavelength is larger than $2\pi p$. Since the transverse wavelength here is $\lambda_T = 2\pi/\alpha$, the integration range should be reduced to the interval $\alpha \in [-1/p, +1/p]$. While the image is no longer stigmatic due to truncation of the integral, the lens nonetheless tends toward a perfect lens since the period of the metamaterial tends toward zero. In other words, contrary to classical lenses, the metamaterial slab is capable of including part of the evanescent waves in the imaging process, thereby overcoming the Rayleigh resolution limit. It might be noted that the amplitude of these evanescent waves is actually larger in a certain region of the slab than at the point source. It can therefore be conjectured that losses inside the left-handed material can be much higher than in classical lossy materials, a fact already pointed out in (Garcia 2002b).

6.4.5 Fabrication of Negative Refractive Index Metamaterials

The practical problem of realizing actual negative refractive index materials was not considered at the time when V. Veselago conducted the first studies on this subject (Veselago 1964). Accordingly, these results were largely forgotten for more than thirty years, until the development of photonic crystals revived interest in this subject.

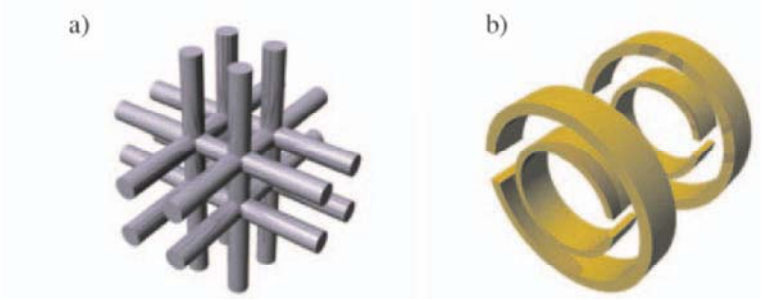

Fig. 6.7. *a.* Three-dimensional structure formed by thin metallic rods exhibiting a low frequency behaviour similar to that of a neutral plasma. *b.* Periodic structure exhibiting a negative magnetic permeability at low frequencies. The elementary pattern consists of LC resonators formed by two concentric split metallic rings

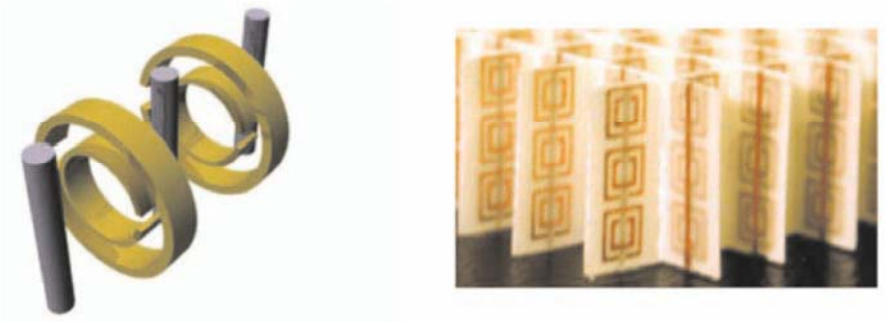

Fig. 6.8. Negative refractive index material fabricated by a research group at the University of San Diego (Smith 2000) *a.* Schematic view showing the combination of two periodic lattices shifted from one other by half a period (conducting wires and double split ring resonators). *b.* View of the actual structure realized from printed boards

In the course of his researches on metallic photonic crystals (see Section 4.2.1 in Chapter 4), JB Pendry observed that crystals formed by conducting rods with a small diameter (Fig. 6.7*a*) presented the same frequency response as non-collisional plasmas (Pendry 1996). Three years later, he suggested an artificial electromagnetic crystal with a negative magnetic permeability (Pendry 1999). This second structure was formed from LC-type resonators consisting of split metallic rings, as represented in Fig. 6.7*b*.

In 2000, a research group from the University of California in San Diego (UCSD) succeeded in fabricating the first artificial material with $\varepsilon < 0$ and $\mu < 0$ in the centimetre wavelength range. The material thus realized was a combination of the two structures previously proposed by JB Pendry (Smith 2000c). More precisely, this artificial material consisted of a two-dimensional lattice of conducting

wires interleaved with double split ring resonators. All these structures were fabricated from printed circuit boards, as represented in Fig. 6.8. The presence of a negative refraction effect was confirmed by microwave measurements (Shelby 2001).

These pioneering works caused a controversy in the scientific community. For instance, doubts were cast as to whether the principle of causality had not been violated (Valanju 2002) in the experiments conducted by RA Shelby *et al* (Shelby 2001). It was also argued that the mere combination of two media, one with $\varepsilon < 0$ and the other with $\mu < 0$, would not allow the propagation of plasma modes (Pokrovsky 2002a). Other authors also pointed out to the fragility of the 'perfect lens' effect, when the losses of the metamaterial were taken into account (Garcia 2002a). This controversy originated, to a large extent, from the desire to explain and describe all the characteristics of negative refractive materials with simple arguments, and, even better, with analytical formulas. A similar situation had arisen a few years earlier with the 'discovery' of the 'superluminal' propagation of light in photonic crystals (Chiao 1997; D'Aguanno 2001), where similar doubts had been raised, in particular with respect to the possible violation of the principle of causality. In this case, however, subsequent numerical simulations clearly demonstrated the impossibility of a superluminal propagation or tunnelling of light (Konsek 2003).

All experiments and numerical simulations conducted with the FDTD method have now vindicated the existence of the negative refraction effect (Grbic 2002; Kärkkäinen 2002; Ziolkowski 2001). Additional confirmation of this phenomenon has offered a direct answer to these criticisms (Garcia 2002b; Maslovsky 2002; Pendry 2002a, 2002b; Veselago 2002).

One of the main results achieved by the UCSD research group, namely the focusing of an electromagnetic wave by a slab with a negative refractive index metamaterial, was reproduced in the experiments conducted by AK Iyer *et al*, where a two-dimensional lattice of LC resonators formed by lumped elements was used (Iyer 2002). From a theoretical point of view, a clear assessment of the issues related to the principle of causality in metamaterials has been presented in (McDonald 2000). It has also been demonstrated that even 'non-perfect' lenses based on metamaterials could exhibit a higher optical resolution than conventional lenses (Maystre 2004; Pokrovsky 2002b; Shen 2002). In the microwave region, it has been shown that the limits imposed on the dispersion of the material can be relaxed through the incorporation of lumped amplifiers in the structure (Tretyakov 2001).

The potential applications of negative refractive index materials to the near infrared and visible ranges started being investigated in parallel to these microwave studies. As a first approximation towards the realization of a perfect lens in the visible range, JB Pendry suggested using a thin silver layer with $\varepsilon < 0$, but $\mu > 0$. In such a simpler system, the conditions for the excitation of surface plasmons must be fulfilled in order to achieve an enhanced transmission of evanescent waves enabling sub-diffraction-limited imaging. First experimental results seem to confirm theoretical predictions (Fang 2005; Melville 2004). Following a different approach, many researches have been directed at obtaining a magnetic response at

short wavelengths, either by using metamaterial structures in the same spirit as for microwave wavelengths (Enkrich 2005; Linden 2004) or by exploiting antisymmetric plasmon resonances (Grigorenko 2005). This actually proves to be a tremendous challenge, as no material, either natural or artificial, is known that would exhibit magnetism in the near-infrared and visible ranges. The first results obtained in this direction and in the exploration of negative-refraction metamaterials (Shalaev 2005; Zhang 2005) appear to be promising for future developments.

More generally, the strong interest in metamaterials and their application to negative refraction should not lead to neglect the potentialities of photonic crystals in the short wavelength regions (Dewar 2001; O'Brien 2002) (see also Fig. 6.5). Contrary to metamaterials, negative refraction can be achieved in photonic crystals by using purely dielectric components, a decisive advantage when it comes to fabricating low-loss devices in the infrared and visible regions. Conversely, photonic crystals must be operated near or above the optical band gap, where the working wavelength is comparable to the size of the elementary motifs. For this reason, a photonic crystal can never be approximated as a homogeneous material. While a numerical experiment has shown that a slab of negative refraction photonic crystal could generate an image of a point source, the image thus obtained was not stigmatic as it did not contain all the energy radiated by the point source (Decoopman 2006). Actually, achieving a transmission equal to one through the 'amplification' of the evanescent waves is possible only in the case of structures with an effective index equal to -1 as well as an effective permittivity and an effective permeability close to -1, as is the case for PLH materials. It is quite clear that the notion of effective parameters quickly approaches its limits when it is applied to a slab of photonic crystal, which, in addition, is never a perfectly isotropic material. Negative refraction photonic crystals can only approximate the optical properties of superlenses.

6.4.6 Electromagnetic Cloaking

Advances in studies on metamaterials have opened new opportunities in the field of electromagnetics and optics. It is now possible to envision systems capable of independently controlling the values of permittivity and permeability at any point of space, in a range including positive as well as negative values. In turn, this property can be used to force electromagnetic fields to avoid an object (Pendry 2006; Leonhardt 2006).

We consider in Fig. 6.9*a* an incident wave (here a plane wave) propagating in a homogeneous medium. In Fig. 6.9*b*, the same incident wave can be seen to illuminate an object. In principle, the latter would scatter light, thereby enabling an observer to easily detect its presence. In order to cancel the scattered field, the object is placed inside a dark sphere of radius R_1, surrounded by a cloaking material extending between the spheres of radii R_1 and R_2, and represented in light grey in Fig. 6.9*b*. The cloaking material is designed in such a way as to cause the line fields to be expelled from the dark sphere, while the field outside the light grey region remains identical to the field in Fig. 6.9*a*.

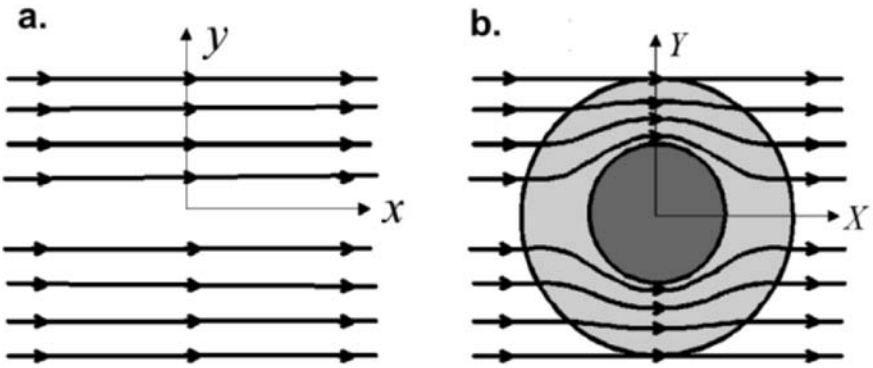

Fig. 6.9. *a.* Incident wave propagating in a homogeneous medium. *b.* Deformation of space in the light grey sphere (cloaking material) excluding all points contained in the dark sphere, while the mapping outside the cloaking material remains identical to that of *a*

In other terms, everything happens as if the electromagnetic wave flows around the dark sphere like a fluid, before returning along its original trajectory without undergoing any perturbation. Quite intuitively, the cloaking material shown in Fig. 6.9*b* must consist of a homogeneous material with a refractive index varying with the distance from the origin, but always smaller than unity. These conditions are suitable for curving the trajectory of light on the one hand, and for recovering the original phase of the field behind the cloaking region on the other hand. An additional requirement imposes that light should be totally transmitted. This actually turns out to be an impedance matching problem for the elementary layers of the cloaking material. This ensemble of conditions imposes the use of anisotropic media, in which the permittivity and the permeability can be independently controlled. Designing a material satisfying these requirements is well within the range of the metamaterial approach to the engineering of electromagnetic materials.

From a mathematical point of view, determining the light trajectories represented in Fig. 9.6*a* amounts to deforming the entire space in such a way as to exclude all points contained within the dark sphere. However, the final mapping must be identical to the original mapping outside the light gray region if the deformation of space is to be limited to a finite region. In addition, the deformation is imposed to be invariant for any rotation with respect to the centre of the spheres.

The required deformation can be obtained from the relations between the Cartesian coordinates *x, y, z* of a point in Fig. 6.9*a* and the Cartesian coordinates *X, Y, Z* of the corresponding point through the mapping process described in Fig. 6.9*b*. It turns out that Maxwell's equations take exactly the same form in the coordinate system *X, Y, Z.* However, both the permittivity and the permeability become tensors dependent on *X, Y, Z.* The components of these tensors can be expressed from functions $X(x, y, z)$, $Y(x, y, z)$, $Z(x, y, z)$, thereby determining the electromagnetic characteristics ε and μ required for the realization of the cloaking material. The in-

terested reader will find the expression of these tensors in (Pendry 2006). The final result is that radiation will be guided around the dark sphere without actually penetrating it. An external observer will not be able to detect the presence of this sphere, and will be led to conclude that the space is void. However, the illusion thus created is restricted to a small range of frequencies.

7 Confinement of Light in Zero-Dimensional Microcavities

The perspective of achieving a better control of the spontaneous emission in optoelectronic devices gave a major impetus to research on photonic crystals in its early developments. Thus, in his founding paper, E. Yablonovitch mentioned as a major incentive in the search for structures with complete photonic band gaps the possibility of inhibiting the spontaneous emission in the spectral range of the photonic band gap (Yablonovitch 1987). A few years later, he also introduced the concept of a single-mode light emitting diode (Yablonovitch 1991b, 1993). Such a device, which ultimately rests on a defect created in a three-dimensional photonic crystal, would allow achieving the complete control of spontaneous emission.

Spontaneous emission plays a major role in optoelectronic devices, either in a positive or in a negative manner. As an example, we may first consider the case of light emitting diodes (LED). These devices represent by far the main share of the market for optoelectronic devices, with high-brightness LEDs totalling 4.2 billions USD on their own in 2006. The emission of a LED is generally ensured by the spontaneous emission of a semiconductor active medium. Accordingly, the efficient extraction of light emission from the semiconductor is essential for maximizing the efficiency of LEDs.

In a laser diode, the spontaneous emission into the lasing mode is useful and even essential, since it acts as a trigger for the amplification by stimulated emission. By contrast, spontaneous emission into all other modes unnecessarily dissipates energy (Yokoyama 1995a). In conventional edge-emitting laser diodes, of the kind used for optical communications or compact disk players, the useful fraction β of the spontaneous emission is as low as 10^{-5}. As a consequence, the current injected at the lasing threshold serves for the most part to compensate for the radiative recombination of the electron-hole pairs by spontaneous emission (Coldren 1995). In principle, increasing β would lead to a reduction by several orders of magnitude of the threshold current of laser diodes, and to a significant increase of their efficiency.

In addition to the improvement of existing devices, the control of the spontaneous emission would open the way to the development of novel devices with very original functions (Burstein 1995; Chang 1996; Yokoyama 1995b). A beautiful example can be found in the form of single-photon sources capable of deterministically emitting a light pulse containing but a single photon. As will be discussed in more detail in Chapter 10, a promising approach towards the actual realization of single-photon sources relies on the Purcell effect, i.e. on the enhancement of the spontaneous emission rate of a single quantum dot in a pillar microcavity. From a

conceptual point of view, another important example is the 'thresholdless laser', that would be achieved in the limit case where $\beta \sim 1$, and where the spontaneous emission would be entirely channelled into the lasing mode. A series of very attractive properties are expected to occur in such a regime, which has largely contributed to stimulating research on semiconductor optical microcavities in the early 1990s (Yamamoto 1991; Yamamoto 1993; Yokoyama 1992).

This brief introduction has highlighted the diversity and the importance of the potential applications that may result in optoelectronics from the control of the spontaneous emission. In this context, photonic crystal microcavities come into competition with other well-established approaches to three-dimensional optical confinement, for instance those based on micropillars and on microdisks. We shall therefore first discuss in general terms the main effects of optical microcavities on the properties of the optical emission, including the physics of thresholdless lasing (Section 7.1). We shall then present the experimental state of the art on this subject in Section 7.2, with a special emphasis on results obtained for optical cavities containing semiconductor quantum dots. From there, we shall compare the main figures of merit of photonic crystal microcavities and other optical microcavities, and discuss their respective assets for the control of spontaneous emission. The first realizations of microcavity-based optical sources will be presented and analysed in Chapter 10.

7.1 Microcavity Sources. Principles and Effects

7.1.1 A Classical Effect: the Angular Redistribution of the Spontaneous Emission and the Example of Planar Microcavities

For any cavity defined between mirrors, the electromagnetic modes of interest are shaped by the boundary conditions imposed by the mirrors. When an emitter is placed inside the cavity, all the physical effects that are expected actually originate from the coupling of the emitter to the cavity modes. If the cavity is not totally enclosed by the mirrors, there remain propagation directions along which the electromagnetic modes involved in these effects form a continuum similar to that of the surrounding homogeneous space (dielectric, air, vacuum). Only the modes 'spreading' over the mirrors will be truly discretized. In order to be detected outside the cavity, the photons need either to propagate through the 'leaky modes' or to be channelled into one of the discrete modes, before being subsequently transmitted through the associated mirrors. In the latter case, it is quite plain that the far-field angular pattern of the emitter will be directly affected by the spatial structure of the underlying cavity modes, and in particular by their lobes and their nodal lines or planes.

The angular redistribution of the spontaneous emission is a classical effect, which has been established for solid state emitters as well as for atoms in microwave or optical cavities. This effect can be illustrated by considering the case of a planar (Fabry-Perot) cavity with an emitter placed in vacuum between two mirrors. These two mirrors are assumed to be parallel, while their respective reflectivities r_1 and r_2 are independent on the frequency and the incidence angle. From an historical perspective, A. Kastler was among the first physicists to consider this case using an elementary classical formalism where polarization effects were neglected (Kastler 1962).

All the relevant modes of the ideal system thus defined are Fabry-Perot modes, which obey the quantification of the wave vector **k** along the z direction normal to the mirrors: $k_z = m\pi/L$, where L is the distance between the mirrors and m is an integer (Fig. 7.1*a*). Denoting by θ the angle formed by the wave vector **k** and the z axis, k_z can also be expressed in the form $k_z = k\cos\theta$, with $k = \omega / c$. The resonant modes are associated with the constructive interferences created by the multiple reflections at the two mirrors. It is under these conditions that the transmission of the cavity described by the Airy function reaches its maximum Fig. 7.1*b*. Outside the cavity, the intensity of the field is distributed over circular fringes, also referred to as rings (Fig. 7.1*c*), whose finesse, i.e. the ratio of the interval of these fringes to their individual width, is given by the classical formula $F = \pi (r_1 r_2)^{1/2} / (1 - r_1 r_2)$, which depends only on the reflectivities of the mirrors (Born 1965). The number of fringes at a given frequency is finite (m_c = integer $[L/(\lambda/2)]$) and corresponds to what could be called the order of the cavity. Inside the cavity itself, the electromagnetic energy is concentrated in resonant modes, with stationary waves forming as a result of the fact that each plane wave is almost totally reflected for $r_1 \sim 1$ and $r_2 \sim 1$.

The efficiency of the coupling between the emitter and resonant modes can be best understood by using the principle of reciprocity. If the emitter is illuminated by a light source located outside the cavity, the field at the emitter will be either reinforced or reduced compared to the situation where no cavity is present. Correspondingly, the coupling will be either enhanced or inhibited. The distribution of the emitted power between the different modes, i.e. between the different fringes, which can be observed outside the cavity (Fig. 7.1*c*), actually depends on the location of the emitter with respect to the 'local electric field' of each mode, and especially with respect to their nodes and antinodes. Accordingly, the angular redistribution of the spontaneous emission caused by the presence of the Fabry-Perot cavity will result in two different effects. First, at a given frequency, the directions of propagation associated with Fabry-Perot modes are favoured over all other directions, as is described by the Airy function. Secondly, the distribution of the power among the different modes, i.e. the different circular fringes, depends on the local value of the field of the mode at the emitter. In the case of a symmetric cavity ($r_1 = r_2$) and of an emitter located at its centre, the coupling occurs only for even modes with an antinode in the centre of the cavity. Odd modes will simply not be coupled, notwithstanding the fact that the Airy function is maximal for the corresponding angle and frequency. Overall the effect induced by the cavity is the suppression of the radiation along non-resonant directions and its concentration

along certain other directions (resonant modes), ideally without any losses occurring in the case of ideal mirrors (Benisty 1998a, 1998b).

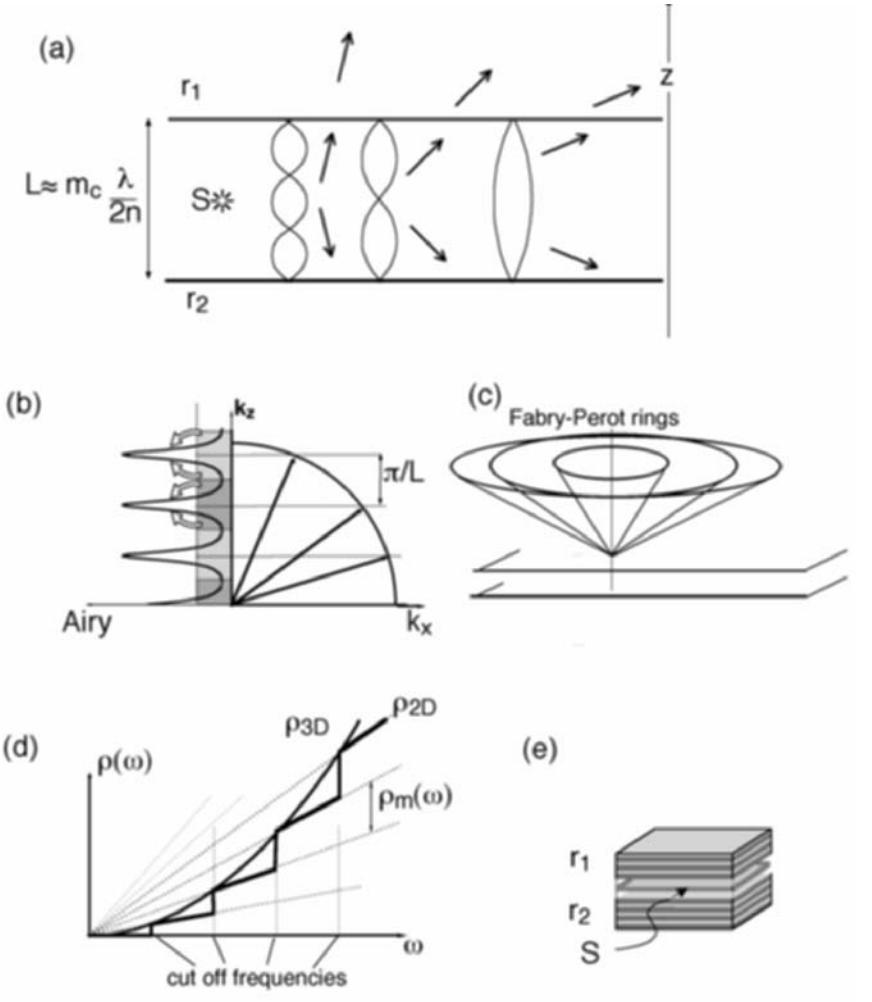

Fig. 7.1. *a.* Fabry-Perot cavity (mirrors with reflectivities r_1 and r_2) with a localized source *S*. Three modes ($m_c \approx 3$) are represented here in the form either of stationary waves or of rays *b.* Quantification of the projection of the wave vector k_z. The locus of **k** describes a circle with radius ω/c, whereas the cavity transmission expressed as a function of k_z evolves like the Airy function *c.* Circular fringes where the emitted radiation energy and the corresponding modes are concentrated *d.* Photonic density of states of the planar microcavity for TE modes *e.* Example of a cavity with Bragg mirrors or with a one-dimensional photonic crystal

Let us now consider the influence of the length L of the cavity. If L is small, then m_c will be small as well, and the emitter will be coupled only to a limited number of resonant modes. In the limit case where m_c is just above unity, all the emitted light can be coupled to a single mode per polarization. This simply means that the source *S,* which originally was isotropic, has been turned into a truly directional source, with a directivity depending on the finesse F of the cavity. One may also select the main output mirror by increasing, in much the same way as in lasers, the transmission (t_1 or t_2) of one of the mirrors with respect to the other. From this simple model, it can be seen that the isotropy of the spontaneous emission completely disappears when the system formed by both the emitter and the cavity is considered. For a polychromatic emission in the cavity, it is also quite apparent that the direction of emission depends on the frequency, this being due to the fact that, for a given mode and for a cavity with a given length, the $\omega\cos\theta$ product is constant. Any increase in the output angle will therefore cause $\cos\theta$ to decrease and will lead to an increase of ω, resulting in a blue shift of the emission.

At this point already, one may perceive the existence of a dynamical effect that will be described in more detail in Section 7.1.2 of this chapter: the change in the overall strength of the coupling to the resonant modes, or in other terms the Purcell effect. Let us note first that the three-dimensional photonic density of states in the cavity (ρ_{2D}) increases stepwise when a new cavity mode appears (Fig. 7*d*, $\omega_m = m\pi/cL$). Therefore, the smaller the value for m, the more different the value of the density of states will be from its value in vacuum ($\sim\omega^2$). Let us for instance consider the case of a dipole emitting in vacuum at the frequency ω, released in a cavity with a length L such that the frequency of the first resonance $\omega_1 = \pi c/L$ is slightly larger than ω. Since $\rho_{2D} = 0$, the TE spontaneous emission of the dipole will be inhibited for TE polarized modes, i.e. for modes whose **E** field is parallel to the plane of the mirrors, as can be seen in Fig. 7.1*d*. When the value for L increases, ω_1 falls under ω, and the spontaneous emission rate changes abruptly due to the appearance of modes characterized by ($k_z = \omega_1/c$, $|\mathbf{k}| = \omega/c$), which provide efficient deexcitation channels for the emitter. As is often the case in the literature, the term 'mode' will be used here both for the discrete set of modes along the z direction (in this sense, 'one mode = one fringe') and for the more genuine photonic modes which form a two-dimensional continuum for each z-quantized value m.

For a more precise study of the spontaneous emission rate, both the exact location and orientation of the emitting dipole need to be accounted for, as is the case in simplified models (Kastler 1962; Benisty 1998a, 1998b) as well as in more elaborated models (Björk 1994; Brorson 1990). The latter models indicate that for a planar cavity confined by ideal mirrors ($r_1 \sim r_2 \sim 1$), the spontaneous emission rate could be enhanced by a factor of 3 compared to its value in vacuum. This however requires that the emitter be polarized parallel to the plane of the cavity and that it be located at its very centre. Even in such an ideal case, the enhancement remains limited. Further, the inhibition of the spontaneous emission is complete in planar cavities only in the case of emitters polarized parallel to the plane of the cavity, and with a transition energy lower than the cutoff of the fundamental

TE mode. TM modes, i.e. modes whose **H** field is parallel to the mirrors, have indeed no cutoff.

Let us now turn to the consideration of more realistic cavities, formed either from Bragg mirrors (Fig. 7.1*e*) or from lossy metallic mirrors. In this case, several additional effects must be given attention. First, a medium with a high index may allow the propagation of perfectly discrete guided modes. 'Leaky' modes may also be present due to absorption. Another series of effects originates from the limited angular and spectral acceptance of Bragg and other distributed mirrors. Within these limits, the phase behaviour of these mirrors is analogous to that of ideal mirrors that would be placed at a certain distance from the first interface with the cavity. The fact that the wave penetrates over a certain depth in the distributed mirror (which is the equivalent of the skin effect for metals) amounts to virtually enlarging the cavity, and therefore to increasing the number m_c of resonances allowed at a given frequency. In the example represented in Fig. 7.1*d*, this means that the total photonic density of states will only exhibit limited relative singularities. To mention but a single numerical example, the total density of states is not modified by more than +/– 20 percent for a GaAs microcavity clad with GaAs/GaAlAs Bragg mirrors. For microcavities confined by metallic mirrors, the penetration of the field is much lower. It can even be demonstrated, by taking into account the phase difference of the wave at the reflection at the mirror, that the first resonance of the cavity is obtained for an optical thickness smaller than $\lambda/2$. The total density of states for such an ultimate cavity is therefore enhanced by a factor of up to 5 (Abram 1998). However, cavities of such a type are rarely used in practice, since the absorption of the mirror limits their quality factor and their transmission, resulting in a lower photon extraction efficiency.

In spite of these limitations, the angular redistribution of the spontaneous emission in planar cavities formed from Bragg mirrors has been used for increasing the extraction efficiency of solid state emitters, and more particularly of semiconductor emitters. Since semiconductors have a high refractive index, the critical angle for total internal reflection is small, and ranges only from 15° to 30°. A large fraction of the light isotropically emitted in the bulk of a chip cannot be transmitted through the interface between the semiconductor and the air. Sandwiching the emitter in a planar microcavity thus allows concentrating the light that would be lost otherwise in a cone with much lower angular aperture. This analysis will be further developed in Chapter 10 when discussing light emitting diodes.

7.1.2 Spontaneous Emission Dynamics in Microcavities

In this section, we shall consider the general situation where the presence of a cavity results in strong singularities in the photonic mode density. The interaction between light and matter will be analysed here in terms of a strong coupling between the field of the cavity and a single emitter. This will lead us to reconsider in more detail the weak-coupling situation previously discussed with respect to planar cavities.

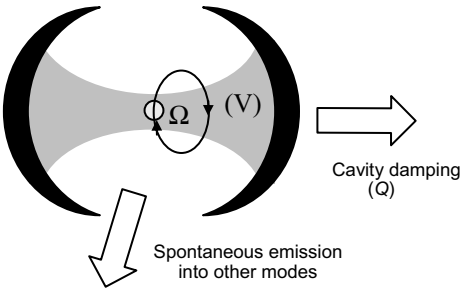

Fig. 7.2. Schematic representation of a single emitter in a cavity

Strong Coupling. Formation of Mixed Exciton-Photon States

Let us consider here a single localized emitter, resonantly coupled to a single lossless cavity mode, as represented in Fig. 7.2. The emitter is assumed to be in an excited state at $t = 0$. In the absence of dissipation, a system of two coupled oscillators, formed by the excited atom on the one hand and of the field of the cavity on the other hand, has thus been created. Each oscillator periodically exchanges its energy with the other, so that the spontaneous emission becomes reversible: thus, a photon emitted by the atom will be reabsorbed, before being re-emitted, and so on. This phenomenon is known in quantum mechanics under the name of Rabi oscillations.

Actually, damping occurs as soon as the coherent interaction is destroyed, or when losses are present, resulting in an exponential decrease of the Rabi oscillations. These phenomena have been intensively studied in atomic physics from the beginning of the 1980s. In particular, famous experiments have been conducted for atomic transitions in the radiofrequency region, using a confocal cavity with superconductor mirrors presenting ultra-small losses (Haroche 1989).

We shall only provide here a short theoretical survey of the physical quantities involved in this interaction, and this will lead us to briefly sketch the quantum theory of fields. Note that this theory will not be used anywhere else in this book (Cohen-Tannoudji 1992; Loudon 1983).

The electric field for a given cavity mode can be written in the form:

$$\vec{\hat{E}}(\vec{r}, t) = i\boldsymbol{\varepsilon}_{\max} \vec{f}(\vec{r}) \hat{a}(t) + \ h.c. \tag{7.1}$$

where $\hat{a}$ is the photon creation operator, $\vec{f}$ is a complex vector which is a function of the space variables and represents the local polarization field ($\vec{f}$ is normalized at one of the antinodes of the field and satisfies Maxwell's equations) and *h.c.* stands for the Hermitian conjugate of the operator in the first term of the right-hand side of Eq. 7.1. The prefactor ε_{max}, which is sometimes improperly referred

to as the 'maximum field per photon', determines the absolute strength of the atom/field coupling. Since the field energy of vacuum (zero photon) for a mode with a frequency ω is $\hbar\omega/2$, i.e. half the quantum of the harmonic oscillator in the fundamental state, ε_{max} can be written in the following form:

$$\boldsymbol{\varepsilon}_{\max} = \sqrt{\hbar\omega / 2\,\varepsilon_0 n^2 V} \tag{7.2}$$

where:

$$V = \frac{1}{n^2} \iiint_{\vec{r}} n(\vec{r})^2 \left|\vec{f}(\vec{r})\right| d^3\vec{r}$$

The physical quantity V in the equation for ε_{max} reduces simply to the usual mode volume in the case where $\vec{f}$ is defined in a medium with a constant refractive index. Nevertheless, as indicated by the second formula, the possibility always exists of defining an effective volume ($V = V_{\text{eff}}$) if the refractive index is variable, as is indeed the case in photonic crystals. In this second formula, $n(\vec{r})$ is the spatially dependent refractive index, while n is the value of the refractive index at the field maximum.

Using the formalism of quantum mechanics, the interaction Hamiltonian is given by the following equation:

$$\hat{H}_{int} = -i\boldsymbol{\varepsilon}_{\max}\vec{d}.\vec{f}(\vec{r}_e)\,|g\rangle\langle e|\,\hat{a} + h.c. \tag{7.3}$$

where |g> and |e> denote respectively the fundamental state and the excited state of the emitter. The assumption is made that the emitter can be described by a two-level system, and that it is located at $\vec{r} = \vec{r}_e$. The dipole moment of the optical transition will be denoted here by $\vec{d}$. The Rabi frequency characterizes the speed at which the system goes from one state to another due to its interaction with the optical field. We shall take for granted here that the Rabi frequency is associated with the dimensioned factor of the Hamiltonian:

$$\hbar\Omega = \left|\boldsymbol{\varepsilon}_{\max}\vec{d}.\vec{f}(\vec{r}_e)\right| \tag{7.4}$$

Using this formalism, the energy levels of the global system in the absence of interaction can be written in the form $|g, 0\rangle$ for the fundamental state, and as $|e, \bar{n}\rangle$ or as $|g, \bar{n}+1\rangle$ for the two degenerate excited states respectively. The second term in each ket stands for the number of photons in the cavity, corresponding to the intensity of the field according to the classical approach. In the case where interactions occur, the degeneracy of the excited levels is lifted, leading to non-degenerate states which are irreducible linear combinations of the uncoupled states $|e, \bar{n}\rangle \pm |g, \bar{n}+1\rangle$ ($\bar{n} = 0,1...$). The energy difference between non-degenerate

states is but the Rabi splitting $2\hbar\Omega\sqrt{n+1}$. It is quite apparent that, while the fundamental state $|g, 0>$ will not be affected, new states will form as a result of the association between the empty cavity and the excited state $|e>$ of the emitter, i.e. $2^{-1/2}(|e, 0> \pm |g, 1>)$. The energy difference between these states is generally referred to as the vacuum Rabi splitting $2\hbar\Omega$. Thus, if the system is originally prepared at $t = 0$ in the excited state with no photon, it should analysed as the linear and symmetrical combination of two states $2^{-1/2}(|e, 0> \pm |g, 1>)$. The energy difference between these states induces a beating at the frequency 2Ω. From a classical point of view, the excitation goes from the emitter to the cavity and conversely.

Still remaining within this formalism, one may introduce two 'decoherence' sources, the leakage of one photon out of the cavity and the deexcitation of the atom through other channels than the emission of one photon in the cavity mode. If two spectral widths $\Delta\omega_c$ and $\Delta\omega_e$ are associated to these two processes respectively, it can be demonstrated that the oscillations which characterize the strong coupling regime subsist only for relatively small linewidths. In the first approximation, strong coupling will be observed if $2\Omega > (\Delta\omega_e + \Delta\omega_c)$. In other terms, the Rabi oscillation needs to be faster than the 'sum' of the two decoherence processes.

The previous inequality reveals the importance of the physical quantities involved in the Rabi pulsation: the electrical dipole strength associated with the optical transition and the cavity field strength, which itself is intimately related to the volume of the cavity. We shall see later in Section 7.2.4 of this chapter that, even in vacuum (Eq. 7.2), impressive field strengths can be obtained for ultimately small volumes. The quality factor $Q = \omega_c / \Delta\omega_c$ of the cavity exerts here its influence through the spectral width $\Delta\omega_c$ of the mode.

It might be recalled here that the strong coupling between a photon and a quantum excitation of matter has been known since quite a long time in the field of solid state physics. In this respect, the study of semiconductor-based planar microcavities has been a unique opportunity to revisit this phenomenon.

In a three-dimensional medium, the phonon polariton due to the coupling between optical phonons and photons is the first example of a strong coupling phenomenon in condensed media (Ashcroft 1976). In semiconductors, the main electronic excitations, i.e. the electron-hole pairs, exhibit a continuous spectrum, which does not in general allow for strong coupling phenomena. The major exception is the exciton resulting from a bound state between one electron and one hole. The dispersion relations for excitons are such that only one optical frequency will be associated to a given three-dimensional wave vector. The wave vector is conserved both in the creation of an exciton by photon absorption and in the emission of a photon by exciton recombination. This selection rule, which is directly related to the translational invariance of the crystal, leads to the formation of mixed exciton-photon particles, known as excitonic polaritons. In a true solid state crystal, these mixed particles are extremely 'fragile', and any disruption in the periodicity of the crystal (surfaces and interfaces) causes these particles to decompose into their elementary constituents, resulting for instance in the leakage of one photon out of the crystal.

In quantum well structures, the excitons are confined in the layers of the quantum layers. The components of their wave vector are well-defined only for directions parallel to the plane of the quantum well ($\mathbf{k}_{//}$). Accordingly, the excitons can couple to the continuum of photonic modes, with all possible values for k_z. However, the situation changes dramatically when the quantum well is embedded in a planar microcavity where k_z is quantified. Due to the translational invariance within the plane of the quantum well, an exciton with momentum $\mathbf{k}_{//}$ can only couple to a photon with the same momentum $\mathbf{k}_{//}$. Under these conditions, k_z and $\mathbf{k}_{//}$ are now interrelated and a strong coupling regime can therefore be achieved, resulting in the formation of microcavity 'polaritons' (Weisbuch 1992). While the photon leakage occurring through the cavity mirrors irremediably contributes to the damping of the Rabi oscillations, it also provides a convenient way of observing these coupled excitations and of analysing their linear and nonlinear properties, for instance in terms of dispersion or saturation. This experimental scheme has allowed different research groups to reproduce, in the field of solid state physics, some of the most fundamental phenomena demonstrated earlier in atomic physics. For instance, it has been tentatively shown that a dense gas of cavity polaritons, which exhibit at first order a bosonic behaviour, could undergo Bose-Einstein condensation at 'ordinary' cryogenic temperatures (Kasprzak 2006). From this point of view, it can be easily understood that photonic crystal structures offer the opportunity of investigating such phenomena under unprecedented conditions.

Weak Coupling and the Purcell Effect

As early as 1946, EM Purcell noted in his pioneering work that the spontaneous emission, rather than being an intrinsic property of an emitter, also depends on the coupling between the emitter and its electromagnetic environment (Purcell 1946). At this time, EM Purcell was essentially interested in the enhancement of the spontaneous emission rather than in its inhibition. It has already been suggested in Section 7.1.1 of this chapter that, even in the case of simple planar microcavities, the spontaneous emission rate can be either enhanced or inhibited. E. Yablonovitch was the first author who suggested the possibility of achieving the total inhibition of spontaneous emission in a three-dimensional photonic band gap material (Yablonovitch 1987). Inhibition of the spontaneous emission also occurs when an emitter is placed in a cavity without any resonant mode at the emission wavelength. This effect has been observed for atoms suitably polarized and released in a cavity with two metallic mirrors, where no resonance was occurring at the atomic frequencies (Jhe 1987).

The Purcell effect can be described in terms of a 'weak' coupling between an emitter and a discrete cavity mode. In other terms, the assumption is made here that, since the quality factor Q of the cavity is relatively low, it loses photons at such a rate that the broadening $\Delta\omega_c$ of the mode is large enough to ensure that $\Omega < \Delta\omega_c$. Let us first assume that the linewidth of the emitter is much smaller than the linewidth of the cavity mode, i.e. $\Delta\omega_e << \Delta\omega_c$. In this case, everything happens as if the emitter were 'seeing' a mode continuum with a spectral density $\rho(\omega)$. The

coupling of the emitter to the cavity mode can be described using the standard formalism with Fermi's golden rule (Cohen-Tannoudji 1973; Ho 1999). The mode density is represented by a Lorentzian function whose width $\Delta\omega_c = \omega/Q$ is dependent on the finite lifetime of the photon in the cavity. By applying a normalization law $\int\rho(\omega)d\omega = 1$ to one mode, the peak value for the mode density turns out to be equal to $\rho_{max}(\omega) = (2/\pi)Q/\omega)$. The other parameters involved in the spontaneous emission process can be adequately rewritten using once more Ω for characterizing the interaction between light and matter. Accordingly, for an emitter at the frequency ω_e, coupled to a single non-degenerate cavity mode at the frequency ω_c, the spontaneous lifetime will be given by the equation:

$$\frac{1}{\tau} = \frac{4\Omega^2 Q}{\omega} \frac{\Delta\omega_c^2}{4\left(\omega_e - \omega_c\right)^2 + \Delta\omega_c^2} \tag{7.5}$$

This value is to be compared with the value of the spontaneous emission rate in the case where the emitter is embedded in a homogeneous medium with index n (Ho 1999):

$$\frac{1}{\tau_{bulk}} = \frac{\left|\vec{d}\right|^2 \omega_e^3 n}{3\pi\varepsilon_0 \hbar c^3} \tag{7.6}$$

where $\vec{d}$ denotes as before the electric dipole associated with the optical transition.

The dynamics of spontaneous emission are therefore modified as soon as the emitter is coupled to the cavity mode. The exaltation (or inhibition) factor for the spontaneous emission is defined as the ratio between the emission rates given in Eqs. 7.5 and 7.6 respectively, and can be expressed in the form of a product of three terms:

$$\frac{\tau_{bulk}}{\tau_{cav}} = \frac{3Q\left(\lambda_c/n\right)^3}{4\pi^2 V} \cdot \frac{\left|\vec{d}.\vec{f}\left(\vec{r}_e\right)\right|^2}{\left|\vec{d}\right|^2} \cdot \frac{\Delta\omega_c^2}{4\left(\omega_e - \omega_c\right)^2 + \Delta\omega_c^2} \tag{7.7}$$

The first term in this equation depends on the intrinsic parameters (Q, V) of the cavity, while the second and third terms are always less than unity and depend on (i) the relative amplitude of the field at the location of the emitter, (ii) the orientation of the dipole with respect to the field of the cavity and (iii) the spectral shift of the emitter with respect to the cavity mode. The first term is usually considered as the factor of merit of the cavity, since it represents the upper bound which can be obtained if the position, orientation and frequency of the emitting dipole are optimal. This factor of merit is the same as the one proposed by EM Purcell:

$$F_p = \left(\frac{\tau_{bulk}}{\tau_{cav}} \right)_{\max} = \frac{3Q(\lambda_c/n)^3}{4\pi^2 V} \tag{7.8}$$

As can be seen, the Purcell factor may assume arbitrarily large values, much larger than unity. If $F_p > 1$, an emitter adequately coupled to the cavity mode will de-excite faster by spontaneous emission in this mode than in all free-space modes. This exaltation of the spontaneous emission predicted by Purcell in 1946 (Purcell 1946) was demonstrated for the first time in spectacular experiments conducted on Rydberg atoms released in a microwave cavity with $\tau_{\text{vacuum}} / \tau_{\text{cav}} = 500$ (Haroche 1989).

In practice, for solid state emitters at room temperature, dephasing mechanisms other than spontaneous emission become so efficient that the homogeneous linewidth of the emitter $\Delta\omega_e$ is larger than $\Delta\omega_c$. Assuming that the condition $\Omega < \Delta\omega_c$ is fulfilled, the preceding calculations remain valid provided however that $\rho(\omega)$ be replaced by:

$$\int L(\omega)\rho_{cav}(\omega)d\omega \tag{7.9}$$

where $L(\omega)$ is a Lorentzian function representing the statistical distribution of the energy around the emission frequency. Assuming the cavity mode and the emitter to be in resonance ($\omega_c = \omega_e$), $1/Q$ must be replaced in Eq. 7.8 by:

1. $1/Q_{\text{em}} = \Delta\omega_e / \omega$ if a significant homogeneous broadening can be observed, i.e. if $\Delta\omega_e >> \Delta\omega_c$,
2. $1/2Q$ if $\Delta\omega_e = \Delta\omega_c$,
3. $1/Q + 1/Q_{\text{em}}$ (as a good approximation) in the general case.

More specifically, the preceding discussion shows that the Purcell effect is considerably attenuated if the emitter has a linewidth much larger than the linewidth of the cavity mode. For this reason, demonstrating the Purcell effect in condensed matter physics took a longer time than would otherwise have been needed. As will be seen in Chapter 10, the lack of adequate solid state emitters still remains an important limitation for the practical implementation of the Purcell effect at room temperature.

A few additional remarks can be made regarding the dimensionality of the cavity. As has been seen in Section 7.1.1, F_p is smaller than 3 in a planar two-dimensional cavity formed by ideal mirrors. By contrast, F_p can be arbitrarily high in zero-dimensional cavities since in this case there are no physical limits for Q. In practice however, the strong coupling regime will be reached for values of Q (or equivalently F_p) exceeding a certain threshold. It now remains to consider the case of one-dimensional cavities, formed for instance by a metallized fibre.

In principle, the photonic density of states of one-dimensional cavities presents singularities for each mode cutoff ($\omega = \omega_i$) and follows a $(\omega - \omega_i)^{-1/2}$ evolution. Likewise, the inverse of the group velocity ($1/v_g = dk/d\omega$), to which the photonic

density of states is proportional, follows the same type of evolution. In actual systems however, the lower the group velocity, the higher the losses, and the properties of one-dimensional systems are necessarily reflective of their finite length. A one-dimensional system with a finite length is equivalent to a zero-dimensional system where damping and decoherence phenomena occur. Experimental and theoretical studies on one-dimensional systems can be found in (Hughes 2004; Viasnoff-Schwoob 2005)

Single-Mode Emission, Low Threshold Microlaser, 'Thresholdless Laser'

Spontaneous emission can be selectively enhanced in one or several microcavity modes by exploiting the Purcell effect which has been described above. Under these conditions, most of the spontaneous emission will be dynamically channeled into these modes. When the emitter is coupled to a single resonant mode, the spontaneous emission factor β becomes (Gérard 1998):

$$\beta = \frac{F}{F+\gamma} \tag{7.10}$$

where F/τ_{bulk} is the emission rate in the cavity mode exalted by the Purcell effect, while γ/τ_{bulk} is the emission rate in the continuum formed by non-resonant modes. In most cases, γ is close to 1, and the value for β tends therefore to approach unity when the Purcell effect is marked. This behaviour can be used both for lasers and for optical devices directly exploiting the spontaneous emission, for instance light emitting diodes or single-photon sources.

The control of spontaneous emission is of primary importance for lasers. A simple solution for minimizing the threshold current of semiconductor lasers is to use a single-mode structure, where only a single mode can benefit from the amplification of the spontaneous emission. The problem then consists in reducing as much as possible the (1 – β) fraction of the spontaneous emission lost in leaky modes, since this parasitic emission consumes needlessly the electron-hole pairs injected in the semiconductor.

The so-called 'thresholdless' laser, that would be achieved for β = 1, is from a conceptual point of view another interesting case (Yokoyama 1992). Contrary to conventional lasers, such a device would ideally convert any electrical signal into an optical signal. The characteristic of this laser would be strictly linear, since any injected electron-hole pair would finally generate a photon, either by spontaneous emission or by stimulated emission. Contrary to standard lasers, where the amplification of the fluctuations by stimulated emission causes an excess noise to occur near threshold, no such noise would be added to the pumping noise in a thresholdless laser.

This second property would allow the conversion of an electrical signal with low amplitude noise into an optical with a low amplitude noise. Indeed, electrical currents can be easily generated with an amplitude noise well below shot noise.

The only condition imposed is that the non-radiative carrier recombinations should be negligible, since any electron loss would otherwise irremediably increase the electrical pump noise.

This type of a laser is said to be 'thresholdless' only in the sense that the traditional 'accidents' occurring near threshold tend to be suppressed when $\beta \rightarrow 1$.This is true as regards both the light-current characteristic and the noise properties of the laser. However, it should be stressed that this device is not a zero-threshold laser. Indeed, two different regimes can be distinguished depending on the average number of photons $\bar{n}$ in the lasing mode. If this number is less than 1, photons are spontaneously emitted, whereas if the number is more than 1, the stimulated emission becomes predominant. In this sense, a threshold can still be defined for such a device ($\bar{n} = 1$). This threshold can be determined experimentally as well. The emitted beam exhibits a spectral coherence only when the stimulated emission becomes predominant. The linewidth of the laser will decrease in inverse ratio to the number of photons in the cavity above threshold and will be essentially imposed by the quality factor Q of the cavity below threshold. The reduction of the linewidth above threshold is known for standard lasers as the Schawlow-Townes law (Schawlow 1958).

For the purpose of discussing the potential interest of photonic crystals in this context, we shall present here a simple model for the description of the main processes involved in a thresholdless laser (Björk 1991). Let us here consider a single-mode cavity assumed to be containing a total number N_t of two-level atoms. N and N_0 here are the number of atoms in the excited state and fundamental state respectively, while $\bar{n}$ is the number of photons in the mode, β is the coupling factor of the spontaneous emission into the mode, $1/\tau$ is the spontaneous emission rate, which can be enhanced by the Purcell effect and is assumed to remain the same for all atoms, P is the pumping rate, g is the gain coefficient, and $\varphi = 1/\tau_{ph}$ is the photon loss rate. If the homogeneous linewidth of the emitters is larger than the linewidth of the cavity mode, the evolution of the coupled system can then be described by a set of two rate equations (RE) for the atom and photon populations respectively (Björk 1991; Morimura 1997; Yamamoto 1993; Yokoyama 1989, 1992). Following the same approach as in these studies, we shall adopt a modified set of equations, where the stimulated emission rate is explicitly expressed as a function of the number of atoms in the ground state N_0, while the number of emitters is imposed by the relation $N_t = N + N_0$. The latter condition is more specifically adapted to account for the saturation effects occurring in quantum dot systems. The model also provides a good physical insight in the physics of quantum well microlasers with single-mode cavity, in spite of a certain overestimate of the saturation effects in this case. The system of rate equations is therefore:

$$\frac{dN}{dt} = P - \frac{N}{\tau} - g\left(N - N_0\right)\bar{n} \tag{7.11}$$

$$\frac{d\bar{n}}{dt} = \beta\frac{N}{\tau} - \varphi\bar{n} + g\left(N - N_0\right)\bar{n} \tag{7.12}$$

From Einstein relations, the spontaneous emission rate in the mode must be equal to the stimulated emission rate induced by a single photon, which implies that $g = \beta/\tau$. It therefore readily follows from these relations that, in the steady-state regime, the microlaser threshold ($\bar{n} = 1$) will be reached for the following pumping rate:

$$P_{th} = \frac{\varphi}{3\beta}\left[1 + 2\beta + 2\xi\left(1 - \beta\right)\right] \tag{7.13}$$

where $\xi = N_t\beta/2\tau\varphi$ is actually nothing other than the average number of spontaneous photons in the mode at transparency ($N = N_0 = N_t/2$). Let us note here that, in the case where $\xi > 1$, the laser threshold will be reached below the transparency threshold, i.e. before the inversion of the atomic medium. Accordingly, lasing will occur without any population inversion. While the fact that ξ is larger than unity might seem surprising, it should be noted that, as β tends towards 1, the emission rate of spontaneous photons remains well beyond the usual values for standard lasers.

The population inversion ratio for the atomic system at threshold can be deduced from Eqs. 7.11 and 7.13:

$$\frac{N - N_0}{N_t} = \frac{1}{3}\left[\frac{1}{\xi} - 1\right] \tag{7.14}$$

This ratio is necessarily less than 100%, and the system can therefore operate in true laser regime only in the case where $\xi > 1/4$.

It might be of interest to analyse the behaviour of microlasers below and above the threshold, by using approximate solutions of Eqs. 7.11 and 7.12 for the two limit cases where $\bar{n} >> 1$ and $\bar{n} << 1$. In the steady-state regime, the resolution of these equations leads to simple analytical expressions for P and N as functions of $\bar{n}$. The output optical power (P_{out}) and the number of excited atoms (N) can therefore be written respectively as:

– for $\bar{n} >> 1$:

$$P_{out} = \varphi\bar{n} \approx P, \qquad N - N_0 = \frac{\varphi\tau}{\beta} = \frac{2N_t}{\xi} \tag{7.15}$$

– for $\bar{n} << 1$:

$$P_{out} = \varphi\bar{n} \approx P\frac{\beta}{1+2\xi(1-\beta)-2P\beta/\varphi} \approx P\frac{\beta}{1+2\xi(1-\beta)}, \qquad N \approx P\tau \qquad (7.16)$$

When the pumping rate is increased, the number of excited atoms linearly increases before saturating above the threshold. This is quite a classical phenomenon. However, since the total number N_t of atoms is finite, saturation may occur for a pumping rate lower than originally expected. In order to convince oneself of the existence of such a possibility, it suffices to observe that, if ξ were smaller than 1/2, the asymptotic limit of N in the second relation (Eq. 7.15) would be higher than N_t. Since obviously such a situation is forbidden, the total inversion will be reached for a certain value of the pump power above which the output power of the microlaser will no longer increase.

On the other hand, the consideration of Eqs. 7.13 and 7.16 allows us to distinguish two different behaviours depending on the value of $2\xi(1 - \beta) = N_t\beta(1 – \beta)/\tau\varphi$ compared to unity. If $2\xi (1 - \beta)$ is lower than, or close to unity, the efficiency below threshold is directly proportional to β. Thus, any increase of β will lead to a decrease of the threshold pump power in approximately the same proportion. If $2\xi (1 - \beta)$ is larger than unity, it will be the predominant term in the denominator of P_{out} (Eq. 7.16). The β factor has a very limited influence not only on the evolution of $\bar{n}$, but also on the microlaser threshold and on the power efficiency below threshold. Actually, in order for β to have a stronger influence, its value needs to be very close to unity. It might be noted here that, for a value for $2\xi (1 - \beta)$ much higher than unity, the pump power at threshold (Eq. 7.13) can be approximated well by the formula $P_{th} = N_t(1 - \beta)/3\tau$. This corresponds to the particular case of standard laser diodes ($\xi > 1$, $\beta << 1$), where the two definitions for the lasing threshold ('$\bar{n} = 1$' and 'gain = loss') lead to estimates of the threshold pump power of the same order. More precisely, P_{th} is 1.5 times lower than the pump power needed for reaching the transparency threshold ($P_{th} = N_t/2\tau$).

The preceding remarks are not without practical implications. Indeed, for semiconductor lasers, $\log(\beta)$ is usually estimated from the amplitude of the 'step' observed in the experimental characteristic $P_{out}(P)$, presented on a logarithmic scale. It is quite clear that, in the case where $2\xi (1 - \beta) >> 1$, the value for β estimated from the measured characteristic will be erroneous. The previous discussion is illustrated in Fig. 7.3. The different possible behaviours of the laser are represented in Figs. 7.3*a* and 7.3*b*, with $N_t/\tau\varphi$ used as a parameter. Fig. 7.3*c* and 7.3*d* represent the corresponding evolutions of the number of emitted photons as a function of the injected pump power.

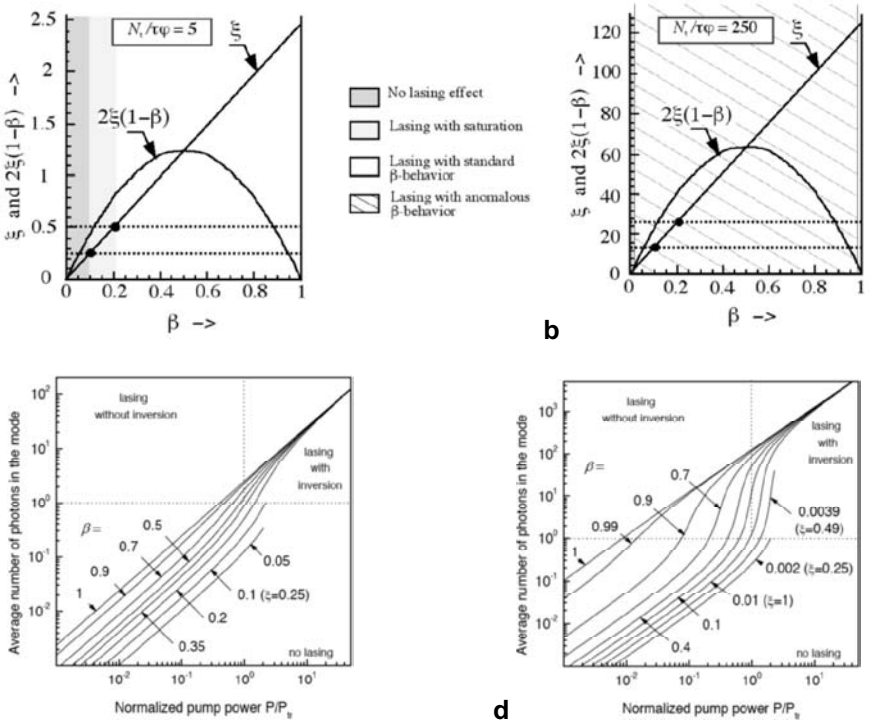

Fig. 7.3. *a.* and *b.* Evolution of ξ and 2ξ (1 - β) versus β for two different values for the parameter $N_t/\tau\varphi$ (*a.* $N_t/\tau\varphi = 4.5$ *b.* $N_t/\tau\varphi = 250$) and microlasers with different behaviours *c.* and *d.* The number of emitted photons as a function of the pump power, in this case the number of electron-hole pairs, for different values for β. The two cases *c* and *d* correspond to the two values for the parameter $N_t/\tau\varphi$ that were chosen in *a* and *b* respectively

Using this simple analytic model, different possible approaches towards the realization of a low-threshold microlaser can be developed:

– a first approach would be to use a true single-mode cavity (β = 1) based on a three-dimensional photonic crystal. This approach is conceptually very powerful: indeed, since ξ does no longer play any role in the equations previously described, it completely removes the constraint imposed on the number of emitters. The pump power at threshold by $P = \varphi$. Indeed, exciting one atom, or creating one electron-hole pair in a semiconductor over the damping time τ_{ph} of the cavity is sufficient for reaching the threshold condition $\bar{n} = 1$, since all the photons are emitted in this case into a single cavity mode. Assuming an emission wavelength around 1 μm and a realistic value for Q around 2000, the threshold would correspond to a pumping rate of 10^{12} electron-hole pairs per second, equivalent to an injection current of 0.16 μA.

– an alternative approach consists in removing the condition imposing a single-mode cavity, and in selecting a microcavity with a high β coefficient, for instance by exploiting the Purcell effect. In view of the remarks previously developed, it is essential to adjust the number of emitters, i.e. the size of the active medium for a semiconductor source, in order for ξ to be neither too large nor too small, while at the same time preventing the gain saturation problem to occur ($\xi > 0.5$). Let us for instance consider two different types of microcavities that will be presented in more detail in Section 7.2.1 of this chapter: first a GaAs/AlAs micropillar, with a 1 μm diameter and a quality factor Q around 2000, and then a microcavity formed by a two-dimensional photonic crystal with a ultimately small volume ($\sim 0.3\ (\lambda/n)^3$) and a quality factor of the same order ($Q = 2000$). Let us insert in each cavity a small fraction of a semiconductor quantum well with a surface of $0.3 \times 0.3\ \mu m^2$. This would correspond to inserting an equivalent number of emitters $N_t \sim 3000$ for a joint density of electronic states equal to $3\ 10^{12}\ cm^{-2}$. The linewidth of this ensemble of emitters, which is of the order of kT, is much larger than the linewidth of the cavity mode (0.6 meV for $\lambda \sim 1$ μm). Assuming the emitter to be in resonance with the cavity mode, the magnitude of the Purcell effect can then be calculated to be of the order of 0.8 for the micropillar, and to be of the order of 16 for the photonic crystal microcavity, since the latter presents a much smaller effective volume (equal to $F = F_p\ \Delta\omega_{cav}/\Delta\omega_{em}$, as has been shown in Section 7.1.2 of this chapter). Assuming the cavity mode to be non-degenerate in both cases, it turns out that $\beta = F/(F + \gamma) \sim 0.45$, $\tau \sim 0.5$ ns for the micropillar and $\beta \sim 0.93$, $\tau \sim 60$ ps for the photonic crystal cavity respectively, while on the other hand, a quality factor equal to 2000 leads to $\varphi \sim 10^{12}\ s^{-1}$. Finally, the values for the main parameters of the laser are $\xi \sim 1.5$, $2\xi(1 - \beta) \sim 1.6$ and $P_{th} \sim 0.3$ μA in the case of the micropillar, and $\xi \sim 27$, $2\xi(1 - \beta) \sim 0.89$ and $P_{th} \sim 0.4$ μA in the case of the photonic crystal cavity. At first sight, it might seem somewhat puzzling that the higher lasing threshold should be obtained for the cavity which actually displays the *largest* value for β. This however can be explained by the much larger value of the term $2\xi(1 - \beta)$ in the photonic crystal cavity. It can clearly be seen here that the optimization of the size of the active medium is an essential step in the design of a microlaser. Actually, reducing the surface of the quantum well down to $60 \times 60\ nm^2$ in the photonic crystal cavity would lead to $\xi \sim 1$ and $P_{th} \sim 0.17$ μA. The latter value is actually very close to the value $P_{th} = 0.16$ μA that would be obtained in the ideal case where $\beta = 1$.
– finally, a completely different approach consists in reducing as much as possible the amount of the cavity losses φ, at the price of a lower value for β. The experiments which have been conducted on silica microspheres are quite representative of this approach (Sandoghdar 1996). For this purpose, the active material, consisting for instance of rare earth atoms, can be embedded in the sphere itself. Another possibility consists in placing an external emitter in the evanescent field of the whispering gallery modes of the sphere. Lasing has been observed at room temperature for a microsphere coupled to a GaAs mesa structure containing a few hundred InAs quantum dots (Steiner 2007).

This discussion shows that the optimization of microlasers could lead to a significant reduction of the threshold current of semiconductor lasers, whose minimum value is currently of the order of 30 μA for the best vertical cavity surface emitting lasers (Huffaker 1997). Conversely, any further decrease of the threshold current will open new perspectives in the field of optical sensors, for instance for environmental or biomedical applications. Further, lasers with simultaneously high values for β, φ and $1/\tau$ could potentially operate at very high modulation frequencies. In order to turn these hopes into reality, it will be necessary to reduce non-radiative recombination processes down to a negligible level. In practice however, this poses a considerable challenge, and the same applies to the electrical pumping of such microstructures.

In this respect, the localization of electron-hole pairs in semiconductor quantum dots seems to be a very attractive method for limiting the diffusion of the charge carriers which takes place towards the defects and the free surfaces, and therefore for reducing the efficiency of the non-radiative recombination processes (Gérard 1996a). For the purpose of discussing the feasibility and potential performances of quantum dot microlasers, let us first consider a microcavity containing an ensemble of quantum dots. At low temperatures, a single quantum dot exhibits a spectrally narrow emission with a typical width of a few μeV in the case of InAs/GaAs quantum dots. Due to their size dispersion, the different quantum dots are more or less in resonance with the cavity mode, and therefore they experience a more or less strong Purcell effect. In turn, the average β factor becomes much smaller than unity when the linewidth of the cavity mode becomes spectrally narrower than the inhomogeneously broadened emission linewidth of the ensemble of quantum dots. The situation is quite different at room temperature, this being due to the strong *homogeneous* broadening in this case of the emission lines of individual quantum dots, which may range from 5 to 10 meV for InAs dots. Assuming a typical value for the inhomogeneous broadening of state-of-the-art quantum dot ensembles (15 meV for InAs quantum dots), it can be seen that a large fraction of the quantum dots contributes to the lasing mechanism.

For a photonic crystal cavity with a volume of $0.3\,(\lambda/n)^3$ and a quality factor equal to 2000, it can be readily demonstrated that a few hundred quantum dots would be necessary for reaching the lasing effect. Having such a large number of dots in so small a cavity could be quite prohibitive in terms of fabrication, since the surface density of quantum dot layers with a good homogeneity is typically of the order of 100 μm^{-2} in the best of cases. From this point of view, the recent improvements in the quality factor Q of photonic crystal microcavities (Akahane 2003) represents a real opportunity. Indeed, the number of emitters required for lasing varies in inverse proportion to the Q factor, and a lasing effect can be reasonably expected in view of the standard level of fabrication of quantum dots.

Let us finally consider a system formed by a single quantum dot in a microcavity. In such a system, lasing can be achieved only in the low temperature regime, where the homogeneous linewidth of the quantum dots becomes sufficiently narrow. In the same way as for micromasers or single-atom lasers (Meschede 1985), quantum fluctuations play a key role in the operation of such a device, and sophisticated quantum models, which would be beyond the scope of the present book,

are necessary for properly describing them. However, our general discussion of microlasers may help us to understand the two main approaches that are currently being investigated for the fabrication of single quantum dot lasers. In the first case, the single quantum dot is coupled to a cavity with a very high quality factor Q and a low loss rate φ. A threshold current as low as 10pA has been predicted for such a system (Pelton 1999). According to the second approach, the laser would be operating in the regime of a very strong Purcell effect (see Section 7.1.2 in this chapter) thanks to the use of a semiconductor microcavity (Gérard 2003). In order to reach the lasing threshold, the emission rate into the cavity mode must be higher than the photon loss rate. We therefore have $1/\tau > \varphi$, whence it follows that $\Delta\omega_{cav} < \Delta\omega_{em}$. If the linewidth $\Delta\omega_{em}$ of the emitter itself is smaller than the Rabi frequency Ω, the system formed by the quantum dots and the cavity will experience a strong-coupling regime (see Section 7.1.2). Let us therefore assume that this regime has been achieved at a low temperature. By increasing the temperature, excitonic dephasing can be progressively increased up to the point where the Rabi oscillation disappears ($\Delta\omega_{em} \sim \Omega$). In such a 'critical' regime, the radiative lifetime τ is of the order of half the period of the unperturbed Rabi oscillation, and is therefore much smaller than the photon lifetime in the cavity $1/\varphi$. In other terms, the quantum-dot-cavity system after emitting a photon is able to emit a second photon before the first one leaks out of the cavity. Single quantum-dot lasing can thus be achieved. Such a laser would operate through the very strong enhancement of the spontaneous emission rate of the quantum dot, and β would therefore be very close to unity. By further increasing the temperature, thereby by reducing the magnitude of the Purcell effect, one would reach a regime where $1/\tau < \varphi$, and therefore lasing would become impossible. In the intermediate regime, a number of original effects are expected to occur. The blinking of the laser emission caused by the fluctuations of the number of charges in the quantum dot is an example of such an effect that would be observable under strong injection conditions. As a first step in this direction, lasing sustained by a few (2-4) quantum dots has been reported for photonic crystal microcavities (Strauf 2006). Interestingly enough, lasing in this experiment was achieved in spite of a detuning between the cavity mode and the fundamental transition of the quantum dots. A homogeneous broadening of the quantum dot transitions under high optical excitation is the key condition for providing gain at the mode energy (Favero 2007). At this stage, the possibility of realizing microcavities containing a single quantum dot (Badolato 2005) will contribute to improving our understanding of lasing mechanisms in few quantum-dot and single quantum-dot lasers.

7.2 Three-Dimensional Optical Confinement in Zero-Dimensional Microcavities

7.2.1. Different Types of Zero-Dimensional Microcavities[1]

Considerable efforts have been devoted during the 1990s towards the development of cavities allowing the confinement of light at the wavelength scale and thus the investigation of cavity quantum electrodynamics (CQED) in solid state systems. For this purpose, two basic phenomena can be used, either alone or in combination. The first is the phenomenon of total internal reflection, used for achieving three-dimensional confinement in microspheres (Braginsky 1989), in microtorus (Armani 2003; Vahala 2003) and in microdisks (Mc Call 1992). The second phenomenon is the distributed Bragg reflection, implemented in one-dimensional dielectric mirrors and more generally in photonic band gap crystals. In micropillars (Jewell 1989), three-dimensional confinement is achieved by a combination of guiding along the axis of the pillars and reflection by one-dimensional Bragg mirrors. By contrast, two-dimensional photonic crystal membranes combine a guiding in the semiconductor slab and a lateral confinement by the photonic crystal. While the highest Q factors have been obtained with microspheres and with microtorus, microdisk, micropillar and photonic crystal microcavities exhibit the smallest volumes V. As will be seen, photonic crystal cavities provide a very attractive combination of high Q and small volume V, with $Q \sim 10^6$ being clearly in a wavelength-scale volume $((\lambda/n)^3)$. Further, these devices can be fabricated using available semiconductor technologies, which opens the perspective of large-scale integration in applications. In what follows, we shall focus on semiconductor microcavities. Different examples of such microcavities are represented in Fig. 7.4. These cavities are not perfect 'photonic boxes' in the stricter sense of the term, because they present a continuum of non-resonant or leaky modes in addition to a discrete series of electromagnetic modes confined along all directions of space. Only the use of three-dimensional photonic crystals would allow the total suppression of leaky modes. Chapter 12 in this book will be devoted to three-dimensional crystals, and more particularly to the advances which have taken place since the pioneering experiments of E. Yablonovitch in the fabrication of these crystals at optical wavelength scales. This being, it should be noted that remarkable results have already been obtained with each of the microcavities represented in Fig. 7.4, both in terms of high Q factors and of small volumes.

[1] A three-dimensional optical confinement results in zero-dimensional microcavities presenting a discrete series of resonant electromagnetic modes, possibly accompanied by a continuum of non-resonant modes. These two terms will be used indifferently in this section.

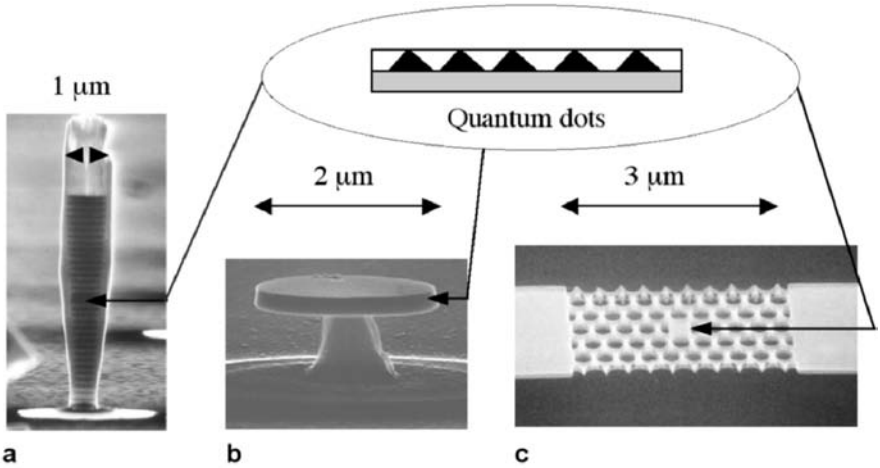

Fig. 7.4. Micrographs of different optical microcavities fabricated at the '*Laboratoire de Photonique et de Nanostructures*' (LPN) in Marcoussis, France *a.* Micropillar *b.* Microdisk *c.* Two-dimensional photonic crystal cavity (Gérard 1999b). Quantum dot layers are incorporated in each cavity. A schematic representation of such a layer is displayed at the top of the figure. The (Q, V, F_p) figures of merit for state-of-the-art active cavities containing quantum dots are respectively (8000, 11 $(\lambda/n)^3$, 54) for micropillars (Sek 2006), (12,000, 6 $(\lambda/n)^3$, 150) for microdisks (Gayral 1999) and (20,000, $(\lambda/n)^3$, 1500) for photonic crystal cavities (Yoshie 2004)

To a large extent, these results were made possible by the fact that 'artificial atoms', i.e. semiconductor quantum dots, can be easily embedded in these cavities, which facilitates their characterization and optimization (Gérard 1996b). Semiconductor quantum dots are generally obtained through a self-organization process. The latter typically occurs during the growth of a thin epitaxial layer exhibiting a strong lattice mismatch with the substrate. Quantum dots have a typical volume of 10^2 - 10^3 nm^3, and they exhibit a high size dispersion. Although the linewidth of an individual quantum dot is relatively narrow in the temperature range of a few Kelvin ($\Delta E \sim 1$ μeV), the luminescence of a quantum dot layer might cover a very broad spectral range. In other terms, an ensemble of quantum dots forms a broadband source with negligible intrinsic absorption losses. Such an internal source is ideally suited for probing the optical properties of quasi-empty microcavities of the kind represented in Fig. 7.4.

Micropillars

Micropillars have received much attention since the first realizations of vertical cavity surface emitting lasers. The possibility that these structures might exhibit interesting features for the enhancement of the spontaneous emission rate and for low-threshold lasing was recognized at the beginnings of the 1990s. In the exam-

ple represented in Fig. 7.4*a*, the micropillars were fabricated by the reactive ion etching (RIE) of a GaAs/AlAs λ-cavity. The cavity was resonant at 0.9 μm, while the radius of the cylinders was varied typically between 1 and 10 μm. Actually, for micropillars with a sufficiently large radius, the mode energies can be quantitatively understood by using a simple model based on the decoupling of the vertical and lateral confinements. The guided photons are vertically confined by the distributed Bragg reflection, but their velocity is modified owing to the lateral confinement. In practice, the resonance condition is the same as for planar microcavity, provided however that the index of the active semiconductor layer be replaced with the effective index of the guided mode (Gérard 1996b). However, for narrow micropillars ($r < 1$ μm), this model turns out not to be adequate, due in particular to the inter-mode coupling which occurs between the guided modes at the interfaces (Lalanne 2004). In such cases, full vectorial electromagnetic calculations are necessary in order to analyse the modal properties of the cavity (Lecamp 2005; Vuckovic 2002b).

Actually, experimental results have revealed that Q decreases for micropillars with a radius smaller than ~ 3 μm (Rivera 1999; Sek 2006; Tezuka 1993). This evolution can be readily explained by the significant roughness of the sidewalls of the pillars. In this respect, the optimization of the fabrication process, and more specifically of the dry etching step, has led to substantial advances, and values for Q as high as 8000 and 30,000 have been reported for a 1.5 μm diameter and a 4-10 μm diameter respectively (Sanvitto 2005; Sek 2006).

The luminescence spectrum of quantum dots embedded in micropillars is typically composed of a series of narrow peaks, associated with resonant modes, and of a broad pedestal, associated with the continuum of non-resonant modes. The influence of the cavity on the emission properties of the quantum dots can then be directly revealed by time-resolved photoluminescence experiments of the kind described in Section 7.2.2. A shorter luminescence decay time, i.e. a shorter lifetime of the excitons, will be observed for quantum dots whose optical transition coincides with a resonant mode.

Microdisks

Semiconductor microdisks of the kind represented in Fig. 7.4*b* allow the propagation of whispering gallery modes. These modes are guided towards the periphery of the microdisk by a phenomenon of total internal reflection, which results in a strong confinement of light (Chang 1996). Microdisks are generally fabricated by using two different types of etching: the semiconductor multilayer at the top of the substrate is etched by RIE into a cylindrical post, while the pedestal of the disk is fabricated by the selective wet etching of a sacrificial layer (Baba 1997; Gayral 1999; Michler 2000c; Mohideen 1994; Slusher 1993). Microdisks provide a more efficient three-dimensional confinement than micropillars, where resonant modes are partially localized, both in the periphery of the cylinder and in the Bragg mirrors. For a microdisk with a small radius ($\lambda/n < r < 20\lambda/n$), the effective surface of the whispering gallery mode with lower quantum radial number is approximately given by $0.86\,\lambda^2(r/\lambda)^{3/2}$, where the different lengths are expressed in mi-

crons (Gérard 1999). The effective vertical thickness h_{eff} of the gallery mode can be estimated by considering the field distribution of the guided mode of the air-confined semiconductor slab which forms the microdisk. For a 250 nm thick GaAs slab, h_{eff} is equal to 175 nm, i.e. to approximately $0.6\,\lambda/n$ in the case where the wavelength is of the order of 1 μm. One finally obtains an effective mode volume equal to $\sim 6\,(\lambda/n)^3$ in the case of a microdisk with a 1 μm radius. Values for Q as high as 20,000, limited by the absorption of the quantum dot array, have been theoretically predicted for such a radius, in spite of the absorption of the quantum dots embedded in the plane of the microdisk. Values for Q equal to 12,000 (Gayral 1999) and to 17000 (Michler 2000c) were experimentally measured for radii equal to 0.9 μm and 2.25 μm respectively. However, it can be noted that significantly higher values can be observed when considering empty cavities. A value for Q equal to 360,000 for a 2 μm radius has thus been estimated from a transmission experiment performed with state-of-the-art GaAs microdisks (Srinivasan 2005). As is the case for micropillars, the photoluminescence spectrum of microdisks reveals narrow peaks due to resonant modes and a broad pedestal associated with leaky modes. A high number of whispering gallery modes associated with the different radial indexes and with the different polarizations can actually be observed. Microdisks are excellent candidates for the study of the Purcell effect in solid state microcavities, as well as for the demonstration of the thresholdless laser or of the strong coupling between light and a quantum dot (see Sections 7.1.2 and 7.2.4 in this chapter).

The most common limitation of microdisks, i.e. the roughness of the edge wall, can be overcome in the specific case of silica disks. Thus, the Q factor of a microtorus can be brought to extremely high values by remelting it with a laser pulse (Armani 2003, 2005; Rokhsari 2005). A number of textbook experiments highlighting extreme aspects of the interaction of light with bulk matter or with interfaces could be carried out on these systems, ranging from optomechanical effects to backscattering and mode splitting or Raman radiation pumping. Laterally coupling an ultra-high-Q microtorus to a fibre also provides a test of photonic tunnelling behaviour over several decades.

Photonic Crystal Microcavities

Until now, three-dimensional confinement in photonic crystal structures has been achieved by designing one-dimensional photonic crystal cavities (Cluzel 2006; Foresi 1997) and, more commonly, two-dimensional photonic crystal cavities, as represented in Fig. 7.4*c*. Both methods rely on a combination of guiding in a semiconductor slab and reflection on photonic crystal mirrors integrated in the slab. New perspectives in integrated optics (see Chapter 9) have stimulated research in these directions. On the other hand, the light line concept introduced in Chapter 5 finds here an interesting application. For the sake of consistency throughout this chapter, we shall briefly outline recent developments in this very active area of research. Attention will be focused on its potential for the fundamental control of light-matter interaction rather than on device applications.

Earlier attempts (Labilloy 1998; Painter 1999a; Vuckovic 2001) involved the 'substrate' approach as well as the 'membrane' approach. As an example, Fig. 7.4*c* represents the scanning electron microscope image of an early two-dimensional photonic crystal microcavity fabricated in a suspended GaAs membrane. The parameters were chosen in such a way as to obtain resonant modes near 1.5 μm (Gérard 1999b). The membrane was used there as a planar waveguide, with the photonic crystal ensuring confinement along in-plane directions. In 2002-2003, it definitely appeared that membrane or air-bridged photonic crystal cavities offered the greatest opportunities for very-high and ultra-high Q values, provided however that the cavities be designed with great care. Contributions by the research group led by S. Noda signalled the emergence of truly low-loss systems. They raised the record to $Q \sim 45{,}000$ in 2003 (Noda 2003) and to 600,000 in 2005 (Song 2005), eventually pushing the limit to $Q \sim 10^6$, which remains unsurpassed since 2006 (Kuramochi 2006). These landmark contributions have signalled the advent of a new era for photonic crystals, which has gained increased credibility for the ultimate control of zero-dimensional confinement.

By allowing the translation of the k-spectrum of localized modes outside the light cone, k-space engineering was instrumental in these advances, and a more detailed account of this method will be offered in Chapter 9. The small mode volume in these photonic crystal systems is of course primarily based on the good vertical confinement ensured by the membrane. As will be reported in Section 9.8.3 of Chapter 9, it came as a surprise that localized modes based on 'shallow' defects, and therefore with a modal profile very close to that of the surrounding crystal, could nevertheless feature extremely small volumes. In addition to experimental studies (Song 2005), an approach toward more deterministic designs than the semi-intuitive approach developed by S. Noda has been proposed in (Englund 2005a).

The combination in the photonic crystal membrane of a strong vertical confinement with a limited penetration of the field in the surrounding photonic crystal allows the formation of defect modes with an effective volume which can be as small as 0.3 $(\lambda/n)^3$ and generally is less than $(\lambda/n)^3$, even for the highest Q modes. After the turn of the millennium, a first series of successes led to the demonstration of sufficiently low out-of-plane losses, obtained using k-space engineering (Vuckovic 2001). For GaAs systems, experiments conducted with state-of-the-art microcavities suceeded in achieving quite impressive figures of merit ($V_{eff} = (\lambda/n)^3$, $Q = 20{,}000$). These results were followed by the demonstration of the highest Purcell factors for all-solid-state microcavities ($F_p = 1500$) (Yoshie 2004). While the highest figures of merit reported to date have been obtained with Si systems (Kuramochi 2006), the promises offered by the future development of III-V semiconductor-based photonic crystal microcavities have been substantiated with the realization of an ultra-high Q cavity mode ($Q \sim 250{,}000$) using a cavity based on the design developed by Noda, but defined in a GaAs membrane (Weidner 2006). As will be seen in Chapters 8 and 9, the high Q values exhibited by all types of microcavities is highly favourable for nonlinear light-matter interaction, whether nonlinearity is of a thermal nature or whether it is due to charge carriers in semiconductors, etc.

As a summary, all zero-dimensional semiconductor microcavities described here provide a much stronger confinement than silica microspheres (V_{eff}= 1000 $(\lambda/n)^3$, $Q = 10^9$) (Collot 1993) and toroid microcavities ($Q = 10^8$) (Armani 2003). Until recently however, the quality factor of semiconductor microcavities was lower by more than five orders of magnitude, even if it was optimistically expected that their small volumes would compensate for this much lower quality factor in the context of CQED experiments. As has been mentioned above, the difference between the Q values of semiconductor and silica microcavities has been reduced to less than 1000, and very high Purcell factors ($F_p >> 1000$) can now be expected from semiconductor cavities. The lower Q-factor (10^4-10^6) of semiconductor cavities compared to silica microspheres and toroid microcavities might even turn out as an advantage, since it relaxes the constraints imposed on the linewidth of the emitter and thus enlarges the variety of emitters which can be used, including for instance quantum wells or quantum dots operated at room temperature. The same argument applies when comparing photonic crystal microcavities to other types of semiconductor microcavities. For applications at room temperature, photonic crystal microcavities with an ultimately small mode volume have a much higher potential than microdisks or micropillars. However, in order that this potential can be fully realized, the non-radiative carrier recombination occurring at the air/semiconductor interfaces will have to be mastered.

7.2.2 Control of the Spontaneous Emission in Weak Coupling Regime. Some Experimental Results

As has already been mentioned in Section 7.1.1 of this chapter, planar microcavities formed by distributed Bragg reflectors modify only marginally the spontaneous emission rate of embedded emitters. This is due for the most part to the penetration of the electromagnetic field in the mirrors, which results in an increase of the effective length of the microcavity. For instance, in the case of the GaAs/AlAs system, a cavity with a 'physical' length equal to λ/n results in a total effective length close to $4\lambda/n$. The measurements of the time-resolved photoluminescence of InAs quantum dots embedded in such a microcavity has revealed only limited variations of the radiative lifetime of quantum dots, which is consistent with theoretical predictions. Indeed, this lifetime turns out to increase or decrease at most by 20%, depending on whether the optical transition energy of the quantum dots is higher or lower respectively than the resonance energy of the microcavity at normal incidence (Bayer 2001). Similar results have been reported for rare-earth atoms embedded in SiO_2/TiO_2 dielectric microcavities (Vredenberg 1993).

At this point, it might be noted that a strongly enhanced luminescence decay rate (×2) had previously been observed for quantum wells and for organic dye molecules embedded in planar cavities (Suzuki 1991). Contrary to quantum dot arrays or to the collections of rare earth-atoms used in the experiments reported above, emitters of this type cannot be considered as being independent light emitters. In this case, the faster luminescence decay rate is due actually to such collective effects as superradiance or stimulated emission.

To this date, the most successful approach towards the observation of a strong enhancement of the spontaneous emission rate (or Purcell effect) for solid state emitters is based on the combination of a zero-dimensional microcavity, in the form for instance of a micropillar or of a microdisk, with semiconductor quantum dots (Gérard 1998). Experiments have been conducted either on ensembles of quantum dots, or on isolated single quantum dots at sufficiently low temperature (5-77K), in order to ensure the monochromatic emission of each of the quantum dots. In the first case, the cavity mode collects the emission from a large number of quantum dots, each with a specific spontaneous emission rate, which depends both on the location of the quantum dot inside the cavity and on its frequency detuning with respect to the cavity mode. At first sight, this might be considered a disadvantage, since the average magnitude of the Purcell effect is much lower than that of a single quantum dot ideally located in the cavity and ideally tuned to the cavity mode. However, this property actually turns out to be an advantage when experimental results are to be quantitatively interpreted. For large ensembles of quantum dots, the average Purcell effect can indeed be modelled from the spatial and spectral statistical distribution of the emitters. By contrast, experiments conducted on single quantum dots should be analysed with much caution, since the exact location of the quantum dot in the cavity is generally either unknown or very poorly known. The experimental results that will be presented in the following will illustrate how complementary these approaches are in practice (Solomon 2001).

In Fig. 7.5*a* are represented photoluminescence decay curves obtained for a collection of quantum dots in a high-F_p (F_p = 32) GaAs/AlAs pillar microcavity. As mentioned in Section 7.2.1 of this chapter, the photoluminescence spectrum consists of a series of sharp peaks corresponding to the resonant cavity modes, and of a weak background emission associated with the emission of quantum dots in the continuum of the non-resonant pillar modes. A multispectral time-resolved setup, based on a streak camera, is used for simultaneously measuring the decay rates of the different types of quantum dots, whether they are in or out of resonance with the fundamental mode of the micropillar. For quantum dots out of resonance with the fundamental mode, the decay rate is very similar to the radiative lifetime of similar InAs quantum dots in a bulk GaAs matrix. By contrast, the photoluminescence decay time is reduced by a factor of 5 for the dots that are in resonance with the fundamental mode of the cavity. This selective reduction of the lifetime of the quantum dots in resonance with this mode confirms the intrinsic nature of the underlying phenomenon, and is a very clear indicative of the Purcell effect. Similar studies conducted for different types of micropillars (Fig. 7.5*b*) have shown that this enhancement of the luminescence decay rate is a function of the Purcell figure of merit F_p defined by Eq. 7.8. More precisely, all these results can be quantitatively interpreted by taking into account the spectral and spatial statistical distributions of the quantum dots with respect to the cavity mode (Gérard 1998, 2003).

Increasing the spectral resolution in the previous experiment also provides an opportunity of studying the dependence of the Purcell effect on the spectral detuning with respect to the mode. As might have been expected from Section 7.1.2, the

enhancement factor of the spontaneous emission rate follows a Lorentzian evolution (see Eq. 7.5), which reflects the contribution of the fundamental mode to the spectral density of modes in the pillar microcavity.

Due to their high Purcell factor, microdisks allow the observation of even greater modifications of the spontaneous emission rate for quantum dots in resonance with a whispering gallery mode. An average enhancement factor of the order of 12 was thus observed for a 1.8 μm diameter microdisk with $Q = 10{,}000$ and $F_p = 160$ (Gayral 2001). Interestingly enough, the radiative lifetime would be about 10 ps for a single quantum dot ideally coupled to the cavity mode. It might also be noted that, for correctly modelling the experiments, it is necessary to take into account the finite value of the relaxation time of the electron-hole pairs injected from the GaAs barrier states to the quantum states of the dots (~30 ps).

Time-resolved photoluminescence experiments have been extended to the case of single quantum dots by embedding, in a micropillar or in a microdisk, a very dilute quantum dot array with a surface density no higher than a few $10^9\,\mathrm{cm}^{-2}$ (Moreau 2001b; Solomon 2001). Here again, the enhancement effect was selectively observed for the isolated quantum dots that were resonantly coupled to a cavity mode. An even more spectacular demonstration of the Purcell effect can be achieved by tuning the energy of a single quantum dot with respect to the mode energy, for instance by varying the temperature of the sample. Following this approach, the spontaneous emission rate of a single quantum dot in a microdisk was found to be enhanced by a factor as high as 6 (Kiraz 2001). Further experiments conducted in the same spirit with micropillars and photonic crystal cavities have highlighted spontaneous emission rate enhancement factors as high as 23 and 28 (Hennessy 2007; Laurent 2005; Varoutsis 2005)

Finally, the Purcell effect can also be demonstrated in a rather simple way by studying the photoluminescence signal as a function of the pump power for a continuous non-resonant excitation of the sample. The emission associated with the fundamental optical transition of a single quantum dot, or a set of quantum dots with identical band gaps, tends to saturate when the first levels in the conduction and valence bands of the dots are completely filled. It is quite obvious that the pumping power required for inducing this saturation effect will be all the higher that the radiative lifetime of the quantum dots is short. Assuming the pumping efficiency to be the same for all quantum dots, be they in or out of resonance, the presence of a Purcell effect results for the different groups of quantum dots in very different evolutions of the photoluminescence signal with respect to the excitation power. Using this approach, an enhancement factor of the spontaneous emission rate close to 18 has thus been observed for InAs quantum dots in a GaAs microdisk (Gayral 2000). This method has also allowed the first observation of a Purcell effect (×10) for an array of quantum dots in a two-dimensional photonic crystal microcavity ($Q = 680$, $F_p = 19$) (Happ 2002).

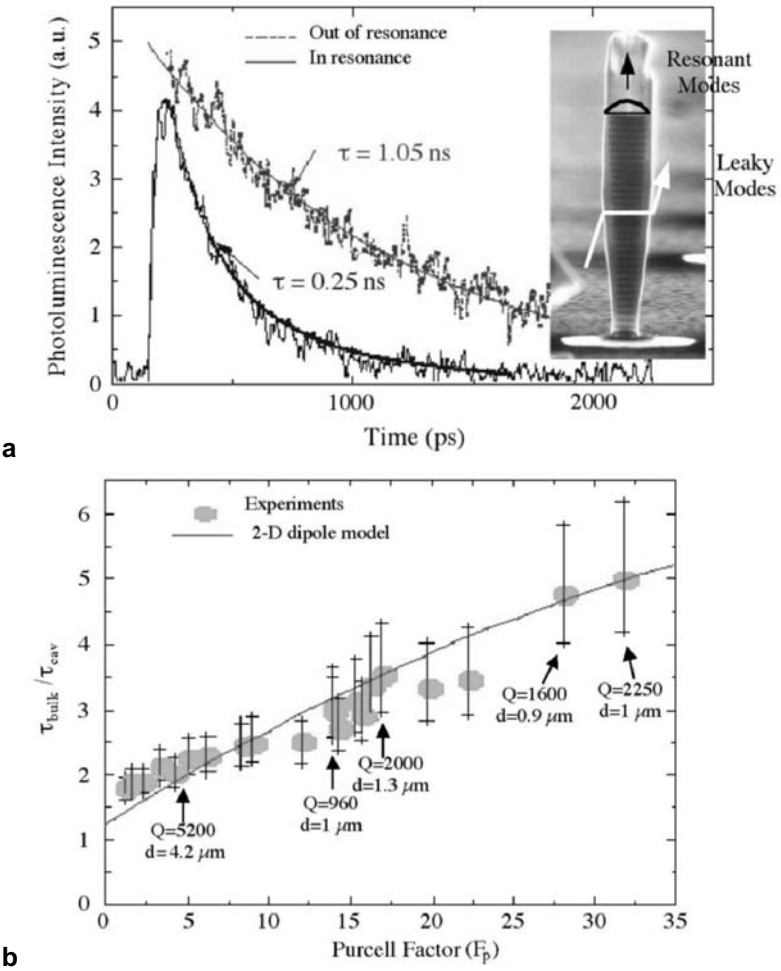

Fig. 7.5. *a.* Time-resolved photoluminescence (PL) signals measured for two groups of quantum dots in a circular micropillar (d = 1 μm, Q = 2250, F_p= 32). The dots in the first group are resonant with the fundamental cavity mode, and exhibit the fastest photoluminescence decay. The dots in the second group are out of resonance and exhibit the slowest photoluminescence decay *b.* Experimental evolution of the relative photoluminescence decay rate τ_{bulk}/τ_{cav} versus the estimated Purcell factor F_p (ovals). The diameter d of the micropillars and the quality factor Q of the cavity are reported for some of the micropillars. The error bars correspond to a time uncertainty of 70 ps relative to τ_{cav}. The solid curves represented in ***a*** and ***b*** were calculated for resonant quantum dots under the assumption that these dots were arbitrarily located in the cavity plane and that their emission frequencies were arbitrarily positioned with respect to the cavity mode frequency. It was further assumed that the emitting dipoles were oriented in the plane and that the relaxation time of the carriers injected in the quantum dots was equal to 35 ps (Gérard 1998, 2003)

The search for spontaneous emission inhibition in semiconductor microcavities presents quite a different challenge than the demonstration of a Purcell effect, because it requires a global reduction of the density of leaky modes in the cavities. In the case of micropillars, this can be achieved for instance by depositing a metallic coating on the sidewalls of the pillars. In a pioneering experiment, the spontaneous emission rate of off-resonance quantum dots has been observed to decrease of approximately one order of magnitude ($\gamma \sim 0.1$), while at the same time the quantum dots that were in resonance with one of the cavity modes displayed the Purcell effect ($F \sim 2.2$) (Bayer 2001). Spontaneous emission inhibition had been observed earlier for quantum wells embedded in a planar cavity defined by metallic metals, below the cut-off for the fundamental TE mode. However, the magnitude of the inhibition ($\gamma \sim 0.6$) was limited in this case due to coupling to the plasmon modes of the mirrors (Bourdon 2000). With the exception of these two attempts involving metals, most experiments have been conducted on photonic crystal structures and cavities. In the same spirit as the scheme originally proposed by Yablonovitch (Yablonovitch 1987), inverse opal three-dimensional photonic crystals have been used to inhibit the spontaneous emission of semiconductor nanocrystals (Lodahl 2004). Experiments have also been conducted with self-assembled quantum dots in two-dimensional photonic crystals. Although they do not display a complete photonic band gap, two-dimensional photonic crystals are highly reflective, and therefore they suppress non-resonant modes over a very large solid angle for laterally propagating light. Strong spontaneous emission inhibition has been observed for collections of InAs quantum dots ($\gamma \sim 0.5$) (Kress 2005) as well as for single quantum dots ($\gamma \sim 0.2$) (Badolato 2007; Englund 2005b) in two-dimensional GaAs photonic crystals.

7.2.3 Single-Mode Coupling of the Spontaneous Emission

A major incentive for the studies conducted during the early 1990s on semiconductor micropillars was the theoretical prediction of a ‘quasi-single-mode’ behaviour of the spontaneous emission ($\beta \rightarrow 1$) within the limit of small pillar diameters and narrow linewidth emitters (Baba 1992). This behaviour can be simply seen as a consequence of the Purcell effect, which selectively enhances the spontaneous emission rate into the resonant micropillar mode and provides a dynamic channeling for the majority of the photons emitted in this mode (Gérard 1998). As has been previously discussed in Section 7.1.2, this effect might be of interest for the development of very-low threshold lasers, and ideally of thresholdless lasers. In the case where the resonant mode of the cavity is non degenerate, Eq. 7.10 leads to $\beta = F/(F + \gamma)$, where γ/τ_0 is the spontaneous emission rate in the continuum of leaky modes, and F/τ_0 is the spontaneous emission rate in the resonant mode, enhanced by the Purcell effect. In the case of micropillars based on GaAs/AlAs Bragg mirrors with a relatively low contrast index, the γ term has been found, both theoretically and experimentally, to be close to unity, with the consequence that β assumes a high value as soon as the Purcell effect becomes pronounced. Among the most spectacular results reported for micropillars of this type, the results ob-

tained by E. Moreau *et al* (Moreau 2001b) and S. Santori *et al* (Santori 2002) deserve a particular mention, since the number of InAs quantum dot emitters was sufficiently low for spectrally resolving the emission of each individual dot. In these experiments, the polarization degeneracy of the fundamental mode was lifted thanks to the use of micropillars with non-circular (e.g. elliptical) cross-sections or, in other terms, by resorting to the use of a form 'birefringence' (see Chapter 8 for more detail). Low-temperature time-resolved photoluminescence measurements performed on the quantum dots yielded $(F + \gamma) \sim 5$ for the dots that were optimally coupled to the resonant mode, while the value for γ was estimated from the emission of non-resonant dots to be near unity. These measurements then led to $\beta \sim 0.8$.

The results discussed above represent an important advance in comparison to those previously achieved with more conventional cavities, where the fundamental mode displays a degeneracy. This degeneracy might be due either to a polarization effect, for instance in the case of micropillars with a circular cross-section, or to a propagation effect, as is the case for microdisks, where two counterpropagating whispering gallery modes may coexist. Indeed, the spontaneous emission rate $\beta = F/(2F + \gamma)$ in these standard microlaser structures reaches at most 0.5 in the strong enhancement regime ($F >> 1$) due to the identical coupling of the emitters with each of the two degenerate cavity modes, which is the usual case for semiconductor emitters. It might also be mentioned that the search for high β values has led to a more efficient control of the polarization of quantum dot emitters. For instance, InAs/GaAs quantum dots have an optical dipole parallel to the plane of the layers, which statistically presents the same amplitude along all directions in this plane. Therefore, when such dots are inserted in a bulk GaAs layer, the emission collected at normal incidence is essentially unpolarized. The same applies to InAs quantum dots in a micropillar with a circular cross-section, this being due to the identical coupling to the two degenerate and cross-polarized fundamental modes. For micropillars with an elliptic cross-section, the degeneracy is lifted, and the fundamental modes are linearly polarized, either along the long axis and or along the short axis of the ellipse. As a result, a very strong linear polarization degree (> 90%) was experimentally observed for the emission of single quantum dots in resonance with either of these modes. The polarization of the quantum dot emission results from the fact that the Purcell effect induces a preferential coupling of these dots to a single linearly-polarized cavity mode. This effect has been exploited for the realization of a source of linearly-polarized single photons. For more detail on this subject, the reader is referred to Chapter 10 of this book and to (Moreau 2001).

As will be discussed in more detail in Chapter 10, the direct measurement of the efficiency of a single-photon source appears as an alternative approach for experimentally probing β. The possibility of actually achieving high values for β in the regime of a strong Purcell effect has thus been vindicated by experimental results on single-photon sources based on quantum dots.

Finally, it might be noted that experimental values for β reported in the literature are much higher for quantum dot single photon sources than they are for quantum well microlasers, for instance vertical cavity surface emitting lasers,

where $\beta \sim 0.04$ (Kuksenkov 1997), microdisk lasers, where $\beta \sim 0.2$ (Slusher 1993) or photonic crystal lasers, where $\beta \sim 0.1$ (Ryu 2004) or $\beta \sim 0.25$ (Park 2004). The reason can be found in the fact that the homogeneous broadening of the emission line of the quantum wells is too strong for allowing any significant enhancement of the spontaneous emission rate by the cavity, especially under the injection conditions attained above the laser threshold. In such structures, the enhancement of the β factor compared to conventional edge-emitting diodes ($\beta \sim 10^{-5}$) is due for the most part to geometrical factors. For microcavities with a comparable geometry, significantly higher β factors can be obtained by using quantum dots at a low temperature as emitters, instead of quantum wells. The narrow band emission of these quantum dots is here the key factor which permits to fully benefit from the Purcell effect for efficiently channelling the emitted photons into the resonant cavity mode.

The observation of such high values for β in quantum-dot microlasers would obviously be of great interest in view of potential application to microlasers. The most direct approach to measuring β in such devices consists in studying the input/output characteristic curve in the vicinity of the laser threshold. In usual cases, the average β factor is strongly reduced, due to both the dispersion of quantum dot band gaps and the homogeneous broadening of quantum dot emissions under high excitation. Values for β in the 20% range have thus been measured for optically pumped micropillars containing a few tens of quantum dots (Reitzenstein 2006). Higher values can be obtained when the gain is predominantly provided by a single quantum dot (Strauf 2006). While a more refined modelling of such a laser remains to be developed, values for β in the 90% range can be derived from simple estimates. These results are most probably explained by the suppression of the detrimental effect caused by inhomogeneous broadening. Recent developments in the field of solid-state microcavity lasers will be presented in more detail in Sections 10.5 and 10.6 of Chapter 10.

7.2.4 Towards Strong Coupling Regime for Solid State 'Artificial Atoms'

Extensive studies have been devoted to the strong coupling of excitons and photons in planar microcavities since the first observation of this phenomenon in 1992 in the case of an active medium consisting of semiconductor quantum wells (Weisbuch 1992). In such a two-dimensional system, both the photonic modes and the excitonic states form continuous bands. However, a coupling between excitions and photons occurs only if the in-plane wave vector is conserved for the optical transition (see Section 7.1.2 in this chapter). This condition ensures the coupling of a given excitonic state to a single photonic mode. It is now clearly established that the properties of this system cannot be properly described save by taking into account the formation of the mixed exciton-photon states, i.e. the cavity polaritons. However, the analogy with the physics of a single atom in a microcavity is limited by the fact that polariton states form bands. For this reason, the dynamic properties of the system are dominated by such scattering processes as

the elastic interactions between polaritons or the inelastic interactions with phonons.

In order to obtain a solid state system that, from a conceptual point of view, would be closer to the 'single atom in a cavity' model of CQED systems, an attractive approach consists in inserting a discrete solid state emitter in a zero-dimensional microcavity. Here again, single quantum dots are the best candidates for such experiments. As will be briefly discussed below (Peter 2005; Reithmaier 2004; Yoshie 2004), experimental demonstrations of a strong coupling regime for such artificial atoms pave the way towards decisive breakthroughs for the development of solid state CQED. Besides the possible realization of single quantum dot lasers (see Section 7.1.2 in this chapter), this will pave the way to the development of novel optoelectronic devices, including photonic switches based on the photon blockade effect (Birnbaum 2005) or quantum logical optical gates operating at the single photon level (Duan 2004). A quantum computing scheme has also been proposed, where quantum dots would be used as the physical support of quantum bits (qubits) for the purpose of creating an effective interaction between distant quantum dots through their coupling to a photonic mode of the usual type (Imamoglu 1999).

The combination of a semiconductor quantum dot and of a zero-dimensional semiconductor microcavity is very attractive if we consider the main significant parameters in the problem. First, the oscillator strength f of the fundamental optical transition of a quantum dot is quite high. Thus, for the InAs/GaAs system, $f = 10$, which corresponds to an electric dipole moment ten times that of actual atoms emitting in the same spectral range. Secondly, semiconductor microcavities display small effective volumes, which leads to the possibility of huge amplitudes for the vacuum field fluctuations in the cavity mode ($\varepsilon_{max} \sim 2.10^5$ V/m for $V_{eff} = (\lambda/n)^3$ and $\lambda \sim 1$ μm). According to Eq. 7.4, the Rabi energy $\hbar\Omega$ is as high as 100 μeV for a single InAs quantum dot located at the antinode of a confined mode ($|\vec{f}| = 1$) with $V_{eff} = (\lambda/n)^3$ and $|\vec{d}| \sim 10^{-28}$ C.m. This value for the Rabi energy is found to be typically two orders of magnitude higher than in CQED experiments conducted on single atoms trapped in optical microcavities (Hood 1998).

However, in order that a strong coupling regime be observed, the Rabi oscillation needs to be faster than all the decoherence phenomena that may affect either the exciton or the photon. This constraint can be roughly expressed in the frequency domain by the approximate condition $2\Omega > \Delta\omega_e + \Delta\omega_c$, already discussed in Section 7.1.2. The broadening of the emission line of the quantum dots at high temperatures, caused by the interaction between phonons and electrons, prevents the observation of the strong coupling regime for temperatures typically higher than 100K. Conversely, at low temperatures, the emission linewidth of the quantum dots becomes negligible in comparison to the Rabi frequency, and in practice cavity losses become the most serious decoherence process. In this case, the relevant necessary condition for achieving a strong coupling regime is $\Delta E_{cav} < 4\hbar\Omega$ (Andreani 1999).

For the purpose of discussing the practical implications of this constraint, we compare in Fig. 7.6 the values for ΔE_{cav} obtained for different state-of-the-art microcavities to the value expected for $4\hbar\Omega$. The latter value was calculated in the

ideal case of a quantum dot located at the antinode of the cavity mode. Prior to 2004 the quality factor of semiconductor microcavities was not high enough to permit the clear observation of the strong coupling regime for a single InAs quantum dot. Since then, novel design rules have led to spectacular improvements in the cavity Q of photonic crystal microcavities (see Section 9.8.3 in Chapter 9). These microcavities now appear to offer the greatest potential in this context, owing to the combination of very small effective volume ($V < (\lambda / n)^3$) and high Q ($Q > 20{,}000$). In 2004, strong coupling regime was achieved for the first time with a single InAs quantum dot in a photonic crystal microcavity (Yoshie 2004).

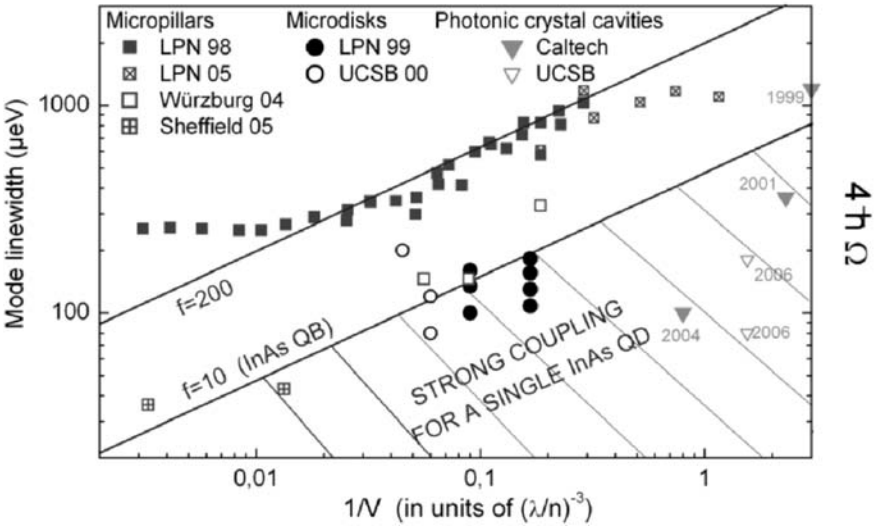

Fig. 7.6. Theoretical estimates of $4\hbar\Omega$ (i.e. twice the Rabi splitting) for a single InAs quantum dot ($f = 10$) and for a single GaAs quantum dot ($f = 200$) formed by an interface defect of a quantum well, plotted as a function of the inverse of the volume of the mode. For the sake of calculations, a single quantum dot emitter is assumed to be ideally coupled to the microcavity mode. This estimate is compared to experimental values for the linewidth of the cavity mode, obtained with different state-of-the art semiconductor microcavities. Experimental data are taken from (Gayral 1999; Gérard 1998; Michler 2000c; Reithmaier 2004; Sanvitto 2005; Strauf 2006; Varoutsis 2005; Yoshie 2001, 2004). The dashed area corresponds to a situation of strong coupling between the cavity and an InAs quantum dot located at the antinode of the mode

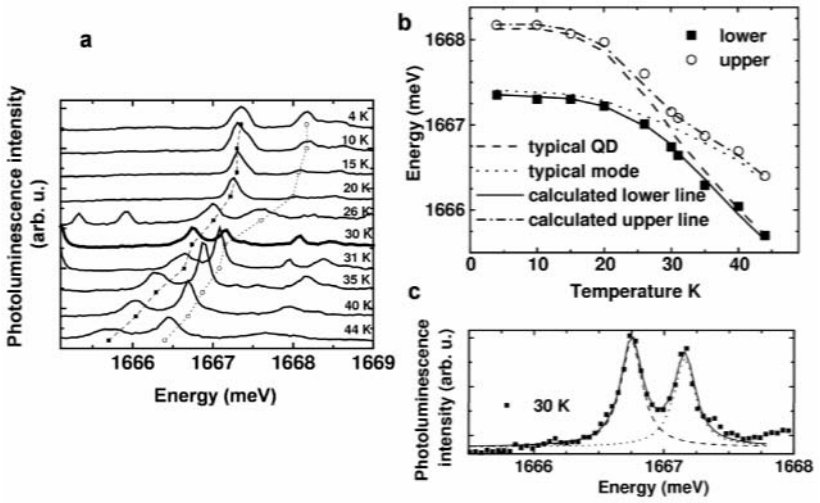

Fig. 7.7. Experimental observation of the vacuum Rabi splitting for a GaAs quantum dot in a microdisk *a.* Photoluminescence (PL) spectra obtained for the microdisk at different temperatures *b.* Energy of the emission line, plotted versus temperature, highlighting the anticrossing behaviour of two lines, associated respectively with the quantum dot and with a whispering gallery mode far from resonance *c.* Enlargement of the photoluminescence spectra, showing the Rabi doublet obtained when the quantum dot is resonantly coupled to the mode (Peter 2005)

Improving the cavity Q is not the only successful strategy towards the strong coupling regime. Thus, another approach has been developed based on the implementation of a quantum dot with larger oscillator strength, as is the case for quantum dots formed by monolayer fluctuations in the thickness of a GaAs/AlAs quantum well (Andreani 1999). Interface defects grown under appropriate conditions defects can be much larger than the Bohr radius of the exciton. In such a case, the confined excitons couple more strongly to light, and they exhibit a larger oscillator strength. Strong coupling regime has been experimentally achieved by placing a GaAs quantum dot in a high-Q microdisk (Peter 2005), or alternatively large InGaAs quantum dots in pillar microcavities (Reithmaier 2004).

These demonstrations of the strong coupling regime were achieved by tuning the fundamental optical transition of a single quantum dot in resonance with a discrete cavity mode through the continuous variation of temperature, as can be seen in Fig. 7.7. A clear anticrossing behaviour, and the formation of a well-balanced Rabi doublet, with the two lines exhibiting similar linewidths, are two spectral signatures of the strong coupling regime.

This success constitutes a very significant milestone for solid-state CQED. However, decoherence still very severely affects the optical properties of the coupled quantum dot-cavity system. The comparison between the linewidth of each component of the Rabi doublet, which reflects the magnitude of the decoherence processes, and the Rabi splitting, shows that the coupled system experiences only

a few (2-3) Rabi oscillations. However, there is still much room for improvement. First, the deterministic positioning of the quantum dot with respect to the cavity mode has been simultaneously demonstrated in the spatial and spectral domains (Badolato 2005). This new possibility will allow the optimization of the emitter-cavity coupling. Secondly, cavity losses remain much larger for active cavities containing quantum dots than they are for empty cavities. The reasons behind this observation are still unclear, but it can be expected that technological advances in the near future will change this state of affairs. In particular, the fabrication of microcavities containing a single quantum dot is a very attractive perspective, which would permit to eliminate the residual absorption or scattering losses induced by other quantum dots.

8 Nonlinear Optics with Photonic Crystals

Thus far, it has been implicitly assumed that photonic crystals interact with electromagnetic waves only through linear processes. This assumption ultimately rested on the fact that the dielectric permittivities of the materials were considered as being independent on the intensity of light. However, as will be illustrated in this chapter, the notion of a photonic crystal can actually be extended to structures formed from nonlinear components, which opens the way to the possibility of hitherto unknown applications.

The transition to nonlinear optics is a necessary step for the further development of photonic crystals, and this is even more true if, as has been prophesized, photonic crystals are to play a role comparable to that of semiconductors in the past. Actually, these expectations are based on the extension of the analogy between electrons and photons to the future development of physics and technology. However, this analogy exists only in the end between certain formal equations. In this sense, concluding from the formal similarity of these equations to the possibility of achieving similar results with photons as with electrons is a very bold move, which rapidly runs into difficulties.

A first difficulty lies in the fundamental difference between the respective statistics of electrons and photons. It is well known that Fermi-Dirac statistics and the Pauli exclusion principle play a fundamental and crucial role for certain key devices in microelectronics. Other differences, like the vector or scalar character of the electromagnetic field or of a wave function respectively, the role of the mass, which causes electrons to stay still and prevents photons from being ever confined *('lazy electron, crazy photon')* should also warn us against overly extending this analogy. In the final analysis, the most significant difference between electrons and photons in this context is undoubtedly the Coulomb force. From a theoretical point of view, the fact that there is no interaction force between photons might first appear as an interesting feature, since it permits to escape the difficult problem of the self-consistent solution to the coupled Schrödinger-Poisson equations and to complete calculations of photonic band gap structures. However, when the problem is to design actual devices based on photonic bandgap materials, the absence of interaction between photons results in the impossibility of directly transferring the principles on which electronic devices are based. Recall that such an essential device in the microelectronic industry as the transistor ultimately rests on the very possibility of displacing electron populations thanks to the presence of other electrons. In this regard, the very possibility of realizing logic and three-terminal devices derives, in the end, from the existence of the Coulomb force.

A prerequisite to the possibility of achieving similar results with photons rather than with electrons is the ability to influence an electromagnetic wave by another. Such a property belongs to the field of nonlinear optics, even if it becomes significant at high optical powers. Whilst linear optics comes down to a one-photon problem, the symmetry between electrons and photons is restored in nonlinear optics: the electrons interact through the Coulomb force, with photons acting as the vectors of these interactions, while the photons interact according to a nonlinear processes: in the latter case, the vector of the interaction is the electron in the potential, which gives the material its nonlinear susceptibility.

Having reviewed the significance of nonlinear optics for photonic crystals, it should be pointed out that nonlinear optics is a very broad field, and that it is necessary to distinguish between phenomena of the second order and phenomena of the third and higher orders. The order corresponds here to the amplitude of the field to which the linear effect is proportional (Yariv 1989).

A large part of this chapter will be devoted to the consideration of phenomena of order 2, i.e. for the most part to frequency conversion phenomena. This is understandable, as early nonlinear experiments with photonic crystals were chiefly concerned with second-order phenomena. However, it should be borne in mind that phenomena of higher order offer a wealth of perspectives, in particular in the field of photonic crystals. The last part of the chapter will therefore be devoted to these third-order nonlinear optical effects, which have been very rapidly emerging as a field of study during the last decade.

8.1 The Problem of Phase Matching

Frequency conversion is a process used in nonlinear optics for the generation of light in spectral regions which often are insufficiently covered by lasers (Armstrong 1962 ; Fejer 1994). Frequency doubling, also referred to as second harmonic generation, is used for instance for producing green light using YAG lasers, while frequency difference and parametrical processes are at the heart of tunable sources, in the mid-infrared as well as in the visible ranges (optical parametrical oscillators). The efficiency of a frequency conversion process is essentially determined by two different parameters: the nonlinear susceptibility $\chi^{(2)}$ of the material on the one hand, and the phase difference between the waves propagating at the frequencies ω and 2ω respectively on the other hand. Indeed, the dispersion of the material induces a difference in the wave number $\Delta k = k^{2\omega} - 2k^{\omega} = 2\omega/c(n^{2\omega} - n^{\omega})$, which itself results in a difference in the propagation speed of these two waves. After a length $L_Q = \pi/\Delta k$, referred to as the 'coherence length', destructive interferences appear between the source wave at the frequency ω and the harmonic wave at 2ω, thereby resulting in a decrease in the efficiency of the nonlinear process. Therefore, in order to achieve an efficient frequency conversion, the value for Δk needs to be low enough in order that the coherence length be as long as possible. However, the ideal situation remains the case where $\Delta k = 0$, a situation referred to as the phase matching condition. This condition can be achieved in bire-

fringent materials, provided however that the various waves propagate with different angles or polarizations.

It thus turns out that the two conditions for an efficient frequency conversion process are the existence of a high value for the linear susceptibility $\chi^{(2)}$ on the one hand, and the possibility of a phase matching on the other hand. Accordingly, although III-V semiconductors, and GaAs in particular, present very high nonlinear coefficients, phase matching by birefringence cannot be achieved with these materials. Indeed, these materials exhibit a cubic symmetry, and they are therefore optically isotropic, which makes them in principle unsuited to frequency conversion. This is precisely the reason why optical heterostructures and photonic crystals are of a great interest for artificially achieving phase matching. The possibility of obtaining different dispersion relations by modifying the Bravais lattice or the air filling factor of a photonic crystal is already known. Likewise, since the design of a photonic structure allows for a large number of degrees of freedom, it is quite obvious that a phase matching condition can be easily achieved with different photonic structures specifically designed for this purpose. However, rather than restricting ourselves to the consideration of structures where the dispersion is designed in such a way as to fulfil the phase matching condition, we shall also examine the case of structures which are periodical only as regards their nonlinear susceptibility. It will be seen that similar properties in terms of frequency conversion can be achieved with these structures.

In this chapter, we describe different approaches for achieving such a phase matching in the case of a nonlinear process of the second order. Under this condition, the material can be completely described by its linear susceptibility $\chi^{(1)}$, which depends on the refractive index[1], and by its nonlinear susceptibility $\chi^{(2)}$, which is the source term of the wave at the frequency 2ω. Two different approaches for the realization of a photonic crystal, in the most general sense of the term, can be distinguished depending on the value of the susceptibility selected for the periodicity of this crystal. We shall first discuss the case of 'classical' photonic crystals, where the linear susceptibility is periodical, and where the dispersion properties of light can be 'modelled' according to the specific requirements imposed by the intended application. We shall then consider the case of materials whose nonlinear susceptibility is periodically structured. These materials are known in the literature as 'quasi-phased-matched materials', and their efficiency for frequency conversion is already well established. Finally, this concept will be extended by considering the case of $\chi^{(2)}$ two-dimensional photonic crystals.

It is to be mentioned that the classification of an optical heterostructure as a 'photonic crystal' has been a matter of debate. Thus, in a recent article published in *Optics and Photonics News*, the creator of the name 'photonic crystal' Eli Yablonovitch insists that the definition of a photonic crystal should encompass the joint requirements of a high index contrast and a two- or three-dimensional struc-

[1] The linear susceptibility links the electric field E to the polarization $P = \varepsilon_0 \chi E$ of the material, which itself is related to the displacement vector D through the equation $D = \varepsilon_0(E + P) = \varepsilon_0 \varepsilon_r E$. Since the refractive index n is defined by the equation $n^2 = \varepsilon_r$, this leads to the equation $\chi = \varepsilon_r - 1 = n^2 - 1$.

ture (Yablonovitch 2007). A more extensive definition would indeed blur the distinction between this concept and, for instance, the very old concept of Bragg mirror, which applies to one-dimensional structures, or the physics of X-ray diffraction by solid state crystals, which have been in textbooks for decades prior to the emergence of photonic crystals. While agreeing completely with the definition given by Eli Yablonovitch, we shall nonetheless proceed to describe in this chapter structures that do not meet these two requirements, for instance one-dimensional structures with form birefringence or structures where only the second-order susceptibility is periodic and without index contrast. We believe, indeed, that these structures fall within the field of photonic crystal physics, since their development has benefited from concepts that first originated in the context of photonic crystal physics. This is more particularly true of the concept of photonic band, which sheds a new light on phase matching in the field of nonlinear optics.

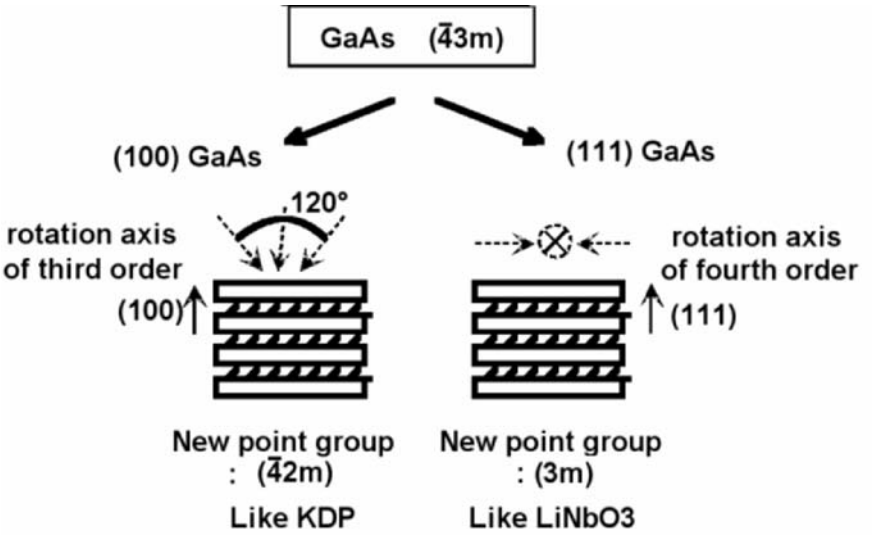

Fig. 8.1. Point groups of multilayer structures containing GaAs. As a bulk material, GaAs is not birefringent. However, the introduction of amorphous layers along the (100) plane of GaAs (*left-hand figure*) disrupts the symmetry of order 3: the point group of the synthetic material thus created is the same as that of the KDP. If the amorphous layers are inserted along the (111) plane, symmetries of order 4 disappear this time: the symmetry group of the resulting material is the 3m point group, to which also belongs niobate lithium. The two materials whose symmetry properties are reproduced at the macroscopic scale are among the most currently used in nonlinear optics

8.2 χ(1) Photonic Crystals

8.2.1 One-Dimensional $\chi^{(1)}$ Photonic Crystals

Phase matching can be achieved through the generation of a phenomenon of 'form birefringence' in a multilayer structure. Since this is the simplest approach toward phase matching through the use of photonic crystals, it might be interesting to proceed from it. This scheme was first successively implemented in 1998 in a GaAs-AlAs oxide (AlOx) multilayer system (Fiore 1998). The optical isotropy of the GaAs is disrupted by the insertion of AlOx layers, which have a different refractive index than GaAs. The difficulties of finding two materials that would simultaneously present both a high nonlinear susceptibility and a high index contrast explains why this technique is still quite recent.

Form birefringence can be explained in intuitive terms from the symmetry of the multilayer structure. Introducing AlOx layers in the GaAs (100) removes the symmetry of order 3: the material obtained in the end belongs to the same point group as the KDP crystal, which is known for both its birefringence and its applications to frequency conversion (Yariv 1989). However, the multilayer structure thus realized still presents the nonlinear characteristics of GaAs, in particular its nonlinear tensor and its value for the coefficient $\chi^{(2)}$, provided however that the AlOx layers, which are amorphous, and therefore present a zero susceptibility $\chi^{(2)}$, are thin enough. On the other hand, the insertion of the AlOx layers in the GaAs (111) causes this time the rotation axes of order 4 of the zinc-blende structure to be disrupted. The symmetry group of the resulting material is the 3m point group, to which belongs also lithium niobate, another well-known birefringent nonlinear material (Yariv 1989). In other terms, this method allows retaining the advantages associated with the microscopic structure at the atomic scale of GaAs, namely its high nonlinear susceptibility, while at the same time permitting the use of a refractive index engineering at the macroscopic scale for achieving the desired dispersion and for reproducing the birefringence of a different material.

The modifications induced on the symmetry of the original structure by the introduction in a GaAs substrate of thin amorphous layers are schematically summarized in Fig. 8.1.

The phenomenon of form birefringence can also be explained from the distribution of the electric field in the multilayers, which depends on the polarization of the wave. This distribution is represented here in Fig. 8.2. Thus, in the case of a wave whose magnetic field is contained in the plane of the layers, i.e. of a transverse magnetic (TM) mode of propagation, the boundary condition at the interfaces imposing that εE be constant causes the electric field to substantially overlap with the medium of lower index, which results in a corresponding decrease of the effective refractive index of the TM mode. On the contrary, when the wave is polarized in the plane of the layers, i.e. in the case of a transverse electric (TE) mode of propagation, the continuity of the electric field at the interfaces ensures that the effective refractive index will remain near the effective index of the layers. Multi-

layer structures are therefore necessarily birefringent. However, only in the case where a high index contrast exists between the layers can a marked birefringence be observed. As an example, the contrast between the refractive indexes of GaAs and AlAs is not high enough for reaching a level of birefringence high enough and for achieving phase matching. It therefore turns out necessary to resort to the use of AlAs oxide, whose refractive index (1.6) is at least two times lower than the refractive index of GaAs, which is higher than 3. This is the reason why, although form birefringence had been suggested as early as 1975 by Van der Ziel (Van der Ziel 1975) as a possible technique for achieving phase matching in semiconductors, more than twenty years passed before this method was experimentally implemented. The decisive breakthrough was made possible only with the control of AlAs oxidation at the beginnings of the 1990s and with the generation of the GaAs/AlAs oxide pair of materials which present a very high index contrast.

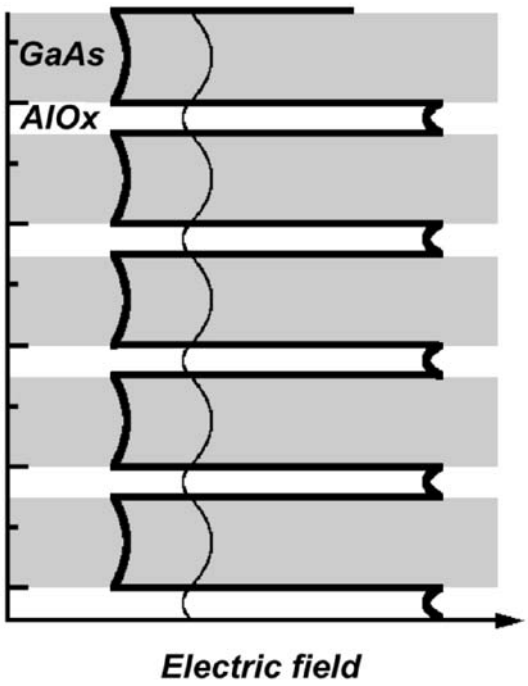

Fig. 8.2. Distribution of the electric field in the multilayers depending on the polarization of the Bloch wave propagating in the plane of the layers, i.e. normally to this figure. The thick line corresponds to TM polarization, i.e. to the case where the magnetic field is in the same plane as the layers: a substantial overlap with the AlOx layers arises in this case. The thin line represents the TE polarization, i.e. the case where the electric field is in the same plane as the layers

For wavelengths larger than the period of the periodic multilayer, the dielectric constants are given by the following simple approximations:

$$\varepsilon_{TE} = \alpha_1 \varepsilon_1 + \alpha_2 \varepsilon_2 \tag{8.1}$$

$$\frac{1}{\varepsilon_{TM}} = \frac{\alpha_1}{\varepsilon_1} + \frac{\alpha_2}{\varepsilon_2} \tag{8.2}$$

where α_1 and α_2 are the filling factors associated with the two materials with permittivities ε_1 and ε_2 respectively. In other terms, if d_1 and d_2 denote the thicknesses of the layers formed by these two materials respectively, then the equation $\alpha_{1,(2)} = d_{1,(2)}/(d_1 + d_2)$ holds true. It can be observed that Eqs. 8.1 and 8.2 are the analogue of the equations expressing the equivalent capacitances of an ensemble of two parallel or series capacitors. This simply results from the fact that the equation for the charge equality $C_1 V_1 = C_2 V_2$ between capacitors in series is formally the analogue of the continuity equation in TM polarization $\varepsilon_1 E_1 = \varepsilon_2 E_2$. Conversely, the equation for the equivalent voltages at the terminals of two parallel capacitors $V_1 = V_2$ is the analogue of the equality between the fields $E_1 = E_2$ for TE waves at the interface between the two materials. These approximations are extremely useful, since they give, in a very simple form, an order of magnitude for the form birefringence.

Such simple analytical formulations are of course highly unusual in the field of photonic crystals, and therefore it would be of the greatest interest if these formulations could be extended to two-dimensional photonic crystals, where the presence of elongated rods results in the same type of birefringence. Unfortunately, it turns out that these formulations are valid only within the approximation of a long wavelength. This region corresponds to the part of the dispersion diagrams which lies in the vicinity of the origin, where the relation $\omega(k)$ is approximately linear (see the first part). Actually, the two equations Eqs 8.1 and 8.2 simply yield the squares ($\varepsilon_r = n^2$) of the slopes at the origins of dispersion relations in TE and in TM polarizations respectively. Using these very simple formulations, it can immediately be seen that the birefringence, i.e. the difference between the square roots of ε_{TE} and ε_{TM}, increases with the index contrast $n_2 - n_1$ between the two materials. This of course is far from being surprising for a phenomenon whose physical origin lies in the discontinuity of the field at the interface between the two materials. This discontinuity appears only in TM polarization, and it is all the more marked that the index step is high. Fig. 8.3 presents two examples of phase matching phenomena associated with form birefringence. Diagrams of this type have been called in the literature 'photon interband transition' (Winn 1999). This denomination, which probably overly extends the well-known analogy between electrons and photons, is not, in our opinion, appropriate. Indeed, the principle of phase matching has been known under this name since quite a few decades already, and phase-matching schemes can be represented, in a very general way, in dispersion diagrams similar to the one represented in Fig. 8.3. However, such diagrams have never been referred to as photon interband transitions in the past.

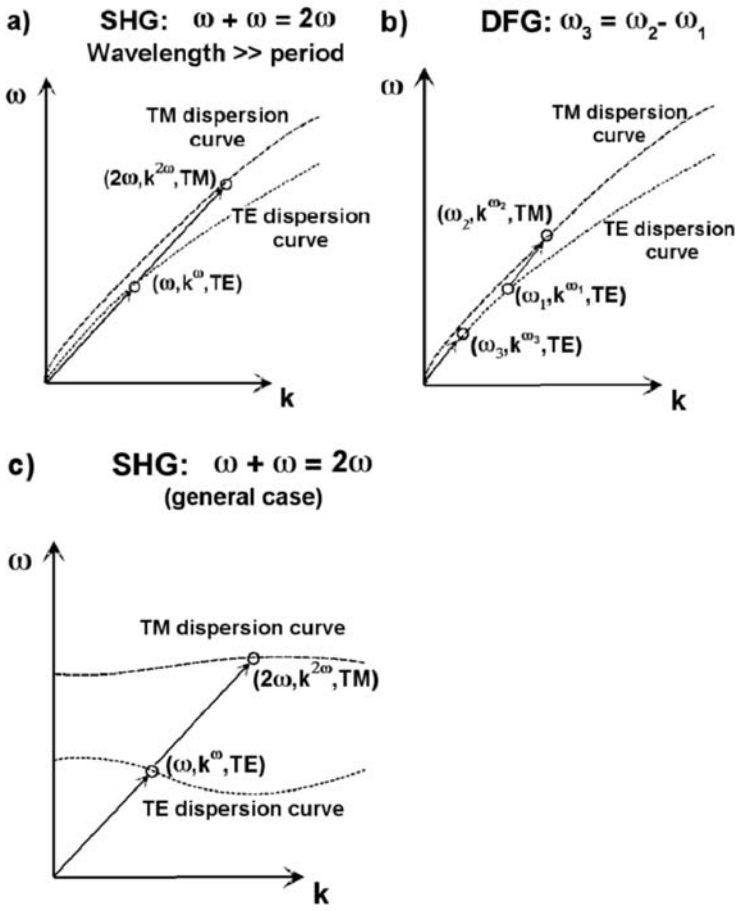

Fig. 8.3. A nonlinear phase matching process allows the coherent transfer of energy between two modes (ω, k) with conservation of the momentum and energy. Such a phase matching phenomenon can always be represented on a dispersion diagram. Two examples of phase matching phenomena relevant to the study of form birefringence are presented here. *a.* Second harmonic generation: this process allows a transfer of energy from a wave (ω, k^{ω}, TE) to a harmonic wave (2ω, $k^{2\omega}$, TM). The phase matching condition is equivalent here to the fact that the two arrows are identical. This ensures both the conservation of energy (identity of the ordinates of the two arrows) and the conservation of the momentum (identity of the abscissas). *b.* The case of frequency difference is similar. *c.* As a general rule, i.e. without any specific restriction to form birefringence, a phase matching phenomenon creates a coupling between two modes which can be represented by a diagram of this type with identical arrows. However, some aspects have not been represented in these diagrams, since the phase matching condition, while being of course necessary, is not sufficient. In particular, an efficient conversion process requires additionally a nonlinear overlap integral between the two modes

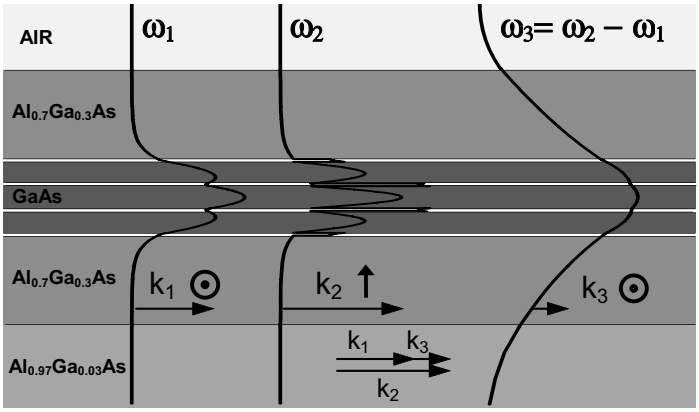

Fig. 8.4. Example of the application of a form-birefringent phase-matched structure to a process of frequency difference. The waveguide used here was realized by molecular beam epitaxy. The guiding structure is clad itself with two AlGaAs confining layers containing 70% of Al, while the waveguide is separated from the GaAs substrate by a thick AlGaAs layers containing 97% of Al. The core of the waveguide itself consists simply of three GaAs layers with a 325 nm thickness and of four AlAs layers (represented by white lines in this figure) with a 40 nm thickness. The fine tuning of the values for the thickness and composition of the different layers allows the implementation of the dispersion relation required for phase matching the nonlinear process. It can be observed that the mode with frequency ω_2 in TM polarization substantially overlaps with the oxide layers, this being due to the discontinuity of the field at the interfaces in this polarization

The efficiency of the phase matching achieved by form birefringence was first demonstrated for a process of frequency difference (Fiore 1998), and later in experiments conducted on second harmonic generation and on parametric fluorescence (De Rossi 2002). Fig. 8.4 displays an example of a structure where the different modes are phase matched by form birefringence, while Fig. 8.5 presents a typical experimental result. The signal obtained during a process of frequency difference follows a sine cardinal evolution and is a function of the wavelength of one of the two pump lasers. This evolution is clearly reflective of the phenomenon of momentum conservation involved here (Fiore 1998).

Semiconductors like GaAs can therefore be used as nonlinear materials with a very high efficiency for frequency conversion in the field of integrated optics. These nonlinearities can be further enhanced by exploiting the properties of quantum well structures (Fiore 1995). This opens the way to the realization of optical parametrical oscillators capable of being continuously in operation at room temperature, as well as that of two-photon compact sources for quantum cryptography. In principle, such devices lend themselves perfectly to fabrication with semi-

conductor technology, and the first experimental measurements of parametrical fluorescence in these structures are reported here in Fig. 8.6. However, research conducted in this direction is presented with severe technological problems, and in particular with the problem of realizing nonlinear waveguides that would exhibit an extremely low amount of loss. One-dimensional $\chi^{(1)}$ photonic crystals can also be used for frequency conversion in schemes where the waves propagate normally to the layers. The first case is when the crystal or the Bragg mirror is operated near the edge of the band gap (Balakin 2001; Dumeige 2001, 2002). Under these conditions, the crystal exhibits a very high dispersion, which can be used for achieving phase matching, while allowing simultaneous exploitation of the resonant amplification of the fields within the layers. Compared to a bulk semiconductor, the enhancement of the efficiency of the frequency conversion process (normalized per unit length of the nonlinear material) results from two distinct effects occurring simultaneously: the high density of states of the electromagnetic field, or in other terms the increase in the amplitude of the field at a resonance in the Bragg structure on the one hand, and phase matching on the other hand. The second case corresponds to a microcavity formed by Bragg mirrors (Berger 1997; Simonneau 1997). The phase matching in the cavity is achieved by adjusting the reflection phases of the mirrors in order to compensate for the phase difference arising between the wave at the frequency ω and the wave at 2ω as they propagate in the cavity. While these two methods are intellectually rich and exciting, their present conversion efficiencies are markedly lower than those obtained in integrated optics, this being essentially due to the limited interaction length. Any significant increase of this length would result in severe technological problems.

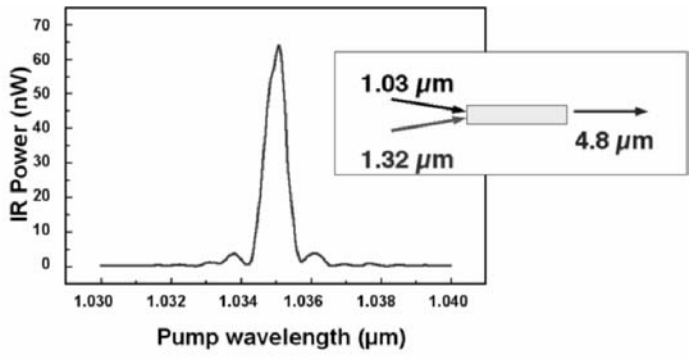

Fig. 8.5. Frequency difference signal represented as a function of the wavelength of one of the Titanium :Sapphire pump lasers. The pumping powers of these two lasers are equal to 0.2 mW and 1.6 mW for pump beams at 1.32 μm and 1.03 μm respectively. The fact that the output signal is quite low (a few ten nW) can be explained by the very high optical losses occurring in the samples, realized in 1998. Since that time, technological advances in the realization of waveguides have led to an enormous reduction of optical losses. Experiments on parametrical fluorescence have also been realized on samples based on the same principles (see Fig. 8.6)

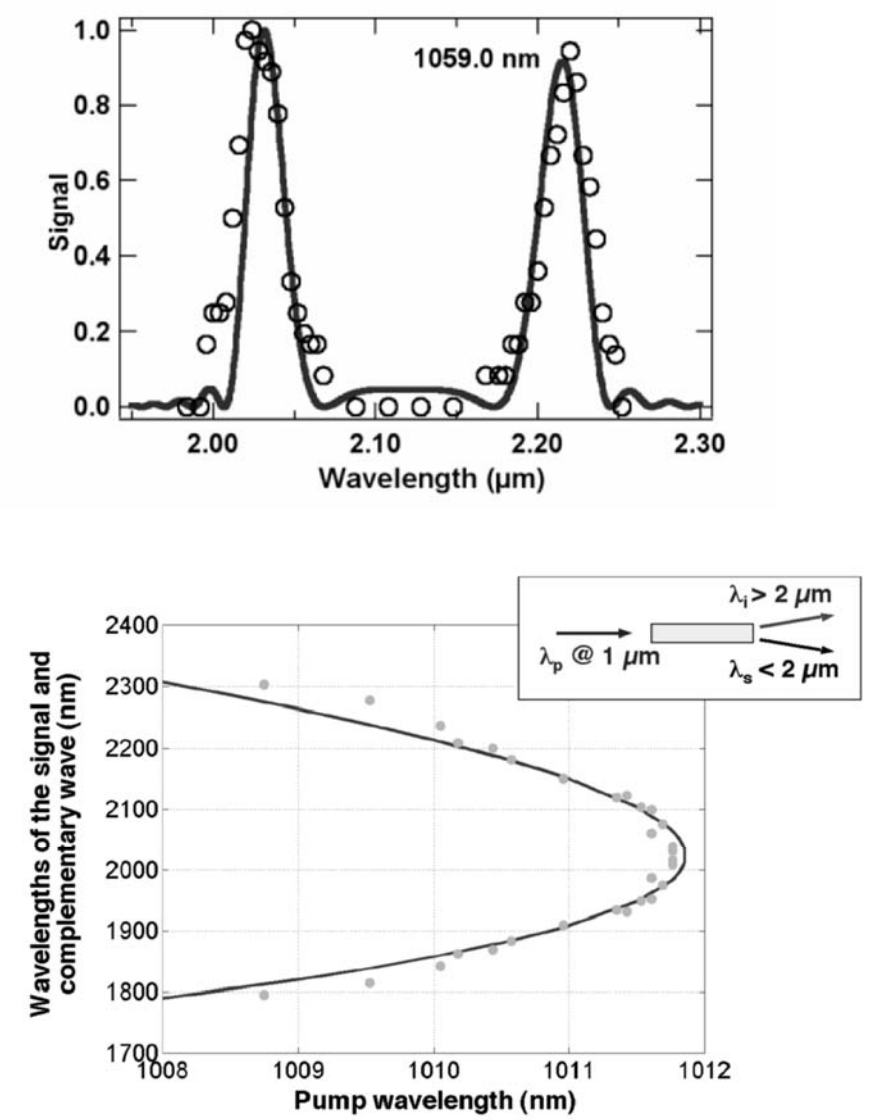

Fig. 8.6. *Top.* Parametrical fluorescence signal for a pumping frequency equal to 1.064 μm. The points correspond to actual experimental measurements, and the continuous curve only serves as a visual cue. A form-birefringent structure can therefore be used as a source for the generation of twin photons *Bottom.* Dependence on the pump wavelength of the wavelengths of the twin photons, associated with the signal and with the complementary wave respectively. This result shows the very high degree of tunability that could be achieved with an optical parametrical oscillator based on these new materials. The sample used in the upper part of the figure is not the same as in the lower part

A different scheme for a photonic crystal microcavity, suggested by Di Falco et *al* (Di Falco 2005), is based on a geometry similar to the one used in the pioneering study by Foresi *et al* (Foresi 1997). The photonic crystal consists of a one-dimensional array of holes drilled in an AlGaAs waveguide rod, with the point defect microcavity itself being associated to a single missing hole in the middle of the photonic crystal. The three-dimensional confinement of light is thus achieved in a small volume through a combination of conventional index guiding and reflection by photonic crystal mirrors. The potential of this structure for nonlinear frequency conversion has been analysed in the context of THz generation by optical rectification (Di Falco 2005). The advantages offered by these photonic structures have also led to has also been investigating their use in the context of four-wave mixing for nonlinear frequency conversion (Di Falco 2004). Although a third-order process is involved in the latter case, this result deserves mention since it can be applied to the production of photon pairs, a problem traditionally addressed through parametric fluorescence based on a second-order nonlinear process.

Finally, we may mention another phase-matching phenomenon observed in a microcavity where a quantum well had been embedded. Through the influence exerted by the quantum well on the dispersion of the cavity, phase matching was achieved in certain configurations for four-wave mixing processes involving two photons at the same frequency ω on the one hand, and two other photons at the frequencies $\omega\Delta$ and $\omega + \Delta$ respectively on the other hand. These experiments were interpreted by using the formalism of cavity polaritons (Savvidis 2001), and the configuration where the phase matching was optimized was given the name of 'magic angle configuration'. However, the phase-matching phenomenon described by the authors is actually similar to a phenomenon reported earlier in a different experiment, where absorption in a quantum well was exploited for controlling the index function (Almogy 1994). Although there may be no 'magic' involved in this phenomenon, it has a place among other phase-matching phenomena (Eastham 2003; Whittaker 2001). Drawing on the description of polaritons generally favoured by researchers in the field of semiconductor microcavities (Baas 2004; Ciuti 2001; Karr 2004a), an extensive literature has been published on this subject, including studies on polariton squeezing (Karr 2004b), polariton pair entanglement, or the production of pairs of photons in coupled microcavities (Diederichs 2006). Unfortunately, the low coupling efficiencies, or equivalently, the high insertion losses inherent to the structures, combined with the non-parametric character of the nonlinear process, which results from the fact that the direction and frequency of output light are imposed by phase matching conditions, has so far hindered the development of actual devices. Applications are expected to include such devices as tuneable sources or twin-photon sources for quantum information applications.

8.2.2 Two-Dimensional $\chi^{(1)}$ Photonic Crystals

As a consequence of the use of the molecular beam epitaxy method for their realization, GaAs/AlOx heterostructures exist only in the form of thin films of a few microns. However, the reason for searching for nonlinear materials with a sufficient thickness lies precisely in the possibility of focusing important energies onto such materials, and correspondingly of achieving high levels of energy at the new frequencies thus generated. In this respect, two-dimensional photonic crystals represent a possible solution for obtaining materials with both a sufficient thickness and a form birefringence. In the same way as for multilayer structures, the latter property results from the very elongated symmetry of these materials. In the general case of two-dimensional photonic crystals, the difference between the dispersion relations of TE and TM modes can clearly be seen from the observation of Figs. 1.9, 1.10, 1.11 and 1.12. The proposal to use the artificial birefringence thus induced in order to achieve phase matching for nonlinear frequency conversion came shortly after the principles of photonic crystals were established (Sakoda 1996). Birefringence, combined with the very structure of two-dimensional photonic crystals formed from holes lattices, can be exploited for materials which generally are not favourable to optical nonlinearities. We shall see in Section 9.5 of Chapter 9 that macroporous silicon is one of the two-dimensional photonic crystals in the optical region which exhibits the best characteristics as regards both the depth of the pores which can be attained (> 100 μm,) and the surface over which a lattice formed by such pores may extend (> 1 cm^2). By construction, a structure realized from macroporous silicon necessarily presents a form birefringence. However, since silicon is centrosymetric, it does not possess nonlinear coefficients of second order. This can be obviated for instance by filling the pores with a nonlinear material, while an alternative approach would consist in relying instead on the third-order nonlinear processes in the silicon, even though processes of third-order are less efficient than processes of second-order. Even for materials where etching very deep holes is not feasible, interesting experiments can be performed by using reflection by two-dimensional photonic crystal slab waveguides. As an example, observation of resonant second harmonic generation has been achieved through the frequency- and momentum-matching between the pump beam and a propagating mode of a two-dimensional photonic crystal slab (Malvezzi 2003). Even if this experimental scheme cannot lead to high conversion efficiencies, it is highly useful for the characterization of photonic crystals, in much the same way as second harmonic generation is currently being used for the characterization of surfaces. Finally, the use of very small high-Q photonic crystal microcavities is yet another approach to second harmonic generation or to frequency conversion using two-dimensional photonic crystals (Di Falco 2006). The strategy is the same as the one discussed in Section 8.2.1, save for the difference that the microcavity here is defined by two-dimensional photonic crystal mirrors based on a planar waveguide instead of being defined by one-dimensional photonic crystal (or Bragg) mirrors formed in a multilayer stack.

8.3. $\chi^{(2)}$ Photonic Crystals

8.3.1 One-Dimensional $\chi^{(2)}$ Photonic Crystals

A one-dimensional $\chi^{(2)}$ photonic crystal is simply a multilayer structure ($\chi'^{(2)}$ - $\chi^{(2)}$) of a well-known type in nonlinear optics, where it is known under the name of 'quasi-phase-matched structure'. It might be noted that, contrary to the previous case where light propagated in the plane of the layers, light now propagates along a direction normal to the layers. Further, $\chi^{(1)}$ is now assumed to be constant in the entire structure, with the consequence that no phenomenon of photonic band gap may occur. The principle of quasi-phase matching, first suggested by N. Bloembergen *et al* in a pioneering work (Armstrong 1962), consists in reversing the sign of the nonlinear coefficient at the end of a coherence length, i.e. when a phase difference accumulates to π between the wave at the frequency ω and the harmonic wave at the frequency 2ω. The sign of the interaction can be reversed, for instance by reversing the crystalline orientation, while leaving unchanged the construction of the harmonic wave. A detailed explanation of the principles of quasi-phase matching is presented here in Fig. 8.7. An excellent review of the literature on this subject is presented in (Fejer 1992).

A large variety of realizations based on quasi-phase matching have been demonstrated, including the 'periodically poled lithium niobate' (PPLN) (Myers 1995), an artificial nonlinear crystal upon which an increasing number of commercial devices are currently being based. Parametric oscillators, frequency doublers (Parameswaran 2002), and optical sources based on different schemes of frequency generation have thus been developed from PPLN crystals (Abernethy 2003). A number of devices for telecommunication applications have also been fabricated from PPLN crystals, with the purpose of implementing all-optical signal-processing functions (Langrock 2006). Twin-photon sources (Tanzilli 2005) or single-photon counters (Diamanti 2006) have been demonstrated in parallel using this type of nonlinear crystal.

The quasi-phase-matching technique has been more recently applied to GaAs crystals, where it has benefited from the development of the so-called 'orientation-patterned GaAs'. Indeed, quasi-phase-matched structures with periodic inversion of the orientation of the crystal have been successfully grown from this material (Skauli 2002). Using the very large second-order nonlinear coefficient of GaAs, and its broad transparency window in the infrared range (up to $\lambda = 17$ μm, to be compared with LiNbO3, which starts to absorb light above $\lambda = 4$ μm), optical parametric oscillators with very impressive characteristics have been developed for the infrared and THz spectral ranges (Kuo 2006; Vodopyanov 2004). This topic is currently under intense scrutiny, this being due to the fact that orientation patterned-GaAs is expected to become a material of choice for optical parametric sources in the mid-infrared.

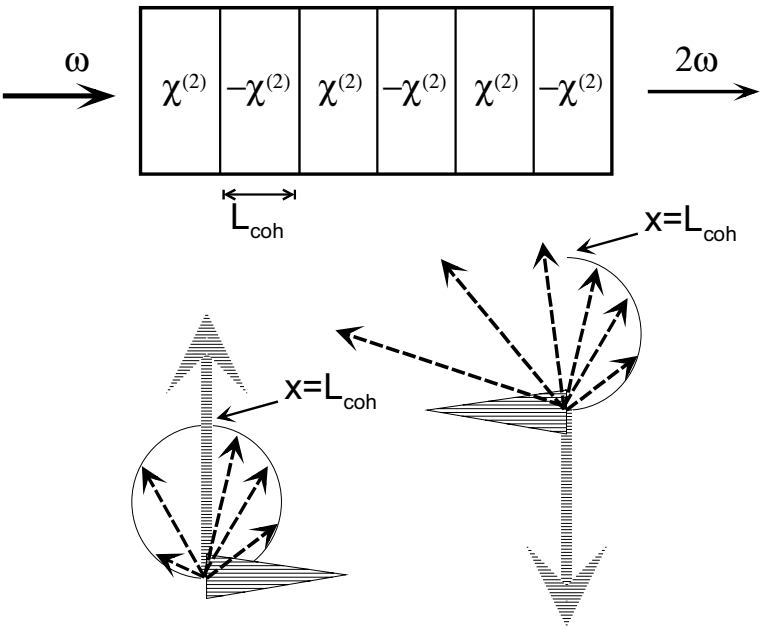

Fig. 8.7. Principles of quasi-phase matching. The quasi-phased matched structure represented at the top of the figure is a $\chi^{(2)}$ photonic crystal. Waves propagate normally to the $\chi^{(2)}$ layers, whose thickness is equal to the coherence length of the nonlinear process. The example considered here is a process of frequency doubling. In the bottom left figure, the broad dashed arrow represents the nonlinear polarization generating the wave at 2ω. The coordinate system is assumed to be rotating with an angular speed equal to $2k^{\omega}$ in order for polarization to remain constant. This nonlinear polarization generates a field in quadrature, which entails that the field at 2ω thus generated will be given at any time by the direction of the triangle represented in dashed lines at the origin. This triangle is assumed to be fixed in the coordinate system used here. By contrast, since $2k^{\omega} \neq k^{\omega}$ the field at 2ω will be rotating in this coordinate system. Different vectors, representing the field at 2ω at different times, are indicated here in the form of bold dashed lines. This field rotates due to the dispersion relation which causes a dephasing of the nonlinear source (whose phase evolves twice as fast as the phase of the pump wave) and of the nonlinear field (which propagates with its own phase). As a consequence, after a certain propagation length, referred to as the coherence length, the harmonic field moves to the left-hand side of the figure. This can be interpreted as an indication that the nonlinear source starts to destructively interfere with the harmonic field. The principles of quasi-phase matching are illustrated in the right-hand part of the figure. After one coherence length, the sign of the nonlinear coefficient is changed by modifying the orientation of the material. This causes the sign of the nonlinear polarization to stay reversed until time is needed, in order for the interaction with the harmonic field to remain constructive

It can be noticed that certain analogies can be drawn between quasi-phased matched structures and Bragg mirrors. More generally, this analogy extends to multilayer structures of the type used in linear optics, where to some extent a linear phase-matching function can be said to be implemented. Thus, it has been demonstrated that the transmission spectrum of multilayer structures depends on the Fourier transform $\chi^{(1)}$, and this property has even been used for developing a method for designing multilayer optical filters on the basis of a Fourier transform principle (Dobrowolski 1978). For instance, in the case of a one-dimensional photonic crystal, the spectral width of the n^{th} band gap is in proportion to the $(n-1)^{th}$ Fourier component of the periodical index function (Yeh 1988). This also explains why, in the case of a perfect Bragg reflector where all layers have an optical thickness equal to $\lambda/4$, the spectral width of the band gaps of even order become zero, exactly as Fourier coefficients of odd order do (see also Section 1.3.2 in Chapter 1). In the case where quasi-phase matching is achieved, the evolution of the field is given by an equation of the form (Fejer 1992):

$$\frac{dE^{2\omega}}{dz} \;\alpha\; \left(E^{\omega}\right)^2 \chi^{(2)}(z)\, exp\left(i(\Delta k)z\right) \tag{8.3}$$

From the previous equation, the harmonic field turns out therefore to be the Fourier transform of the nonlinear susceptibility function $\chi^{(2)}$:

$$E^{2\omega} \;\alpha\; \int \left(E^{\omega}\right)^2 \chi^{(2)}(z) \exp\left[i(\Delta k)z\right]\, dz \tag{8.4}$$

Considered in this way, the principle of quasi-phase matching becomes quite clear. Assuming here that the function $\chi^{(2)}$ has a component $\exp(-i\Delta kz)$, the harmonic field increases constructively over a large distance. This is exactly what happens when $\chi^{(2)}$ is constant and when $\Delta k = 0$, or when $\chi^{(2)}$ is periodical with a period $2L_{coh}$, where $L_{coh} = \pi/\Delta k$ is the coherence length. The fisrt situation corresponds to the phase matching by birefringence of a material, while the latter situation corresponds to quasi-phase matching.

Drawing on this analogy between $\chi^{(1)}$ multilayers (Bragg mirrors) and $\chi^{(2)}$ multilayers (quasi-phase matched materials), a large number of quasi-phase matched structures have been realized. This can be paralleled to the great variety of Bragg multilayer structures. Examples of quasi-phase matched structures include structures with a wide band frequency response, obtained through the use of a variable period ('chirped structures') (Bortz 1994) or structures intended at widening or compressing a pulse in the nonlinear domain (Arbore 1997) in much the same way as, in linear optics, multilayer mirrors are used for compensating the intrapulse frequency shift of femtosecond lasers. In the following section, we further explore this analogy between $\chi^{(1)}$ periodical structures and $\chi^{(2)}$ periodical structures, by turning this time to the consideration of two-dimensional structures.

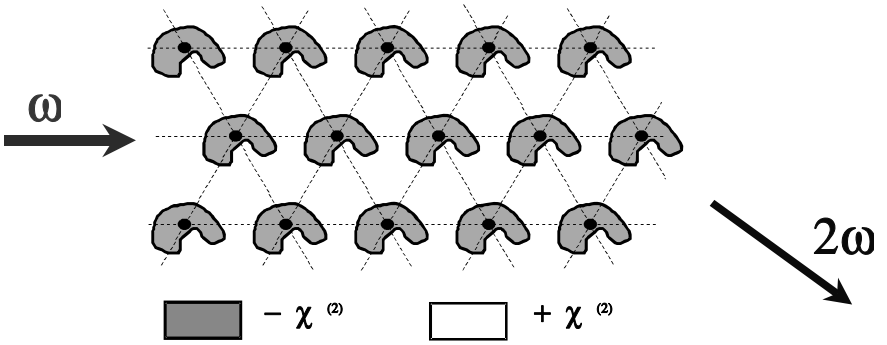

Fig. 8.8. Two-dimensional $\chi^{(2)}$ photonic crystals. The frequency conversion of a wave emerging from a composite material follows a nonlinear Bragg's law

8.3.2 Two-Dimensional $\chi^{(2)}$ Photonic Crystals

After discussing successively one and two-dimensional $\chi^{(1)}$ structures and one-dimensional $\chi^{(2)}$ structures, it is quite natural to turn to the consideration of the periodical structuring of $\chi^{(2)}$ in two dimensions. An example of a two-dimensional $\chi^{(2)}$ photonic crystal is represented here in Fig. 8.8). This problem was first theoretically addressed in 1998 (Berger 1998), and the first experiments on this topic were conducted by N. Broderick *et al* (Broderick 2000).

Let us here consider the case of a plane wave propagating in a medium formed by $\chi^{(2)}$ cylinders perpendicular to the plane represented in Fig. 8.8. In such a case, the linear susceptibility is constant, with the consequence that no anomalous dispersion or photonic band gap phenomenon occurs. We are therefore presented with a generalization to the two-dimensional case of the principle of quasi-phase matching. It can be demonstrated that a harmonic wave can develop efficiently in the crystal, provided that the conservation of the momentum of the photons is ensured through the possible contribution of a wave vector **G** of the reciprocal lattice:

$$\mathbf{k}^{2\omega} - 2\mathbf{k}^{\omega} - \mathbf{G} = 0 \tag{8.5}$$

A relatively straightforward argument (Berger 1998) shows that this momentum conservation leads to the formulation of a nonlinear Bragg's law, which ex-

presses the wavelength of the harmonic wave obtained in the crystal by frequency doubling as a function of the walk-off angle θ between the fundamental and the harmonic waves, i.e. the angle formed by the two directions of propagation at ω and 2ω:

$$\lambda^{2\omega} = \frac{2\pi}{G}\sqrt{\left[1 - \frac{n^{\omega}}{n^{2\omega}}\right]^2 + 4\frac{n^{\omega}}{n^{2\omega}}\sin^2\theta} \tag{8.6}$$

This equation represents a generalization of Bragg's law describing the refraction of X-rays by crystals to the field of nonlinear optics. Actually, the classical form of Bragg's law can be retrieved by imposing that $n^{\omega} = n^{2\omega}$, which leads to the equation $\lambda^{\omega} = 2d\sin\theta$ where $d = 2\pi/G$ is the distance between two reticular planes. The frequency conversion process can therefore be likened to the diffraction of an ensemble of nonlinear sources (at 2ω), excited with a certain phase relation by the fundamental wave at the frequency ω, and collectively emitting in accordance with the Huygens-Fresnel principle. This analogy also allows the introduction of various concepts first developed in the context of the diffraction of X-rays by solid state crystals, like for instance the non-linear Ewald sphere, the rotating crystal method or the nonlinear Laue method (Berger 1998). The first experimental study of two-dimensional $\chi^{(2)}$ crystals was conducted in 2000 with lithium niobate (Broderick 2000), and provided evidence for the generalized Bragg's law described above. A first application for this type of structures is the frequency or wavelength tuning of nonlinear processes. Indeed, for a given frequency ω, the possibility always exists, by some rotation of the $\chi^{(2)}$ crystal, of finding an incidence at which phase matching can be achieved. The versatility of this method, without equivalent in one-dimensional quasi-phase-matched materials, compares only to that of the rotating crystal method applied to the X-ray analysis of solid state crystals, where the rotation of the crystal can always be used for finding a direction allowing the diffraction of X-rays. A second possible application is the cascading of different nonlinear processes occurring along different directions of propagation, which has been experimentally demonstrated (Broderick 2000). Further studies have included the observation of third and fourth harmonic generation in $\chi^{(2)}$ photonic crystals (Broderick 2002), of second harmonic generation in the visible range (Peng 2003; Xu 2004) or of wavelength interchange in the telecommunication range (Chowdhury 2001). The wide variety of degrees of freedom in these structures opens the possibility of envisioning many complex interactions, involving multiple-phase-matching or multicolour parametric frequency generation (Saltiel 2000). However, such multiple interactions are often achieved at the expense of efficiency.

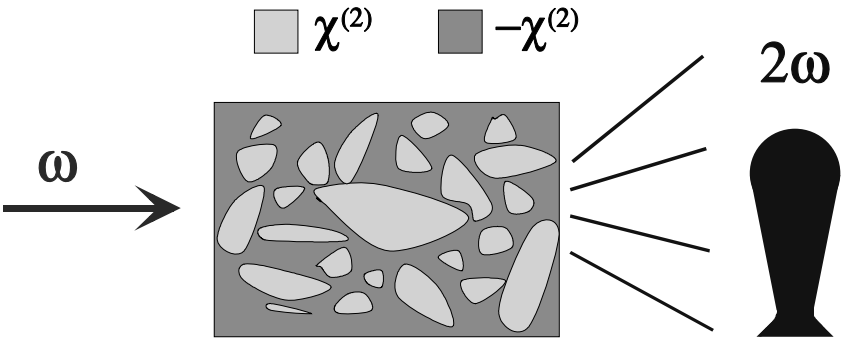

Fig. 8.9. Two-dimensional $\chi^{(2)}$ photonic crystal structure. The shapes of the $\chi^{(2)}$ regions are chosen in such a way as to force the nonlinear emission of the structure under illumination to assume a certain requested shape (nonlinear holography)

A further refinement of the notion of a nonlinear photonic crystal has led to the proposal of nonlinear materials which, rather than being periodically structured in two dimensions, would be structured in such a way as to adapt the harmonic wave to the spatial distribution of the fundamental excitation wave (Berger 1999). This leads to the possibility of developing a genuine nonlinear holography, according to a principle schematically represented in Fig. 8.9. Although this concept opens interesting perspectives, its practical implementation presents a series of difficulties. Thus, assuming a certain spatial distribution of the pump wave, the problem consists in structuring the nonlinear material in such a way as to finally obtain the desired nonlinear emission. In other terms, the problem which needs to be solved within the framework of nonlinear optics is the inverse of the Huygens-Fresnel principle.

8.4 Photonic Crystals with Third Order Susceptibility

It has been pointed out already, in the introduction to this Chapter, that nonlinear optics will be a crucial stage for the further development of photonic crystals. These structures are indeed expected to play an important role in the manipulation of light. In the same way as the path of an electron can be manipulated in a transistor using other electrons, it is hoped that photonic crystals will open the way to the manipulation of light by light. This goal is at the very heart of third-order nonlinear optics.

As has been described earlier, second-order effects are mostly used either to modify the frequency of light (frequency doubling, difference frequency generation, parametric fluorescence) or to control it through an electric field. Frequency conversion can also be achieved by exploiting a third-order process such as four-

wave mixing, where the signal and idler photons are generated from an intense pump pulse. Here again, phase matching is a crucial step. The same applies to the management of other third-order effects, for example the minimization of the spontaneous Raman scattering. Promising results in this field have been obtained using photonic crystal fibres (Fan 2005; Fulconis 2005; Rarity 2005). These fibres will be described at greater length in Chapter 11 of this book. However, it is clear that third-order effects are essentially adapted to the control of the phase and/or intensity of light by light at either same or a different frequency. Specific third-order processes such as self-modulation effects can also occur within a single light pulse. A pioneering work along these directions was carried out by M. Scalora *et al* (Scalora 1994), who investigated intensity-dependent pulse transmission and pulse reshaping in one-dimensional photonic band-gap materials with a third-order coefficient. The interested reader will find in (Lin 1998) another pioneering work on two-dimensional photonic band gaps applied to the realization of an optical limiter in the visible. Since that time, an abundant literature has been published on third-order nonlinear effects in one-, two- and three- dimensional photonic crystals.

An important example of third-order nonlinear effect observed in photonic crystals is optical bistability (Centeno 2000; Fatih 2003; Soljacic 2003; Tanabe 2005; Yacomotti 2006; Yanik 2003). Light propagating through a waveguide is typically made to interact with a Kerr medium placed in a high-quality-factor cavity. The transmitted power is at first a linear function of the input power. At a certain level of input power P_{off}, the refractive index of the medium in the cavity is modified, for instance by two-photon absorption (Tanabe 2005). This causes the incident light to become out of resonance, and transmission to suddenly switch off. After restoring input power to its original level, the system remains in low transmission mode until an incident power lower than P_{off} is reached. Transmission thus depends on the history of the system: this is the principle of bistability (Gibbs 1985), a concept which can be used for the implementation of optical memories and more generally of all-optical information processing systems.

Bistable photonic crystal devices have been proposed for operating optical flip flop circuits where information is memorized and processed with incoming data (Shinya 2006). Such ultra-small devices are likely to become key components of future all-optical high-speed circuits. More generally, the use of high-Q photonic crystals microcavities with reduced volume is of a great interest for bistable devices, since it allows operating these devices at a low incident power and with high contrast ratios between the two stable states. On the other hand, the development of high-performance devices relies on a crucial improvement of photonic crystal technology, namely the suppression of the out-of-plane radiation loss of two-dimensional photonic crystals, which leads to the possibility of achieving high quality factors (Akahane 2003) and very high quality factors (Kuramochi 2006; Notomi 2005; Weidner 2006) in photonic crystal waveguides. It has already been shown in Chapter 7 that two unique features of photonic crystals, i.e. the fact that they simultaneously have a high-Q and a low volume, equal to a few tens of thousands and to less than 10^{-13} cm^{-3} respectively, are perfectly suited for achieving Purcell effects. Likewise, these properties of photonic crystals are of great in-

terest for ultralow-power all-optical switching (Weidner 2007). Powers of the order of a few tens of femtojoules have been experimentally observed (Tanabe 2005), and it is theoretically expected that the single-photon level can be reached (Soljacic 2005). Figure 8.10 presents results obtained with a GaAs waveguide-cavity system where the high-Q cavity is side-coupled to the photonic crystal waveguide (Weidner 2007).

More generally, the exciting possibility of designing photonic crystals with desired photonic band properties is an additional key element which has been instrumental in the success of photonic crystals in the field of third-order nonlinearities (Inoue 2005). For instance, structures can be designed allowing to considerably slow down light at a certain frequency for the purpose of increasing its interaction with matter. Slowing down light has thus been discussed for one-dimensional structures, for example fibre gratings (Zhou 2005a). Structures involving interference schemes between coupled cavities in a photonic crystal waveguide have been designed in such a way as to present a very high sensitivity to the modulation of the refractive index. This offers new and exciting perspectives on the stopping and time reversal of light using photonic crystals (Sandhu 2006; Yanik 2004a, 2004b, 2004c).

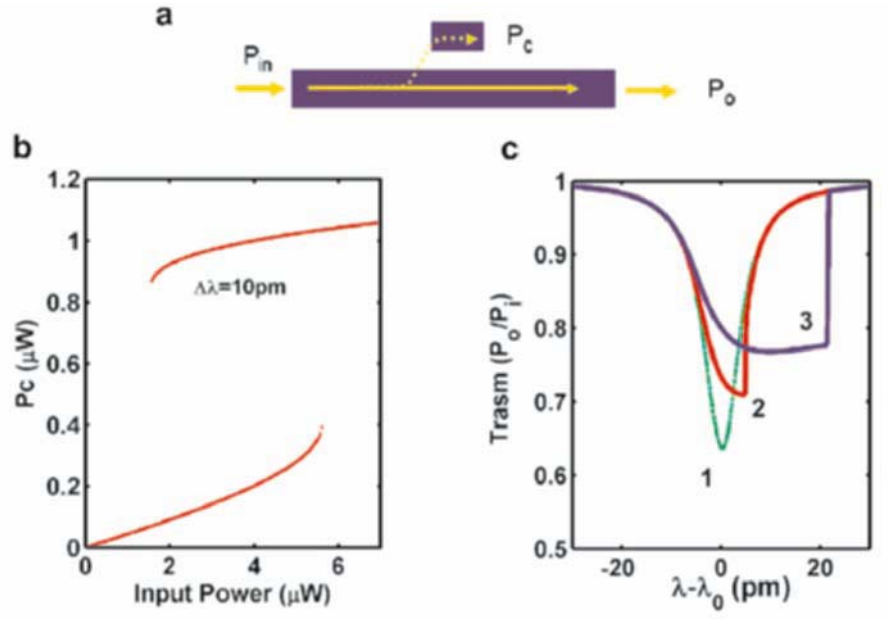

Fig. 8.10. *a.* Schematics of the photonic crystal waveguide-cavity configuration used in (Weidner 2007). *b.* Power emitted from the cavity Pc, plotted as a function of the input power for a wavelength detuning equal to –11pm. *c.* Transmission spectra of the side-coupled system near resonance of the cavity for three different input powers: 0.2 μW (1), 1 μW (2) and 2.2 μW (3)

The control of light speed finds applications in diverse areas, and in particular for all-optical switching. This is a strategic function in all-optical telecommunication networks, and a field where photonic crystal devices can provide competitive solutions. Different factors of merit for an all-optical switch can be identified, including the amount of power needed to control light and the response time of the device (Bristow 2003; Raineri 2004), which itself depends on the physical mechanism involved in the third-order nonlinear processes (Mondia 2005). Photonic crystal waveguides have demonstrated an excellent potential with respect to each of these two factors. The response time has thus been decreased down to the picosecond range using a Mach-Zehnder-type all-optical switch (Nakamura 2004), thereby demonstrating the degree of maturity gained by the integration of photonic crystal devices. Another crucial factor of merit is the capability of coupling the photonic crystal device to a fibre or to another telecommunication integrated device. This factor should not be neglected, and it will probably become a key element for the success of this technology In this respect, the pioneering work reported by the research group directed by O. Painter should be mentioned here (Barclay 2005). The authors succeeded in achieving a fibre-to-cavity coupling efficiency reaching 44% thanks to an original coupling design, and were finally able to observe a bistable behaviour for a 250 μW power at the fibre input. The very fact that the result was given in terms of fibre input power rather than by using an estimate of the power actually coupled into the device is certainly a sign that these devices are beginning to reach the stage of practical applications.

Part III

Fabrication, Characterization and Applications of Photonic Bandgap Structures

Introduction to Part III

The last part of this book will be devoted to a survey of the potential applications of photonic crystals to different fields, as well as to the fabrication and characterization methods which are the most suited to these crystals. The miniaturization of existing optical devices and the exploitation of novel properties of the kind presented in the second part of this book are among the main incentives for the development of photonic crystals. This applies not only to semiconductor devices in planar integrated optics, discussed in Chapter 9, but also to microsources (Chapter 10) and optical fibres (Chapter 11). We also devote a specific chapter to the subject of three-dimensional photonic crystals (Chapter 12). Since the fabrication of these devices remains a difficult process, they may seem 'futuristic' compared to other existing types of photonic crystals. However, these photonic crystals also foreshadow the development of a future three-dimensional optoelectronics. Finally, in order for this survey to be as complete as possible, we shall examine in Chapter 13 the potential applications that are currently expected for photonic crystals in the long wavelength range, i.e. in the field of microwave devices and antennas. In spite of its distinctive features, it is becoming increasingly apparent that the microwave region share many common aspects with optics.

9 Planar Integrated Optics

9.1 Objectives, New Devices and Challenges

Planar integrated optics plays a key role in many fundamental optoelectronic devices. These devices can be conveniently classified according to the materials on which they are based.

Thus, doped silica/silica systems are used for the fabrication of passive integrated devices with an extremely tight tolerance. As an example of such devices, we may mention phased arrays or 'PHASARs', which are integrated spectrometers intended at multiplexing or demultiplexing signals.

Semiconductors, and more specifically III-V semiconductors, are essential to the operation of laser diodes and compact optical amplifiers used for generating and reinforcing signals. Almost all such devices include a waveguide for maximizing the interaction between light and matter. Semiconductors also allow the implementation of a large variety of optoelectronic functions and nonlinear optical functions, provided however that the carrier dynamics can be adequately controlled, in particular at the picosecond time scale, which now corresponds to bit rates much higher than 100 Gbits/s. Dielectric materials with high electro-optical coefficients are more particularly interesting for the realization of modulators or very fast nonlinear functions (without carrier) used for the generation of signals by the frequency sum or difference of two signals. Lithium niobate ($LiNbO_3$) is an example of such a material, which in addition can be polarized. Finally, attempts at introducing organic materials are continually being made, for the realization either of low-cost devices or of optical backplanes in board-to-board interconnects. In addition, some of these organic media present a thermal drift of the refractive index $dn/dT < 0$, in direct contrast to the standard case, where $dn/dT > 0$. Such a property is of particular interest for the compensation of the thermal drift.

As suggested by the mention of temperature compensation, integrated optics is already a few decades old, enough to find solutions to such problems as the insensitivity to polarization or parasitic reflections. For all the functions mentioned above, the pioneering devices have been indeed developed in the 1960s. Contrary to electronic integration, optical integration has not developed at the fast pace of Moore's law: no more than two or three functions can currently be cascaded on sixteen channels, and more commonly on two or four channels only. The reasons

for the limits imposed on integration are far from being trivial. A first limitation is the higher cost of fabrication of small-scale device. Another limitation lies in the necessity of a coupling of these devices to single-mode fibres with at least a sub-micrometer resolution, without any excessive reflection: the easy mounting of 'optical chips' on 'optical printed circuit boards' still remains a remote prospect. A third limitation is the existence of incompatible technologies, and the necessity of resorting to a hybrid integration of devices: for instance, chips realized with different technologies (lasers, modulators, etc.) are embedded on a board where an adequate optical circuit has been defined. During the telecom bubble of the late 1990s, the demand for a rapid production of such hybrid devices by an exponentially expanding market diverted research groups from monolithic integration. However, this approach is now being reconsidered, especially in view of the recent breakthroughs in the field of 'silicon (nano)photonics', where a silicon platform is used with minimal addition of exogeneous components, for instance e.g. III-V lasers. The technological advances facilitating such an integration are only maturing slowly across the different fields involved in this process. For the time being, the realization of optical chips as compact and versatile as electronic chips remains a distant dream, even if the silicon chip company Intel has now integrated possible chip-scale optical interconnects in its roadmaps (see for example http://www.intel.com/research/platform/sp/).

In this context, the concept of photonic crystal has aroused considerable expectations. After an early naive period, the possibility of implementing integrated optical functions using photonic crystals really started being investigated at the turn of the millennium. A more complex picture of photonic crystals has thus emerged, and we are now in a position to understand how the basic properties of photonic crystals, which have been described in the second part of this book, can be turned into applications to integrated optics.

As will be seen in this chapter, two-dimensional crystals remain by far the main focus of attention. The main advantages of two-dimensional photonic crystals, namely their simpler fabrication and easier modelling, lead to the possibility of completely controlling the incorporation of defects or the implementation of certain original dispersion effects. Conversely, planar integrated optics provide an elegant method for 'freezing' the third dimension in the two-dimensional problem. By starting from a slab with a single-mode behaviour along the third direction, a photonic crystal type structuring is then defined on this slab. To some extent, this amounts to considering the world as being two-dimensional, as in Edwin A. Abbott's 'Flatland' (Abbott 1992).

In such a two-dimensional world, the use of photonic crystals as 'optical insulators' naturally leads to envision the possibility of realizing optical circuits bounded by such insulators in order to channel, analyse and combine an increasing number of optical signals in a more compact form than the solutions previously developed in the field of integrated optics. In particular, the classical guiding method used in integrated optics, i.e. index guiding, leads to severe limitations as regards the curvature of bends. This is more particularly true for low index contrasts, as is the case with doped silica /silica systems. For this reason, index guiding does not lend itself very well to miniaturization, since several

square centimetres can be necessary for implementing a single optical function. Similar considerations apply to devices or functions based on resonant cavities. It is hoped that these limitations can be overcome through the use, in the form either of waveguides or cavities, of defects artificially engineered in two-dimensional photonic crystals. More specifically, there are expectations that waves guided in photonic crystal defects will be able to follow bends at the wavelength scale, i.e. for instance at the micrometer scale. Even if catching up Moore's law remains beyond reach, such a decisive breakthrough would lead to a tremendous acceleration of the evolution towards integration.

Photonic crystals with a strong index contrast also provide the possibility of exploiting the Bloch waves of photonic transmission bands, which are markedly different from usual plane waves propagating in unbounded homogeneous media. This stake had been clearly perceived by Philip St. J. Russell in his pioneering work on one-dimensional integrated optical structures in the 1980s. One of the effects expected to occur near a band edge is the superprism or ultra-refraction effect, already discussed in Chapter 6. It might be recalled here that the wave vector exhibits an enhanced dependence on the frequency ω in the vicinity of a band edge, since $\mathrm{d}\omega/\mathrm{d}k$ becomes zero in one dimension. This effect is interesting for the demultiplexing of very close signals, for instance with a relative frequency spacing $\Delta\omega/\omega = 0.1\%$. When propagating through a superprism, the different frequencies translate into different wave vectors, which can then be converted into widely different propagation angles, for instance with a 10° divergence, eventually allowing the spatial separation of the signals.

This mux/demux function is necessary for the analysis of an entire series of signals carried by a comb of nearby frequencies (wavelength division multiplexing, WDM). All these signals need to be regenerated, routed, etc. However, in many cases, a single channel, consisting more precisely of a narrow frequency band, must be separated or injected into a fibre. This is the case for instance when a transmission bus line goes by a user: it needs to leave the signal addressed to this user (drop) and to insert the signal received from him (add). This add/drop function is currently one of the most intensively researched functions. A simple scheme for implementing this function consists in the selective coupling of a guided wave to an optical resonator: energy is transferred to the resonator only at the frequency of the resonator, and not at any other frequency. After energy has been transferred, it must then be directed onto another element, for instance a detector or another waveguide. Such a system should ideally be reconfigurable by means of electro-optical elements.

A completely different use of the geometry of two-dimensional photonic crystals will be described in Chapter 11 when considering the case of microstructured fibres. Contrary to planar integrated optics, discussed in the present chapter, the propagation of waves in these fibres occurs along the invariant direction of the crystal (see also Fig. 5.5 in Chapter 5). This is a most important distinction, which can be summarized by saying that attention focuses in this case on the transverse rather than on the longitudinal control of light. Chapter 11 will be more specifically devoted to these fibres, which are also referred to as 'photonic crystal fibres'. Prototypes of such photonic crystal fibres have been the first two-

dimensional photonic crystal device to reach market around the year 2004. This has been made possible by both their relative simplicity, which results from the fact that they are fabricated from a unique material (SiO_2), and by their input/outputs, which are almost as simple as those of usual fibres,

In all these cases, confinement and guiding are two key functions. We shall therefore begin this chapter with a brief survey of classical optical guiding, based on a refractive index step rather than on periodicity. Different applications in this field will then be described, and the choices to be made for actual two-dimensional photonic crystals will be discussed. Finally, we address certain problems which have not been satisfactorily answered so far, and which are likely to remain intensively investigated during the next decade. For engineers looking for innovations in the field of integrated optics, it is quite clear that the advent of photonic crystals around the year 2000 is of great significance. Even if actual applications of photonic crystals were to remain of a limited scope in the near future, their influence on concepts and their role in the drive toward miniaturization of highly resonant systems cannot be ignored.

9.2 Fundamentals of Integrated Optics and Introduction of Photonic Crystals

9.2.1 Conventional Waveguides

As a wave propagates away from its source, it generally tends to diverge and to decay. The guiding of light is intended at obviating this effect. The analogue of the potential step, which confines for instance water in a canal or electrons in a copper wire, is the refractive index step between the core and its cladding with lower index. As will be seen later, such a pure index confinement can be achieved in certain simple configurations. However, since by construction this confinement is not omnidirectional, its implementation is quite delicate in certain critical parts of actual devices. In this respect, photonic crystals bring a more elegant and general answer to the problem of confinement, at the price of course of an increased complexity.

The fundamental phenomenon involved in ordinary index confinement is the total internal reflection of a plane wave propagating from a medium with a high index n_2 towards a plane interface formed by a dielectric with an index $n_1 < n_2$, at an incidence angle θ beyond the critical angle $\sin \theta_c = (n_1/n_2)$. This results in the generation, on the side with the lower index, of an evanescent wave, whose amplitude decreases exponentially as the distance to the interface increases.

The two edges of our light channel are therefore two such plane and parallel interfaces, separated by a distance L from one another and clad with two, possibly different, indices n_1 and n_3, sandwiching the core with higher index n_2. We now need to account for the wave aspect of the problem, and to search for har-

monic solutions at the pulsation ω in the absence of any source. In the planar waveguide geometry, which presents an invariance along two directions, the six components of the electromagnetic field can be separated into two groups of three components respectively, referred to as TE and TM polarizations (see Section 1.1.5 in Chapter 1). Thus, in much the same way as for infinite two-dimensional crystals, the time-harmonic Maxwell's equations reduce to a scalar equation involving one of these two groups of three components. Using the same reference axes as in Fig. 9.1*a*, where x is the propagation axis and (xz) is the plane of the invariant directions, the TE and TM polarizations are associated with the component groups (H_x, E_z, H_y) and (E_x, H_z, E_y) respectively. The scalar equation may involve either E_z or H_z. From a mathematical point of view, the problem is to search for solutions satisfying the two boundary conditions between the field propagating in the core and decreasing evanescent waves in the claddings. Since the system is separable and invariant along the z axis, it appears that, in TE polarization, E_z assumes the following form:

$$E_z = A(y) \times exp(ik_x x) \times exp(-i\omega t) \tag{9.1}$$

where $A(y)$ satisfies an equation deduced from Eq. 1.6a, which turns out to be completely analogous to the one-dimensional Schrödinger equation if one substitutes $-\omega^2/c^2 n^2(y)$ to the potential $V(y)$ and the opposite of the squared propagation constant $-k_x^2$ to the energy eigenvalue E. This analogy is more particularly valid in TE polarization, and is less so in TM polarization. Thus considered, higher indices can be viewed as potential wells and the claddings as potential barriers. The conclusion can therefore be drawn that the spectrum of the solutions for k_x^2 is partly discrete with discrete solutions $A_p(y)$ and adequate constants $k_x^{(p)}$, with the sign here being arbitrary. Two solutions (modes) $A_1(y)$ and $A_2(y)$ have been schematically represented in Fig. 9.1*a* in the case of a symmetric waveguide. Note the alternate parities for the fields $A_p(y)$ of the modes of such a waveguide.

In this symmetric case, the number of allowed discrete solutions is intuitively dependent on the number of oscillations that a wave may complete between the two interfaces when approaching the critical angle. $A_p(y)$ is actually of the form $\cos(k_y y)$ or $\sin(k_y y)$ in the core, where:

$$k_x^2 + k_y^2 = n_2^2 \omega^2/c^2 \tag{9.2}$$

Let us now reconsider the total internal reflection condition. Actually, this condition means that k_x needs to be large enough to prevent the wave from coupling to the continuum of radiation modes of the cladding with index n_1, i.e. to modes whose wave vector is bounded by $n_1\omega/c$.

Since the equation $k_x = k_2 \sin\theta = n_2(\omega/c)\sin\theta$ also holds, the relation $\theta > \theta_c$ can be rewritten in the form:

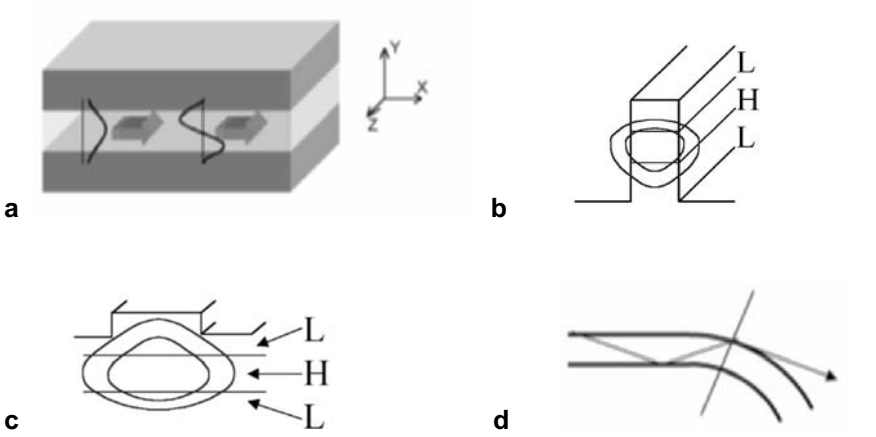

Fig. 9.1. *a.* Planar waveguide and profiles of its first two modes $A_1(y)$ and $A_2(y)$ *b*. Deep-etched ridge waveguide c. Shallow-etched ridge waveguide *d.* Bend and role of the critical angle. H and L in figures *b* and *c* are for high-index and low-index, respectively

$$k_x > n_2\,(\omega/c)\,\sin\theta_c = n_1\omega/c \tag{9.3}$$

The lowest value allowed for k_x by the total internal reflection condition is therefore $k_x = n_1\omega/c$. Accordingly, the highest possible value for k_y will be $k_y = (\omega/c)\sqrt{n_2^2 - n_1^2}$, while the number of oscillations has an upper bound $k_y L/\pi$ with this value for k_y. By using simply $(\omega/\pi c)=(2/\lambda)$, and taking into account the fundamental mode which does not complete a full oscillation, the number of allowed modes turns out to be equal to:

$$\textit{Number of modes} = 1 + \text{Integer}\,[(L/(\lambda/2))\ \sqrt{n_2^2 - n_1^2}\,] \tag{9.4}$$

From this equation, it can be seen that in order to achieve a single-mode guiding, i.e. to 'freeze' the third degree of freedom of light to a single discrete value, it is necessary that the value for the thickness L should be relatively small. Indeed, while L is small in the case of a high index contrast ($\sqrt{n_2^2 - n_1^2} \sim n_2$ and $L \sim \lambda/2n_2$, it becomes much larger for lower index contrasts, up to ($L \sim \lambda/2\sqrt{2n\Delta n}$), within the limit of a small index step $\Delta n = n_2 - n_1$, as is the case for instance with doped silica /silica. In practice, the concept universally used in integrated optics is that of the effective refractive index, which depends on the mode p and is defined as follows:

$$n_{eff}^{(p)} = k_x^{(p)} c/\omega. \tag{9.5}$$

The considerations developed above show that all guided modes satisfy the relation $n_1 < n_{eff} < n_2$. In the case of a single-mode planar waveguide, everything takes place as though the waveguide were a block of material with index n_{eff}, where, however, the beams would never vertically diverge, i.e. along y.

The asymmetric case has been extensively discussed in the literature (Marcuse 1974). We shall contend ourselves here with noting that, in such a case, the conditions for single-mode guiding, and even for the very possibility of such a guiding to exist, do no longer assume a simple form.

Another case which can be algebraically analysed in a one-dimensional fashion is that of fibres whose index profile presents an azimuthal invariance. Proceeding to an adequate transformation of variables, and under the assumption of an $\exp(im\phi)$ azimuthal dependence, ϕ can be eliminated, leaving only the radial variable. In other terms, the 'azimuthal quantum number' is set to the value m. For each value of m, one has then to solve a one-dimensional equation whose solution $A_n(r)$ is indexed by an integer radial number n. In order to go any further, the use of Hankel or Bessel functions would become necessary (see Appendix A devoted to the multipole method, where these functions appear).

Lateral Confinement and Stripe Waveguides

Let us now return to planar waveguides, and let us assume that $\omega = \omega^{(p)}(k_x)$ is the dispersion relation of the p^{th} mode. The guiding condition $k_x > n_1\omega/c$ means that the dispersion curve of a lossless guided mode necessarily lies below the 'light line' whose equation $k_x = n_1\omega/c$ defines the limit of grazing incidence in the cladding (see Chapter 5). An asymmetric waveguide presents but a single genuine light line, which is the 'lowest' one in the $\omega = \omega(k_x)$ diagram and is associated with the cladding with higher index. In such a case, the regions of the dispersion diagram extending between the light lines of the two claddings correspond to waves propagating both in the core and in the higher index cladding, but undergoing a total internal reflection at the interface with the lower index cladding.

Let us now consider an additional lateral confinement of the waveguide (Coldren 1995; Tamir 1990). For this purpose, let us define stripes in the planar waveguide, by etching away material, in order to force the optical signals to follow certain specified trajectories. Two limit cases might be considered: first, that of a 'strong' guiding created by using a deep-etched ridge, as represented in Fig. 9.1*b*, and that of a 'weak' guiding, where a simple 'dielectric load' (Fig. 9.1*c*) is used for laterally confining a mode of the waveguide. In such a system, we need to restrict ourselves to the case of a straight channel waveguide if a genuine propagation constant is to be defined. Within this assumption, the two previously decoupled polarizations become coupled, and all six components of the electromagnetic field are rigorously nonzero for the eigenmodes of this waveguide.

Nevertheless, it is often possible to still consider the modes as being quasi-TE or quasi-TM, especially if the in-plane width defined by the lithography is larger than the thickness L of the core. The latter is generally small in order to achieve a single-mode regime for the basic planar waveguide. The thickness of the core is controlled by wafer-scale thin-film deposition techniques In the case of the deep-etched ridge waveguide represented in Fig. 9.1*b*, simple considerations apply to the effective index n_{eff}. Due to the additional confinement enforced along the lateral directions, this effective index will be smaller than the effective index of the originally non-etched planar waveguide n_{eff}^{planar}. In the case of the dielectric load represented in Fig. 9.1*c*, the confinement is enforced by adding material, and n_{eff}^{planar} will obviously be lower than the index n_{eff} of the channel-guided mode due to the presence of the load for the latter. In the specific case of a quasi-TE mode propagating in such a dielectric-loaded waveguide, horizontal guiding can often be described adequately enough by starting with two different planar effective indices: n_{eff}^{stripe}, calculated as if the stripe had no lateral boundary, and n_{eff}^{planar}, calculated in the absence of the load. The lateral guiding can thus be regarded, in the plane of the waveguide, as resulting from the confinement of the wave by the one-dimensional profile $n_{eff}^{planar} / n_{eff}^{stripe} / n_{eff}^{planar}$. However, it is necessary to proceed cautiously at this point, since the main component of the field in the 'plane' of the interface is not E_z, but H_z. In the z-x plane, we are therefore in a TM-like situation.

Since semiconductors present a high index n, they lend themselves to the realization of waveguides with index steps $\Delta n \sim 0.1$- 0.5 much higher than those of silica fibres, where $\Delta n \sim 0.01$. As a consequence, the modes tend to be very small, and to have a width well in the sub-micron range, which contrasts with the modes of fibres whose typical width is of the order of 8 μm. The coupling between a fibre and a semiconductor waveguide will therefore be very weak unless a taper structure is used, where the mode of the waveguide can adiabatically extend both laterally and vertically without coupling to the extra modes that may exist in the enlarged region.

These waveguides already allow the realization of very sophisticated devices, intended more particularly at telecommunication applications. Examples of such applications include beam splitters and couplers, demultiplexers of the 'PHASAR' type (Smit 1996), which exhibit a high spectral dispersion, Mach-Zehnder interferometers used for signal modulation in telecommunication technologies (Bigo 2006), etc. In this context, it can be of interest to adopt a monolithic approach and to integrate sources in these devices. Indeed, not only does such an approach allow the size of optical switchboards to remain small enough, but it may also enable such advanced functions as wavelength transposition at the nodes of WDM networks. A specific issue associated with photonic crystals and all high-index systems, the dependence on polarization, can be ignored for integrated laser sources, since these devices have a fixed polarization and are quasi-TE polarized in most instances.

As has been mentioned earlier in the chapter, the limited curvature of the bends is one of the main factors that restrict the compact integration of these functions. It also results in very important losses as soon as the radius falls down

below a certain relatively high critical value, which typically is of the order of a few hundred microns and is directly determined by the lateral index step $\Delta n_{eff} = n_{eff}^{stripe} - n_{eff}^{planar}$. This issue can be best understood by considering a simple ray tracing model, where the problem consists in not exceeding the critical angle when arriving from a straight onto a curved section of the waveguide. The angular margin between the equivalent angle in the straight waveguide and the critical angle thus determines the critical radius (Fig. 9.1*d*). Silica/doped silica structures are the most penalized in this respect, because they require radii at the centimetre scale. At the opposite extreme, silicon-on-silica structures, generally known as SoI (silicon-on-insulator) structures, and where Δn can be larger than 2, allow radii of a few microns.

SoI substrates are widely used and they represent a major supply in the microelectronic industry. Until recently, the realization of abrupt bends in deep-ridge SoI waveguides was hampered by the power and coherence losses resulting from the roughness of the walls of the waveguide. For single-mode deep-ridge waveguides, these losses tended to be unacceptable as soon as the propagation distance reached the order of 1 mm. Another negative effect associated with these high contrasts was the important polarization conversion at the bends. Since 2003 however, significant advances in silicon fabrication technology for photonics have resulted in impressive performances. In this respect, the use of SoI in CMOS foundries has proven very effective, even if it implies demanding requirements at design stage.

9.2.2 Photonic Crystals in Integrated Optics

We shall now disccuss the interest of two-dimensional photonic crystals for integrated optics. Owing to their band gaps, these crystals should ensure a new form of lateral guiding, which is believed to be superior, from a physical point of view, to index guiding. Actually, several different advantages are expected from such a guiding (Benisty 2006): (i) the miniaturization of bends by exploiting the property of photonic crystals of 'blocking' light, and therefore of preventing its leakage, (ii) the realization in a single technological step of a number of different functions such as guiding, dispersion (superprisms), filtering (microcavities) as well as coupling and confinement functions (laser mirrors). These issues are discussed by T. Baba in (Baba 2007).

Basic Devices

Fig. 9.2 presents a series of applications of photonic crystals in the field of integrated optics. Straight and bent waveguides, represented in Fig. 9.2*a*., are the most elementary application in this respect. Other simple functions consist in separating signals depending on their polarization or their wavelength, as in the case of the polarization beam splitter represented in Fig. 9.2*b*. All these functions rely in a relatively direct way on the concept of photonic band gap, used for opening or closing broad transmission windows in the spectrum, which are not

the same for the different polarizations. Optical telecommunications provide a convenient gauge for spectrum bandwidth. It might be recalled here that the aggregated transmission bandwidth of optical fibres can be increased by simultaneously exploiting a few dozen wavelength channels, spaced by 100 GHz (0.8 nm) between 1530 and 1560 nm, and with a 25 to 40 GHz bandwidth each. Telecommunication operators now offer the possibility of using a 50 GHz spacing (0.4 nm), and plan to extend this technique to neighbouring bands. A single fibre would thus carry 128 channels, each to be routed at a different node in an optical network. Used in combination with techniques offering bandwidth efficiencies higher than 1bit/s/Hz (Bigo 2006), this results in the possibility of achieving a multi-THz bandwidth capability.

In this context, more sophisticated function can be implemented, including the demultiplexing of all these channels onto a set of physically distinct waveguides, in much the same way as a dispersive glass prism does with a white light beam. The superprism effect represented in Fig. 9.2*c* (see also Section 6.3 in Chapter 6), and the miniature in-plane echelette-type gratings represented in Fig. 9.2*d*, are two possible solutions to this problem. Presently, arrays of distributed waveguides, referred to either as arrayed waveguide gratings (AWG) or as phased arrays (PHASAR), are used for the multiplexing and demultiplexing of channels (Fig 9.2*e*). These systems offer high performances, and surpassing them is quite an exciting challenge.

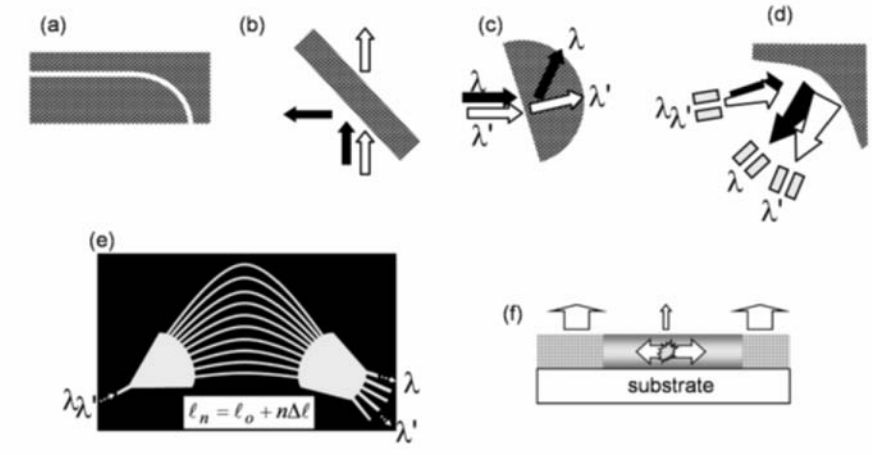

Fig. 9.2. Applications envisioned for photonic crystals *a.* Straight and bent waveguides *b.* Polarization beam splitters (TE and TM beams are represented in the form of black and white arrows respectively) *c.* Superprism (beams with different frequencies are represented by black and white arrows) *d.* Miniature monolithic reflective gratings *e.* Spectrometer, known as 'Phasar' or 'AWG', based on an array of waveguides with geometrically increasing lengths. The length increment $\Delta\lambda$ is a multiple of a central wavelength, for which the phase front at the exit is naturally focused at the central exit

The add/drop function, which consists in filtering a single wavelength out of a multiplicity of signals, in order either to extract it or to insert it into a network, can be achieved by inserting two microcavities in a photonic crystal, and more precisely in a doubly degenerate resonant system. Of course, these microcavities must resonate at exactly the intended frequency, while being adequately coupled to the waveguide carrying the multiple signals.

Lateral guiding and partially reflective mirrors can also be implemented in laser diodes. These two functions are more particularly interesting for semiconductor lasers based on the coupling of two cavities, which are known for their frequency tunability (see Section 9.2 in this chapter), and for master oscillator power amplifier (MOPA) systems, adapted to the high power laser diodes used for the pumping of fibre amplifiers.

The dimensions and transduction energy in modulators can be strongly reduced when light is made to spend a longer time in an electro-optical medium structured in such a way as to slow down the Bloch waves and minimize their group velocity $d\omega/dk$. Nonlinear functions, including signal regeneration of the 2R type (reshaping and reamplifying) gain similar benefits from a slow-light regime. Finally, an optical buffer memory is a long-sought device, which should be capable of storing in a controlled manner an optical data flow at the demanding 40 Gbits/s rate, hence at a ~ 1 ns time scale (i.e. at least 10 bit times). This has been recently achieved in two studies (Asano 2006; Tanabe 2007).

Light Extraction

The properties of photonic crystals can also be used for the extraction of light. This applies equally to the light guided in a channel waveguide and to the more randomly directed spontaneous emission of a light-emitting diode (LED) (Fig. 9.2*f*). The ultimate objective here is to prevent the active semiconductor region from radiating along unwanted directions, and more particularly in the direction of the substrate and of the lateral sides of the active region. The photonic crystal can act along these directions by suppressing all unwanted photon modes, especially guided modes.

A heuristic demonstration of this effect, albeit at a cryogenic temperature, has been reported in (Fujita 2005). In principle, this effect could benefit light-emitting diodes, which today represent the largest share of the market for optoelectronic components, and the largest number of devices sold per year (several billions). Indeed, the extraction efficiency of LEDS remains low, from 2 to 20%, depending on the technology used for their fabrication. Planar microcavities have already demonstrated their potential for achieving an optical confinement in the vertical direction and the angular redistribution of the spontaneous emission (see Section 7.1.1 in Chapter 7). A state-of-the-art survey of planar microcavities will be presented in Section 10.1 of Chapter 10.

Most planar structures, even those realized in laboratory, still present, regardless their 'vertical' extraction performances, a noticeable density of in-plane guided modes. A naive solution would be to use photonic crystals for preventing the propagation of these modes. However, the realization of a good quality *p-n*

junction in the very middle of a 'holey' photonic crystal structure remains a delicate issue from a technological point of view. In the short term, the main application which can be expected for photonic crystals in this field would be to use them in the vicinity of the device for the extraction of the guided light arriving from the active region. Here again, these issues will be discussed at a greater length in Chapter 10, devoted to microsources.

Choice of the Two-Dimensional Crystal

The consideration of the ideal two-dimensional geometry described in the first part of this book (see Section 1.3.3 in Chapter 1) shows that the type of lattice where band gaps are the most likely to appear are typically lattices consisting of a triangular array of holes. Indeed, these lattices exhibit a Brillouin zone approaching a circle, a property which tends to favour the overlap of the band gaps in the different symmetry directions. The period a is set in such a way that a band gap will appear for at least one polarization at the wavelengths of interest, such as 1.3 µm and still more 1.55 µm (Fig. 9.3).

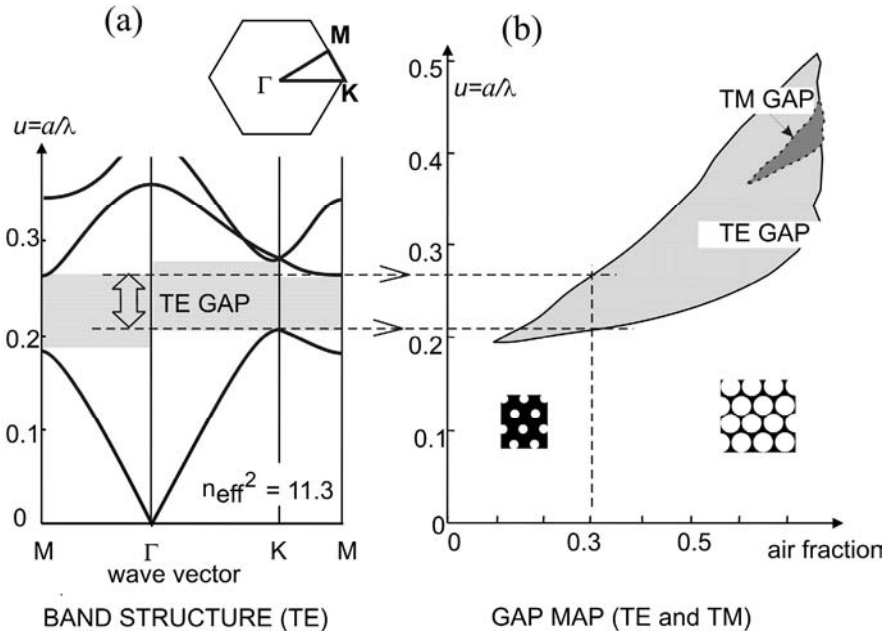

Fig. 9.3. Triangular photonic crystal *a.* Band diagram in TE polarization for $f = 30\%$ and $\varepsilon = 11.3$ *b.* Associated 'gap map': the TE and TM band gaps are represented as functions of the air-filling factor *f.* The number of plane waves used here is $N = 127$

As a first approximation, the matrix index to be used in two-dimensional simulations for accurately predicting the behaviour of the crystal used for the guiding is the effective index n_{eff} of the fundamental guided mode. The consideration of the 'gap map' presented in Fig. 9.3*b*, which shows a typical value for the effective index $n_{eff} \sim 3.4$, indicates that the frequency range should fall within the limits $0.2 < a/\lambda < 0.5$, hence that the period a should be between 300 and 700 nm. The air-filling factor f may range from 0.2 to 0.75, while the period will be increasing with f at a fixed value for λ.

It might be noted that, unfortunately, a 'direct' photonic crystal, consisting of dielectric columns in the air, would not be adapted at all to dielectric guiding in the third dimension. From a practical point of view, this results from the fact that channel waveguides would have to be created in this case by omitting rows of columns. While the first calculations for an in-plane two-dimensional propagation had led to seemingly encouraging results (Mekis 1996), the importance of radiation losses in these structures became apparent when properly taking into account the third dimension along the axis of the columns. There would still remain the possibility of introducing a dielectric type defect, in the form for instance of a row of columns with a larger diameter or a higher refractive index. While this solution is not without justification from a theoretical point of view, experimental evidence remains scarce. A practical difficulty is that these columns need to be held on a substrate located at a distance large enough from the guided wave. The comparison with the difficulties already encountered in the 'standard' case, where holes were drilled in a planar waveguide, can be useful for understanding the difficulties presented by a photonic crystal formed by such dielectric columns.

Choice of the Planar Waveguide

We now turn to the problem of choosing the most appropriate planar waveguide that can be etched with the photonic crystal pattern described above. This question is still unsettled, and it will probably remain so for some time. A convenient classification consists in distinguishing between waveguides with a high vertical index contrast, and waveguides with a low vertical index contrast, as these two types of waveguides have been investigated along distinctly different lines. The highest index contrast can be found between a semiconductor and the air. In order to realize such a semiconductor membrane, a specific technology must be used for holding it by the edges or on posts. We also include in this category the case of semiconductor layers on low-index layers ($n < 1.7$), since the physics of these systems are quite similar. All these systems will be referred to hereafter as 'membrane waveguides'.

For lower index contrasts, as is typically the case for industrial optoelectronic devices like laser diodes, the waveguide is often buried or sandwiched between two cladding layers with relatively high indices n_1 and n_3 ($n > 2.5$). Of course, intermediate situations may exist, for instance that of silicon clad with silicon nitride ($n = 2.2$) or that of GaN-based LEDs, (see Chapter 10). However, the objec-

tive of an optoelectronic integration justifies the use of a low index-contrast cladding, as the latter is compatible, for instance ,with electrical injection.

In the next section of this chapter, we shall successively consider buried and membrane waveguides. In this context, we shall make use of the crucial concept of 'light line', already introduced in the second part of this book (Chapter 5). Here the use of this concept will be taken a step further. The quantification of losses is a constant subject of attention in the area of integrated optics. Therefore, after having established the possibility of coupling to a continuum of radiative modes, it will be necessary to determine the amount of guided energy which is lost. This requires particular care in the case of Bloch modes, especially when it comes to analysing precisely how and why they acquire an imaginary wave vector *k"*.

Quantification of Losses in Bloch Modes

When the vertical dimension *y* is taken into account, the Bloch modes of a generic structure with in-plane *x*-*z* periodicity read as:

$$E_z = \sum_m A^m(y)\ \exp[i(k_x + G_m^x)x]\ \exp[i(k_z + G_m^z)z] \quad \exp(-i\omega t) \tag{9.6}$$

where *m* spans the two-dimensional reciprocal lattice vectors $\{G_m^x, G_m^z\} \equiv \{G_m\}$. Other field components will have similar forms with different functions A^m. The plane wave expansion in Eq. 9.6 should be seen both (i) as a generalization of Eq. 9.1 and (ii) as a Fourier expansion of the periodic part of $E_z(x,y,z)$ in the form of *y*-dependent terms $A^m \exp[i(k_x + G_m^z)x]\exp[i(k_z + G_m^z)z]$, where *m* is a two-dimensional index. The physics of the investigated processes requires most of the time the consideration of only a few values for *m.* For instance, contradirectional coupling in the fundamental gap can be described by only two values. Of particular interest is the fact that A^m only depends on *y*. Therefore, if only a few values for *m* are necessary, assessing the relationship with the non-photonic-crystal case described in Eq. 9.1 can be managed easily.

We shall now consider the two situations that can arise for a guided mode, depending on whether its dispersion curve lies below or above the light line. For this purpose, we shall consider a generic periodic structure, in the form of a partially perforated guiding layer with index n_2 disposed on a cladding layer with lower index n_1, as represented in Fig. 9.4.

For lossless modes below the light line, spatial harmonics $A^m(y)$ vanish as $y \to \pm\infty$. In other words, $A^m(y)$ displays an $\exp(\pm ik_y^m y)$ dependence, where the vertical wave-vector component k_y^m associated to G_m is purely imaginary both in the air and in the substrate with index n_1:

$$k_y^{m(air)} = i\sqrt{\left|\omega^2/c^2 - k_x^2 - k_z^2 - G_m^2\right|}$$
$$k_y^{m(sub)} = -i\sqrt{\left|n_1^2\omega^2/c^2 - k_x^2 - k_z^2 - G_m^2\right|} \tag{9.7}$$

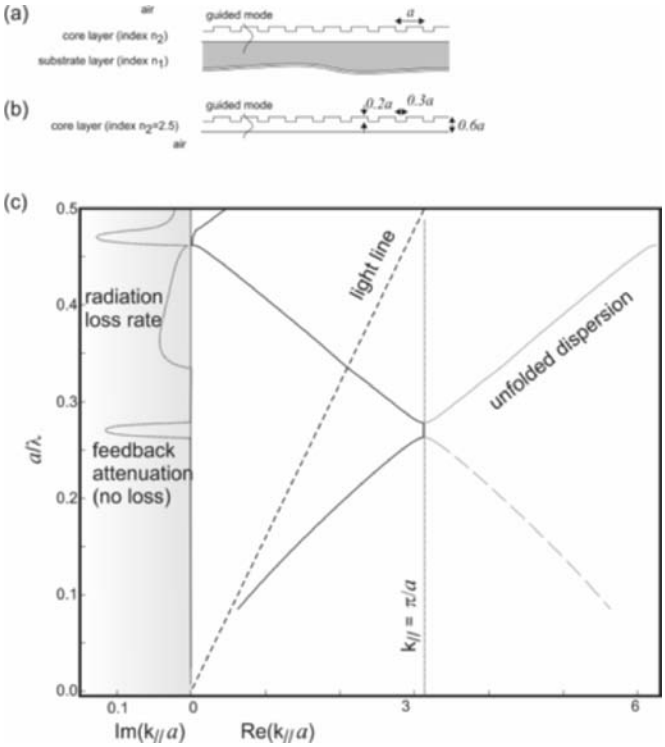

Fig. 9.4. *a.* Schematic representation of a generic corrugated waveguide (one-dimensional photonic crystal structure) with periodic corrugations of period *a b.* In this example, the core has an index $n_2 = 2.5$ and a $0.6a$ thickness, while the lower cladding is air. The periodic corrugations are rectangular-shaped with a $0.2a$ depth and a $0.3a$ width (30% air-filling factor) *c.* Dispersion and extinction of TE Bloch modes, shown in the right part and in the left part of the figure respectively. Extinction is represented on a shaded background, and with a different horizontal scale. Around the first gap, attenuation is due only to optical feedback (backscattering of the propagating wave). Once the light line is crossed ($a/\lambda \geq 0.33$), radiation losses arise. Around the second gap ($a/\lambda \approx 0.47$), attenuation results both from radiation losses and from optical feedback. As can be seen in the extended Brillouin zone for frequencies outside the gap (grey curves in the right-hand side of the figure) dispersion is similar to that obtained for the non-corrugated waveguide, at least when radiation losses are limited (David 2007)

Modes above the light line are coupled to a continuum, and at least one of the spatial harmonics $A^m(y)$ does not vanish as $y \to \pm\infty$. The existence of radiative losses along the vertical y-direction implies in turn a spatial decay along the direction of propagation, for instance, along the x-direction. This means that k_x acquires an imaginary part k''. In this case, the Poynting vector of the mode decreases with an $\exp(-2k''x)$ behaviour at any (y, z) position. While the time-harmonic dependence is thus preserved, the wave becomes inhomogeneous, and more precisely it becomes physically divergent either in the x or in the $-x$ direction.

Eq. 9.7 remains valid nonetheless. A possible theoretical approach for quantifying the real and imaginary parts of k_x, and more generally $k_{//}$, consists in using the scattering matrix method combined with a 'pole search' technique. This basically means solving an equation of the form $\det[\boldsymbol{S}(\omega, k_x, k_z)] = 0$, where $\boldsymbol{S}(\omega, k_x, k_z)$ is the scattering matrix, while an iterative process is used in order to estimate the imaginary parts of k_x and k_z. A clear relationship exists between this approach and the methods described in Chapter 2, with the provision however that the scattering matrix here is taken in the sense of Whittaker and Culshaw (Whittaker 1999). The interested reader is referred to more recent studies (Nevières 2003; Tikhodeev 2002) for the exact resolution of the matrix equation appropriate to wave scattering in periodically structured layers. Besides, it can be noted that the 'pole search' technique (Sipe 1982) has some relation with the phenomenological method of polology and with the discussion of plasmons developed in Chapter 4.

Fig. 9.4*c* shows the results of calculations performed using the previous method in the simplest case of a one-dimensional membrane-type photonic crystal (Fig. 9.4*b*), invariant in the z-direction (David 2007). The dispersion equation is solved here for a real frequency ω and a complex wave vector k_x. One may also proceed the other way around, by looking for the imaginary part of frequency in order to describe the temporal decay of energy launched homogeneously in space at some initial time. The first step in the 'pole search' technique consists in searching for the approximate amount of leakage $A^m(y)$ using the simplifying assumption that k_x is real. From this, it is then possible to determine how much energy is lost per unit length, and thus to find an imaginary value of k_x from which the process can be iterated in order to obtain a higher order $A^m(y)$ etc.

As can be seen in Fig. 9.4*c*, the imaginary part of $k_{//}$ appears to be nonzero in several occurrences. The fundamental gap here is well below the light line. Although an imaginary $k_{//}$ component occurs at this band gap, it only reflects Bragg backscattering, a phenomenon addressed by the coupled mode theory. The rectangular-shaped corrugation of the membrane shown in Fig. 9.4*b* induces in this case a rectangular-shaped modulation of the effective index with a relative amplitude $\Delta n/\langle n \rangle \approx 4.8\%$. In turn, this leads to a relative gap width $(2/\pi)\,\Delta n/\langle n \rangle \approx 3\%$. Correspondingly, the imaginary part of $k_{//}a$ reaches its peak value at about 3% of the value of its real part $k_{//}a = \pi$. Above the gap, radiation losses are cancelled out ($\mathrm{Im}(k_{//}) = 0$), provided that the dispersion curve remains below the light line.

After crossing the light line, radiation losses abruptly increase ($\mathrm{Im}(k_{//}) \neq 0$) until they reach a certain maximum, and then they gradually decrease until approaching the second gap. Following the usual convention, only the $m = 0$ harmonic is found to be leaky. However, the main harmonic is not actually the $m = 0$ harmonic, but rather the unfolded branch shown in the right-hand side of the dispersion diagram, which, within a symmetry, is the more natural prolongation of the guided mode. After passing the gap, a complex series of phenomena occur, causing $\mathrm{Im}(k_{//})$ first to go down to zero, then to peak to a large value, before resuming a more steady course in the highest frequency band. Around the second gap, attenuation has two origins, and is due partly to Bragg reflection and partly to radiation losses, as is the case in second-order DBR and DFB laser diodes (Kazarinov 1985).

The discussion above can be easily extended to the case of a periodically corrugated structure on a substrate with index larger than air (Fig. 9.4*a*). In this case, the light line is lowered (slope c/n_1), and the leaky region is shifted downwards until it encompasses the fundamental gap. The evolution of $\mathrm{Im}(k_{//})$ reported in Fig. 9.4*c* thus helps us to understand that, in any case, two phenomena contribute to losses in two-dimensional Bloch modes, either separately or in combination. The complete description of the band gap situation would certainly be more complex. The general argument given above applies, but it is also necessary to account for boundary conditions, which play a large role in finite structures. Thus, the behaviour of locally scattered light must be fully defined in a finite mirror, since it can be 'recaptured' depending on the optical elements present in the environment of the photonic crystal.

Moreover, it appears that most photonic crystal devices do not actually exploit extended two-dimensional Bloch modes, but rather line defects, etc. It is therefore necessary to consider reality in all its complexity. For example, a conservative definition of modes 'below the light line' is still possible for line defects, provided that no loss occurs in the cladding with highest index, etc. By contrast, no simple statement can be made for the complementary situation 'above the light line'. The region of the defect and its lateral cladding may indeed have different vertical structures, as can be seen for instance in Fig. 9.5*e*, and a three-dimensional approach becomes necessary. Actually, even in the case of the superprism, which is one of the Bloch-mode structures with the more two-dimensional character (see Section 6.3 in Chapter 6,), a large effort is required in order to adapt waves at its outer interfaces, where similar three-dimensional aspects appear. The only exception considered here will be the two-dimensional photonic band edge laser described in Section 10.3 of Chapter 10, and involving for instance a perforated symmetric semiconductor membrane whose cladding has a unique, well-defined index at all points.

A precise quantitative analysis of losses in two-dimensional photonic crystal structures is therefore necessary when it comes to designing practical realizations. For this purpose, we summarize in the following the fabrication techniques used for the definition of the photonic crystal patterns for both types of photonic

crystal waveguides. This will also provide us with the opportunity to discuss the main implementations of photonic crystal waveguides.

Practical Implementations and Mask Writing Technology

The first step in the fabrication process is generally the exposure of the resist-coated wafer where the required patterns are to be defined, followed by a development step in order to proceed to the deposition or to the etching. Due to the typical size of the features, of the order of 100 nm, and of the required accuracy (about 10 nm or less), the most adequate method for the definition of photonic crystal patterns in semiconductor substrates is the electron-beam (e-beam) lithography: a focused electron beam, with a typical spot size below 10 nm, scans all the parts of the resist which are to be dissolved (Fig. 9.5*a*). In the case of a positive resist such as the polymethyl methacrylate (PMMA) resist commonly used for e-beam lithography, the exposed region is subsequently dissolved in an adequate solution. A typical lithography step, as well as the subsequent exposure and etching steps are schematically represented here in Fig. 9.5*a*. An example of pattern defining a high-Q cavity is schematically represented in Fig.9.5*b*.

The possibility of using deep-ultraviolet (DUV) lithography with the projection of a mask at a high resolution has also been demonstrated recently. This method should be preferred for mass production as its throughput is an order of magnitude higher than with serial e-beam lithography. Further, this method is undoubtedly in a position of benefiting from the current advances in the miniaturization of silicon microelectronics, where the size of the grids for transistor gates is expected to fall well below 100 nm within the next few years.

Finally, the possibility of using laser holography has also been considered (see Section 12.2.1 in Chapter 12). For the time being, this technique allows only the fabrication of uniform crystals, and does not seem to be well-suited to the realization of 'periodicity defects' in photonic crystals, which is essential for the implementation of genuine optoelectronic devices.

After having defined a correct mask and the corresponding set of etching steps, the three main possible implementations are represented in Fig.9.5*c*,*d*,*e*. A straight photonic crystal waveguide has been chosen here as a visual example. It consists of a line of missing holes along a dense direction of the photonic crystal. The membrane (Fig. 9.5*c*) is apparently the simplest case, but its fabrication process is quite complex from a technological point of view. The case of a low-index substrate is generally the simplest in terms of etching (Fig. 9.5*d*). The case of a buried waveguide is of great interest as regards technological integration, but its implementation imposes very demanding requirements in terms of deep etching. We consider in Section 9.3 the substrate approach (either buried or simply on a low-index cladding), before turning to the membrane approach in the next section.

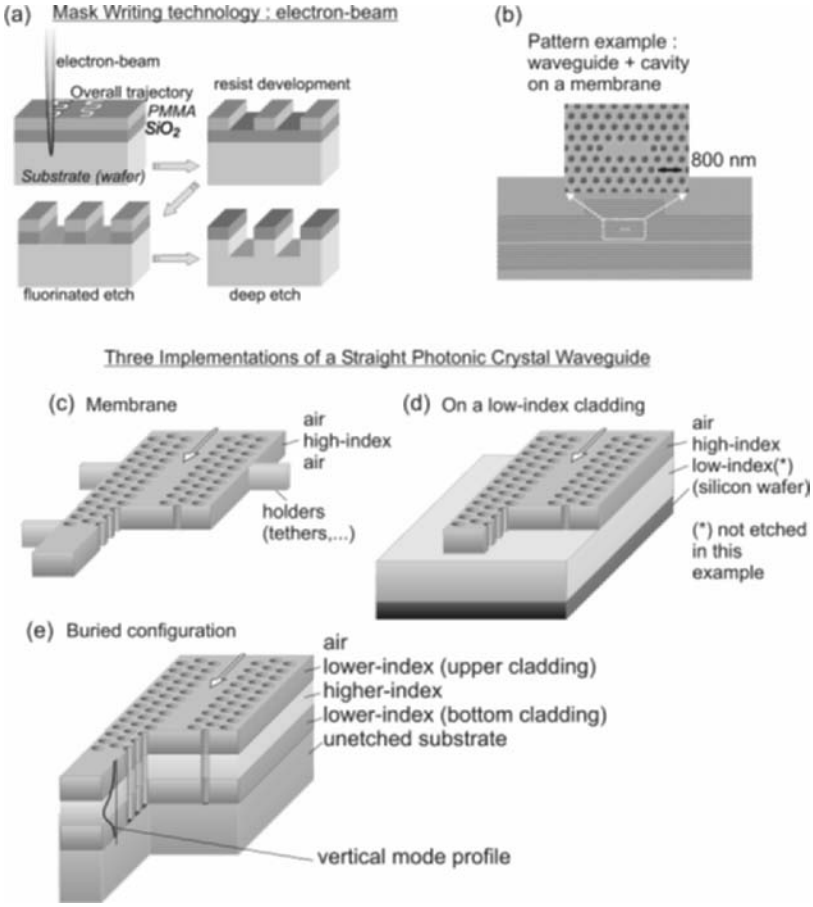

Fig. 9.5. An example of mask writing technology and the three main implementations of a photonic crystal straight waveguide that can be produced: *a.* Electron-beam lithography technique and application to the etching process. The semiconductor/SiO_2/PMMA tri-layer structure is first exposed to the scanning electron beam (the global trajectory of the beam is represented by the serpentine pattern. The scanning beam is stopped during each return scan). The exposed PMMA is then dissolved by wet etching, while the unprotected silica is removed by dry etching with fluorinated plasma. The residual PMMA is finally removed in order to perform the deep dry-etching of the semiconductor material (GaAs, InP, Si…) using reactive ions from an adequate plasma *b.* Micrograph of a waveguide–cavity system carved into a photonic crystal consisting of a triangular lattice of holes in a GaAs membrane. The period of the lattice is here around 400 nm. The crystal presented here was fabricated at CNRS LPN and Thales TRT *c.* Straight photonic crystal waveguide defined on a membrane *d.* Same object defined on a low-index cladding *e*. Same object defined in a buried configuration, the multilayer structure corresponding, for instance, to a standard laser diode. The vertical mode profile is sketched.

9.3 Planar Photonic Crystals in the Substrate Approach

9.3.1 DFB and DBR Laser Diode Structures

We begin the detailed study of planar photonic crystals by considering the 'substrate approach', i.e. the case of planar waveguides where the index of at least one of the two claddings is close to the index of the core layer. The light line is therefore very low, a situation which in principle favours the leakage of light. These systems are quite ubiquitous in semiconductor optoelectronics, since buried waveguides are the essential photonic structure of edge-emitting laser diodes (Fig. 9.5*e*). Owing to the simultaneous electronic and optical confinement properties of semiconductor multilayer stacks, these structures are also known under the name of 'double heterostructures', invented in 1963 and for which Z.I. Alferov and H. Kroemer were awarded the Nobel prize in 2000.

From a technological point of view, the main issue here is the depth of the holes. From an historical point of view, laser diode waveguides were first processed into gratings in the 1970s in the wake of the seminal article by Kogelnik and Shank (Kogelnik 1971) with the development of distributed feedback (DFB) laser diodes and distributed Bragg reflector (DBR) laser diodes (see Chapter 5 for more detail). Let us briefly consider here these devices. In both DFB and DBR laser diodes, the gratings are etched with a very limited depth, 50 or 100 nm in such a way as to be localized in the upper tail of the guided mode profile. The subsequent regrowth on top of a layer with a relatively small index difference ($\Delta n = 0.15$) tends to further smooth the index modulation. These gratings are intended at enforcing the longitudinal single-mode operation of the laser by favouring feedback only for the guided waves whose half spatial period ($\lambda /2n_{\text{eff}}$) coincides with the pitch of the lattice Λ, exactly as it is the case in the Bragg backscattering of X-rays by a very large number of equidistant atomic planes. The gratings can be etched either along the entire active region, as is the case for DFB lasers, or in the region immediately surrounding the latter, as in DBR lasers, in a passive section injected with a separated electrode. An additional interest of the injection in a separate section of the DBR laser is that it leads to minimizing the absorption and/or to modulating the real and imaginary effective index by shifting or modifying the backreflection peak. For a 1.55 μm emission, the value for the pitch Λ in these InP-based devices is equal to 220 nm for first-order feedback and to 440 nm for second-order feedback: the first-order feedback can be used in this case for outcoupling light. This simply results from the fact that the effective index of InP/GaInAsP/InP waveguides is typically around 3.2. The interaction length is typically larger than 200 μm, which is approximately the length of the active region. This clearly shows the weakness of the interaction between the laser wave and the grating, since about 1000 periods are needed in order to obtain any sizeable effect. The directional stopband thus obtained has only a 1-2 nm width.

9.3.2 Photonic Crystals, a Strong Perturbation for Guided Modes

In order to create a photonic crystal, and thus to obtain larger one or two-dimensional band gaps, the interaction must be reinforced. For this purpose, a first approach consists in increasing the etch depth h in order to reach the centre of the core: if the etched region is left unfilled, this allows achieving an index contrast 3 : 1 between the semiconductor and the air. Unfortunately, in terms of photonic performances, if the etching is not carried until the lower cladding, the local interruption of the guiding may result in an extremely large leakage. Etching deeper into the core layer actually causes the effective index in the core of the waveguide to decrease, and the dispersion curve of the guided mode to rise until the fundamental gap lies above the light line of the substrate. Im($k_{//}$) may thus become almost comparable to Re($k_{//}$) (Fig. 9.4*c*). The wave is repelled towards the lower cladding, and only a few periods are necessary before it totally leaks into the substrate (Chen 1996a). This effect will be all the more marked than the effective index of the wave is high.

Under such conditions, not only is the coupling to the cladding modes allowed, but it will even be maximized if the etching is performed at the centre of the core. This situation corresponds to the top of the 'loss bell' in Fig. 9.6, which schematically represents the losses as a function of the etch depth h for a simple planar structure, i.e. without upper cladding layer. When losses reach their maximum value, large singularities generally occur due to the fact that dimensions are of the order of the half-wavelength. The sides of the bell show a more regular evolution. For shallow gratings (Fig. 9.6*a*) and small h, diffraction efficiency scales like h^2, resulting in a steady decrease of the losses, as can be seen in the left-hand side of the curve. For deeply etched structures (Fig. 9.6*c*) and large h, the perfectly etched substrate under the core acts only as a tunnelling channel for leakage through the bulk substrate with index n_1, without allowing itself the propagation of guided modes. This causes an abrupt decrease of the losses in this case.

Since 1996 and the pioneering article by TF Krauss, it is generally recognized that is necessary, in order to ensure the guiding that the etching be performed also through the lower cladding, until the entire vertical profile $A(y)$ of the field of each guided mode is intercepted by the holes (Krauss 1996a). In other terms, it is necessary to pass beyond the loss bell of Fig. 9.6*d*. From a mathematical point of view, and in the ideal case where no holes are present, the field profile extends at infinity and decreases exponentially in the cladding with the form $\exp(-y/L)$, where L is the decay length of the evanescent wave, as given by the classical formula:

$$L_{\text{decay}} = \lambda / [2\pi\sqrt{n_{eff}^2 - n_1^2}] \tag{9.6}$$

As an example, in the case of a GaAs core and of a $Ga_{0.2}Al_{0.8}As$ cladding, where $n_{eff} - n_1 \sim 0.3$, the decay length is $L_{decay} = 50$ nm for $\lambda = 1$ μm, whereas for

an InGaAsP core (n = 3.35) and InP cladding (n = 3.17) where $n_{eff} - n_1 \sim 0.1$, the decay length is equal to L_{decay} = 200 nm at λ = 1.55 µm.

In all these cases, the etching depth needs to be significantly larger than the thickness of the core of the waveguide, resulting in a high aspect ratio as well as in a delicate technological process. In this context, there are two main reasons for preferring the TE polarization over the TM polarization. First, the profile of a TE mode is much more confined than that of a TM mode. Secondly, band gaps appear in TE polarization for much smaller air-filling factors.

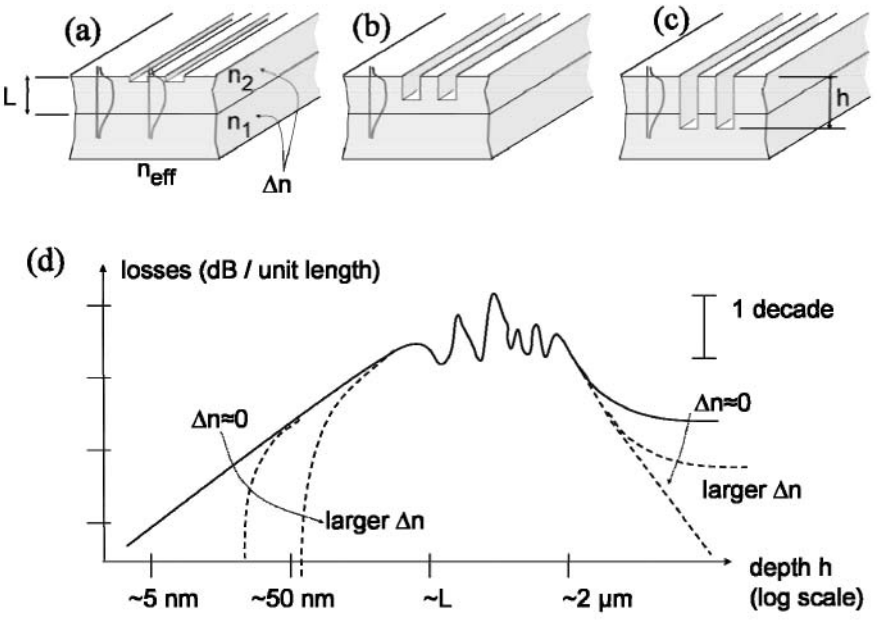

Fig. 9.6. Grating etched at a variable depth in a semiconductor waveguide and schematic representation of the losses as a function of the etch depth *a.* DFB type grating. Such gratings are more commonly buried *b.* Grating etched halfway through the core *c.* Grating etched throughout the core *d.* Schematic 'loss bell' diagram. For the sake of clarity, the singular features which may occur, especially in case *b*, have been minimized. The solid line represents a generic scenario valid for vanishing Δn. The dashed line represents scenarii for increasing Δn, where n_{eff} becomes lower than n only beyond a certain threshold depth. Similarly, leakage to the cladding may steadily disappear for large depth and large Δn, since in this case only an 'effective' cladding with relatively low index is seen by the guided mode.

9.3.3 Choice of the Diameter of the Holes and of the Period of the Crystal

For a triangular lattice of holes with a given period a and a buried waveguide with typical effective index $n_{eff} = 3.34$, a ratio $\phi/a = 0.35$ between the diameter ϕ of the holes and the period is enough to cause an omnidirectional TE band gap to appear. This corresponds to an air-filling factor no higher than 15%. By contrast, a ratio $\phi/a = 0.75$, corresponding to an air-filling factor $f = 60\%$, would be required in order to simultaneously obtain complete TE and TM band gaps.

In the latter case, the holes become so large and are separated by such small semiconductor veins that 10 nm fluctuations in the thickness of these veins are likely to have a noticeable influence on the properties of the photonic crystal device. Another reason for adopting a relatively small diameter for the holes pertains to the fact that the profile of the guided field in the etched region will not be significantly different from its profile in the non-etched region, a favourable feature for optoelectronic integration. Thus, a guided wave, arriving for instance from a crystal free region will propagate into the crystal region without undergoing any significant mismatch nor radiation loss, provided however that its frequency be in one of the transmission bands of the crystal.

The solution of using small holes, and thus of having small air-filling factors *f,* also leads to the possibility of a relatively independent analysis of the guiding along the vertical and lateral directions. In other terms, this entails that an approximation of the form $A(y) \times B(x, z)$ for the guided waves will be more acceptable in such a case.

Unfortunately, as far as applications are concerned here, favouring one polarization over the other does not appear, in principle, to be an ideal solution. Indeed, with the exception of lasers, polarization-insensitivity is a requirement for integrated optical devices receiving their signals from fibres. A possible solution, known as 'polarization diversity' consists in separating the TE and TM polarizations immediately after the input. The TM polarized signal is then converted into a TE polarized signal and injected in a circuit duplicating the TE polarization. The two signals are finally recombined in the two orthogonal polarization states at the output.

Thus far, we have paid little attention to the upper cladding of the waveguide. For planar waveguides with the simplest designs, like in Fig. 9.6 for instance, this layer is simply absent, since the waveguide is directly realized by the mere deposition of a layer with index n_2 on a substrate with index $n_1 < n_2$. Thus, two different regimes occur for the evanescent tails of the guided modes, with air being of course the medium where the propagation velocity is the highest. We shall see later, with the help of the 'light line' formalism, that important losses may arise in this regime at the bends of integrated photonic circuits. These losses can therefore be significantly reduced by starting from a genuinely buried waveguide (Fig. 9.7*a*), where the index profile is $n_1/n_2/n_1$/air or $n_1/n_2/n_3$/air, hence with a relatively low index step $(n_2 - n_3) << n_2$. As a consequence of the presence of this additional cladding layer, the etch depth, denoted here by h, increases. However, this increase can be minimized by reinforcing the confinement on the side of the sub-

strate, in such a way as to obtain indices satisfying the relation $n_1 < n_3 < n_2$. A truly optimal solution requires an in-depth modelling, either in three dimensions or at least in the *yz* plane (Bogaerts 2001; Lalanne 2001).

9.3.4 Specific Parameters for InP- and GaAs-Based Systems

In Table 9.1 are presented typical values of the relevant parameters in TE polarization for photonic crystal buried waveguides, realized either on an GaAs or an InP substrate. These two types of waveguides are adapted to operate at wavelengths around 1 μm and 1.55 μm respectively. In either cases, the air-filling factor is assumed to be equal to $f = 30\%$. This assumption allows the limitation of the vertical modification of the profile of the guided modes in the section of the waveguide under consideration.

Table 1. Parameters for photonic crystals etched in buried waveguides grown on GaAs and InP substrates, and displaying TE photonic band gaps around 1 μm and 1.55 μm, respectively (the air-filling factor is the same in both cases, and is equal to $f = 30\%$

Substrate	Lower cladding	Core	Upper cladding	Δn	Period a [nm]	Diameter ϕ [nm]	Height h [nm]
GaAs	$Ga_{0.2}Al_{0.8}As$ ≥ 400 nm	GaAs ~250 nm	$Ga_{0.8}Al_{0.2}As$ ~300 nm	0.2-0.5	220-300	110-160	≥750
InP	InP[a]	GaInAsP[b]	InP ~300 nm	0.1-0.2	330-550	180-280	≥1500

[a] undoped buffer layer

[b] $Ga_xIn_{1-x}As_yP_{1-y}$ lattice-matched to InP

It can be seen from this table that for the value of the air filling factor $f = 30\%$, corresponding to $\phi \sim 0.6a$, the aspect ratio h/ϕ of the holes is higher than 5 in GaAs ($\phi \sim 160$ nm) and still higher in InP ($\phi \sim 280$ nm), where it is more than 7. With this in mind, we shall devote the next section to a discussion of the dry etching methods which permit to achieve such high aspect ratios.

9.3.5 Deep Etching

The most traditional anisotropic dry etching technique is reactive ion etching (RIE). The term 'anisotropic' refers to the fact that the sidewalls are vertical at the edges of the mask. By comparison, a pure chemical etching results in significantly undercut sidewalls which follow the crystallographic planes. At the opposite extreme, a pure physical etching, such as milling by Ar+ ion bombardment, erodes the material, which results in rounded sidewalls. When correctly adjusted, the RIE technique produces patterns similar in the <110> and <1-10> directions of the <001> plane for a standard III-V substrate. In its standard version, this technique is based on the use of a plasma produced by a simple RF discharge, and different gas inlets containing in particular silicon tetrachloride, methane and

hydrogen. The rectification by the plasma produces the bias voltage required for accelerating the ions towards the sample holder. This method has been instrumental for the first applications of photonic crystals to the field of integrated optics (Smith 2000c, 2000d), by allowing in particular the realization of holes in GaAs with an aspect ratio $h/\phi = 5$.

However, RIE etching tends to become less efficient for aspect ratios of 4 in InP, this being due to the lower volatility of the In-containing residues. These limits can be overcome using modified methods based on the independent control of the plasma density and its energy, i.e. the bias. In order to enhance the plasma density, energy can be injected either by RF electron cyclotron resonance reactive ion etching (ECR-RIE) or by inductively coupled plasma reactive ion etching (ICP-RIE). The latter method seems very promising, especially for silicon, GaAs or InP, and is being increasingly documented (Combrié 2005, Pommereau 2004). Since several years, silicon etching by ICP-RIE has clearly become suitable for the realization of photonic crystal patterns with large size ($\phi >> 1$ μm). Finally, we may mention another method which has also been successfully implemented in laboratory, the chemically-assisted ion-beam etching (CAIBE). In this method, an Ar^+ ion beam is used for milling the sample, while at the same time an active chemical species, like chlorine, is introduced above the sample in order to form volatile compounds, for instance indium compounds. The CAIBE method has been used in particular in the first experimental attempts directed at the realization of three-dimensional photonic crystals at optical wavelengths (see Chapter 12).

9.4 Membrane Waveguide Photonic Crystals

9.4.1 Free-Standing Membranes

The idea of etching a photonic crystal in a membrane held only by its edges was first introduced around 1994, when researchers in optoelectronics started exploiting processes used in the fabrication of micro-opto-electro-mechanical systems (MOEMS). As far as applications to integrated optics are concerned here, these membranes are defined with a typical thickness ranging from 200 to 400 nm, ideally forming a single-mode planar waveguide. The tremendous advantage of these membranes is that their realization requires a relatively small etching depth, hardly larger than the thickness mentioned above. Such an etching depth is enough to access the underlying 'sacrificial' layer, i.e. a layer that will be subsequently removed by selective dissolution, as represented in Figs. 9.7*b* and 9.7*c*. These membranes present an index $n = 3$ or higher, and they naturally behave as a relatively good 'trap' for light. In comparison with buried waveguides (see Fig. 9.7*a* as well as Figs. 9.5*e*), the effective index of the unpatterned membrane is quite low, and typically $n_{eff} \approx 2.8$ for a 270 nm semiconductor membrane suspended in the air at the 1.5 μm wavelength. The critical angle varies from 16 to

18° with respect to the normal of the membrane, resulting in a very sharp-angled light cone in the dispersion diagram. The band gaps of a photonic crystal etched in the layer of the membrane overlap only to a limited extent with this cone. In the case where a straight waveguide is introduced in the membrane (Fig. 9.5*c*), it is now known under which parameters and conditions the in-plane guided modes lie below the light cone and are therefore lossless. Accordingly, all the advantages offered by waveguides (Fig. 9.1) will be retained and, conversely, all the functions that are expected from photonic crystals, like the possibility of radiation-free bends or the coupling with cavities with a very high Q factor, can be tested. More precisely, the only residual losses for modes of straight waveguides are expected to result only from irregularities and fluctuations associated with the fabrication process. Further, the latter losses might even be very low in the case of a photonic crystal device, since the radiation associated with an irregularity can itself be inhibited, resulting only in the generation of an evanescent wave. However, in all cases where the translational invariance is disrupted on purpose (bends, cavities), the limitations are those of the modal engineering and of the design of the structure itself. This is documented, among others, in (Asano 2006b; Chutinan 2002; Englund 2005; Sauvan 2005; Yoshie 2001), and this complex topic is far from being exhausted.

Membrane technology has been regularly improving over the last few years, especially for InP-based systems. In order to realize a membrane, it is necessary to dissolve the underlying sacrificial layer. In this respect, the chemistry of wet etching of GaInAsP quaternaries allows a great latitude in this process, and it permits, in particular, to dissociate the design of the heterostructure, for instance as an active structure, from the technological constraints associated with the formation of the membrane. Further, the use of membranes has been extensively explored during the 1990s for the realization of numerous micromechanical devices and all-semiconductor tuneable vertical cavities (Dantec 1999). A further advantage of the InP system is the low rate of the non-radiative recombinations, notwithstanding the vicinity of the interfaces between the air and the semiconductor. This results in a much better luminescence efficiencies than in comparable GaAs-based structures. InP systems typically present recombination rates ten to a hundred times lower than GaAs systems. In particular, InP systems have been used for realizing the first optically pumped photonic crystal laser operating up to room temperature (Painter 1999a), a decisive achievement which was instrumental in demonstrating within the scientific community the relevance of the photonic crystal approach. The topic will be discussed in more detail in Chapter 10 on microsources.

As far as alternative materials are concerned, the FESTA group in Tsukuba (Kawai 2001) has first succeeded in fabricating perfect free-standing GaAs membranes with a proven gap. These membranes were exploited for the design of such complex devices as the Mach-Zehnder modulators that will be discussed later in this chapter (Asakawa 2006). GaAs-GaInP Al-free heterostructures have also been reported as a particularly good basis for the fabrication of membranes (Combrié 2006a). Another possibility for fabricating membranes is to use the silicon-on-insulator (SoI) technology, which allows the production of perfect

crystalline Si membranes on top of a silica layer with a few hundred nanometers by dissolving the underlying silica in hydrofluoric acid etchants (Loncar 2002a). Many striking achievements from the 2003-2007 period are based on this approach.

Etching a membrane only requires a relatively low aspect ratio between the depth and the diameter. Since a membrane typically presents a thickness between 200 and 400 nm, this ratio should be no higher than unity. It is also much easier to obtain vertical sidewalls along the entire height than with buried waveguides systems, and the latitude in the design of the geometrical parameters of the lattice increases accordingly. Thus, it was with membrane systems rather than with buried systems that it has been possible to reach high air-filling factors, well above 50% and even approaching 70%. In this extreme case, the holes were separated only by extremely small veins, and the TM band gap tended to coincide with the high-frequency TE band gap. The counterpart of this benefit is that the amount of material left in the membrane is drastically reduced. For this reason, the membrane can no longer be described in terms of a two-dimensional model, where the effective index of the waveguide is used as the two-dimensional matrix index, and it becomes necessary to resort to the methods of three-dimensional electromagnetism, with all their unavoidable complexity.

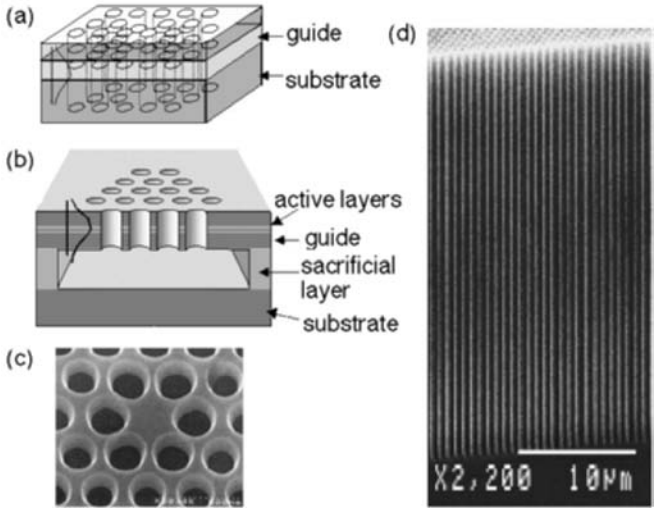

Fig. 9.7. *a.* Photonic crystal etched in a buried waveguide, shown for reference *b.* Membrane photonic crystal, fabricated by dissolving a sacrificial layer, made accessible by the presence of the holes, during a wet etching process. Active layers have also been embedded here *c.* Example of a microcavity formed by a single missing hole in a photonic crystal (Yoshie 2001) *d.* Example of a realization in macroporous silicon (Rowson 1999a). Note the remarkable perfection of the columns over several dozen microns

In some respects, the successful development of high performance structures based on membranes has turned them into a benchmark for electromagnetic design. In counterpart, accuracy requirements necessarily impose the use of three-dimensional modelling, even in the case of 'normal' holes and large veins between holes (air-filling factor $f \sim 30\%$).

9.4.2 Reported Membranes

An interesting variant of the free-standing membrane is based on the report of a membrane on a low-index substrate, for instance silica with index $n = 1.48$ to mention a common configuration. Such an arrangement answers a series of mechanical problems inherent to membranes, in particular the risk for the membrane to stick when drying. Further, it also leads to a better thermal management of these devices, even if silica remains a poor thermal conductor. Another technique implemented by the Sandia group in New Mexico in the course of their collaboration with the Massachusetts Institute of Technology (MIT) on Ga(Al)As systems relies on the use of 'AlOx', a non-stœchiometric aluminum oxide obtained by the lateral oxidization of Al-rich GaAlAs layers. The original waveguide used in these experiments consists of a GaAs core deposited onto a thick $Al_{0.95}Ga_{0.05}As$ layer (60-200 nm). The latter is selectively oxidized, typically in a water vapour atmosphere at 450°C, which leads to its conversion into quasi-alumina with index $n \sim 1.6$.

In principle, since etching is performed only after the report of the membrane on the substrate, the latter, which may consist for instance of silica, can be perforated for all the systems mentioned above. However, other choices can be made. For instance, if a non-perforated substrate is used, the light line decreases following a $1/n$ law, and goes from unity (air) for a free-standing film to typically 2/3 for a non-perforated substrate. The risk exists of greatly reducing the photonic band gaps, leaving only very restricted regions for the propagation of possible lossless guided modes. Nevertheless, it was with such a system that early investigations on straight waveguides were conducted in 1999 by the group of T. Baba from Yokohama University (Baba 1999).

9.5 Macroporous Silicon Photonic Substrates

Macroporous silicon does not fall into any of the categories presented above, and it is generally considered as an outsider in integrated optics. This material, obtained from a bulk *n*-doped Si crystal or wafer, is invariant along the third dimension. For this reason, it is undoubtedly the material which most resembles the ideal two-dimensional photonic crystal. As can be seen in Fig. 9.7*d*, a photoelectrochemical etching carried out in a hydrofluoric acid based electrolyte is performed for obtaining pores with an aspect ratio higher than 50, perfectly aligned along the <100> direction normal to the usual polished face of the wafer. In the

absence of an adequate preparation of the surface, the location of the pores will be determined by the native defects of the electrochemically active interface, resulting in a certain disorder in their distribution. In practice, this defect is avoided by first imprinting etch pits at specified locations using a classical photolithographic process followed by a chemical etching with a potassium hydroxide solution. A large and very uniform lattice of holes extending over more than one centimetre square can be obtained using an holography technique, where the photomask is defined from the fringe pattern resulting of the interference of three laser beams (Berger 1997b). More detail on this technique will be presented in Section 12.2.1 of Chapter 12. The choice of the period for the lattice of pores is intimately related to the *n*-doping level, which therefore needs to be correctly anticipated. Since a free carrier screening process is involved in the selection mechanism of the sizes of the pores, the period varies in inverse ratio to the doping level. An inappropriate doping may for instance result in the spontaneous appearance of unwanted 'interstitial' pores. The advantages offered by this system must therefore be balanced with these different factors when designing such a device. Thus, in order to obtain good quality holes, the holes must be thought as being uniformly distributed over the entire device, since a hole without neighbours would be prone to instabilities.

Since the pioneering studies by U. Grüning *et al,* where a complete photonic band gap was reported around 5 μm for both TE and TM polarizations (Grüning 1996), important advances have taken place towards the control of photonic crystals formed from macroporous silicon at telecommunication wavelengths (Rowson 1999a). The example represented in Fig. 9.7*d* convincingly demonstrates that these photonic crystals are among the new materials which could be used for achieving the transition from 'free space' optics to integrated optics.

More precisely, if these systems are to be realistically used in integrated optics, then light needs to be confined both vertically, i.e. along the axis of the pores, and horizontally, i.e. in the plane of periodicity. For the realization of cascaded optical functions, such a confinement is much preferable to the use of a simple collimated light beam that would evolve with an intrinsic divergence along the pores. An elegant solution for simultaneously achieving a vertical confinement and a single-mode guiding consists in reducing the diameter of the pores over a certain height Δh. For narrower holes, a guiding effect is achieved due to the fact that the average index of the slab with height Δh is higher than the average index in the surrounding medium. Various authors (Rowson 1999b; Schilling 2001) have demonstrated that the diameter of the pores could be modulated within some appropriate range by simply varying the current during the photo-electrochemical etching process (Fig. 9.8).

In order to simultaneously achieve a single-mode behaviour, an optimized coupling with fibres, and a relative insensibility to the residual imperfections due to the fabrication process, both the height Δh and the variation of the diameter need of course to be optimized. A possible solution for achieving the in-plane confinement along the horizontal direction consists in the in-filling of selected pores with a polymer material, which leads to an increase of the local average index. It has been experimentally demonstrated that pores with a 0.65 μm diameter

could be filled over a 10 μm height with a polymer exhibiting a good transparency in the 1550 nm window (David 2002). However, in order to fill the desired set of pores, it turned out necessary to resort to a complementary lithographic technology, for to instance e-beam lithography, in order to mask all but the desired region and to have the patterns of the waveguide aligned with the axis of the photonic crystal (Birner 2001). In spite of these relative difficulties, macroporous silicon remains a promising material. Indeed, not only is this material of a relatively low cost for the study of photonic crystal waveguides, but it allows the realization of pores at depths that would be out of reach with any other techniques. It can reasonably be expected that these promises will be fulfilled in the forthcoming years.

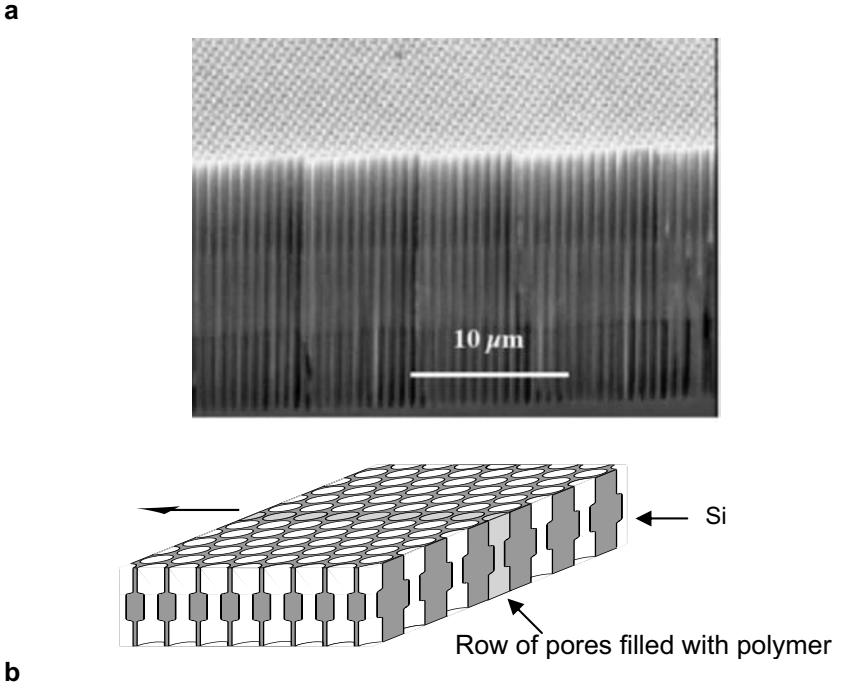

Fig. 9.8. *a.* Micrograph of a planar waveguide defined in a macroporous silicon photonic crystal adapted to telecommunication wavelengths (period 0.65 μm). The vertical confinement is achieved through the modulation of the diameter of the pores along the vertical direction. This diameter is typically 250 nm in the core of the waveguide, whereas it reaches 420 nm in the cladding regions. The total depth of the pores is more than 20 μm *b.* Schematic representation of a macroporous silicon waveguide with confinement of light along both the vertical and the horizontal directions. The horizontal confinement is achieved by filling one or several rows of pores with a transparent polymer

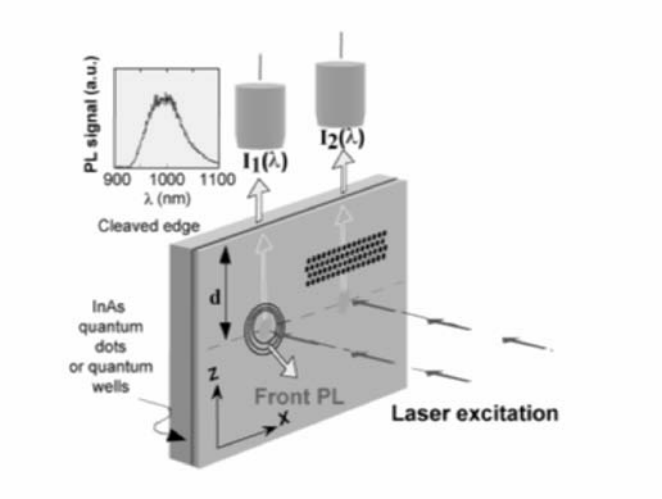

a

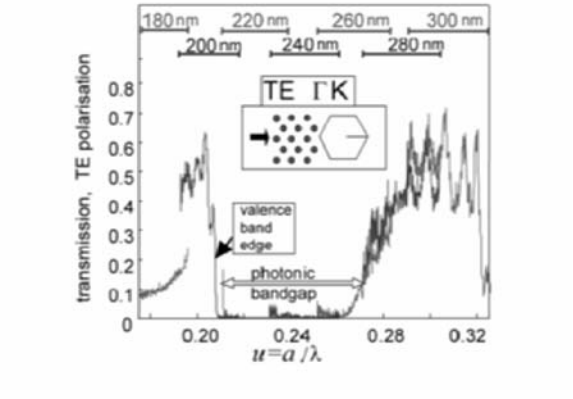

b

Fig. 9.9. *a.* Principle of the internal light source method used for the characterization of photonic crystals in integrated optics: a localized laser spot generates electron-hole pairs in a quantum well or in a layer of quantum dots. Radiative recombinations (photoluminescence) occur and the corresponding photons are emitted in the waveguide in the form of circular waves. The reabsorption of these photons is low enough to allow a substantial fraction of the light to reach a cleaved edge located at a distance *d* from the source ranging from 50 to 100 µm. If light propagates through a photonic crystal structure etched in this waveguide, the transmission of the crystal can be determined by comparing the resulting signal I_2 to the reference signal I_1 *b.* Example of a measurement realized by combining seven transmission spectra measured for seven photonic crystals with different periods, indicated here above the graph. The spectra are plotted against the normalized frequency $u = a/\lambda$, represented in abscissa

9.6 Characterization Methods for Photonic Crystals in Integrated Optics

9.6.1 Internal Light Source Method

When a photonic crystal reduces to a very small 20 μm × 2 μm^2 object, etched in a GaAs or InP substrate with for instance a 4 × 8 mm^2 area, the question arises of the most appropriate method for determining its transmission. The solution of using an external source raises difficulties as regards the possibility and the reproducibility of the coupling. However, as will be seen hereafter in Section 9.6.2, a few solutions to these problems exist. This being, the idea of generating light inside the structure itself obviates most of these difficulties, and we shall now proceed to describe the methods used for inducing such an internal source.

In the specific case of III-V semiconductors, this is achieved by inserting photoluminescent layers in the core of the waveguide during the epitaxial growth process. These layers can be reduced to a single quantum well with a thickness of a few nanometers. They may also consist of a series of self-assembled quantum dots, based for instance on InAs, a system which has been known since about 1985 and which exhibits a large inhomogeneous broadening (see Chapter 7). By pumping with a visible laser focused with the objective of a microscope, as represented in Fig. 9.9*a*, the recombination of the electron-hole pairs created in the core of the waveguide occurs mostly in the lower energy quantum well or in the quantum boxes with the lower energy. The optical cladding, formed for instance by $Al_xGa_{1-x}As$ in the case of a GaAs substrate and a GaAs core, also plays the role of a confinement barrier for the electrons and the holes.

A substantial fraction of the generated photons, which typically is of the order of 40 percent, is coupled to the guided mode, while the remaining photons are coupled to the continuum formed by the non-guided radiating modes. For multimode waveguides, as in the case of blue GaN-based LEDs and lasers, InGaN quantum wells may be used, with the GaN cladding being pumped by an ultraviolet laser (David 2005, 2006a) (see also Section 10.1.3 in Chapter 10). The vertical position of the InGaN source within the waveguide then determines the excitation efficiency of each guided mode, since this excitation depends on the value of $|A^{(p)}(y)|^2$ at the location of the quantum well. In more precise terms, an overlap integral between this function and the electron-hole wave function needs to be calculated.

This localized photoluminescence source can then be used as a 'lamp' for illuminating the waveguide and the device under test. This source can be easily positioned at the desired location, and a signal $I_2(\lambda)$ is collected at a cleaved edge after the propagation of light in the photonic crystal under consideration (Labilloy 1997, 1999). Layers with a good epitaxial quality often present a uniform photoluminescence efficiency, and the intensity of the source is therefore the same at any point of the sample. In the case where uniformity is an issue for the

normalization of the signal, it suffices to measure the light spectrum $I_I(\lambda)$ after a simple free propagation in the waveguide up to the cleaved edge.

However, even in the case where a single quantum well is inserted in the core, reabsorption effects occur within a relatively limited length, of the order of 100 μm. Indeed, no pumping at all takes place elsewhere in the waveguide, and the generated photons, whose energy is about the same as that of the fundamental transition of the quantum well, only undergo a band-to-band absorption caused by the latter. It is not easy to indicate a unique value for reabsorption due to the very nature of the band gap region, where the absorption coefficient rapidly evolves from a zero value to a bulk value equal to $10^4 cm^{-1}$, with often an excitonic maximum occurring between these two values. After propagating over typically 100 μm, the spectrum of the guided light reduces to its low energy content, this being due to the fact that reabsorption affects essentially its high energy part. The effective wavelength range for spectral measurements therefore decreases down to $\Delta\lambda = 20$ nm for an $In_xGa_{1-x}As$ quantum well grown on a GaAs waveguide. The relative spectral width available is therefore approximately $\Delta\lambda/\lambda \sim 2\%$ for a central wavelength $\lambda \sim 950$ nm.

In order to characterize the crystal over a broader spectral range, one may take advantage of the fact that, in the first order, the transmission depends only on the normalized frequency a/λ. The technique known as 'lithographic tuning' can then be applied, by using a series of samples with the same air-filling factor f, but with gradually increasing periods a. The transmission data are finally plotted on a single graph as a function of a/λ. It can be easily calculated that, in the case of a source with a 2% relative width, measurements have to be carried over approximately thirty different crystals in order to cover a broad spectral range in a continuous fashion ($\Delta\lambda/\lambda > 50$ %).

An internal source with a much broader and useful spectral range can be obtained by using InAs quantum dots (or quantum wires), whose characteristics and luminescence have already been addressed in Chapter 7. Quantum dot layers can be produced through a self-organizing process during the growth by molecular beam epitaxy (MBE) of materials with a high positive mismatch of the lattice parameter. Quantum dot sources have been widely adopted for GaAs studies (Benisty 1999; Labilloy 1999; Olivier 2001b; Reese 2001; Viasnoff-Schwoob 2005) as well as for InP studies (Letartre 2001; Nomura 2006; Pottier 1999; Seassal 2002). In order to increase the spectral width of the source as much as possible, the InAs growth conditions are chosen in such a way as to produce inhomogeneous dots. The distribution of the sizes of these dots will result in different electronic confinement energies, and therefore in a larger spectral width. A spectral width ranging 150 from 250 nm around 1050 nm can thus be obtained on GaAs, corresponding to a useful spectral width $\Delta\lambda/\lambda \sim 15$-$25$ %. Along with this 'spectral dilution' of the source, reabsorption also decreases by a factor of ten or more, resulting in a typical modal absorption of the order of $20 - 30\ cm^{-1}$ per quantum dot layer. A risk, when going to critical epitaxial growth conditions in terms of surface, flux and temperature, is the spatial inhomogeneity of the photoluminescence efficiency. This effect can be obviated by using two or three quantum dot layers.

With a spectral width of $\Delta\lambda/\lambda \sim 10$ - 15 %, a couple of structures with different periods are sufficient to cover the photonic band gap, and even extended spectral regions beyond this gap. Fig. 9.9*b* presents an example where measurements were carried out over seven photonic crystals with different periods in order to cover almost a frequency octave in terms of the normalized frequency $u = a/\lambda$, ranging from 0.175 to 0.325 (Labilloy 1999). In these experiments, the spectral range was further limited to short wavelengths ($\lambda < 1060$ nm) due to the intrinsic properties of the silicon-based CCD device. In the absence of such a limitation, four samples would have been enough. The dispersion of the material is also the cause of the small mismatches which can be observed in the diagram ($\partial n / \partial\lambda \approx -8\times10^{-4}$ nm^{-1}, and therefore $\Delta n \sim 0.1$ across a 125 nm spectral range).

This internal light source method can also be used for membrane-type photonic crystals (Park 2001; Pottier 1999; Seassal 2002). However, since the edges of the membrane are not necessarily regular, the optical transition from the membrane to the non-etched region may not be reproducible. It is therefore preferable, either to cleave within the thin film to be analyzed, which also presents difficulties, or to extract light by using an output grating located after the crystal in order to outcouple the measured beam towards the air (Fig. 9.10*a*). In addition, the extraction characteristics should be carefully modelled and calibrated using adequate experimental means.

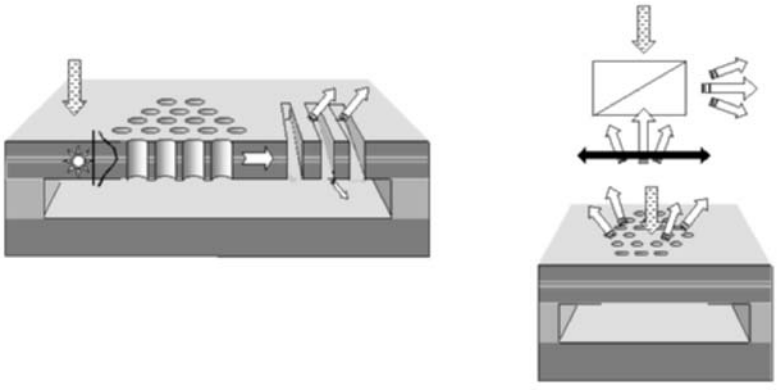

Fig. 9.10. Internal excitation of a membrane *a.* In order to avoid the effects of the non-reproducible optical transmission which may occur at the edges of the membrane, the light is collected by means of an extraction grating placed before the cleaved facet of the sample *b.* The photoluminescence diffracted at the boundaries of a microcavity is directly collected. A dichroic beam splitter is used in the experimental arrangement in order to separate the diffracted signals from the exciting beam with shorter wavelength

We shall later discuss some of the issues associated with the study of completely closed resonators. In this case, the spectral characteristics of the resonances that are expected to occur (cavity peaks) can be measured from the out-of-plane diffraction. This observation applies to membrane waveguides as well as to buried waveguides. Light is then collected normally to the plane of the waveguide, either along approximately the same axis as the exciting beam, or simply through the same objective, by using in the latter case an adequate beam splitter (Fig. 9.10*b*). These considerations on resonators can be extended to the end-fire method, assuming in this case that light be guided first to the vicinity of the investigated cavity in order to have it interact with the cavity.

9.6.2 End-Fire Method

External sources present obvious advantages when it comes to selecting the wavelength (down to a 0.1 pm accuracy), the intensity or the spatial profile of the injected mode. The coupling of the light emitted by an external source into a photonic crystal structure can be achieved through the edge of the waveguide, either by cleaving the sample or by using a grating coupler similar to the one represented of Fig. 9.10*a*, but located at the input end of the waveguide.

Let us focus for instance on the injection by a cleaved edge. Different types of geometry can be considered for characterizing the photonic crystal structure:

- the photonic crystal lies isolated in a planar waveguide, as in the example represented in Fig. 9.11*a*. The situation is similar to that of the internal light source represented in Fig. 9.9*a*, with a spot located just at the edge of the sample. A significant divergence of the injected light occurs in this case. The intensity of the wave decreases with $1/r$, but the residual absorption (an $\exp(-\alpha r)$ factor) can be low due to the fact that the waveguide has no absorbers at all, i.e. that it forms a passive system. In other terms, absorption will not significantly affect the signal until distances of the order of 1 mm are reached, since α can be no higher than 10 cm^{-1} under these conditions.
- light is injected into a single-mode ridge waveguide, which channels light to the structure under study. In the example represented in Fig. 9.11*b*, this structure is a photonic crystal waveguide (Talneau 2001). In order to collect light as efficiently as possible, it should be injected only in the desired polarization, for instance in TE polarization with $E = E_z$. The polarization at the level of the access waveguide should of course be maintained in the photonic crystal, as is usual in integrated optics (see Chapter 5 for polarizations and conventions).

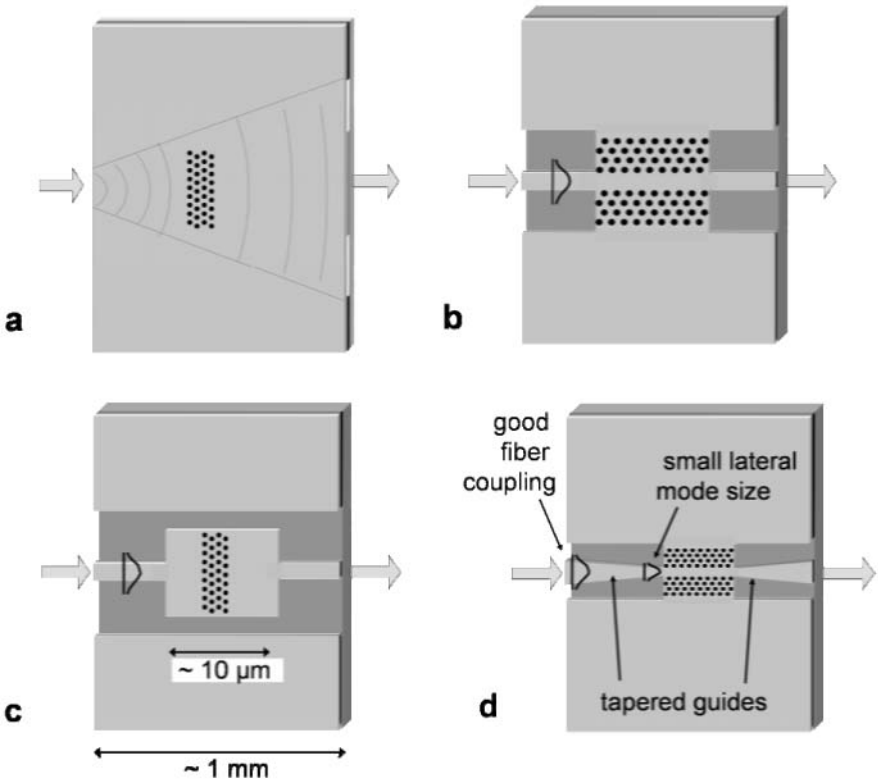

Fig. 9.11. End-fire method *a.* Injection in a simple planar waveguide. The decrease in the transmission caused by the crystal under study is revealed by the shadow appearing on the opposite edge *b.* Injection in a deep-etched ridge waveguide, leading to the photonic crystal waveguide under study *c.* Intermediate geometry where light is injected in a ridge waveguide leading to an enlarged region containing the photonic crystal under study. The divergence of light is less marked than in case *a,* and the detected signal is therefore less attenuated *d.* Same as *b*, with the difference that the ridge sections are adiabatically tapered in order to provide good coupling both with the fibre and with the narrow photonic crystal waveguide

- the photonic crystal lies in an enlarged region of a straight ridge waveguide, as in the example shown in Fig. 9.11*c*. This intermediate situation is also reported in (Chow 2000; Lin 2000, 2001a).
- the adiabatically tapered section of a waveguide is used in order to facilitate the coupling of the mode of the fibre to the photonic crystal waveguide, as shown in Fig. 9.11*d*. The larger mode size (~ 2 µm) at the entrance of the waveguide is in accordance with the beam waist size of a typical microlensed fibre, while the mode size on the side of the photonic crystal waveguide can be reduced to 'nanophotonic' dimensions, of the order of $\lambda/n \sim 0.5$ µm.

The sources used in these experiments are typically fibre or semi-conductor lasers with an external cavity providing a spectral tunability range of the order of $\Delta\lambda/\lambda = 6$ percent. In the long wavelength range (mid-infrared), the only tuneable coherent sources are optical parametric oscillators, which however are difficult to operate. In the short wavelength range, towards visible wavelengths, tuneable solid state lasers like Ti : sapphire lasers are often the most appropriate. Finally, we may mention here the specific category of amplified spontaneous emission sources. The spectral width of these sources is of the order of kT, i.e. of a few percents in terms of $\Delta\lambda/\lambda$, and they present a lower coherence, a convenient feature for avoiding spurious interferences. The so-called supercontinuum sources can also be considered. As can be understood, it is often necessary to use a battery of several sources or samples in order to fully investigate a photonic band gap.

The end-fire injection at a cleaved edge requires very accurate alignments as regards the angles and the positions. It also requires a beam with an aperture matched as much as possible to the guided mode, thus with an elliptic shape and a linear polarization. A beam with a mismatched shape may excite other modes than the fundamental mode. This also justifies the use of long single-mode ridge waveguides for accessing the photonic structure. Indeed, since the parasitic modes are of a radiative nature, they will eventually escape from the ridge waveguide towards the substrate, and therefore they will not be taken into account in the measurements.

Improved In-Coupling Tapers

End-fire coupling from a fibre to a membrane-based waveguide results in a considerable change in the area of the modes, from ~ 60 μm^2 to ~ 0.1 μm^2, a factor of about 500. In order to achieve this transition, it is very useful to resort to tapers integrated on a chip, and combined with microlensed fibres. Tapers would deserve a chapter on their own, as regards both their design and their fabrication technology. Let us briefly mention that two families of tapers exist, 'interferometric' and 'adiabatic' tapers. In 'interferometric tapers', a number of scatterers cause a wide beam to interfere destructively at most points save at the entrance of the narrow waveguide. Adiabatic tapers, on the other hand, exploit the expansion of modes in the deconfinement regime, which allows the modified modes to be captured in another, larger waveguide at a different height. Contrary to the scheme represented in Fig. 9.11*d*, the width of the ridge waveguide is drastically reduced on the side of the fibre in order to obtain a semiconductor tip much smaller than $\lambda/2$. By contrast, the coupling configuration on the side of the membrane photonic crystal device can remain unchanged. The reproducible fabrication of such waveguide tapers places high demands on technology, for instance on high-resolution lithography, for the production of tips with reproducible 50 nm radius. Results reported by S. McNab and by M. Notomi are representative of the solutions favoured for managing this issue (McNab 2003; Notomi 2004).

9.6.3 Wide-Band Transmission-Reflection Spectroscopy

The methods presented above are not well-suited to 'bulk' photonic crystals like macroporous silicon. Here again, an external source is needed. However, this source should present an appropriate output beam in order to probe samples with a thickness of a few ten micrometers, for instance a collimated beam with a 50 μm diameter. In order to gain an accurate insight into the influence of the different length scales involved here, for instance the size of the holes, the period of the lattice and the three dimensions of the crystal, the use of a source with a very wide band, extending over two or three octaves, is preferable. Contrary to measurements on planar waveguides, there is obviously no risk that cutoff effects due to guided modes might occur. The different conditions enumerated here can be fulfilled by using a Fourier transform spectrometer coupled to a microscope equipped with a Cassegrain-type reflective objective presenting a slight central obscuration. The size of the spot can thus be reduced to a few ten micrometers, and there is no need of using any particular spatial filter along the trajectory of the beam. Such an arrangement has been used for measuring the reflection spectra of macroporous silicon photonic crystals in the mid-infrared, ranging from about 1.3 to 20 μm (Rowson 1998). The wideband transmission method can also be applied to microstructured fibres in the visible and near-infrared regions. The reader is referred to Chapter 11 for more detail on the latter subject.

9.7 Losses of Photonic Crystal Integrated Optical Devices

9.7.1 Analysis of Losses in Planar Photonic Crystal Waveguides

The losses of photonic crystals in integrated optics have several causes. Two of them are the same as in classical waveguides, i.e. absorption, in the form either of bulk or surface absorption, and scattering by sub-wavelength irregularities. In addition to these two mechanisms, the out-of-plane radiation losses induced by the crystal itself are a specific and additional loss mechanism. Depending on their value, these losses may critically restrict the potential applications of photonic crystals. We shall discuss here this issue, with a special emphasis on the relations between theory and experiments.

The theoretical considerations developed in Section 5.4 of Chapter 5 predict that any guided mode below the light line will be lossless. This however supposes that the crystal extends at infinity. In practice, the transition from a standard waveguide (a non etched region) to a perforated region may result in losses, even if the mode propagating in the crystal lies under the light line. This leads to the necessity of formally separating the losses into two distinct contributions, the losses due to the propagation in the photonic crystal itself on the one hand and the losses resulting from the input/output transitions on the other hand. The total

losses are a combination of these two distinct losses, and to some extent they can be viewed as a coherent combination of their contributions. However, in the common case where the incident wave has a frequency in the photonic band gap and where it penetrates over a very limited length in the crystal, this distinction becomes useless.

For buried waveguides, the guided modes most often lie above the light cone, and out-of-plane losses may arise for any wave geometry. A simple approach suggested for accounting for these losses in a two-dimensional simulation relies on the use of a complex refractive index in the air holes $n = 1 + in''$ (Benisty 2000). This amounts to considering that the energy leaking out of the plane of the waveguide is actually dissipated in the air of the holes, i.e. in the regions where there is no guiding (Krauss 1996a). This analogy can be justified by certain theoretical considerations that will be summarised hereafter.

In the spectrum represented in Fig. 9.9*b*, the high-frequency band edge is less abrupt, not only than the low frequency band edge, but also than the band edge predicted in a two-dimensional lossless simulation where the effective index of the waveguide in the absence of the holes was used as the matrix index. This difference can be explained by the in-plane fractional overlap of the air holes and the photonic modes, which is significantly smaller at the lower band edge than at the upper band edge, as can be seen in the one-dimensional examples considered in Section 1.3.2 of Chapter 1 (see for instance Fig. 1.6). This is an additional confirmation that the losses are 'localized' in the air holes. A further reasoning leads to considering the actual system as a perturbation to another separable and lossless system (Benisty 2000). This amounts to considering each hole as a dipole excited by the guided field and radiating in all directions. This local approach can be adapted to any type of structure, either regular or not (straight waveguides, bends, cavities with any shape and symmetry, etc), and it is therefore distinctly different from the collective modal approach based on infinitely extended modes. However, the dipole strength is directly dependent on the strength of the 'leaky' component of the Bloch wave, i.e. the component associated with the wave vector lying above the light line. This observation reconciles the local and collective approaches. The local radiating dipole approach can also be exploited in the frequent case where the holes are insufficiently deep due to the limitations of etching technology. In such a case, the dipole is now associated with the excess material at the bottom of the hole (Lalanne 2001). The respective contributions of each component of the waveguide, i.e. of the cladding and the core respectively, can thus be extracted (Ferrini 2003a, 2003b, 2004).

Let us turn now to the losses resulting from the finite etch depth. It can be demonstrated that these losses are, in the first order, proportional to the fractional overlap of the vertical profile of the field with the non-etched region, i.e. to the part of the field that does not overlap with the holes. In practice, the optical intensity decreases very rapidly as the depth increases. For instance, in a GaAs system corresponding to the values presented in Table 9.1, it decreases from a factor $e = 2.718$ every ~ 50 nm. Increasing the etch depth by only 50 nm can therefore be decisive. Let us finally mention that this approach can also be used for determining the influence of the shape of the holes, for instance their conicity (Ferrini

2003a, 2003b). In this case, the application of this method consists in modulating the fraction of excess material (compared to an infinite perfect hole) with respect to the etch depth. This semi-analytical approach permits to reach certain simple physical conclusions which can be useful for minimizing the losses of any photonic crystal structure, for instance by selecting optimized heterostructures or etching conditions (Ferrini 2004; Pommereau 2004).

Losses in Membrane Photonic Crystals

Losses in two-dimensional photonic crystal membranes have not been the subject of any comprehensive study reviewing significant data and methods. A first reason stems from the complex nature of the physics of systems with high index contrast in all three directions. A simplified system, where dimensionality was reduced to two, has been discussed in Section 9.2.2 (see Figs. 9.4*a* and *c*). A second reason is that research on membranes has been directed for the most part at cavities and channel waveguides, providing in turn to a useful set of data for these lower-dimensional structures. The superprism (see Section 6.3 in Chapter 6) might be a suitable candidate for investigating the loss characteristics of genuine two-dimensional membrane photonic crystals. However, in view of the difficulty, at the present time, of obtaining a satisfactory behaviour of superprisms in integrated optics, the status of two-dimensional membrane photonic crystals remains to be established, especially as regards their transmission bands. Research on nonlinear resonances or double resonances may give a new impulse to studies on canonical two-dimensional periodic systems (Mondia 2003; Raineri 2005).

9.7.2 Measurement of Propagation Losses in Straight Photonic Crystal Channel Waveguides

In a straight channel waveguide, i.e. in a line defect, defined for instance by a missing row in a triangular crystal, genuine propagation losses occur for modes located above the light cone. Due to the scale difference between the lengths of the waveguide (100 μm or more) and of the coupling region to such a waveguide (~1 μm), the coupling and propagation losses can be separated unambiguously

It is no longer possible, for measuring propagation losses, to resort to the cut-back method which had previously been transposed from fibres to long ridge waveguides, and where the length of a given waveguide was progressively reduced by repeated cleavage under constant injection conditions. Indeed, this method would require an initial length as large as 2 mm of photonic crystal waveguide. This is much more than the 10 to 200 μm which can be currently obtained using e-beam lithography, and which also correspond to the typical length of many envisioned miniature applications. Alternative techniques, based on the characterization methods described earlier, include:

– the use of the internal source method for comparing the attenuation undergone by waveguides realized from the same substrate, but with different lengths

(pseudo-cutback method). The accurate positioning of the spot, which is necessary in order to induce a similar excitation of the waveguide from a modal point of view, can be easily achieved (Smith 2000c).

- the use of the end-fire method for comparing the losses associated with photonic crystal waveguides of different lengths excited under identical conditions (Talneau 2001; Lin 2000a). The excitation conditions can be indeed fixed by long single-mode access ridge waveguides, as represented in Figs. 9.11*b* and 9.11*c*. However, the cleaved facets induce a large amount of reflection, which cannot be easily eliminated when using highly coherent laser sources. An interesting alternative consists in considering these facets as mirrors with a known and reproducible reflectivity, and the whole sample as a Fabry-Perot cavity. When scanning a tuneable source, the analysis of the fringe contrast allows the evaluation of the cumulated losses arising during propagation between the facets, which include the coupling losses and the genuine propagation losses. The two contributions can then be retrieved separately by comparing samples with different lengths. More exactly, one determines the difference between the propagation losses of the ridge waveguide and those of the photonic crystal. The ridge waveguide itself can be calibrated using the same technique.
- the direct exploitation of the Fabry-Perot reflections at the ends of photonic crystal waveguides without resorting to access waveguides. In order to draw accurate comparisons between photonic crystal waveguides with different lengths, the termination of the crystal must be kept the same for each waveguide. Only GaAs technology currently offers the possibility of cleaving membrane photonic crystal waveguides at reproducible crystal positions, i.e. at the symmetry planes, where the membrane exhibits a singular mechanical weakness. However, even in this case, drawing comparisons between two waveguides remains a delicate task when it must performed in the regime of ultimate low losses, for instance a few dB/cm. Measurements must be accompanied by numerical simulations of the modal reflectivity if significant loss data are to be retrieved from a given sample (Combrié 2006a).
- the measurement of the light scattered above and along the photonic crystal waveguide, with the end-fire method being used for the injection of light into the waveguide. This restricts the observation to those modes which are lossy in the collection angle. The precise measurement of the total scattered light is obviously hampered by the substrate and by the complex evolution of the rays radiating in it in the case where the latter is not absorptive.

The losses of a waveguide are obviously dependent on its in-plane width. In a system with a strong in-plane index contrast, a waveguide larger than $\sim \lambda/2n$ becomes multimode, but the fundamental mode extends less and less in the photonic crystal as the width increases, as in a standard 'refractive' waveguide. This leads to a significant reduction of the losses, which approximately scale as $1/(\text{width})^2$. Propagation losses can thus be made acceptably low with a relatively limited width, corresponding for instance to three to five missing rows (Kotlyar 2004; Zimmerman 2004). The risk of coupling to extra modes of these

waveguides should not be excessively feared in miniature geometries. Besides, a number of specific modal characteristics can be engineered for the sake of minimizing and even exploiting adverse effects (Viasnoff-Schwoob 2005).

A series of technological improvements have been instrumental in reaching very low losses in W1-type structures on membranes. In view of recent advances in the ongoing race toward low losses, the 1dB/cm value can now be considered as attainable (Jafarpour 2004; McNab 2003; Notomi 2004; Sugimoto 2004; Tanaka 2004).

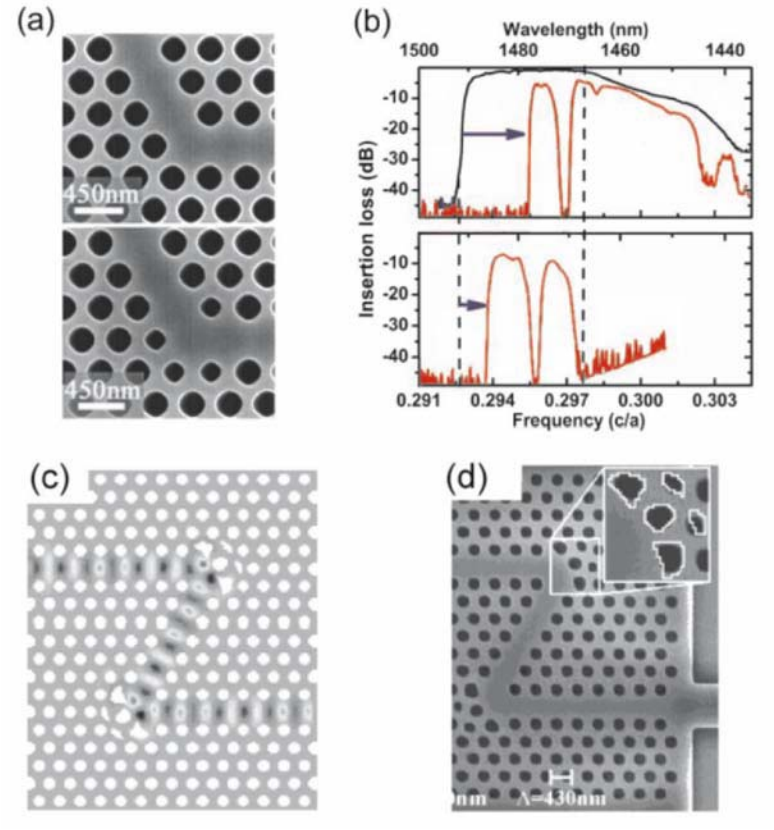

Fig. 9.12. Photonic crystal bends with good transmission performances *a.* SEM views of 60° bends fabricated from photonic crystal membranes (Assefa 2006). *Upper part.* Simple bend with photonic crystal holes of a constant diameter. *Lower part.* Modified bend in which four holes adjacent to the bend corner have smaller radii. *b.* Measured transmission spectra of 20 cascaded bends (*red*) and comparison with a straight waveguide with a 181 μm length (*black*). *Upper part.* Simple bends as in *a* (top). *Lower part.* Modified bends as in *a* (bottom). In this case, transmission is shifted to the slow light region at long wavelengths. The maximum transmission reaches ≈ 98% for one bend *c.* Topology-optimized 120° bends in a W1 geometry. Snapshot of the magnetic field (Têtu 2005) *d.* Corresponding SEM image of the fabricated structure

9.7.3. Losses in the Slow-Light Regime

The tail of an even W1 mode (or similarly of a Wx mode, where x is a fraction around unity) is characterized by a clear cut-off with a zero group velocity towards $k = \pi/a$, far into the lossless operation region of membrane systems. The group index $n_g = c/v_g$ is used for assessing slow-light performance. The second important parameter is the bandwidth over which such a slow-light regime can be achieved. It is quite clear that a compromise between these two parameters must be found. However, the terms of such a compromise are not established yet. This slow-light regime near the W1 main mode cut-off has attracted considerable attention since the pioneering results by M. Notomi in 2001, which demonstrated group indices approaching the $n_g = 100$ symbolic value in narrow bands (Notomi 2001a). The relationship of losses to n_g or v_g is obviously of importance. While incoherent losses, for instance losses due to absorption, usually tend toward a $1/v_g$ scaling, the resonant nature of the waveguide modes entails that coherence is very likely to play a role, as is the case, for example, in very high-Q toroid microcavities. Following the studies conducted by S. Hughes at NTT, it is now recognized that, in the slow-light regime, losses associated to coherent backscattering mechanisms can increase at an even faster rate than $1/v_g$ (Hughes 2005; Kuramochi 2006). In this respect, the investigation of losses in waveguides with variable length conducted by the IBM group has provided a useful benchmark (McNab 2003).

9.7.4 Waveguide Bends in Photonic Crystals and Bend Losses

The bends in a photonic crystal waveguide raise a complicated design issue, which originates in the fact that these bends disrupt the very periodicity of the waveguide. Thus, the input mode, which may for instance be the fundamental mode, tends to couple to all output modes. The multimodal nature of a waveguide is obviously a major obstacle to achieving a good bend transmission. Ideally, no higher-order mode should be excited, be it on the transmitted side or on the reflected side. This issue is somehow related to that of furtive electromagnetic obstacles, and in particular aircrafts, which should not scatter waves along certain directions.

At this point, we need to comment on the well-known numerical simulation realized by the MIT group, which predicted a near-unity transmission in 90° bent photonic crystal waveguides (Mekis 1996). Actually, the two-dimensional photonic crystal considered for this simulation was a crystal formed by dielectric columns, where an air waveguide had been created by removing one row of rods. Under these conditions, the wavelength in the waveguide remains significantly larger than the period of the crystal. As a consequence, the wave does not undergo any significant diffraction. On the contrary, in an experimental waveguide, the photonic crystal is formed by a lattice of air holes, and the waveguide itself consists of one or several missing rows of holes. Accordingly, such a waveguide

exhibits the higher index in the whole system, and since the wavelength λ/n is small, the wave propagating in the waveguide is diffracted by its corrugated boundaries.

A number of possible improvements, based on a variety of different configurations, have been suggested. Thus far, good performances are obtained only at the price of a lower bandwidth, with the resulting bandwidths being of the same order as the WDM 'C' band (30 nm at 1550 nm, i.e. 2 %) (Figs 9.12*a*,*b*). The influence exerted by several different factors, for instance by the polarization of the field, and more generally the physical limits of these devices, remain unclear. For this reason, there is still room for improvement in their design. In practice, and leaving aside the issue of modal reflection, the measurement of a bent waveguide proceeds essentially by comparing it to a straight waveguide with identical length (Figs 9.12*b*, *bottom*).

Historically, the bend designs proposed by A. Chutinan *et al* in 2002 were among the first to be device grade in terms of performances (Chutinan 2002). To date, the results obtained by K. Asakawa *et al* in Tsukuba provide a practical benchmark from an experimental point of view (Asakawa 2006; Tanaka 2005). As an example, these authors have implemented with a high degree of success the topology-optimized photonic crystal structures elaborated in (Borel 2004; Têtu 2005). As non-intuitive as these structures might seem (Figs. 9.12*c*,*d*), they nonetheless exhibit extremely good performances, with a transmission approaching 100 percent over wide frequency bandwidths. However, interest in sharp bends in photonic crystal waveguides has somewhat declined in the recent years as a direct consequence of the impressive results independently obtained on sharp bends of simple ridge waveguides in the SoI technology. Further, as will be seen in more detail Section 9.8, it has been found that clever multichannel devices could be designed from photonic crystal cavities without resorting to bent waveguides.

9.7.5 Photonic Crystal Resonators and Quality Factors

Realizing a resonator by adding two in-plane confinements to an integrated optical configuration necessarily results in a certain leakage of light along the third dimension. This is caused by the fact that the k-spectrum of the confined in-plane field presents a continuum of spatial Fourier components within the light cone at wave vectors down to $k = 0$. The resulting losses must be controlled and minimized for both types of vertical waveguides, i.e. for waveguides in the substrate and in the membrane approaches respectively. For membrane waveguides, the resonators can be designed in such a way as to minimize the fraction of the 'leaking' k-components, i.e. those within the light cone (Akahane 2003a; Englund 2005; Song 2005; Yoshie 2001).

In the case of buried waveguides, no such possibility exists, and as a result, the problem is more open-ended. The trivial solution, which consists in increasing the size of the resonators, is of limited interest. Indeed, the behaviour of the modes tends in this case towards that of delocalized plane waves, thereby result-

ing in a multiplication of the number of these modes. As a consequence, one tends to lose the interesting features of microcavities for light emission (see Chapters 7 and 10) or to decrease the free spectral range for filtering applications. However, the underlying physics are far from being trivial and interesting modes may exist in relatively large cavities. An analogous situation is that of whispering gallery modes, whose volume is much smaller than that of the microdisk inside which they are confined. An alternative deconfinement strategy consists in creating a very localized, albeit 'shallow' defect, i.e. a weak modification of a band gap material. Some striking successes of this strategy will be presented later in the course of this chapter.

For an isolated resonator consisting of a set of missing or smaller holes drilled in a large uniform photonic crystal, the method described in Fig. 9.10*b* allows the direct determination of the quality factor from the spectral width of the observed peaks in the diffracted photoluminescence. This simply results from the fact that the presence of a resonant microcavity mode enhances the field in the cavity. The same applies to the physical edges of the cavity, which results in a resonance peak in the spectrum (Benisty 1999; Lin 2001a; Park 2001; Pottier 1999; Reese 2001; Yoshie 2001). A spatial filtering can be used for optimizing the collected signal by eliminating the photoluminescence directly emitted through the upper surface of the cavity, i.e. without the guiding and diffraction processes, which does not exhibit a structured spectrum.

A major drawback of this method lies in the fact that luminescence efficiency is hampered due to the close proximity of the etched sidewalls. Use of this method tends therefore to be restricted to cavities ranging from three to a hundred missing rows, which allow for the existence of a large number of modes. Among these modes, only modes with wavefronts aligned with the edges of the crystal have a sizeable fraction of their emission oriented along the vertical direction (Smith 2000d). In the case of an elementary microcavity with a 1 μm side or diameter, realized in a GaAs-based photonic crystal, there typically exist more than five modes in a 100 nm spectral range. Most of these modes present complicated wavefronts, which never give rise to a plane wave in the normal direction, but radiate in different scattering lobes. Indeed, due to the complex relation between the phases of the radiating elements, i.e. the holes around the resonator, the far field tends to present destructive interferences under most circumstances, in much the same way as in dark-field and phase-contrast microscopies. It is far easier to proceed to the classification of modes with respect to their symmetry in the case of ultimately small cavities, since the cancellations and reinforcements between a limited number of modes are more clear-cut. A sizeable fraction of power can then be captured for usual geometries.

Another obstacle is the presence, in the cavity, of a 'load' associated with the absorption of the luminescent system. While this effect can be reduced by resorting to an optical pumping, there is no simple method for determining the transparency point with respect to the pump power (see Chapter 7 for the type of modelling involved here). The risk exists of actually measuring a laser, whose spectral linewidth can be much narrower than that of the 'cold' cavity, i.e. the cavity in the absence of the load. In spite of the interest of such a property, let us

remind ourselves that we are primarily interested here in the determination of the quality factor of microcavities. Other 'useful' loads can be devised, for instance the optical fibre pick-ups used either for weakly confined modes (Barclay 2005) or for more confined modes (Hwang 2005, 2006)

Let us now describe in more detail the case of some hexagonal cavities. In a triangular crystal, the hexagonal cavities have sides consisting of dense rows and form a series of canonical cavities. It is convenient to name these cavities according to the number of periods along each side. Thus, a microcavity with a single missing hole will be termed H1, a microcavity with seven missing holes H2, etc. The amplitude maps of the magnetic fields of two modes of an H2 cavity are shown in Fig. 9.13. These two modes are non-degenerate modes. Such modes are much easier to analyse than doubly degenerate modes, which unfortunately are twice as many. The analogy between these resonant modes and the energy levels of the canonical benzene molecule is useful for understanding the degeneracy of the modes. The mode represented in Fig. 9.13*a* is of the 'radial' type, with wavefronts that tend to align to the edges of the cavity. A similar mode with a wavefront aligned along the sides, albeit with a different intensity at the apices, can also be observed. The mode represented in Fig. 9.13*b* is analogous to the so-called whispering-gallery modes, typical of microdisks, as will be seen in Chapter 10. There are no simple rules for the evolution of the modes when the size of the cavity digitally increases to H3, H4, etc.

The smaller the cavity, the lower will be its quality factor, at least as long as similar loss mechanisms are at play. Thus, H1 cavities present the lowest quality factor. This being, there is no simple rule for the evolution of the Q factors either. In one-dimensional Fabry-Perot cavities, the quality factor is given by the equation $Q = mF$, where $m = L/(\lambda/2n)$ is the order of the cavity and F is dependent only on the reflectivity of the mirror. However, the first modes of interest in H1 cavities are double degenerate dipole modes, and a monopole mode in the gap can be found only by diminishing the radius of the surrounding holes (Park 2001). By lifting the degeneracy in such a way that the field had minimal Fourier components within the light cone, the Caltech group reached in 2001 the value of $Q = 2800$, thereby opening the way to ultracompact resonators for telecommunication applications within the WDM framework.

The next section will be devoted to an account of the recent improvements which have been taking place following early studies on H1 and H2 cavities. We also provide a survey of the numerous photonic crystal devices which have emerged during the same period.

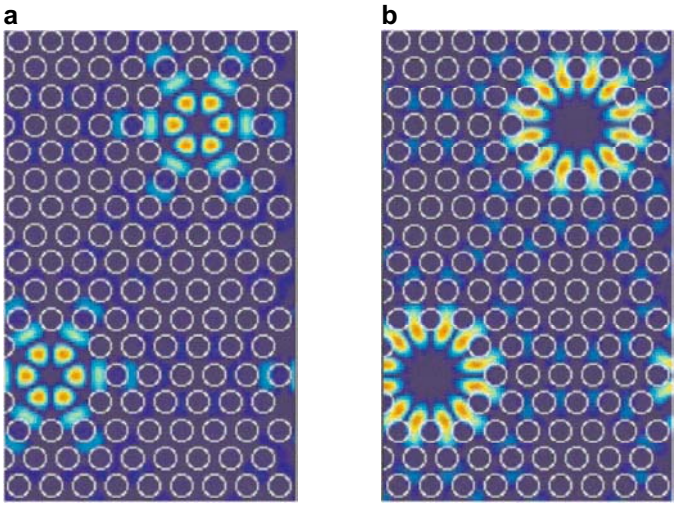

Fig. 9.13. Amplitude maps of the magnetic fields of two TE modes of 'H2' microcavities, calculated through a two-dimensional numerical simulation *a.* Mode of the 'radial' type. The lobes near the edges of the cavity are elongated. Accordingly, since the phase of the mode is the same at the different holes of the periphery, the mode can radiate along the direction normal to the plane *b.* Mode of the 'whispering-gallery' type: the phase of the mode alternates at the periphery. The air-filling factor is equal to $f = 0.40$, and the dielectric constant to 10.5. Both these two modes lie within the photonic band gap of the crystal at a short distance from the normalized frequency $u = a/\lambda = 0.3$

9.8 Photonic Crystal Devices and Functions : Recent Developments

9.8.1 Classification of devices

The years 2002 to 2006 have witnessed huge improvements in the Q factors of microcavities, which have reached the value of about 1,000,000. These improvements have been demonstrated in passive cavities, for instance cavities on silicon membranes. As has been underlined in Section 9.7, these advances have coincided with the advent of very low-loss W1 waveguides. In turn, this has enabled the better characterization of passive cavities through resonant energy transfer from an adjacent waveguide. Recent milestones in the development of coupled waveguide-microcavity systems include:

– early studies on microcavity-waveguide coupling in substrate-type photonic crystals,

- the design of coupled-resonator optical waveguides, formed by a series of coupled cavities,
- updated results on very-high-Q cavities.

While it is natural to focus on the best results, it might also be useful to provide a more general classification of emerging photonic crystal devices. The following enumeration lists these different types of photonic crystal devices, together with some brief comments:

- Polarization splitting and converting devices, used for separating the TE and TM polarizations. This is of particular interest for implementing desired functions under TE polarization, which in general can be more easily handled in planar photonic crystals.
- Broadband splitters and combiners. The splitting function is often necessary when performing several processing operations on the same signal.
- Tapers and couplers. These devices are used for coupling different types of waveguides together, or for coupling a fibre from the outside world to a planar waveguide.
- Modulators, and in particular Mach-Zehnder modulators. The latter are widely used for the processing of optical signals in telecommunication technologies (Bigo 2006). In the context of photonic crystal devices, a Mach-Zehnder modulator consists in ensemble of splitters, bends and straight sections, plus a modulating arm for implementation of an electro-optic effect.
- Slow-light devices, based on the direct exploitation of the low group velocity regions of photonic crystal waveguides. These systems, as well as a number of other competitive systems such as microrings, offer delay management and dispersion management functions which are useful at various stages in the context of high-bit-rate optical telecommunication networks.
- Spectrometer-type devices of a resonant nature, where a set of microcavity-type resonances is used in order to select some spectral component of an optical signal. This category also includes devices based on a ‘mini stopband’ effect (see Section 5.2.5). While this phenomenon is not formally of the microcavity type, it is rather resonant in character.
- Spectrometer devices based on modified arrays of waveguides,
- Spectrometer devices based on the superprism effect in two-dimensional photonic crystals,
- Spectrometer devices based on successive cutoff waveguides. Light not transmitted at the transition between a first (waveguide) and a second, slightly narrower waveguide at cutoff, is channelled onto some other optical path for this purpose.
- Nonlinear ‘gating’ devices. In these devices, which generally are of a resonant nature, the all-optical modulation of a signal beam by a control beam is achieved by taking advantage of the resonant enhancement of at least one of the fields.

In the following, we first consider coupled waveguide-microcavity systems.

9.8.2 Coupled Resonators and Waveguides

The coupling of a resonator to the 'external world' is a necessary step on the way to exploiting the properties of a resonator in an actual device. This is required in particular for selectively inserting or extracting a single wavelength from a multicolour signal (with a WDM resolution, $Q = \Delta\lambda/\lambda$ should lie between 3000 and 100000), propagating in a waveguide. While some of the earliest proposals may have been unrealistic in terms of fabrication (Fan 1996, 1998), the first configurations successfully implemented with some significance for applications include the following realizations:

- the lateral coupling of an H7 cavity to a W3 waveguide, represented in Fig. 9.14*a* (Smith 2001). At this stage of the characterization process, the luminescence signal in the cavity modes is locally induced by a pump laser beam focused onto the sample. It is then transferred onto the waveguide, and the light in this waveguide is subsequently channelled in the direction of a cleaved edge. Light is then collected in the same way as in other experiments conducted with internal light sources. The lateral coupling between a cavity and a waveguide is favoured here by the coupling occurring between the different in-plane guided modes, as described in Section 5.2.5 of Chapter 5. This phenomenon results in the formation of a ministop band with a width equal to 10 nm around $\lambda = 1000$ nm. Another application of this mini-stopband for the realization of a miniature spectrometer will be described below. For the range of coupling parameters considered in the experiments, and within the limits of experimental resolution, the quality factors of resonant modes ($Q \sim 800$) were found not to be degraded.
- H2 or H3 cavities cascaded with photonic crystal waveguides (Olivier 2002b). The Hn cavities are coupled to waveguides by their apices, which, intuitively, is not an optimal solution. In the example presented in Figs. 9.14*b* and *c*, this drawback was circumvented by using a cavity with a larger size. The inverse solution would be to change the orientation of the waveguide from 30°, which would result in a relatively strong corrugation of the waveguide, with larger and more numerous mini-stopbands than Wn waveguides with a similar physical width.
- a coupled-cavity waveguide, also referred to as a coupled resonator optical waveguide (CROW) (Olivier 2001a; Yariv 1999). An example of such a waveguide is presented here in Fig. 9.14*d*, while the phenomena of transmission minibands and minigaps associated with it are clearly visible on the spectra presented in Fig. 9.14*e*. This system is actually a good model for photonic engineering, and it provides in particular the possibility of controlling the group velocity by simply varying the degree of coupling between the cavities. The reader interested in other studies on nanophotonic 'CROWs' is referred for instance to the work by F. Xia *et al*, where striking results based on microrings integrated on a SoI platform are reported (Xia 2007).

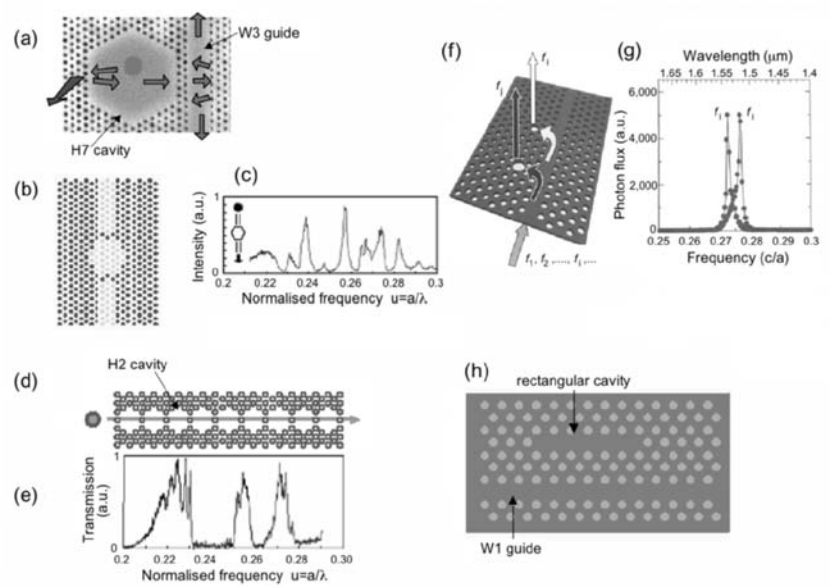

Fig. 9.14. Coupling between a waveguide and a cavity *a.* H7 cavity laterally coupled to a W3 waveguide (Smith 2001) *b.* Cavity adapted to in-line coupling with a W3 waveguide and inserted in such a waveguide (Olivier 2002a) *c.* Transmission spectrum for the cavity represented in *b* *d.* Example of a coupled-cavity waveguide, also referred to as a coupled resonator optical waveguide (CROW) consisting of nine H2 cavities *e.* Transmission spectrum represented as a function of the normalized frequency $u = a/\lambda$, measured using the internal light source method (Olivier 2001a) *f.* Defects consisting of enlarged holes coupled to a W1 waveguide *g.* Transmission spectrum measured along the vertical direction above the defect (Noda 2000) *h.* Rectangular cavity consisting of a few missing holes coupled to a W1 waveguide (Seassal 2002)

– a cavity based on a single modified hole, in this case an enlarged hole (Noda 2000), and coupled to a W1 waveguide (Figs. 9.14*f* and *g*). The selective drop of a wavelength with a quality factor close to 500 was thus obtained. It is not necessarily easy to determine whether the critical coupling condition was achieved in these experiments, i.e. whether the radiation of the cavity towards the air was actually equal to losses in the direction of the waveguide. This actually is quite a generic issue. While the determination of cavity emissions is a delicate issue, the coupling itself can be more easily modelled due to its non-resonant character. For this reason, experimental results often rely on a sufficiently realistic estimate of the coupling. This allows to deduce the Q factor of the 'cold cavity', i.e. of the cavity if it were isolated, from the Q factor of the 'loaded' cavity, when the emission of the cavity in the waveguide is a significant, and even a predominant channel. It might be noted that no convincing evidence demonstrating a coupling between a H1 cavity and a waveguide has

been established thus far. Among various factors, this can be ascribed to the dipolar nature of the relevant modes of H1 cavities.

– rectangular cavities, consisting actually of sections of W1 waveguides, which themselves are coupled to another W1 waveguide, as represented in Fig. 9.14*h* (Seassal 2002). These results were among the first on elongated cavities resembling straight waveguides, and were in the continuity of previous works reported by the same authors on the group velocity in W1 waveguides (Letartre 2001).

In the following section, we shall provide an updated survey of research on very high-*Q* cavities on membranes conducted in the period 2003-2006.

9.8.3 Very high-*Q* cavities

Recent evolutions towards very high-*Q* cavities have been taking place following the first results at the turn of the millennium.

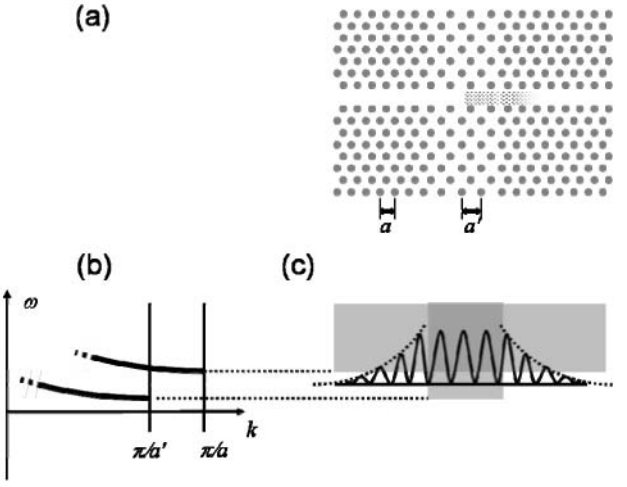

Fig. 9.15. Principles of the 'ultra-high *Q* cavity' designed by Noda's group *a.* Waveguide formed by a single row of missing holes with a modified central area, extending in this case in a region of the photonic crystal with larger period $a'>a$ *b.* Schematic band structures of two waveguides with periods a' and a respectively. The larger period causes the cutoff frequency of the even waveguide mode to decrease at the edge of the Brillouin zone *c.* Schematics of the field confinement in the photonic heterostructure thus created, similar to the confinement of electrons in a quantum well. The modal volume remains small owing to the rapid decay of the evanescent field, which itself results from the 'heavy' effective mass observed in the dispersion diagram *b* at the edge of the Brillouin zone

These results have been due to the continued effort of the Kyoto group on elongated cavities of the Ln type consisting of a small line of n missing holes in the photonic crystal (Akahane 2003a). The authors found that variations in the behaviour of Ln cavities occurred depending on n, and related these variations to the different emission patterns and different phases of the in-plane field at each edge of the cavities.

The fine tuning of the position of the holes at the edges of the cavities led to the first major increase in the Q factor, which reached the value of 45,000 in the studies conducted by Akahane on a silicon membrane (Akahane 2003a). The authors argued that the 'gentle confinement' of the field ensured by tuning the hole position resulted in a mode with a more Gaussian-like envelope in the real space. This translated into a Fourier spectrum of the in-plane field characterized by two peaks (those of a standing wave in a W1 waveguide) with minimal broadening and minimal amount of k-components in the region of the light cone. It still remains somewhat controversial whether the in-plane field and its component have a completely unambiguous relationship to far-field radiation (Sauvan 2005). Far-field radiation involves the coupling of in-plane fields with scatterers described by the dielectric constant. Further, since the field is three-dimensional, with different maps in each plane, the consideration of the field in the middle of the slab cannot provide the entire information. It does however provide a convenient way to 'spy' in a first approach the possible trends of cavity modes in terms of leakage. P. Lalanne and C. Sauvan further demonstrated how the lower group velocity and the better mode matching could account for the higher Q of this cavity.

The fine tuning of the position of the holes on the edge sides has also been considered, and has led to values for Q reaching 100,000 for the best design. This particular design had been closely 'missed' by Y.Akahane *et al.* in 2003.

Another step forward was made at the beginning of 2005, when the same group succeeded in reaching the value of 600,000, and then the value of around 1,000,000 (Song 2005). This corresponds to photon lifetimes around 1 ns, as has been recently evidenced by two different groups (Asano 2006b; Tanabe 2007). Beyond the symbolic value of this achievement, it is now becoming apparent that cavity design has reached a point where it is no longer the limiting factor: The limits to such ultra-high Q values are rather to be found in their fabrication process and in other technical aspects, including thermal stability during measurements and residual adsorbed water absorption. Since the optical path is of the order of 1 m (1 ns corresponds to 30 cm) across a thin piece of silicon with surfaces exposed to the air, sensitivity to absorbing species becomes an issue (Asano 2006b). For certain designs, Q values of the order of 20,000,000 appear to be attainable in ideal structures, and further advances are likely to take place in the area of high-Q 'nanocavities'. It has indeed been shown that the Q factor could increase by a decade at the price of only a logarithmic increase of the mode volume.

For a different membrane material such as GaAs, impressive quality factors, of the order of ~ 250,000, have also been achieved (Weidner 2006).

The design of these ultra-high Q 'nanocavities' is at once very simple and yet very clever. It rests on the natural cut-off of a W1 waveguide, and uses it to create a waveguide heterostructure with only a shallow 'photonic well' (Fig. 9.15). The optical field in the central region is therefore very well matched to the field of the evanescent 'half-Bloch-mode' in the barrier regions, formed by the same waveguide with a difference of only a few percent in the hole pitch. In the most recent versions of these structures, developed by the competing NTT group, shifts less than 10 nm in the holes of the basic waveguide are sufficient for creating this shallow defect (Kuramochi 2006; Tanabe 2007).

An interesting point to consider is that a shallow defect may nonetheless provide a reasonably well-confined cavity, with a volume remaining in the cubic wavelength regime $(\lambda/n)^3$. The key to this effect is the particularly 'heavy' photonic mass of the W1 waveguide in the region considered here. Using an analytic continuation to imaginary k values in the barrier regions, this translates into a large imaginary part of k (k"), of the order of a substantial fraction of π/a, in spite of the very small frequency difference. Since the volume is determined essentially by $1/k$", this ensures a small volume, of the order of the unit-cell volume, within a relatively small numerical factor (Asano 2006a, 2006b).

Since then, both these cavities and those previously described have been used in device demonstrations. In particular, the NTT team has used them for implementing nonlinear optical functions, as will be reported in the next section.

9.8.4 Other Devices and Optical Functions

This brief review will be aimed at showing that photonic crystals have both the potential and the momentum to become a disruptive technology in the field of integrated optical devices. The degree of accuracy that will be achieved in the fabrication of microstructures and nanostructures, and more generally the future advances that will be taking place in the field of micro- and nanotechnology, will be decisive factors for the evolution of integrated optical devices based on photonic crystals.

Polarization Splitting and Converting Devices

Polarization is an important issues in integrated optics. A popular scheme for achieving polarization independence is the polarization diversity approach, which requires first to split the TE and TM polarizations, and then to convert TM into TE, before recombining them in their initial, distinct polarization channels, hence without interferences. The gap maps of both the triangular and square lattices of holes contain numerous regions where only a TE gap and no TM gap exist. This property can be used to divert a TE wave by means of a slab of photonic crystal. This has been studied at design stage, but a number of practical difficulties, especially at the interfaces, have prevented thus far its realization. A further step is to convert one polarization into another. Existing bulk polarization rotation schemes will not be detailed here. Instead we shall emphasize that the high index contrast

used for photonic crystals can be similarly used for implementing very high form birefringence. Polarization rotation requires the eigenmode axis of the photonic crystal to be rotated with respect to the standard axis. This property can be achieved by means of an array of slots etched at a large angle with respect to the usual vertical direction, and such a structure has been shown to perform polarization rotation within only a few microns **(**Kotlyar 2005**)**. Another scheme for polarization diversity, proposed by the Ghent research group, consists in using a surface coupler based on two-dimensional square lattices, where slight distortions can be introduced for directionality purposes (Taillaert 2006). These devices can also be considered for use as taper devices, provided that they accept the mode of a standard optical fibre at the input, which should be delivered to a thin single-mode waveguide (with the same width at a first stage).

Broadband Splitters and Combiners

Beam-splitting and combining are important functions in standard integrated optics. They can be implemented either through use of a Y junction, in which case the realization of the tip of the Y-branch is a critical lithographic step, or through so-called multi-mode interference (MMI) devices. The latter devices are based on the Talbot effect, i.e. on the coherent diffraction of coherent multiple sources at a small distance. Implementations of the Y-type splitter have been proposed by different groups, and acceptable performances have been obtained after adjusting the Y region in order to avoid coupling to any extra mode (Boscolo 2002a). Recent results, based on different optimization approaches for the Y junction, can be found in (Asakawa 2006; Ayre 2005; Borel 2004; Têtu 2005). Another popular proposal, implemented with some degree of success (Leuenberger 2005) is the broadband codirectional coupler, based on two waveguides positioned in close proximity and coupled by an evanescent wave. The bandwidth is large if the symmetric and antisymmetric supermodes of the waveguide pair have a sufficient spectral coverage with unperturbed characteristics. The combiner operation is less documented to our knowledge.

Tapers and couplers

The coupling of light between different waveguides, or between a fibre and a waveguide, requires an adaptation either of the size or of the aperture. The tapers used for coupling a broader W3 waveguide to a narrower W1 waveguide are an example in the area of photonic crystals of devices permitting such an adaptation. Indeed, it is in general more difficult to couple directly from such a waveguide to a fibre. A progressive variation in the size of the holes has been proposed for this purpose in (Talneau 2002), and this proposal has also been used for the realization of bends and splitters. Other approaches have been developed for other types of waveguides. In any case, the termination of W1-type waveguides is a crucial parameter when it comes to assessing the extended performances of any coupling system. The surface coupler mentioned above, and based on one or two-dimensional photonic crystals on a high-index contrast layer, in particular on SoI,

is also relevant in this context, insofar as it can be used for coupling from a fibre to an in-plane (broad) waveguide (Taillaert 2006).

Mach-Zehnder modulators

Modulators, and more specifically Mach-Zehnder (MZ) modulators, are important devices in the field of optical telecommunications (Bigo 2006). A good Mach-Zehnder interferometer must satisfy several demanding requirements; no reflections should occur at bends, losses at the level of the Y splitters should remain small, and a good balance should be maintained between the two branches in an unbiased reference case. The modulation scheme must then be defined, for instance through carrier injection or through other electro-optical or nonlinear optical effects. In this respect, the most striking results were undoubtedly achieved by the FESTA group in Tsukuba (Asakawa 2006). Their studies were conducted mostly on GaAs membranes, by using selectively grown quantum dots in the middle of the MZ structure in order to achieve the all-optical control of the transmission by a control beam at an extra entrance of the MZ device. Very short response times have been demonstrated using arrangements already established for other MZ modulators, thereby demonstrating the interest of photonic crystal research used in combination with existing solutions for addressing the numerous aspects of real-world devices. In a different approach, the IBM group has succeeded in designing a MZ system tuneable by direct electro-optic effect from a silicon photonic crystal, by using a clever lateral doping scheme **(**Vlasov 2005**).** The device was operated in the low group velocity region of the photonic crystal.

Slow Light Devices based on direct exploitation of the Low-Group-Velocity Regions of Photonic Crystal Waveguides

Devices based on the exploitation of the low group velocity of photonic crystal waveguides are increasingly attracting interest. The archetypal low-group velocity region arises at the cutoff region of narrow W*x*, W1 or other similar waveguides with different *x* values. The first signatures of a very slow group velocity were undoubtedly reported in the pioneering article by Notomi (Notomi 2001a). This initial result has been followed by several others from various leading groups, with varying degrees of success and measurement accuracy, either for membranes (Asakawa 2006; Combrié 2006a; Dulkeith 2005; McNab 2003; Notomi 2004; Vlasov 2005, 2006), or for SoI systems (Settle 2006). CROW systems have also been investigated (O'Brien 2007; Talneau 2006). Although all these waveguides will not necessarily translate into actual devices, it is clear that they allow variable group delays to be generated simply by operating at different wavelengths (Combrié 2006b; Talneau 2006; Vlasov 2005). The use of coupled resonant devices such as CROWs is certainly a promising route. It has been recently demonstrated that coupled microrings with a 10-20 μm diameter could be used for achieving a 500 ps delay with a bandwidth over 20 GHz, and thus that 10 bits could be delayed in a perfectly functional way by telecom standards (Xia

2007). A similar achievement for devices based purely on photonic crystals would undoubtedly be a milestone in this area.

Resonant-Type Spectrometer Devices

A first type of spectrometer device is based on the use of a series of local resonances. Each of these resonances picks up a corresponding frequency and removes it partially or entirely from a bus waveguide.

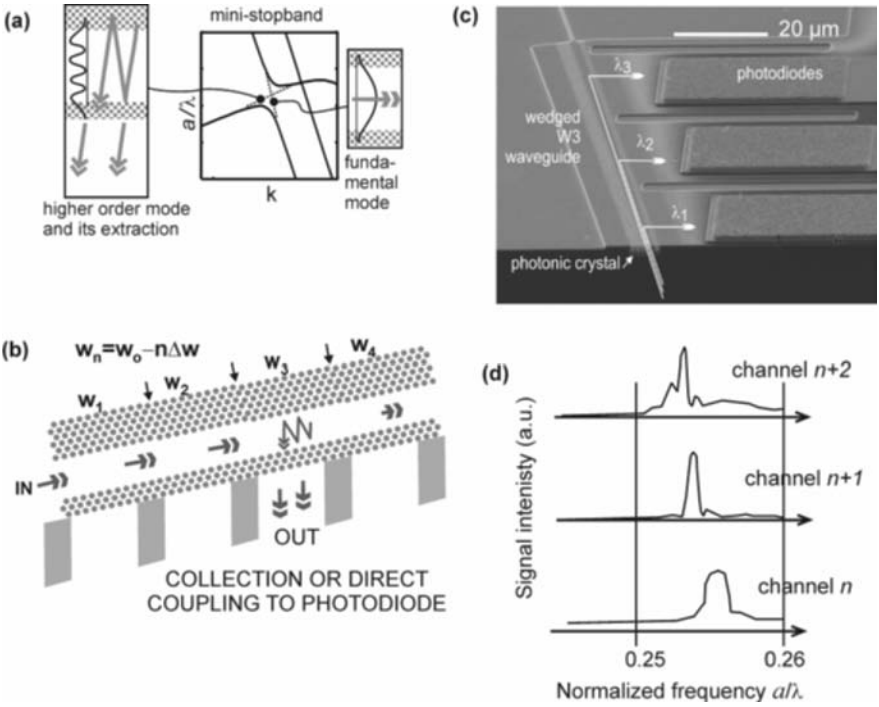

Fig. 9.16. Spectrometer based on mini-stopband *a.* Use of a mini stopband for the extraction of light at a defined *k* and frequency *b.* Step-wedged device for demultiplexing several channels. The width reduction induces a reduction in the extracted wavelength *c.* Micrograph of a device designed by HHI, Berlin, based on a design developed at the CNRS Palaiseau, and featuring integrated 1.5 µm photodiodes and a W3 waveguide *d.* Optical output of a similar device based on W7 waveguide with a *Q* factor up to 500. Details can be found in (Martinelli 2007)

Since 2002, this idea has prompted intense research activity by the Kyoto group (Akahane 2003b; Song 2003), and further studies on this subject have been conducted by the NTT group (Notomi 2004). The cavities used here are of the elongated type, while the waveguides are, broadly speaking, of the W1 type. A detailed discussion of these designs requires the consideration of complex technical issues, and the interested reader is referred to the corresponding articles (Shinya 2005). Nevertheless, the basic rules of cavity-to-waveguide coupling underlie these designs.

Spectrometers based on a mini-stopband in a W3 or in a similar multimode waveguide (Martinelli 2007; Viasnoff-Schwoob 2005) deserve a special mention. The resonant cavity can be said in this case to be 'inside the waveguide', since the same element is used as a waveguide for the fundamental mode and as a resonator akin to a Fabry-Perot resonator for higher-order modes (Fig. 9.16). The fact for the waveguide to be wedge-shaped, either in a continuous or in a stepwise fashion, ensures a series of channels to be dropped by this waveguide. This system rests on the omnidirectional reflection offered by two-dimensional photonic crystals, and in particular on the fact that they allow the guiding of modes up to Fabry-Perot-type modes, which would not be possible in ordinary waveguides. Selectivity is ensured by a slow higher-order mode, which also ensures greater compactness (Kamp 2006). A basic version of this spectrometer has thus been elaborated before being used in monolithic association with a laser for controlling the wavelength of the latter. Since the short footprint of the device ($< 10\ \mu m$) allows operation in an unpumped, absorbing active region, no passive layer was needed for implementing this spectrometer. This mesoscopic pattern of wave interaction could lend itself more easily than others to the design of fault tolerant systems (Olivier 2003).

Spectrometer Devices based on Modified Arrays of Waveguides

Another approach for the development of spectrometer devices is based on the idea of revisiting the traditional arrayed waveguide gratings (AWG), also known as 'phasar' (phased array) devices. The possibility to tune the velocity of the wave rather than its physical path opens the way to very different implementations of this idea. However, practical realizations of this approach have not been attempted thus far.

Spectrometer Devices based on Two-dimensional Photonic Crystal Dispersion and on the 'Superprism' Effect

Superprisms are based on the exploitation of the specific refractive properties of Bloch modes in photonic crystals, which have been discussed in Chapter 6. Actually, the first realizations of superprism devices (Kosaka 1998, 1999) were not based on an integrated-optical geometry. For more recent waveguide configurations, an angular deviation as large as 10° for a 20 nm spectral shift around 1300 nm has been achieved by the groups directed by TF Krauss at St Andrews (Wu 2002) and by T. Baba in Yokohama (Baba 2002). Intrinsically multimode

waveguides with a large width were used at the superprism input in order to provide an incident beam with weak divergence. Different configurations have been proposed by A. Lupu *et al.* One of these configurations allows the study of the superprism effect along different axes of the crystal (Lupu 2004), while another tolerates the use of waveguides with narrow input (Lupu 2006). Since then, it has become increasingly clear that a critical issue is that of the interfaces between the superprism and the rest of the system. In particular, it is necessary to minimize or eliminate the spurious reflections which arise elsewhere in the prism, especially in the case of a strongly multicoloured signal. Indeed, due to crosstalk, it becomes much more difficult in this case to control optical paths (Momeni 2006). Leaving aside this issue, it should be noted that the footprint remains large compared to other designs. However, this device deserves attention, if only for the reason that it exemplifies the potential of using Bloch modes rather than classical waves.

Successive Cutoff Waveguides

In these systems, light not transmitted at the transition between a first and a second, slightly narrower waveguide at cutoff is channelled onto some other optical path for this purpose (Niemi 2005). These devices are to some extent a variant of successive resonant systems (Shinya 2005; Viasnoff-Schwoob 2005).

Nonlinear 'Gating' Devices.

These devices are in general resonant devices, with either a microcavity or a band-edge resonance. All-optical modulation of a signal beam by a control beam is achieved by exploiting the resonant enhancement of one of the fields (Notomi 2005; Raineri 2005; Yacomotti 2006). A full in-plane nonlinear interaction has been reported in a work of the NTT group (Tanabe 2007).

10 Microsources

10.1 High-Efficiency Light-Emitting Diodes

10.1.1 Solutions for the Extraction of Light without Confinement

The efficiency or quantum yield of a light-emitting diode (LED) is the product of two factors η_1 and η_2. The first factor, also referred to as the internal quantum yield, quantifies the efficiency of the conversion of the injected electrons into internal photons. The second factor represents the efficiency of the extraction of photons from the semiconductor towards air. The internal quantum yield η_1 may easily reach typical values of the order of 90 percent, while in many instances η_2 is less than a few percents due to the strong refractive index of the semiconductor material itself ($n \approx 3$). This results from the phenomenon of total internal reflection, which occurs for all internal angles above the critical angle, i.e. for angles such that $\theta > \theta_c = \sin^{-1}(n)$, and from the fact that the cone of the half-angle θ_c represents therefore only a fraction $\eta_2 \approx 1/4n^2$ of the 4π steradians over which an isotropic emitter radiates. We may here consider an emitter placed in GaAs and with an isotropic spontaneous emission radiation pattern, in the form for instance of an electron-hole pair (Fig. 10.1*a*). In this case, and neglecting Fresnel reflections, only 2% of the spontaneous emission escapes the GaAs/air interface. This figure is doubled if the semiconductor is encapsulated in epoxy, as is common for light-emitting diodes ($n = 1.5$ for epoxy). For GaN-based light-emitting diodes, massively used for visible lighting, the refractive index of the emitting medium goes down to 2.5. A further factor of 2 can thus be gained, which brings the extraction efficiency η_2 to 8%. However, such a value remains in absolute terms fairly low.

Several different solutions have been devised for collecting a larger number of photons (Delbeke 2002). An example is the use of thick transparent layers sandwiching the entire active semiconductor. Such thick layers allow the extraction of the light emitted sideways that would otherwise be reabsorbed within a few tens of microns (Fig. 10.1*b*). This type of LED provides efficiencies in the 5-20 % range, and it is used in particular in the signalling market owing to both its simplicity and intermediate cost. Still higher efficiencies can be obtained by relying on purely

geometrical considerations for optimizing the geometrical shape of the chip in such a way as to allow most rays to escape the device after at most one total internal reflection. By using a truncated inverted pyramid structure, the company AGILENT has thus achieved an external quantum yield $\eta_1.\eta_2$ higher than 50 %. This configuration, shown in Fig. 10.1*c*, is now being employed in the GaP-based orange LEDs used for the signalling of battery-powered work (Krames 1999).

Another solution consists in removing the initial substrate of the LED and in reporting the active epilayers onto a metallic mirror. As delicate as this process might be, it is becoming increasingly well mastered. The light not directly extracted remains trapped between the metal and the semiconductor/air interface, and the trick consists in redirecting these photons into the extraction cone prior to any possible re-absorption. This can be achieved for instance through the wavelength-scale texturing of the upper interface, as represented in Fig. 10.1*d* (Windisch 1999). In order to preserve a high brightness, it is of interest to devise textures that will redirect the trapped photons from a few microns. A possibility is to use structures with a strong index contrast, which provide an efficient coupling with free-space continuum modes. The properties of these structures have already been described in Chapter 9 when discussing losses of integrated-optical systems, and they will now be considered with respect to the objective of maximizing losses. Note that losses can similarly be quantified through the imaginary part of the wave vector of leaky modes.

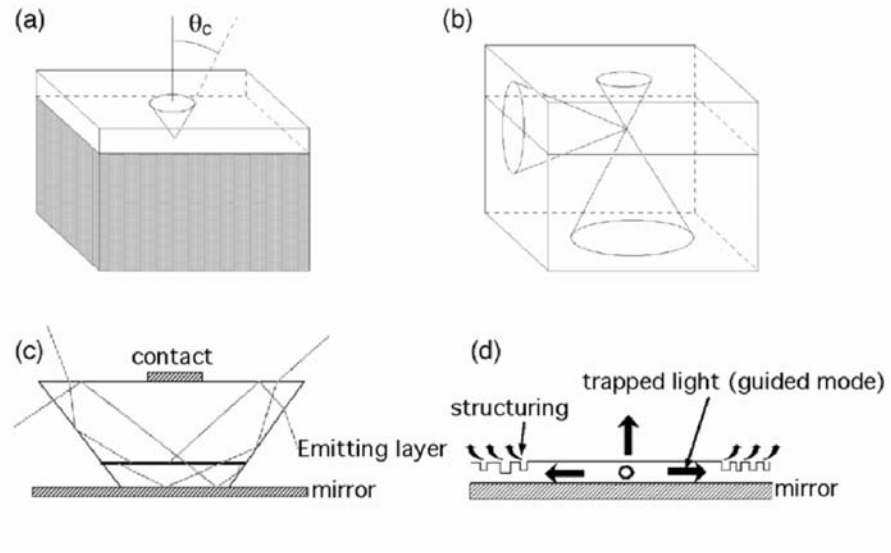

Fig. 10.1. *a.* Single extraction cone in a classical LED structure grown onto an absorbing substrate *b*. Extraction cones at the six faces of a parallelepiped *c.* Cross-section of the truncated inverted pyramid structure suggested by Agilent *d.* Substrate-less structure with extraction of the trapped light using a textured surface

The use of a metallic mirror allows a certain degree of freedom for the design of its shape. The mirror is deposited on the grown layers, and the chip is flipped over in order to extract light through the thinned substrate. An array of small (~10 μm, i.e. still in the regime of geometric optics) pyramids or microprisms capped by metal ensures the efficient redirection of light, as shown by recent realizations by the OSRAM Company (for more information on this subject, see http://www.gaasmantech.org/Digests/2005/2005papers/6.1.pdf).

10.1.2. Enhanced Extraction Efficiency through Planar Confinement

When an emitter is placed in a planar cavity, its emission is concentrated into annular rings or lobes, as it has been described in Section 7.1. This angular redistribution of the spontaneous emission can be exploited in order to increase the extraction efficiency η_2 (Fig. 10.2). The relative spectral emission width ($\Delta\omega/\omega$) of LEDs remains moderate at room temperature, and it typically assumes values between 2 and 20 %. In order to estimate the conditions required for the actual enhancement of the extraction efficiency when planar mirrors are placed before the source, the assumption will be made that the emission is monochromatic. As the consideration of Fig. 7.1 allows us to understand, a genuine enhancement of the extraction corresponds to the case of a single resonance of the Airy function in the extraction cone ($\theta < \theta_c$) (Fig. 10.2*a*).

The above condition amounts to imposing a minimum spacing between the Airy peaks, i.e. a sufficiently small cavity order $m_c = L/(\lambda/2n)$. This condition can be expressed in quantitative terms as follows:

$$m_c < 2n^2/NA^2 \tag{10.1}$$

where NA is the numerical aperture (see Fig. 10.2*a*). This formula can be generalized to any required aperture by replacing n with n/NA, where $NA = 0.2$ for typical silica fibres, $NA = 0.5$ for plastic optical fibres and $NA = 1.5$ for a semiconductor LED with encapsulating epoxy.

For an emitter that would be identically coupled to all cavity modes, the extraction efficiency simply reduces to:

$$\eta = 1/m_c \tag{10.2}$$

In the case of a monochromatic emitter at a specified wavelength $\lambda = \lambda_{em}$, designing a 'good' microcavity LED (MCLED) amounts to optimizing individually all the constitutive elements schematized in Fig. 10.2*b* (Benisty 1998a, 1998b):

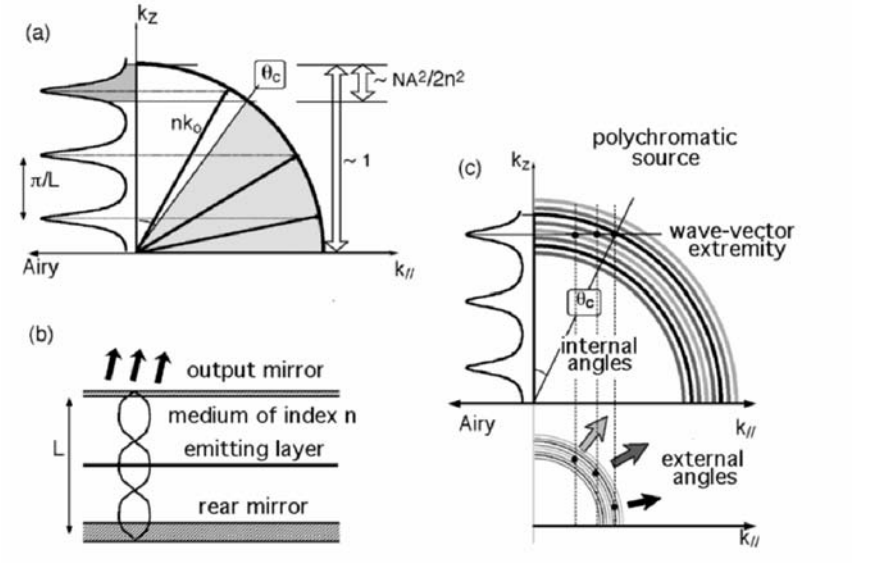

Fig. 10.2. *a.* The Airy function and the locus of the wavevector for a monochromatic source represented in a diagram with axes $k_{//}$ and k_z. Note the extraction cone *b.* Elements of a microcavity LED *c.* Spectral narrowing and angular dependence of the emission for a polychromatic source: same diagram as *a*, with the addition of a schematic representation of the wavevectors in air (*lower figure*). The vertical lines joining the two figures provide for the conservation of $k_{//}$ which underlies Snell-Descartes law of refraction

- the back mirror should be as reflective as possible, but this should not, however, result in any excessive increase of the cavity order m_c. A metallic mirror with a reflectivity $R = 0.9$ may thus be preferable to a Bragg mirror whose reflectivity reaches $R = 0.99$. Indeed, such a high reflectivity is achieved at the cost of a penetration depth of a few half-wavelengths, and of even higher values for substrates like InP. Further, in the latter case, it is difficult to grow Bragg mirror epilayers with strong index contrast without risking severe problems in terms of stress and dislocation,
- the tuning of the cavity should be realized in such a way as to position the Airy peak (at λ_{em}) in the extraction window as optimally as possible. The length L of the cavity must therefore be slightly larger than $m_c(\lambda/2n)$, which corresponds to the value for normal-incidence resonance familiar to Fabry-Perot practitioners. By proceeding in this manner, the emission angular lobe is made to correspond to directions of emission substantially inclined with respect to the normal direction, up to 30-45° in the case of an extraction in the air,
- the emitting layer(s) should be located at the antinode(s) of the cavity mode profile, as is the case for vertical cavity surface emitting lasers (VCSELs),
- the exit mirror, i.e. in the present case the upper mirror, should have a reflectivity suitable for the construction of an Airy resonance. The reflectivity does not

need to be as high as in the case of VCSELS, where the problem is not to shape the spontaneous emission, but to compensate for the minute gain of sub-μm thick active layers Since the gain is of a few percents, the reflectivity of the mirrors in VCSELS must be in the 99-100% range. By contrast, a first order approximation for the adequate reflectivity of the upper mirror in the MCLED yields $R \sim 1-m_c NA^2/n^2 \sim$ 40-80 % (Benisty 1998a, 1998b). Under these conditions, the cavity reaches an appropriate finesse, and the Airy peak represented in Fig. 10.2*a* tends to become narrow enough for validating the efficiency value predicted by Eq. 10.2. Since metals tend to present significant transmission losses, they are excluded in favour of one-dimensional photonic crystals (Bragg mirrors) and even, in certain specific cases, of a simple semiconductor/air interface ($R = 0.3$). The optimization of the exit mirror illustrates how the control of spontaneous emission leads to revisiting cavity concepts, more particularly in terms of size and finesse.

Having reviewed the physics underlying the case of a monochromatic emission, the influence of the spectral width of the emitter can be more easily assessed (the 'material's Q', as represented in Fig. 10.2*c*). The monochromatic approximation presented here remains valid as long as the relative spectral width $\Delta\omega/\omega \approx \Delta\lambda/\lambda$ does not exceed the ratio $\Delta k_z/k_z$ corresponding to the extraction cone (Fig. 10.2*a*). This ratio can also be equated to the quantity $NA^2/2n^2$ introduced above. For large spectral widths, the use of the planar cavity amounts to an angular redistribution of the emission according to its spectral components, but without resulting in any overall net gain. The spectral narrowing along a given direction may nonetheless present a specific interest. This is the case for the coupling of light with an optical fibre, since spectral filtering limits the excessive effects of spectral dispersion on the further transmission of the signal.

Quantitatively, the overall efficiency reaches $\eta = 23\%$ at $\lambda = 980$ nm for GaAs microcavities enclosed with a metallic mirror on one side and a Bragg mirror with reflectivity $R = 60$ % on the other (De Neve 1997a, 1997b). This value could be further enhanced to 29 % at $\lambda = 980$ nm by replacing the back mirror with a Bragg mirror with strong index contrast (AlOx/GaAs layers) and the upper mirror with the simple air/GaAs interface respectively (Rattier 2002). The theoretical limit is actually closer to 40 %, but lateral current injection through extremely thin layers (< 50 nm) would become quite difficult in this case. For red LEDs emitting at 650 nm and marketed for coupling with plastic optical fibres (by OSRAM-OS), the use of Bragg mirrors (one-dimensional photonic crystals) remains limited due to the weak index contrast $\Delta n \sim 0.25$ which can be obtained with their constitutive materials. For this reason, alternative metallic mirror technologies have been developed.

Microcavity effects and single-mirror enhancement effects are also to be considered for organic LEDs (OLEDs), an area where gains in efficiency can be achieved in spite of the low refractive index of the emitting material ($n \sim 1.7$).

10.1.3 Increase of the Extraction Efficiency using Two-Dimensional Photonic Crystals

General aspects

Two-dimensional photonic crystals are considered as suitable candidates for increasing the emission efficiency of LEDs beyond the limit values reached in planar cavities. Not only is the fabrication of Bragg mirrors with strong index contrast difficult, but planar microcavities do not remove the significant photon leakage which occurs through the guided modes propagating in the active layer plane. Indeed, the different layers of the microcavity tend to form a waveguide, and this horizontal emission, which may represent up to 50% of the total emission, is not detected. A two-dimensional photonic crystal placed at the periphery of the emitting area can be used as a reflector for exploiting this radiation. The reflector allows 'recycling' the guided photons by absorbing them and by giving them a new opportunity of being emitted in the mode of the planar microcavity (Benisty 1998a, 1998b). However, this phenomenon is of a practical interest only in the case where the internal quantum yield η_1 is very high, and the emission in leaky modes, i.e. in continuum modes that are neither guided nor resonant, is negligible (Rattier 2002).

A different approach relies on the use of the photonic crystal as a second order grating in order to diffract the guided light towards air in its first order (Boriditsky 1999, Delbeke 2002). This configuration is more deterministic than the random texturing of the surface of a thin film, represented in Fig. 10.1*d* (Windisch 1999). One of the problems which arise here is the relative sizes of the emitting and extracting areas. In order to avoid any undesirable increase in the apparent size of the source and the associated brightness penalty, different solutions have been experimentally investigated, where only the guiding regions at the periphery of the emitting area are structured with two-dimensional photonic crystals (Delbeke 2002, Rattier 2002). In this context, it is worth mentioning the intrinsic difficulty of calibrating photoluminescence measurements in configurations where the active medium is textured. This difficulty arises from the fact that such textures may significantly affect the actual efficiency of the pumping efficiency of the active medium. More detail on this subject can be found in the articles published in the special issue of the *IEEE J. Selected Topics in Quantum Electronics*, vol. 8, 2002.

More radically, an extraction of 100% has been predicted for membrane-based two-dimensional photonic crystals when the frequency of the emitter lies either in a complete band gap or in an allowed band of higher order (Fan 1997). In the first case, in-plane propagation is forbidden, while in the second case the emission is channelled into the photonic crystal modes that are efficiently coupled to free-space modes. The membrane configuration is akin to the so-called 'band edge lasers' that will be examined shortly hereafter in Section 10.3. Actually, an in-depth analysis reveals that as far as the extraction of luminescence is concerned, an identical 100 % performance can be obtained using other types of diffraction gratings (Rigneault 2000). At this stage, it is necessary to pay close attention to the fact that most of the 'guided modes' are actually above the light cone, as can be seen

for instance in Fig.9.4*c*. A series of questions thus arise. First, on which side does the leakage of these modes occur, i.e. on the upper or lower side of the device? Indeed, the behaviour of light will be different in each case since the two sides of the device do not present the same reflectivity/absorption and spectral/angular characteristics. Secondly, what are the competing extinction mechanisms (reabsorption, scattering by undesired inhomogeneities) when light is launched in these modes? Finally, is the leakage strong enough to allow the capture of light before it reaches the edge of the chip, where controlling its behaviour becomes more difficult?

Another critical point for structures with a perforated emitting area, and more particularly for perforated membranes, is the possibility that important non-radiative recombination phenomena may occur at the close and numerous etched interfaces. A number of issues arise when implementing electrical pumping in membranes or in thin layers on insulators. Similar problems arise for the 'band-edge' lasers and microlasers described in Sections 10.3 and 10.4 respectively. In the mid-term perspective, compromising the electrical and thermal performances of such mass-produced devices as light-emitting diodes is out of the question. This implies that the control of spontaneous emission should comply with existing technological constraints.

This condition leads to favouring techniques initially restricted to the extraction of the guided modes, and eventually allowing the inclusion of a transfer scheme by means of a mirror. The use of the omnidirectional extraction properties of Archimedean lattices, described in Chap. 3, is one of the directions which are currently being investigated (Rattier 2003).

GaN-based LEDs

Lighting applications are a powerful motivation for the development of GaN-based LEDs with high extraction efficiency. These applications range from general lighting applications, an area where the cost and efficiency of GaN-based LEDS are now believed to compete efficiently with fluorescent 'tube' sources, to cell phone and display backlighting (the largest market for white LEDs in the mid-2000s), as well as to car and shop lighting. Luminus Devices, a MIT-originated company, has even proposed to incorporate photonic crystals in the LEDs used for the backlighting of expensive LCD TV screens, where LEDs generally provide improved colour (gamut) rendering. In this context, several studies have specifically addressed photonic crystal extraction in GaN-based LEDs with the aim of achieving a more in-depth understanding of extraction mechanisms.

Let us briefly recall that light extraction in GaN blue-green-white LEDs is intrinsically higher than in GaAs-based devices, due to the lower refractive index ($n = 2.5$) of the former. However, in order to compensate for the mismatch between the epitaxial layers and the substrate, a thick GaN layer (~ 3 μm), inside which the emitting InGaN quantum wells are located, is generally used. This 3 μm-thick layer forms a waveguide allowing propagation of about 20 guided modes at the blue 450 nm wavelength (the substrate index is $n = 1.7$ for sapphire). Since the thickness of the photonic crystal cannot be much larger than the wavelength if the fabrication process is to remain accurate, most of the guided modes

only 'skim' below the surface without being actually extracted. Thus, only 40 % of the modes were seen in a typical experiment (David 2005), and the mean free path of light was well in excess of 100 μm. In order to alleviate this poor extraction of guided modes, the use of a 'cap layer mode' has been proposed in (David 2006a). In this scheme, the quantum wells are grown inside a GaN cap layer separated from the thick GaN layer by an $Al_xGa_{1-x}N$ cladding barrier with index $n \sim 2.4$. The cap layer is designed in such a way as to create a single-mode waveguide, whose mode can thus interact well with the surface grating, i.e. with the photonic crystal. The light emitted is therefore prevented from populating the 'unextractable' modes of the thick layer. Of course, for GaN as for other systems, the use of a metallic mirror at the rear side of the device will provide, once etching and injection difficulties are solved, a good solution for further enhancing the extraction efficiency (David 2006b). The possibility of an omnidirectional extraction through the use of Archimedean lattices has also been considered for GaN-based LED systems (David 2006c).

Zinc oxide (ZnO), which basically emits around 370 nm, is another material that will probably receive wide consideration in the future. This material lends itself quite well to the design of photonic structures, but is more difficult in terms of electrical injection, quantum well introduction, etc. The market for this material is expected to lie mostly at the UV end of the LED spectra, for instance the water purification mass market. Efforts directed at tuning its emission in the visible range are also being undertaken, in order to reduce the gap in material efficiency which still exists for wavelengths around the peak eye sensitivity (yellow and amber).

10.2 Ridge-Type Waveguide Lasers confined by Photonics Crystals

The most classical geometry for semiconductor lasers is that of the waveguide edge-emitting laser, which presents a typical output mirror reflectivity of ~30 percent for a cleaved facet in the absence of optical processing. As has been previously discussed in Chap. 9 in the context of integrated optics, both the ridge waveguide and the end mirrors can be based on photonic crystals. For ridge waveguides, a practical interest of air-hole photonic crystals is that electrical continuity can be more easily achieved with these crystals than with deep-ridge waveguides. As far as end mirrors are concerned, the use of a one-dimensional or two-dimensional photonic crystal defined through the etching of a waveguide may ensure a high reflection coefficient for guided modes ($R > 0.97$). The reduction of optical losses at these mirrors leads to very short cavity lasers. As an example, we mention here the fabrication of an ultra-short cavity GaAs/GaAlAs laser (12 μm) using one-dimensional air/GaAs deep etched mirrors created with the ECR-RIE etching method (Rennon 2001) (Fig. 10.3*a*). In principle, these short cavity lasers have a very small active volume and a threshold current far beyond the submilli-

ampere threshold. However, the possibility of achieving such threshold currents will depend on the resolution of other technological problems.

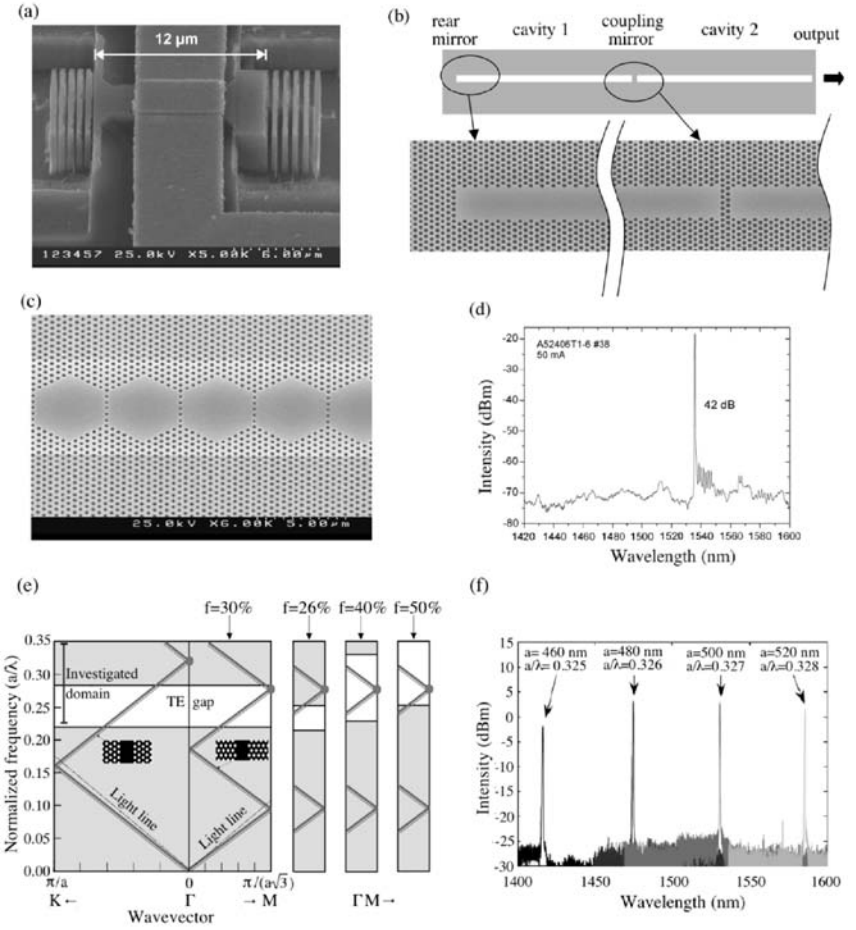

Fig. 10.3. *a.* Short waveguide laser based on one-dimensional photonic crystal mirrors (Rennon 2001) *b*. Ridge photonic crystal laser with two coupled cavities: principle and side view (SEM micrographs) (Happ 2001) *c*. Laser consisting of a set of hexagonal cavities coupled together *d*. Corresponding single-mode emission spectrum with a high rejection of secondary modes (Happ 2003) *e*. *Left.* Schematic representation of the band diagram of the triangular lattice, and folding of the fundamental mode of the waveguide in the ΓK and ΓM directions (substrate approach; air-filling factor $f = 30\%$). *Insets.* W_3 and W_{2-3} waveguides. *Right.* Evolution of the band diagram near the M-point when the value for f increases from 26 to 55% *f*. Measured emission spectra of a W1 waveguide laser in a square symmetry for four different diameters of the photonic crystal holes, i.e. for four different air-filling factors (Checoury 2005a).

A further reason for interest in photonic crystal mirrors and waveguides is that they offer a possibility of revisiting earlier single-mode laser configurations, like the so-called C^3 laser, or *Cleaved Coupled Cavity* laser (Agrawal 1993, Tsang 1983). The development of these lasers was abandoned in the 1970s and 1980s due to technical difficulties. The compound cavities of these lasers were indeed created from the mechanical assembling of two separated cavities through the mere juxtaposition of two chips. As may easily be imagined, the phase of the coupling was quite imprecise. By contrast, a well-designed photonic crystal mirror should offer a well-defined phase for the coupling, as has been demonstrated by T. Happ *et al* (Happ 2001). Fig. 10.3*b* presents an example of a laser constituted of two coupled linear cavities, both of which were entirely carved inside a two-dimensional photonic crystal. An elaborate two-channel tunable source with a wavelength tuning range of 30 nm around $\lambda \sim 1530$ nm has thus been designed based on the integration of two such lasers on the same chip (Manhkopf 2004). The outputs of the lasers were coupled into a single waveguide using a photonic crystal Y-coupler.

A rather extreme case of a coupling-based system is that of a laser using a waveguide formed by coupled hexagonal cavities, such as the CROW (Coupled Resonator Optical Waveguide) proposed by A. Yariv *et al* (Yariv 1999). Such a device, represented here in Figs. 10.3*c* and 10.3*d*, has been fabricated at the University of Würzburg, and a single-mode emission has been achieved (Happ 2003).

Let us now return to more 'canonical' photonic crystal waveguides, by noting that the periodic corrugation of the edges of the waveguides can be used for optical feedback. The main difference in this respect with classical DFB (Distributed Feedback) lasers (Agrawal 1993; Casey 1978) is that the periodic modulation of the refractive index is strong and two-dimensional, which may possibly result in a two-dimensional photonic gap preventing lateral losses. Fig. 10.3*e* shows a schematic representation of the band diagram of the triangular lattice in the InP substrate approach, along with the folding of the fundamental mode of the waveguide in the ΓK and ΓM directions. As in the usual case of DFB, mode folding, and hence DFB lasing, occur for $\Lambda/\lambda = (1,2,3,\ldots)/2n_{\mathrm{eff}}$, where Λ is the period of the corrugations along the waveguide and n_{eff} is the effective index of the core of the waveguide.

In the ΓK orientation of the waveguide (Fig. 10.3*e*, *left*) and for a standard air-filling factor (~ 30 %), the fundamental mode does not fold in the gap whatever the width of the waveguide is. Accordingly, DFB laser action on this mode can only take place outside the band gap. In practice, the period a of the lattice is usually chosen to be larger than ~ 350 nm in order to ensure accurate fabrication of the photonic crystal with the deep etch technique. For a laser emission around $\lambda = 1550$ nm, this corresponds to normalized frequencies a/λ above ~ 0.225. Only the region extending around the second folding of the fundamental mode (Γ-point) can be reached in experiments conducted under these conditions. Lasing in this region has thus been observed for the W3 laser (3 rows of missing holes), and was found experimentally to be single-mode with a side-mode suppression ratio larger than 40 dB (Checoury 2004). The selection mechanism based on band-edge dependent losses is actually similar to that reported earlier by Henry and Kazarinov

for a second-order DFB laser (Kazarinov 1985). The same behaviour has also been reported for the narrow W1 waveguide square-lattice laser. The emission wavelength of the laser was tuned over ~170 nm by varying the lattice period from 460 to 520 nm (Checoury 2005a), as described in Fig. 10.3*f*. By contrast, no such lasing has been obtained thus far from the W1 waveguide triangular-lattice laser. For these structures, laser emission has been achieved only in the membrane approach. In this case, the lasing mode was a relatively high-order mode located in the 'lossless' region within the gap and below the light line (Sugitatsu 2003).

For waveguides oriented in the ΓM direction of the triangular lattice, i.e. for so-called $W_{i-(i+1)}$ waveguides, whose width is determined by alternating i and $(i+1)$ missing holes, the period of the corrugations is $\sqrt{3}$ times larger than it is the case for the ΓK direction. As can be seen in the right-hand side of Fig. 10.3*e*, only the third fold of the fundamental mode can be found to be within the relevant range of normalized frequencies. Accordingly, the behaviour of the laser can be expected to be similar to that of third-order DFB lasers. However, for large air-filling factors and wide gaps, emission can take place deep in the TE band gap, with the consequence that the characteristics of the laser will be strongly modified. It has thus been shown that an increase of the air-filling factor from ~ 28 to 55% simultaneously allows the reduction of the laser threshold by a factor of three and the increase of the laser efficiency by a factor greater than ten (Checoury 2005b, 2006). This emphasizes the interest of operating waveguide lasers in a photonic gap, and even, in the substrate approach, in a two-dimensional gap. Not only does the fact of operating deep in a two-dimensional gap eliminate in-plane losses, but it also reinforces the confinement of the modes in the dielectric core of the waveguide, thereby reducing the out-of-plane losses occurring at the photonic crystal holes around the core.

The superiority of photonic crystal waveguide lasers over classical ridge lasers remains to be fully demonstrated, in view in particular of the fact that the efficiency of the electrical pumping is limited by the carrier recombination occurring at the photonic crystal holes. Nevertheless, the use of photonic crystals opens unprecedented perspectives for the association of lasers with miniature guided-optical devices (filters, bends, optical 'plates', etc. See Chap. 9) as well as for the monolithic integration of distinct lasers over a single chip in a single technological stage. In addition to the high added value of large-scale integrated systems, these perspectives bring about a certain amount of physical simplification, which results from the fact that photonic crystals ensure the operation of the resulting device in a single (TE) polarization mode. For lasers, this opens the possibility of abstracting, in first and even in second approximation, from the behaviour of the optical chain in the other polarization.

10.3 Bulk Photonic Crystal Band Edge Lasers

In the preceding examples of semiconductor microsources, the photonic crystal was located at the periphery of the active region, thereby acting either as a reflector or as a diffraction coupler. In the following sections, we shall consider examples of semiconductor microsources where the photonic crystal, or alternatively a defect of limited dimensions in the crystal, is located within the core of the emitting region.

It is now a well-established fact that the dispersion curve of materials can be dramatically altered through their periodic structuring. More specifically, group velocities close to zero can be obtained near the edges of the photonic band gap as well as at the Γ symmetry point of the Brillouin zone (see Section 6.1.2). Propagation modes presenting an almost flat dispersion curve over almost the entire Brillouin zone may also exist. It should be borne in mind, however, that the latter modes result from a degeneracy effect (see Section 1.3.3). As a rule, lower group velocities correspond to longer time constants in the interaction between an optical medium and the propagating light. Accordingly, all processes involved in this interaction can be dramatically reinforced if certain conditions are met. This applies to the case of the nonlinear frequency conversion process (Sakoda 1996), as well as to the case of stimulated emission (Dowling 1994; Sakoda 1999a). It has been demonstrated that for an inverted medium, the stimulated gain is in inverse proportion to the group velocity and that lasing can be produced in a photonic crystal without requiring the use of cavity mirrors.

The enhancement of the stimulated emission in photonic crystals was first predicted through the modelling of the propagation of wave packets in the time domain (Dowling 1994). The description has been supplemented by other methods, developed for instance in (Quang 1997), which have addressed, in particular, the fluorescence of a photonic crystal near the edge of the band gap. A detailed formulation of the stimulated gain in two and three-dimensional crystals has been suggested by K. Sakoda *et al* (Sakoda 1999a, 1999b, 2001). As a first approximation, the lasing mechanism appears to be the same as for the DFB lasers currently in use in optical telecommunication systems. To some extent, lasers based on 'bulk' photonic crystals can be viewed as the two- and three-dimensional extensions of DFB lasers. In all cases, and provided that no defect has been created inside the periodic structure, lasing occurs at the edges of the band gap, i.e. in frequency domains where the distributed feedback of the propagating waves is marked, but where the propagation of the waves themselves is not forbidden. A DFB laser thus tends to simultaneously lase at two distinct frequencies at the two opposite edges of the band gap. In order to operate in single mode, a defect must be created inside the periodic structure, thereby creating a phase jump in the distributed Bragg grating. An example of such a method can be found in (Utaka 1986). In spite of these similarities, a significant difference remains between DFB lasers and 'bulk' photonic crystal lasers. Indeed, the one-dimensional grating of conventional DFB lasers is seldom etched to the point where the active layer is reached. As a consequence, the periodic modulation along the laser is essentially a

modulation of the refractive index. By contrast, in the case of photonic crystal band-edge lasers, the active layer is structured. Although the index modulation remains predominant due to the high index contrast between the air holes and the semiconductor, the modulation of the laser gain is no longer negligible. Thus, a comparison can be drawn to some extent between band-edge photonic crystal lasers and the so-called gain coupled DFB lasers (Kogelnik 1972)

Laser emission in band-edge microsources based on the use of two-dimensional bulk, i.e. defectless photonic crystals has been experimentally demonstrated by several groups (Inoue 1999; Kopp 1998; Monat 2002; Notomi 2001b; Ryu 2002a). An underlying objective is to realize microlasers with large emitting areas without resorting to the use of cavity mirrors. In such a case, there would be obviously no need neither for aligning nor for tuning the cavities, and to some extent the realization of such a laser would come down to cutting up a given two-dimensional photonic crystal at the desired size. Indeed, laser light can be extracted in this case from the whole surface of the crystal, provided however that diffraction effects occur in photonic bands of a sufficiently high order. It could be argued that such an extraction technique is identical to that used in more conventional high-power semiconductor lasers, which are equipped with a one-dimensional diffraction grating of second order. Actually, while a second-order grating behaviour may indeed be found in certain two-dimensional photonic crystal band-edge lasers, new situations may also occur where, for instance, several directions in the photonic crystal are involved in the distributed feedback effect, as can be seen in Fig. 10.4 (Notomi 2001b). Interestingly enough, it can be noted that the first 'bulk' photonic crystal lasers were made of polymer layers pre-structured in the form of a two-dimensional grating. To some extent, this reproduces in two dimensions the first experiments on DFB lasers conducted more than thirty years ago, where doped gelatin layers were used (Kogelnik 1971).

Experiments based on semiconductor photonic crystal membranes have led to very good performances. A lasing effect was thus obtained, for InGaAsP membranes, over a ~ 50 μm^2 emitting area, with optical pump powers as low as 35 μW (Ryu 2002a). The operating temperature was equal to 80 K. In another experiment, a similar lasing threshold was obtained at room temperature from an InAsP quantum well ($\lambda = 1.5$ μm) membrane pumped over a ~ 9 μm^2 emitting area (Mouette 2003). The photonic crystal consisted of a graphite lattice designed in such a way as to ensure a low curvature band in the emission wavelength range of the quantum wells. The photonic crystal membrane was transferred onto silicon using the SiO_2-SiO_2 bonding technique.

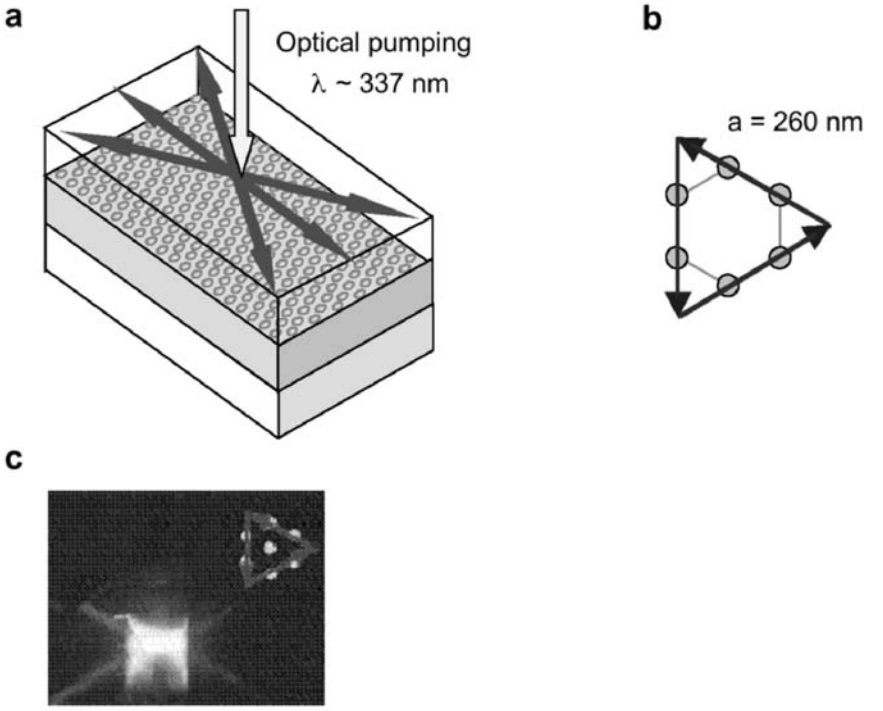

Fig. 10.4. *a.* Schematics of an optically pumped bulk photonic crystal band-edge laser with examples of optical feedback directions *b.* Optical feedback involving simultaneously three directions of a triangular photonic crystal *c.* Photograph showing the trajectories of the rays inside the organic photonic crystal laser used as a reference (Notomi 2001b). The operating conditions are as represented in *b*. The photograph is taken from the upper surface of the laser (scattered light) using a CCD camera

10.4 Photonic crystal VCSELs

Vertical cavity surface emitting lasers (VCSEL) are a familiar geometry for surface-emitting semiconductor lasers. In these lasers, one or more emitting layers is or are located in a small cavity vertically bounded by two semiconductor Bragg reflectors. The Bragg reflectors used in this configuration can be advantageously replaced by photonic crystal membranes, since the latter are much more compact while simultaneously exhibiting a similar reflectivity (Seassal 2005). A very high reflectivity (> 99.8 %) has thus been achieved by optimizing the resonant coupling of an incoming electromagnetic wave to slow Bloch modes at the Γ point in a photonic crystal membrane (Boutami 2006). A schematic representation of a VCSEL with a photonic-crystal reflector is shown in Fig. 10.5*a*. The distributed

Bragg reflector (DBR) generally used at the bottom of VCSELs, whose typical thickness lies in the 5-10 μm range for the InP system, is replaced in this case by a thin photonic crystal membrane ($\sim\lambda/2n_{eff} \sim 0.26$ μm) separated from the active region by a ($\lambda/2$) air cavity. The hybrid VCSEL schematized in Fig. 10.5*a* was successfully operated near $\lambda = 1.5$ μm under optical pumping (Boutami 2007). Electrical pumping of a similar photonic-crystal VCSEL in the AlGaAs system ($\lambda = 0.85$ μm) has also been reported (Huang 2007).

For VCSELs as well as for the photonic crystal LEDs presented in Section 10.1.3, another reason of interest of photonic crystals is the fact that they can be used for the lateral confinement of the emitted mode. In this case, two situations may occur depending on whether the photonic crystal is operated in the band gap or not.

If the lateral photonic crystal is used in the band gap, the mode(s) of the VCSEL is or are confined both in-plane and vertically. The properties of the modes will obviously depend on the respective strength of the confinement in the two different directions. For a large emitting area, lasing tends to start in the horizontally guided modes. As a result, most of the advantages associated with VCSELs tend to be lost. By contrast, small emitting areas should result in a greater potential for applications. However, the practical fabrication of these structures is still limited by the requirement of a high-aspect-ratio dry etch of sub-μm patterns through a multilayer stack with typically a 5 μm thickness.

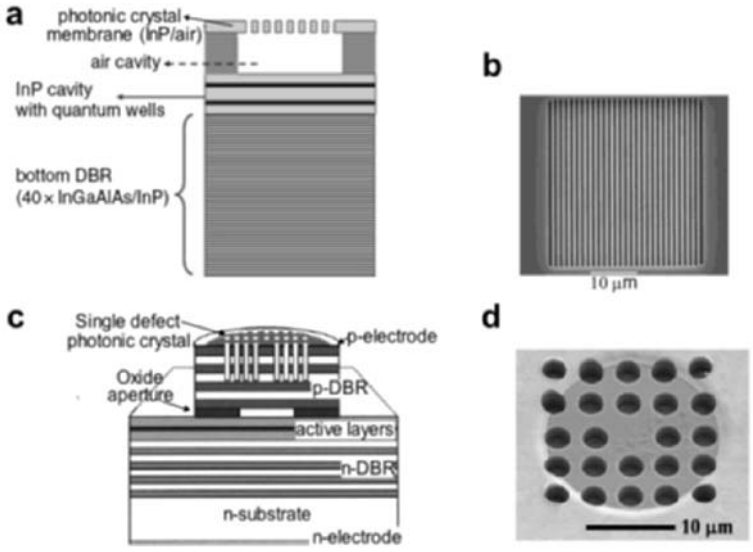

Fig. 10.5. *a.* Schematics of a VCSEL with a photonic crystal reflector in the InP system *b.* Scanning electron microscope (SEM) top view of the photonic crystal reflector developed in (Boutami 2007) *c.* Schematics of a VCSEL with lateral index modulation provided by a photonic crystal *d.* SEM top view of the square lattice photonic crystal used in (Lee 2004)

From a more practical point of view, two-dimensional photonic crystals can be used for the purpose of laterally modulating the refractive index of VCSELs rather than for creating a two-dimensional photonic band gap. In this case, the photonic-crystal VCSEL 'mimics' a slice of microstructured fibre, with all the benefits associated with transverse mode control (Fig. 10.5*c*). For a sufficiently large emitting area, the modal properties of the device can be understood through the decoupling of the vertical and lateral confinements. Guided photons are vertically confined by distributed Bragg reflection, while the transverse mode profile is determined by the lateral modulation of the refractive index. In much the same way as microstructured fibres can be single-mode even if their core has a much larger diameter than the wavelength, photonic crystal VCSELs with large emitting area can be designed in such a way as to support the propagation of only the fundamental mode. The typical periodicity of the structure can be of several microns, as is the case for microstructured fibres, while the patterns are not necessarily to be etched throughout the entire thickness of the VCSEL mirrors (Danner 2004; Song 2002). Such VCSELs are of interest for achieving single-mode operation at high injection currents. The control of spontaneous emission and light polarization can also be enhanced compared to ordinary VCSELs. Single-mode powers in the 1-10 mW range have thus been obtained from photonic crystal VCSELs (Lee 2004) and from VCSELs with holey structures in the GaAs/AlGaAs system (Furukawa 2004).

10.5 Microcavity Lasers

As has been seen in Section 7.1.3, the increase of the coupling factor of the spontaneous emission β to a given cavity mode and the simultaneous reduction of the active layer volume may potentially provide microcavity lasers with very original and interesting properties. While the best performances to date in terms of threshold current have been reported for VCSELs with small emitting areas and for microdisk lasers, rapid advances in the performances of two-dimensional photonic crystal microlasers have been observed since 2000. Electrical pumping is a delicate issue in the design of these devices. Thus far, it has been reported only in a few experiments that required challenging technological problems to be solved (Park 2004; Seo 2007).

After briefly reviewing the best results obtained for these different microlasers, we then proceed to identify their respective limitations using the didactic model set out in Section 7.1.3.

The most recent technological advance in the development and optimization of VCSELs has been the introduction of an oxide ring just above the active layer containing the quantum wells or dots for the purpose both of localizing the carrier injection and of laterally confining the optical mode (Fig. 10.6*a*).

A record threshold current of 36 μA, the lowest ever achieved for all semiconductor lasers, has thus been reported in the continuous wave (cw) regime for the (In)GaAs/GaAlAs system at 300K (Bond 1998; Huffaker 1997). To date, this sys-

tem remains by far the most advanced as regards both its material quality and the very structure of the device. The active layer generally consists of a single or several quantum wells emitting at around $\lambda = 0.98$ μm. The reduction in the actual lateral size of this device, which generally is accompanied by a significant increase of the β factor, is limited here by the diffraction of the oxide ring. Indeed, an optimal diameter exists for the latter, beyond which strong diffraction effects may take place. This optimal diameter can be typically achieved for a lateral size equal to 2 μm by placing the oxide layer at a field node of the laser mode so as to minimize the amount of optical losses. The value for β is about 0.04 in the best case (Kuksenkov 1997).

Advances in the fabrication of microdisk lasers, and the reduction of their lateral dimensions, have been instrumental in achieving a better carrier injection in these lasers and a significant improvement of their threshold current in the cw regime (Fig. 10.6*b*). The lowest threshold currents reported to date are around 40 μA (Fujita 2000). Microdisk lasers are fabricated in the InGaAsP/InP system, which exhibits moderate non-radiative carrier recombinations at the air/semiconductor interfaces. The best threshold performance was obtained for a disk with a diameter of 2.7 μm and a β factor equal to 0.1 (Fujita 2001).

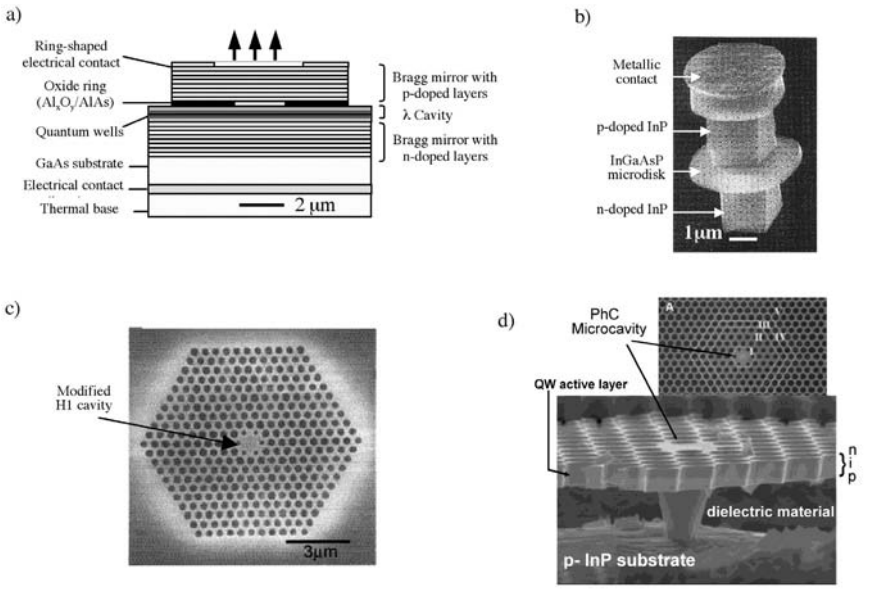

Fig. 10.6. *a.* Schematic view of a VCSEL with small emitting area fabricated from a GaAs substrate *b.* Micrograph of a microdisk laser (Fujita 2000) *c.* Micrograph of a photonic crystal microcavity laser (Park 2001) *d.* Cross-sectional SEM image of the electrically driven single-cell photonic crystal laser demonstrated in (Park 2004) *Inset.* Top view of the structure, showing the size of the chirped patterns. The regions from I to V correspond to photonic crystal holes with increasing diameter

Minimizing non-radiative carrier recombination at the air/semiconductor interfaces is a crucial issue for photonic crystal microcavity lasers. The approach generally used for circumventing this difficulty consists in using either the InGaAsP/InP system (Painter 1999b) or an active medium with quantum dots (Yoshie 2002). In the latter case, the carrier diffusion at the interfaces can be dramatically reduced (Gérard 1996a). Several groups have reported an optically pumped laser emission for InGaAsP quantum wells in microcavities with a very small effective volume ($V < (\lambda / n)^3$) (Loncar 2002b; Painter 1999b; Park 2001; Ryu 2002b). All these microcavities were realized from suspended membranes (Fig. 10.6*c*). In the first experiments performed using a microcavity with a small Q-factor ($Q = 250$), the emission of the laser was maintained up to the temperature of 143 K for a threshold pump power of 7 mW, a value that would correspond to a very high current density of several $kA.cm^{-2}$ in the case of an electrically pumped laser. At such a current density, it is well known that the non-radiative Auger recombinations become prohibitive in the InGaAsP system. Fortunately, better quality factors that were made possible by an optimized geometry of the defect in the microcavity have led to the demonstration of lasing at 300K under pulsed excitation, and to a significant reduction of the threshold pump power down to 220 μW for a microcavity with a Q factor equal to ~ 2000 (Loncar 2002b; Park 2001). Low threshold lasing at 300K has also been reported for a small band edge laser using a graphite lattice of holes in an InP membrane transferred onto Si (Mouette 2003) (see Section 10.3). In this case, improved performance was due to the significant reduction of the heating effects in the reported membrane. In terms of threshold pump power, very impressive results have been obtained from a L3 defect photonic crystal microcavity laser fabricated in a GaAs membrane containing five layers of self-assembled InAs quantum dots as the active gain material (Nomura 2006). Continuous-wave (cw) lasing at 300K was observed for the first time in this approach, with a pump power absorbed at threshold in the active layers as low as 4 μW. Such a radical improvement can be explained for the most part by the very high Q (~19,000) of the small L3 microcavity (see Section 9.8.3 for more detail), which allows laser action with a small number of active quantum dots coupled to the lasing mode (~ 250).

However, the membrane approach is penalized by the difficulty of implementing an electrical excitation, and by the strong reinforcement of the heating effects. For this reason, the possibility of cw laser action in electrically pumped photonic crystal microcavity lasers at room temperature still remains to be demonstrated. Thus far, electrical pumping of photonic crystal microcavity lasers has been achieved only under pulsed conditions. Fig. 10.6*d* presents one of the most striking realizations, that of an electrically pumped single-cell photonic crystal laser fabricated in the InP/InGaAsP system (Park 2004; Seo 2007). This laser operates either on a monopole mode or on a hexapole mode of a modified H1 cavity, with the field node being located at the centre of the cavity in such a way that the central post used for current injection induces only a weak perturbation. However, even if a relatively high cavity Q (~ 3400) and a low averaged threshold current (~ 100 μA) can be achieved, poor heat sinking still prevents the continuous wave operation of the laser. In this respect, the use of quantum dots instead of quantum

wells as the active laser medium appears here again as the most promising route toward reduction of the laser threshold and toward continuous wave operation under electrical pumping.

While it is quite apparent that microcavity lasers have dramatically progressed in the last recent years, their current performances are still far from the ultimate performances expected for 'thresholdless' lasers (where $I_{th} \sim 0.1$ μA for $Q \sim 2000$ as discussed in Section 7.1.3). For each type of microlasers, their physical limitations can be identified by estimating the ξ and β parameters involved in the rate equation model in Section 7.1.3. Recall that ξ denotes the average number of spontaneous photons in the lasing mode at transparency.

In the case of InGaAsP quantum well structures, realized either from microdisks (Fujita 2001) or from photonic crystal microcavities (Park 2001; Seo 2007), the value for ξ lies between a few tens and a few hundreds. The laser threshold can be relatively well estimated by assuming that non-radiative recombinations can be neglected. In principle, a lower threshold could be achieved by decreasing the value for ξ through a diminution of the 'number of emitters', i.e. by reducing either the number of quantum wells or their active areas, or alternately by using a quantum dot active medium as will be discussed later.

From this point of view, the GaAs VCSEL presented in (Huffaker 1997) has already a high level of optimization, since the active medium consists of a single InGaAs quantum well. From the relatively low value found for β (~ 0.04) measured for very similar structures (Kuksenkov 1997), it can be deduced that $\xi \sim 2$ (with $N_T/S \sim 4\ 10^{12}$ cm^{-2}, $S \sim 5$ μm^2, $\varphi \sim 10^{12}$ s^{-1}, $\tau \sim 10^{-9}$ s), and, from Eq. 7.13, the threshold current I_{th} can be predicted to be about 2 μA. The performances of the laser are actually limited in the first place by the heating effects induced on active layers by the electrical injection in this special configuration. This simultaneously results in a broadening of the gain curve, in an increased carrier loss through non-radiative recombinations and in additional electrical leakages. Any eventual improvement of the device can therefore be expected to result essentially from the optimization of the electrical injection (Huffaker 1997).

We shall finally consider the case of the quantum dot photonic crystal microcavity laser described in (Nomura 2006), which operates under continuous wave pumping at 300K. The L3 laser microcavity has a 0.8 μm^2 emitting surface, and contains five layers of InAs quantum dots with a total density of 10^{11} cm^{-2} per surface unit. We may consider that only a limited fraction *f* of the quantum dots are coupled to the lasing mode, and that this fraction is close to the ratio of the homogeneous linewidth for a single quantum dot (~10 -20 meV) to the inhomogeneous linewidth for the ensemble of quantum dots (35 meV). Using experimentally measured values for β (0.22) and Q (19,000), the average number of photons in the mode can be estimated to be equal to $\xi \approx 2$ at the transparency threshold. It is quite clear that the size of the active medium is already well optimized, and that the Purcell effect plays an essential role in the laser operation through the large value of β. In the absence of non-radiative carrier recombinations, the laser threshold calculated from Eq. 7.13 would be equal to ~ 0.071 μW, assuming an optical pumping with a 100 percent efficiency. In practice, several effects may actually contribute to increasing the laser threshold:

- the pump beam is only partially absorbed (15 %) in the photonic membrane,
- the optically pumped area is much larger (12 μm^2) than the emitting surface of the photonic crystal cavity (0.8 μm^2),
- some quantum dots in the cavity are pumped while not being coupled to the lasing mode. This effect actually increases the laser threshold by a factor of two.

The laser threshold can thus be estimated, by taking into account all these effects, to be of the order of 15 μW, not far from the experimentally found value of 25 μW. The residual difference is most likely to be explained by non-radiative recombinations, which result from the fact that quantum dots do not completely inhibit carrier diffusion at 300K (Nomura 2006). This being said, the main limiting factor in these experiments appears to be the large width of the pump beam, and its poor matching to the cavity mode.

In spite of their relatively low β factor, VCSELs thus appear to offer the best compromise among microlasers, in terms of threshold performances, ease of fabrication and practical use (due to their directive emission). Simultaneously achieving good optical, thermal and electrical properties remains a major issue for photonic crystal lasers. Two main directions can be followed in order to obtain a continuous wave photonic crystal laser diode operating at 300K: the use of quantum dots as the active material, and the optimization of photonic crystal microcavities in the substrate approach. Indeed, not only does the use of a small ensemble of quantum dots permit to obtain low laser thresholds in high-Q cavities, but it also alleviates to a large extent the thermal management problem in the membrane approach. This was illustrated by the successful operation of optically pumped structures at room temperature. On the other hand, the substrate approach is recognized as offering good heat sinking and high power operation, even if it is at the cost of an increase in the effective volume of the cavity mode and of a lower Q factor. In view of the impressive advances in the field of photonic crystal cavities and lasers over the last ten years, it can be reasonably expected that major developments will occur for photonic crystal microlasers in the mid-term perspective.

10.6 Potential Interest of Single-Photon Sources

A single-photon source is an optoelectronic device capable of generating on demand a light pulse containing but a single photon. The development of single-photon sources, and more generally the generation of non-classical states of light by solid state devices are key issues for the practical implementation of the concepts of quantum information science (Bouwmeester 2000).

In the midterm, the most promising field of application for single-photon sources is likely to be quantum cryptography. Single-photon sources are indeed expected to permit the implementation of the intrinsically secure transmission protocols proposed in the early eighties which rely on the polarization state of single photons for the encoding of information (Bennett 1992). The fundamental princi-

ples of quantum mechanics ensure that a complete knowledge of the polarization state of a photon cannot be obtained from measurements save from a polarization basis known beforehand. By contrast, in conventional optical communications, each light pulse contains a plurality of photons. This would potentially allow an eavesdropper to proceed to several measurements and to retrieve precise information concerning the common polarization state of these photons.

These quantum cryptography protocols have already been validated for conventional telecommunication systems based on optical fibres using strongly attenuated laser sources delivering on average less than 0.1 photon per pulse. It is quite obvious that a coherent source is but a very rough approximation of the properties of a real single photon source, since the probability for a given light pulse not to contain any photon is predominant. Additionally, a non-zero probability exists that it might contain two photons or more. Two main problems thus arise (Brassard 2000):

1. multi-photon pulses can be exploited by a potential eavesdropper for extracting information. In order to limit the amount of information that could be accessed by such an eavesdropper, it is therefore necessary to operate in a regime of strong attenuation
2. in practice, the distance range for secure communication is limited by the losses occurring in the channel, and by the dark counts ('false positives') of the detectors. Indeed, errors induced on quantum keys by dark counts can be corrected only insofar as the bit error rate remains typically smaller than 10%. Obviously, this problem becomes all the more acute for light pulses with a weak intensity.

When using attenuated lasers, the maximum secure transmission length will be the result of a compromise between these two conditions. For realistic quantum cryptography systems on optical fibres, the replacement of attenuated lasers with perfect single photon sources would typically lead to increasing the maximum secure length by a factor of 2. Alternately, at constant channel length the bit rate per pulse could be increased by two orders of magnitude (Brassard 2000).

Single-photon pulses are quantum states of light. As such, they cannot be generated by 'classical' sources such as a black body or a laser. The most efficient strategy for the on-demand production of single photons relies on the pumping of a single quantum system. For solid state systems, the triggered generation of single photons has been reported using a variety of isolated emitters: a molecule (Lounis 2000), a coloured centre inside a diamond crystal (Kurtsiefer 2000, Brouri 2000), a semiconductor nanocrystal (Michler 2000a), or a semiconductor self-assembled quantum dot (Michler 2000b; Moreau2001a). However, the practical interest of molecules and nanocrystals is limited due to their degradation under optical excitation, a phenomenon known as photobleaching. Presently, quantum dots appear most likely to be adopted for practical application in quantum cryptography, as they combine two major specific advantages. Not only can they be pumped relatively easily by electrical injection (Yuan 2002), but optical microcavities can further be used in order to adjust their emission properties and to collect more efficiently their emission (see Section 7.2). A single-mode single photon

source has been realized by placing a single InAs quantum dot inside a GaAs/AlAs pillar microcavity (Moreau 2001b; Santori 2002). When the quantum dot is in spectral resonance with the cavity mode, it undergoes a strong Purcell effect (see Section 7.1.2), and its spontaneous emission is drastically funnelled into this mode. Last but not least, the directional emission of the pillar microcavity allows single photons to be very efficiently collected. A photon collection with an efficiency higher than 40 % has thus been independently measured in two different laboratories (Moreau 2002; Pelton 2002). Further, the use of anisotropic cross-sections allows to lift the polarization-degeneracy of the fundamental micropillar mode (Gayral 1998) and to control the linear polarization of single photons (Moreau 2001b). In practice, this property is extremely interesting for communication protocols based on polarization encoding, due to the continued necessity of preparing single photons in a given polarization state prior to any encoding of information. When non-polarized single photon sources are used, half of the photons get lost at this stage of the preparation.

Finally, a 'plug-and-play' single photon source for quantum cryptography should combine three main properties: an emission in the telecom spectral window (Ward 2005; Zinoni 2006), a high efficiency in a genuine single mode (space and polarization) and an electrical pumping. Thus far, these three properties have been separately demonstrated. Their combination in a single device now appears to be within reach, and it will probably be achieved in a near future with InAs quantum dots embedded in GaAs/AlAs micropillars.

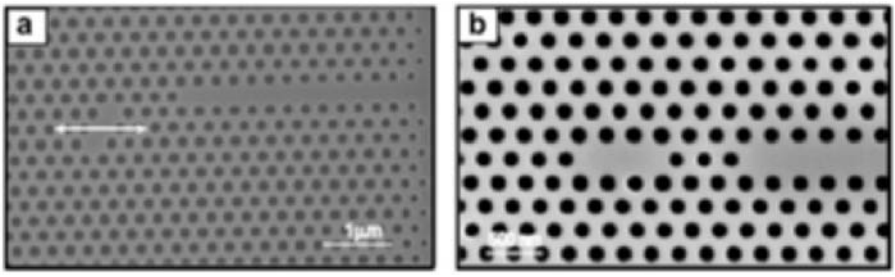

Fig. 10.7. Scanning electron microscope images of two integrated photonic crystal cavity-waveguide systems (Faraon 2007). In both cases, a few photonic crystal holes are used in order to mediate the coupling of a high-Q L3 cavity to a W1 waveguide *a.* Fabricated tilted cavity (four-hole separation). A cavity-guide coupling efficiency as high as 90 % was measured in this case *b.* Fabricated straight cavity (three-hole separation)

In this context, the potential interest of photonic crystal microcavities results from two significant limitations of single photon sources based on a single quantum dot embedded in a micropillar. These limitations are of an intrinsic and of an extrinsic nature respectively:

1. the generation of single photon pulses relies on the strong Coulomb interaction between the electrons and the holes trapped inside the quantum dot (Gérard 1999). It rests upon a very simple principle: several electron-hole pairs are first injected into the quantum dot by means of a non-resonant pulsed optical or electrical excitation. These pairs, usually known as excitons, relax towards the dot ground state through a radiative cascade; each emitted photon has a specific energy, which depends on the number p of electron-hole pairs remaining in the dot at this stage of the sequential recombination process. Therefore, a spectral filtering of the single-exciton emission line of the quantum dot ($p = 1$) results, after each excitation cycle, in a triggered light pulse containing the very last photon emitted by the quantum dot. A requirement for implementing this protocol is, quite obviously, that the exciton and multi-exciton ($p > 1$) lines of the quantum dot should be spectrally separated at the scale of their linewidth. In practice, the electron-phonon interaction tends to broaden these lines, with the consequence that this approach applies only to temperatures lower than 100 K for InAs quantum dots. By contrast, nanocrystals, as well as certain molecules, are able to generate single photons at room temperature. The coupling of such an emitter to the resonant mode of a microcavity based on two-dimensional photonic crystal is a very appealing approach. First, the 'open' or 'holey' nature of such cavities allows the selection of an adequate emitter, thereby ensuring spectral resonance and the optimization of its position at the antinode of the resonant mode. Further, in spite of the broad linewidth of these emitters at room temperature, the very small modal volume of the cavities is likely to ensure a strong Purcell effect, and therefore a good coupling of the spontaneous emission to the cavity mode, which should result in an efficient photon collection. As stated earlier, the main limiting factor for this approach appears to be related to the limited stability of the emitters.

2. The efficiency of single photon sources based on quantum dots placed in micropillars has been experimentally found to be systematically lower than the spontaneous emission coupling coefficient β in the resonant cavity mode, which can be estimated from the magnitude of the Purcell effect using Eq. 7.10 (see Section 7.1.2). This effect directly results from the additional extrinsic optical losses which are mostly due to scattering by the rough cylindrical sidewalls of the micropillar. This effect is particularly marked for small-diameter micropillars ($d < 2$ μm typically for GaAs/AlAs) and for micropillars with highly-reflective Bragg mirrors. Since in the latter case the intrinsic losses, which are related to the finite reflectivity of the mirrors, are low, the properties of the cavities tend to be extremely sensitive to the existence of additional extrinsic losses. The optimization of micropillars for high-efficiency sources must therefore result from a compromise between the search for a strong Purcell effect,

favoured by a decrease of intrinsic losses, and the necessity of minimizing the effects of extrinsic losses (Barnes 2002). When all these effects are taken into account, it can be demonstrated that the external efficiency of such single photon sources is typically limited to 70 % with a state-of-the-art processing of GaAs/AlAs micropillars (Barnes 2002). In this respect, the use of photonic crystal microcavities might very well represent a decisive breakthrough that will contribute to pushing back this limitation (Gérard 2004). Let us indeed consider an isolated cavity constructed in a two-dimensional photonic crystal, displaying a high quality factor Q_{iso} and containing a single quantum dot in resonance with the cavity mode. Supposing that this cavity can be coupled to a photonic waveguide without increasing the vertical losses of the cavity, the efficiency of the single photon source will be given simply by $\eta = \beta (1 - Q/Q_{iso})$, where Q is the quality factor of the loaded cavity. Let us assume that the quality factor Q_{iso} of the isolated cavity is of the order of 20,000 (Badolato 2005; Yoshie 2004) and let us further adjust the efficiency of the coupling to the waveguide in such a way that the quality factor Q of the loaded cavity be of the order of 500. For a typical cavity mode volume equal to $(\lambda/n)^3$, the following values can be derived from Eqs. 7.8 and 7.10 respectively: $F_p \sim 40$ and $\beta \sim 98$ %. Since by construction the coupling of the cavity to the waveguide is the main loss mechanism for the cavity, the efficiency of this source is therefore equal to $\eta \approx 96\%$. While extensive simulations might be necessary to optimize the overall design, cavity-waveguide coupling efficiencies as high as 90 % have already been demonstrated for the system presented in Fig. 10.7 (Faraon 2007).

3. The use of photons as elementary carriers of quantum information is attractive due to the ability of photons to propagate over long distances. Quantum information processing with photons exploits particular quantum states of light, such as indistinguishable single photons or polarization-entangled photon pairs. While such states can be generated from bare quantum dots, microcavity effects prove here again to be very useful for approaching the 'perfection' of quantum states, as well as for improving the efficiency of the photon source. Let us first consider the issue of single-photon indistinguishability. In the case of an isolated emitter, the story of each single photon emission event is the same save for their emission time. Thus, after temporal resynchronization, two such single photon pulses become identical. This would not be the case for a solid-state emitter, which is subject to decoherence processes. For self-assembled quantum dots, the electron-phonon interactions and the Coulomb interactions between the quantum dot exciton and the surroundings charges are the two dominant sources of decoherence. The latter effect can be minimized by operating at low temperature and under resonant pumping, which ensures that quantum dots will exhibit a narrow emission linewidth in the range of a few μeV (Kammerer 2002; Santori 2002). However, this linewidth remains ten times larger than the intrinsic linewidth associated to the exciton radiative lifetime. A possible strategy for generating 'near'-indistinguishable single photons is based on the exploitation of the Purcell effect in a micropillar (Santori 2002; Varoutsis 2005) or in a photonic crystal cavity (Laurent 2005), where the radiative recombina-

tion rate can be made faster than decoherence processes. This strategy has been validated by photon coalescence measurements. Photon pairs can also be generated by exploiting the sequential two-step recombination of a biexciton in a quantum dot (Gérard 1999). Since the biexciton is a well-defined zero-spin state, recombination can follow two different pathways, depending on which bright exciton is left in the quantum dot at the intermediate stage (Benson 2000). For a quantum dot displaying a circular symmetry, the two bright exciton states are degenerate, and therefore the two pathways cannot be distinguished. In such an ideal case, the photon pair is emitted in an entangled polarization state, a desirable feature for quantum information processing. In practice however, the degeneracy of bright excitons is lifted by the non-circular shape of the quantum dot (Bayer 2002). Different approaches, including thermal annealing (Langbein 2004) and the application of a transverse electric or magnetic field have been used for the purpose of reducing this bright exciton splitting, which for InAs/GaAs quantum dots is in the range of a few tens of μeV. Entangled photon pairs have thus been produced by combining the technique of thermal annealing with the use of a magnetic field to cancel the residual splitting (Young 2006). In this context, an interesting alternative could be the exploitation of the Purcell effect in a photonic crystal microcavity. The strong enhancement of the exciton radiative recombination rate, and the resulting broadening of the two bright exciton lines, would allow restoring the entanglement as soon as the exciton linewidth becomes larger than the exciton splitting. In addition, the use of a microcavity would also ensure the directional emission of the photon pairs, which is of interest in view of practical applications.

11 Photonic Crystal Fibres

11.1 Another Implementation of Periodic Structures

As has been exposed in the preceding chapters, photonic crystals in the near-infrared and visible regions were primarily conceived for the purpose of achieving a complete control of electromagnetic waves in semiconductor materials. At the same time, however, various hitherto unforeseen applications involving other types of materials have progressively appeared along the 'tree' of photonic crystals. The most striking illustration of the unexpected fruitfulness of such generic concepts as that of a photonic crystal is most probably the photonic crystal fibre (PCF) and more generally the microstructured optical fibre (MOF), also known as holey fibre (HF). For an insight into state-of-the-art performances achieved with microstructured optical fibres, the reader is referred to (Bjarklev 2003; Russel 2003, 2006), where further references are also presented.

In conventional optical fibres, which have been the basis of the terrestrial telecommunication industry since the first demonstration of fibres with a high transmission capacity in the spectral window extending around 1550 nm, light is guided owing to the phenomenon of total internal reflection (TIR). The guiding itself occurs inside a silica core with an optical index higher than the optical index of the medium forming the cladding, which is made from silica as well. The index step is created by using a different doping for the core and the cladding respectively. Most of the time, only the core is doped, and the cladding itself is made of pure silica. In this respect, microstructured optical fibres present a completely different structure. As can be seen in Figs. 11.1 and 11.2, these fibres appear in the form of silica matrices drilled with a number of parallel holes periodically organised into a two-dimensional array. While the periodic arrangement of the air holes would justify the use of the term 'photonic crystal fibre', this name should be more specifically reserved to those fibres where the propagation inside a defect with a low index is ensured by a true photonic bandgap effect. The defect consists in most cases in an air hole with large diameter at the centre of the structure, as is represented in Fig. 11.2*a*. For this reason, photonic crystal fibres of this type are also referred to as hollow-core photonic crystal fibres (HC-PCFs) or as hollow-core photonic bandgap fibres (HC-PBG fibres). True photonic band gap effects can also be exploited in all-solid fibres consisting of a pure or doped silica core surrounded by a cladding made of a background material (generally pure silica) containing a two-dimensional array of high-index inclusions of doped silica. These fibres are known as all-solid PBG fibres. It is to be noted at this point that solid-core holey fibres, whose guiding principle is not based on photonic bandgap

effects, but on a modified form of total internal reflection, are also frequently but improperly called 'photonic crystal fibres'. In order to avoid any confusion, these fibres will be referred to in the following as TIR-MOFs, or simply as MOFs.

In the first years following the invention of holey fibres in 1996, most results were actually concerned with solid-core microstructured optical fibres, examples of which can be seen in Figs. 11.2*b* and *c*. The study and the fabrication of these fibres are indeed much simpler than it is the case for hollow-core microstructured optical fibres. As mentioned above, propagation in these solid-core microstructured optical fibres occurs through a specific form of modified total internal reflection where photonic bandgap reflection is not necessarily involved. In this chapter, after providing a brief description of the fabrication process used for the realization of microstructured fibres, we then proceed to describe the main properties and applications of TIR-MOFs. Hollow-core PCFs and all-solid PBG fibres will finally be addressed in the second part of the chapter.

11.2 Fabrication of Microstructured Optical Fibres

The preform of a microstructured optical fibre is created by carefully stacking silica tubes and rods in an arrangement with the desired geometry. In the arrangement thus designed, some tubes in the periodic array can be replaced by rods in order to provide some specific optical functionality. The tubes and the rods, whose diameter lies in the millimetre range, are assembled at the macroscopic scale, which ensures the easy manipulation of the individual elements. The arrangement is generally set and fixed in a large supporting silica tube with a thin rim, and the whole constitutes the preform.

By heating the preform at a high temperature, for instance at around 1800°C, the silica softens to the point where it can be drawn using a similar technique to the one employed for the fabrication of classical fibres. This process is schematically represented here in Fig. 11.1. A miniaturized version of the original array of silica tubes and rods is thus obtained upon completion of the drawing process. It is often necessary to proceed in two steps if a sufficiently high reduction factor is to be reached. The preform, which typically is 3-4 cm in diameter, is first drawn to form a cane with a diameter of about 2 mm. The cane is then sleeved in a silica tube with large rim, before drawing once more this assembly in order to obtain the desired fibre, whose typical diameter is equal to 125 μm. The most fascinating feature of this technique, which rests on an extremely simple concept, is the perfection of the miniaturized version thus realized. As can be observed in the micrographs presented in Fig. 11.2, the final structure exhibits a lateral period which lies in the micrometer range, i.e. three orders of magnitude below the period of the preform. The structure exhibits in this case a quasi-perfect regularity, without any apparent deformation. Nevertheless, the possibility still exists in practice that noticeable deformations may arise. At this point, it might be noted that the interstitial holes between the individual tubes and rods can be either preserved or filled depending on the drawing parameters (temperature of the furnace, internal and ex-

ternal pressure in the tubes, drawing speed, etc). As will be seen, this may dramatically influence propagation performances in hollow-core as well as in solid-core photonic bandgap fibres.

The standard fabrication process represented in Fig. 11.1 concerns for the most part silica glass MOFs. For non-silica glasses, like tellurite or chalcogenure glasses, other fabrication processes, for instance extrusion, are used (Monro 2006). In the latter method, the realization of the preform proceeds by injecting molten glass inside a grid with the desired inclusion structure (Kumar 2002). Extruded jacketing tubes can also be realized using the same technique. Different geometries or hole shapes can be obtained in microstructured polymer optical fibres realized either by drawing preforms made from commercially available polymethylmethacrylate (PMMA) (van Eijkelenborg 2003) or by using careful drilling techniques (Barton 2004). Like in the standard stack-and-draw process represented in Fig. 11.1, the pattern formed by the holes may undergo modifications during the drawing of the fibre.

The design of these structures allows a large number of degrees of freedom, including the use either of hollow capillaries, or of solid rods, the number of individual elements, their diameter, their profile, the material from which they are made, their periodic arrangement, etc. This results in a great variety of possible realizations. Photonic crystal fibres thus open to the possibility of a proper engineering system of the refractive index.

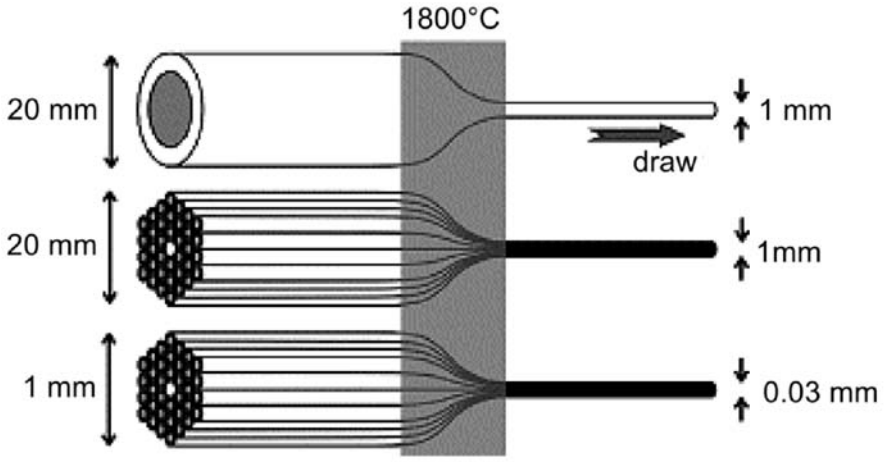

Fig. 11.1. Schematic principle of the fabrication of microstructured optical fibres, or 'holey' fibres

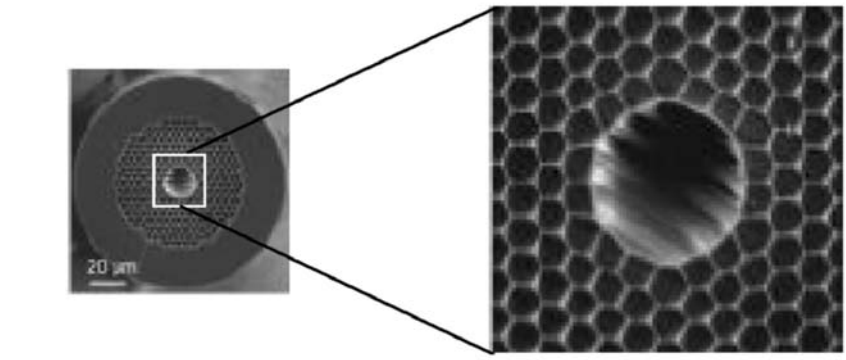

a

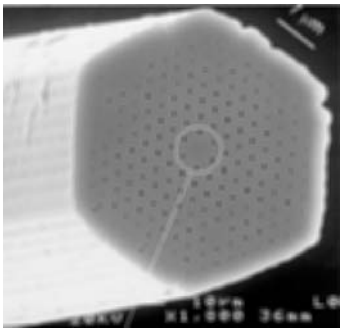

b

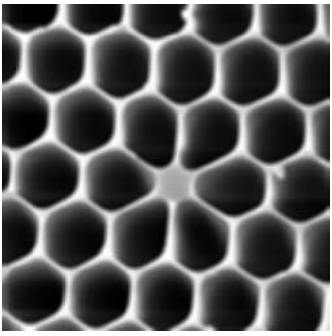

c

Fig. 11.2. Examples of microstructured optical fibres (MOF), displaying the variety of structures which can be obtained using the fabrication process described in Fig. 11.1. The perfection of the structure at the sub-micrometer scale can be noticed. Contrary to the solid-core microstructured optical fibres represented in *b* and *c*, the fibre represented in *a* has a hollow core. In this case, the confinement of light is achieved through a photonic bandgap reflection at the periodic structure which surrounds the central core

11.3 Solid-Core Microstructured Optical Fibres

11.3.1 Confinement Losses and Second Mode Transition

As a model of a microstructured optical fibre (MOF), we shall consider here an infinite matrix pierced with a finite number of parallel holes forming the cladding region. The core is a solid region which corresponds to one or more missing holes in the centre of the cladding. Due to the finite dimensions of the confining region, all electromagnetic modes of such a structure are leaky modes (Kuhlmey 2002; White 2002a; Snyder 1983). Each leaky mode is associated with a complex effective index n_{eff} which itself is linked to the propagation constant along the fibre axis β by the equation $n_{eff} = \beta/k_0$, where k_0 is the wave number of light ($k_0 = 2\pi/\lambda$).

The confinement losses L of the guided modes, expressed in decibels per meter, can be determined from the imaginary part of n_{eff} using the following equation:

$$L = \frac{40\pi}{\ln(10)\lambda} Im(n_{eff}) 10^6 \tag{11.1}$$

where λ is expressed in micrometers. It might be emphasized here that confinement losses may occur even in the case where material absorption is completely neglected. The most common type of MOF consists of a subset of a triangular lattice formed by air holes where the central hole is missing. Several different parameters are used for the description of the fibre: the period Λ of the lattice subset, the diameter d of the holes and the number N_r of hole rings. These parameters are schematically represented in Fig. 11.3. For a structure with a λ/Λ ratio low enough, the confinement losses L decrease almost exponentially with N_r and decrease also with the d/Λ ratio.

One of the earliest known and perhaps most surprising properties of MOFs is the possibility for these fibres of being endlessly single-mode (Birks 1997). This behaviour cannot be achieved with classical fibres, due to the fact that at short wavelengths a multimode regime is irreparably reached. Indeed, as the wavelength decreases, the normalized cutoff frequency of an increasing number of modes tends to be smaller than the limit frequency $V = k_0.a.NA$, where a is the radius of the core and $NA = (n_{co}^2 - n_{cl}^2)^{1/2}$ is the numerical aperture, with n_{co} and n_{cl} being the refractive indices of the core and the cladding respectively (Yariv 1997)[1]. The endlessly single-mode behaviour of MOFs can be explained in qualitative terms as follows: in the short-wavelength region, the fraction of the electromagnetic field which spreads in the cladding remains confined in the silica between neighbouring

[1] The numerical aperture NA in the expression of the normalized spatial frequency V is independent on the wavelength in the case of standard fibres. It measures the light-gathering capability of the fibre, and is defined as the sine of the maximum external angle of the entrance ray (measured with respect to the axis of the fibre) trapped in the core by total internal reflection.

holes, and the equivalent index of the cladding region tends toward the index of the silica, which is the same as the index of the core. Thus, the index contrast, and hence the numerical aperture of the fibre, become increasingly lower as the wavelength decreases. Accordingly, all guided modes present a larger extension in the cladding, and additional losses tend to eliminate high-order modes.

Actually, a MOF where the confinement of light is due exclusively to a finite number of rings of holes presents an infinite number of modes, all of which are leaky modes. Following the qualitative explanation outlined above, the relative losses of the different modes must be compared in order to determine whether the MOF is single-mode or not. If the modes present such relative losses that, after a given propagation length, all the modes save one have leaked away, the MOF can be considered to be single-mode for this specific propagation length. However, this definition of a single-mode MOF is not entirely satisfactory, on several counts: not only does this definition depend on the actual propagation length, but it also depends on the period of the lattice and on the number of hole rings. In the limit case of an infinite number of rings, no MOF could possibly be single-mode if such a definition were admitted.

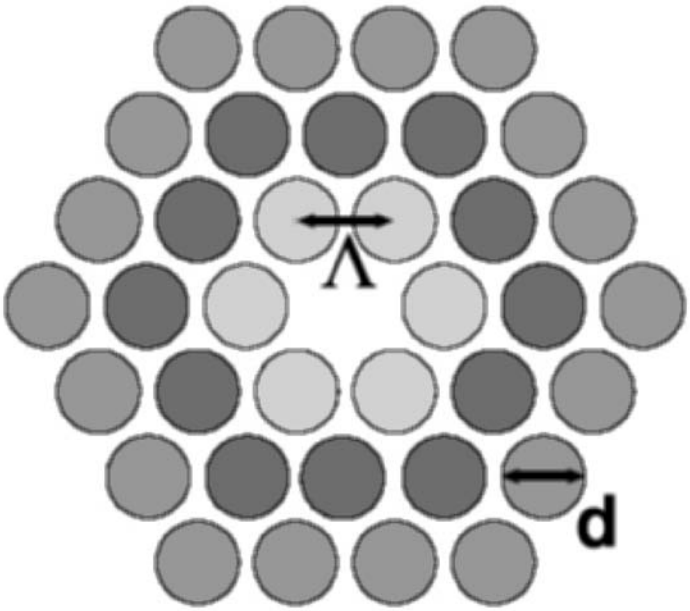

Fig. 11.3. Cross-section of an idealized solid-core MOF with three rings of holes (the holes are coloured with a different shade of grey for each individual ring). $N_r = 3\Lambda$ is the period of the triangular lattice, and d is the diameter of the holes. The solid core is formed by a single missing hole at the centre of the structure

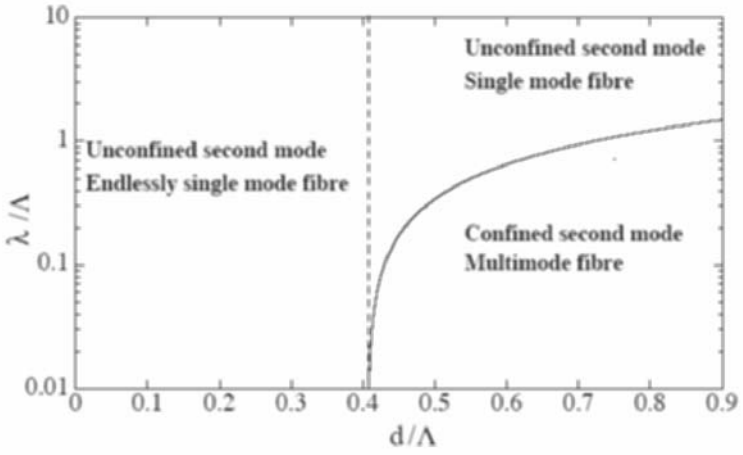

Fig. 11.4. Transition diagram of the second mode for a solid-core MOF. This diagram was obtained for a MOF based on a subset of a triangular lattice of circular holes inside a silica matrix. The solid line corresponds to the loci of the transition of the second mode. In the upper region of the (d/Λ, λ/Λ) plane, the fundamental mode is the only mode confined inside the core of the MOF (single mode regime), whereas in the lower region of the plane, the second mode is confined as well (multimode regime). The vertical dashed line represents the approximate limit of the endlessly single-mode regime

A possible solution for achieving a more precise characterization of single-mode MOFs is by studying the second mode[2] of such a fibre as a function of the parameters associated with it. This second mode actually undergoes a transition inside the core of the MOF from an unconfined state to a confined state. This transition can therefore be identified with a cutoff, which is observable on the loss curves for all the values of N_r under study. The higher the value for N_r, the steeper the transition is. The transition curve for the second mode is represented here in Fig. 11.4, where the normalized hole diameter d/Λ and the normalized wavelength λ/Λ were taken as reference parameters. As can be seen from the consideration of this figure, the (d/Λ, λ/Λ) plane divides into two regions. Below the transition curve, the second mode is confined, while above the transition curve, it is not confined and extends spatially. It might be noted that the curve intersects with the abscissa axis at $d/\Lambda = 0.406$, and that, below this limit value for d/Λ, the second mode never becomes confined. As a consequence, the fundamental mode is the only mode which remains potentially confined at any wavelength: the MOF is therefore endlessly single-mode.

At long wavelengths, the electromagnetic field in the cladding spreads increasingly in the holes surrounding the core. In the limit case of long wavelengths, the

[2] The second mode is defined as the mode whose real part approaches the most the real part of the fundamental mode.

MOF can be viewed as a cylindrical waveguide with a silica core whose index is equal to the index of silica (n_s), surrounded by a cladding with a lower index $n_{cl} = [f n_a^2 + (1 - f) n_s^2]^{1/2}$, where n_a is the air index and f is the air filling factor, as given by $f \sim 0.91(d/\Lambda)^2$ for a standard cladding consisting of a triangular lattice of air holes. The numerical aperture tends toward a maximum value equal to $[f(n_s^2 - n_a^2)]^{1/2}$. Thus, in a simplifying approach, a solid-core MOF can be seen as a leaky waveguide with a numerical aperture decreasing with the wavelength.

11.3.2 Attenuation and Bend Loss

In practice, the leakage of the fundamental mode of a MOF to the continuum of modes represents a propagation loss lower than 0.01 dB/km, provided however that the number of hole rings be sufficiently high (5 or more). The effective attenuation of MOFs is thus dominated by intrinsic losses associated to Rayleigh scattering, to material absorption and to diffusion at the silica/air interfaces. Since MOFs are made of pure silica glass without dopant, these intrinsic losses can be actually lower than those of standard single-mode fibres. The threshold attenuation is estimated to be equal to 0.14 dB/km at $\lambda = 1.55$ μm. At this wavelength, the measured attenuation of MOFs manufactured with low-water-peak high-purity silica glass tubes and rods, for which efforts have been directed toward reducing the roughness at the silica/air interfaces, has already been found to be as low as 0.28 dB/km for propagation lengths over a few kilometres (Tajima 2003) and as 0.3 dB/km for distances over 100 km (Kurokawa 2006). Such performances open the possibility of using MOFs in long-haul telecommunication applications.

In standard fibres, the macrobending loss of the guided modes increases with the wavelength, this being due to the fact that the electromagnetic field becomes less confined in the core. This remains true for MOFs. However, contrary to standard fibres, they also present a macrobending edge at short wavelengths, which results from the fact that the index contrast between the core and the cladding decreases with the wavelength. The critical wavelength below which the macrobending loss dramatically increases to the point where it becomes unacceptable is proportional to $R^{-1/2}$, where R is the radius of curvature (Nielsen 2004). Even though this critical wavelength is in most cases significantly shorter than the operating wavelengths, this may nonetheless be a limiting factor for the use of large-mode area MOFs.

11.3.3 Chromatic Dispersion Properties

The chromatic dispersion, or equivalently the group velocity dispersion, plays a fundamental role in conventional fibre optics (Okoshi 1982), be it in the linear or in the nonlinear optical regimes (Agrawal 2001), and this remains true when microstructured optical fibres are considered (Ranka 2000; Dudley 2002; Ferrando 2003). For a given propagation mode, the chromatic dispersion D_c is linked to the spectral evolution of the effective index n_{eff} by the following equation:

$$D_c = -\frac{\lambda}{c}\frac{d^2 n_{eff}}{d\lambda^2} \tag{11.2}$$

where n_{eff} depends on the indexes of the core and of the cladding, as well as on the distribution of the field over the two regions of the fibre (Pagnoux 2003).

Quite early in the development of MOFs, it was recognized that these new waveguides could exhibit specific and interesting dispersion properties owing to the non-conventional spectral behaviour of the effective index of the mode, which itself is induced by the evolution of the equivalent index of the cladding with the wavelength. MOFs were therefore considered as good candidates for the management of chromatic dispersion in optical systems (Mogilevstev 1998; Ferrando 2000b; Knight 2000). It appeared that the control of the chromatic dispersion is indeed much more powerful in MOFs than in conventional optical fibres thanks to a higher index contrast and to a greater number of available geometrical parameters, including the diameters of the holes, the period of the lattice and more generally the location of the holes in the array.

The systematic study of the chromatic dispersion in MOFs (Ferrando 2000b) really began when a vector description of the guided modes was developed, either in terms of periodic boundary conditions (Ferrando 2000a) or by means of a vectorial finite element method (Bréchet 2000a). Nevertheless, the finite cross-section of MOF must be accounted for in order to accurately describe the chromatic dispersion and thus correctly determine propagation losses (Kuhlmey 2003).

The chromatic dispersion management of MOFs can thus be achieved in a variety of different ways. For instance, a special design for MOFs has been suggested, where the diameters of the inclusions are made to increase with the distance from the axis of the fibre until a maximum diameter is reached. An ultra-flattened chromatic dispersion associated with a low amount of propagation losses was predicted for these fibres (Renversez 2003). In principle, if such a structure with only three different hole diameters were used, only seven rings of low-index inclusions would be needed for reaching a 0.2 dB/km loss level at $\lambda = 1.55$ µm with a dispersion exhibiting a variation amplitude below $3.0\ 10^{-2}$ ps nm^{-1} km^{-1} in the (1.5 - 1.6 µm) wavelength range. This value for N_r compares favourably with the eighteen rings which are required in the case of a usual MOF consisting of identical inclusions. A dispersion lower than 1.2 ps nm^{-1} km^{-1} was experimentally achieved between the 1000 and 1600 nm wavelengths using a fibre consisting of eleven rings of holes with diameter $d = 0.58$ µm and $\Lambda = 2.59$ µm (Reeves 2002). The dispersion of MOFs can also be cancelled at wavelengths under 1300 nm, even in the case where a high material dispersion exists. As an example, a MOF with a silica core with a diameter equal to 0.5 µm surrounded by holes fifty times this size was found to exhibit a zero dispersion at $\lambda = 560$ nm, in spite of a material dispersion equal to –360 ps nm^{-1} km^{-1} (Knight 2000).

The price to pay for a greater flexibility in the choice of the chromatic dispersion is that the latter can be very sensitive to the diameter and pitch of the holes, in particular those located in the central rings of inclusions (Labonté 2006). For ex-

ample, the dispersion of a fibre with eleven rings of holes described above (Reeves 2002) remains close to zero around 1300 nm, but it becomes lower than –6 ps $nm^{-1}km^{-1}$ below 1150 nm and above 1550 nm when the diameter and the pitch of the holes are slightly decreased from 0.58 μm and 2.59 μm to 0.57 μm and 2.47 μm respectively. The control of geometrical parameters is therefore a crucial issue for the fabrication of MOFs with the desired performances.

11.3.4 Main Applications of Solid-Core Microstructured Optical Fibres

The industry landscape for MOFs has significantly changed over the last few years. As a result of mergers, only a few startups and small-size companies are currently manufacturing and selling those fibres. On the other hand, several major companies in the telecommunication field produce MOFs for their own internal research use, while MOFs are being realized in an increasing number of academic laboratories in Europe, Asia, Australia and North-America.

As a result of their technological maturity, a variety of applications can be envisioned for solid-core microstructured optical fibres. At least five main types of applications can be distinguished:

1. optical communications (Himeno 2005; Reeves 2002;Tajima 2003),
2. rare-earth doped lasers (Furusawa 2001; Limpert 2003; Wadsworth 2000),
3. optical amplifiers (Knight 1998a; Hougaard 2003),
4. supercontinuum generation (Dudley 2002; Ranka 2000),
5. polarization-maintaining applications (Ortigosa-Blanch 2000).

Devices of a more ‘exotic’ type, including sensors (MacPherson 2001), have also been proposed (Eggleton 2001).

1. MOFs are very attractive media for high-bit-rate large-capacity and long-distance transmission, because they provide dispersion and mode-field diameters that would not be achievable with conventional single-mode fibres. Large-mode field diameters allow increasing the transmitted power without any undesirable increase of non-linear effects. High bit-rate soliton transmission can also be implemented, provided that dispersion be suitably managed (Kurokawa 2006). The endlessly single-mode properties of MOFs also allow the implementation of dense wavelength division multiplexing (DWDM) techniques in enlarged spectral regions (Nakajima 2005). Finally, suitably designed dual-concentric-core MOFs can be efficiently used as dispersion compensating devices, owing to the fact that they exhibit a very large negative dispersion in the 1.55 μm spectral region and are able to compensate for the positive dispersion of standard fibres (Gérôme 2004; Varshney 2006).

2 and 3. Single-mode MOFs can be designed with a silica core of a much larger diameter than would be possible with conventional fibres, where a single-mode behaviour generally imposes the use of a core with small diameter, unless a high

level of precision can be achieved in the management of the index contrast between the core and the cladding. By contrast, the core of a single-mode MOF can be more than fifty times larger than the working wavelength (Knight 1998b). Large-core MOFs, represented for instance in Fig. 11.2*b*, present an immediate interest as regards the transmission of high optical power as well as the realization of rare-earth doped lasers and optical amplifiers (Hilaire 2006; Jeong 2004; Shirakawa 2005). The interested reader is referred to (Roy 2006) for a review of specific designs of MOFs which can be used for efficient amplification and lasing.

4. MOFs can also be designed in such a way as to present modes with a very small size, as is the case for the fibre represented in Fig. 11.2*c*. This property tends to ensure a high degree of optical nonlinearity. Appropriate group velocity dispersion combined with large third-order non-linearity was used to generate supercontinua under pumping with femtosecond (Husakou 2001; Ranka 2000), picosecond (Coen 2001), nanosecond (Dudley 2002) pulses or with a continuous wave (Avdohkin 2003). Supercontinua generated from MOFs generally extend from the infrared to the visible ranges. Multi-wavelength pumping schemes (Champert 2004) or the use of MOFs with scalable core diameters (Kudlinski 2006) allow a larger extension of supercontinua from the IR (> 1700 nm) to the UV domain (< 350 nm).

5. In principle, perfect hexagonal MOFs do not exhibit optical birefringence, due to their threefold rotational symmetry. In practice however, any imperfection in the fabrication process irremediably leads to shape birefringence. Even if a low birefringence can be maintained with an accurate fabrication technique, the very manufacturing process of MOFs lends itself actually much more to the realization of highly birefringent fibres. Thus, a twofold rotational symmetry can be induced easily in a MOF with a quasi-elliptical core created for instance by removing two neighbouring holes. In such a MOF with $d = 1.2$ μm and $\Lambda = 1.46$ μm, a birefringence (effective index difference between the two polarization modes) as high as 4×10^{-3} has thus been measured, resulting in a beat length as short as 0.39 mm at $\lambda = 1.55$ μm (Mélin 2003). Another solution consists in resorting to air holes with different sizes, symmetrically placed along the periphery of the pure silica core. Such a fibre was reported in (Ortigosa-Blanch 2000) where small holes with a diameter $d = 0.4$ μm were introduced among larger holes of diameter $d = 1.16$ μm inside a periodic array with period $\Lambda \approx 2$ μm. The beat length in this fibre reached 0.56 mm at $\lambda = 1.55$ μm.

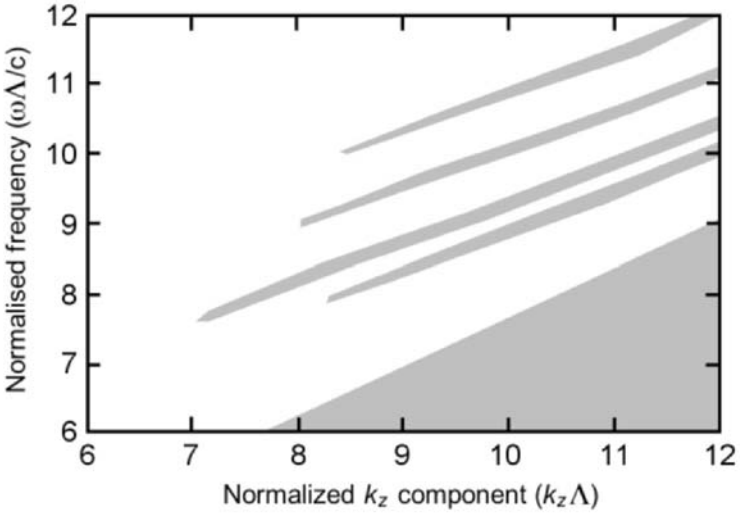

Fig. 11.5. Mapping of the photonic band gaps (represented in grey) calculated for the cladding of a photonic crystal fibre with a triangular lattice of circular holes inside a silica matrix (Birks 1995). The normalized frequency ($\omega\Lambda/c$) is represented as a function of the normalized wave vector component along the invariance axis ($k_z\Lambda$), where Λ is the period of the lattice. Only the four narrow bands at high frequencies correspond to proper photonic band gaps of the crystal, while the triangular frequency band at low frequencies corresponds in fact to refractive modes inside the fibre

11.4 True Photonic Crystal Fibres (PCF)

11.4.1 Photonic Bandgap Cladding

The use in fibre technology of photonic band-gap claddings can be traced back to the 1970s, at the time when the theory of Bragg fibres with concentric layers was first advanced (Yeh 1978). The very first experimental demonstration of guiding in such a Bragg fibre with low-index core was achieved in 2000 (Bréchet 2000b). Two more years were needed before convincing demonstrations of low loss propagation in hollow-core Bragg fibres were achieved, first in the mid-IR at $\lambda = 10.6$ μm (Temelkuran 2002), and then in the near IR (Kuriki 2004). Today however, photonic band-gap fibres or true photonic crystal fibres are more generally described in the form of two-dimensional periodic arrays of inclusions inside a silica matrix, where the propagation of light occurs due to a low-index defect created at the centre of the array. At the very beginning of research on genuine PCFs, i.e. at the end of the 1990s, inclusions always consisted of air holes, with the low-index

defect being an additional air hole, as represented in Fig. 11.2*a*. More recently, a new generation of all-solid photonic bandgap fibres has been developed, in which the two-dimensional periodic inclusions in the cladding are high-index solid rods and the core is made of pure or doped silica. In the following, we shall first focus on propagation mechanisms in hollow-core PCFs with cladding air holes.

Actually, the physics underlying such periodic arrays of holes are different from that of the two-dimensional photonic band gaps created in semiconductors and described in Chapter 9, because light propagates in this case along the invariance axis, i.e. perpendicularly to the cross-section of the fibre. Indeed, in spite of the relatively low index contrast between silica and the air, the periodic structuring of the fibre dramatically modifies the modal behaviour of the fibre waveguide. Since the so-called 'out-of-plane component', i.e. the wave vector component k_z of the modes guided along the propagation axis, is significantly higher than the two other components k_x and k_y along the transverse directions, a photonic band gap can no longer be defined as a frequency domain where the propagation of light is forbidden for any direction within the (x, y) plane, and it should be defined instead as a frequency domain where no (k_x, k_y) state is allowed for a given value of k_z (see Chapter 5). If a defect is created at the centre of the periodic structure, a propagation mode will be allowed for an appropriate value of the k_z component, and the light propagating will be confined inside the core of the fibre.

As an illustration, Fig. 11.5 represents a mapping of the photonic band gaps calculated for a silica fibre where the photonic crystal consisted of a triangular lattice of holes with an air-filling factor f equal to 0.45 (Birks 1995). The presentation adopted in this figure differs somewhat from those previously used throughout the present book, insofar as the forbidden frequencies are represented here as functions of the k_z wave vector component. Actually, two different types of frequency domains where the propagation of light into the cladding is forbidden need to be distinguished: the first domain extends from the lower frequencies and its upper boundary corresponds approximately to the straight line defined by the equation $\omega/c = k_z/n_{eq}$ where n_{eq} is the equivalent index of the composite material (silica + air holes). In fact, n_{eq} can be viewed as the effective index of the mode with lowest order allowed in the photonic crystal considered as an infinite medium (fundamental space-filling mode). Since n_{eq} depends on the way the field extends into the cladding, it also depends on the wavelength. As has been stated already in this chapter, $n_{eq} = \sqrt{\varepsilon_m}$ with $\varepsilon_m = (1 - f)\,\varepsilon_{silica} + f\,\varepsilon_{air}$ in the long wavelength limit, whereas in the short wavelength limit, n_{eq} tends toward $\sqrt{\varepsilon_{silica}}$. The domain below the line $\omega/c = k_z/n_{eq}$, which appears in Fig 11.5 in the form of a grey triangle, corresponds to the classical guiding in fibres by total internal reflection, which entails that as long as $k_z/n_{eq} \geq \omega/c$ ($= k_{free\ space}$), the wave propagating in the core will remain confined inside the fibre for the simple reason that no refraction angle exists that would allow the transmission to occur from the core to the cladding region.

A second type of frequency domains where propagation is forbidden can be discerned in Fig. 11.5 in the form of the four narrower grey bands. These four frequency domains, which are located at high frequencies, correspond to the proper guiding imposed by the photonic crystal, and associated with Bragg reflections.

These band gaps can be obtained for all polarizations of the electromagnetic field. It might be emphasized here that, contrary to planar optics involving semiconductors, photonic band gaps can be achieved in the visible and near-infrared ranges without requiring the need of a (sub)-micrometric period of holes. This simply arises from the fact that the guided light propagates along the invariance axis rather than within the periodicity plane, thereby resulting in lower values for k_x and k_y. In principle, breaking the periodicity of the crystal by creating a central hole with a different size, as is represented in Fig. 11.2*a*, should allow the propagation of one or several guided modes with a frequency in narrow bands similar to those represented in Fig. 11.5 (Knight 1996). Such guided modes were first achieved in practice by using a graphite-type hexagonal lattice of holes (Knight 1998a). More detail on these lattices can be found in Section 1.3.3 of Chapter 1. These results were generalized the following year to triangular lattices of holes with different profiles (Cregan 1999).

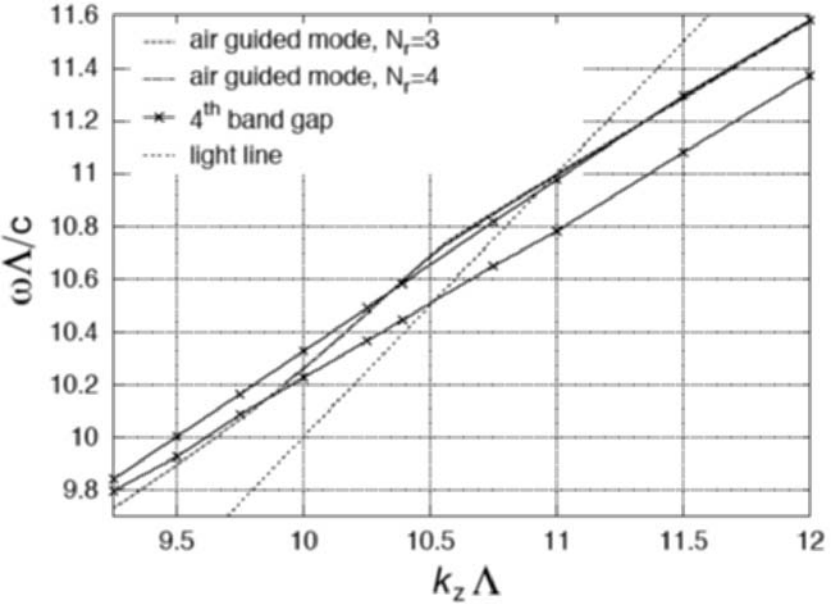

Fig. 11.6. *Dashed curves.* Dispersion curves of the fundamental air-guided modes for two photonic crystal fibres with a core of the same diameter (φ = 13.1 μm, and n_{core} = 1.0), but with different numbers of cladding layers (N_r = 3 and N_r = 4 respectively). The cladding consists in either case of a periodic lattice of holes drilled inside silica (n_{matrix} = 1.39), with a period Λ = 5.7816 μm and a hole diameter d = 4.026 μm. *Solid curves with crosses.* Boundaries of the fourth band gap for the infinite lattice of holes (n_{hole} = 1.0, n_{matrix} = 1.39). *Thin dashed curve.* Light line $\omega = ck_0$

11.4.2 Losses of Photonic Crystal Fibres with Finite Cladding

Let us here consider a hollow-core PCF with a finite photonic crystal cladding. The genuine dispersion curve of the air-guided mode in such a fibre can be calculated in the way described in Fig. 11.6 for a lattice with parameters similar to Fig. 11.5. Actually, the dispersion curve of the fundamental air-guided mode of the finite photonic crystal fibre does not lie totally within a given band gap, in the present case in the fourth one, but crosses its boundaries at certain frequencies. This phenomenon can be readily explained by the simple fact that the modal dispersion curve was calculated for finite structures with either three or four hole rings, whereas the band gap had been calculated for the case of an infinite lattice of holes. Nevertheless, at most frequencies, the dispersion curve remains above the light line, which demonstrates that the real part of the effective index of the mode is actually smaller than one. Indeed, the distribution of the field which can be calculated using one of the elaborate methods described in Sections 2.2 and 2.3 in Chapter 2 vindicates the conclusion that defect modes are proper air-guided modes propagating inside the hollow core of the PCF.

As is also the case for solid-core MOFs, the losses of the confined fundamental mode of hollow-core PCFs have been found to decrease almost exponentially with the number of rings of air holes for wavelengths located in the band gap. The wavelength associated with the lower loss level increases slightly with the number N_r of hole rings surrounding the core, while the slope of the loss curve increases with N_r around the optimal wavelength. If the operating wavelength is far from this optimum, the losses then reach a considerable level, with the consequence that the hollow-core MOF simply becomes unusable. This behaviour is consistent with the relative narrowness of the photonic band gaps which can be observed in Fig. 11.5. Contrary to solid-core MOFs, photonic crystal fibres allow an efficient guiding of light only over limited spectral ranges. For a detailed theoretical analysis of the loss characteristics of hollow-core as well as solid-core MOFs, the reader is referred to the works by Kuhlmey (Kuhlmey 2002a, Kuhlmey 2002b, Kuhlmey 2003).

The performances of HC-PCFs are strongly influenced not only by the number of rings, but also by the geometry of the hollow core as well. In order to evaluate this influence, it is necessary to determine precisely the characteristics of the guided modes versus the shape of the core, in particular the associated field distribution, the effective index and the field leakage to the continuum of modes. A full-vector finite element method including anisotropic perfect matched layers (PMLs) has proved to be an appropriate method for carrying out numerically this study (Saitoh 2003). Three HC-PCFs with a common d/Λ value equal to 0.9, but with different cross-sections, are represented in Fig. 11.7. In all three cases, the core was obtained by removing the seven central elements in the primary preform. The cross-section of the core is varied by carving the silica at the periphery of the core. As expected, due to field boundary conditions, the field distribution of the fundamental mode which can be excited in the first band gap of the cladding around $\lambda/\Lambda = 0.67$ depends on the cross-section of the core. Accordingly, the dispersion and effective area of the mode are also dependent on the cross-section of

the core in the spectral region of interest. Moreover, it can be noted that, except in the case of the type-3 fibre, a significant part of the field is located in the silica region extending around the core, thereby favouring the excitation of leaky 'surface modes'. The major consequence is that the leakage loss in the mid-gap region of type-2 and type-1 HC-PCFs with 10 hole rings, expressed in dBs, is respectively one and two orders of magnitude higher than the leakage loss of type-3 fibres (Saitoh 2003).

For any HC-PCF, there exists a wavelength of minimum attenuation, referred to as λ_c, which depends on the structure of the fibre and varies in proportion to the transverse dimension of the fibre (Cregan 1999). The loss of a mode propagating in the hollow core is due for the most part to its coupling to the radiation modes of the cladding and to surface modes. The guided light can also be scattered to non-guided modes due to the roughness of the surface at the silica/air interfaces. The net attenuation induced by this scattering is proportional to $1/\lambda_c^3$ instead of $1/\lambda^4$ for Rayleigh scattering in bulk media (Roberts 2005). A particular effort must therefore be directed toward minimizing the roughness of the surface if low propagation losses are to be achieved. On the other hand, coupling to radiation modes and surface modes can be reduced by diminishing the spatial overlap between the guided mode and the silica/air interfaces. This can be achieved, either separately or in combination, by enlarging the diameter of the core, by adjusting the shape of the cross-section of the core or by increasing the air-filling factor in the cladding.

For a HC-PCF with a core consisting of 19 missing elementary cells (the central hole and the two neighbouring rings of holes), surrounded by a resonant silica/air cladding with an air-filling factor of 99.8 %, theoretical investigations show that the minimum attenuation that would be realistically attainable is of the order of 0.2 dB/km at $\lambda = 1.6$ μm and 0.13 dB/km at $\lambda = 1.9$ μm (Roberts 2005). This is to be compared to conventional fibres, where Rayleigh scattering in silica imposes a minimal attenuation of 0.15 dB/km at $\lambda = 1.55$ μm. Operating HC-PCFs at longer wavelengths should lead to even smaller scattering losses, with the risk, however, of a simultaneous increase of infrared absorption losses in the silica domains where a small fraction of light is localized. HC-PCFs might also be optimized by using fibres with a larger air core, created for instance by removing a third ring of holes (i.e. with 37 missing elementary cells). However, this would allow the propagation of many high-order modes that could efficiently couple to surface modes. In addition, this would also increase the bend loss of the fibre.

From an experimental point of view, the measured losses of hollow-core silica PCFs have been continuously decreasing from 1999 to 2005 (Cregan 1999; Broeng 1999; Mangan 2004; Roberts 2005; Smith 2003). The lowest reported loss is 1.2 dB/km at $\lambda = 1.62$ μm in a HC-PCF with a 19-cell core and a silica/air cladding whose air-filling factor is equal to 99.5 % (Roberts 2005). For such low-loss fibres, Rayleigh scattering caused by the gas contained in the hollow core is responsible for a large part of the residual attenuation. Accordingly, a dramatic decrease of the Rayleigh scattering might be experienced provided that vacuum could be achieved inside the core.

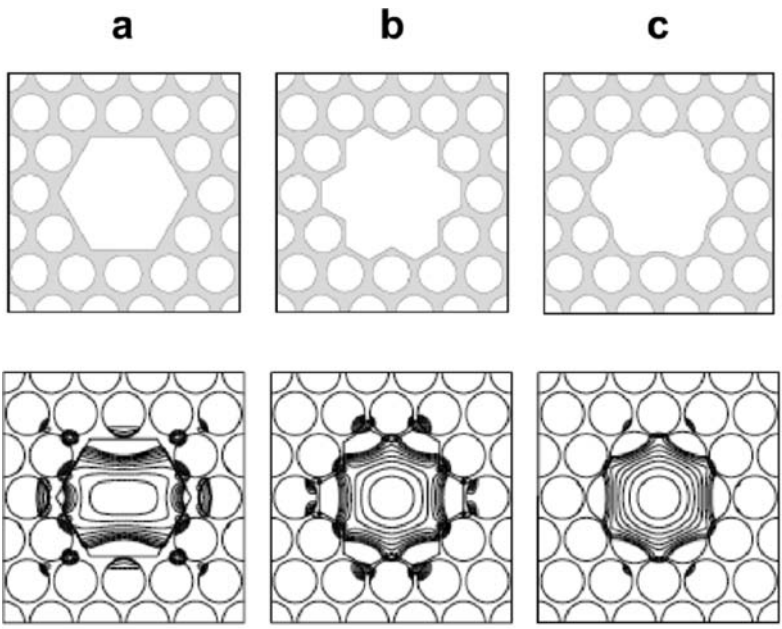

Fig. 11.7. *Top.* Cross-sections of hollow-core photonic crystal fibres (HC-PCFs) of type-1 *(a)*, type-2 *(b)* and type-3 *(c)* for d/Λ=0.9. *Bottom* Intensity profiles of the horizontally polarized fundamental mode for the different fibres (λ/Λ=0.67) (Saitoh 2003)

11.4.3 Photonic Crystal Fibres with Optimized Structures

The very first experimental demonstration of the propagation of light in an air core was achieved in a fibre with a graphite-type lattice of holes (Knight 1998a). However, air guiding was rapidly demonstrated in a more convincing fashion with HC-PCFs based on a triangular lattice of air holes in the cladding (Cregan 1999). The first such PCF, whose air-filling factor is equal to 0.39, is presented here in Fig.11.8*a*. As described in the previous section, extensive researches have been subsequently conducted in order to reduce the loss of HC-PCFs through the optimization of the geometrical parameters, whilst retaining the overall structure. An example of a low-loss HC-PCF has thus been presented in Fig.11.2*a* (Roberts 2005). Some sophisticated versions of these fibres, providing additional attractive propagation properties, have also been proposed. As an example, a twofold symmetric arrangement of elliptical patterns can be introduced in the silica ring surrounding the core in order to provide a high birefringence and a differential leakage loss between the two polarization modes of the HC-PCF (Roberts 2006).

In parallel to the studies previously mentioned, original fibre structures were designed with the aim of overcoming the drawbacks of standard HC-PCFs, i.e.

their intrinsically narrow transmission bandwidth, and the difficulty of fabricating them when a small pitch (< 2 μm) is necessary for short wavelength applications. An important example of such an original structure is the Kagomé fibre, represented in Fig. 11.8*b*, whose cladding consists of a regular hexagonal lattice of triangles joined at their apexes (Couny 2006a). The photonic band gaps in Kagomé fibres are located at normalized frequencies $k\Lambda$ significantly higher than in conventional HC-PCFs. The net result is that short wavelength (visible, and even UV) light can be guided in the hollow core whilst using a large pitch of a few tens of microns. Furthermore, the band gaps are broadened, and the chromatic dispersion of Kagomé fibres is flatter than those of conventional HC-PCFs, which makes them suitable for applications to non-linear optics (high-harmonic generation, soliton delivery, etc) and to gas sensing.

In conventional HC-PCFs, the low-index material consists of air holes, while the high-index background material, generally made from silica, forms a connected structure of quasi-triangular rods joined by bridges. An alternative design, represented in Fig. 11.8*c*, consists in using a low-index solid as the background material, with the high-index inclusions being formed by a periodic array of isolated circular rods in the cladding (Luan 2004). Modes able to propagate in the core of these fibres have effective indices which are only slightly lower than the index of the background material. Besides, each high-index inclusion is able to guide its own modes with effective indices comprised between the index of the inclusion and that of the background material. When a mode of the inclusion reaches its cutoff, its effective index simultaneously reaches the same value as the index of the background material. Thus, at the corresponding frequency, quasi-phase matching occurs between this mode and the modes of the core, thereby allowing the energy of the later to couple into the inclusions. In an array of close inclusions, the coupling between the identical modes of the individual inclusions gives rise to supermodes whose cutoff frequencies are very close to one another. This creates frequency bands within which light propagating in the low-index core can couple into the inclusions. In other words, the fibre with low-index core and high-index inclusions presents transmission minima associated to the mode cutoffs of the high-index inclusions. Conversely, it transmits light in the photonic band gaps of the cladding that are located far from these cutoffs. It might be noted that the frequency positions of the transmission bands depend for the most part on the index and diameter of the inclusions, and only to a limited extent on their geometrical arrangement (White 2002b). Solid-core fibres with isolated high-index inclusions clearly operate following the same principles as antiresonant reflecting optical waveguides (ARROWs) (Argyros 2005; Litchinitser 2003).

These fibres, also known as all-solid two-dimensional photonic band gap (SC-PBG) fibres, have the very attractive feature of combining the original dispersion characteristics associated to the band gap with the possibility of doping the core, either for Bragg grating inscription or for light emission. Improved structures, where the interstitial air holes between the cladding rods are preserved, have been shown to exhibit reduced confinement loss and bend sensitivity (Bétourné 2007).

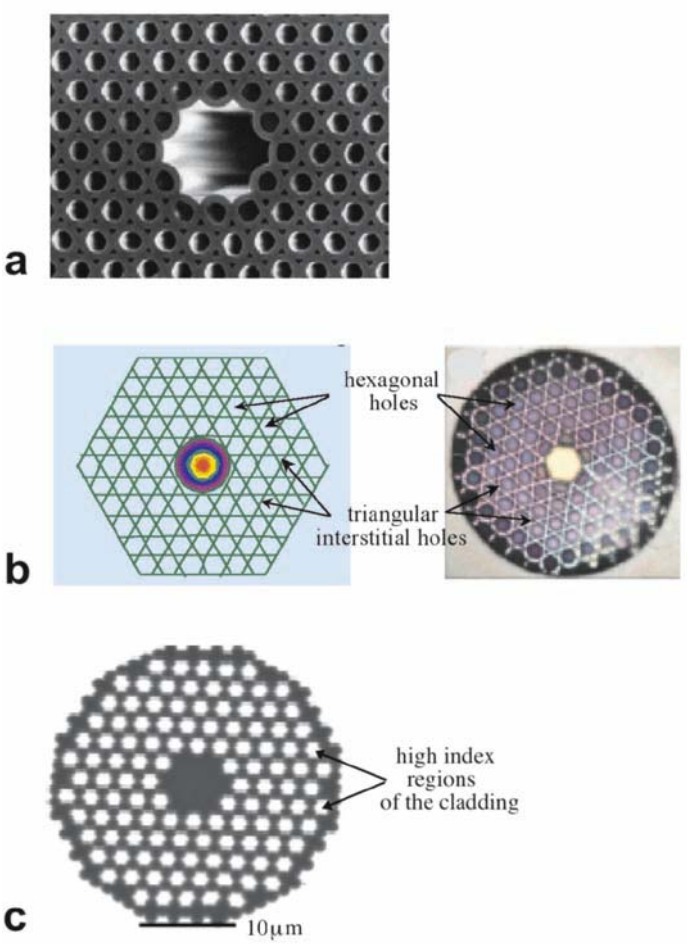

Fig. 11.8. Cross-sections of different photonic crystal fibres (PCFs). *a.* Very first PCF able to guide light in a hollow core thanks to a triangular lattice of holes in the cladding (Cregan 1999) *b.* Kagomé fibre *Left.* Schematic representation *Right.* Optical micrograph (Couny 2006a) *c.* Solid-core photonic bandgap (SC-PBG) fibre (Luan 2004)

11.4.4 Main Applications of Photonic Crystal Fibres

It is very likely that the development of hollow-core photonic crystal fibres (HC-PCFs) and solid-core photonic bandgap (SC-PBG) fibres will open the way to a large variety of applications. This is particularly true for HC-PCFs, and their use should lessen the constraints imposed on the properties of waveguides by the nature of the material used for the core of the fibre. Another series of possible appli-

cations for these fibres is the reinforcement of the interaction between light and a gas filling the core of the fibre. On the other hand, SC-PBG fibres are very attractive candidates for applications requiring single-mode propagation of light beams with in-fibre spectral filtering. We describe some of these aspects in more detail hereafter.

A first possible application of hollow-core photonic crystal fibres would be their use as efficient waveguides for the propagation of light in wavelength ranges where silica and glasses undergo strong absorption. This is particularly the case in the infrared range, beyond the third telecommunication window (Amezcua-Correa 2006). Application to the UV domain can also be envisioned, provided that the cross-section of the fibre is small enough, and that the roughness of the silica/air interfaces is sufficiently low.

HC-PCFs are also attractive for the transfer of high optical powers, as is already the case for solid-core MOFs with cores of a large diameter. Further, hollow-core PCFs should exhibit a lower optical nonlinearity, a lower damage threshold, and a lower Fresnel coefficient at their extremities than solid-core MOFs, provided however that the residual absorption in the hollow core is small enough. Let us here recall that the air is more absorbing than silica at telecommunication wavelengths. An example of a hollow-core PCF used at high optical levels with a reduced nonlinearity was presented by DG Ouzounov *et al* (Ouzounov 2003), where megawatt optical solitons were generated inside the core of a fibre filled with xenon gas.

Applications of hollow-core PCFs may also be developed in the opposite direction, involving nonlinear processes in active molecular gases. Indeed, both the confinement of light and the length of interaction can be dramatically increased when compared to conventional gas systems. A stimulated Raman scattering was thus achieved inside a hollow-core PCF filled with hydrogen and with a length of one meter, leading to Stokes and anti-Stokes energy thresholds almost two orders of magnitude lower than those previously obtained with optical systems (Benabid 2002a). In similar experiments, the core of a few-meter long HC-PCF was filled with very low-pressure acetylene in order to observe electromagnetically induced transparency and saturable absorption for different absorption lines of the gas, with the latter being pumped by a low power laser beam (Couny 2006b; Light 2006). Electromagnetically induced transparency has even been demonstrated in the nanowatt regime by replacing acetylene with low-pressure rubidium vapour (Ghosh 2006). Such performances open exciting prospects for all-fibre compact applications requiring a precise control of the frequency, and in particular for applications pertaining to dense wavelength division multiplexing, frequency metrology and atomic clocks.

Beyond the well-identified applications of hollow-core photonic crystal fibres which have been mentioned here, more ‘exotic’ applications of these fibres, not necessarily relying on the concept of a photonic crystal, can be envisioned. Examples of such applications include:

– the realization of gas lasers from holey fibres,

– the realization of gas sensors from coiled-up holey fibres, allowing simultaneously the gas flow and the injection of a light beam. Here again, the use of hollow-core PCFs would result in a considerable increase of the effective length of interaction between light and the gas. Such a device would be similar to the high quality factor Fabry-Perot cavities currently in use for this type of detection, with the additional advantage of providing a robust and relatively easy optical alignment.

Before leaving the subject of HC-PCFs, let us finally mention an application which, as futuristic as it might seem, is quite seducing nonetheless. The possibility of using light for trapping objects of small dimensions, ranging from atoms to microspheres, has been recognized for already quite a long time: not only is this trapping mechanism involved in the cooling of atoms using laser beams, but it is also play a role in the concept of the optical tweezers which are currently in use, for instance in biology. Similarly, we may envision the possibility of a hollow-core photonic crystal fibre that could be used indifferently for the guiding of light and for the transfer of atoms or small nanoparticles. Such a fibre would present the same advantages for the transfer of matter as for the transfer of light, i.e. the possibility of controlling at will the direction, orientation and curvature of the matter or light beam. The realization of such highly localized and easily movable 'matter sprinklers' would be an unexpected and quite interesting application of photonic crystals to a bottom-up approach to the fabrication of nanostructures. This idea is now supported by convincing experiments where hollow-core photonic crystal fibres were used for ensuring the propagation of small spheres with a size of a few micrometers using pump beams with relatively low power injected at the end of the fibre (Benabid 2002b). Further, it has been shown that the side illumination of HC-PCFs is efficient enough for the guiding of cold atoms in the core (Fatemi 2005). Side illumination offers a number of advantages compared to end excitation. These advantages include the decoupling of the injection device from the vacuum chamber and the possibility of launching light at multiple locations along the fibre.

Let us finally illustrate the interest of the in-fibre spectral filtering which occurs in solid-core photonic bandgap fibres. Since the core of the fibre is solid, it can be doped with active ions such as Yb^{3+} ions in order to achieve laser emission in the near infrared. Conventional Yb-doped fibres, whose emission process is based on a 3-level system with a pump excitation at $\lambda = 915$ nm, produce a laser emission at $\lambda = 980$ nm which itself can be used for pumping Er-doped amplifiers. However, the reabsorption of the emitted light and its conversion into a parasitic amplified spontaneous emission (ASE) at $\lambda = 1030$ nm dramatically limits the efficiency of conventional Yb-doped fibre lasers. In order to eliminate ASE along the fibre, it is therefore necessary to introduce spectrally selective loss around $\lambda = 1030$ nm. A very elegant solution to this problem would consist in using a SC-PBG Yb-doped fibre with a cladding whose photonic band gap is chosen in such a way as to forbid the propagation of the ASE (1030 nm) while allowing the propagation of the pump emission (915 nm) and laser emission (980 nm). The first results reported on such a spectrally selective laser are promising (Bigot 2007).

12 Three-Dimensional Structures in Optics

Three-dimensional photonic crystals were at the origin of the very notion of photonic crystal, and to a large extent they still represent the 'holy Grail' at which all experimental realizations are directed. The reason lies in the fact that only photonic crystals presenting a three-dimensional periodicity are capable of providing an omnidirectional band gap with the complete suppression of the radiative states in the corresponding frequency range. In turn, controlling the density of radiative states would allow to achieve an absolute control of the radiative properties of the light emitters incorporated inside crystals. Different consequences are expected to follow from the realization of this objective. Examples of potential applications are the complete inhibition of the spontaneous emission, the localization of light over defects acting as zero-dimensional microcavities, the three-dimensional guiding of light or the realization of band-edge lasers based on strictly periodic bulk photonic crystals, described in Section 10.3.

The realization of three-dimensional photonic crystals at optical wavelengths represents a tremendous challenge. Thus far, none of the technologies developed for the fabrication of three-dimensional photonic crystals can be considered to be either predominant or completely established, due of course to the difficulty inherent to the structuring of matter at sub-μm scales. Reaching the same degree of technological mastery as in the microwave region is still a remote prospect for the fabrication of three-dimensional photonic crystals in the optical region. Indeed, the first three-dimensional structures were realized as early as the beginnings of the nineties in the field of microwaves, leading to the considerable development of the studies devoted to photonic crystals which has been taking place ever since (Yablonovich 1991a).

This chapter begins with a review of the three-dimensional structures which have been suggested so far for application to the optical region. While some of these structures have already been fabricated with currently available technological means, other structures presented in the course of this chapter seem to be realizable, but they have not been demonstrated yet. For this reason, the specific aspects associated with the fabrication of three-dimensional crystals will be addressed only in the second part of this chapter. Finally, this chapter concludes with a description of different experiments intended at exploiting the properties of three-dimensional crystals, both in the infrared range (metallic structures) and in the visible range (opals).

12.1 Geometrical Configurations proposed for Three-Dimensional Structures

The choice of a specific geometry for a three-dimensional structure is always more or less in direct relation with the fabrication techniques which are available to an experimentalist. Nevertheless, two general classes of structures can be distinguished, depending on whether an omnidirectional photonic band gap is desired or whether partially forbidden bands are considered to be enough, provided however that the three-dimensional periodicity of the photonic crystal is preserved. As has been seen in the first part of this book, band gaps of lowest order are often the largest and the most robust ones. In contrast, high-order gaps are much more sensitive to the disorder of the crystal, and this fact is of particular significance when searching for an omnidirectional band gap. The irregularities in the structure that result from the fabrication process can never be entirely neglected when working at the very boundaries of technological possibilities, as is the case in the optical region.

12.1.1 Structures with Omnidirectional Photonic Band Gaps

It would be reasonable to assume that a lattice with a Brillouin zone as close as possible to a sphere is the most likely to exhibit an omnidirectional band gap of low order. However, numerical tests conducted on structures presenting a fcc lattice geometry have revealed that the shape of the Brillouin zone is not the only factor which determines the presence of omnidirectional photonic band gaps, and that the symmetry of the structure also exerts a decisive influence in this respect. The first structure exhibiting such an omnidirectional photonic band gap was correctly predicted by Ho, Chan and Soukoulis in 1990 (Ho 1990). This structure consisted of dielectric spheres placed according to a diamond crystalline lattice. For such a structure, complete band gaps may exist both for high-index dielectric spheres in the air and for air spheres in a dielectric medium. This requires of course that both the size of the spheres and the dielectric constants be adequately chosen. A more detailed explanation of the necessity of breaking the symmetry of the fcc lattice (with a single ‘atom’ per unit cell) in order to open a complete band gap can be found in (Ho 1990) and in (Yablonovitch 1994).

However, the diamond lattice structure consisting of spherical ‘atoms’ is quite difficult to realize at the sub-μm scale. These difficulties led E. Yablonovitch to propose the now famous ‘Yablonovite’, which was briefly introduced in the preface to this book (Fig. 12.1). In this structure, the fcc geometry with two atoms per unit cell is reproduced by drilling three series of holes inside a block of dielectric material. The directions of the hole axes reproduce the <110>, <101> and <011> directions of the diamond lattice, while the surface of the crystal corresponds to the <111> crystal plane. The symmetry of such a structure is thus similar to that of the diamond lattice, and its omnidirectional photonic band gap, located between

the second and third permitted bands, presents a relatively low sensitivity to the irregularities resulting from the fabrication.

In the wake of the first demonstration of 'Yablonovites' in the microwave region (Yablonovitch 1991a), several more or less successful efforts were directed at the realization of 'Yablonovites' in the optical wavelength region.

A different type of structure exhibiting the same symmetry as the diamond lattice is the so-called 'woodpile' or 'layer-by-layer' structure. Either name refers to the fabrication scheme itself. Such structures have been advanced and actually implemented for the realization of three-dimensional crystals exhibiting complete band gaps in the optical region. The details of the fabrication of these structures will be exposed later in the course of this chapter.

It might be mentioned here that the same layer-by-layer method has also been applied for the realization of simple cubic structures. Provided that the index contrast is high enough, such a structure exhibits a complete band gap for a high air-filling factor. This band gap is relatively narrow, albeit of low order (Lin 2001b; Zavieh 1999).

The continuous advances occurring in the field of micro and nano-fabrication lead us to anticipate that periodic three-dimensional structures with a very high degree of precision will be realized within a few years. A few structures with higher-order omnidirectional band gaps have already been suggested for fabrication, and some of them have been actually realized. However, the presence of omnidirectional band gaps in these structures has not been formally confirmed thus far by experimental measurements.

It has thus been predicted that, under certain conditions, fcc structures may present an omnidirectional gap between the eight and the ninth permitted bands. This leads to believe that artificial opals could provide complete higher-order gaps, provided however that their regularity can be perfectly mastered.

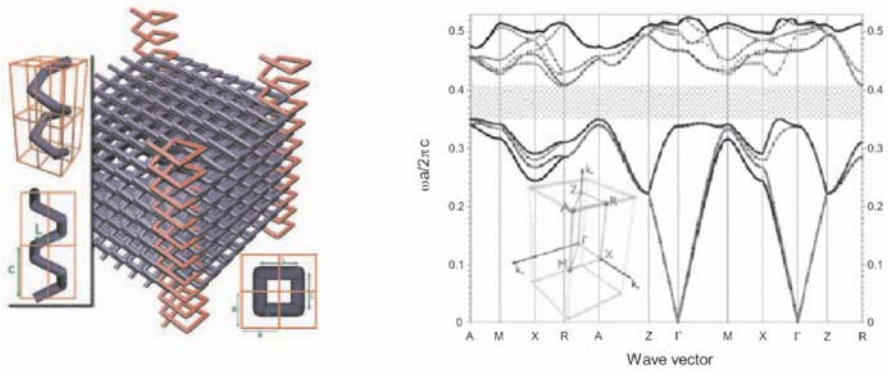

Fig. 12.1. *Left.* Schematic view of a chiral structure. *Right*. Calculated band diagram (Toader 2001)

S. John *et al* have for their part suggested chiral structures consisting of square spirals placed according to a simple tetragonal lattice, represented here in Fig. 12.1 (Toader 2001). A complete forbidden band with a 15 percent relative width was predicted for an index contrast equivalent to the index contrast between a semiconductor and the air.

Among the other structures from this 'exotic' family, the 'woven' photonic crystal suggested by Y.-C. Tsai *et al* may also be mentioned (Tsai 1999). This crystal is actually a special form of the woodpile (or layer-by-layer) structure with the difference however that the dielectric fibres forming the different layers are interwoven rather than being contained within their respective planes. In much the same way as for the original woodpile structure, two successive layers are shifted from a quarter of the horizontal period in the horizontal plane. This method requires that fibres with two different dielectric constants be used in order to cancel the C4 symmetry which prevents complete band gaps from being opened up.

Metallic photonic crystals are a special case among the variety of three-dimensional photonic crystals. Due to the strong interaction, described in Chapter 4, between electromagnetic waves and metallic lattices, the existence of complete band gaps is only to a very limited extent determined by the symmetry of the lattice. In certain cases, this interaction can even be strong enough to compensate for the lack of symmetry of the crystal. It has been seen already that resorting to metallic crystals is a solution that should be privileged in the field of microwaves. More specifically, metallic crystals realized from connected elements present a complete photonic band gap which extends from the zero-frequency (see Section 4.2 in Chapter 4), and the periodicity as well as the size of the constitutive elements of metallic crystals can be significantly smaller than the wavelength at the gap edge. While these small dimensions with respect to the wavelength are an advantage in the microwave region, they may however represent a drawback in the optical region due to the present limits of modern nano-fabrication techniques. In this context, the interest of metals rather lies in the fact that they exhibit a relatively high dispersion of their dielectric constant in the visible wavelength range, a property which in principle could be exploited for realizing new optical EM structures.

As has been described in Section 4.1, the dielectric constant of metals can be approximated by using the Drude dielectric function of the type $\varepsilon_0[1-\omega_p^2/\omega^2]$, and for some metals the plasmon frequency ω_p lies at the boundary between the UV and visible regions. The excitation of plasmons entails relatively high optical losses. The amount of these losses might be too high for allowing the realization of optical microcavities with a high Q-factor, but it is low enough for the realization of efficient passband optical filters.

Before turning in Section 12.1.2 to the description of incomplete bandgap three-dimensional structures, the existence of omni-directional optical reflectors not requiring the use of three-dimensional photonic crystals deserves mention. Thus, dielectric multilayer stacks (one-dimensional Bragg mirrors) with a high index contrast can be realized, where the light arriving from a low-index medium, for instance the air, will be reflected by the structure at any incidence angle and for any polarization of the field (Winn 1998; Chigrin 1999). The stacks do not

actually present a complete band gap. However, the incident wave is not coupled to the propagation modes of the crystal, but only to a multilayer mode whose propagation direction is contained within the light cone determined by the critical angle. Due to the existence of this critical angle, a partial band gap (for directions contained within the light cone) is enough for reflecting all incident rays.

Finally, as far as omnidirectional band gaps are concerned, this review would not be complete if it did not mention the fact that studies similar to those presented on three-dimensional photonic crystals have been conducted on acoustic three-dimensional crystals. Of course, certain strong analogies exist between these two types of waves, as well as between their propagation modes (Sigalas 1992). Thus, fundamental complete band gaps for fcc lattices have been predicted in the case of elastic waves (Suzuki 1998). The specificity of acoustic crystals lies in the physical existence of longitudinal acoustic waves.

12.1.2 Incomplete Band Gap Three-Dimensional Structures

It might sometimes be interesting to employ three-dimensional periodic structures in situations where omnidirectional gaps are not necessary. This is the case, for instance, for bulk band edge three-dimensional lasers (Enoch 2002a; Sakoda 1999b). A different example is given by the photonic crystal used for achieving phase matching in a frequency doubler (see Chapter 8). Such situations tend for a large part to reduce the constraints imposed upon the geometry of the structures to be realized. In practice, this opens the possibility of using three-dimensional structures created by self-organization, as none of these structures exhibit omnidirectional band gaps of low order.

The idea of realizing nanoscopic structures through self-organization is quite seducing. At the risk of oversimplifying, the underlying idea is that the structure can be realized simply by placing all necessary constituent elements in a test tube and by shaking the latter. The apparent simplicity of this method, combined with its intrinsic parallelism, explains the intense research activity surrounding self-organized structures.

In the case of photonic crystals, research has been concerned for the most part with artificial opals created through the sedimentation of sub-mm monodisperse spheres of latex or silica. The lattices thus obtained exhibit the spatial configuration corresponding to the minimal potential energy, i.e. an fcc- type geometry. As has been mentioned already, fcc lattices may only present complete photonic band gaps of high-order, and under the condition that a high index contrast exists. These high-order bands are extremely sensitive to the irregularities resulting from the fabrication process, and even low dispersions of the size of the spheres, down to 2 percent (Li 2000) or of the air-filling factor may cause this gap to vanish.

A different, albeit very specific, example of a self-organized three-dimensional structure is the structure obtained through an autocloning process. This method proceeds from a pre-structured substrate, upon which alternated layers of different dielectric materials are successively deposited by RF sputtering, as is schematically described in Fig. 12.2. The deposition of each layer is balanced with its si-

multaneous etching by the sputtered ions. Under actual autocloning conditions, the topology of each deposited layer reproduces the shape of the underlying substrate. As a consequence, the vertical periodicity of the three-dimensional crystal is determined by the alternation of the dielectric layers, while its horizontal periodicity is determined by the initial structuring of the substrate. However, the resulting three-dimensional structures do not present the diamond lattice symmetry, and therefore they cannot possess complete gaps of low order. The possibility of achieving complete gaps through the combination of auto-cloning and a subsequent plasma etch of vertical holes, as represented here in Fig. 12.2, has been theoretically investigated (Notomi 2000b), but the experimental demonstration of this method remains to be established.

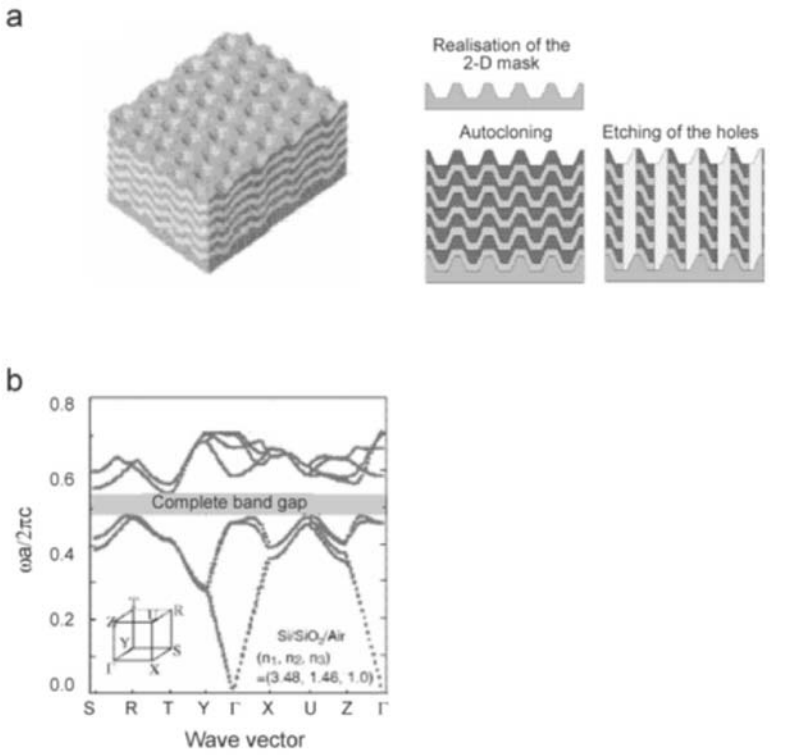

Fig. 12.2. ***a.*** *Left.* Schematic view of the hexagonal crystal with alternate dielectric layers, fabricated using the autocloning technique. *Middle and right.* Method proposed for the fabrication of an autocloned structure with a complete photonic band gap: the autocloning process is followed by the plasma etching of vertical holes (Notomi 2000b) *b.* Band diagram calculated for a structure with a complete band gap: each vertical period is formed by a Si/SiO_2 bilayer while the air holes are organized according to a triangular lattice

As a summary, it may be concluded that the structures which can be obtained by self-organization methods do not present much diversity, and that the insertion of intentional defects in these structures is almost impossible. The major advantage of self-organization techniques is to be found in the fact that they allow the realization of three-dimensional photonic crystals with a relatively large size. Nevertheless, in order to extend to the realization of very regular structures, this method will need to achieve a higher degree of maturity.

12.2 Examples of Fabrication Processes and Realizations of Three-Dimensional Photonic Crystals in the Optical Region

12.2.1 Complete Band Gap Structures

Yablonovites

A considerable technological effort has been devoted worldwide to the realization of Yablonovites adapted to the near-infrared and visible ranges. This was motivated by the correct assumption that Yablonovites could be easily realized using existing micro-fabrication methods, and, most of all, that their very design could facilitate the realization of three-dimensional structures.

The first attempts in this direction were conducted by etching bulk GaAs using the chemically assisted ion beam etching (CAIBE) method. This technique allows indeed the etching of materials at arbitrary angles with respect to the surface of the sample. However, these attempts did not succeed insofar as they did not permit the realization of Yablonovites with a depth larger than three vertical periods (Cheng 1996b). Indeed, the etching depth was limited by resistance to etching of the mask which defines the geometry of the whole structure. As has been previously described, the realization of a Yablonovite requires that three series of holes be etched at different angles through the same mask. In this respect, the maximal three period depth allowed by this method was not sufficient for the development of applications, and no significant advance can be expected from this technology in the near future.

An alternative approach for the fabrication of Yablonovites relies on the use of a polymer periodic mould structured like a Yablonovite. This mould is then filled with a high-index material before being finally eliminated: a high-index Yablonovite structure can thus be obtained. Sub-μm moulds with a thickness of several periods were fabricated by X-ray lithography using a variant of the LIGA process (Ehrfeld 1998), originally been developed for the fabrication of structures, either periodic or not, with a depth of several hundred microns. In practice, a layer of polymer resist with a thickness of the order of 10 μm is exposed to a collimated soft X-ray beam along the three crystalline directions <110>, <101> and <011>.

Each of these directions forms an angle of 35°26 with respect to the normal to the surface of the sample (crystal plane <111>). Exposure is achieved through a mask opaque to X-rays, inside which a triangular grid of holes has been defined beforehand. Only the regions of the resist which are exposed to the X-rays become soluble in an appropriate solvent. After the dissolution of these regions, the mould can be filled, either with a high-index dielectric material or with a metal. Fig. 12.3 presents an example of such a Yablonovite realized by X-ray lithography (Cuisin 2002): the structure considered here has a 1.2 μm period. Six periods in the vertical direction are visible on the SEM image of the cleaved sample, represented in the upper left of the figure. The polymer Yablonovite was then filled with copper using an electro-deposition technique, as can be seen from the lower micrographs in Fig. 12.3.

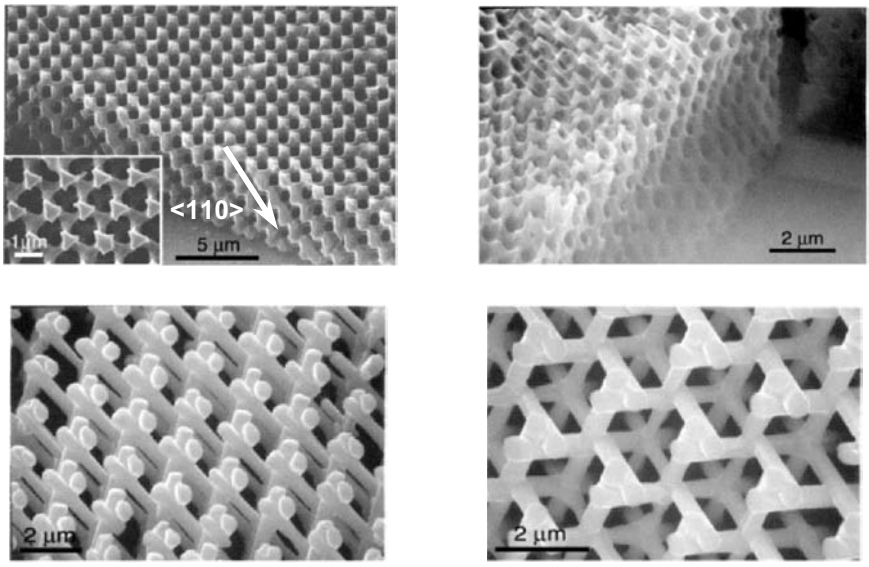

Fig. 12.3. Scanning electron microscope (SEM) images of Yablonovites fabricated by X-ray lithography (Cuisin 2002). *Top (left and right).* Views of a Yablonovite mould formed from a polymethyl-methacrylate (PMMA) resist, a polymer sensitive to X-rays. The insert in the left-hand figure represents the upper surface of the Yablonovite mould: the imperfect contact between the mask and the PMMA resist has resulted here in the formation of a slightly distorted hexagonal lattice. *Bottom (left and right).* Micrographs of the copper Yablonovite obtained by dissolving the mould after filling it with PMMA by copper electrodeposition

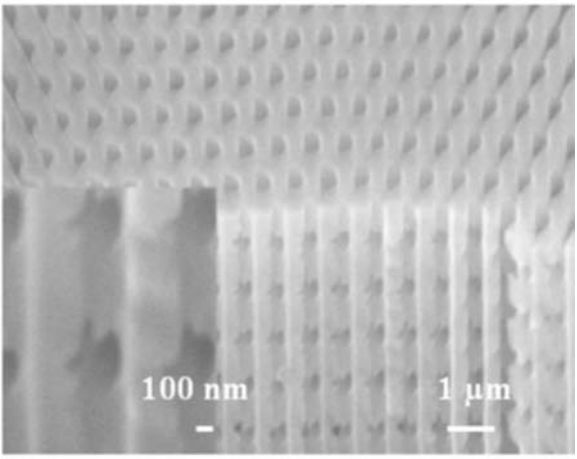

Fig. 12.4. Micrograph of a Yablonovite directly fabricated from silicon by combining a photo-electrochemical etching (macroporous silicon etching) with a focused ion beam (FIB) etching (Chelnokov 2000). The left side of the image displays an enlarged view of the holes which emerge laterally from the silicon substrate

Five period-thick yablonovite structures have also been fabricated directly from bulk silicon by combining a photo-electrochemical etching (macroporous silicon etching) with a focused ion beam (FIB) etching (Chelnokov 2000). In the example displayed in Fig. 12.4, the first series of holes drilled in the silicon, i.e. the vertical holes, are arranged in a lattice of macropores of the same type as the lattice presented in Section 9.5. The two other series of holes of the Yablonovite are obtained by an oblique FIB drilling at the angle of 51° instead of 60° with respect to the normal of the sample: the Yablonovite structure thus obtained is therefore slightly distorted. A complete photonic band gap was nonetheless reported around the 3 μm wavelength under these conditions (Chelnokov 2000). It should be pointed out that the FIB drilling is performed sequentially, i.e. that only one hole is drilled at a time. As a consequence, this technology is not well-suited to the realization of large crystals or for the realization of a large number of crystals.

Woodpile Structures

Modern microfabrication technologies are for the most part based on thin-film processes. As an example, the so-called 'woodpile' structures, whose geometry has been described in Section 12.1.1, are obtained by a standard thin-film processing. More precisely, the semiconductor layers are deposited one by one and dry-etched so as to form a periodic lattice of horizontal rods. The rods of two suc-

cessive layers are perpendicular with respect to one another, thereby forming a square grid, as can be seen in Fig. 12.5. Two successive grids are shifted with respect to one another along the diagonal of the square motif by half the diagonal. A set of two grids, i.e. four adjacent layers, constitutes a period of a crystal where the intersections of the rods reproduce the distribution of atoms inside the diamond lattice. It is apparent that the fabrication of a woodpile structure is quite a complicated task, and that it requires a sub-μm precision processing. No less than seventeen technological steps are required in order to obtain a single crystal period using the standard techniques of silicon microelectronics. An example of a structure realized with this method can be seen in the right-hand part of Fig. 12.5 (Fleming 1999; Lin 1999a). In spite of this complexity, structures adapted to the 1.5 μm wavelength range and with a three period thickness have been realized in silicon and in III-V materials (GaAs and InP) (Noda 1999), as well as in chalcogenide glass (Feigel 2000). Since the layers of the crystal are structured one after another, the insertion of waveguides or of microcavities is a relatively straightforward process. Three-dimensional microcavities (Lin 1999b), as well as linear waveguides with a 90 degree bend (Noda 2002b), have been experimentally demonstrated. Single-mode waveguide configurations with woodpile structures have also been proposed on the basis of numerical simulations (Kawashima 2006). All measurements of the optical properties of structures without defects have been found to be in a very good agreement with theoretical predictions. There appear to be numerous perspectives for woodpile structures, especially in view of the rapid advances occurring continuously in the field of planar micro-fabrication processes, which lead to increasingly sophisticated realizations.

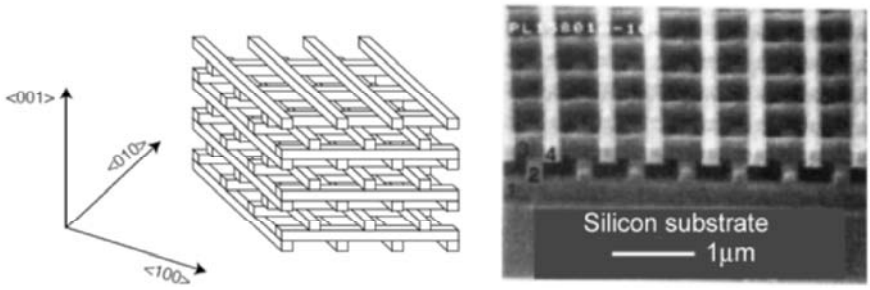

Fig. 12.5. *Left.* Schematic view of a 'woodpile' structure. *Right.* Scanning electron microscope image of a 'woodpile' structure fabricated using the techniques of silicon microelectronics (Fleming 1999). The structure considered here consists of four layers, which together constitute the period of a photonic crystal reproducing the diamond lattice. The photonic band gap is located at around 1.5 μm

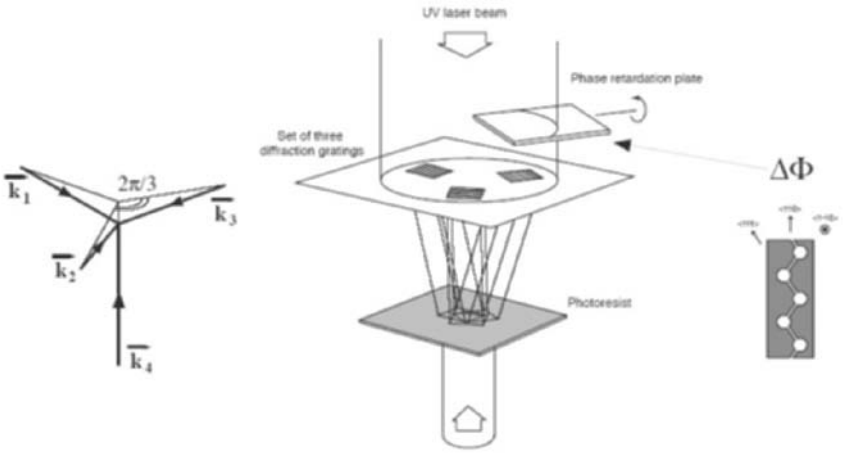

Fig. 12.6. *Middle.* Experimental arrangement of four laser beams used for the realization of a fcc lattice by interferential construction inside a UV photoresist (Chelnokov 1999). *Left.* Schematic representation of the wave vectors associated with the different beams. *Right.* Translation of the interferential patterns using a phase retardation plate

Other Fabrication Methods

Several other methods have been suggested for the direct fabrication of 'diamond' lattices. Among these different methods, which may appear more or less unusual, multiple-beam interference laser holography and two-photon absorption lithography are of a particular interest.

Laser Holography. Periodic three-dimensional structures can be obtained by 'freezing' into a photosensitive resist layer with a large thickness the interference patterns of at least four laser beams operating at the same wavelength, typically in the UV range (Campbell 2000; Shoji 2000). Depending on the precise nature of the resist, the patterns are then developed by dissolving either the weakly or the strongly irradiated regions. The angles, polarizations and respective phases of the laser beams are defined in such a way as to obtain the desired spatial symmetry in the final interference lattice (Chelnokov 1999; Mei 1995). The arrangement displayed in Fig. 12.6 represents an experimental configuration proposed for the fabrication of the diamond lattice (Chelnokov 1999). The use of a phase retardation plate across the path of one of the beams permits to vary the position of the interference patterns inside the resist layer, which makes possible the construction of the fcc structure with two atoms per unit cell. Thanks to the improved contrast in the development process of currently available photoresists, configurations close

to that of Fig. 12.6 have been successfully used for the fabrication of three-dimensional holographic crystals from polymers with submicrometric patterns and partial band gaps at near-infrared wavelengths (Kondo 2006; Scrimgeour 2006). Further, additionally combining this holographic method with infilling techniques, for instance atomic layer deposition, is expected to allow the realization of very large, albeit strictly periodic (i.e. without intentional defects) photonic crystals with three-dimensional bandgaps.

Two-Photon Absorption Photolithography. This method represents another example of the use of a laser light for the realization of three-dimensional photonic crystals. Rapid photo-prototyping is already a well-developed technology, which consists in using a strongly focused laser beam for writing, point by point and layer by layer, the desired patterns onto a thick layer of photo-polymerizing resist. Taking into account the laser wavelength (in the blue) typically used for the laser and the limited numerical aperture of the focusing optics, the minimal size for the patterns must be equal to at least 1 μm. For the fabrication of photonic crystals, this resolution has been significantly improved by using a two-photon absorption process. In this case, the wavelength at which the writing laser operates is long enough to prevent any direct absorption by the resist, but it must also be chosen in such a way that the second harmonic of the emission of the laser is located inside the absorption band of the resist, which typically is in the blue or in the near-UV. Under these conditions, the illumination of the resist by the laser results in its local polymerization. Since the efficiency of the two-photon process is proportional to the square of the local photon flux, the intensity of the laser must be increased, yet without causing an excessive heating of the resist. An infrared Ti : Saphire laser in mode-locking regime is used for this purpose. Mode-locked sub-picosecond optical pulses are generated at the $\lambda \sim 800$ nm wavelength, while the two-photon absorption occurs at half this wavelength ($\lambda \sim 400$ nm). The laser pulses present a high optical peak power, but a low average power, which is perfectly suited to laser writing. The two-photon absorption process and the subsequent polymerization of the resist only occur in the close vicinity of the focal point of the writing beam, where the photon flux is maximal. The patterns are created by moving the focal point along the three axes. The non-polymerized resist is then removed using an appropriate solvent.

Periodic as well as aperiodic three-dimensional structures with pattern sizes of less than 1 μm have thus been realized from polymer. Optical transmission spectra measured on the periodic structures represented in Fig. 12.7 have revealed the presence of forbidden photonic bands at wavelengths close to 4 μm (Sun 1999). In spite of the sequential writing mode used there, which results in an actual decrease of the resolution, this technique holds promise for telecommunication wavelengths in the 1.3-1.5 μm ranges (Deubel 2004). A similar, albeit somewhat different technique consists in using conformable phase masks in conjunction with transparent photopolymers and two-photon effects, thereby allowing the formation of complex, but well-defined three-dimensional nanostructures in a single exposure step (Jeon 2006). In principle, all these different types of polymer structures can be used as moulds for the deposition of a material with high index contrast.

12.2.2 Incomplete Band Gap Structures

As indicated, the present section will be mainly devoted to the consideration of three-dimensional photonic crystals created by self-organization. While self-organization brings a number of distinctive advantages, its lack of flexibility explains that only three-dimensional photonic crystals with partial band gaps have thus far been obtained with this method.

Artificial Opals

Much in the same way as atoms organise into solid-state crystals, uniform latex or silica spheres released in a colloidal solution organise into fcc lattices. An ordered sedimentation can be achieved through the use of a gravitational field, for instance in a centrifuge, by causing very slowly the solvent of the colloidal solution to evaporate, or by filtering through microporous substrates the solution where the spheres are contained. The orientation of the 'crystallized' lattice of spheres can be forced by prestructuring the substrate where the sedimentation takes place. The structures composed of self-organized spheres thus obtained are referred to as artificial opals, since their microscopic structure, which can be seen in Fig. 12.8, reproduces the structure of natural opals.

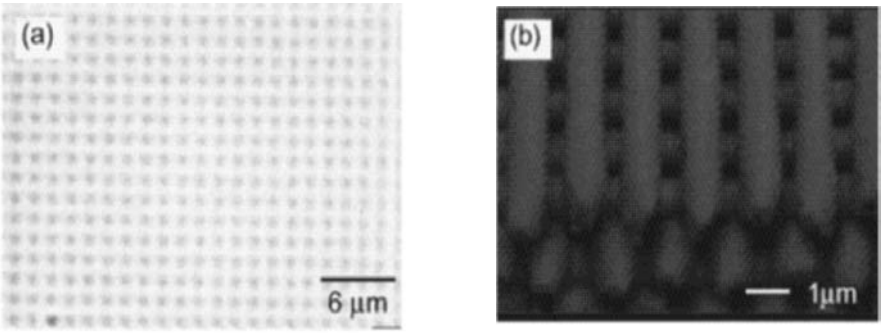

Fig. 12.7. *a.* Top view of a diamond-like structure fabricated by two-photon absorption photolithography (Sun 1999). The horizontal period of the lattice is 1.4 μm. *b.* Cross-section view of the same structure, obtained by scanning electron microscopy

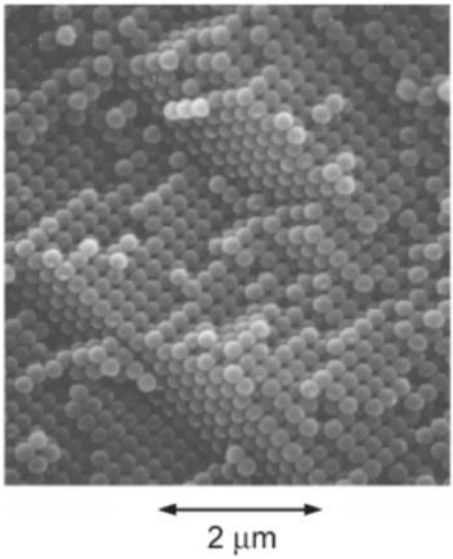

Fig. 12.8. Micrograph of a direct opal (Romanov 1997). The cleaved facet of the structure reveals the presence both of ensembles of spheres with a square symmetry, associated with the <100> planes, and of ensembles of spheres with an hexagonal symmetry, associated with the <111> planes

Although the spheres actually tend to 'crystallize' inside the lattice with the minimal potential energy, i.e. inside the fcc lattice, the energy of the fcc lattice is unfortunately very close to the energy of the hexagonal close packed (hcp) lattice (Wood 1997). As a consequence, artificial opals generally present a significant concentration of stacking defects. This often results in perturbations affecting the optical characteristics of photonic crystals based on artificial opals. However, the uniformity of the structures realized has been constantly improving, due to the use either of pre-structured substrates (Braun 2001) or of a high-pressure gaseous flux during sedimentation (Xia 1999).

Recent studies seem to open new perspectives for self-organized structures through the use of spheres of different types or different sizes (Jiang 2001). The use of non-spherical particles for the realization of self-organized structures has also be considered (Snoeks 2001).

The optical index of the silica or latex spheres from which artificial opals are formed is close to 1.5. In order to increase the index contrast, the voids between the spheres can be filled in with a higher index material. The initial opal matrix is then eliminated, either by chemical dissolution or by thermal processing (calcination). The resulting structure is referred to as an inverse opal. An example of such a structure is presented in Fig. 12.9. Like direct opals, the symmetry of inverse opals remains the same as that of an fcc lattice, and as a consequence, they do not exhibit complete band gaps. It has been theoretically demonstrated that, in the case

of inverse opals with a strong index contrast (i.e. > 2.8) a complete band gap could exist between the eight and the ninth permitted bands. Unfortunately, the existence of such a high-order forbidden band can be ruined by the presence of even the slightest local variations in the parameters of the crystal.

To this day, inverse opals have been fabricated from such various materials as selenium (Braun 2001), vanadium oxide (Golubev 2001), silicon (Blanco 2000), titanium oxide (Holland 1998), indium phosphide (Romanov 1997), cadmium selenide (Vlasov 1999), II-VI semiconductors (Braun 1999) or tin sulfide SnS_2 (Romanov 2001). It remains, however, to be demonstrated that these structures are really capable of providing complete band gaps.

Since the possibility exists of inserting different types of materials in the voids extending between the spheres, artificial opals can be used as a testbed for the eventual development of controllable optical photonic crystals. It has thus been suggested that the control of the photonic band gaps could be achieved, either by varying the temperature, or by applying an external electrical field (Bush 1999; Yoshino 1999). Artificial silicon-based opals impregnated with liquid crystals have been fabricated for this purpose. Another approach would consist in using the 'metal-semiconductor' phase transition which occurs in vanadium oxide at temperatures close to room temperature (Golubev 2001).

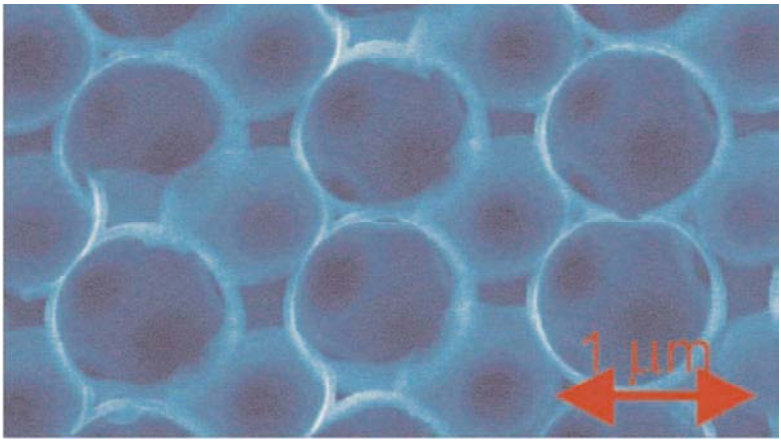

Fig. 12.9. Scanning electron microscope image of the cleaved <110> facet of an inverse opal formed from silicon (website: http://www.icmm.csic.es/cefe/). The direct opal used as mould was filled by chemical vapour deposition (CVD) of silicon. The image shows a lattice of air spheres surrounded by thin silicon shells, a structure which actually is inherited from the fcc lattice of the direct opal. Adjacent spheres are connected to one another by small circular windows resulting from a sintering process

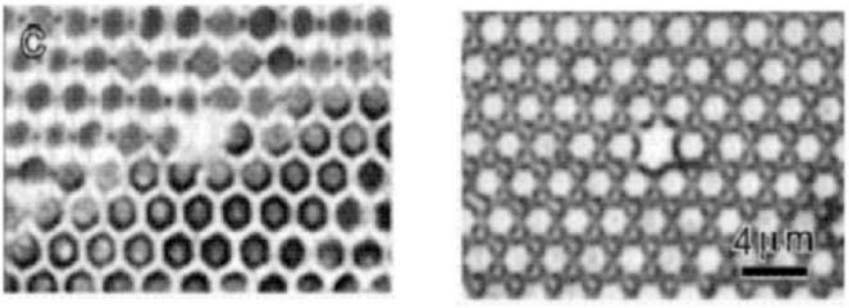

Fig. 12.10. Triangular lattice with a 2 μm period, formed by air bubbles inside a polystyrene layer (Srinivasarao 2001). *Left*. Structure observed in reflection. *Right*. Structure observed in transmission. In both cases a krypton laser (568 nm) was used as the illumination source. The defects of the lattice are also clearly visible

It has been previously emphasized that self-organization processes were not well-suited to the incorporation of defects during the sedimentation of the spheres. Some authors have suggested to overcome this difficulty by using two-photon absorption lithography (Lee 2002), a method presented earlier in Section 12.2.1. Three-dimensional optical waveguides were thus created inside an inverse opal by injecting a photosensitive polymer inside the opal before locally polymerizing it by means of a strongly focused IR laser beam. A minimal waveguide width of 1.5 μm was achieved, with the boundaries of the waveguides being defined with a precision of the order of 100 nm.

As a summary, the use of colloidal crystals as three-dimensional photonic crystals is reaching a higher degree of maturity, and structures obtained with this method are being constantly improved as regards both their size and their uniformity. The wavelengths of the band gaps extend over both the visible and IR regions. The index contrast can be further enhanced by the fabrication of inverse opals, a technique which is becoming increasingly reliable, by using for example the so-called atomic layer deposition technique (King 2005). Artificial opals allow rapid advances in the experimental investigation of different aspects associated with three-dimensional photonic crystals in the optical region. However, the problem of stacking defects will need to be addressed before this technology can be definitively considered as having reached the same degree of maturity as traditional lithography techniques.

Let us finally mention the growing number of more ‘exotic’ methods which have been developed for the fabrication of three-dimensional structures by self-organization. An example of such a method is the insertion of uniform air bubbles inside a polystyrene layer for the realization of the original structure represented in Fig. 12.10 (Srinivasarao 2001). The existence of photonic band gaps in the infrared region was demonstrated for this structure. Another example, which has potential applications in the field of microwaves, is the realization of periodic three-

dimensional lattices using magnetic particles (Saado 2001). Finally, three-dimensional 'crystals' have been obtained in dusty plasmas, i.e. in plasmas containing charged solid particles of microscopic size (Thomas 1994).

Autocloning

Suggested in 1997 by Japanese researchers (Kawakami 1997), autocloning structures can be classified either among self-organized structures or among layer-by-layer structures. This technique rests on a balance between three processes occurring simultaneously: the sputtering deposition of dielectric layers, their physical etching by ions accelerated perpendicularly to the surface, and the redeposition of neutral particles torn from the deposited layer by the accelerated ions. The subtle balance thus achieved between these three processes results in the repetition of the topology of a pre-structured growth substrate from one deposited layer to the other (Kawakami 1999). However, due to the restricted possibilities offered in the choice of the relief and materials, and more particularly to the impossibility of inserting air layers inside the structure, complete band gaps cannot be achieved with this method. As has been described earlier (Fig. 12.2), another technological step, i.e. an additional plasma etching, would be necessary in order to actually obtain a complete band gap (Notomi 2000b).

In spite of these shortcomings, autocloning was one of the first techniques which demonstrated the possibility of realizing actual devices based on three-dimensional crystal photonic crystals, even in the absence of a complete band gap. Examples of such devices are the extremely efficient polarizers and phase retardation plates fabricated with this technique (Sato 2002). Their structure can be seen in Fig. 12.11*b*. Ultra-refractivity and superprism effects have also been demonstrated using the same technology.

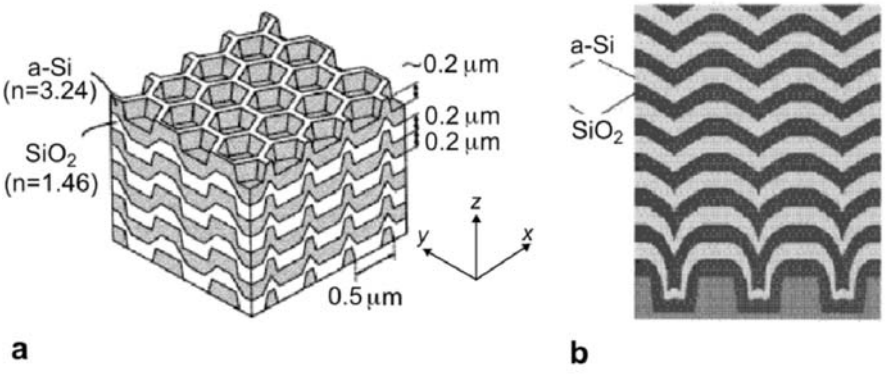

Fig. 12.11. Photonic crystal fabricated by autocloning and used either as a polarizer or as a phase retardation plate device (Sato 2002). *a.* Schematic three-dimensional view. *b.* Cross-section view of the actual crystal, obtained by scanning electron microscopy

Furthermore, autocloning can be employed for the fabrication not only of three-dimensional photonic structures and discrete devices, but of slab and channel waveguides as well, which are two key components of integrated optics (see Chapter 9). By way of example, suffice it to mention the fabrication of channel waveguides with a very low propagation loss, of the order of 0.1 dB/mm (Ohkubo 2004). This result may rightly be viewed as a milestone as regards the practical fabrication of circuits containing functional components such as chromatic dispersion equalizers and wavelength filters.

12.3 Metallic Three-Dimensional Photonic Crystals in the Optical Region

As far as applications are considered, one of the most convincing realizations of metallic three-dimensional photonic crystals in the optical region has been presented by researchers from the Sandia laboratories. An example of the structure thus obtained is represented in Fig. 12.12 (Fleming 2002). Metallic woodpile structures with a 4.2 μm period were fabricated using a method similar to that used for the realization of dielectric layer-by-layer structures. Reflection and transmission measurements performed on the structure revealed a complete photonic band gap extending from the 8 μm to the 20 μm wavelength, in agreement with theoretical predictions, while a 30 dB attenuation per elementary cell (each individual cell consisting of four planar layers) was demonstrated. The structures thus created could stand temperatures up to 1500°C, and one of the applications envisioned for these structures was the modification of the emission spectra produced by incandescent light sources. An example of such an application would be the enhancement of the emission efficiency in the visible part of the spectrum by suppressing the emission in the mid-IR wavelength range. Another potential application would be the use of these structures for improving the efficiency of thermo-electric converters.

One of the main features of the woodpile structures previously described is their small metal filling factor (28%). A smaller volume fraction of metal tends to reduce the optical losses of the crystal (Leung 1998), and a ~ 60% light transmission has been observed in the permitted bands of the structures thus fabricated (Fig. 12.12).

Artificial opals containing metal particles represent another technological approach towards the realization of three-dimensional metallic photonic crystals in the optical region. Opal crystals composed of metallic spheres disconnected from one another have thus been suggested by A. Moroz (Moroz 1999). Theoretical studies followed by experiments conducted in the microwave region (Zhang 2000) have vindicated the possibility of achieving ‘robust’ band gaps in the visible and infrared regions using periodic structures of dielectric spheres coated with metal. In fact, actual opal structures containing metals are based on dielectric opals whose voids are filled either with silver by chemical deposition (Zhou 2000) or with liquid metals by impregnation under pressure (Zakhidov 2001). The use of

silver, in spite of its tendency to oxidize in the air, is motivated by the fact that it has a reflectivity higher than 98% in the visible range, and that the corresponding plasmon wavelength is located in the near UV range. Forbidden bands have thus been actually obtained for opals filled with a very low fraction of silver (Zhou 2000). However, interpretation of the results was complicated by the fact that silver had been deposited in a polycrystalline phase.

As a summary, metallic photonic crystals can operate efficiently at wavelengths ranging from the mid-infrared to the microwave region. In the visible range, the existence of intrinsic metallic losses imposes the utilization of metals with very low metal filling factors (10-20%), for instance silver. For this very reason, it would be difficult to realize microcavities containing metals with a high quality factor in the visible range.

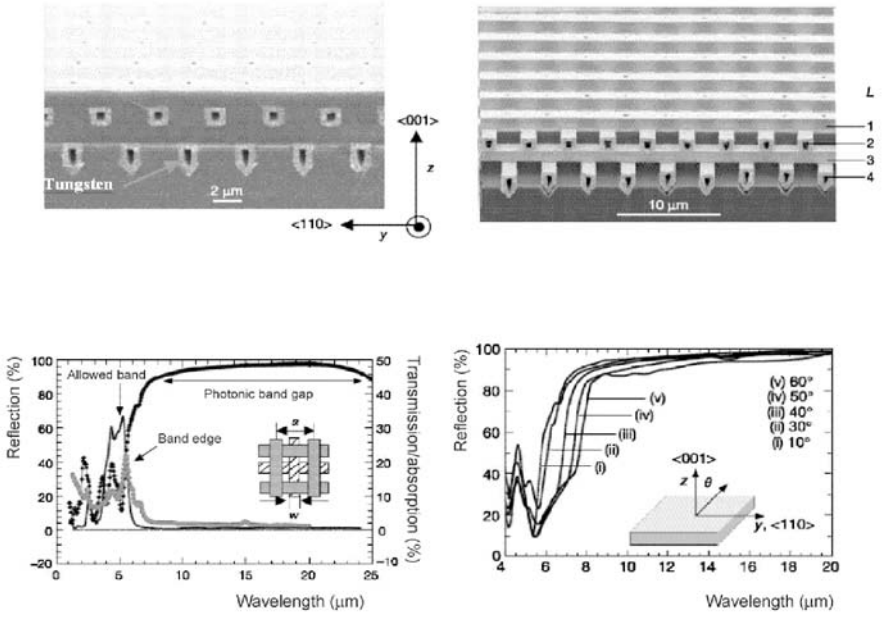

Fig. 12.12. Woodpile metallic photonic crystal formed from tungsten rods with a 4.2 μm period (Fleming 2002). *Top*. Micrographs of the fabricated structure. *Bottom (left)* Reflection and transmission (absorption) spectra measured between the ~1 and the 25 μm wavelengths *(right)* Reflection spectra measured at different incidence angles

12.4 Three-Dimensional Photonic Crystals and Light Emitters

In spite of technological difficulties, three-dimensional photonic crystals have now become a reality in the visible and near-infrared spectral regions. At least one of the proposed technologies, the woodpile or layer-by-layer structures, allows the realization of photonic crystals with complete band gaps at optical telecommunication wavelengths. It is plain, however, that research devoted to the development of micro-structuring and micro-assembling technologies must be pursued before the concept of three-dimensional photonic crystal can be successfully translated into actual applications, and before the total control of light emission can be really achieved.

It has been demonstrated that the variations in the local density of the radiative states induced by a photonic crystal should result in significant changes affecting the radiative lifetime of an emitter placed inside the crystal, especially in the case where the band gap of the crystal is complete (see Section 7.1.2). In this respect, it might be noted that, while the pioneering experiments conducted on artificial opals were not successful, a spatial redistribution of the spontaneous emission was nonetheless observed (Megens 1999; Petrov 1998). At that time, the low index contrast and the absence of any reference value for the radiative lifetime of the dye used as an internal emitter in the opal were offered as an explanation for these results. However, convincing experimental results demonstrating a reduction of the radiative lifetime by a factor of 5 were later reported in 2002 (Koenderinck 2002a, 2002b). UV lasing in artificial inverted opals was demonstrated using atomic layer deposition of amorphous/polycrystalline ZnO, although it should be noted that very high optical pumping powers were necessary for achieving such a result (Scharrer 2006).

Modifications of the thermal emission spectrum (black body radiation) were also demonstrated in the presence of three-dimensional crystals, either metallic (Fleming 2002) or dielectric (Lin 2000b). However, in view of the continuous advances occurring in the field of micro- and nano-fabrication, it is reasonable to believe that results obtained in the mid-infrared and far-infrared ranges will sooner or later find their way to the near-infrared and visible ranges. It thus appears that the objective of realizing the original scheme of a single light emitter in a three-dimensional photonic crystal microcavity is on its way to becoming a reality.

13 Microwave and Terahertz Antennas and Circuits

As has been mentioned already, the idea of achieving a control of the dielectric permittivity in the microwave region through the use of one, two or three-dimensional periodical ensembles of metallic elements is far from being a novelty. Already during the 1960s, the propagation of waves in two-dimensional periodical structures or in three-dimensional stacks of spheres had started being investigated, using at this time the concept of an artificial dielectric (Harvey 1959). However, the new interest for periodical structures in the field of microwaves has largely extended beyond these limits. First, it is quite apparent that microwave devices, which often can be more easily realized than their optical equivalents, have permitted the validation and the simpler demonstration of a series of new effects related to photonic crystals (Danglot 1998; Gadot 1997; Lourtioz 1999 ; Özbay 1996 ; Pendry 1996 ; Shelby 2001 ; Sievenpiper 1996, 1998, 1999a ; Smith 2000b ; Yablonovitch 1991a, 1991b). In the microwave region itself, the detailed study of three-dimensional structures, the analysis of periodicity defects, the combination of photonic crystals with active devices, the increase in frequencies well beyond the gigahertz, and more generally the development of modelization and characterization methods, were still in their infancy at the time of artificial dielectrics. Finally, from a practical point of view, the combination of photonic crystals with microwave circuits and antennas has led to envisioning the possibility of several important applications, even if it is too early, in view of the great variety of currently existing microwave techniques, to assess their actual potentialities. In what follows, we shall first present in Section 13.1 the different possibilities of applications of photonic crystals to antennas. We shall then discuss in Section 13.2 the specific advantages offered by metallic photonic crystals, and the possibility of making them controllable or reconfigurable by the introduction of electronic components. The first experiments involving metamaterials, described in Section 6.4 of Chapter 6, will also be mentioned in this context. We shall then consider in Section 13.3 the potential applications of ultra-compact photonic crystals for microwave circuits. The extension in frequency up to the terahertz (THz) will be illustrated in Section 13.4. Finally, in Section 13.5, we shall take one step further towards optics by presenting how certain concepts originally developed in the field of microwaves can be applied to optics, and how certain experiments based on the use of THz photonic crystals may announce the realization of similar experiments at shorter wavelengths.

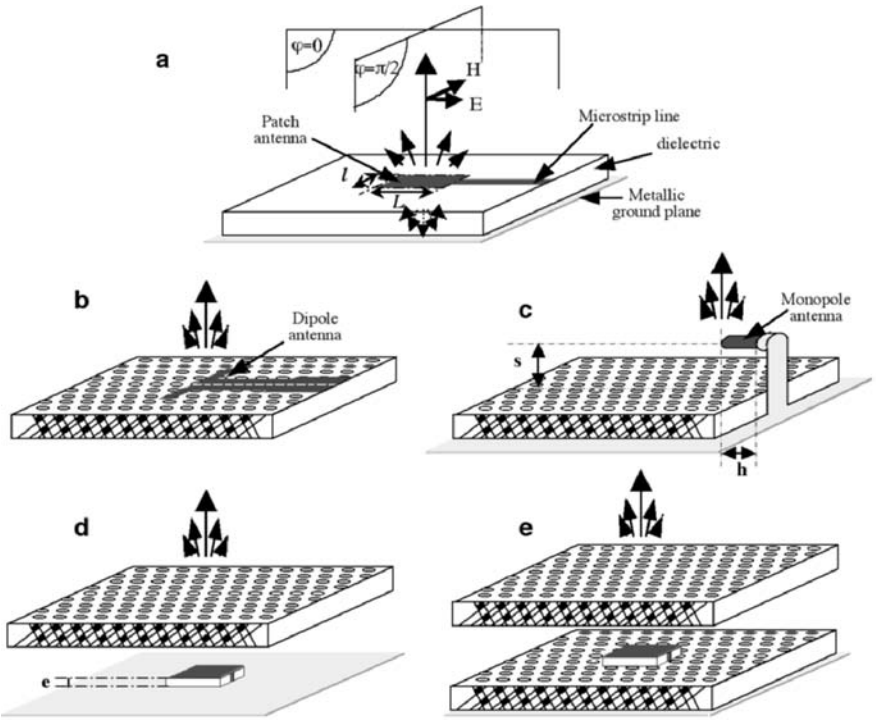

Fig. 13.1. Schematic representations of antennas and of their association with photonic crystals *a.* Simple patch antenna and definition of the E and H planes *b*. Dipole antenna on a photonic crystal substrate in a coplanar geometry *c.* Monopole antenna with a photonic crystal mirror *d.* Patch antenna with a photonic crystal radome, parallel in this case to the antenna *e.* Patch antenna with photonic crystal substrate and radome. In all these cases except *b,* the use of a ground plane, represented in grey, is made necessary. In cases *d* and *e*, the patch antenna is supplied by a coaxial cable, whereas, in case *a,* it is supplied by a microstrip line

13.1 Photonic Crystal Antennas

A great variety of antennas exist, designed for different fields of applications and for equally different performances. Among the basic forms used for antennas, one may distinguish monopole antennas, dipole antennas and patch antennas, which are often arranged in arrays. An antenna can be supplied in different ways, either simply with a coaxial cable, or more commonly by coplanar lines or microstrip

lines, which are the two main types of connections in microwave circuits. Thus, in Fig. 13.1*a* is represented the classical scheme of a patch antenna supplied by a microstrip line on a dielectric substrate, with the ground plane being mounted on the rear side. The interest in the potential use of photonic crystals in this context stemmed from the observation that an important part of the radiation emitted by antennas could be lost in dielectric substrates with a permittivity higher than that of the air. This prompted the idea that the radiation of the antenna could be totally inhibited under the plane of the antenna simply by replacing the substrate with a photonic band gap material, as represented in Fig. 13.1*b* (Brown 1993, 1994). In addition, it was believed that this would also allow suppressing the unwanted couplings occurring between antennas arrayed on the same substrate, and induced by surface waves. Later, other forms of applications of photonic structures to antennas have emerged. Photonic crystals have thus been used as antenna reflectors, as in Fig. 13.1*c* (Kesler 1996), as radomes, also referred to as superstrates, as in Fig. 13.1*d* (Thevenot 1999), or even simultaneously as substrates and supertstrates, as shown in Fig. 13.1*e* (Akalin 2001). In the following, we successively review these different forms of applications of photonic crystals to antennas.

13.1.1 Photonic-Crystal Antenna Substrates

Two different types of photonic-crystal antenna substrates have been successively developed. While the first such substrates were realized from entirely dielectric structures, high impedance surfaces were later developed from metallodielectric photonic structures (see Chapter 4 for more detail). We shall successively present these two types of antenna substrates following this order.

Dielectric Photonic-Crystal Substrates

The first experiments intended at using photonic crystals as antennas substrates were conducted by ER Brown *et al* (Brown 1993). The configuration used in these experiments is schematically represented here in Fig. 13.1*b* for a dipole antenna and a three-dimensional photonic crystal of the Yablonovite type. Contrary to conventional substrates of the kind represented in Fig. 13.1*a*, it is quite obvious that the electromagnetic field radiated by the antenna cannot propagate in the photonic crystal if the emission frequency lies in the omnidirectional band gap. It might be noted here that the radiation of an antenna is typically measured in two principal planes perpendicular to one another, as can be seen in Fig. 13.1*a*. These two planes, referred to as planes *E* and *H*, are respectively parallel to the electric and magnetic field radiated at infinity by the antenna. In addition to its frequency, different characteristics are relevant for a radiating antenna, in particular its efficiency, its directivity and the preferential polarization of its emission. In the first experiments carried out by ER Brown *et al*, a promising reduction of the energy loss occurring within the substrate itself was achieved. However, surface modes (see Section 1.4.6 in Chapter 1) remained another source of losses for the antenna,

since the presence of these modes results in parasitic lobes in the radiation diagram measured at a great distance. In principle, for any orientation of the surface of a three-dimensional crystal, a certain termination, i.e. a position of the interface between the air and the crystal inside the elementary mesh, exists for which no surface mode may propagate (Joannapoulos 1995b). In addition, a complete optimization requires that the phase be zero at the interface, in order to create an antinode of the field on the antenna. This situation is the exact opposite to what is the case with a metallic surface. Thus, in a second study in 1994, ER Brown *et al* (Brown 1994) succeeded in demonstrating that the radiation of a dipole antenna placed on a Yablonovite substrate, as represented in Fig.13.1*b*, could be optimized for certain terminations of the Yablonovite, provided however that the dipole be correctly positioned and oriented on the terminating surface. A similar study was conducted some time after for a photonic crystal of the 'woodpile' type (Cheng 1995). Unfortunately, it becomes apparent, when operating at frequencies equal to a few gigahertz, that devices based on three-dimensional photonic crystals have significant drawbacks in terms of compactness, since four periods of photonic crystal typically correspond to a ~ 50 cm thickness. For this reason, in the frequency ranges that are currently used in most applications, be they civil or military-oriented, research has shifted to structures allowing the realization of more compact devices.

Substrates realized from High Impedance Surfaces

The high impedance surfaces described in Section 4.4.6 of Chapter 4 have turned out to be the photonic structures best suited to antenna substrates, both in terms of compactness and as regards the possibility of exploiting the properties of photonic band gaps (Sievenpiper 1999a, 1999b). Fig. 13.2 (*left*) displays a schematic representation of a patch antenna inserted in a square lattice of metallic blocks which forms the high impedance surface. As can be seen in the cross-section view, each metallic block is connected to the ground plane by a metallic stud in order to create the inductive element of the high impedance surface (see Section 4.4.6 in Chapter 4). The arrangement represented in Fig. 13.2 is exactly the same as in the experiments reported by Y. Qian *et al* in 1999 (Qian 1999).

In this arrangement, the patch antenna is supplied by a microstrip line with a characteristic impedance equal to 50 Ω. The emission frequency of the antenna is the same as the resonance frequency of the cavity. The latter is located between the metallic plate and the ground plane, and its lateral dimensions are identical with those of the metallic plate itself. For a $TM_{m,n,0}$ mode, where the indices *m*, *n* and 0 correspond to the propagation axes *Ox, Oz* and *Oy* respectively (see Fig. 13.2), the transverse magnetic field extends for the most part in the plane of the substrate, and the cavity is bounded by vertical magnetic walls and horizontal electric walls, with the latter being formed by metallic planes. The resonance frequency of the cavity is given, in the first approximation, by the equation:

$$f_{m,n} = \frac{c}{2\sqrt{\varepsilon_r}} \sqrt{\left(\frac{m}{a}\right)^2 + \left(\frac{n}{b}\right)^2} \tag{13.1}$$

where ε_r is the dielectric permittivity of the substrate, while a are b the lengths of the two sides of the metallic plate.

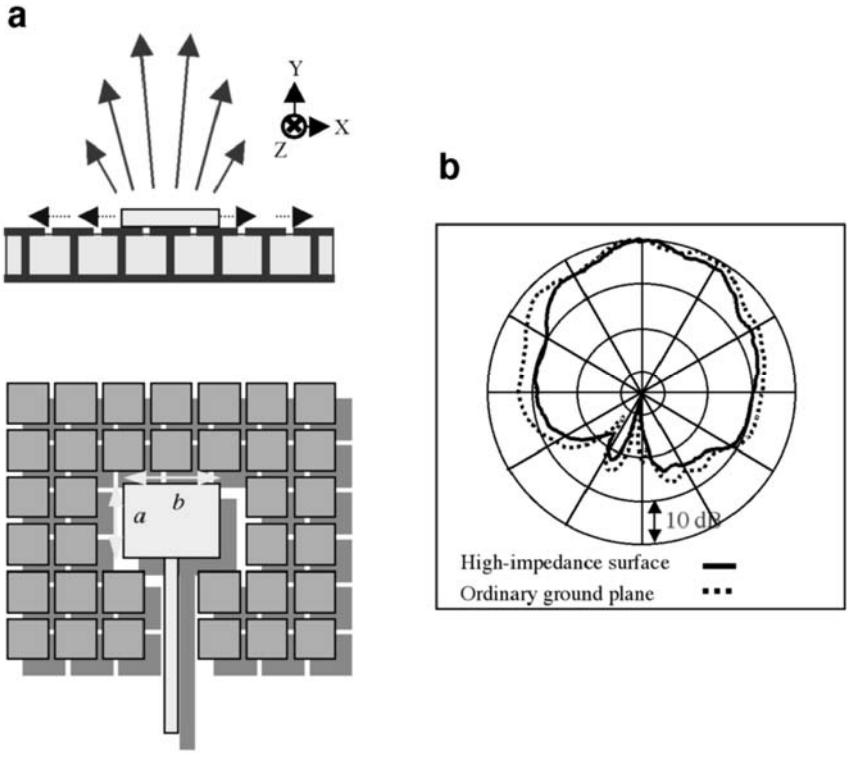

Fig. 13.2. *a.* Cross-section view (*top*) and top view (*bottom*) of a patch antenna on a high impedance surface. The principal emission of the antenna, represented by vertical arrows, is increased, while the surface waves, represented by horizontal arrows, are suppressed *b.* Radiation diagrams measured in the cases where the antenna is placed on a conventional substrate and on a substrate with a high impedance surface. The measurements are carried out in the plane *E* (*see* Fig. 13.1*a*). The amplitude is normalized for the two diagrams, revealing the decrease of the radiation in the horizontal direction (Qian 1999)

In order for the antenna to operate, the dimensions of the surface grid must be selected in such a way as to have the emission frequency of the antenna fall within the photonic band gap. Actually, assuming the emission of the antenna to be generated in a TM mode, no coupling to a TE surface mode may occur. As a consequence, the actual band gap will extend well beyond the band gap in TM polarization (see Section 4.6 in Chapter 4 and Fig. 4.14, *bottom*), resulting in an additional degree of tolerance. The period of the lattice is typically several times smaller than the length of the patch antenna. Near the frequency of the band gap, the surface impedance reaches such a high level that the propagation of surface waves is no longer allowed. Accordingly, the radiation of the antenna will be enhanced in terms both of efficiency and of directivity, this being due to the fact that the diffraction effects induced by the edges of the substrate are, in principle, suppressed. Fig. 13.2 (*right*) presents a comparison between the radiation of an antenna placed on a conventional substrate and that of an antenna placed on a substrate with a high impedance surface (Sievenpiper 1995b). It can be observed that, in the presence of the photonic structure, the radiation of the antenna in the horizontal direction and its radiation on the rear side are significantly reduced.

In the experiment conducted by Y. Qian *et al* (Qian 1999), the dimensions of the patch antenna were 3.05 x 4.27 mm^2, while the permittivity of the dielectric material, consisting of Duroid with a 0.64 mm thickness, was equal to $\varepsilon_r = 10.2$. The emission frequency of the antenna placed on a 'conventional' metallic plane was experimentally measured to be equal to ~ 14 GHz, a value close to the value calculated by using the simplified formula given in Eq.13.1. In the configuration where a substrate with a high impedance surface was used, the surface grid had a 2.43 mm period, while the square metallic blocks had a 2.23 mm side and were separated from one another by a 0.2 mm distance. Under these conditions, the complete photonic band gap was theoretically estimated to range from 8.6 to 12.66 GHz, while the actual band gap in TM polarization extended to 27.36 GHz. As can be seen in the right-hand part of Fig. 13.2, the radiation of the antenna placed on the high-impedance surface is significantly reduced in the horizontal direction and on the rear side. The increase in the effective power on the front side was found to be equal to ~ 1.6 dB, corresponding to an effective percentage of 45 %. This clearly shows that a complete modelization of the system formed by the antenna and the high impedance substrate will be necessary in order to better match the antenna to the substrate, and thus to enable the more advanced optimization of the device .

13.1.2 Photonic-Crystal Antenna Mirrors

As for antenna substrates, the first studies on the application of photonic crystal mirrors to antennas were carried out by considering volume structures realized from two or three-dimensional crystals, as represented in Fig. 13.1*c* (Kesler 1996 ; Sigalas 1996, 1997). Some of the issues associated with these photonic crystal mirrors have been discussed already in Sections 5.1.1, 5.1.2 and 5.1.3. In this respect, one of the most interesting cases to consider is the situation where specular

reflection is the only possible diffraction order of the photonic grating (see Section 5.1.2 in Chapter 5). The phase conditions on reflection of the photonic crystal are markedly different from those of a standard metallic plane. Thus, the reflected waves may combine with the waves that are directly emitted by the antenna, resulting in both a greater intensity and a higher directivity of the far-field radiation. More precisely, the conformation of the radiation of the antenna results from the strong angular dependence of the reflection coefficient. The crystal may thus, for instance, exhibit a band gap for some angles of incidence, while not for others.

Within a photonic band gap, the phase of the reflection coefficient of a photonic crystal follows, as a first approximation, a linear evolution as a function of the frequency *f*. This is illustrated in Fig. 13.3*a* in the case of a two-dimensional crystal formed by dielectric rods extending in the air. While this linear evolution can actually be verified whatever the incidence angle θ is, (Kesler 1996), the slope of this evolution changes with θ, and the reflection coefficient can therefore be written in the form:

$$\Gamma_{PC}(\theta,f)=\exp\left[i\left(A(\theta)-B(\theta)f\right)\right] \tag{13.2}$$

where A and B are functions of θ. Eq. 13.2 is valid only if the crystal is perfectly reflective, with a reflectivity equal to unity within the band gap. Actually, the frequency and angular dependences can be reintroduced in Eq. 13.2 by considering that, for each incidence angle, reflection occurs on a virtual metallic plane located inside the crystal, and at a distance $d(\theta)$ from the surface of the crystal (Fig. 13.3b). Assuming the metal to be a perfect reflector whose phase on reflection follows a law of the form $\Phi(\theta)$, the reflection coefficient considered at the surface of the crystal can thus be expressed as follows:

$$\Gamma_M(\theta)=\exp\left[i\left(\Phi(\theta)-2kd(\theta)\cos\theta\right)\right]=\exp\left[i\left(\Phi(\theta)-\frac{4\pi f}{c}d(\theta)\cos\theta\right)\right] \tag{13.3}$$

Eq. 13.2 can be retrieved from this equation under the following assumption:

$$\Phi(\theta)=A(\theta) \quad \text{and} \quad d(\theta)=\frac{cB(\theta)}{4\pi\cos\theta} \tag{13.4}$$

For the calculation of the radiation diagram of a dipolar antenna placed in the vicinity of the surface of the crystal, the assumption can then be made that, along a given direction, the field is the superposition of the field that would be emitted by the dipole in the absence of the crystal, and of the field due to the virtual image generated by the equivalent reflective plane. Of course, the field is calculated in the half-plane which extends around the crystal. As an example, let us here consider a dipole with a small height h, where a uniform current propagates, and whose axis is parallel to the dielectric rods of the two-dimensional crystal. In the

absence of the crystal, the field lines would assume the form of circles in the plane H perpendicular to the axis of the dipole. Denoting by s the distance between the dipole and the surface of the crystal, the image generated in the equivalent reflective plane will be located at a distance $s + d(\theta)$ from the other side of this surface. The total field radiated in the direction θ follows in this case the following proportionality law:

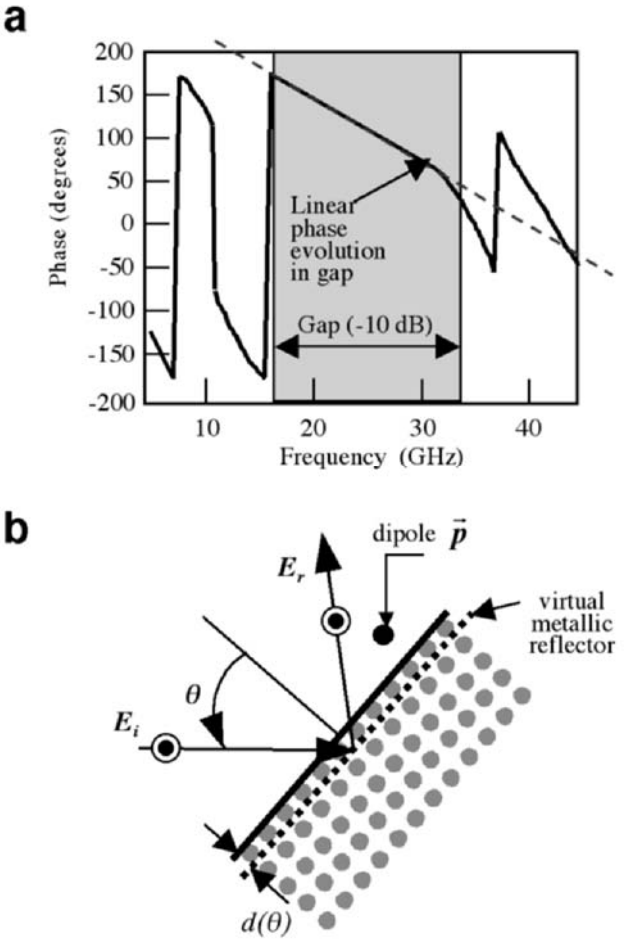

Fig. 13.3. *a.* Frequency dependence of the phase of the refection coefficient of a photonic crystal formed by a square lattice of dielectric rods ($\varepsilon = 4.2$) with a 2 mm radius. The period of the lattice is equal to 9 mm (Kesler 1996). The incidence angle is assumed to be zero *b.* Metallic reflector equivalent to the photonic crystal, for an incidence angle θ

$$E_{tot}(\theta) = E_i(\theta) + E_r(\theta) \;\alpha\; \exp\left[i\left(\Phi(\theta) - 2k\left(s + d(\theta)\right)\cos\theta\right)\right] \tag{13.5}$$

where $\Phi(\theta)$ is as previously defined in Eq. 13.4. The application of Eq. 13.5 supposes that $\Phi(\theta)$ and $d(\theta)$ have been calculated beforehand for each particular value of θ. The radiation diagrams obtained with this simplified calculation method have turned out to be consistent with the experimental values measured for two-dimensional crystals formed from dielectric rods (Carbonell 1998; Kesler 1996). The most favourable conditions for achieving a narrow emission beam and a good efficiency of the dipole have generally been obtained for a distance $s = \lambda/4$ between the dipole and the crystal. By comparison to the 'classical' case where the radiating dipole is at a distance $\lambda/4$ from a metallic plane, the efficiency of the dipole has thus been increased by a factor ranging from 1 to 2 dB. It should be pointed out, however, that the simplified calculation method presented here does not allow the determination of the detailed structures which appear in the emission lobes experimentally measured, and which can be simulated using more sophisticated methods, in particular the FDTD method (Carbonell 1998). Further, this method does not allow the prediction of the finer modifications appearing in the radiation diagrams when the dipole is moved parallel to the surface of the crystal.

Clearly, high impedance metallic structures can be used for the realization not only of antenna substrates, as described in the previous section, but also of antenna mirrors, which may also derive benefits from the compactness of these structures. The phase changes on reflection are in this case quite different from those that would be obtained with a perfect metallic mirror. For the sake of simplicity, we assume that we are in a regime of normal incidence. The impedance at the surface is defined in this case by the equation

$$Z_s = \frac{E_{tot}}{H_{tot}} = \frac{E_i + E_r}{H_i + H_r} \tag{13.6}$$

where E_{tot} and H_{tot} are the electric and magnetic fields at the surface respectively, while (E_i , H_i) and (E_r, H_r) correspond to the incident and reflected waves respectively. For the incident wave and the reflected wave propagating in the air, the impedance is given by the equation:

$$\left|\frac{E_i}{H_i}\right| = \left|\frac{E_r}{H_r}\right| = \eta \approx 377\Omega \tag{13.7}$$

while on the other hand the phase change on reflection is defined by the equation

$$\Delta\Phi = \mathrm{Im}\left\{\ln\left(\frac{E_r}{E_i}\right)\right\} \tag{13.8}$$

By combining Eqs. 13.6 and 13.7 with appropriate signs, and by reintroducing the result in Eq. 13.8, one reaches the following equation:

$$\Delta\Phi = \mathrm{Im}\left\{ \ln\left(\frac{Z_s - \eta}{Z_s + \eta} \right) \right\} \tag{13.9}$$

When the value for Z_s is very small, we are led back to the case of a perfect metal, where $\Delta\Phi = \pm\pi$. Conversely, for high impedance structures, Z_s assumes large values in the vicinity of the resonance, and $\Delta\Phi = 0$. This means that the radiating element, in the form either of a dipole or a patch antenna, can be placed at a very small distance from the high impedance surface. In such a case, the efficiency of the antenna can be expected to be higher than the efficiency obtained when the radiating element is located at a distance $\lambda/4$ from a metallic reflective plane. Since the tangentiel magnetic field at the surface tends towards zero, high impedance surfaces have also been given the name of 'perfect magnetic conductors'.

13.1.3 Photonic Crystal Antenna Radomes or Superstrates

The configuration formed by an antenna equipped with a photonic radome (also referred to as a superstrate) is schematically represented in Fig. 13.1*d*. Radomes are generally used for controlling the emission of an antenna and/or for protecting it from any external detection. The radome may cover the antenna, either partially or totally, with an inclination which can be variable with respect to the plane of the latter. In the example represented in Fig. 13.1*d*, the photonic radome totally covers the antenna and is used in emission mode. We shall discuss in Section 2 of this chapter the possibility of alternately operating in emission mode or in 'discretion' mode through the use of 'controllable' photonic crystals. The radome, which is often tilted with respect to the plane of the antenna, ensures in such a case the angular filtering, both in emission and in reception, along certain off-axis directions of propagation. In the example represented in Fig. 13.1*d*, the photonic radome is parallel to the plane of the antenna, resulting in an enhanced filtering in the principal direction of emission due to a cavity effect. Indeed, the emitting antenna is located in the asymmetric cavity formed by the photonic radome and the metallic ground plane. Depending on the distance between the radome and the ground plane, and thus on the position of the cavity frequency with respect to the emission frequency of the antenna, the emission can be either reinforced or attenuated. When a reinforcement of the emission occurs, the spatial filtering is reinforced as well, and the radiated electromagnetic field can thus be concentrated in a relatively narrow emission lobe.

The group of B. Jecko and A. Reineix from the University of Limoges has investigated in a detailed manner the configuration formed by an antenna and a photonic radome. This configuration is represented here in Fig. 13.1*d* (Thevenot 1999). The best results in terms of antenna gain, of directivity of the emission and

of overall cost of the system have been obtained for a one-dimensional photonic crystal limited to only three periods (Fig 13.4). The basis of the antenna is formed by a rectangular metallic plate placed on a dielectric substrate ($\varepsilon = 2$), which itself lies on a ground plane. The photonic radome consists for its part of three dielectric plates ($\varepsilon = 9.6$) separated with air. The radome and the antenna are arranged in such a way as to form a $\lambda/2$ cavity, where λ is the Bragg wavelength of the one-dimensional crystal. Under these experimental conditions, the resonance was found to be of the order of 20 GHz. At this frequency, the power emitted by the antenna is concentrated for the most part in a narrow emission lobe, whose width corresponds to an effective width of the emitting area equal to ~ 120 mm, i.e. more than 25 times the width of the patch antenna. The antenna gain has thus been increased by ~ 24 dB, due to the presence of the radome. This value is close to the value of 27 dB given by the formula:

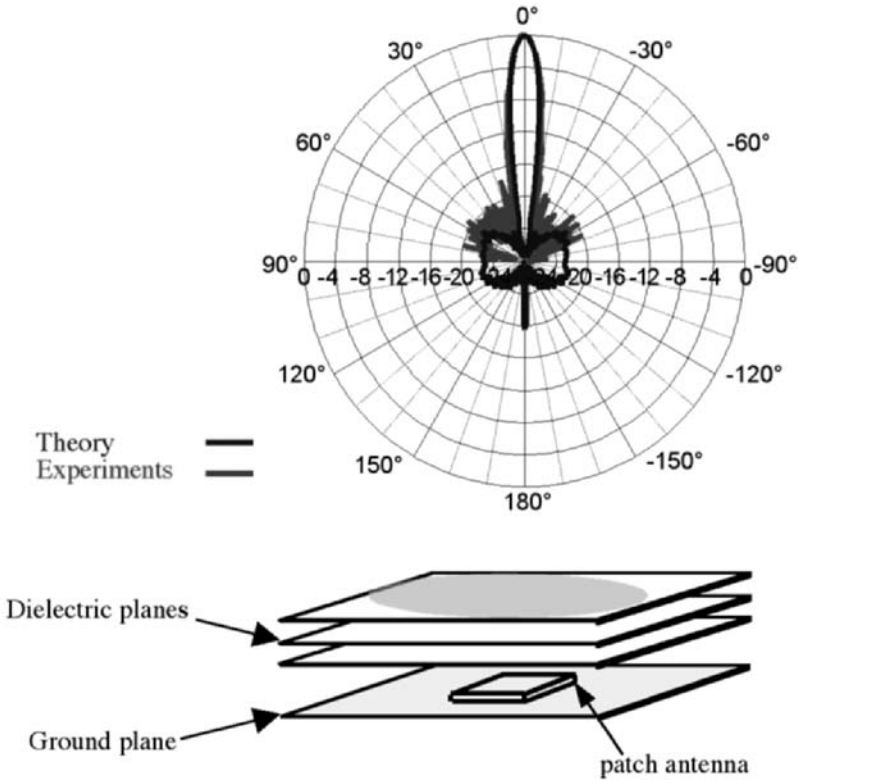

Fig. 13.4. *a.* Patch antenna equipped with a one-dimensional photonic crystal radome (Thevenot 1999) *b.* Radiation diagram of the antenna in the plane *E*. The values obtained from experimental measurements and from numerical simulations using the FDTD method are represented by black and dark grey lines respectively

$$G = 10 \log [4\pi S/\lambda^2] \tag{13.10}$$

where S is the effective emitting area. Accordingly, the amplitudes of the secondary lobes were found to be 20 dB lower than the amplitude of the principal lobe of the antenna. The radiation diagram measured in the plane E parallel to the electric field is represented here in Fig. 13.4, which shows that these results are consistent with numerical simulations realized with the FDTD method.

A diagram almost identical to the latter, revealing the same agreement between experimental measurements and theoretical values, was obtained in the plane H (Thevenot 1999). At the same time, a theoretical study addressing the case of a dipolar antenna placed between a radome and a one-dimensional photonic substrate (Fig. 13.1*e*) demonstrated the same effects, namely the enhancement of the antenna gain and that of the directivity of the antenna (Akalin 2001). Actually, the angular refinement of the emission can be interpreted as an effect induced by a planar cavity (see Section 10.1.2 in Chapter 10), even if the cavity involved here is of a rather special type. Both the effective emitting area and the numerical aperture are dependent on the quality factor of the cavity (see Fig. 10.2).

13.2 Controllable Structures and Metamaterials

13.2.1 Principles and Characteristics of Electrically Controllable Photonic Crystals

The use of metallic structures in the microwave region facilitates the insertion of electrically active elements in photonic crystals. This property is at the origin of the very concept of an active or 'controllable' photonic crystal, which was first suggested by two French research groups working at the University of Orsay and at the University of Lille respectively (Lourtioz 1999). In practice, electrically controllable two-dimensional photonic crystals have been fabricated by periodically inserting p-i-n diodes along metallic wires or metallic strips arranged in arrays. Depending on the applied voltage, the diodes can be either in an on-state or in an off-state. When the diodes are in the on-state, the properties of the crystal are the same as those of a lattice of continuous metallic wires, which have been described in Section 4.2.4 of Chapter 4. When the diodes are in the off-state, the properties of the crystal are the same as those of a lattice consisting of discontinuous wires with dielectric inserts (see also Section 4.2.4). These lattices impose less limitations on the propagation of electromagnetic waves (Economou 1993). Thus, starting from the zero frequency, a valence (transmission) band appears instead of the plasmon-type band gap. As will be seen in Section 13.2.2 of this chapter, one may also envision the possibility of an arrangement where only a few wires would be equipped with diodes. In this case, instead of modifying the behaviour of the

photonic crystal as a whole, one modifies its properties locally though the creation of 'active'defects.

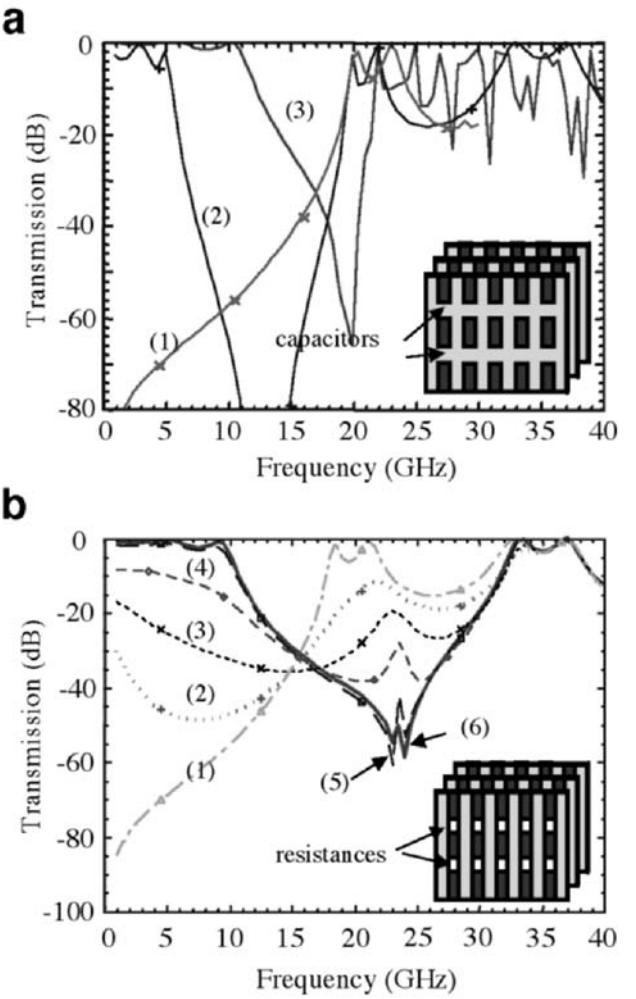

Fig. 13.5. Transmission spectra calculated for photonic crystals with metallic strips, where capacitances *(a)* or resistances *(b)* are periodically inserted along the strips. Three-layer crystals, formed by three printed circuits, are represented in the inserts. The printed circuit boards are separated from one another by 6 mm. For each circuit, the distance between two neighbouring metallic strips is equal to 4 mm, as is the distance between two neighbouring capacitance (or resistances) along a strip. The incident wave is TM polarized. In *a,* curve (1) corresponds to the absence of capacitance while curves (2) and (3) correspond to capacitance values equal to 0.3 and 30 fF respectively. In *b*, the curves (1) to (6) correspond to resistance values equal to 0, 50, 150, 500, 5000 and 15000 Ω respectively

A p-i-n diode can actually be schematically represented by an equivalent circuit containing a capacitor and a resistance connected in parallel. The behaviour of the photonic crystal is dependent on the respective values of the capacitance or of the resistance. In Fig. 13.5 are represented the transmission spectra calculated in two extreme cases for a two-dimensional p-i-n diode photonic crystal, realized with the standard technology used for printed circuits. The crystal presents a square symmetry, and it is further assumed in both cases that the incident wave is TM polarized, i.e. that the field **E** is parallel to the wires. Calculations were performed using an FDTD model, where each individual diode was simulated by an RC-type localized circuit. Fig. 13.5*a* corresponds to the situation where the capacitor plays the predominant role in the circuit equivalent to the diode, i.e. in the case where $R = \infty$. As might have been expected, the first plasmon-type band gap is replaced under these conditions by a valence band, whose edge progressively shifts towards high frequencies as the capacitance value increases. The transmission spectrum is not otherwise modified. A completely different behaviour can be observed when the resistance plays the predominant role in the circuit equivalent to the diode ($C \sim 0$, Fig. 13.5*b*). In this case, not only the first band, but also the bands of higher order as well are strongly modified. The lower the resistance is, the more changes occur in the spectrum. All the results achieved with the FDTD modelization represented in Fig. 13.5 have been experimentally vindicated (de Lustrac 1999; Brillat 2002). Thus, by changing the polarization voltage applied to the diodes, and hence the value of the resistance equivalent to each diode, the photonic crystal can be tuned continuously from an on-state corresponding to a high transmission to an off-state corresponding to a strong reflection.

13.2.2 Electrically Controllable Photonic Crystal Antennas

Electrically controllable photonic crystals can be implemented in microwave antennas, in the form either of active radomes or of spatial filters, and different studies have been conducted along these lines (Collardey 2002; de Lustrac 2001; Poilasne 2000). Fig. 13.6*a* presents results obtained with an active radome in a configuration similar to the one described in Fig. 13.4 (de Lustrac 2001). The antenna used in this configuration is a patch antenna, while the radome, which is placed parallel to the antenna, is formed by three printed circuit boards where p-i-n diodes have been soldered with a regular spacing along parallel metallic strips. The distance between two nearby strips (4 mm) and the distance between the printed circuit boards (9 mm) were selected in such a way as to obtain an emission frequency of the antenna in the low frequency region of the first transmission band of the two-dimensional photonic crystal, as can be observed in the curve (1) in Fig. 13.5*b*. The radome is located at a small distance from the antenna, which allows reducing the amount of leaky waves on either side of the structure while at the same time optimizing the impedance matching between the photonic crystal and the antenna.

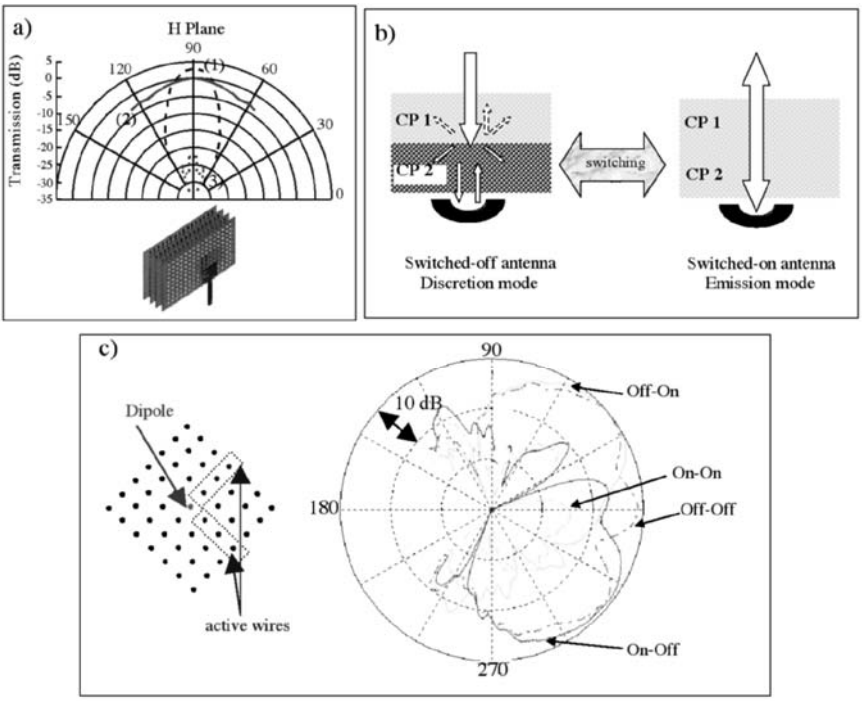

Fig. 13.6. *a.* Patch antenna with an active photonic crystal radome (de Lustrac 2001). The radome was fabricated with the standard technology used for the realization of printed circuits *(insert).* The radiation diagram of the antenna measured in the absence of the radome reveals a large emission lobe (2). This lobe becomes narrow when the radome is in the transmission state (1). A 30 dB attenuation is obtained when the radome is in the reflection state (3) *b.* Principle of a composite photonic crystal radome (PC1 + PC2) used for the reduction of the radar equivalent surface of the antenna (Collardey 2002). When the two crystals are in the transmission state, the radiation of the antenna is transmitted, and the antenna can receive external signals. When the active crystal PC2 is switched to the reflection state, the transmission decreases, and the diffraction and refraction effects induced by the interface between the two crystals PC1/PC2 contribute to the reduction of the radar equivalent surface of the antenna *c.* Schematic representation of a dipole antenna placed at the centre of a photonic crystal consisting of metallic wires where two rows of wires contain active elements (Poilasne 2000) (*left*). Radiation diagrams measured for the different states of the two series of active elements (*right*). The on-state (resp. off-state) is conductive (resp. non conductive)

As can be seen in Fig. 13.6*a*, the use of an active radome allows the complete control of the radiation diagram of the antenna.When the diodes are in the on-state, the radome transmits the radiation, and beam-shaping effects similar to those described in Section 13.1.2, can be exploited for increasing the directivity of the antenna. This results in an improvement of the antenna gain by comparison with the situation where the radome is not be present. When the diodes are in the off-state, the radome reflects the radiation of the antenna, and the transmitted level decreases by nearly 30 dB.

Fig. 13.6*b* presents a different configuration where the active radome is formed by an ensemble of two photonic crystals (referred to in this figure as PC1 and PC2) with the same mesh, albeit with significantly different periods. The photonic crystal located at the smaller distance from the antenna (PC2) is an electrically controllable crystal (Collardey 2002). The problem addressed here is to prevent the antenna from being detected when it is not in emission mode. Using the appropriate teminology, the problem is therefore to reduce the 'radar equivalent surface' (RES) of the antenna.

Two different situations may thus arise. When the antenna is in emission mode, the conditions are selected in such a way as to ensure that the two crystals will be in the transmission state, and that no significant transmission or diffraction loss is induced by the interface. Conversely, when the PC2 crystal is in the reflection state, not only does the transmission of the antenna strongly decrease, but the refraction and/or diffraction effects occurring at the interface between PC1 and PC2 contribute to the reduction of the reflection of the external waves, thus resulting in a significant attenuation of the radar equivalent surface along certain directions of observation.

Fig. 13.6*c* shows the application of an active photonic crystal to the spatial filtering and to the switching of antenna arrays (Poislane 2000). Contrary to the two previous schemes, here a dipolar antenna is inserted in a photonic crystal formed by metallic wires. The frequency of the emitting dipole is (2 GHz) in the first band gap of the crystal with square symmetry. Only a few wires located in two rows perpendicular to one another contain active elements. Actually, these two rows of wires form two waveguides, which are independent from one another within the crystal. Three different situations may arise then. When all elements are in the on-state, everything happens as if the metallic wires were continuous, and the radiation emitted by the antenna towards the outside decreases down to a very low level. When the active elements of only one series are in the on-state, the radiation of the antenna will be transmitted only through a single waveguide. The simultaneous commutation of the two series therefore allows switching the antenna array from one direction to the other. Finally, when all the elements are in the off-state, the radiation of the antenna is transmitted through the two waveguides, and the emission lobe may become in this case very large. These results suggest the possibility of developing low-cost antennas where the directions of emission would be controlled by photonic crystal structures.

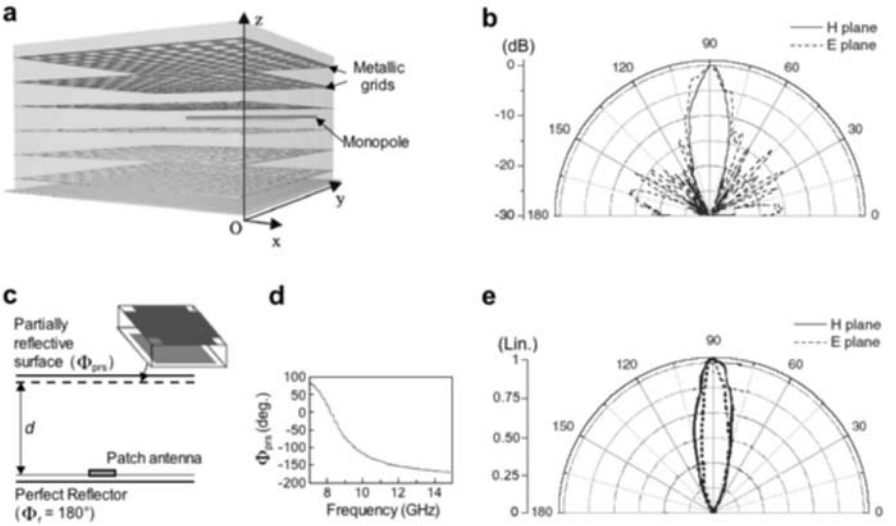

Fig. 13.7. *a.* Monopole antenna placed in a metamaterial with index much smaller than unity, formed by a stack of perforated metallic grids (Enoch 2002) *b.* Radiation diagrams in dB scale of the antenna measured in the *H* and *E* planes, respectively. *c.* Patch antenna placed in an ultracompact (~ λ/60) cavity bounded on the upper side by a partially reflective surface (Ourir 2006b). *Insert.* Elementary pattern of the partially reflective surface *d.* Evolution of the phase at reflection, measured for the partially reflective surface. *e.* Radiation diagrams in linear scale of the antenna, measured in the *H* and *E* planes respectively

13.2.3 Antennas and Metamaterials

Most of the applications of photonic crystals to antennas described above were based essentially on the exploitation of the amplitude response of the photonic crystal (on- and off-states). However, another possibility consists in exploiting the phase response as well as different refractive effects of the kind discussed in Chapter 6 in relation with metamaterials. The idea of using a 'perfect' lens associated with a negative refractive index represents a possible solution for achieving the control of the far-field radiation of the antenna. The antenna in this case is located outside the metamaterial. Another possibility consists in inserting the emitting element inside the metamaterial itself. If the effective refractive index of the metamaterial is very small with respect to unity, the emitted radiation will emerge from the metamaterial in a cone with a very narrow aperture. In other terms, the emitted beam will present a high directivity, which generally is a highly desirable feature for applications. This effect was reported in the studies by S. Enoch *et al* (Enoch 2002a, 2002b). In these experiments, the metamaterial was formed by a stack of perforated metallic grids assembled in a foam with a refractive index

close to unity (Figs. 13.7*a*, *b*). Such a structure exhibits at low frequencies the same behaviour as a charge plasma, whose effective index, which is described by Drude's formula given in Section 4.1.1, can be much smaller than unity. The radiation diagram measured for a monopole antenna located at the centre of this stack reveals the existence of a very narrow lobe corresponding to an angular aperture equal to 8.9° and 12.5° in the *H* plane and in the *E* plane respectively (Fig. 13.7*b*).

A different approach (Figs.13.7*c*,*d*,*e*) consists in placing the antenna in a small cavity bounded by a metallic ground plane on one side and a metamaterial-based partial reflector on the other side (Ourir 2006a, 2006b; Zhou 2005b). The configuration is similar to that of the photonic crystal radomes described in Section 13.1.3, with the difference however that the phase of the reflection coefficient associated to the metamarial-based reflector Φ_{prs} presents the original property of being strongly dependent on the frequency (Fig. 13.7*d*), contrary to the reflection phase of the metallic ground plane, Φ_r, which remains close to π. When $(\Phi_{prs}+\Phi_r)$ approaches zero, the resonance condition $d = \lambda(\Phi_{prs} + \Phi_r)/4\pi \pm N\lambda/2$ can be achieved for cavities with a very small thickness ($N = 0$). Ultracompact antenna systems ($d \sim \lambda/60$) with directive emission have thus been obtained in this way, as can be seen in Fig.13.7*e* (Ourir 2006b).

13.3 Microwave Circuits and Ultra-Compact Photonic Crystals

13.3.1 Ultra-Compact Photonic Crystals

In the field of microwaves as in integrated optics (see Chapter 9), the realization of circuits imposes the use of of extremely compact structures. It has been seen earlier, in Section 13.1.1 of this chapter, that high impedance surfaces could be used for the realization of antenna substrates with a limited thickness while at the same time allowing the concept of a photonic band gap to be used. It has also been seen that the electromagnetic behaviour of these structures could be analysed in terms of localized components, inductances and capacitances, with a band gap at the frequency ω defined by the equation $LC\omega^2 = 1$ (see Section 4.4.6 in Chapter 4). In the examples presented in Figs. 4.13 and 13.2 of high impedance surfaces, the capacitances resulted from the existence of gaps between the metallic patches while the inductances were associated with the metallic 'rods' which connect, inside the substrate, the patches to the ground plane. Despite the limited thickness of these structures, their design remained nonetheless essentially three-dimensional. In this respect, the specificity of ultra-compact photonic crystals lies in the fact that they are intended at being used in circuits based on microstrip or coplanar lines. In such circuits, the two types of elements, i.e. the capacitors and the inductances, coexist on the same metallic plane.

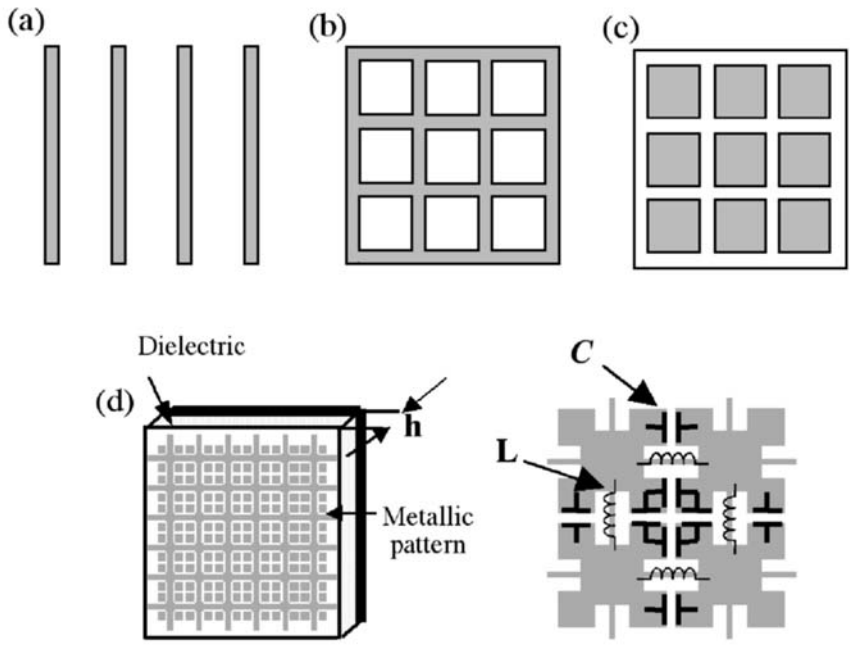

Fig. 13.8. Schematic illustration of the progression from metallic grids to ultra-compact photonic crystals for microwave circuits *a.* One-dimensional inductive grid *b.* Two-dimensional inductive grid *c.* Two-dimensional capacitive grid *d. Left.* Ultra-compact photonic crystal realized by the structuring of the ground plane following a 'Jerulasem cross' periodic pattern *Right.* Circuit equivalent to the elementary cell of the ultra-compact photonic crystal

Fig. 13.8, which represents different types of periodical metallic patterns, shows the increasing level of complexity arising with such structures. One-dimensional lattices of metallic wires or metallic strips represented in Fig. 13.8*a* have long been used as polarization-selective filters owing to the inductive couplings arising between the wires. An ensemble of two lattices crossed in the form of a grid, as illustrated in Fig. 13.8*b*, may act as a high-pass filter for the two polarizations. Conversely, the dual system consisting of periodic metallic contacts separated from one another and represented in Fig. 13.8*c*, involves capacitive couplings, and it behaves like a low-pass filter. Finally, the 'Jerusalem cross' pattern, represented in Fig. 13.8*d*, and first suggested by the group of T. Itoh at the University of California (Los Angeles) (Coccioli 1999; Yang 1999a) simultaneously combines inductive effects and capacitive effects: a genuine electromagnetic band gap can thus be achieved around the frequency ω defined by $LC\omega^2 = 1$. The equivalent circuit corresponding to an elementary cell is represented in the right-hand part of Fig. 13.8*d* by an ensemble of capacitors and inductances: the capaci-

tors are associated with the 'gaps' between the metallic blocks, while the inductances are associated with the wires connecting the central regions of these metallic blocks.

In order to realize an ultra-compact photonic crystal, it is therefore sufficient to structure the metallic ground plane of a microwave circuit, without having to modify the dielectric region which forms the core of the guiding lines. This is a decisive advantage in terms of cost and simplicity of the design, compared to conventional dielectric photonic crystals. Actually, the resulting geometry is analogous to that of surface selective surfaces (Chan 1995), with the difference however that one considers here a guided wave instead of an external incident wave. An electromagnetic wave propagating along the lines of the circuit will be sensitive to the filtering induced by the structuring of the ground plane. As for planar integrated optics (see Chapter 9), the two-dimensional periodicity of the patterns allows this filtering to be effective in all the directions in the plane. Effects associated with the refractive indexes (or with the propagation speeds of the waves) can also be exploited in the vicinity of the band gaps. In particular, a strong increase of the group index may result, for a given wavelength, in the possibility of reducing the size of the circuit, which is a substantial advantage for applications at low frequencies.

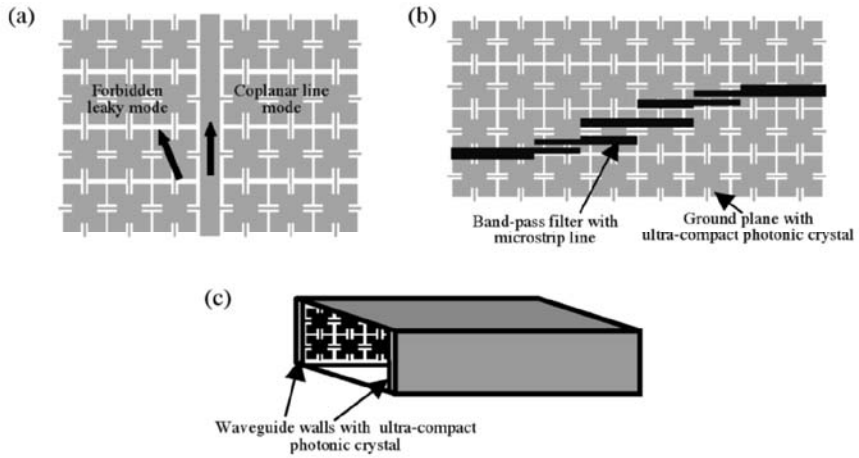

Fig. 13.9. *a.* Top view of a coplanar line where the ground planes on either side of the central conductor exhibit an ultra-compact photonic crystal structure. This configuration prevents the propagation of parasitic waves between the front-mounted ground lines and the rear-mounted ground plane *b.* Top view of microstrip line band-pass filter. The fundamental band is imposed by the coupled cavities defined on the front side. The 2ω component is suppressed due to the ultra-compact photonic crystal realized in the rear ground plane *c.* Schematic representation of a hollow waveguide with ultracompact photonic crystal

13.3.2 Microwave Filters and Waveguides realized from Ultra-Compact Photonic Crystals

Different applications of ultra-compact photonic crystals have been suggested, and a few examples of such applications, which are illustrated in Fig. 13.9, will be presented in this section. The first example shown in this figure (Fig. 13.9*a*) is that of coplanar circuits (Yang 1999a). As its name indicates, the metallic connections in such a circuit generally lie in the same plane, a coplanar line being formed by a central conductor surrounded by two ground lines. Such a configuration allows the optimization of the performances in terms of frequency of the circuits, while at the same time allowing to reduce the dielectric 'gaps', and more specifically the thickness of the substrate. However, when this thickness becomes too small, a second metallic ground plane is mounted on the rear side in order to rigidify the substrate. Whereas guiding should exclusively occur under the central conductor, the risk exists that parasitic waves may be guided between the rear-mounted ground plane and the front-mounted ground lines, In this respect, the creation of an ultra-compact photonic crystal through the structuring of the ground lines on the front side can be viewed as an elegant solution to the problem of preventing the propagation of parasitic waves, irrespective of their direction of propagation.

In the second example of an application of ultra-compact photonic crystals represented in Fig. 13.9*b*, an ultra-compact photonic crystal is used as a band-pass filter in a microstrip line circuit (Yang 1999a). In such a circuit, guiding will occur in the region of the dielectric which extends between the front-mounted metallic strip and the rear-mounted ground plane. Band-pass filters are generally realized by using coupled-cavity structures, represented in Fig. 13.9*b* by dark bands. The rigidity of the filter depends on the quality factor of each cavity, while the spectral width varies with the number of cavities. One of the main drawbacks associated with these structures results from the fact that the filter allows the propagation of waves at all the harmonic frequencies of the fundamental frequency. As an example, the component at the 2ω frequency can be suppressed through the use of a ground plane structured in such a way as to prevent the propagation of this component. In other terms, one takes advantage here of the double structuring of the metallic lines of the circuit, which results in the definition of coupled cavities on the front side and of an ultracompact photonic crystal on the rear side. The optimization of the performances of the filter at simultaneously ω and 2ω depends of course on the position of the strips on the front side with respect to the ultra-compact photonic crystal patterns on the rear side.

The third example represented in Fig. 13.9 is a hollow waveguide with an ultra-compact photonic crystal structuring of its sidewalls (Yang 1999b). These hollow waveguides are related to the microstructured hollow fibres described in Section 11.3 of Chapter 11. The fact that the wave is guided in the air allows high powers to be injected. In general, microwave waveguides are bounded by metallic sidewalls which impose a zero field. Conversely, the replacement of metal with a photonic crystal behaving as a 'perfect magnetic conductor' results in reflective walls without any phase change at the reflection (see Section 13.1.2 in this chapter). In such a case, the guided wave exhibits almost a constant amplitude at all

points of the waveguide and fills the entire volume, resulting in an increases by a factor ~ 2 of the power transmission capabilities of the waveguide.

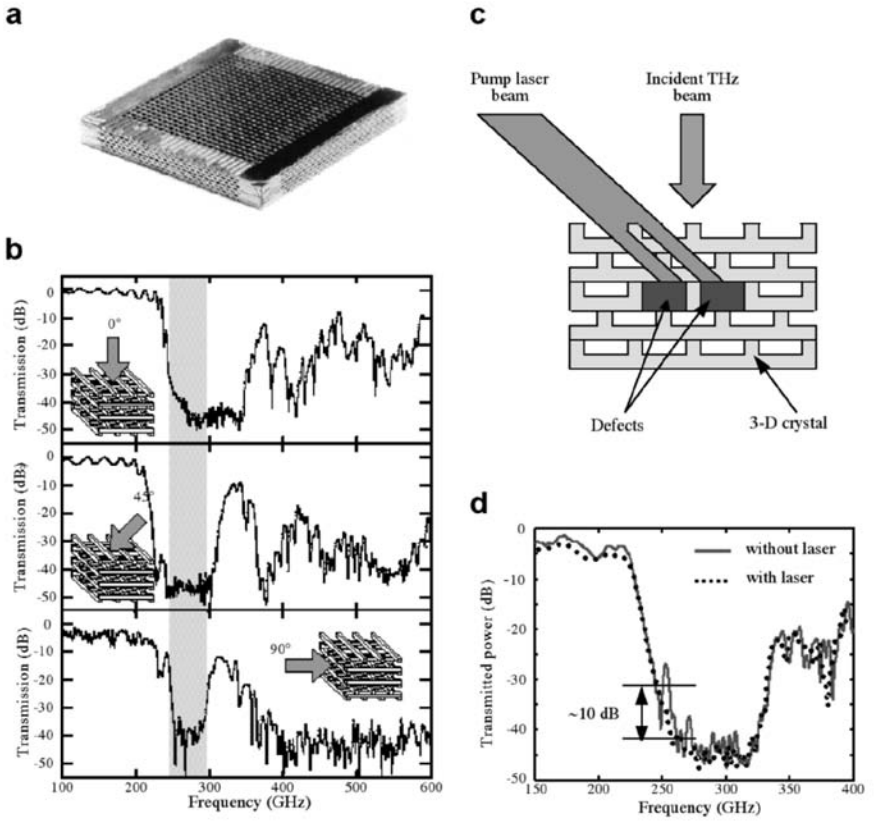

Fig. 13.10. *a.* THz photonic crystal of the 'woodpile' type realized by the mechanical etching of a silicon substrate (Chelnokov 1997). *b.* Transmission spectra measured for three different directions of the incident wave, revealing the existence of a complete photonic band gap. *c.* Principle of a THZ controllable filter based on a three-dimensional photonic crystal where defects were introduced (Chelnokov 1998) *d.* Transmission spectra measured along the <100> direction in the absence of illumination (*continuous lines*) and under illumination (*dots*)

13.4 From Microwaves to Terahertz Waves

Terahertz (THz) waves, also referred to as submillimiter waves or as far infrared, occupy an intermediate position between microwaves and the near-infrared in the frequency spectrum. These waves have typical wavelengths ranging from a few ten microns to the millimeter, hence frequencies ranging from approximately ~200 GHz to a few terahertz. For this reason, techniques related to these waves have generally a hybrid character between microwave and optical techniques. Thus, the THz emission sources include such diverse systems as gas lasers, for instance lasers optically pumped by means of a carbonic gas laser (Lourtioz 1981), semiconductor lasers, for instance quantum cascade lasers (Köhler 2002), systems for the frequency doubling or tripling of microwave emitters (Siegel 1999) as well as emitters similar to those used for microwaves, like for instance *impatt* or *Gunn* diodes (Eisele 1998), albeit with an optimization of their frequency response. The existence of a specific technique of THz spectroscopy can be mentioned in this context. This technique is based on the exploitation of the free-space radiation of antennas connected to semiconductor switches, with the latter being triggered by an infrared laser operating in a regime of (sub)picosecond pulses (Garet 1997). This technique is commonly used for the characterization of photonic structures adapted to the THz region.

The field of applications for THz waves is less extended than that of microwaves, this being due to the fact that the absorption of these waves in the atmosphere reduces the distance of propagation in free space at most frequencies of interest. This however can be turned into an advantage when information is transmitted over short distances (indoor telecommunications) or in highly diluted media (satellite communications), since in this case the absorption occurring over longer distances leads to the possibility of discretizing the information transmission. At a different level, THz spectroscopy provides specific information concerning vibration/rotation spectra of molecules, with possible applications to the environment, to chemistry or to astronomy. Finally, THz spectroscopy is well suited to the measurement of charge densities in relatively dense plasmas. These different applications justify the interest in THz waves, and consequently in photonic crystals in this region. From an historical point of view, another reason for this interest lies in the fact that the THz region, as a field of investigation for photonic structures, can be more easily accessed than optics, while at the same time offering the perspective of a rapid transfer of the results achieved in the THz range to the infrared and visible ranges.

In particular, it might be recalled here that the three-dimensional photonic crystal structures of the ‘woodpile’ type that were described in Section 12.2.1 of Chapter 12, were first developed in the THz field from semiconductor materials (Özbay 1994a, 1994b). Fig. 13.10*a* represents an example of such a three-dimensional structure realized from a silicon substrate (Chelnokov 1997). The fabrication method used here is significantly different from the method used for the realization of the first such structures, where each lattice in the three-dimensional stack was realized by chemical etching. In the case under consideration, grooves are

etched on each side of a silicon substrate by means of a programmable silicon dicing saw of the kind used in the electronic industry. In principle, mechanical etching can be applied to any type of substrate, and any value can be selected for the angle between the grooves mechanically etched on either side of the substrate. The grooves have a 360 μm width and they are spaced from one another by 135 μm, while the remaining silicon 'rods' have a 135 μm^2 cross-section. The rods of two adjacent lattices in the stack are directed along two directions perpendicular to one another, as in the case of the original 'woodpile' structure described in Section 12.2.1. Transmission measurements carried out for a stack of eight layers, corresponding to 4 periods of a three-dimensional crystal at variable incidence angles have indeed revealed the existence of a complete band gap, which extends from 240 to 290 GHz (Fig. 13.10, *bottom left*).

The possibility of realizing a THz modulation filter controllable by infrared beam has been demonstrated by inserting defects, in the form of small silicon blocks, in the photonic crystal represented in Fig. 13.10 (Chelnokov 1998). The structure where these defects were introduced has been previously described in Chapter 1 (Fig. 1.17).

The principle of this modulation filter is schematically represented in Fig. 13.10*d*. Each small silicon block forms actually a cavity whose quality factor depends on the absorption induced by the infrared laser beam. The absorption at THz frequencies is due to the photocreation of electrons and holes in the silicon, and the variation in transmission of the crystal is measured by injecting a THz beam from above the crystal. The actual behaviour of the modulator is illustrated in Fig. 13.10*d*, which represents the transmission spectrum of the crystal along the <100> direction under two different conditions of illumination. In the absence of illumination by a laser beam, the spectrum exhibits a resonance peak with a width equal to ~ 4 GHz within the band gap (at 253 GHz). The fact that the resonance is only moderately pronounced has already been addressed in Section 1.4.1 of Chapter 1. In the presence of the laser beam operating with a ~300 mW illumination power, this resonance peak totally disappears. This corresponds approximately to a 10 dB amplitude modulation of the THz filter. Beyond this specific application to filtering, the experiment reported in Fig. 13.10 also opens the way to the possibility of realizing submillimeter sources optically pumped by infrared laser.

13.5 From Microwaves to Optics

It is not unusual that the development of microwave devices and systems may announce that of future optical devices and systems. Similarly, the study of microwave devices often leads to the development of new analysis and modelization methods, which eventually will find their way into optics. In this respect, more than in any other else, the thematic of photonic crystals can be seen as a link between the fields of microwaves and optics. In this section, we shall present several examples of such possible transfers from one field to the other.

13.5.1 Impedance Matching of Photonic Waveguides

The problem of impedance matching is a most classical problem for electronic circuits. Each transmission line can be associated to a characteristic impedance Z_C which depends on the inductance and on the capacitance per unit length of the transmission line. In the most usual case, $Z_C = 50\ \Omega$. This impedance can also be defined as the ratio between the amplitudes of the electric and magnetic fields of the wave propagating along the line (see Eqs. 4.40 and 4.42). When the line ends with a charge impedance Z_L, the impedance matching, or in other terms the optimization of the electromagnetic power contained in the charge, can be indifferently determined either from the reflection coefficient at the end of the line Γ_L or from the standing wave ratio (SWR), which are respectively defined as follows:

$$\Gamma_L = \frac{Z_L - Z_C}{Z_L + Z_C} \quad \text{and} \quad SWR = \frac{1+|\Gamma_L|}{1-|\Gamma_L|} \tag{13.11}$$

An optical waveguide is of course analogous to a microwave transmission line. This leads to the possibility of defining a characteristic impedance for optical waveguides. The charge at the extremity of the waveguide will thus be associated with some perturbation of the waveguide, such as a bend, a widening of the waveguide or the presence of a cavity. However, the difference between a photonic crystal waveguide and a standard waveguide lies precisely in the periodicity of the former, and therefore in its non-uniformity. The study conducted by S. Boscolo *et al* (Boscolo 2002b) has nonetheless demonstrated that the notion of characteristic impedance Z_B, which may be referred to as the 'Bloch impedance', can also be introduced in this context. This however requires that the the ratio E/H be considered along the transverse direction wih respect to the propagation of the wave. Thus, for a TM wave propagating in a channel waveguide created in a two-dimensional photonic crystal formed by dielectric rods (Fig. 13.11), the field E extends along the Oz axis, and the 'Bloch impedance' can be written as follows:

$$Z_B = \frac{\int \eta_B(x,0)\,\mathrm{Re}\{P_y(x,0)\}dx}{\int \mathrm{Re}\{P_y(x,0)\}dx} \tag{13.12}$$

where:

$$\eta_B(x,y) = \frac{E_z(x,y)}{H_x(x,y)}$$

and where $P_y(x, 0)$ represents the longitudinal component of the Poynting vector in the $y = 0$ plane.

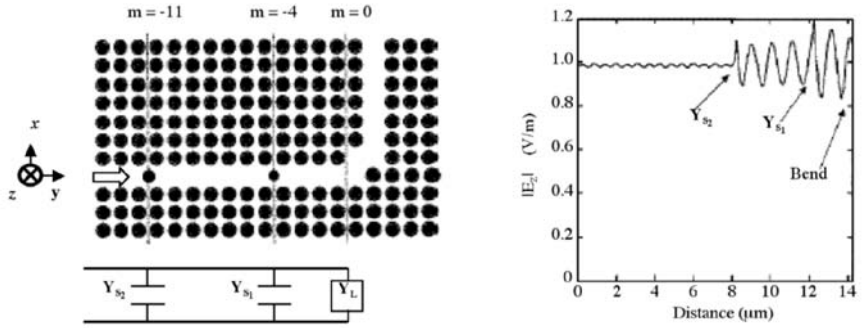

Fig. 13.11. *Left.* Bend in a two-dimensional photonic-crystal waveguide with a square symmetry and equivalent scheme of an impedance-matched transmission line. *Right.* Modulus of the electric field along the main waveguide. The introduction of the two defects allows the impedance matching of the waveguide, resulting in a lower standing wave ratio before Y_{S2}

Likewise, in the case where a perturbation, in the form for instance of a bend as in Fig. 13.11, is induced at the extremity of the waveguide, a charge impedance Z_L can also be defined, with the consequence that the impedances calculated at different distances from the perturbation (rows formed by rods with rank $m < 0$ in Fig. 13.11) can be expressed as a function of Z_B and Z_L, as in the case of a conventional transmission line (Boscolo 2002). Under such conditions, it becomes possible to apply the various impedance matching techniques developed in the field of RF waves to photonic crystal waveguides. One of these techniques consists in placing localized impedances (stubs), parallel to the transmission line, at two different points before the perturbation. In principle, only two impedances with adequately selected values are sufficient for reducing the standing wave ratio in the transmission line, and thereby for optimizing the energy transmission at the end of the line.

This phenomenon can be observed in the example represented in Fig. 13.11. The two localized impedances are obtained by placing two dielectric rods with different radii along the axis of the waveguide in the rows $m = -4$ and $m = -11$ respectively (Fig. 13.11, *left*). In this case, it can be observed that the oscillations of the field beyond the second central rod ($m \leq -11$) tend to disapear (Fig. 13.11, *right*): the standing wave ratio thus tends towards unity. This impedance matching technique turns out to be relatively robust in terms of wavelength, as shown by the fact that reflection losses are kept no higher than 20 dB over a relative spectral range $\Delta\lambda/\lambda \sim 1\%$. This method for the impedance matching of photonic waveguides can thus be extended to other types of perturbations and to other types of photonic crystal structures.

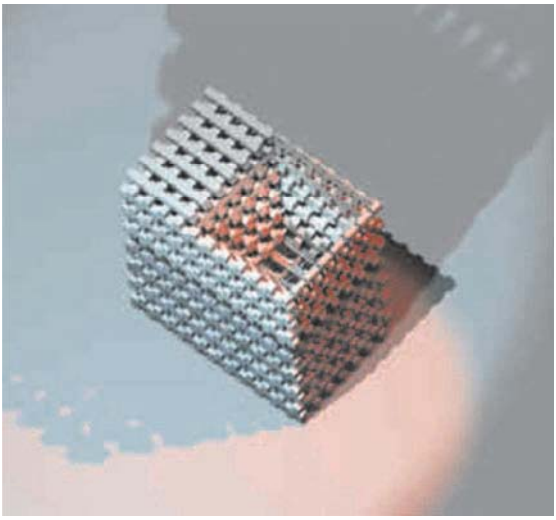

Fig. 13.12. Schematic representation of a THz pixel of the passive imaging system developed within the STARTIGER framework for the 250 and 300 GHz frequencies (STARTIGER 2003). The detecting/mixing element is embedded in a three-dimensional photonic crystal realized by mechanical machining. The aperture on the upper side, with a form similar to that of microwave receiving horns, allows illumination of the pixel

13.5.2 Photonic Crystal THz Imaging System

Imaging is one of the most important fields of applications for optical systems. Each frequency range provides specific information concerning the scene to be 'imaged'. Of course, the visible range is for us the most familiar region. Terahertz detection, like infrared detection, provides information on the temperature of objects present in a scene, with the specificity however that the THz radiation emitted by these objects can be transmitted through smoke and clouds, as well as through such materials as glass, plastics, cloth and even sufficiently thin walls. THz imaging systems are more practical than microwave imaging systems, and, in certain cases, they can be substituted to these systems for observations from small platforms, in particular satellite boarded platforms. While some commercial systems already exist, three-dimensional silicon photonic crystals, of the type presented in Section 4, open the way to the realization at low cost of three-dimensional architectures, where not only the detection elements (pixels) and the

photonic substrate would be integrated, but also the receiving horns and the connection lines themselves, as can be seen in the example represented in Fig. 13.12 (Gonzalo 2002; STARTIGER 2003). In such an architecture, the existence of the photonic band gap allows isolating the active elements from the pixels as well as from the substrate, thereby preventing diaphony problems from arising. The selection of the termination of the crystal at the location of the emitter also provides the possibility of matching impedances, and thus of optimizing the level of the detected signal. In view of the development of fabrication techniques of three-dimensional photonic crystals (see Section 13.4 in this chapter), it is likely that this experiment on a THz imaging system will be extended to shorter wavelengths.

13.5.3 'Microwave Inspired' Nanostructures and Nanodevices

The development of 'microwave inspired' nanostructures and nanodevices based on the use of metals and dielectrics represent a real opportunity in the field of subwavelength optics. Whereas dissipative loss generally limits the use of metals at optical frequencies, the situation changes radically when optical structures involving small metal filling factors and/or small optical paths at the micrometre scale are used. The miniaturization of metallo-dielectric structures thus appears, besides photonic crystals, as another possible way towards optical connections. The use of surface plasmon polaritons has also been proposed as a way of overcoming the problem of losses for an optical emitter close to a metallo-dielectric interface (Barnes 1999) (see Section 4.4).

Several examples of such 'microwave inspired' structures and devices are shown in Fig.13.13. The intimate relation between photonic crystals and metamaterials has already been emphasized in Section 6.4 as regards the control of the refractive index and, more generally, the electromagnetic properties of periodic structures. Fig. 13.13*a* shows an example of a metamaterial structure consisting in a miniaturized version of the periodic array of metallic split ring resonators developed at microwave frequencies (see Section 6.4.5). This structure is formed by gold nanorings deposited on glass (Enkrich 2005). Magnetic resonances, and hence mu values different from one, have been claimed by the authors at both the 0.8 and 1.5 μm wavelengths for an oblique incidence and a non-zero magnetic field component perpendicular to the plane of the ring resonators. It is worth noting that the metamaterial structure in Fig.13.13*a* is very similar to the frequency selective surfaces (FSS) developed much earlier in the gigahertz and terahertz domains (Bozzi 2000; Chan 1995). The interested reader is also referred to (Labeke 2006; Monacelli 2005) for more recent developments concerning FSSs in the infrared and visible ranges.

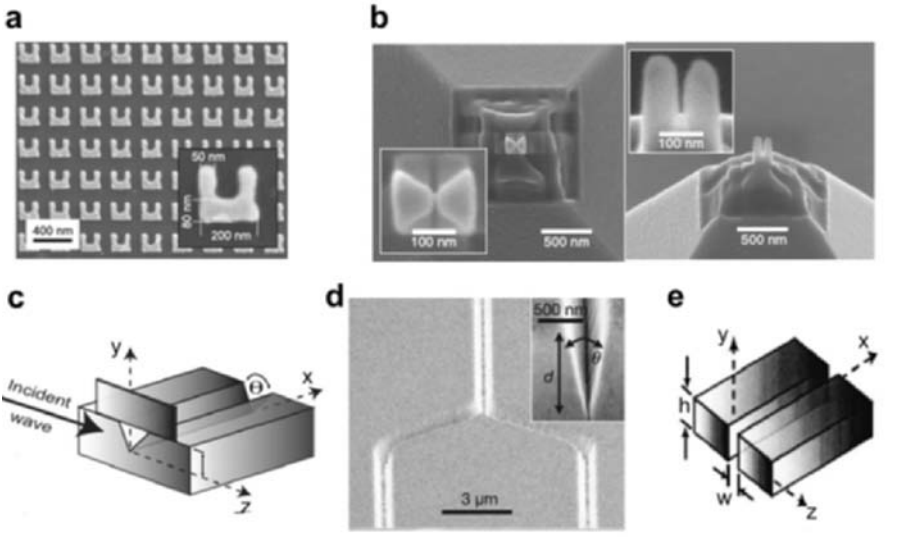

Fig. 13.13. *a.* Electron micrograph of an array of split rings, with the dimensions of an individual split ring shown in the inset on the right-hand side of the figure (Enkrich 2005) *b.* Optical bow-tie antenna fabricated at the apex of an AFM tip (Farahani 2005) *Left.* Top view *Right.* Side view *c.* Schematic representation of a V-groove metallic waveguide studied in (Gramotnev 2004) *d.* Electron micrograph of a plasmonic Y-splitter based on V-groove waveguides (Bozhevolnyi 2006) *e.* Schematic representation of a nanoscale gap plasmon waveguide studied in (Pile 2005)

Throughout this chapter, metallic antennas have been presented as emblematic components for microwave applications. Nanometric versions of microwave antennas are currently being developed with the aim of realizing near-field optical probes combining a spatial resolution well below the diffraction limit with a high optical transmission efficiency (Cubucku 2006; Fromm 2004; Groeber 1997). White light generation can even be achieved under pulse laser illumination (Muhlschlegel 2005). Another interest of metallic nanoantennas lies in the possibility of enhancing the light emission of a single quantum emitter in the same way as radio antennas enhance radio emission (Farahani 2005). However, contrary to radio antennas, the optical antenna is strongly influenced by electron resonances in the metal, including surface plasmon resonances (see Section 4.4). Fig.13.13*b* shows an example of a bow-tie nanoantenna used in close interaction with a single quantum dot for modifying its radiative transition rate (Farahani 2005). The nanoantenna was fabricated at the apex of a Si_3N_4 atomic force microscope (AFM) cantilever tip. After evaporation of a homogeneous 40 nm thick aluminium film, the bowtie-shaped metallic structure was sculptured from the film using a focused ion beam milling technique.

Metallic waveguides are basic components in microwave systems, and the exploitation of surface plasmon polaritons in their nanometre scale analogues ap-

pears as an efficient way to achieve the extreme miniaturization of optical circuits. Different waveguide structures have been proposed, some of which are represented in Figs.13.13*c*, *d*, *e*. Very promising results have been obtained with V-shaped grooves milled in metal films (Fig.13.13*c*, *d*), where the electromagnetic wave can propagate over tens of micrometres along the bottom of the groove (Bolzhevolnyi 2006; Gramotnev 2004; Pile 2005). Y-splitters, Mach-Zehnder interferometers and waveguide ring resonators based on such V-groove shaped waveguides have been realized with reasonably low insertion loss ($\leq$ 3dB) and small footprints ($\leq$ 200 μm^2) (Bolzhevolnyi 2006). The propagation of surface plasmons has also been demonstrated for nanowaveguides formed by a dielectric (air) gap in a thin metal membrane or film, as represented in Fig.13.13*e* (Pile 2005). The fabrication of these structures is expected to be simpler than that of V-grooves. Other hybrid waveguide structures combining metals and dielectrics are currently being studied for the nanometric focusing of light (Wang 2004) and more generally for the realization of ultracompact integrated optics (Charbonneau 2005).

Conclusion and Perspectives

More than a decade after the first demonstration of photonic band gaps, photonic crystals remain fascinating in view not only of their analogy with solid state crystals, but most of all of the unique opportunity of bringing together knowledge and experience from different fields of research, ranging from solid state physics to optics, microwaves and microelectronics The large variety of approaches presented in this book reflect the complexity and breadth of this topic. Furthermore, its heuristic usefulness has led to its inclusion in graduate curricula in optics and electronics.

Beyond these remarks of a general character, it has been seen in this book that photonic crystals have paved the way to the development of a new generation of optical devices with ultimate dimensions and properties, i.e. optical devices at the wavelength scale. Among these devices, microstructured silica fibres are likely to become the first photonic-crystal-based product to reach the marketplace. In the field of semiconductors, the transition from concept to actual applications took more time than originally expected. Not only was it necessary to address numerous technological difficulties, but existing devices in optical communications had already at this time achieved a high level of sophistication. Fortunately enough, most of these difficulties are currently in the process of being solved thanks to the advances which have been taking place in the fields of microtechnology and nanotechnology. One of the major breakthroughs expected to occur during the next decade is the fabrication of two and three-dimensional photonic crystals in which ultra-small waveguides and microcavities could be incorporated on demand. More generally, it should be borne in mind that the elementary patterns of photonic crystals in the near-infrared region, i.e. at telecommunication wavelengths, are typically in the range of one hundred nanometers, with aspect ratios ranging from one to ten. For this reason, the accuracy required for the fabrication of efficient devices can be estimated to be of the order of ten nanometers, and even less. This is about the same accuracy scale as for mainstream silicon microelectronics.

Photonic crystals are also at the very origin of the parallel which is now being increasingly drawn between nanoelectronics and nanophotonics. In addition to the miniaturization of optical devices and systems that they allow, one of the guiding ideas in the practical development of photonic crystals is the possibility of fabricating, in a limited number of technological steps, the main constitutive elements of future large-scale-integration photonic circuits. In simple terms, this would provide a practical ‘toolkit’ for the design of circuits in optics and optoelectronics, combining the most advanced lithography and etching processes. Different meth-

ods are now being proposed for the computer-assisted design of the first elementary photonic circuits. Hybrid circuits where photonic circuits would be associated on the same chip to electronic circuits are also being proposed. One of the decisive advantages of using optical rather than electrical signals is the perspective of a much weaker interaction between the signals themselves.

As a result of the easier control of the two-dimensional topology of planar integrated optics, considerable advances on two-dimensional photonic crystal devices have been taking place during the last decade. In particular, thanks to the numerous modelling and characterization studies that have been conducted on photonic waveguides, the scientific community has gained a clearer understanding of the limitations of the two main alternatives, i.e. highly-confined and weakly-confining photonic crystal waveguides, corresponding to membrane waveguides and to buried photonic crystal waveguides respectively. Several approaches have been developed for reaching an acceptable level of loss. This problem remains the most critical issue as far as applications to actual devices are concerned, especially with respect to the implementation of such optical functions as the filtering, the guiding or the emission of light. It is expected that systems based on photonic crystals will soon be mature enough to compete with the most performing demultiplexer systems in optical telecommunications, such as waveguide arrays or the so-called 'phasars'. The encouraging results obtained on light bends, on mode matching systems and on 'add-drop' filters, where photonic crystal waveguides are combined to microcavities, demonstrate that photonic crystals hold even greater promises for a great variety of miniature active devices.

The perspective offered by the past decades clearly indicates that we are only at the beginnings of the first microsources and nonlinear optical devices based on the use of photonic crystals, and that a potential exists for much lower thresholds of optical nonlinearities, for instance in very high-Q cavities. Taking a broader view, the approach to 'light management' by highly structured dielectrics, whether it has been successful or not in its different applications, has undoubtedly created an environment for the growth of the two neighbouring fields of plasmonics and metamaterials. These domains dramatically expand the perspectives of the metallo-dielectric structures discussed in this book.

Mentioning the practical applications of photonic crystals without recognizing the important theoretical perspectives opened by the modelling studies conducted on this subject would be an unforgivable omission. This book, not only in its first part, but also in its second part devoted to the optical properties of photonic crystals and to the design of miniature photonic devices, has hopefully provided the reader with an insight into the extraordinary breadth of the problems posed by photonic crystals in terms of electromagnetic modelling. Difficult problems need to be solved for each specific situation, for instance in the case where a three-dimensional analysis is necessary, and even more so when the crystal is formed from composite elements such as metamaterials, or when it is combined with active elements such as emitters or nonlinear materials. It can be safely predicted that the dynamic process started by theoretical studies on photonic crystals will continue to generate new ideas for electromagnetic modelling.

Finally, one of the original dreams of the pioneers of research on photonic crystal, i.e. achieving the complete control of light with a single emitter in photonic crystal microcavities, now seems to be within reach. The perspective of developing practical implementation schemes for quantum cryptography is presently a strong incentive towards achieving this goal. Even if other options are available, the relevance of photonic crystal microcavities in this context is no longer disputed. Photonic crystals are no longer in their infancy, and it is now to be hoped that the continuous advances arising in micro- and nanotechnology, combined with the intellectual appeal of the questions raised by photonic structures, will enable them to flourish during the next decade.

Appendices

Appendix A. Scattering Matrix Method: Determination of the Field for a Finite Two-Dimensional Crystal formed by Dielectric Rods

This appendix will be devoted to a more complete and detailed exposition of the scattering matrix method, also referred to as the multipole method or as the modal method, which has been introduced in Section 2.3 of Chapter 2. We more specifically consider the problem of the determination of the field in two-dimensional photonic crystals formed by an array of dielectric rods in the air.

A.1 Incident Field

In the coordinate system represented in Fig. A.1, the incident field illuminating the array of rods can be written as follows:

$$E_z^i = exp\left(ik_0 n_{ext}\left(x\,sin\,\Theta^{inc} - y\,cos\,\Theta^{inc}\right)\right) \tag{A.1a}$$

A.2 Field inside the Rods

Inside an arbitrary dielectric rod with permittivity $\varepsilon_{r,int}$, the total field satisfies the following equation:

$$\nabla^2 E_z + k_0^2 \varepsilon_{r,int} E_z = 0 \tag{A.2}$$

We shall use a system of local polar coordinates (r_j, θ_j) with an origin located at the centre of the j^{th} rod. For a fixed value of r_j, the field is a periodic function of θ_j with a period 2π, and therefore it can be written in the form of a Fourier series:

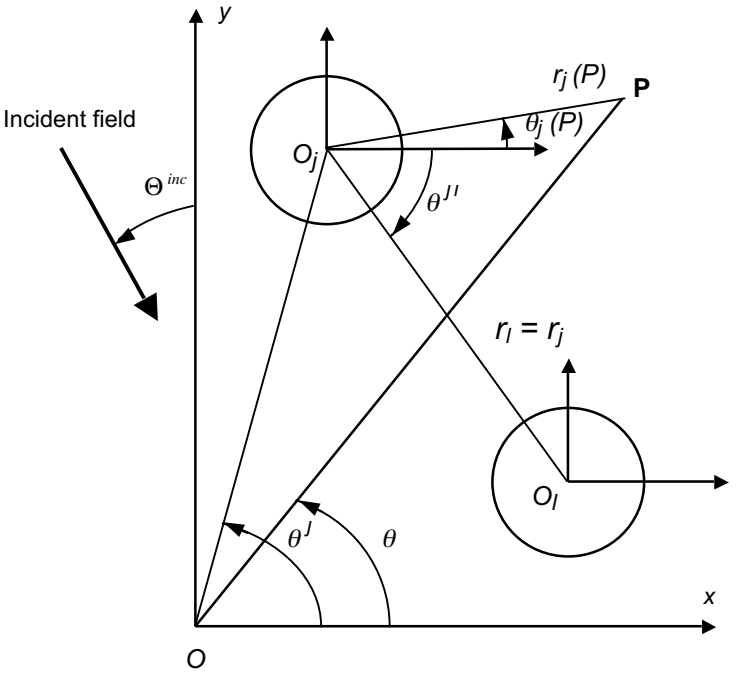

Fig. A.1. Representation of the coordinate system

$$E_z\left(r_j,\theta_j\right)=\sum_{m=-\infty,+\infty}E_{z,m}\left(r_j\right)exp\left(im\theta_j\right) \tag{A.3}$$

We shall use the expression in polar coordinates of the scalar Laplacian:

$$\nabla^2 \mathrm{V}=\frac{\partial^2 V}{\partial r_j^2}+\frac{1}{r_j}\frac{\partial V}{\partial r_j}+\frac{1}{r_j^2}\frac{\partial^2 V}{\partial \theta_J^2} \tag{A.4}$$

Let us now introduce the expression of the field given by Eq. A.3 in Eq. A.4. A straightforward calculation demonstrates that the Fourier coefficients satisfy the following equation:

$$\forall m \qquad \frac{d^2 E_{z,m}}{dr_j^2}+\frac{1}{r_j}\frac{\partial E_{z,m}}{\partial r_j}+\left(k_0^2\varepsilon_{r,int}-\frac{m^2}{r_j^2}\right)E_{z,m}=0 \tag{A.5}$$

Assuming that $r'_j = k_0\, n_{int} r_j$, and proceeding to some simplifications, this equation becomes:

$$\forall m, \qquad \frac{d^2 E_{z,m}}{dr_j'^2} + \frac{1}{r_j'}\frac{\partial E_{z,m}}{\partial r_j'} + \left(1 - \frac{m^2}{r_j'^2}\right) E_{z,m} = 0 \tag{A.6}$$

We are therefore led back to Bessel's equation. The general solution of this equation is given by:

$$E_{z,m} = c'_{j,m} J_m\left(r_j'\right) + d'_{j,m} Y_m\left(r_j'\right) = c'_{j,m} J_m\left(k_0 n_{int} r_j\right) + d'_{j,m} Y_m\left(k_0 n_{int} r_j\right) \tag{A.7}$$

where J_m and Y_m are Bessel functions of the m^{th} order of the first and second kinds respectively (Abramovitz 1970).

The right-hand side of Eq. A.7 can also be written in the following form:

$$E_{z,m} = \left(c'_{j,m} + id'_{j,m}\right) J_m\left(k_0 n_{int} r_j\right) - id'_{j,m}\left(J_m\left(k_0 n_{int} r_j\right) + iY_m\left(k_0 n_{int} r_j\right)\right) \tag{A.8}$$

Let us here remind ourselves that the definition of the Hankel function of m^{th} order of the first kind is:

$$H_m^{(1)}(u) = J_m(u) + iY_m(u) \tag{A.9}$$

It thus turns out that Eq. A.8 can be rewritten in the form:

$$E_{z,m} = c_{j,m} J_m\left(k_0 n_{int} r_j\right) + d_{j,m} H_m^{(1)}\left(k_0 n_{int} r_j\right) \tag{A.10}$$

where the coefficients $c_{j,m}$ and $d_{j,m}$ can be easily deduced from $c'_{j,m}$ and $d'_{j,m}$.

It shall be later demonstrated that this new expression of the field is the most adequate for a physical interpretation of the two terms appearing in its right-hand side. Introducing this expression for $E_{z,m}$ in Eq. A.3, we arrive at an expression of the total field in the rod in terms of a Fourier-Bessel expansion:

$$E_z\left(r_j, \theta_j\right) = \sum_{m=-\infty,+\infty} \left[c_{j,m} J_m\left(k_0 n_{int} r_j\right) + d_{j,m} H_m^{(1)}\left(k_0 n_{int} r_j\right)\right] exp\left(im\theta_j\right) \tag{A.11}$$

It can be noted that, in the specific case of the field inside the rods, all coefficients $d_{j,n}$ become zero. Indeed, the Hankel function $H_m^{(1)}(s)$ presents a singularity

at $s = 0$. Since the field cannot be singular, the corresponding terms have to be removed from the expression of the field, and therefore, for $r_j < R$:

$$E_z\left(r_j, \theta_j\right) = \sum_{m=-\infty,+\infty} c_{j,m} J_m\left(k_0 n_{int} r_j\right) \exp\left(im\theta_j\right) \tag{A.12}$$

The determination of the field inside the rods thus reduces to the calculation of the coefficients $c_{j,m}$ of the Fourier-Bessel expansion given in the right-hand side of Eq. A.12.

A.3 Field in the Vicinity of a Rod

The calculations which have led to the expression of the field inside the rods can be reproduced almost identically for the regions outside the rods.

Thus, it can be demonstrated that the field outside the rods satisfies the following Helmholtz equation:

$$\nabla^2 E_z + k_0^2 \varepsilon_{r,ext} E_z = 0 \tag{A.13}$$

Let us now consider the circular region surrounding the j^{th} rod and extending to the nearest point of the immediately neighbouring rod. This region is represented by the light grey area in Fig 2.10 of Chapter 2. In this region, the value of the refractive index is constant and equal to n_{ext}. Using the same coordinate system and the same mathematical development as in the preceding section, it can be demonstrated that the field in this region assumes the form of a Fourier-Bessel series similar to the series given in Eq. A.11:

$$\begin{aligned} E_z\left(r_j, \theta_j\right) = & \sum_{m=-\infty,+\infty} a_{j,m} J_m(k_0 n_{ext} r_j) \exp(im\theta_j) \\ & + \sum_{m=-\infty,+\infty} b_{j,m} H_m^{(1)}(k_0 n_{ext} r_j) \exp(im\theta_j) \end{aligned} \tag{A.14}$$

In this case however, it is no longer possible to demonstrate that the coefficients $b_{j,m}$ are zero. Indeed, no physical argument prevents the field from being singular at the origin, since this origin does not belong to the ring itself.

Nevertheless, the two terms appearing in the right-hand side of Eq. A.14 can be given a physical interpretation, which rests on the properties of Bessel functions. The field in the ring can indeed be decomposed into three different components:

– the incident plane wave, i.e. the source, given by Eq. A1,

- the field scattered by the j^{th} rod. From the radiation condition at infinity, this field must propagate away from this rod,
- the fields scattered by the all other rods in the direction of the j^{th} rod. These fields behave with respect to this rod as an incident field. Accordingly, the total incident field at the j^{th} rod is formed by these fields and by the incident plane wave, i.e. the source term.

In order to identify each physical component in Eq. A.14, we observe first that the total incident field at the j^{th} rod is necessarily generated by sources located outside this rod. This field must therefore satisfy a Helmholtz equation *inside* this rod without presenting any singularity. This property allows us to conclude that the total incident field is contained in the first sum of Eq. A.14, and therefore that the second sum represents the field scattered by the j^{th} rod. The only remaining question is whether this second sum represents the totality, or whether it corresponds to only a part of the field scattered by the j^{th} rod. In the first case, the first sum would represent the total incident field on this rod, whereas in the second case it would also contain a part of the field scattered by the j^{th} rod complementary to the second sum. This question can be answered by observing that, from causality, the field scattered by the j^{th} rod must propagate away from this rod. It can be demonstrated that the only Fourier-Bessel functions satisfying this condition are the Hankel functions of the first kind. For instance, apart from a multiplying factor, the Hankel function of zeroth order of the first kind is but the Green's function solution for the Helmholtz equation in a homogeneous space with permittivity $\varepsilon_{r,ext}$, under the assumption of a radiation condition at infinity:

$$\nabla^2\left[-\frac{i}{4}H_0^{(1)}\left(k_0 n_{ext} r_j\right)\right] + k_0^2 \varepsilon_{r,ext}\left[-\frac{i}{4}H_0^{(1)}\left(k_0 n_{ext} r_j\right)\right] = \delta(x)\delta(y) \qquad \text{(A.15)}$$

From a physical point of view, the Green's function thus defined represents the field that would be generated by an infinitely thin linear source located along the z axis, i.e. parallel to the rods, the space being assumed to be homogeneous and with a permittivity $\varepsilon_{r,ext}$. In order to verify that Hankel functions of the first kind satisfy the radiation condition at infinity for any order, it suffices to consider their asymptotic expression at infinity (Abramovitz 1970):

$$H_m^{(1)}\left(k_0 n_{ext} r_j\right) \cong \sqrt{\frac{2}{\pi k_0 n_{ext} r_j}}\, exp\left[i\left(k_0 n_{ext} r_j - m\frac{\pi}{2} - \frac{\pi}{4}\right)\right] \qquad \text{(A.16)}$$

The second sum in Eq. A.14 represents a field scattered by the j^{th} rod. On the contrary, an arbitrary term of the first sum cannot represent a scattered field since, from Eq. A.9, J_m (s) can be written in the form:

$$J_m(s) = H_m^{(1)}(s) + \overline{H}_m^{(1)}(s) \tag{A.17}$$

where $\overline{H}_m^{(1)}(s)$ denotes the complex conjugate of $H_m^{(1)}(s)$. It is quite apparent from Eq. A.16 that $\overline{H}_m^{(1)}(s)$ does not satisfy the radiation condition. This definitely demonstrates that the first sum in Eq. A.14 represents the total incident field striking the j^{th} rod and the second sum the field scattered by the j^{th} rod.

Let us now proceed to the determination of the contribution of the incident source field to the first sum. This field is given by Eq. A.1a, and at any arbitrary point *P* of space (Fig. A.1), it can be written in the form:

$$E^j(P) = exp(i\mathbf{k}.\mathbf{OP}) \tag{A.1b}$$

where $(k_0 n_{ext} \sin\Theta^{inc}, -k_0 n_{ext} \cos\Theta^{inc})$ are the coordinates of the incident wave vector **k**. Writing vector **OP** as the sum of vectors $\mathbf{OO_j}$ and $\mathbf{O_jP}$, we arrive at the following equation:

$$\begin{aligned} E^i(P) &= exp\left(i\mathbf{k}.\left(\mathbf{OO}_j + \mathbf{O}_j\mathbf{P}\right)\right) \\ &= exp\left[ik_0 n_{ext} r^j \sin\left(\Theta^{inc} - \theta^j\right)\right] exp\left[ik_0 n_{ext} r_j(P) \sin\left(\Theta^{inc} - \theta_j(P)\right)\right] \end{aligned} \tag{A.18}$$

where r^j, θ^j denote the polar coordinates of the origin O_j of the local coordinate system in the general *xy* system represented in Fig. A.1. Let us now use the following formula, given in (Abramovitz 1970):

$$exp\left(i\xi \sin(u)\right) = \sum_{m=-\infty}^{m=+\infty} J_m(\xi) exp(imu) \tag{A.19}$$

The application of Eq. A. 19 leads to the following expression for $E^i(P)$:

$$\begin{aligned} E^i(P) = {} & exp\left[ik_0 n_{ext} r^j \sin\left(\Theta^{inc} - \theta^j\right)\right] \times \\ & \sum_{m=-\infty,+\infty} exp\left(im\Theta^{inc}\right) J_m\left(k_0 n_{ext} r_j(P)\right) exp\left(-im\theta_j(P)\right) \end{aligned} \tag{A.20a}$$

Since $J_{-m}(s) = (-1)^m J_m(s)$, *m* can be replaced by $-m$ in Eq. A.20a. This will simplify the comparison with the terms in Eq. A.14:

$$E^i(P) = exp\left[ik_0 n_{ext} r^j \sin\left(\Theta^{inc} - \theta^j\right)\right]\times \sum_{m=-\infty,+\infty} (-1)^m exp\left(-im\Theta^{inc}\right) J_m\left(k_0 n_{ext} r_j(P)\right) exp\left(im\theta_j(P)\right) \quad \text{(A.20b)}$$

Eqs. A.20a and A.20b give the development of the incident source field into Fourier-Bessel series in the coordinate system associated with the j^{th} rod. Going back to Eq. A.14, it is now possible to distinguish the coefficients of the Fourier-Bessel series associated with the source field from the coefficients associated with the field scattered by the other rods. These two sets of coefficients will be denoted by $a_{j,m}^{source}$ and $a_{j,m}^{rods}$ respectively, and their sum is equal to $a_{j,m}$. From Eq. A.20b, $a_{j,m}^{source}$ can be identified with the following expression:

$$a_{j,m}^{source} = (-1)^m exp\left(ik_0 n_{ext} r^j \sin\left(\Theta^{inc} - \theta^j\right) - im\Theta^{inc}\right) \quad \text{(A.21)}$$

The three components of the field in the ring surrounding the j^{th} rod can therefore be expressed respectively as follows:

– the source term is:

$$E_{z,j}^{source}\left(r_j,\theta_j\right) = \sum_{m=-\infty,+\infty} a_{j,m}^{source} J_m\left(k_0 n_{ext} r_j\right) exp\left(im\theta_j\right) \quad \text{(A.22)}$$

– the field scattered by the other rods in the direction of the j^{th} rod is:

$$E_{z,j}^{rods}\left(r_j,\theta_j\right) = \sum_{m=-\infty,+\infty} a_{j,m}^{rods} J_m\left(k_0 n_{ext} r_j\right) exp\left(im\theta_j\right) \quad \text{(A.23)}$$

– the field scattered by the j^{th} rod is:

$$E_{z,j}^{d}\left(r_j,\theta_j\right) = \sum_{m=-\infty,+\infty} b_{j,m} H_m^{(1)}\left(k_0 n_{ext} r_j\right) exp\left(im\theta_j\right) \quad \text{(A.24)}$$

It has been demonstrated that the total field in the ring can be expressed in terms of three series of coefficients: $a_{j,m}^{source}$, $a_{j,m}^{rods}$ and $b_{j,m}$, among which only the first coefficient is known. Before proceeding to the calculation of these components, an observation must be made on Eq. A.24. The expression given by this equation for the field scattered by the j^{th} rod in the circular region surrounding it

(see Figure 2.10 in Section 2.3 of Chapter 2) extends actually to the whole space surrounding this rod. While this result can be rigorously demonstrated from the properties of Fourier-Bessel functions (Maystre 2002), we shall content ourselves with admitting that the field scattered by the j^{th} rod is generated by sources, i.e. by dipoles, located in this rod. It can be noted that, by contrast, Eq. A.23 cannot be extended to the whole space, since the field generated by the dipolar sources located in the other rods ($\neq j$) may present singularities inside these rods.

The validity of Eq. A.24 in the whole space outside the j^{th} rod is a decisive property. It entails that the field represented by the coefficients $b_{j,m}$ actually is the field scattered by the j^{th} rod in the direction of the other rods, which itself is also a part of the field represented by the coefficients $a_{l,m}^{rods}$ $l \neq j$. Hence, if we now consider the balance of the total incident field at the l^{th} rod, i.e. if we add the incident source field to the fields scattered by all other rods in the direction of the l^{th} rod, we should now be in the position of expressing the coefficients $a_{l,m}$, $m \in [-\infty,+\infty]$ in terms of the coefficients $a_{l,m}^{source}$, $m \in [-\infty,+\infty]$ and $b_{j,m}$, ($m \in [-\infty,+\infty]$, $j \neq l$). For this purpose, it is necessary first to solve a mathematical problem: indeed, the incident field at the l^{th} rod is expressed in a local coordinate system associated with this rod, whereas the fields scattered by the other rods are expressed in the local coordinate system associated with these rods.

The representation of all fields in the unique coordinate system associated with the l^{th} rod can be achieved by using Graf's formula (Abramovitz 1970). This formula expresses in a mathematical form a physically very intuitive result: the field scattered by the j^{th} rod along the direction of the l^{th} rod satisfies in the vicinity of this rod a Helmholtz equation without exhibiting any singularity. This field can therefore be expressed in the form of a Fourier-Bessel series containing only Bessel functions of the first kind. Using the notations presented in Fig. A.1, this formula can be written, in the case where $r_l(P) \leq r_l^{\,j} = O_l O_j$, in the following form:

$$H_m^{(1)}\left(k_0 n_{ext} r_j(P)\right) exp\left(im\theta_j(P)\right) \tag{A.25}$$
$$= \sum_{q=-\infty}^{+\infty} exp\left(i(m-q)\theta_l^{\,j}\right) H_{q-m}^{(1)}\left(k_0 n_{ext} r_l^{\,j}\right) J_q\left(k_0 n_{ext} r_l(P)\right) exp\left(iq\theta_l(P)\right)$$

Eqs. A.24 and A.25 allow expressing the field scattered by the j^{th} rod in the direction of the l^{th} rod in the coordinate system with origin O_l. Therefore, in the case where $r_l(P) \leq r_l^{\,j} - R$:

$$E_{z,j}^d(P) = \tag{A.26a}$$
$$\sum_{m=-\infty}^{+\infty} b_{j,m} \sum_{q=-\infty}^{+\infty} \exp\left(i(m-q)\theta_l^{\,j}\right) H_{q-m}^{(1)}\left(k_0 n_{ext} r_l^{\,j}\right) J_q\left(k_0 n_{ext} r_l(P)\right) \exp\left(iq\theta_l(P)\right)$$

or, by reversing the indices m and q:

$$E_{z,j}^{d}(P) = \sum_{q=-\infty}^{+\infty} b_{j,q} \sum_{m=-\infty}^{+\infty} \exp\left(i(q-m)\theta_l^j\right) H_{m-q}^{(1)}\left(k_0 n_{ext} r_l^j\right) J_m\left(k_0 n_{ext} r_l(P)\right) \exp\left(im\theta_l(P)\right) \tag{A.26b}$$

The field $E_{z,l}^{rods}$ in the ring surrounding the l^{th} rod, which is obtained by replacing the index j by the index l in Eq. A.23, can be identified to the sum of the fields scattered by the $N-1$ other rods $\sum_{j\neq l} E_{z,j}^{d}$. The sum of these fields can be deduced from equations similar to Eq. A.26b. This identification leads to the following equation:

$$a_{l,m}^{rods} = \sum_{j\neq l} \sum_{q=-\infty,+\infty} b_{j,q}\, exp\left(i(q-m)\theta_l^j\right) H_{m-q}^{(1)}\left(k_0 n_{ext} r_l^j\right) \tag{A.27}$$

Adding the coefficient $a_{l,m}^{source}$ of the source field given by Eq. A.22 to the coefficients $a_{j,m}^{rods}$, $a_{l,m}$ can be expressed in terms of the coefficients $b_{j,q}$ of the fields scattered by the other rods:

$$\begin{aligned} a_{l,m} = {} & (-1)^m\, exp\left(ik_0 n_{ext} r^l\, sin\left(\Theta^{inc} - \theta^l\right) - im\Theta^{inc}\right) \\ & + \sum_{j\neq l} \sum_{q=-\infty,+\infty} b_{j,q}\, exp\left(i(q-m)\theta_l^j\right) H_{m-q}^{(1)}\left(k_0 n_{ext} r_l^j\right) \end{aligned} \tag{A.28}$$

Appendix B. Magneto-Photonic Crystals

This appendix will briefly describe some aspects related to magneto-photonic crystals. These structures have indeed potential applications for the design of non-reciprocal optical devices and, more generally, for the control of optical devices by a magnetic field.

Magneto-photonic crystals are periodic structures where one or several individual constituents are formed by magneto-optical materials, i.e. materials whose optical properties can be modified under application of a static or quasi-static magnetic field. The dielectric permittivity of such materials is represented by a 3×3 tensor, where each individual element depends on the magnetic field **H** (Landau 1984). For a non-zero value of H, the tensor is anti-symmetric, and various optical effects may occur depending on the orientation and intensity of the field and on the physical properties of the material itself. One of the most popular effects in this context is probably the Faraday effect, wherein the polarization of a linearly polarized plane wave is rotated in the presence of a magnetic field parallel to the wave vector. Thus, optical isolators based on the non-reciprocal Faraday effect are used in a number of experimental setups for the purpose of minimizing the backward reflection of optical sources. In the more general context of non-reciprocal phenomena, ferromagnetic materials are of particular interest because these materials exhibit a spontaneous magnetisation even in the absence of an external magnetic field. Metallic ferromagnetic materials have thus been successfully applied for the development of novel optical isolators integrated with semiconductor optical amplifiers (SOA) at telecommunication wavelengths. The theoretical concept of this integrated isolator was proposed in 1999 (Takenaka 1999; Zaets 1999) and first demonstrated in 2004 (Vanwolleghem 2004). A ferromagnetic contact with transverse magnetization was used for inducing differential losses between the two counter-propagating TM-polarized waves in the SOA waveguide. The amplifier medium of the SOA was able to compensate only for the losses of one of the two waves, while the transparency threshold was far from being reached for the other wave.

The main motivation for the use of magneto-optical materials in photonic crystals stems from the possibility of strongly enhancing magneto-optical effects through the confinement of light, and of controlling the optical properties of the photonic crystals themselves through the reorientation of the magnetization. Resonant effects in one-dimensional photonic crystal defects have thus been exploited by researchers for the sake of enhancing magneto-optical phenomena. As an example, considerable enhancements of the Faraday rotation were predicted and observed by Inoue *et al* and Fedyanin *et al* when a magneto-optical material is in-

cluded as a defect in one-dimensional Bragg-mirror-like photonic crystals (Fedyanin 2004; Inoue 1998). More generally, multilayer structures with random arrangement of dielectric and magneto-optical layers have been shown to exhibit strongly enhanced magneto-optical rotations in a rather similar light confinement process (Inoue 1997). However, only limited research has been devoted to the study of magneto-photonic crystals with dimensionality higher than one, and, more generally, to the investigation of the photonic band structures of this new class of photonic crystals. The first calculations of the band structures of one-dimensional magneto-photonic crystals in a non-perturbative approach were reported by A. Figotin *et al* in a pioneering study in 2003 (Figotin 2003). Optical non-reciprocity in these crystals was predicted by the authors, i.e. the possible existence of an asymmetric photonic band structure with $\omega(\vec{k}) \neq \omega(-\vec{k})$. They demonstrated that this optical non-reciprocity necessarily requires that none of the symmetry operations present in the symmetry group of the crystal should transform the wave vector $\vec{k}$ of the Bloch function into its opposite $-\vec{k}$. The occurrence of a symmetry operation violating the condition above is a sufficient condition for the reciprocity of the band structure for this particular direction. For one-dimensional photonic crystals where waves are assumed to propagate normally to the layers, it has been demonstrated that achieving spectral non-reciprocity requires the incorporation of a birefringent material in addition to magneto-optical materials and isotropic dielectrics. However, the demonstration was conducted for one-dimensional stacks where the magneto-optical layers consisted of ferrites. Since the magnetic permeability of ferrites is tensorial, their use is actually limited to the microwave regime.

Using a full vectorial anisotropic plane wave expansion algorithm (Johnson 2001), M. Vanwolleghem *et al* theoretically demonstrated the possibility of obtaining an asymmetric band structure for certain classes of two-dimensional magneto-photonic crystals, thereby identifying the necessary conditions for the symmetry of the spatial pattern of the unit cell of the crystals, as well as for the direction of magnetization (Vanwolleghem 2006a). The authors also showed that, even in the absence of non-reciprocity, the possibility always exists of tuning the band gap of the crystal through reorientation of the magnetization. However, as successful as these first investigations have been, there is a clear need for numerical approaches more powerful than existing methods, not only for the purpose of conducting more detailed studies of non-reciprocal effects in the band structures of magneto-photonic crystals, but also for the development of optical components based on magneto-photonic crystals.

In parallel with the first theoretical studies on magneto-photonic crystals, original schemes of optical devices have been proposed. A new version of a magneto-optical isolator integrated with a semiconductor optical amplifier has thus been suggested where the planar ferromagnetic contact would be replaced by a distributed Bragg grating ferromagnetic photonic crystal (Vanwolleghem 2006b). A strong reinforcement of the optical isolation is expected to occur near the band edge of the one-dimensional magneto-photonic crystal. In a similar context, Li *et al* have experimentally studied one-dimensional magneto-photonic crystal waveguides where a resonant defect had been inserted for the enhancement of the

Faraday rotation (Li 2005). A theoretical model (Belotelov 2005), followed by a numerical assessment (Jalali 2005), has also been proposed for the study of Faraday rotation in the case of two-dimensional magneto-photonic crystals. A three-port Y-junction optical circulator has been proposed by Wang *et al* based on two-dimensional magneto-photonic crystals where three W1 photonic crystal waveguides are coupled to a H1 cavity (Wang 2005) The field patterns of this optical circulator are represented here in Fig. B.1*a,b,c*. For a magnetization perpendicular to the plane of the H1 cavity, the presence of the magneto-optical material causes the two doubly degenerate modes of the cavity to split into two counter-rotating modes at different frequencies. Figs. B.1*b* and B.1*c* show the transmission/isolation properties of the magneto-optical circulator by comparison with the case where no magnetic material is used (Fig. B.1*a*). The feasibility of realizing such a magneto-optical circulator in a bismuth-iron-garnet (BIG)/air photonic crystal at 1550 nm was also considered by the authors. Finally, other optical devices might be envisioned following the study by Kono *et al*, who proposed an optical isolation based on non-reciprocal phase shifts in two-dimensional magneto-photonic crystal waveguides (Kono 2005).

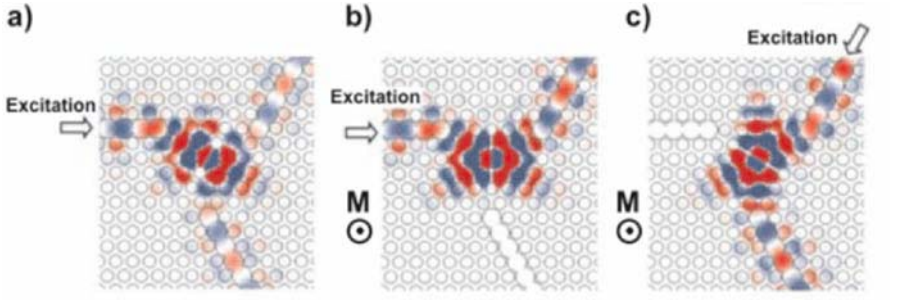

Fig. B.1. Calculated field patterns of the three-port junction optical circulator studied in (Wang 2005). Red and blue colours represent large positive and negative values of the field, respectively. Each of the three W1 waveguides connected to the H1 cavity is constructed by enlarging the radius of a row of air holes. *a.* Photonic crystal with non-magneto-optical material. *b.* Photonic crystal with a magneto-optical material. The cavity is excited at the input port. The magnetization is perpendicular to the plane of the cavity. *c.* Photonic crystal with a magneto-optical material. The cavity is excited at the output port. The magnetization is perpendicular to the plane of the cavity

Appendix C. Stigmatism of a Slab of Perfect Left-Handed Material: Integral for the Total Field

In this appendix, we shall present some expressions, more detailed than was possible in Section 6.4.3 of Chapter 6, for the stigmatism of a 'perfect lens' consisting of a slab of 'perfect left-handed material' (PHLM). We consider more specifically the problem of determining the electromagnetic field in the different regions of space when the PHLM slab is illuminated by a point source S. The parameters used in this appendix have been defined in Sections 6.4.2 and 6.4.3.

The field radiated by this point source at a point M located above the slab is given by the equation (Morse 1953):

$$E^S = H_0^{(1)}(k_0 SM) \tag{C.1a}$$

where $H_0^{(1)}$ is the Hankel function of the first kind and zeroth order, i.e. the Green function of the two-dimensional Helmholtz equation in air.

Using a classical formula (Morse 1953), the Hankel function at a point M can be expressed in the form of a sum of plane waves above and below the point source in the upper region (see Fig. 6.6 in Section 6.4):

$$H_0^{(1)}(k_0 SM) = \frac{1}{\pi} \int_{\alpha=-\infty}^{+\infty} \frac{1}{\beta(\alpha)} \exp\left(i\alpha x + i\beta(\alpha)\left|y - y_S\right|\right) d\alpha \tag{C.1b}$$

$$\text{with : } \beta(\alpha) = \sqrt{k_0^2 - \alpha^2} \quad \text{or} \quad i\sqrt{\alpha^2 - k_0^2} \tag{C.1c}$$

Below the point source, $y - y_S$ is negative, and therefore $|y - y_S| = y_S - y$. Accordingly, Eq. C.1b assumes the form:

$$H_0^{(1)}(k_0 SM) = \frac{1}{\pi} \int_{\alpha=-\infty}^{+\infty} \frac{1}{\beta(\alpha)} \exp\left(i\alpha x - i\beta(\alpha)\left[y - y_S\right]\right) d\alpha \tag{C.1d}$$

This equation shows that the slab is illuminated by a sum of plane waves with a propagation constant α in x and $\beta(\alpha)$ in y. Calculating the field at any point of

space is therefore very easy. From the entire set of equations from Eqs. 6.25 to 6.32 in Section 6.4.2 of Chapter 6, we know the expression for the field generated at any point of space by a single homogeneous plane wave illuminating the slab. For deriving integral equations for the field in each region of space, it therefore suffices to sum the contributions of all plane waves in Eq. C.1d with amplitudes $\frac{1}{\pi}\frac{\exp\left(i\beta(\alpha)y_S\right)d\alpha}{\beta(\alpha)}$. For example, the field below the slab will be written in the form:

$$\text{if } y < -e, \quad E = \frac{1}{\pi}\int_{\alpha=-\infty}^{+\infty}\frac{\exp\left(i\beta(\alpha)y_S\right)}{\beta(\alpha)}t(\alpha)\exp\left(i\alpha x - i\beta(\alpha)y\right)d\alpha \qquad \text{(C.2a)}$$

where $t(\alpha)$ is as given by Eq. 6.32. It should be noted however that the integration in Eq. C.2a extends from $\alpha = -\infty$ to $\alpha = +\infty$, and therefore that $\beta(\alpha)$ takes imaginary values outside the interval $\alpha \in [-k_0, +k_0]$. In this case, the incident homogeneous plane wave in Eq. C.1d becomes an evanescent wave. Indeed, since $\beta(\alpha) = i\sqrt{\alpha^2 - k_0^2}$, the plane wave assumes the form:

$$\exp\left(i\alpha x - i\beta(\alpha)y\right) = \exp\left(i\alpha x + \chi(\alpha)y\right), \text{ with } \chi(\alpha) = \sqrt{\alpha^2 - k_0^2} \qquad \text{(C.2a)}$$

Such a wave will be referred to as an 'incident evanescent wave' in the following, even though it would be more appropriately termed an 'incident anti-evanescent wave' since its amplitude increases exponentially with y, contrary to evanescent waves. It is worth noting that the equations from Eq. 6.25 to Eq. 6.32 in Section 6.4.2 hold for waves of this kind, and therefore that expressions of the field such as Eq. C.2a can be used.

Thus, combining Eqs. C.2a and 6.32 leads to the following equation for the field below the slab:

$$E = \frac{1}{\pi}\int_{\alpha=-\infty}^{+\infty}\frac{1}{\beta(\alpha)}\exp\left(i\alpha x - i\beta(\alpha)\left[y - y_S + 2e\right]\right)d\alpha \qquad \text{(C.2zb)}$$

Obviously, the expression for transmitted field will be the same as the expression for the field radiated by the point source, but with a translation of $-2e$ in y. Bearing in mind that the expression of the field radiated by the point source given by Eq. C.1d is only valid below the point source, we are thus led to the conclusion that, below the ordinate $y = y_S - 2e$, the field transmitted by the slab identifies with

the field that would be radiated by a point source placed at the point F (Fig. 6.6 in Chapter 6) of coordinates $x = 0$, $y = y_S - 2e$. The image at point F of the point source S is therefore stigmatic, and has the same intensity as S (Pendry 2000). Interestingly, a similar study of the field inside the slab shows the existence of another stigmatic image of S, which is located at point $\tilde{S}$ and is symmetric to S with respect to the upper interface of the slab.

References

Abbott EA (1992) Flatland, a Romance of Many Dimensions. Dover Publications, New York

Abernethy JA (2003) Novel devices in periodically poled lithium niobate. University of Southampton, Faculty of Engineering and Applied Science, Optoelectronics Research Centre, PhD Thesis

Abram I, Robert I, Kuszelewicz K (1998) Spontaneous emission control in semiconductor microcavities with metallic or Bragg mirrors. IEEE J Quant Elect 34 : 71

Abramovitz M, Stegun I (1970) Handbook of Mathematical Functions. Dover Publications, New York

Agrawal GP (2001) Nonlinear Fiber Optics. Academic Press, 3rd edition

Agrawal GP, Dutta N (1993) Semiconductor Lasers. Van Nostrand Reinhold, New York

Akahane Y, Asano T, Song BS, Noda S (2003a) High-Q nanophotonic in a two-dimensional photonic crystal. Nature 425 : 944-947

Akahane Y, Asano T., Song BS, Noda S (2003b) Investigation of high-Q channel drop filters using donor-type defects in two-dimensional photonic crystal slabs. Appl Phys Lett 83 : 1512-1514

Akalin T, Danglot J, Vanbesien O, Lippens D (2001) A highly directive dipole antenna embedded in a Fabry-Perot type cavity. IEEE Microwave and Wireless Components Lett 12 : 48-50

Albert JP, Jouanin C, Cassagne D, Bertho D (2000) Generalized Wannier function method for photonic crystals. Phys Rev B 61 : 4381

Almogy G, Yariv A (1994) Second harmonic generation in absorptive media. Optics Lett 19 : 1828

Amezcua-Correa R, Petrovitch MN, Broderick NGR, Richardson DJ, Delmonte T, Watson MA, O'Driscoll EJ (2006) Broadband Infrared Transmission in a Hollow-Core Photonic Bandgap Fibre Free of Surface modes. Tech. Digest of ECOC : paper We4.4.4

Anderson PW (1985) The question of classical localization. A theory of white paint? Phil Mag B 52 : 505-509

Andreani LC, Panzarini G, Gérard JM (1999) Strong-coupling regime for quantum boxes in pillar microcavities: theory. Phys Rev B 60 : 13276

Angot A (1982) Compléments de Mathématiques (in French). Masson, 6th edition, Paris New York

Arbore MA, Galvanauskas A, Harter D, Chou MH, Fejer MM (1997) Engineerable compression of ultrashort pulses by use of second-harmonic generation in chirped-period-poled lithium niobate. Optics Lett 22 : 1341

Argyros A, Birks T, Leon-Saval S, Cordeiro CMB, Russell PSJ (2005) Guidance properties of low-contrast photonic bandgap fibres. Opt. Express 13 : 2503-2511

Armani DK, Kippenberg T.J, Spillane SM, Vahala KJ (2003) Ultra-high Q toroid microcavity on a chip. Nature 421 : 925-928

Armstrong JA, Bloembergen N, Ducuing J, Pershan PS (1962) Interactions between light waves in a non linear dielectric. Phys Rev 127 : 1918

Asakawa K, Sugimoto M, Watanabe K, Ozaki N, Mizutani A, Takata Y, Kitagawa Y, Ishikawa H, Ikeda N, Awazu K, Watanabe A, Nakamura S, Ohkouchi S, Inoue K, Kristensen M, Sigmund O, Borel PI, Baets R (2006) Photonic crystal and quantum dot technologies for all-optical switch and logic device. New J Phys 8 : 208-220

Asano T, Song BS, Akahane Y, Noda S (2006a) Ultrahigh-Q Nanocavities in Two-Dimensional Photonic Crystal Slabs. IEEE J Sel Top in Quantum Electron 12 : 1123-1134

Asano T, Song BS, Noda S (2006b) Analysis of the experimental Q factors (> 1 million) of photonic crystal nanocavities. Opt Express 14 : 1996-2002

Ashcroft NW, Mermin ND (1976) Solid State Physics. Saunders College Publishing

Assefa S, McNab SJ, Vlasov YA (2006) Transmission of slow light through photonic crystal waveguide bends. Opt Lett 31 : 745-747

Astratov VN, Bogomolov VN, Kapyanskii AA, Prokofiev AV, Samoilovich LA, Samoilovich SM, Vlasov YuA (1995) Optical spectroscopy of opal matrices with CdS embedded in its pores: quantum confinement and photonic band gap effects. Nuovo Cimento D17 : 1349

Astratov VN, Stevenson RM, Culshaw IS, Whittaker DM, Skolnick MS, Krauss T.F, De La Rue RM (2000) Heavy photon dispersions in photonic crystal waveguides. Appl Phys Lett 77 : 178-180

Avdokhin AV, Popov SV, Taylor JR (2003) Continuous-wave, high-power, Raman continuum generation in holey fibers. Opt Lett 28 : 1353-1355

Ayre M, Karle TJ, Wu L, Davies T, Krauss TF (2005) Experimental verification of numerically optimized photonic crystal injector, Y-splitter, and bend. IEEE Journal on Selected Areas in Communications 23 : 1390-1395

Baas A, Karr JPh, Romanelli M, Bramati A, Giacobino E (2004) Optical bistability in semiconductor Microcavities in the nondegenerate parametric oscillation regime: analogy with the optical parametric oscillator. Phys Rev B 70 : 161307 -

Baba T (2007) Photonic crystals: Remember the light. Nature Photonics 1 : 11-12

Baba T, Fujita M, Sakai A, Kihara M, Watanabe R (1997) Lasing characteristics of InGaAsP-InP strained quantum well microdisk injection lasers with diameter of 2-10 μm. IEEE Photon Technol Lett 9 : 878-

Baba T, Fukaya N, Yonekura J (1999) Observation of light propagation in photonic crystal optical waveguides with bend. Electron Lett 35 : 654-655

Baba T, Hamano T, Koyama F (1991) Spontaneous emission factor of a microcavity DBR surface emitting laser. IEEE J Quant Electron 27 : 1347-

Baba T, Hamano T, Koyama F, Iga K (1992) Spontaneous emission-factor of a microcavity DBR surface emitting laser (II), effect of electron confinement. IEEE J Quant Electron. 28 : 1310-

Baba T, Matsumoto T. (2002) Resolution of photonic crystal superprism. Appl Phys Lett 81 : 2325-2327

Badolato A, Henessy K, Atatüre M, Dreiser J, Hu E, Petroff PM, Imamoglu A (2005) Deterministic coupling of single quantum dots to single nanocavity modes. Science 308 : 1158-1161

Balakin AV, Bushuev VA, Mantsyzov BI, Ozheredov IA, Petrov EV, Shkurinov AP, Masselin P, Mouret G (2001) Enhancement of sum frequency generation near the photonic band gap edge under the quasi phase matching conditions. Phys Rev E 63 : 046609

Baliarda CP, Romeu I, Cardama A (2000) The Koch monopole: a small fractal antenna. IEEE Trans Antennas Propag 48 : 1773-1781

Bao KD, McPhedran RC, Nicorovici NA, Poulton CG, Botten LC (2000) The electromagnetic modes and homogenization for a cubic lattice of spheres. Physica B 279 : 162-163

Barclay PE, Srinivasan K, Painter O (2005) Nonlinear response of silicon photonic crystal microresonators excited via an integrated waveguide and fiber taper. Opt Express 13 : 801-820

Barnes WL (1999) Electromagnetic crystals for surface plasmon polaritons and the extraction of light from emissive devices. IEEE J Lightwave Technol 17 (1999) 2170-2182

Barnes WL, Björk G, Gérard JM, Jonsson P, Wasey J, Worthing P, Zwiller V (2002) Solid-state single photon sources : light collection strategies. Eur Phys J D 18 : 197-

Barnes WL, Kitson SC, Preist TW, Sambles JR (1997) Photonic surfaces for surface plasmon-polaritons. J Opt Soc. Am 14 : 1654-1661

Barnes WL, Preist TW, Kitson SC, Sambles JR (1996) Physical origin of photonic energy gaps in the propagation of surface plasmons on gratings. Phys Rev B 54 : 6227-6244

Barton G, van Eijkelenborg MA, Henry G, Large MCJ, Zagari J (2003) Fabrication of microstructured polymer optical fibres. Opt Fib Tech 10 : 325-335

Bayer M, Ortner G, Stern O, Kuther A, Gorbunov A, Forchel A, Hawrylak P, Fafard S, Hinzer K, Reinecke TL, Walck CK, Reithmaier JP, Klopf F, Schäfer F (2002). Fine structure of neutral and charged excitons in self-assembled InGaAs/GaAs quantum dots. Phys Rev B 65 : 195315

Bayer M, Reinecke TL, Weidner L, Larionov A, Mc Donald A, Forchel A (2001) Inhibition and Enhancement of the Spontaneous Emission of Quantum Dots in Structured Microresonators. Phys Rev Lett 86 : 3168-

Belotelov VI, Doskolovich LL, Zvezdin AK (2007) Extraordinary Magneto-optical effects and transmission through metal-dielectric plasmonic sytems. Phys Rev Lett 98 : 077401 (1-4)

Belotelov VI, Zvezdin AK (2005) Magneto-optical properties of photonic crystals. J Opt Soc Am B 22 : 286-292

Benabid F, Knight JC, Antopoulous G, Russell P St.J (2002a) Stimulated Raman scattering in hydrogen-filled hollow-core photonic crystal fiber. Nature 298 : 399–402

Benabid F, Knight JC, Russell P St.J (2002b) Particle levitation and guidance in hollow-core photonic crystal fiber. Opt.Express 10 : 1195–1203

Benisty H, De Neve H, Weisbuch C (1998a) Impact of planar microcavity effects on light extraction: I. basic concepts and analytical trends. IEEE J Quant Electron 34 : 1612-1631

Bénisty H, De Neve H, Weisbuch C (1998b) Impact of planar microcavity effects on light extraction : II. Selected exact simulation and role of photon recycling. IEEE J Quant Electron. 34 : 1632-1643

Benisty H, Labilloy D, Weisbuch C, Smith CJM, Krauss TF, Béraud A, Cassagne D, Jouanin C (2000) Radiation losses of waveguide-based two-dimensional photonic crystals : positive role of the substrate. Appl Phys Lett 76 : 532-534

Benisty H, Lalanne P, Olivier S, Rattier M, Weisbuch C, Krauss TF, Smith CJM, Jouanin C, Cassagne D (2002) Finite-depth and intrinsic losses in vertically etched two-dimensional photonic crystals. Optical and Quantum Electronics 34 : 205-215

Benisty H, Lourtioz, JM., Chelnokov A, Combrié S, Checoury X, (2006). Recent Advances Toward Optical Devices in Semiconductor-Based Photonic Crystals. IEEE Proc 94 : 997-1023

Benisty H, Weisbuch C, Labilloy D, Rattier M, Smith CJM, Krauss TF, De La Rue RM, Houdré R, Oesterle U, Cassagne D (1999) Optical and confinement properties of two-dimensional photonic crystals. J Lightwave Technol 17 : 2063-2077

Bennett CH, Brassard G, Ekert AK (1992) Quantum cryptography. Sci Am 267 : 50-

Benson O, Santori S, Pelton M, Yamamoto Y (2000) Regulated and entangled photons from a single quantum dot. Phys Rev Lett 84 : 2513-2516

Bérenger JP (1994) A perfectly matched layer for the absorption of electromagnetic waves. J Computational Physics 14 : 185-200

Berger V (1997b) Second harmonic generation in monolithic cavities. J Opt Soc Am B 14 : 1351-

Berger V (1998) Nonlinear photonic crystals. Phys Rev Lett 81 : 4136-

Berger V (1999) Photonic crystals for nonlinear optical frequency conversion in : Benisty H *et al.* (eds) Confined Photon Systems : fundamentals and applications. Springer, Heidelberg

Berger V, Gauthier-Lafaye O, Costard E (1997a) Fabrication of a 2D photonic bandgap by a holographic method. Electron Lett. 33 : 425-426

Bétourné A, Bouwmans G, Quiquempois Y, Perrin M, Douay M (2007) Improvements of solid-core photonic bandgap fibers by means of interstitial air holes. Opt. Lett. 32 : 1719-1721

Bigo S (2006) Special Issue on Technologies for next generation optical networks. IEEE Proc 94 : 869-1035

Bigot L, Pureur V, Bouwmans G, Quinquempois Y (2007) Ytterbium-doped 2D solid-core photonic bandgap fiber for laser operating at 980 nm. Tech Digest of ECOC 2007 : paper Mo.1.4.5

Birks T.A, Knight JC, Russel PStJ (1997) Endlessly single-mode photonic crystal fiber. *Opt Lett* 22 : 961–963

Birks TA, Roberts PJ, Russell PStJ, Atkin DM, Shepherd T.J (1995) Full 2-D photonic bandgaps in silica/airstructures. Electron Lett 31 : 1941-1942

Birnbaum KM, Boca A, Miller R, Boozer AD, Northrup TE, Kimble HJ (2005) Photon blockade in an optical cavity with one trapped atom. Nature 436 : 87-

Birner A, Wehrspohn RB, Gösele UM, Busch K (2001) Silicon-based photonic crystals. Adv Mater 13 : 377-388

Bjarklev A (2003) Photonic crystal fibers, Springer, New-York

Björk G (1994) On the spontaneous lifetime change in an ideal planar microcavity-Transition from a mode continuum to quantized modes. IEEE J Quant Electron 30 : 2314-

Björk G, Yamamoto Y (1991) Analysis of semiconductor microcavity lasers using rate equations. IEEE J Quant Electron 27 : 2386-2396

Blanco A, Chomski E, Grabtchak S, Ibiskate M, John S, Leonard SW, Lopez C, Meseguer F, Miguez H, Mondia JP, Ozin GA, Toader O, van Driel HM (2000) Large-scale synthesis of a silicon photonic crystal with a complete three-dimensional bandgap near 1.5 micrometers. Nature 405 : 437-440

Bloch F (1928) Uber die Quantenmechanik der Electronen in Kristallgittern. Z. Physik 52 : 555-600

Bogaerts W, Bienstman P, Taillaert D, Baets R, De Zutter D (2001) Out-of-plane sacttering in photonic crystal slabs. IEEE Phot Technol Lett 13 (6) : 565-567

Bohren CF, Huffman DR (1984) Absorption and scattering of light by small particles. Wiley, New York, Chap. 9

Bond A, Dapkus PD, O'Brien J (1998) Aperture placement effects in oxide confined vertical cavity surface emitting lasers. IEEE Photon Technol Lett 10 : 1362-

Borel PI, Harpoth A, Frandsen L, Kristensen M, Shi P, Jensen JS, Sigmund O (2004) Topology optimization and fabrication of photonic crystal structures. Opt Express 12 : 1996-2001

Born M, Wolf E (1965) Principles of Optics. Pergamon Press

Boroditsky M, Krauss T.F, Coccioli R, Vrijen R, Bhat R, Yablonovitch E (1999) Light extraction from optically pumped light-emitting diode by thin-slab photonic crystal. Appl Phys Lett 75 : 1036-1038

Bortz ML, Fujimura M, Fejer MM (1994) Increase acceptance bandwidth for quasi-phase matched second harmonic generation in LiNbO3 waveguides. Electron Lett 30 : 34-

Boscolo S, Conti C, Midrio M, Someda CG (2002b) Numerical analysis of propagation and impedance matching in 2-D photonic crystal waveguides with finite length. J Lightwave Technol 20 : 304-310

Boscolo S, Midrio M, Krauss T (2002a) Y junctions in photonic crystal channel waveguides: high transmission and impedance matching. Opt Lett 27 : 1001-1003

Bossavit A (1989) Simplicial finite elements for scattering patterns in electromagnetism. Comput Method Appl Mech Eng 76 : 299-316

Bourdon G, Robert I, Adams R, Nelep K, Sagnes I, Moison JM, Abram I (2000) Room temperature enhancement and inhibition of spontaneous emission in semiconductor microcavities. Appl Phys Lett 77 : 1345-1347

Boutami S, Ben Bakir B, Leclercq JL, Letartre X, Rojo-Romeo P, Garrigues M, Viktorovitch P, Sagnes I, Legratiet L, Strassner M (2006) Highly selective and compact tunable MOEMS photonic crystal Fabry-Perot filter. Opt Express 14 : 3129-3137

Boutami S, Ben Bakir B, Regreny P, Leclercq JL, Viktorovitch P (2007) Compact 1.55 μm room-temperature optically pumped VCSEL using photonic crystal mirror. Electron Lett 43 : 282-283

Bouwmeester A, Ekert A, Zeilinger A (2000) The physics of quantum information. Springer, Berlin

Bozhevolnyi SI, Volkov VS, Devaux E, Laluet J-Y, Ebbesen TW (2006) Channel plasmon subwavelength waveguide components including interferometers and ring resonators. Nature 440 : 508-511

Bozzi M, Perregrini L (2000) Frequency selective surfaces in the gigahertz and terahertz region : analysis and experimental results. SPIE Proceedings (The-International-Society-for-Optical-Engineering) 4111 : 141-151

Braginsky VB, Gorodetsky ML, Ilchenko VS (1989) Quality factor and non-linear properties of optical whispering gallery modes. Phys Lett A 137 : 393-

Brassard G, Lütkenhaus N, Mor T, Sanders BC (2000) Limitations on practical quantum cryptography. Phys Rev Lett 85 : 1330-

Braun PV, Wiltzius P (1999) Electrochemically grown photonic crystals. Nature 402 : 603-604

Braun PV, Zehner RW, White CA, Weldon MK, Kloc C, Patel SS, Wiltzius P (2001) Epitaxial growth of high dielectric contrast three-dimensional photonic crystals. Adv Mater 13 : 721-724

Bréchet F, Marcou J, Pagnoux D, Roy P (2000a) Complete analysis of the characteristics of propagation into photonic crystal fibers, by the finite element method. Opt Fib Tech 6 : 181-191

Bréchet F, Roy P, Marcou J, Pagnoux D (2000b) Singlemode propagation into depressed-core-index photonic-bandgap fibre designed for zero-dispersion propagation at short wavelengths. Electron Lett 36 : 514-515

Bridges T.J, Pollack MA (1970) Variable metal mesh coupler for far infrared lasers. Appl Opt 9 : 2511-2516

Brillat T, De Lustrac A, Gadot F, Akmansoy E (2002) The use of controllable photonic bandgap (CPBG) materials: an antenna application. Optical and Quantum Electronics 34 : 265-277

Bristow AD, Wells JPR, Fan WH, Fox AM, Skolnick MS, Whittaker DM, Tahraoui A, Krauss TF, Roberts JS (2003) Ultrafast nonlinear response of AlGaAs two-dimensional photonic crystal waveguides. Appl Phys Lett 83 : 851

Broderick N, Bratfalean RT, Monro TM, Richardson D, Martijn de Sterke C (2002) Temperature and wavelength tuning of second-, third-, and fourth-harmonic generation in a two dimensional hexagonally poled nonlinear crystal. J Opt Soc Am B 19 : 2263

Broderick NGR, Ross GW, Offerhaus HL, Richardson DJ, Hanna DC (2000) Hexagonally Poled Lithium Niobate : A two-dimensional nonlinear photonic crystal. Phys Rev Lett 84 : 4345-

Broeng J, Sondergaard T, Barkou SE, Barbeito PM, Bjarklev A (1999) Waveguidance by the photonic bandgap effect in optical fibres. Journal of Optics A 1 : 477–482

Brorson SD, Yokoyama H, Ippen EP (1990) Spontaneous emission rate alteration in optical waveguide structures. IEEE J Quant Elect.ron 26 : 1492-

Brouri R, Beveratos A, Poizat JP, Grangier P (2000) Photon antibunching in the fluorescence of individual color centers in diamond. Opt Lett 25 : 1294-

Brown ER, Parker CD, McMahon CD (1994) Effect of surface composition on the radiation pattern from a photonic planar dipole antenna. Appl Phys Lett 64 : 3345-3347

Brown ER, Parker CD, Yablonovitch E (1993) Radiation properties of a planar antenna on a photonic-crystal substrate. J Opt Soc Am B 10 : 404-407

Burstein E, Weisbuch C (1995) Confined electrons and photons : New physics and applications. Plenum, New-York

Bush K, John S (1999) Liquid crystal photonic band gap materials : the tunable electromagnetic vacuum. Phys Rev Lett 83 : 967-970

Campbell M, Scharp D, Harrison M, Denning R, Tuberfield A (2000) Fabrication of photonic crystals for the visible spectrum by holographic lithography. Nature 404 : 53-56

Carbonell O (1998) Electromagnetic analysis of active and passive devices for space applications. Ph.D. thesis, Lille University

Carroll L (1871) Through the Looking-Glass, and What Alice Found There. MacMillan and Co., London

Casey HC, Panish MB (1978) Heterostructure Lasers. Academic Press

Cassagne D (1997) Matériaux à Bandes Interdites Photoniques. PhD thesis (in French) Montpellier University

Cassagne D, Jouanin C, Bertho D (1996) Hexagonal photonic band gaps. Phys Rev B 53 : 7134-

Centeno E, Felbacq D (2002) Optical bistability in finite nonlinear bidimensional photonic crystal doped by a microcavity. Phys Rev B 62 : R 7683

Champert PA, Couderc V, Leproux P, Février S, Tombelaine V, Labonté L, Roy P, Froehly C, Nérin P (2004) White-light supercontinuum generation in normally dispersive optical fiber using original multi-wavelength pumping system. Opt Express 12 : 4366-4371

Chan CH (1995) Analysis of frequency selective surfaces in : Wu TK Frequency selective surface and grid array (pp. 27-85). Wiley Inter-Science, New York

Chan YS, Chan CT, Liu ZY (1998) Photonic band gaps in two dimensional photonic quasicrystals. Phys Rev Lett 80 : 956-

Chang RK, Campillo AJ (1996) Optical processes in microcavities. World Scientific, Singapore

Charbonneau R, Lahoud N, Mattiusi G, Berini P (2005) Demonstration of integrated optics elements based on long-ranging surface plasmon polaritons. Opt Express 13 : 977-984

Checoury X, Boucaud P, Lourtioz JM, Derouin E, Drisse O, Poingt F, Legouezigou L, Legouezigou O, Pommereau P, Duan GH (2006) Tailoring holes for improving the efficiency of single-mode photonic crystal waveguide lasers on InP substrate. Appl Phys Lett 89 : 071108

Checoury X, Boucaud P, Lourtioz JM, Gauthier-Lafaye O, Bonnefont S, Mulin D, Valentin J, Lozes-Dupuy F, Pommereau F, Cuisin C, Derouin E, Drisse O, Legouezigou L, Lelarrge F, Poingt F, Duan GH (2005a) 1.5 µm room-temperature emission of square-lattice photonic-crystal waveguide lasers with a single defect line. Appl Phys Lett 86 : 151111

Checoury X, Boucaud P, Lourtioz JM, Pommereau F, Cuisin C, Derouin E, Drisse O, Legouezigou L, Lelarrge F, Poingt F, Duan GH, Mulin D, Bonnefont S, Gauthier-Lafaye O, Valentin J, Lozes F, Talneau A (2004) Distributed feedback regime of photonic crystal waveguide lasers at 1.5 µm. Appl Phys Lett 85 : 2011-

Checoury X, Crozat P, Boucaud P, Lourtioz JM, F. Pommereau, Cuisin C, Derouin E, Drisse O, Legouezigou L, Legouezigou O, Lelarrge F, Poingt F, Duan GH, Bonnefont S, Mulin D, Valentin J, Gauthier-Lafaye O, Lozes-Dupuy F, Talneau A (2005b) Single-mode in-gap emission of medium-width photonic crystal waveguides on InP substrate. Opt Express 13 : 6947-6955.

Chelnokov A, Rowson S, Lourtioz JM, Berger V, Courtois JY (1999) An Optical Drill for the Fabrication of Photonic Crystals. J Opt A : Pure and Applied Optics 1 : L3-L6

Chelnokov A, Rowson S, Lourtioz JM, Duvillaret L, Coutaz JL (1997) Terahertz characterization of mechanically machined 3D photonic crystal. Electron Lett 33 : 1981-1983

Chelnokov A, Rowson S, Lourtioz JM, Duvillaret L, Coutaz JL (1998) Light controllable defect modes in a three-dimensional photonic crystals. Electron Lett 34 : 1966-1967

Chelnokov A, Wang K, Rowson S, Garoche P, Lourtioz JM (2000) Near-infrared Yablonovite-like photonic crystals by focused-ion-beam etching of macroporous silicon. Appl Phys Lett 77 : 2943-2945

Chen JC, Haus HA, Fan S, Villeneuve PR, Joannopoulos JD (1996) Optical filters from photonic band gap air bridges. IEEE J Lightwave Technol 14 : 2575-

Cheng C, Scherer A, Arbet-Engels V, Yablonovitch E (1996) Lithographic band gap tuning in photonic band gap crystals. J Vac Sci Technol B 14 : 4110-4114

Cheng SD, Biswas R, Ozbay E, McCalmont S, Tuttle G, Ho KM (1995) Optimized antennas on photonic band gap crystals. Appl Phys Lett 67 : 3399-3401

Cheng SSM, Li LM, Chan CT, Zhang ZQ (1999) Defect and transmission properties of two-dimensional quasiperiodic photonic band-gap systems. Phys Rev B 59 : 4091-

Chew WC, Gürel L, Wang YM, Otto G, Wagner RL, Liu QH (1992) A generalized recursive algorithm for wave-scattering solutions in two dimensions. IEEE Trans Microwave Theory and Techniques 40 : 716-723

Chiao RY, Steinberg AM (1997) Tunnelling times and superluminality. Prog Optics 37 : 345-405

Chigrin D, Lavrinenko A, Yarotsky D, Gaponenko S (1999) Observation of total omnidirectional reflection from a one-dimensional dielectric lattice. Applied Physics A: Materials Science & Processing, 68 : 25-28

Chow E, Lin SY, Johnson SG, Villeneuve PR, Joannopoulos JD, Wendt JR, Vawter GA, Zubrzycki W, Hou H, Alleman A (2000) Three-dimensional control of light in a two-dimensional crystal slab. Nature 407 : 983-986

Chowdury A, Staus C, Boland BF, Kuech TF, McCaughan L (2001) Experimental demonstration of 1535 and 1555 nm simultaneous optical wavelength interchange with a nonlinear photonic crystal. Opt Lett 26 : 1353-

Chul-Sick Kee, Jae-Eun Kim, Hae Yong Park, Ikmo Park, Lim H (2000) Two-dimensional tunable magnetic photonic crystals. Phys Rev B 61 : 15 523-5

Chutinan A, Okano M, Noda S (2002) Wider bandwith with high transmission through waveguide bends in two-dimensional photonic crystal slabs. Appl Phys Lett 80 : 1698-1700

Ciuti C, Schwendimann P, Quattropani A (2001) Parametric luminescence of microcavity polaritons. Phys Rev B 63 : 041303

Cluzel B, Picard E, Charvolin T, Hadji E, Lalouät L, de Fornel F, Sauvan C, Lalanne P (2006) Near field spectroscopy of low-loss waveguide integrated microcavities. Appl Phys Lett 88 : 051112

Coccioli R, Yang Fei-Ran, Itoh T (1999) Aperture-coupled patch antenna on UC-PBG substrate. IEEE Trans Microwave Theory and Tech 47 : 2123-2130

Coen S, Chau AHL, Leonhardt R, Harvey JD, Knight JC, Wadsworth WJ, Russell PStJ (2001) White-light supercontinuum generation with 60-ps pump pulses in a photonic crystal fiber. Opt Lett 26 : 1356-1358

Cohen-Tannoudji C, Diu B, Laloe F (1973) Mécanique quantique (in French). vol.1, Hermann, Paris

Cohen-Tannoudji C, Dupont-Roc J, Grymberg G (1992) An introduction to quantum electrodynamics and Photons and atoms. Wiley, New York

Coldren LA, Corzine SW (1995) Diode lasers and photonic integrated circuits. Wiley, New York

Collardey S (2002) Applications des matériaux à bande interdite photonique à la réduction de la S.E.R. d'un réseau d'antennes. PhD thesis (in French), Rennes University

Collot L, Lefèvre-Seguin V, Brune M, Raymond JM, Haroche S (1993) Very-high Q whispering – gallery mode resonances observed on fused silica microspheres. Europhys Lett. 23 : 327-

Combrié S, Bansropun S, Lecomte M, Parillaud O, Cassette S, Benisty H, Nagle J (2005) Optimization of an inductively coupled plasma etching process of GaInP/GaAs based material for photonic band gap applications, J Vac Sci Technol B 23 : 1521-1526

Combrié S, De Rossi A, Morvan L, Tonda S, Cassette S, Talneau A (2006b) Time-delay measurement in singlemode, low-loss photonic crystal waveguides. Electron Lett 42 : 86-88

Combrié S, Weidner E, De Rossi A, Bansropun S, Cassette S, Talneau A, Benisty H (2006a) Detailed analysis by Fabry-Perot method of slab photonic crystal line-defect waveguides and cavities in aluminium-free material system. Opt. Express 14 : 7353-7361

Couny F, Benabid F, Light PS (2006a) Large-pitch Kagome-structured hollow-core photonic crystal fibre Opt. Lett. 31 : 3574-3576

Couny F, Light PS, Benabid F, Russell PSJ (2006b) Electromagnetically induced transparency and saturable absorption in all-fiber devices based on $^{12}C_2H_2$-filled hollow-core photonic crystal fiber. Opt. Comm. 263 : 28-31

Cregan RF, Mangan BJ, Knight JC, Birks TA, Russel PStJ, Roberts PJ, Allan DC (1999) Single-mode photonic bandgap guidance of light in air. Science 285 : 1537-39

Cubucku E, Kort EA, Crozier B, Capasso F (2006) Plasmonic laser antenna. Appl Phys Lett 89 : 093120

Cuisin C, Chelnokov A, Decanini D, Peyrade D, Chen Y, Lourtioz JM (2002) Sub-micrometer dielectric and metallic structures fabricated from resist templates. Optical and Quantum Electronics 34 : 13-26

D'Aguanno G, Centini M, Scalora M, Sibilia C, Bloemer MJ, Bowden CM, Haus JW, Bertolotti M (2001) Group velocity, energy velocity and superluminal propagation in finite photonic band gap structures. Phys Rev E 63 : 36610-

Danglot J, Carbonell J, Fernandez M, Vanbésien O, Lippens D (1998) Modal analysis of guiding structures patterned in a metallic photonic crystal. Appl Phys Lett 73 : 2714-

Danner AJ, Raftery JJ Jr, Yokouchi N, Choquette KD (2004) Transverse modes of photonic crystal vertical-cavity lasers. Appl Phys Lett 84 : 1031-1033

Dantec NL, Benyattou T, Guillot G, Spisser A, Seassal C, Leclercq JL, Viktorovitch P, Rondi D, Blondeau R (1999) Tunable microcavity based on InP-Air Bragg mirrors. IEEE J Sel Top in Quant Electron 5 : 111-114

Dautray R, Lions JL (1984) Analyse mathématique et calcul numérique pour les sciences et techniques (in French). Masson, Paris

David A, Benisty H, Weisbuch C (2007) Optimization of Light-Diffracting Photonic-Crystals for High Extraction Efficiency LEDs. Journal of Display Technology 3 (2) : 133-148

David A, Fujii T, Matioli E, Sharma R, Nakamura S, DenBaars SP, Weisbuch C, Benisty H (2006c) GaN light-emitting diodes with Archimedean lattice photonic crystals, Appl Phys Lett 88 : 073510

David A, Fujii T, Moran B, Nakamura S, DenBaars SP, Weisbuch C, Benisty H (2006b) Photonic crystal laser lift-off GaN light-emitting diodes, Appl Phys Lett 88 : 133514

David A, Fujii T, Sharma R, McGroddy K, Nakamura S, Denbaars SP, Hu E, Weisbuch C, Benisty H (2006a) Photonic-crystal GaN light-emitting diodes with tailored guided modes distribution. Appl Phys Lett 88 : 061124

David A, Meier C, Sharma R, Diana FS, DenBaars SP, Hu E, Nakamura S, Weisbuch C, Benisty H (2005) Photonic bands in two-dimensionally patterned multimode GaN waveguides for light extraction, Appl Phys Lett 87 : 101107

David S (2003) Étude de composants à cristaux photoniques dans la filière silicium pour les longueurs d'onde des télécommunications optiques (in French). Ph.D. Thesis, Orsay University

David S, Chelnokov A, Lourtioz JM (2000) Wide angularly isotropic photonic bandgaps from 2D photonic crystals with archimedean-like tiling. Opt Lett. 25 : 1001-

David S, Chelnokov A, Lourtioz JM (2001) Isotropic photonic structures : Archimedean-like tilings and quasi-crystal. IEEE J Quant Electron 37 : 1427-

David S, Chelnokov A, Lourtioz JM (2002) Lateral Confinement in Macroporous Silicon Crystals. J Opt A : Pure and Applied Optics 4 : 468-473

de Lustrac A, Gadot F, Akmansoy E, Brillat T (2001) High-directivity planar antenna using controllablephotonic bandgap material at microwave frequencies. Appl Phys Lett 78 : 4196-4198

de Lustrac A, Gadot F, Cabaret S, Lourtioz JM, Brillat T, Priou A, Akmansoy E (1999) Experimental demonstration of electrically controllable photonic crystals at centimeter wavelengths. Appl Phys Lett 75 : 1625-1627

De Neve H (1997b) Study and realisation of microcavity based LEDs. PhD Thesis, University of Gent

De Neve H, Blondelle J, Vandaele P, Demeester P, Baets R, Borghs G (1997a) Recycling of guided mode light emission in planar microcavity light emitting diodes. Appl Phys Lett 70 : 799-

De Rossi A, Berger V, Calligaro M, Leo G, Ortiz V, Marcadet X (2001) Parametric fluorescence in oxidized aluminum gallium arsenide waveguides. Appl Phys Lett 79 : 3758-

Decoopman T, Tayeb G, Enoch S, Maystre D and Gralak B (2006) Photonic Crystal Lens: From Negative Refraction and Negative Index to Negative Permittivity and Permeability. Phys Rev Lett 97 : 073905

Decoopman T, Tayeb G, Enoch S, Maystre D and Gralak B (2006) Photonic Crystal Lens: From Negative Refraction and Negative Index to Negative Permittivity and Permeability. Phys Rev Lett 97 : 073905

Defos du Rau M (1997) PhD Thesis (in French), University of Bordeaux

Delbeke D, Bockstaele R, Bienstman P, Baets R, Benisty H (2002) High-Efficiency Semiconductor rsonant-Cavity Light-Emitting Diodes: A Review. IEEE J Selected Topics in Quant Electron 8 : 189-206 ; see other articles in the same issue of this journal.

Della Villa A, Enoch S, Tayeb G, Capolino F, Pierro V, Galdi V (2006) Localised modes in photonic quasicrystals with Penrose-type lattice. Opt Express 14 : 10021-10027

Deubel M, von Freymann G, Wegener M, Pereira S, Busch K, Souhkoulis CM (2004) Direct Laser Writing of Three-Dimensional Photonic Crystal Templates for the Telecommunication Regime. Nature Mater. 3 : 444-447

Dewar G (2001) Candidates for μ<0, ε<0 nanostructures. Intern J Modern Physics B 15 : 3258-3265

Di Falco A, Conti C, Assanto A (2004) Wavelength shifting in photonic bandgap microcavities with isotropic media. Appl Phys Lett 85 : 4585

Di Falco A, Conti C, Assanto A (2005) Terahertz pulse generation via optical rectification in photonic crystal microcavities. Opt Lett 30 : 1174

Di Falco A, Conti C, Assanto A (2006) Impedance matching in photonic crystal microcavities for second harmonic generation. Opt Lett 31 : 250

Diamanti E, Langrock C, Fejer M, Yamamoto Y, Takesue H (2006) 1.5 micron photon counting optical time domain reflectometry with a single photon detector based on upconversion in a periodically poled lithium niobate waveguide. Opt Lett 31 : 727

Diederichs C, Tignon J, Dasbach G, Ciuti C, Lemaitre A, Bloch J, Roussignol Ph, Delalande C (2006) Parametric oscillations in vertical triple cavities. Nature 440 : 904

Dobrowolski JA, Lowe D (1978) Optical thin film synthesis program based on the use of Fourier transform. Appl Optics 17 : 3039-

Dobson DC (1999) An efficient method for band structure calculations in 2D photonic crystals. J Comput Phys 149 : 363-376

Dowling JP, Scalora M, Bloemer MJ, Bowden CM (1994) The photonic band edge laser: a new approach to gain enhancement. J Appl Phys 75 : 1896-1899

Drude P (1890) Ann. D. Phys. 39

Duan LM, Kimble HJ (2004) Scalable photonic quantum computation through cavity assisted interactions. Phys Rev Lett 92 : 127902

Dudley JM, Provino L, Grossard N, Maillotte H, Windeler R, Eggleton B, Coen S (2002) Supercontinuum generation in airsilica microstructured fibers with nanosecond and femtosecond pulse pumping. J Opt Soc Am B 19 : 765–771

Dulea M, Severin M, Riklund R (1990) Transmission of light through deterministic aperiodic nonFibonaccian multilayers. Phys Rev B 42 : 3680-

Dulkeith E, McNab SJ, Vlasov YA (2005) Mapping the optical properties of slab-type two-dimensional photonic crystal waveguide., Phys Rev B72 : 115102 (1-9)

Dumeige Y, Sagnes I, Monnier P, Vidakovic P, Abram I, Meriadec C, Levenson A (2002) Phase matched frequency doubling at photonic band edges : efficiency scaling as the fifth power of the length. Phys Rev Lett 89 : 043901-

Dumeige Y, Vidakovic P, Sauvage S, Sagnes I, Levenson JA, Sibilia C, Centini M, D'Aguanno G, Scalora M (2001) Enhancement of Second Harmonic Generation in a 1D Semiconductor Photonic Band Gap. Appl Phys Lett 78 : 3021-

Eastham PR, Whittaker DM (2003) Steady states of a $\chi^{(3)}$ parametric oscillator with coupled polarizations. Phys Rev B 68 : 075324-

Ebbesen TW, Lezec HJ, Ghaemi HF, Thio T, Wolff PA (1998) Extraordinary Optical Transmission through Sub-Wavelength Hole Arrays. Nature 391: 667-669

Economou EN, Sigalas MM (1993) Classical wave propagation in periodic structures : Cermet versus network topology. Phys Rev B 48 : 13434-13438

Eggleton BJ, Kerbage C, Westbrook PS, Windeler RS, Hale A (2001) Microstructured optical fiber devices. Opt Express 9 : 698–713

Ehrfeld W, Schmidt A (1998) Recent developments in deep X-ray lithography. J Vac Sci Technol B 16 : 3526-3534

Eisele H, Haddad GI (1998) Two terminal millimeter wave sources. IEEE Trans Microwave Theory and Tech 46 : 739-746

Elachi C (1976) Waves in active and passive periodic structures at microwave frequencies. Proc IEEE 64 : 1666-

Elsherbeni AZ, Kishk AA (1992) Modeling of cylindrical objects by circular dielectric and conducting cylinders. IEEE Trans on Antennas and Propagation 40 : 96-99

Englund D, Fattal F, Waks E, Solomon G, Zhang B, Nakaoka T, Arakawa Y, Yamamoto Y, Vuckovic J (2005b) Controlling the spontaneous emission rate of single quantum dots in a 2D photonic crystal. Phys Rev Lett 95 : 013904

Englund D, Fushman I, Vuckovic J (2005a) General recipe for designing photonic crystal cavities. Opt Express 13 : 5961-5976

Enkrich C, Wegener M, Linden S, Burger S, Zschiedrich L, Schmidt F, Zhou JF, Koschny Th, Soukoulis CM (2005) Magnetic Metamaterials at Telecommunication and Visible Frequencies. Phys Rev Lett 95 : 203901

Enoch S, Gralak B, Tayeb G (2002a) Enhanced emission with angular confinement from photonic crystals. Appl Phys Lett 81 : 1588-1591

Enoch S, Popov E, Nevière M, Reinisch R (2002c) Enhanced light transmission by hole arrays. J Opt A: Pure Appl Opt 4 : S83-S87

Enoch S, Tayeb G, Maystre D (1999) Numerical evidence of ultrarefractive optics in photonic crystals. Opt Commun 161: 171-176

Enoch S, Tayeb G, Sabouroux P, Guérin N, Vincent P (2002b) A metamaterial for directive emission. Phys Rev Lett 89 : 213902-1/4

Fan J, Migdall A, Wang LJ (2005) Efficient generation of correlated photon pairs in a microstructured fiber. Opt Lett 30 : 3368-

Fan S, Villeneuve PR, Joannopoulos JD (1997) High extraction efficiency of spontaneous emission from slabs of photonic crystal. Phys Rev Lett 78 : 3294-

Fan S, Villeneuve PR, Joannopoulos JD, Haus HA (1996) Channel drop tunneling through localized states. Phys Rev Lett 80 : 960-963

Fan S, Villeneuve PR, Joannopoulos JD, Haus HA (1998) Channel drop filters in photonic crystals. Optics express 3 : 4-11

Fang N, Lee H, Sun C, Zhang X (2005) Sub-diffraction-limited optical imaging with a silver lens. Science 308 : 534-537

Farahani JN, Pohl DW, Eisler H-J, Hecht B (2005) Single Quantum Dot Coupled to a Scanning Optical Antenna: A Tunable Superemitter. Phys Rev Lett 95 : 017402

Faraon A, Waks E, Englund D, Fushman I, Vuckovic J (2007) Efficient photonic crystal cavity-waveguide couplers. Appl Phys Lett 90 : 073102-

Fatemi F, Bashkansky M, Moore S (2005) Side-illuminated hollow-core optical fiber for atom guiding. Opt. Express 13 : 4890-4895

Favero I, Berthelot A, Cassabois G, Voisin C, Delalande C, Roussignol Ph, Ferreira R, Gérard JM (2007). Dephasing in semiconductor quantum dots at low temperature : a probe of the carrier dynamics in the environment. Phys Rev B 75 : 073308

Fedyanin A, Aktsipetrov O, Kobayashi D, Nishimura K, Uchida H, Inoue M (2004) Enhanced Faraday and nonlinear magneto-optical Kerr effects in magneto-photonic crystals. J Magn Magn Mater 282 : 256-

Feigel A, Kotler Z, Sfez B, Arsh A, Klebanov M, Lyubin V (2000) Chalcogenide glass-based three-dimensional photonic crystals. Appl Phys Lett 77 : 3221-3224

Fejer MM (1994) Nonlinear optical frequency conversion. Phys Today, May 1994, p 25

Fejer MM, Magel GA, Jundt DH, Byer RL (1992) Quasi-Phase-Matched Second Harmonic Generation : Tuning and Tolerances. IEEE J Quant Electron 28 : 2631-

Felbacq D (1994) Étude théorique et numérique de la diffraction de la lumière par des ensembles de tiges parallèles (in French). PhD Thesis (in French), University of St Jerome (Marseille)

Felbacq D, Bouchitté G (1997) Homogeneization of a set of parallel fibers. Waves in Random Media 7 : 245-256

Felbacq D, Guizal B, Zolla F (1998) Limit analysis of the diffraction of a plane wave by a stratified periodic medium. J Math Phys 39 (9) : 4604-4607

Felbacq D, Maystre D, Tayeb G (1995) Localization of light by a set of parallel cylinders. Journal Modern Optics 42 : 473-482

Felbacq D, Tayeb G, Maystre D (1994) Scattering by a random set of parallel cylinders. J Opt Soc Am A 11 : 2526-2538

Ferrando A, Silvestre E, Miret JJ, Andrés P (2000b) Nearly zero ultraflattened dispersion in photonic crystal fibers. Opt Lett 25 : 790–792

Ferrando A, Silvestre E, Miret JJ, Andrés P, Andrés MV (2000a) Vector description of higher-order modes in photonic crystal fibers. J Opt Soc Am A 17 : 1333–1340

Ferrando A, Zacarés M, Fernandez de Cordoba P, Binosi D, Monsoriu JA (2003) Spatial soliton formation in photonic crystal fibers. Optics Express 11 : 452–459

Ferrini R, Berrier A, Dunbar LA, Houdré R, Mulot M, Anand S, De Rossi S, Talneau A (2004) Minimization of out-of-plane losses in planar photonic crystals by optimising the vertical waveguide, Appl Phys Lett 85 : 3998-3400

Ferrini R, Houdré R, Bénisty H, Qiu M, Moosburger J (2003a) Radiation losses in planar photonic crystals : two-dimensional representation of hole depth and shape by an imaginary dielectric constant. J Opt Soc Am B 20 : 469-478

Ferrini R, Lombardet B, Wild B, Houdré R, Duan GH (2003b) Hole depth- and shape-induced radiation losses in bi-dimensional photonic crystals, Appl Phys Lett 82 : 1009-1011

Figotin A, Vitebskiy I (2003) Electromagnetic uni-directionality in magnetic photonic crystals. Phys Rev B 67 : 165210-

Figotin A, Vitebsky I (2001) Non reciprocal magnetic photonic crystals. Phys Rev E 63 : 066609-1/17

Fiore A, Berger V, Rosencher E, Bravetti P, Nagle J (1998) Phase matching using an isotropic nonlinear material. Nature 391 : 463-

Fiore A, Rosencher E, Vinter B, Weill D, Berger V (1995) Second order optical susceptibility of biased quantum wells in the interband regime. Phys Rev B 51 : 13192

Fleming JG, Lin SY (1999) Three-dimensional photonic crystal with a stop-band from 1.35 to 1.95 μm. Opt Lett 24 : 49-51

Fleming JG, Lin SY, El-Kady I, Biswas R, Ho KM (2002) All-metallic three-dimensional photonic crystals with a large infrared bandgap. Nature 417 : 52-55

Foresi JS, Villeneuve PR, Ferrera J, Thoen E.R, Steinmeyer G, Fan S, Joannopoulos JD, Kimmerling EC, Smith HI, Ippen EP (1997) Photonic bandgap microcavities in optical waveguides. Nature 390 : 143-145

Fromm DP, Sundaramurthy A, Schuck PJ, Kino G, Moerner WE (2004) Gap-dependent optical coupling of single 'bowtie' nanoantennas resonant in the visible. Nano Lett 4 : 957-961

Fujita M, Takahashi S, Tanaka Y, Asano T, Noda S (2005) Simultaneous inhibition and redistribution of spontaneous light emission in photonic crystals, Science 308 : 1296-1298

Fujita M, Ushigome R, Baba T (2000) Continuous wave lasing in GaInAsP microdisk injection laser with threshold current of 40 μA. Electron Lett 36 : 790-

Fujita M, Ushigome R, Baba T (2001) Large spontaneous emission factor of 0.1 in a microdisk injection laser. IEEE Photon Technol Lett 13 : 403-

Fulconis J, Alibart O, Wadsworth WJ, Russel PSJ, Rarity JG (2005) High brightness single mode source of correlated photon pairs using a photonic crystal fiber. Opt Express 13 : 7572

Furukawa A, Sasaki S, Hoshi M, Matsuzono A, Moritoh K, Baba T (2004) High-power single-mode vertical-cavity surface-emitting lasers with triangular holey structure. Appl Phys Lett 85 : 5161-5163

Furusawa K, Malinowski AN, Price JH, Monro TM, Sahu JK, Nilsson J, Richardson DJ (2001) Cladding pumped ytterbium doped fiber laser with holey inner and outer cladding. Optics Express 9 : 714–720

Gadot F (1998) Modélisation et caractérisation expérimentale des matériaux à bandes interdites photoniques (BIP) en micro-ondes (in French). PhD Thesis, University of Orsay

Gadot F, Chelnokov A, De Lustrac A, Crozat P, Lourtioz JM, Cassagne D, Jouanin C (1997) Experimental demonstration of complete photonic bandgap in graphite structure. Appl Phys Lett 71 : 1780-1782

Garcia N, Nieto-Vesperinas M (2002a) Is there an experimental verification of a negative index of refraction yet? Opt Lett 27 : 885-887

Garcia N, Nieto-Vesperinas M (2002b) Left-handed materials do not make a perfect lens. Phys Rev Lett 88 : 207403-1/3, see also answer from: Pendry 2003

Garet F (1997) Génération optoélectronique d'impulsions électromagnétiques ultracourtes : application à la spectroscopie THz. PhD Thesis (in French), University of Annecy

Gayral B, Gérard JM (2000) Strong Purcell effect for InAs quantum boxes in high-Q wet-etched microdisks. Physica E7 : 641-

Gayral B, Gerard JM, Legrand B, Costard E, Thierry-Mieg V (1998) Optical study of GaAs/AlAs pillar microcavities with elliptical cross-section. Appl Phys Lett 72 : 1421-

Gayral B, Gérard JM, Lemaître A, Dupuis C, Manin L, Pelouard, JL (1999) High-Q wet-etched GaAs microdisks containing InAs quantum boxes. Appl Phys Lett 75 : 1908-

Gayral B, Gérard JM, Sermage B, Lemaître A, Dupuis C (2001) Time-resolved probing of the Purcell effect for InAs quantum boxes in GaAs microdisks. Appl Phys Lett 78 : 2828-

Gérard JM (2003) Solid-state cavity quantum electrodynamics with self-assembled quantum dots in P. Michler (ed.) Single Quantum Dots: Physics and Applications, Topics of Applied Physics, Springer, Heidelberg

Gérard JM, Barrier JM, Marzin JY, Kuszelewicz R, Manin L, Costard E, Thierry-Mieg V, Rivera T (1996b) Quantum boxes as active probes for photonic microstructures : the pillar microcavity. Appl Phys Lett 69 : 449-

Gérard JM, Cabrol O, Sermage B (1996a) InAs quantum boxes : highly efficient radiative traps for light emitting devices on Si. Appl Phys Lett 68 : 3123-3125

Gérard JM, Gayral B (1999) Strong Purcell effect for InAs quantum boxes in three-dimensional solid-state microcavities. J Ligthwave Technol 17 : 2089-

Gérard JM, Izraël A, Marzin JY, Padjen R, Ladan FR (1993) Photonic bandgap of two-dimensional dielectric crystals. Solid State Elect 37 : 1341-

Gérard JM, Sermage S, Gayral B, Costard E, Thierry-Mieg V (1998) Enhanced spontaneous emission for InAs quantum boxes in a monolithic optical microcavity. Phys Rev Lett 81 : 1110-

Gérôme F, Auguste JL, Blondy JM (2004) Design of dispersion-compensating fibers based on a dual-concentric-core photonic crystal fiber. Opt Lett 29 : 2725-2727

Ghosh S, Bhagwat AR, Renshaw CK, Goh S, Gaeta AL, Kirby BJ (2006) Low-light-level optical interactions with rubidium vapor in a photonic band-gap fiber. Phys Rev Lett 97 : 023603

Gibbs HM (1985) Optical bistability, controlling light with light (Academic, Orlando)

Golubev VG, Davydov VY, Kartenko NF, Kurdyukov DA, Medvedev AV, Pevtsov AB, Scherbakov AV, Shadrin EB (2001) Phase transition-governed opal-VO2 photonic crystal. Appl Phys Lett 79 : 2127-2129

Gonzalo R, Martinez B, Mann CM, Pellemans H, Bolivar PH, De Maagt P (2002) A low-cost fabrication technique for symetrical and asymmetrical layer-by-layer photonic crystals at submillimeter-wave frequencies. IEEE Trans. Microwave Theory and Tech 50 : 2384-2392

Gralak B, Enoch S, Tayeb G (2000) Anomalous refractive properties of photonic crystals. J Opt Soc.Am A 17 : 1012-1020

Gramotnev DK, Pile DFP (2004) Single-mode subwavelength waveguide with channel plasmon-polaritons in triangular grooves on a metal surface. Appl Phys Lett 85 : 6323-6325

Granet G, Guizal B (1996) Efficient implementation of the coupled waves method for metallic gratings in TM polarization. J Opt Soc Am A 13 : 1019-1023

Grbic A, Eleftheriades GV (2002) Experimental verification of backward-wave radiation from a negative refractive index metamaterial. J Appl Phys 92 : 5930-5935

Greffet JJ (1991) Waves in random media 3 : S65-S73

Grigorenko AN, Geim K, Gleeson HF, Zhang Y, Firsov AA, Khrushchev IY, Petrovic J (2005) Nanofabricated media with negative permeability at visible frequencies. Nature 438 : 335-337

Groeber RD, Schoelkopf RJ, Prober DE (1997) Optical antenna: towards a unit efficiency near-field optical probe. Appl Phys Lett 70 : 1354-1356

Grüning U, Lehmann V, Ottow S, Busch K (1996) Macroporous silicon with a complete 2D PBG centered at 5 µm. Appl Phys Lett 68 : 747-749

Guenneau S, Nicolet A, Zolla F, Geuzaine C, Meys B (2001) A finite element formulation for spectral problems in optical fibers. COMPEL 1 : 120-131

Guenneau S, Zolla F (2000) Homogenization of three-dimensional finite photonic crystals. Proceedings PIERS 27 : 91-127

Guida G, Maystre D, Tayeb G, Vincent P (1998) Homogeneization of two-dimensional metallic photonic crystals. Journ Opt Soc Am JOSA A 15 : 2308-2315

Happ T, Kamp M, Forchel A, Gentner JL, Goldstein L (2003) Two-dimensional photonic crystal coupled-defect laser diode. Appl Phys Lett 82 : 4-6

Happ T, Markard A, Kamp M, Forchel A, Srinivasan A (2001) Single-mode operation of coupled-cavity lasers based on two-dimensional photonic crystals. Appl Phys lett 79 : 4091-4093

Happ TD, Tartakovskii I, Kulakovskii VD, Reithmaier JP, Kamp M, Forchel A (2002) Enhanced light emission of InGaAs quantum dots in a two-dimensional photonic crystal defect microcavity. Phys Rev B 66 : R041303-

Haroche S, Kleppner D (1989) Cavity quantum electrodynamics. Physics Today 42 : 24-

Harvey A (1959) Wave propagation in periodic structures: Electric Filters and crystal lattices. IRE Trans 8 : 30-

Harvey A (1963) Microwave Engineering. Academic Press, New-York

Hennessy K, Badolato A, Winger M, Gerace D, Atatüre M, Gulde S, Fält S, Hu EL, Imamoglu A (2007) Quantum nature of a strongly coupled single quantum dot cavity system. Nature 445 : 896-899

Hessel A, Oliner AA (1965) A new theory of Wood's anomalies on optical gratings. Appl. Optics : 332-354

Hilaire S, Pagnoux D, Roy P, Février S (2006) Numerical study of single mode Er-doped microstructured fibers: influence of geometrical parameters on amplifier performances. Opt Express 14 : 10865-10877

Himeno K, Matsuo K, Ning Guan, Wanda A (2005) Low-bending-loss single-mode-fibers for fiber-to-the-home. J Lightwave Technol 23 : 3494-3499

Hippert F, Gratias D (1994) Lectures on Quasicrystals. Les Éditions de Physique (Hippert F, Gratias D eds), Les Ulis

Ho K, Chan C, Soukoulis C (1990) Existence of a Photonic Gap in Periodic Dielectric Structures. Phys Rev Lett 65 : 3152-3155

Ho K, Chan C, Soukoulis C, Biswas R, Sigalas M (1994) Photonic bandgaps in three dimensions : new layer by layer periodic structures. Solid State Communications 89 : 413-416

Ho ST, Wang, L, Park S (1999) Spontaneous emission control and microcavity light emitters conversion in : Benisty H *et al.* (eds) Confined Photon Systems : Fundamentals and Applications (pp. 243-297). Springer, Heidelberg

Holland BT, Blanford CE, Stein A (1998) Synthesis of macroporous minerals with highly ordered three-dimensional arrays of spheroidal voids. Science 281 : 538-540

Hood CJ, Chgapman MS, Lynn TW, Kimble HJ (1998) Real-time cavity-QED with single atoms. Phys Rev Lett 80 : 4157-

't Hooft GW (2001) Comment on Negative refraction makes a perfect lens. Phys Rev Lett 87: 249701

Hougaard KG, Broeng J, Bjarklev A (2003) Low pump power photonic crystal fibre amplifiers. Electron Lett 39 : 599–600

Huang MCY, Zhou Y, Chang-Hasnain CJ (2007) A surface-emitting laser incorporating a high-index-contrast subwavelength grating. Nature Photonics 1 : 119-122

Huffaker DL, Deppe DG (1997) Improved performance of oxide-confined vertical-cavity surface emitting lasers using a tunnel injection active region. Appl Phys Lett 71 : 1449-1451

Hughes S (2004) Enhanced single-photon emission from quantum dots in photonic crystal waveguides and nanocavities. Opt Lett 29 : 2659-2661

Hughes S, Rammuno L, Young JF, Sipe JE (2005) Extrinsic optical scattering loss in photonic crystal waveguides: role of fabrication disorder and photon group velocity. Phys Rev Lett 94 : 033903 1-4

Husakou AV, Herrmann J (2001) Supercontinuum generation of higherorder solitons by fission in photonic crystal fibers. Phys Rev Lett 87 : 203901-

Hutley MC, Maystre D (1976) The total absorption of light by a diffraction grating Optics Commun 19 : 431-436

Hwang IK, Kim GH, Lee YH (2006) Optimization of Coupling Between Photonic Crystal Resonator and Curved Microfiber. IEEE J Quantum Electron 42 : 131-136

Hwang IK, Kim SK, Yang JK, Kim SH, Lee S, Lee YH (2005) Curved-microfiber coupling for photonic crystal light emitter Appl Phys Lett 87 : 131 107 (4)

Imamoglu A, Awschalom D, Burkard G, DiVincenzo DV, Loss D, Sherwin M, Small A (1999) Quantum Information Processing Using Quantum Dot Spins and Cavity QED. Phys Rev Lett 83 : 4204-

Inoue K, Sasada M, Kawamata J, Sakoda K, Haus JW (1999) A two-dimensional photonic crystal laser. Jpn J Appl Phys 38 : L157-L159

Inoue M, Arai K, Fujii T (1998) Magneto-optical properties of one-dimensional photonic crystals composed of magnetic and dielectric layers. J Appl Phys 83 : 6768-6770

Inoue M, Fujii T (1997) A theoretical analysis of magneto-optical Faraday effect of YIG films with random multilayer structures. J Appl Phys 81 : 5659-5661

Inoue SI, Aoyagi Y (2005) Design and fabrication of two-dimensional photonic crystals with predetermined nonlinear optical properties. Phys Rev Lett 94 : 103904

Iyer AK, Eleftheriades GV (2002) Negative Refractive Index Metamaterials Supporting 2-D Waves. IEEE International Microwave Symposium Digest : 1067-1070, Seattle WA (June 2-7)

Jafarpour A, Chow E, Reinke CM, Huang J, Adibi A, Grot A, Mirkarimi LW, Girolami G, Lee RK, Xu Y (2004) Large-bandwidth ultra-low-loss guiding in bi-periodic photonic crystal waveguides. Applied Physics B77 : 409-414

Jalali AA, Friberg AT (2005) Faraday rotation in a two-dimensional photonic crystal with a magneto-optic defect. Opt Lett 30 : 1213-1215

Jeon S, Malyarchuk V, Rogers JA (2006) Fabricating three-dimensional nanostructures using two-photon lithography in a single exposure step. Opt Express 14 : 2300-2308

Jeong Y, Sahu JK, Payne DN, Nilsson J (2004) Ytterbium-doped large-core fiber laser with 1.36 kW continuous-wave output power. Opt Express 12 : 6088-6092

Jewell JL, Mc Call SL, Scherer A, Houh HH, Whitaker NA, Gossard AC, English JH (1989) Transverse modes, waveguide dispersion, and 30ps recovery in submicron GaAs/AlAs microresonators. Appl Phys Lett 55 : 22-

Jhe W, Anderson A, Hinds EA, Meschede D, Moi L, Haroche S (1987) Suppression of spontaneous decay at optical frequencies: Test of vacuum-field anisotropy in confined space. Phys Rev Lett 58 : 666-

Jiang P, Ostojic GN, Narat R, Mittleman DM, Colvin VL (2001) The fabrication and bandgap engineering of photonic multilayers. Adv Mater 13 : 389-393

Joannopoulos JD (1995a) The magical world of photonic crystals in : Soukoulis C (ed) Photonic band gap materials

Joannopoulos JD, Meade RD, Winn JN (1995b) Photonic Crystals. Princeton University

John S (1984) Electromagnetic absorption in a disordered medium near a photon mobility edge. Phys Rev Lett 53 : 2169-2173

Johnson S, Joannopoulos J (2001) Bloch iterative frequency-domain methods for Maxwell equations in a plane wave basis. Opt Express 8 : 173-

Kammerer C, Voisin C, Cassabois G, Delalande C, Roussignol Ph, Klopf F, Reithmaier JP, Forchel A and Gérard JM (2002) Line narrowing in single semiconductor quantum dots: toward a control of environment effects. Phys Rev B 66 : 041306 (R)

Kamp M, Scherer H, Ulzhöfer C, Völker B, Forchel A, Janiak K, Heidrich H, Brénot R, GH Duan (2006) Tunable Photonic Crystal Laser with Integrated Wavelength Monitor, presented at ECOC'06, Cannes, paper, Tu3.4.2

Kärkkäinen MK (2002) Illustration of wave propagation in DNG materials in : Digest of the XXVII URSI/IEEE Convention on Radio Science, Espoo, Finland (Oct. 17-18, 2002) : pp. 31-33, http://www.hut.fi/Units/Radio/URSI02/ursi_karkkainen_b.pdf

Karr JP, Baas A, Giacobino E (2004a) Twin polaritons in semiconductor microcavities Phys Rev A 69 : 063807

Karr JP, Baas A, Houdré R, Giacobino E (2004b) Squeezing in semiconductor microcavities in the strong coupling regime. Phys Rev A 69 : 031802

Kasprzak J, Richard M, Kundermann S, Baas A, Jeambrun P, Keeling JMJ, Marchetti FM, H. Szymanska M, André R, Staehli JL, Savona V, Littlewood PB, Deveaud B, Le Si Dang (2006) Bose-Einstein condensation of exciton-polaritons. Nature 443 : 409-414

Kastler A (1962) Atomes dans un interféromètre de Fabry-Pérot. Applied Optics 1 : 17-

Kato H, Matsushita T, Takayama A, Egawa M, Nishimura K, Inoue M (2003) Theoretical analysis of optical and magneto-optical properties of one-dimensional magnetophotonic crystals. J Appl Phys 93 : 3906-3911

Kawai N, Inoue K, Carlsson N, Ikeda N, Sugimoto Y, Asakawa K (2001) Confined Band Gap in Air-Bridge Type of Two-Dimensional AlGaAs Photonic Crystal. Phys Rev Lett 11 : 2289-2292

Kawakami S (1997) Fabrication of submicrometre 3D periodic structures composed of Si/SiO_2. Electron Lett 33 : 1260-1261

Kawakami S, Kawashima T, Sato T (1999) Mechanism of shape formation of three-dimensional periodic nanostructures by bias sputtering. Appl Phys Lett 74 : 463-465

Kawashima S, Okano M, Imada M, Noda S (2006) Design of compound-defect waveguides in three-dimensional photonic crystals. Opt Express 14 : 6303-6307

Kazarinov RF, Henry CH (1985) Second-order distributed feedback lasers with mode selection provided by first-order radiation losses. IEEE J Quantum Electron 21 :144-150

Kesler MP, Maloney JG, Shirley BL, Smith GS (1996) Antenna design with the use of photonic band-gap material as all-dielectric planar reflectors. Microwave Opt Technol Lett 11 : 169-174

Kim M, Dainty JC, Friberg AT, Sant AJ (1990) Experimental study of enhanced backscattering from one- and two- dimensional random rough surfaces. J Opt Soc Am A 7 : 569-577

King JS, Heineman D, Graugnard E, Summers CJ (2005) Atomic deposition in porous structures: 3D photonic crystals. Applied Surface Science 244 : 511-516

Kiraz A, Michler P, Becher C, Gayral B, Imamoglu A, Zhang L, Hu E. (2001) Cavity-quantum electrodynamics using a single InAs quantum dot in a microdisk structure. Appl Phys Lett 78 : 3932-

Kitson SC, Barnes WL, Sambles JR (1996) Full Photonic Band Gap for surface modes in the visible. Phys Rev Lett 77 : 2670-2673

Kittel Ch (1958) Introduction à la Physique de l'Etat Solide (in French). Dunod, Paris

Kittel Ch (1971) Introduction to Solid State Physics. John Wiley & Sons

Kleppner D (1981) Inhibited spontaneous emission, Phys Rev Lett 47 : 233-236

Knight JC (2003) Photonic crystal fibres. Nature 424 : 847-851

Knight JC, Arriaga J, Birks TA, Ortigosa-Blanch A, Wadsworth WJ, Russell PStJ (2000) Anomalous dispersion in photonic crystal fibers. IEEE Photon Technol Lett 12 : 807–809

Knight JC, Birks TA, Russell PStJ, Atkin DM (1996) All-silica single-mode fiber with photonic crystal cladding. Opt Lett 21 : 1547-1549

Knight JC, Birks TA, Russell PStJ, de Sandro JP (1998b) Large mode area photonic crystal fibre. Electron Lett 34 : 1347-1348

Knight JC, Broeng J, Birks TA, Russell PStJ (1998a) Photonic bandgap guidance in optical fibers. Science 282 : 1476-1478

Kœnderinck AF, Bechger L, Schriemer HP, Lagendijk A, Vos W (2002a) Broadband five-fold reduction of vacuum fluctuations probed by dye photonic crystals. Phys Rev Lett 88 : 143903-

Kœnderink AF, Johnson PM, Galisteo Lopez JF, Vos WL (2002b) Three-dimensional photonic crystals as a cage for light. Comptes Rendus de l'Académie des Sciences 3 : 67-77

Kogelnik H, Shank CV (1971) Stimulated Emission in a Periodic Structure. Appl Phys Lett 18 : 152-154

Kogelnik H, Shank CV (1972) Coupled-wave theory of distributed feedback lasers. J Appl Phys 43 : 2327-2335

Köhler R, Tredicucci A, Beltram F, Beere H, Linfield E, Davies AG, Ritchie DA, Iotti RC, Rossi F (2002) Terahertz semiconductor heterostructure lasers. Nature 417 : 156-159

Kohn W, Rostoker N (1954) Solution of the Schrödinger Equation in Periodic Lattices with an Application to metallic Lithium. Phys Rev 94 : 1111-1120 (KKR method, see also : Korringa 1947)

Kondo T, Juodkazis S, Mizeikis V, Misawa H, Matsuo S (2006) Holographic lithography of periodic two and three-dimensional microstructures in photoresist SU-8. Opt Express 14 : 7943-7953

Kong JA (2000) Electromagnetic Wave Theory. EMW Publishing

Kono N, Koshiba M (2005) Three-dimensional finite element analysis of nonreciprocal phase shifts in magneto-photonic crystal waveguides. Opt Express 13 : 9155-9166

Konsek SL, Pearsall TP (2003) Dynamics of electron tunneling in semiconductor nanostructures. Phys Rev B 67 : 45306-

Kopp VI, Fan B, Vithana HKM, Genack AZ (1998) Low threshold lasing at the edge of a photonic stop band in cholestérol liquid crystals. Opt Lett 23 : 1707-1709

Korringa J (1947) On the Calculation of the Energy of a Bloch Wave in a Metal, Physica (Utrecht) 13 : 392- (KKR method, see also : Kohn 1954)

Kosaka H, Kawashima T, Tomita A, Notomi M, Tamamura T, Sato T, Kawakami S (1998) Superprism phenomena in photonic crystals. Phys Rev B 58 : 10096-10099

Kosaka H, Kawashima T, Tomita A, Notomi M, Tamamura T, Sato T, Kawakami S (1999) Photonic crystals for micro lightwave circuits using wavelength-dependent angular beam steering. Appl Phys Lett 74 : 1370-1372

Kotlyar MV, Bolla L, Midrio M, O'Faolain L, Krauss TF (2005) Compact polarization converter in InP-based material Opt Express 13 : 5040-5045

Kotlyar MV, Karle T, Settler D, O'Faolain L, Krauss T.F (2004) Low-loss photonic crystal defect waveguides in InP. Appl Phys Lett 84 : 3588-3590

Krames MR, Ochiai-Holcomb M, Höfler GE, Carter-Coman C, Chen EI, Tan. IH, Grillot P, Gardner NF, Chui HC, Huang SA, Stockman JW, Kish FA, Craford MG, Tan TS, Kocot C P, Hueschen M, Posselt J, Loh B, Sasser G, Collins D (1999) High-power truncated-inverted-pyramid $(Al_xGa_{1-x})_{0.5}In_{0.5}P/GaP$ light-emitting diodes exhibiting >50% external quantum efficiency. Appl Phys Lett 75 : 2365-2367

Krauss TF, De La Rue RM (1996b) Exploring the two-dimension photonic bandgap in semiconductors in Soukoulis CM (Ed) Photonic Band Gap Materials (pp. 427-436). Kluwer Academic Publishers, Dordrecht

Krauss TF, De La Rue RM, Brand S (1996a) Two-dimensional photonic-bandgap structures operating at near-infrared wavelengths. Nature 383 : 699-702

Kress A, Hofbauer F, Reinelt N, Kaniber M, Krenner HJ, Meyer R, Böhm G, Finley JJ (2005) Manipulation of the spontaneous emission dynamics of quantum dots in two-dimensional photonic crystals. Phys Rev B 71 : 241304(R)

Kretschman E (1971) The determination of the optical constants of metals by excitation of surface plasmons. Z Phys 241 : 313-324

Kruusing A, Mellikov E (2001) Photoconductive patterns in semiconductors for electromagnetic field control : A review. Proceedings-of-the-SPIE (The-International-Society-for-Optical-Engineering) 4415 : 22-32

Kudlinski A, George AK, Knight JC, Travers JC, Rulkov AB, Popov SV, Taylor JR (2006) Zero-dispersion wavelength decreasing photonic crystal fibers for ultraviolet-extended supercontinuum generation. Opt Express 14 : 5715-5722

Kuhlmey B, de Sterke M, McPhedran RC, Robinson P, Renversez G, Maystre D (2002b) Microstructured Optical fibers : where's the edge. Optics Express 10 : 1285-1290

Kuhlmey B, Renversez G, Maystre D (2003) Chromatic dispersion and losses of microstructured optical fibers. Applied Optics 42 : 634-639

Kuhlmey B, White TP, Renversez G, Maystre D, Botten LC, Martijn de Sterke C, McPhedran RC (2002a) Multipole method for microstructured optical fibers II : Implementation and results. J Opt Soc Am B 10 : 2331-2340

Kuksenkov DK, Temkin H, Lear KL, Lou HQ (1997) Spontaneous emission factor in oxide-confined vertical cavity surface emitting lasers. Appl Phys Lett 70 : 13-

Kumar Ravi Kanth VV, George AK, Reeves WH, Knight JC, Russell PStJ, Omenetto FG, Taylor AJ (2002) Extruded soft glass photonic crystal fiber for ultrabroad supercontinuum generation. Optics Express 10 : 1520–1524

Kuo PS, Vodopyanov KL, Fejer MM, Simanovskii DM, Yu X, Harris JS, Bliss D, Weyburne D (2006) Optical parametric generation of a mid-infrared continuum in orientation-patterned GaAs. Opt Lett 31 : 71-

Kuramochi E., Notomi M, Mitsugi S, Shinya A, Tanabe T, Watanabe T (2006) Ultrahigh-Q photonic crystal nanocavities realized by the local width modulation of a line defect, Appl Phys Lett 88 : 041112

Kuriki K, Shapira O, Hart S, Benoit G, Kuriki Y, Viens JF, Bayindir M, Joannopoulos JD, Fink Y (2004) Hollow multilayer photonic bandgap fibers for NIR applications. Opt. Express 12 : 1510-1517

Kurokawa K, Tajima K, Tsujikawa K, Nakajima K, Matsui T, Sankawa I, Haibara T (2006) Penalty-Free Dispersion-Managed Soliton Transmission Over a 100-km Low-Loss PCF. J Lightwave Technol 24 : 32-37

Kurtsiefer C, Mayer S, Zarda S, Weinfurter H (2000) Stable solid-state source of single photons. Phys Rev Lett 89 : 290-

Labeke DV, Gerard D, Guizal B, Baida FI (2006) An angle-independent Frequency Selective Surface in the optical range. Opt Express 14 : 11945-11951

Labilloy D, Benisty H, Weisbuch C, Krauss TF, Houdré R, Oesterle U (1997) Use of guided spontaneous emission of a semiconductor to probe the optical properties of two-dimensional photonic crystals. Appl Phys Lett 71 : 738-740

Labilloy D, Benisty H, Weisbuch C, Krauss TF, Smith CJM, Houdré R, Oesterle U (1998) High-finesse disk microcavity based on circular Bragg reflector. Appl Phys Lett 73 : 1314-

Labilloy D, Benisty H, Weisbuch C, Smith CJM, Krauss TF, Houdré R, Oesterle U (1999) Finely resolved transmission spectra and band structure of two-dimensional photonic crystals using InAs quantum dots emission. Phys Rev B 59 : 1649-1652

Labonté L, Roy P, Pagnoux D, Louradour F, Restoin C, Mélin G and Burov E (2006) Experimental and numerical analysis of the chromatic dispersion dependence upon the actual profile of small core microstructured fibres. J Opt A: Pure Appl Opt 8 : 933-938

Lalanne P, Benisty H (2001) Ultimate limits of two-dimensional photonic crystals etched through waveguides : an electromagnetic analysis. J Appl Phys 89 : 1512-1514

Lalanne P, Hugonin JP, JM Gérard (2004) Electromagnetic study of the Q of pillar microcavities in the small diameter limit. Appl Phys Lett 84 : 4726-4728

Lalanne P, Morris GM (1996) Highly improved convergence of the coupled wave method for TM polarization. J Opt Soc Am A 13 : 779-784

Landau L, Lifchitz E (1969) Électrodynamique des milieux continus (Physique Théorique Tome VIII, in French). Ed. MIR, Moscou

Landau L, Lifshitz L, Pitaevskii LI (1984) Electrodynamics of Continuous Media. Pergamon Press, New-York

Landolt-Börnstein (1982) Numerical Data and Functional Relationship in Science and Technology in: O. Madelung (dir) New Series group III, vol. 17, Springer Verlag, Berlin

Langbein W, Borri P, Woggon U, Stavarache V, Reuter D, Wieck AD (2004) Control of fine structure splitting and biexciton splitting in InGaAs quantum dots by annealing. Phys Rev B 69 : 161301.

Langrock C, Kumar S, McGeehan JE, Willner AE, Fejer MM (2006) All optical signal processing using chi(2) nonlinearities in guided wave devices. IEEE J of Lightwave Technology 24 : 2579

Laurent S, Varoutsis S, Le Gratiet L, Lemaître A, Sagnes I, Raineri F, Levenson A, Robert-Philip I, Abram I (2005) Indistinguishale single photons from a single quantum dot in a two-dimensional photonic crystal cavity. Appl Phys Lett 87 : 163107

Lawandy NM, Johnston SA, Martorell J (1988) Birefringence and polarization dependence absorption in sheared colloidal crystals. Opt Commun 65 : 425-429

Le Vassor d'Yerville M (2002) Modélisation de cristaux photoniques bidimensionnels de hauteur finie (in French). Ph.D. Thesis, University of Montpellier II

Lecamp G, Lalanne P, Hugonin JP, Gérard JM (2005) Energy transfer through laterally confined Bragg mirrors and its impact on pillar microcavities. IEEE J Quant Electron 41 : 1323-1329

Lee KH, Baek JH, Hwang IK, Lee YH, Lee GH, Ser JH, Kim HD, Shin HE (2004) Square-lattice photonic-crystal vertical-cavity surface-emitting lasers. Opt Express 12 : 4136-4143

Lee PT, Lu TW, Tsai FM, Lu TC, Kuo HC (2006) Whispering gallery mode of modified octagonal quasiperiodic photonic crystal single-defect microcavity and its side-mode suppression. Appl Phys Lett 88 : 201104

Lee TDM, Parker GJ, Zoorob ME, Cox SJ, Charlton MDB (2005) Design and simulations of highly symmetric photonic quasi-crystals. Nanotechnology 16 : 2703-2706

Lee W, Pruzinsky S, Braun PV (2002) Multi-photon polymerisation of waveguide structures within three-dimensional photonic crystals. Adv Mater 14 : 271-274

Leonhardt U (2006) Optical conformal mapping. Science 23:1777-1780

Letartre X, Seassal C, Grillet C (2001) Group velocity and propagation losses measurement in a single-line photonic-crystal waveguide on InP membranes. Appl Phys Lett. 79 : 2312-

Leuenberger D, Ferrini R, Dunbar LA, Houdré R, Kamp M, Forchel A (2005) Codirectional couplers in GaAs-based planar photonic crystals. Appl Phys Lett 86 : 081108 (1-3)

Leung WY, Tuttle G, Sigalas MM, Biswas R, Ho KM, Soukoulis CM (1998) Optimising the Q value in three-dimensional metallic photonic band gap crystals. J Appl Phys 84 : 4091-4095

Li L (1996) Use of Fourier series in the analysis of discontinuous periodic structures. J Opt Soc Am A 13 : 1870-1876

Li R, Levy M (2005) Bragg grating magnetic photonic crystal waveguides. Appl Phys Lett 86 : 251102

Li ZY, Zhang XD, Zhang ZQ (2000) Disordered photonic crystals understood by a perturbation formalism. Phys Rev B 61: 15738-15748

Light PS, Couny F, Benabid F (2006) Low optical insertion-loss and vacuum-pressure all-fiber acetylene cell based on hollow-core photonic crystal fiber. Opt. Lett. 31 : 2538-2540

Limpert J, Schreiber T, Nolte S, Zellmer H, Tunnermann T, Iliew R, Lederer F, Broeng J, Vienne G, Petersson A, Jakobsen C (2003) Highpower air-clad large-mode-area photonic crystal fiber laser. Optics Express 11 : 818–823

Lin HB, Tonucci RJ, Campillo AJ (1998) Two-dimensional photonic bandgap optical limiter in the visible. Opt Lett 23 : 94-96

Lin SY, Chow E, Johnson SG, Joannopoulos JD (2001a) Direct measurement of the quality factor in a two-dimensional photonic-crystal microcavity. Opt Lett 26 : 1903-1905

Lin SY, Chow E., Johnson SG, Joannopoulos JD (2000a) Demonstration of highly efficient waveguiding in a photonic crystal slab at the 1.5 μm wavelength. Optics Lett 25 : 1297-1299

Lin SY, Fleming JG (1999a) A three-dimensional optical photonic crystal. J Lightwave Technol 17 : 1944-1947

Lin SY, Fleming JG, Chow E, Bur J, Choi KK, Goldberg A (2000b) Enhancement and suppression of thermal emission by a three-dimensional photonic crystal. Phys Rev B 62 : R2243-2246

Lin SY, Fleming JG, Lin R, Sigalas MM, Biswas R, Ho KM (2001b) Complete three-dimensional photonic bandgap in a simple cubic structure. J Opt Soc Am B 18 : 32-35

Lin SY, Fleming JG, Sigalas MM, Biswas R, Ho KM (1999b) Photonic band-gap microcavities in three dimensions. Phys Rev B 59 : R15579-R15582

Lin SY, Hietala VM, Wang L, Jones ED (1996) Highly dispersive photonic band-gap prism. Opt Lett 21 : 1771-1773

Linden S, Enkrich C, Wegener M, Zhou J, Koschny T, Soukoulis CM (2004) Magnetic response of metamaterials at 100 Terahertz. Science 306 : 1351-1353

Litchinitser N, Dunn S, Usner B, Eggleton B, White T, McPhedran R, Martijn de Sterke C (2003) Resonances in microstructured optical waveguides. Opt. Express 11 : 1243-1251

Lodahl P, van Driel AF, Nikolaev IS, Irman A, Overgaag K, Vanmaekelbergh D, Vos W (2004) Controling the dynamics of spontaneous emission from quantum dots in photonic crystals. Nature 430 : 654-657

Lombardet B, Dunbar LA, Ferrini R, Houdré R (2005) Fourier analysis of Bloch wave propagation in photonic crystals. J Opt Soc Am B 22 : 1179-1190

Loncar M, Nedeljkovic D, Pearsall TP, Vuckovic J, Scherer A, Kuchinsky S, Allan, DC (2002a) Experimental and theoretical confirmation of Bloch-mode light propagation in planar photonic crystal waveguides. Appl Phys Lett 80 : 1689-1691

Loncar M, Yoshie T, Scherer A, Gogna P, Qiu Y (2002b) Low-threshold photonic crystal laser. Appl Phys Lett 81 : 2680-

Lord Rayleigh, JW Strutt (1892) On the influence of obstacles arranged in rectangular order upon the properties of a medium. Philos Mag 34 : 481-502

Loudon R (1983) The Quantum Theory of Light. Oxford University Press, Oxford

Lounis B, Moerner WE (2000) Single photons on demand from a single molecule at room temperature. Nature 407 : 491-

Lourtioz JM (1981) Lasers submillimétriques continus pompés optiquement par laser CO2. PhD Thesis (in French), University of Orsay

Lourtioz JM, Berger V (1998) Les matériaux à bandes interdites photoniques (in French). Images de la Physique (ed. CNRS) : 37-43

Lourtioz JM, de Lustrac A, Gadot F, Rowson S, Chelnokov A, Brillat T, Ammouche A, Danglot J, Vanbésien O, Lippens D (1999) Toward controllable photonic crystals for centimeter and millimeter wave devices. J Lightwave Technol 17 : 2025-2031

Luan F, George AK, Hedley TD, Pearce GJ, Bird DM, Knight JC, Russell PSJ (2004) All-solid photonic bandgap fiber. Opt. Lett. 29 : 2369-2371

Luo C, Johnson SG, Joannopoulos JD, Pendry JB (2002) All-angle negative refraction without negative index. Phys Rev B 65 : R201104-

Lupu A, Cassan E, Laval S, Melhaoui LE, Lyan P, Fedeli JM (2004) Experimental evidence for superprism phenomena in SOI photonic crystals. Opt Express 12 : 5690-5696

Lupu A, De Lustrac A, Ourir A, Lourtioz JM, Checoury X, Centeno E, Cassagne D, Albert JP, Pommereau F, Legouezigou L, Drisse O, Legouezigou O, Derouin E, Duan GH (2006) Discontinuous wavelength super-refraction in photonic crystal superprism. Opt Express 14 : 2003-2013

Malvezzi AM, Vecchi G, Patrini M, Guizzetti G, Andreani LC, Romanato F, Businaro L, Di Fabrizio E, Passaseo A, De Vittori M (2003) Resonant second harmonic generation in a GaAs photonic crystal waveguide. Phys. Rev. B 68 : 161306

Man W, Megens M, Steinhardt PJ, Chaikin PM (2005) Experimental measurements of the photonic properties of icosahedral quasicrystals. Nature 436 : 993-996

Mangan BJ, Farr L, Langford A, Roberts PJ, Williams DP, Couny F, Lawman M, Mason M, Coupland S, Flea R, Sabert H, Birks TA, Knight JC, Russell PSJ (2004) Low loss (1.7 dB/km) hollow core photonic bandgap fiber. Proc. Opt. Fiber. Commun. Conf : paper PDP24

Manhkopf S, Arlt M, Kamp M, Colson V, Duan GH, Forchel (2004) A Two-channel tunable laser diode based on photonic crystals. IEEE Photon Technol Lett 16 : 353-355

Maradudin AA, Michel T, McGurn AR, Mendez ER (1990) Enhanced backscattering of light from a random grating. Ann Phys 203 : 255-307

Marconi G, Franklin S (1919) Reflector For Use In Wireless Telegraphy And Telephony, US patent

Marcuse D (1974) Theory of Electric Optical Waveguides. New York: Academic

Martinelli L, Benisty H, Drisse O, Derouin E, Pommereau F, Legouézigou O, Duan GH (2007) Fine Impact of Lithographic Grid Irregularity Assessed on Photonic Crystal Device Selectivity. IEEE Phot Technol Lett 19 : 282-284

Maslovsky SI (2002) Negative refraction and causality in : Digest of the XXVII URSI/IEEE Convention on Radio Science (Oct. 17-18, 2002) Espoo, Finland, pp. 110-111 (http://www.hut.fi/Units/Radio/URSI02/ursi_maslovski.pdf).

Maxwell Garnett JC (1904) Colours in metal glasses and metal films, Phil Trans Roy Soc A 203 : 385-

Maxwell Garnett JC (1906) Colours in metal glasses, in metallic films, and in metallic solutions II, Phil Trans Roy Soc A 205 : 237-

Maystre D (1982) General study of grating anomalies from electromagnetic surface modes in Boardman AD (ed) Electromagnetic surface modes (Chapter 17, pp 661-724), John Wiley & Sons, Chichester

Maystre D (1993) Diffraction Gratings. SPIE Milestones series, vol MS83

Maystre D (1994a) Electromagnetic study of photonic band gaps. Pure Appl Opt 3 : 975-993

Maystre D and Enoch S (2004) Perfect lenses made with left-handed materials: Alice's mirror? J Opt Soc Am A 21: 122-131

Maystre D, Dainty JC (1991) Modern Analysis of Scattering Phenomena. Hilger, New-York

Maystre D, Nevière M (1977) Sur une méthode d'étude théorique quantitative des anomalies de Wood des réseaux de diffraction, application aux anomalies de plasmons (in French). Nouv Rev Optique 8 : 165-174

Maystre D, Petit R (1976) Brewster incidence for metallic gratings. Optics Commun 17 : 196-200

Maystre D, Saillard M (1994b) Localization of light by randomly rough surfaces: concept of localiton. J Opt Soc Am A 11 : 680-690

Maystre D, Saillard M, Tayeb G (2002) Special methods of wave diffraction, Academic Press, New York

Mc Call SL, Levi AFJ, Slusher RE, Pearton SJ, Logan RA (1992) Whispering-gallery mode microdisk lasers. Appl Phys Lett 60 : 289-

Mc Phedran RC, Maystre D (1977) On the theory and solar application of inductive grids. Appl Phys 14 : 1-20

McCall SL, Platzman PM, Dalichaouch R, Smith D, Schultz S (1991) Microwave propagation in two-dimensional dielectric lattices. Phys Rev 67 : 2017-

McDonald KT (2000) Negative Group Velocity. ArXiv, 0008013., http://arxiv.org/abs/physics/0008013

McNab S, Moll N, Vlasov Y (2003) Ultra low-loss photonic integrated circuit with membrane-type photonic crystal waveguides. Opt Express 11 : 2927-2939

McPherson WN, Gander MJ, McBride R, Jones JDC, Blanchard PM, Burnett JG, Greenaway AH, Mangan B, Birks TA, Knight JC, Russell PStJ (2001) Remotely addressed optical fibre curvature sensor using multicore photonic crystal fibre. Optics Commun 193 : 97-104

Meade RD, Rappe AM, Brommer KD, Joannopoulos JD, Alerhand OL (1993) Accurate theoretical analysis of photonic bandgap materials. Phys Rev B 48 : 8434-8437

Megens M, Schriemer HP, Lagendijk A, Vos WL (1999) Fluorescence lifetimes and linewidths of dye in photonic crystals. Phys Rev A 59 : 4727-4731

Mei D, Cheng B, Hu W, Li Zh, Zhang D (1995) Three-dimensional ordered patterns by light interference. Optics Lett 20 : 429-431

Mekis A, Chen JC, Kurland I, Villeneuve PR, Joannopoulos JD (1996) High transmission through sharp bends in photonic crystals waveguides. Phys Rev Lett 77 : 3787-3790

Mélin G, Cavani O, Gasca L, Peyrilloux A, Provost L, Réjeaunier X (2003) Characterization of a polarization maintaining microstructured fiber. Tech Digest of ECOC, We1.7.4

Melville DOS, Blaikie RJ, Wolf CR (2004) Submicron imaging with a planar silver lens. Appl Phys Lett 84 : 4403-4405

Meschede D, Walther H, Müller G (1985) One-atom maser. Phys Rev Lett 54 : 551-554

Michler P, Imamoglu A, Mason M, Carson M, Strouse G, Buratto S (2000a) Quantum correlations among photons from a single quantum dot at room temperature. Nature 406 : 968-

Michler P, Kiraz A, Becher C, Schoenfeld W, Petroff PM, Zhang L, Hu E, Imamoglu A (2000b) A quantum dot single photon turnstile. Science 290 : 2282-

Michler P, Kiraz A, Zhang L, Becher C, Hu E, Imamoglu A (2000c) Laser emission from quantum dots in microdisk structures. Appl Phys Lett 77 : 184-

Mie G (1908) Beiträge zur Optik trüber Medien, speziell kolloidaler Metallösungen. Ann. d. Phys. 25 (4) : 377-

Mogilevstev D, Birks TA, Russell PS (1998) Group-velocity dispersion in photonic crystal fibers. Opt Lett 23 : 1662–1664

Moharam MG, Gaylord TK (1986) Rigorous coupled wave analysis of metallic diffraction gratings. J Opt Soc Am A 3 (11) : 1780-1787

Mohideen U, Hobson WS, Pearton SJ, Ren F, Slusher RE (1994) GaAs/AlGaAs microdisk lasers. Appl Phys Lett 64 : 1911-

Momeni B, Huang J, Soltani M, Askari M, Mohammadi S, Rakhshanderoo M, Adibi A (2006) Compact wavelength demultiplexing using focusing negative index photonic crystal superprisms. Opt Express 14 : 2413-2422

Monacelli B, Pryor JB, Munk BA, Kotter D, Boreman GD (2005) Infrared Frequency Selective Surface Based on Circuit-Analog Square Loop Design. IEEE Trans Antennas Propag 53 : 745-752

Monat C, Seassal C, Letartre X, Regreny P, Rojo-Romeo P, Viktorovitch P, Le Vassor d'Yerville M, Cassagne D, Albert JP, Jalaquier E, Pocas S, Aspar B (2002) InP-based two-dimensional photonic crystal on silicon : in-plane Bloch mode laser. Appl Phys Lett 81 : 5102-5104

Mondia JP, van Driel HM, Jiang W, Cowan AR, Young JF (2003) Enhanced second-harmonic generation from planar photonic crystals. Optics Lett 28 : 2500-2502

Mondia JP, Wee Tan H, Linden S, van Driel HM, Young JF (2005) Ultrafast tuning of two-dimensional planar photonic crystal waveguides via free-carrier injection and the optical Kerr effect. J Opt Soc Am B 22 : 2480-

Monge D (2000) Description des propriétés optiques des cristaux photoniques à l'aide d'une méthode basée sur les fonctions localisées. Ph.D. Thesis (in French), University of Montpellier

Monro TM, Ebendorff-Heidepriem H (2006) Progress in microstructured fibers. Annual Rev Mat Research 36 : 467-495

Moreau E, Robert I, Gérard JM, Abram I, Manin L, Thierry-Mieg V (2001b) Single-mode solid-state single photon source based on isolated quantum dots in pillar microcavities. Appl Phys Lett 79 : 2865-

Moreau E, Robert I, Manin L, Thierry-Mieg V, Gérard JM, Abram I (2001a) Quantum cascade of photons in semiconductor quantum dots. Phys Rev Lett 87 : 183601-

Moreau E, Robert I, Manin L, Thierry-Mieg V, Gérard JM, Abram I (2002) A single mode single photon source based on isolated quantum dots in a micropillar. Physica E 13 : 418-

Morimura S, Ujihara K (1997) Rate equation analysis of a microcavity laser with a finite number of molecules in the mode volume. Jap Journ Appl Phys 36 (part 1) : 4307-

Moroz A (1994) Inward and outward integral equations and the KKR method for photons. Journal of Physics: Condensed Matter 6 (1) : 171-182

Moroz A (1995) Density-of-states calculations and multiple-scattering theory for photons. Phys Rev B 51 : 2068-2081

Moroz A (1999) Three-dimensional complete photonic band gap structures in the visible. Phys Rev Lett 83 : 5274-5277

Morse PM and Feshbach H (1953) Methods of theoretical physics. Mc Graw Hill Book Company, New York

Mouette J, Seassal C, Letartre X, Rojo-Romeo P, Leclercq JL, Regreny P, Viktorovitch P, Jalaguier E, Perreau P, Moriceau H (2003) Very low threshold vertical emitting laser operation in InP graphite photonic crystal slab on silicon. Electron Lett 39 : 526–528

Mühlsclegel P, Eisler HJ, Martin OJF, Hecht B, Pohl DW (2005) Resonant optical antennas. Science 308 : 1607-1609

Myers LE, Miller GD, Eckardt RC, Fejer MM, Byer RL, Bosenberg WR (1995) Quasi-Phase-Matched 1.064 μm-pumped optical parametric oscillator in bulk periodically poled LiNbO3. Opt Lett 20 : 52-

Nakajima K, Jian Zhou, Tajima K, Kurokawa K, Fukai C, Sankawa I (2005) Ultra-wide band single-mode transmission performance in a low-loss photonic crystal fiber. J Lightwave Technol 23 : 7-12

Nakamura H, Sugimoto Y, Kanamoto K, Ikeda N, Tanaka Y, Nakamura Y, Ohkouchi S, Watanabe Y, Inoue K, Ishikawa H, Asakawa K (2004) Ultra-fast photonic crystal/quantum dot all-optical switch for future photonic networks. Opt Express 12 : 6606-

Nevière M (1980) The homogeneous problem in Petit R (ed) Electromagnetic Theory of Gratings (Chapter 5, pp 123-157), Springer Verlag, Berlin

Nevière M, Popov E (2003) Light Propagation in Periodic Media: Differential Theory and Design, Marcel Dekker vol. 81, New York

Nicorovici NA, Mc Phedran RC, Botten LC (1995) Photonic band gaps for arrays of perfectly conducting cylinders. Phys Rev E 52 : 1135-1145

Nielsen M, Mortensen N, Albertsen M, Folkenberg J, Bjarklev A, Bonacinni D (2004) Predicting macrobending loss for large-mode area photonic crystal fibers. Opt Express 12 : 1775-1779

Niemi T, Frandsen LH, Hede KK, Harpoth A, Borel PI, Kristensen M (2006) Wavelength-division demultiplexing using photonic crystal waveguides. IEEE Phot Technol Lett 18 : 226-228

Nishizawa, H, Nakayama T (1997) Magneto-optic anisotropy effect on photonic band structure. J Phys Soc Jpn 66 : 613-617

Noda S, Chutinan A, Imada M (2000) Trapping and emission of photons by a single defect in a photonic bandgap structure. Nature 407 : 608-610

Noda S, Imada M, Okano M, Ogawa S, Mochizuki M, Chutinan A (2002) Semiconductor three-dimensional and two-dimensional photonic crystals and devices. IEEE J Quant Electron 38 : 726-735

Noda S, Yamamoto N, Kobayashi H, Okano M, Tomoda K (1999) Optical properties of three-dimensional photonic crystals based on III-V semiconductors at infrared to near-infrared wavelengths. Appl Phys Lett 75 : 905-907

Nomura M, Iwamoto S, Watanabe K, Kumagai N, Nakata Y, Ishida S, Arakawa Y (2006) Room temperature continuous-wave lasing in photonic crystal nanocavity. Opt Express 14 : 6308-6315

Notomi M (2000a) Theory of light propagation in strongly modulated photonic crystals: refraction like behavior in the vicinity of the photonic band gap. Phys Rev B 62 : 10696-10705

Notomi M, Shinya A, Mitsugi S, Kira G, Kuramochi E, Tanabe T (2005) Optical bistable switching action of Si high Q photonic crystal nanocavities. Opt Express 13 : 2678

Notomi M, Shinya A, Mitsugi S, Kuramochi E, Ryu HY (2004) Waveguides, resonators and their coupled elements in photonic crystal slabs. Opt Express 12 : 1551-1561

Notomi M, Suzuki H, Tamamura T (2001b) Directional lasing oscillation of two-dimensional organic photonic crystal lasers at several photonic bandgaps. Appl Phys Lett 78 : 1325-1327

Notomi M, Tamamura T, Kawashima T, Kawakami S (2000b) Drilled alternating-layer three-dimensional photonic crystals having a full photonic band gap. Appl Phys Lett 77 : 4256-4258

Notomi M, Yamada K, Shinya A, Takahashi J, Takahashi C, Yokohama I (2001a) Extremely large group-velocity dispersion of line-defect waveguides in photonic crystal slabs. Phys Rev Lett 87 : 253902

Nozaki K, Baba T (2006) Lasing characteristics of 12-fold symmetric quasi-periodic photonic crystal slab nanolasers. Jap J Appl Phys 45 (n° 8A) : 6087-6090

O'Brien D, Settle MD, Karle T, Michaeli A, Salib M, Krauss TF (2007) Coupled photonic crystal heterostructure nanocavities. Opt. Express 15 : 1228-1233

O'Brien S, Pendry JB (2002) Magnetic activity at infrared frequencies in sructured metallic photonic crystals. J Phys Condens Matter 14 : 6383-6394

O'Donnel KA, Mendez ER (1987) Experimental study of scattering from characterized random surfaces. J Opt Soc Am A 4 : 1194-1205

Ohkubo H, Ohtera Y, Miura K, Akutsu N, Hikage M, Kawakami S (2004) Reduction of propagation loss to 0.1 dB/mm : Flat core channel waveguides consisting of periodic structures. IEEE Photon Technol Lett 16 : 1068-1070

Okoshi T (1982) Optical Fibers. Academic Press, New York

Olivier S (2002b) Nouvelles structures miniatures dans des cristaux photoniques bidimensionnels planaires pour les fonctions de l'optique intégrée (in French). Ph. D. Thesis, University of Paris VI

Olivier S, Benisty H, Weisbuch C, Smith CJM, Krauss TF, Houdré R, Oesterle U (2003) All-Photonic crystal add-drop filter exploiting low group-velocity modes. Opt Lett 28 : 2246-2248

Olivier S, Rattier M, Benisty H, Smith CJM, De La Rue RM, Krauss TF, Oesterle U, Houdré R, Weisbuch C (2001b) Mini stopbands of a one dimensional system: the channel waveguide in a two-dimensional photonic crystal. Phys Rev B 63 : 113311-

Olivier S, Smith C, Benisty H, Weisbuch C, Krauss TF, Houdré R, Oesterle U (2002a) Cascaded photonic crystal guides and cavities: spectral studies and their impact on integrated optics design. IEEE J Quant Electron 38 : 816-824

Olivier S, Smith C, Rattier M, Benisty H, Weisbuch C, Krauss T, Houdré R, Oesterlé U (2001a) Miniband transmission in a photonic crystal coupled-resonator optical waveguide. Optics Letters 26 : 1019-1021

Ortigosa-Blanch A, Knight JC, Wadsworth WJ, Arriaga J, Mangan BJ, Birks TA, Russel PstJ (2000) Highly birefringent photonic crystal fibres. Opt Lett 25 : 1325-1327 - and references therein.

Ourir A, De Lustrac A, Lourtioz JM (2006a) All-metamaterial based subwavelength cavities (λ/60) for ultrathin directive antennas. Appl Phys Lett 88 : 084103 (1-3)

Ourir A, De Lustrac A, Lourtioz JM (2006b) Optimization of metamaterial based subwavelength cavities for ultracompact directive antennas. Microwave Opt Technol Lett 48 : 2573-2577

Ouzounov DG, Ahmad FR, Müller D, Venkataraman N, Gallagher MT, Thomas MG, Silcox J, Koch KW, Gaeta AL (2003) Generation of megawatt optical solitons in hollow-core photonic band-gap fibers. Science 301 : 702-1704

Özbay E, Michel E, Tuttle G, Biswas R, Ho KM, Bostak J, Bloom DM (1994a) Double-etch geometry for millimeter-wave photonic bandgap crystals. Appl Phys Lett 65 : 1617-1619

Özbay E, Michel E, Tuttle G, Biswas R, Ho KM, Bostak J, Bloom DM (1994b) Terahertz spectroscopy of three-dimensional photonic bandgap crystals. Opt Lett 19 : 1155-1157

Özbay E, Temelkuran B, Sigalas M, Tuttle G, Soukoulis CM, Ho KM (1996) Defect structures in metallic photonic crystals. Appl Phys Lett 69 : 3797-

Pacradouni V, Mandeville WJ, Cowan AR, Padon P, Young JJ, Johnson SR (2000) Photonic band structure of dielectric membranes periodically textured in two dimensions. Phys Rev B 62 : 4204-

Pagnoux D, Peyrilloux A, Roy P, Fevrier S, Labonte L, Hilaire S (2003) Microstructured air-silica fibres : recent developments in modelling, manufacturing and experiments. Ann Télécommun 58 : 1238-1274

Painter O, Lee RK, Scherer A, Yariv A, O'Brien JD, Dapkus PD, Kim I (1999b) Two-dimensional photonic band-gap defect mode laser. Science 284 : 1819-1821

Painter OJ, Husain A, Scherer A, O'Brien JD, Kim I, Dapkus D (1999a) Room-temperature photonic crystal defect laser at near-infrared wavelengths in InGaAsP. J Lightwave Technol 17 : 2082-2088

Parameswaran KR, Kurz JR, Roussev RV, Fejer MM (2002) Observation of 99% pump depletion in single pass second harmonic generation in a periodically poled lithium niobate waveguide. Opt Lett 27 : 43-

Park HG, Hwang JK, Huh J, Ryu HY, Lee YH, Kim JS (2001) Nondegenerate monopole-mode two-dimensional photonic band gap laser. Appl Phys Lett 79 : 3032-3034

Park HG, Kim SH, Kwon SH, Ju YG, Yang JK, Baek JH, Kim SB, Lee YH, (2004) Electrically Driven Single-Cell Photonic Crystal Laser. Science 305 : 1444-1447

Patrini M, Galli M, Marabelli F, Agio M, Andreani LC, Peyrade D, Chen Y (2002) Photonic Bands in patterned Silicon-on-insultao waveguides. IEEE J Quant Electron 38 : 885-890

Pelton M, Santori C, Vuckovic J, Zhang B, Solomon G, Plant J, Yamamoto Y (2002) Efficient Source of Single Photons : A Single Quantum Dot in a Micropost Microcavity. Phys Rev Lett 89 : 233602-

Pelton M, Yamamoto Y (1999) Ultralow threshold laser using a single quantum dot and a microsphere cavity. Phys Rev A 59 : 2418-2421

Pendry JB (1994) Photonic band structures. Journ Mod Phys 41 : 209-229

Pendry JB (1996b) Calculating photonic band structures. J Phys Condens Matter 8 : 1085-1108

Pendry JB (2000) Negative refraction makes a perfect lens. Phys Rev Lett 85 : 3966-3969

Pendry JB (2001a) A Reply to the Comment by G. W. 't Hooft. Phys Rev Lett 87: 249702

Pendry JB (2001b) A Reply to the Comment by J. M. Williams. Phys Rev Lett 87: 249704

Pendry JB (2003b) Comment on : Left-Handed Materials Do Not Make a Perfect Lens (see Garcia 2002b), Phys Rev Lett 91 : 099701-

Pendry JB, Holden AJ, Robbins DJ, Stewart WJ (1998) Low frequency plasmons in thin-wire structures. J Phys Condens Matter 10 : 4785-4809

Pendry JB, Holden AJ, Robbins DJ, Stewart WJ (1999) Magnetism from conductors and enhanced nonlinear phenomena. IEEE Trans Microw Theory 47 : 2075-2084

Pendry JB, Holden AJ, Stewart WJ, Youngs I (1996a) Extremely low frequency plasmons in metallic mesostructures. Phys Rev Lett 76 : 4773-4776

Pendry JB, Schurig D, Smith DR (2006) Controlling Electromagnetic fields. Science 312: 1780-1782

Pendry JB, Smith DR (2003a) Comment on : Wave Refraction in Negative-Index Media Always Positive and Very Inhomogeneous (see : Valanju 2002). Phys Rev Lett 90 : 029703-

Peng LH, Peng LH, Hsu CC, Shih YC (2003) Second harmonic green generation from two dimensional chi(2) nonlinear photonic crystal with orthorhombic lattice structure. Appl Phys Lett 83 : 3447

Peter E, Senellart P, Martrou D, Lemaître A, Hours J, Gérard JM (2005) Exciton-photon strong coupling regime for a single quantum dot embedded in a microcavity. Phys Rev Lett 95 : 067401

Petit R (1980) Electromagnetic Theory of Gratings. Springer Verlag, Heidelberg

Petrov EP, Bogomolov VN, Kalosha II, Gaponenko SV (1998) Spontaneous emission of organic molecules embedded in a photonic crystal. Phys Rev Lett 81 : 77-80

Pile DFP, Ogawa T, Gramotnev DK, Matsuzaki Y, Vernon KC, Yamaguchi K, Okamoto T, Haraguchi M, Fukui M (2005) Two-dimensionally localized modes of a nanoscale gap plasmon waveguide. Appl Phys Lett 87 : 261114

Pohl DW and Courjon D (1993) Near Field Optics. Kluwer Academic Publisher, Dordrecht

Poilasne G, Poulingen P, Mahdjoubi K (2000) Study of beam splitting using periodic metallic photonic band-gap materials. Microwave Opt Tech Lett 25 : 36-

Pokrovsky AL, Efros AL (2002a) Electrodynamics of metallic photonic crystals and problem of left-handed materials. Phys Rev Lett 89 : 093901-

Pokrovsky AL, Efros AL (2002b) Diffraction in left-handed materials and theory of Veselago lens. Cond Mat 0202078 (http://xxx.lanl.gov/abs/cond-mat/0202078)

Pommereau F, Legouézigou L, Hubert S, Sainson S, Chandouineau JP, Fabre S, Duan GH, Lombardet B, Ferrini R, Houdré R (2004) Fabrication of low loss two-dimensional InP photonic crystals by inductively coupled plasma etching, J Appl Phys 95 : 2242-2246

Popov E, Bozhkov B, Nevière M (2001a) Almost perfect blazing by photonic crystal rod grating. Applied Optics : 2417-2422

Popov E, Nevière M (2001b) Maxwell equations in Fourier space: fast-converging formulation for diffraction by arbitrary shaped, periodic, anisotropic media. J Opt Soc Am A 18 : 2886-2894

Pottier P, Seassal C, Letartre X, Leclercq JL, Viktorovitch P, Cassagne D, Jouanin C (1999) Triangular and Hexagonal High Q-Factor 2D Photonic Bandgap Cavities on III-V Suspended Membranes. J Lightwave Technol 17 : 2058-2062

Powell JL, Craseman B (1965) Quantum Mechanics. Addison-Wesley, Reading

Purcell EM (1946) Spontaneous Emission Probabilities at Radiofrequencies. Phys Rev 69 : 681

Qian Y, Coccioli R, Sievenpiper D, Radisic V, Yablonovitch E, Itoh T (1999) A microstrip patch antenna using novel photonic band-gap structures. Microwave Journal : 67-76

Quang T, John S (1997) Resonance fluorescence near a photonic band edge : Dressed-state Monte Carlo wave-function approach. Phys Rev A 56 : 4273-4277

Raether H (1988) Surface Plasmons on Smooth and Rough Surfaces and on Gratings. Springer Verlag, New York

Raineri F, Cojocaru C, Monnier P, Levenson A, Raj R, Seassal C, Letartre X, Viktorovitch P (2004) Ultrafast dynamics of the third order nonlinear response in a two dimensional InP-based photonic crystal. Appl Phys Lett 85 : 1880-

Raineri F, Cojocaru C, Raj R, Monnier P, Levenson A, Seassal C, Letartre X, Viktorovitch P (2005) Tuning a two-dimensional photonic crystal resonance via optical carrier injection. Opt Lett 30 : 64-66

Ranka JK, Windeler RS (2000) Nonlinear interactions in air-silica microstructures optical fibers. Optics and Photonics News : 20-25

Rarity JG, Fulconis J, Duligall J, Wadsworth WJ, Russel PSJ (2005) Photonic crystal fiber source of correlated photon pairs. Opt Express 13 : 534-

Rattier M, Benisty H, Schwoob E, Weisbuch C, Krauss TF, Smith CJM, Houdré R, Oesterle U (2003) Omnidirectional and compact guided light extraction from Archimedean photonic lattices. Appl Phys Lett 83 : 1283-1285

Rattier M, Benisty H, Stanley R, Carlin JF, Houdré R, Oesterle U, Smith CJM, Weisbuch C, Krauss TF (2002) Towards Ultra-High Efficiency Aluminum Oxide Microcavity Light-Emitting Diodes : Guided Mode Extraction by Photonic Crystals. IEEE J Sel Topics in Quant Electron 8 : 238-247

Reese C, Becher C, Imamoglu A, Hu E, Gerardot BD, Petroff PM (2001) Photonic crystal microcavities with self-assembled InAs quantum dots as active emitters. Appl Phys Lett 78 : 2279-2281

Reeves WH, Knight JC, Russell PStJ (2002) Demonstration of ultra-flattened dispersion in photonic crystal fibers. Optics Express 10 : 609-613

Reineix A, Jecko B (1996) A new photonic bandgap equivalent model using Finite Difference Time Domain. Ann Télécommun 51 : 656-662

Reithmaier JP, Sek G, Löffler A, Hofmann C, Kuhn S, Reitzenstein S, Keldysh LV, Kulakovskii VD, Reinecke TL, Forchel A (2004) Strong coupling in a single quantum dot semiconductor microcavity system. Nature 432 : 197-200

Reitzenstein S, Bazhenov A, Gorbunov A, Hofmann C, Münch S, Löffler A, Kamp M, Reithmaier JP, Kulakovskii VD, Forchel A (2006) Lasing in high-Q quantum dot micropillar cavities. Appl Phys Lett 89 : 051107

Rennon S, Klopf F, Reithmaier JP, Forchel A (2001) 12-micron-long edge-emitting quantum-dot microlaser. Electron Lett 37 : 690-691

Renversez G, Kuhlmey B, McPhedran RC (2003) Dispersion management with microstructured optical fibers: Ultra-flattened chromatic dispersion with low losses. Optics Letters 28 : 989-991

Rigneault H, Lemarchand F, Sentenac A (2000) Dipole radiation into grating structures. J Opt Soc Am A 17 : 1048-1058

Rivera T, Debray JP, Legrand B. Gérard JM, Manin-Ferlazzo L, Oudar JL (1999) Optical losses in plasma-etched AlGaAs microresonators using reflection spectroscopy. Appl Phys Lett 74 : 911-

Roberts P, Couny F, Sabert H, Mangan B, Williams D, Farr L, Mason M, Tomlinson A, Birks T, Knight J, Russell PSJ (2005) Ultimate low loss of hollow-core photonic crystal fibres. Opt. Express 13 : 236-244

Roberts PJ, Williams DP, Sabert H, Mangan BJ, Bird DM, Birks TA, Knight JC, Russell PSJ (2006) Design of low-loss and highly birefringent hollow-core photonic crystal fiber. Opt. Express 14 : 7329-7341

Rokhsari H, Kippenberg TJ, Carmon T, Vahala KJ (2005) Radiation-pressure-driven micromechanical oscillator. Opt Express 13 : 5293-5301

Romanov SG, Johnson NP, Fokin AV, Butko VY, Yates HM, Pemble ME, Sotomayor Torres CM (1997) Enhancement of the photonic gap of opal-based three-dimensional gratings. Appl Phys Lett 70 : 2091-

Romanov SG, Maka T, Sotomayor Torres CM, Muller M, Zentel R (2001) Emission in a SnS2 inverted opaline photonic crystal. Appl Phys Lett 79 : 731-733

Rowson S, Chelnokov A, Lourtioz JM (1999a) Two-dimensional photonic crystals in macroporous silicon photonic crystals : from mid-infrared to telecommunication wavelengths (1.3-1.55 μm). J Lightwave Technol 17 : 1989-1995

Rowson S, Chelnokov A, Lourtioz JM (1999b) Macroporous silicon : photonic crystal substrates at 1.55 µm. 25 th European Conference On Optical Communication ECOC'99, Nice, Sept 99

Rowson S, Chelnokov A, Lourtioz JM, Carcenac F (1998) Reflection and transmission characterisation of a hexagonal photonic crystal in the mid infrared. J Appl Phys 83 : 5061-

Roy P *et al* (2006) Photonic crystal fibres for lasers and amplifiers. C.R. Physique 7 : 224-232

Russell PStJ (2003) Photonic crystal fibers. Science 299 : 358-362

Russell PStJ (2006) Photonic-crystal fibers. J Lightwave Technol 24 : 4729-4749

Ryu H, Kim S, Park H, Hwang J, Lee Y, Kim J (2002b) Square lattice photonic bandgap single-cell laser operating in the lowest order whispering gallery mode. Appl Phys Lett 80 : 3883-

Ryu HY, Kwon SH, Lee YJ, Lee YH, Kim JS (2002a) Very-low-threshold photonic band-edge lasers from free-standing triangular photonic crystal slabs. Appl Phys Lett 80 : 3476-3478

Ryu HY, Notomi M, Kuramoti E, Segawa T (2004) Large spontaneous emission factor (>0.1) in the photonic crystal. Appl Phys Lett 84 : 1067-1069

Saado Y, Golosovsky M, Davidov D, Frenkel A (2001) Fabrication of artificial crystals with tunable lattice constant via self-assembly of floating magnetic particles. Synthetic Metals 116 : 427-432

Saitoh K, Koshiba M (2003) Leakage loss and group velocity dispersion in air-core photonic bandgap fibers. Opt. Express 11 : 3100-3109

Sakoda K (1995) Transmittance and Bragg reflectivity of two-dimensional photonic lattices. Phys Rev B 52 : 8992-8995

Sakoda K (1999a) Enhanced light amplification due to group-velocity anomaly peculiar to two- and three- dimensional photonic crystals. Optics Express 4 : 167-176

Sakoda K (2001) Optical Properties of Photonic Crystals. Springer Verlag, Heidelberg New York

Sakoda K, Ohtaka K (1996) Sum-frequency generation in a two-dimensional photonic lattice. Phys Rev B 54 : 5742-5749

Sakoda K, Ohtaka K, Ueta T. (1999b) Low-threshold laser oscillation due to group-velocity anomaly peculiar to two- and three-dimensional photonic crystals. Optics Express 4 : 481-489

Saltiel S, Kivshar Y (2000) Phase matching in nonlinear chi(2) photonic crystals. Opt Lett 25 : 1204- and 25 : 1612-

Sandhu S, Povinelli M, Yanik MF, Fan S (2006) Dynamically tuned coupled resonators delay lines can be nearly dispersion free. Opt Lett 31 : 1985-

Sandoghdar V, Treussart F, Hare J, Lefèvre-Seguin V, Raimond JM, Haroche S (1996) Very low threshold whispering-gallery-mode microsphere laser. Phys Rev A : R1777-

Santori C, Fattal D, Vuckovic J, Solomon G, Yamamoto Y (2002) Indistinguishable photons from a single-photon device. Nature 419 : 594-

Sanvitto D, Daraei A, Tahraoui A, Hopkinson M, Fry PW, Whittaker DM, Skolnick MS (2005) Observation of ultrahigh quality factor in a semiconductor microcavity. Appl Phys Lett 86 : 191109

Sato T, Miura K, Ishino N, Ohtera Y, Tamamura T, Kawakami S (2002) Photonic crystals for the visible range fabricated by autocloning technique and their application. Optical and Quantum Electronics 34 : 63-70

Sauvan C, Lalanne P, Hugonin JP (2005) Slow-wave effect and mode-profile matching in photonic crystal microcavities. Phys Rev B71 : 165118-1-4

Savvidis PG, Ciuti C, Baumberg JJ, Whittaker DM, Skolnick MS, Roberts JS (2001) Off-branch polaritons and multiple scattering in semiconductor microcavities. Phys Rev B 64 : 075311-

Scalora M, Dowling JP, Bowden CM, Bloemer MJ (1994) Optical limiting and switching of ultrashort pulses in nonlinear photonic band gap materials. Phys Rev Lett 73 : 1368

Scharrer M, Yamilov A, Wu X, Cao H, Chang RPH (2006) Ultraviolet lasing in high-order bands of three-dimensional ZnO photonic crystals. Appl Phys Lett 88 : 201103

Schawlow AL, Townes CH (1958). Infrared and optical masers. Phys Rev 112 : 1940-1949

Schilling J, Müller F, Matthias S, Wehrsporn RB, Gösele U, Busch K (2001) Three-dimensional photonic crystals based on macroporous silicon with modulated pore diameter. Appl Phys Lett 78 : 1180-1182

Schwartz L (1961) Méthodes mathématiques pour les Sciences Physiques (in French). Hermann, Paris

Scrimgeour J, Sharp DN, Blanford ChrF, Roche OM, Denning RG, Turberfield AJ (2006) Three-dimensional Optical Lithography for photonic Microstructures. Adv Mater 18 : 1557-1560

Seassal C, Désières Y, Letartre X, Grillet C, Rojo-Romeo P, Viktorovitch P, Benyattou T (2002) Optical Coupling Between a Two-Dimensional Photonic Crystal-Based Microcavity and Single-Line Defect Waveguide on InP Membranes. IEEE J Quant Electron 38 : 811-815

Seassal C, Monat C, Mouette J, Touraille E, Ben Bakir B, Hattori HT, Leclercq JL, Letartre X, Rojo-Romeo P, Viktorovitch P (2005) InP Bonded Membrane Photonics Components and Circuits: Toward 2.5 Dimensional Micro-Nano-Photonics. IEEE J Sel Top in Quantum Electron 11 : 395-407

Sek G (2006) Low-dimensional Systems and Nanostructures. Physica E 32 : 471-475

Sek G, Hofmann C, Reithmaier JP, Löffler A, Reitzenstein S, Kamp M, Keldysh LV, Kulakovskii VD, Reinecke TL, Forchel A (2006) Investigation of strong coupling between single quantum dot excitons and single photons in pillar microcavities. Physica E 32 : 471-475

Senechal M (1995) Quasicrystals and Geometry. Cambridge Univ. Press, Cambridge

Seo MK, Jeong KY, Yang JK, Lee YH, Park HG, Kim SB (2007) Low threshold current single cell hexapole mode photonic crystal laser. Appl Phys Lett 90 : 171122-

Settle M, Salib M, Michaeli A, Krauss TF (2006) Low loss silicon on insulator photonic crystal waveguides made by 193nm optical lithography. Opt Express 14 : 2440-2445

Shalaev VM, Cai W, Chettiar UK, Yuan HK, Sarychev AK, Drachev VP, Kildishev AV (2005) Negative index of refraction in optical Metamaterials. Opt Lett 30 : 3356-3358

Shelby RA, Smith DR, Schultz S (2001) Experimental verification of a negative index of refraction. Science 292 : 77-

Shen JT, Platzman PM (2002) Near field imaging with negative dielectric constant lenses. Appl Phys Lett 80 : 3286-3288

Shinya A, Mitsugi S, Kuramochi E, Notomi M (2005) Ultrasmall multi-channel resonant-tunneling filter using mode gap of width-tuned photonic-crystal waveguide. Opt Express 13 : 4202-4209

Shinya A, Mitsugi S, Tanabe T, Notomi M, Yokohama I, Takara H, Kawanishi S (2006) All optical flip flop circuit composed of coupled two port resonant tunneling filter in two dimensional photonic crystal slab. Opt Express 14: 1230

Shirakawa A, Ota J, Musha M, Nakagawa K, Ueda K, Folkenberg JR, Broeng J (2005) Large-mode-area erbium-ytterbium-doped photonic-crystal fiber amplifier for high-energy femtosecond pulses at 1.55 μm. Opt Express 13 : 1221-1227

Shoji S, Kawata S (2000) Photofabrication of three-dimensional photonic crystals by multibeam laser interference into a photopolymerizable resin. Appl Phys Lett 76 : 2668-2671

Siegel PH, Smith RP, Martin S, Gaidis M (1999) 2.5 THz GaAs monolithic membrane diode mixer. IEEE Trans Microwave Theory and Tech 47 : 596-604

Sievenpiper D (1999b) High impedance electromagnetic surfaces. Ph. D. Thesis, Univ. California, Los Angeles

Sievenpiper D, Sickmiller M, Yablonovitch E (1996) 3D wire mesh photonic crystals. Phys Rev Lett 76 : 2480-2483

Sievenpiper D, Yablonovitch E, Winn J, Fan S, Villeneuve P, Joannopoulos D (1998) 3D metallo-dielectric photonic crystals with strong capacitive coupling between metallic islands. Phys Rev Lett 80 : 2829-2832

Sievenpiper D, Zhang L, Broas R, Alexopoulos N, Yablonovitch E (1999a) High-impedance electromagnetic surfaces. IEEE Transactions on Microwave Theory and Techniques 47 : 2059-2074

Sigalas MM, Biswas R, Ho KM (1996) Theoretical study of dipole antennas on photonic band-gap materials. Microwave and Opt Technol Lett 13 : 205-209

Sigalas MM, Biswas R, Li Q, Crouch D, Leung W, Woodbury RJ, Lough B, Nielsen S, Mc Calmont S, Tuttle G, Ho KM (1997b) Dipole antennas on photonic band-gap crystals – experiment and simulation. Microwave Opt Technol Lett 15 : 153-158

Sigalas MM, Economou EN (1992) Elastic and acoustic wave band structures. J Sound Vibration 158 : 377-

Sigalas MM, Soukoulis CM, Biswas R, Ho KM (1997a) Effect of the magnetic permeability on photonic bandgaps. Phys Rev B56 : 959-962

Silberstein E, Lalanne P, Hugonin JP, Cao Qing (2001) Use of grating theories in integrated optics. J Opt Soc Am A : 2865-2875

Silvester P, Pelosi G (1994) Finite elements for wave electromagnetics, IEEE Press, New York

Simonneau C, Debray JP, Harmand JC, Vidakovic P, Lovering DJ, Levenson JA (1997) Second-harmonic generation in a doubly resonant semiconductor microcavity. Optics Letters 22 : 1775-

Sipe JE, Becher J (1982) Surface energy transfer enhanced by optical cavity excitation: a pole analysis. J Opt Soc Am 72 : 288-

Skauli T, Vodopyanov KL, Pinguet TJ, Schober A, Levi O, Eyres LA, Fejer MM, Harris JS, Gerard B, Becouarn L, Lallier E (2002) Measurement of the nonlinear coefficient of orientation-patterned GaAs and demonstration of highly efficient second-harmonic generation. Opt Lett 27 : 628

Slusher RE, Levi AFJ, Mohideen U, Mc Call SL, Pearton SJ, Logan RA (1993) Threshold characteristics of semiconductor microdisk lasers. Appl Phys Lett 63 : 1310-

Smit MK, van Dam C (1996) PHASAR-Based WDM Devices, Principles, Design and Applications. IEEE J Sel Topics in Quant Electronics 2 : 236-250

Smith CJM, De La Rue RM, Rattier M, Olivier S, Benisty H, Weisbuch C, Krauss TF, Houdré R, Oesterle U (2001) Coupled guide and cavity in a two-dimensional photonic crystal. Appl Phys Lett 78 : 1487-1489

Smith CJM, Krauss T.F, Benisty H, Rattier M, Weisbuch C, Oesterle U, Houdré R (2000d) Directionnally dependent confinement in photonic-crystal microcavities. J Opt Soc Am B 17 : 2043-2051

Smith CJM. Benisty H, Olivier S, Rattier M, Weisbuch C, Krauss TF, De La Rue RM, Houdré R, Oesterle U (2000c) Low-loss channel waveguides with two-dimensional photonic crystal boundaries. Appl Phys Lett 77 : 2813-2815

Smith CM, Venkataraman N, Gallagher MT, Müller D, West JA, Borrelli NF, Allan DC, Koch KW (2003) Low-loss hollow-core silica/ air photonic bandgap fibre. Nature 424 : 657–659

Smith DR, Kroll N (2000b) Negative Refractive Index in Left-Handed Materials. Phys Rev Lett 85 : 2 2933-2936

Smith DR, Padilla WJ, Vier DC, Nemat-Nasser S, Schultz S (2000a) Composite medium with simultaneously negative permeability and permittivity. Phys Rev Lett 84 : 4184-4187

Snoeks E, Blaaderen A, van Dillen T, van Kats CM, Velikov K, Brongersma L, Polman A, Colloidal assemblies modified by ion radiation. Nucl Instr Methods Phys Res, Sect B Beam interact Mater Atoms : 178 : 62-68

Snyder AW, Love JD (1983) Optical Waveguide Theory. Chapman & Hall,

Soljacic M, Lidorikis E, Joannopoulos JD, Hau LV (2005) Ultralow power all optical switching. Appl Phys Lett 86 : 171101

Soljacic M, Luo C, Joannopoulos JD, Fan S (2003) Nonlinear photonic crystal microdevices for integration. Opt Lett 28 : 637-

Solomon GS, Pelton M, Yamamoto Y (2001) Single-mode spontaneous emission from a single quantum dot in a three-dimensional microcavity. Phys Rev Lett 86 : 3903-3906

Song BS, Noda S, Asano T (2003) Photonic Devices Based on In-Plane Hetero Photonic Crystals. Science 300 : 1537-1539

Song BS, Noda S, Asano T, Akahane (2005) Y Ultra-high Q photonic double-heterostructure nanocavity. Nature Materials 4 : 207-210

Song DS, Kim SH, Park HG, Kim CK, Lee YH (2002) Single-fundamental-mode photonic-crystal vertical-cavity surface-emitting lasers. Appl Phys Lett 80 : 3901-3903

Soto-Crespo JM, Nieto-Vesperinas M (1989) Electromagnetic scattering from very rough random surfaces and deep reflection gratings. J Opt Soc Am A 6 : 367-384

Srinivasan K, Borselli M, Johnson TJ, Barclay PE, Painter O, Stintz A and Krishna S (2005) Optical loss and lasing characteristics of high quality factor AlGaAs microdisk resonators with embedded quantum dots. Appl Phys Lett 86 : 151106

Srinivasarao M, Collings D, Philips A, Patel S (2001) Three-dimensionally ordered array of air bubbles in a polymer film. Science 292 : 79-83

STARTIGER (Space Technology Advancements by Resourceful Targeted & Innovative Groups of Expert and Researchers) (2003) THz Imaging and Technology. http://www.startiger.org/tech.htm,

Stefanou N, Modinos A (1998) Impurity bands in photonic insulator. Phys Rev B 57 : 12127-12133

Steiner S, Hare J, Lefèvre-Seguin V, Gérard JM (2007) Room temperature lasing of InAs/GaAs quantum dots in the whispering gallery modes of a silica microsphere. Opt Express 15 : 10052-10060

Strauf S, Hennessy K, Rahker MT, Choi YS, Badolato A, Andreani LC, Hu EL, Petroff PM, Bouwmeester D (2006) Self-tuned gain in photonic crystal lasers. Phys Rev Lett 96 : 127404

Sugimoto Y, Tanaka Y, Ikeda N, Tanaka K, Asakawa K, Sakaki H, Ishida K (2004) Low propagation loss of 0.76 dB/mm in GaAs-based single-line-defect two-dimensional photonic crystal slab up to 1 cm in length. Opt Express 12 : 1090-1096

Sugitatsu A, Noda S (2003) Room temperature operation of a 2D photonic crystal slab defect-waveguide laser with optical pump. Electron Lett 39 : 213-215

Sun HB, Matsuo S, Misawa H (1999) Three-dimensional photonic crystal structures achieved with two-photon-absorption, photopolymerisation of resin. Appl Phys Lett 74 : 786-788

Suzuki M, Yokoyama H, Brorson SD, Ippen EP (1991) Observation of spontaneous lifetime change of dye-containing Langmuir-Blodgett filmsin optical microcavities. Appl Phys Lett 58 : 998-

Suzuki T, Yu P (1998) Complex elastic wave band structures in three-dimensional periodic elastic media. Mech Phys Solids 46 : 115-138

Taflove A (1995) Computational Electrodynamics: the Finite-Difference Time-Domain method. Artech House, Boston

Taillaert D, Bogaerts W, Bienstman P, Krauss TF, Daele PV, Moerman I, Vertsuyft S, Mesel KD, Baets R (2002) An Out-of-Plane Grating Coupler for Efficient Butt-Coupling Between Planar Waveguides and Single-Mode Fibers. IEEE J. Quant Electron 38 : 949-955

Taillaert D, Van Laere F, Ayre M, Bogaerts W, van Tourhout D, Bienstman P, Baets R (2006) Grating Couplers for Coupling between Optical Fibers and Nanophotonic Waveguides. Jap J Appl Phys 45 : 6071-6077

Tajima K, Zhou J, Kurokawa K, Nakajima K (2003) Low water peak photonic crystal fibers. Tech Digest of ECOC, Th4.1.6

Takenaka M, Nakano Y (1999) Proposal of a novel semiconductor optical waveguide isolator. Proceedings of the 11th Intern Conf on Indium Phosphide and Related Materials, Davos, Switzerland : 288-292

Talneau A, Aubin G, Uddhammar A, Berrier A, Mulot M, Anand S (2006) Highly dispersive photonic-crystal-based coupled-cavity structures. Appl Phys Lett 88 : 201106 (1-3)

Talneau A, Gouezigou LL, Bouadma N (2001) Quantitative measurements of low propagation losses at 1.55 μm on planar photonic crystal waveguides. Optics Lett 26 : 1259-1261

Talneau A, Lalanne P, Agio M, Soukoulis CM (2002) Low-reflection photonic-crystal taper for efficient coupling between guide sections of arbitrary widths. Opt Lett 27 : 1522-1524

Tamir T (ed) (1990) Guided Wave Optoelectronics. Springer Verlag, Heidelberg

Tanabe T, Notomi M, Kuramochi E, Shinya A, Taniyama H (2007) Trapping and delaying photons for one nanosecond in an ultrasmall high-Q photonic-crystal nanocavity. Nature Photonics 1 : 49-52

Tanabe T, Notomi M, Mitsugi S, Shinya A, Kuramochi E (2005) Fast bistable all optical switch and memory on silicon photonic crystal on chip. Opt Lett 30 : 2575

Tanabe T, Nishiguchi K, Shinya A, Kuramuochi E, Inokawa H, Notomi M, Yamada K, Tsuchizawa T, Watanabe T, Kukuda H, Shinojima H, Itabashi S (2007) Fast all-optical switching using ion-implanted silicon photonic crystal nanocavities. Appl Phys Lett 90: 031115

Tanaka Y, Asano T, Hatsuta R, Noda S (2004) Analysis of a line-defect waveguide on a silicon-on-insulator two-dimensional photonic-Crystal slab. J Lightwave Technol 22 : 2787-2792

Tanaka Y, Sugimoto Y, Ikeda N, Nakamura H, Kanamoto K, Asakawa K, Inoue K (2005) Design, fabrication, and characterization of a two-dimensional photonic-crystal symmetric Mach–Zehnder interferometer for optical integrated circuits. Appl Phys Lett 86 : 141104 (1-3)

Tanzilli S, De Riedmatten H, Tittel W, Zbinden H, Baldi P, De Micheli M (2005) Highly efficient photon pair source using periodically poled lithium niobate waveguides. Electron. Lett 37 : 26-

Temelkuran B, Hart SD, Benoit G, Joannopoulos JD, Fink Y (2002) Wavelength-scalable hollow optical fibres with large photonic bandgaps for CO_2 laser transmission. Nature 420 : 650-653

Têtu A, Kristensen M, Frandsen LH, Harpoth A, Borel PI, Jensen JF, Sigmund O (2005) Broadband topology-optimized photonic crystal components for both TE and TM polarizations. Opt Express 13 : 8606–8611

Tezuka T, Nunoue SY, Yoshida H, Noda T (1993) Spontaneous emission enhancement in pillar-type microcavities. Jpn J Appl Phys 32 : L54-L57

Thevenot M, Cheype C, Reineix A, Jecko B (1999) Directive photonic bandgap antennas. IEEE Trans Microwave Theory and Tech 47 : 2115-

Thomas H, Morfill G, Demmel V, Goree J (1994) Plasma crystal: coulomb crystallisation in a dusty plasma. Phys Rev Lett 73 : 652-655

Tikhodeev SG, Yablonskii AL, Muljarov EA, Gippius NA, Ishihara T (2002) Quasiguided modes and optical properties of photonic crystal slabs. Phys Rev B 66 : 045102

Toader O, John S (2001) Proposed Square spiral microfabrication architecture for large three-dimensional photonic band gap crystals. Science 292 : 1133-1135

Tretyakov SA (2001) Meta-materials with wideband negative permittivity and permeability., Microwave and Optical Technology Lett 31 : 163-165

Tsai YC, Pendry JB, Shung KWK (1999) Absolute three-dimensional photonic band gap in the infrared regime in woven structures. Phys Rev B 59 : R10401-R10404

Tsang T, Olsson NA, Linke RA, Logan RA (1983) High-speed direct single-frequency modulation with large tuning note and frequency emission in cleaved-coupled-cavity microseconductor lasers. Appl Phys Lett 42 : 650-

Ulrich R (1967) Far infrared properties of metallic mesh and its complementary structure. Infrared Phys 7 : 37-55

Ulrich R, Renk F, Genzel L (1963) Tunable submillimeter interferometers of the Fabry-Perot type. IEEE Trans Microwave Theory and Techniques MTT-11 : 363-371

Utaka K, Akiba S, Sakai K, Matsushima Y (1986) λ/4-shifted InGaAsP/InP DFB lasers. IEEE J Quant Electron QE-22 : 1042-1051

Vahala K (2005) Optical microcavities. Nature 424 : 839-646

Valanju PM, Walser RM, Valanju AP (2002) Wave Refraction in Negative-Index Media: Always positive and Very Inhomogeneous. Phys Rev Lett 88 : 187401

Van Der Ziel JV (1975) Phase matched harmonic generation in a laminar structure with wave propagation in the plane of the layers. Appl Phys Lett 26 : 60-62

Van Driel HM, Vos WH (2002) Multiple Bragg wave coupling in photonic-band-gap crystals. Phys Rev B 62 : 9872-9875

van Eijkelenborg MA, Argyros A, Barton G, Bassett IM, Fellew M, Henry G, Issa NA, Large MCJ, Manos S, Padden W, Poladian L, Zagari J (2004) Recent progress in mi-

crostructured polymer optical fibre fabrication and characterization. Opt Fib Tech 9 : 199-209

Vanwolleghem M, Dagens B, Gogol P, Beauvillain P (2006b) Integrated optical isolator equipped with a Bragg grating. French patent n°06 10344

Vanwolleghem M, Gogol P, Beauvillain P, Lourtioz JM (2006a) First Theoretical Evidence of Optical Non-Reciprocity and Band Gap Tunability in Two-Dimensional Magneto-Photonic Crystals. Proceedings of the Intern Conf CLEO/QELS 2006 (vol 1) : QTuC2

Vanwolleghem M, Van Parys W, Van Thourhout D, Baets R, Lelarge F, Gauthier-Lafaye O, Thedrez B, Wirix-Speetjens R, Lagae L. (2004) Experimental demonstration of nonreciprocal amplified spontaneous emission in CoFe clad semiconductor optical amplifier for use as an integrated optical isolator. Appl Phys Lett 85 : 3980-3982

Varoutsis S, Laurent S, Kramper P, Lemaître A, Sagnes I, Robert-Philip I, Abram I (2005) Restoration of photon indistinguishability in the emission of a semiconductor quantum dot. Phys Rev B 72 : 041303(R)

Varshney SK, Florous NJ, Saitoh K, Koshiba M, Fujisawa T (2007) Numerical investigation and optimisation of a photonic crystal fiber for simultaneous dispersion compensation over S+C+L wavelength bands. Opt Comm 274 : 74-79

Veselago VG (1964) Uspekhi Physicheskikh Nauk (in Russian) 92 : 517-526

Veselago VG (1968) The electrodynamics of substances with simultaneously negative values of ε and μ. Soviet Physics Uspekhi 10 : 509-514

Veselago VG (2002) About the wording of Fermat's principle for light propagation in media with negative refraction index (http://physics.ucsd.edu/~drs/publications/veselago-preprint-2002.pdf).

Viasnoff-Schwoob E, Weisbuch C, Benisty H, Olivier S, Varoutsis S, Robert-Philip I, Houdré R, Smith CJMS (2005) Spontaneous Emission Enhancement of Quantum Dots in a Photonic Crystal Wire. Phys Rev Lett 95 : 183901

Vlasov YA, McNab SJ (2006) Coupling into the slow light mode in slab-type photonic crystal waveguides. Opt Lett 31 : 50–52

Vlasov YA, O'Boyle M, Hamann HF, McNab SJ (2005) Active control of slow light on a chip with photonic crystal waveguides. Nature 438 : 65-69

Vlasov YA, Yao N, Norris DJ (1999) Synthesis of photonic crystals for optical wavelengths from semiconductor quantum dots. Adv Mater 11 : 165-169

Vlassis M, McPhedran RC, Nicorovici NA (1996) Radiation modes of multiple core fibres. Opt Commun 129 : 256-272

Vodopyanov KL, Levi O, Kuo PS, Pinguet TJ, Harris JS, Fejer MM, Gérard B, Becouarn L, Lallier E (2004) Optical parametric oscillation in quasi-phase-matched GaAs. Opt Lett 29 : 1912-

Vos WL, Driel HMV, Megens M, Koenderink AF, Imhof A (2001) Experimental probes of the optical properties of photonic crystals in Soukoulis CM (dir) Photonic Crystals and Light Localization in the 21st Century (pp. 191-218), Kluwer Academic Publishers, Dordrecht

Vredenberg AM, Hunt NE.J, Schubert EF, Jacobson DC, Poate PM, Zydzik GJ (1993) Controlled atomic spontaneous emission from Er^{3+}in a transparent Si/SiO_2 microcavity. Phys Rev Lett 71 : 517-

Vuckovic J, Loncar M, Mabuchi H, Scherer A (2002a) Optimization of the Q factor in photonic crystal microcavities. IEEE J Quant Electron 38 : 850-856

Vuckovic J, Lonkar M, Mabuchi H, Scherer A (2001) Design of photonic crystal microcavities for cavity QED. Phys Rev E 65 : 016608-

Vuckovic J, Pelton M, Scherer A, Yamamoto Y (2002b) Optimization of three-dimensional micropost microcavities for cavity quantum electrodynamics. Phys Rev A 66 : R023808-

Wadsworth WJ, Knight JC, Reeves WH, Russel PStJ (2000) Yb3+- doped photonic crystal fibre laser. Electron Lett 36 : 1452–1454

Wang B, Wang GP (2004) Metal heterowaveguides for nanometric focusing of light. Appl Phys Lett 85 : 3599-3601

Wang K (2006) Light wave states in two-dimensional quasiperiodic media. Phys Rev B 73 : 235122

Wang Z, Fan S (2005) Optical circulators in two-dimensional magneto-optical photonic crystals. Opt Lett 30 : 1989-1991

Wannier GH (1937) The structure of electronic excitation levels in insulating crystals. Phys Rev 52 : 191-

Ward MB, Karimov OZ, Unitt DC, Yuan ZL, See P, Gevaux DG, Shields AJ, Atkinson P, Ritchie DA (2005) On-demand single-photon source for 1.3 μm telecom fiber. Appl Phys Lett 86 : 201111-

Weidner E, Combrié S, de Rossi A, Tran NVQ, Cassette S (2007) Nonlinear and bistable behavior of an ultrahigh-Q GaAs photonic crystal nanocavity. Appl Phys Lett 90 : 101118

Weidner E, Combrié S, Tran NVQ, de Rossi A, Nagle J, Cassette S, Talneau A, Benisty H (2006) Achievement of ultrahigh quality factors in GaAs photonic crystal membrane nanocavity. Appl Phys Lett 89 : 221104

White TP, Kuhlmey B, McPhedran RC, Maystre D, Renversez G, Martijn de Sterke C, Botten LC (2002a) Multipole method for microstructured optical fibers I: formulation. J Opt Soc Am B 10 : 2322–2330

White TP, McPhedran RC, Martijnde Sterke C, Litchinitser NM, Eggleton BJ (2002b) Resonance and scattering in microstructured optical fibers. Opt Lett 27 : 1977-1979

Whittaker DM (2001) Classical treatment of parametric processes in a strong-coupling planar microcavity. Phys Rev B 63 : 193305-

Whittaker DM, Culshaw IS (1999) Scattering-matrix treatment of patterned multilayer photonic structures. Phys Rev B 60 : 2610-2618

Wiersma D, Bartolini P, Lagendijk A, Righin R (1997) Localization of light in a disordered medium. Nature 390 : 671-673

Williams J M (2001) Some problems with negative refraction. Phys Rev Lett 87: 249703

Windisch R, Heremans P, Knobloch A, Kiesel P, Döhler GH, Dutta, B, Borghs G (1999) Light-emitting diodes with 31% external quantum efficiency by outcoupling of lateral waveguide modes. Appl Phys Lett 74 : 2256-2258

Winn JN, Fan S, Joannopoulos JD, Ippen EP (1999) Interband transitions in photonic crystals. Phys Rev B 59 : 1551-1554

Winn JN, Fink Y, Fan S, Joannopoulos J (1998) Omnidirectional reflection from a one-dimensional photonic crystal. Optics Letters 23 : 1573-1575

Wood RG (1902) Optical resonances from granular films and fogs of the alkali metals. Phil Mag 6 : 396-

Woodcock LV (1997) Entropy difference between the face-centred cubic and hexagonal close-packed crystal structures. Nature 385 : 141-143

Wu L, Mazilu M, Karle T, Krauss TF (2002) Superprism phenomena in planar photonic crystal. J Lightwave Technol 38 : 915-918

Xia F, Sekaric L, Vlasov YA (2007) Ultracompact optical buffers on a silicon chip. Nature Photonics 1 : 65-71

Xia Y, Gates B, Park SH (1999) Fabrication of three-dimensional photonic crystals for use in the spectral region from ultraviolet to near-infrared. J Lightwave Technol 17 : 1956-1962

Xu P, Ji SH, Zhu SN, Yu XQ, Sun J, Wang HT, He JL, Zhu YY, Ming NB (2004) Conical second harmonic generation in a two dimensional chi(2) photonic crystal : a hexagonally poled LiTaO3 crystal. Phys Rev Lett 93 : 133904

Yablonovitch E (1987) Inhibited spontaneous emission in solid state physics and electronics. Phys Rev Lett 58 : 2059-

Yablonovitch E (1993) Photonic band-gap structures. J Opt Soc Am B 10 : 283-

Yablonovitch E (1994) Photonic crystals. Journ. of Mod Phys 41 : 173-194

Yablonovitch E (2007) Photonic crystals : what's in a name ? Optics and Photonics News March 2007, page 12.

Yablonovitch E, Gmitter T.J, Leung KM (1991a) Photonic band structures : the face-centered- cubic case employing non-spherical atoms. Phys Rev Lett 67 : 2295-

Yablonovitch E, Gmitter T.J, Meade RD, Rappe AM, Brommer KD, Joannopoulos J (1991b) Donor and acceptor modes in photonic band structures. Phys Rev Lett 67 : 3380-

Yacomotti AM, Raineri F, Vecchi G, Monnier P, Raj R, Levenson A, Ben Bakir B, Seassal C, Letartre X, Viktorovitch P, Di Cioccio L, Fedeli JM (2006) All optical bistable band edge Bloch modes in a two-dimensional photonic crystal. Appl Phys Lett 88 : 231107

Yacomotti AM, Raineri F, Vecchi G, Monnier P, Raj R, Levenson A, Ben Bakir B, Seassal C, Letartre X, Viktorovitch P, Di Cioccio L, Fedeli JM (2006) All-optical bistable band-edge Bloch modes in a two-dimensional photonic crystal. Appl Phys Lett 88 : 231107

Yamamoto Y (1991) Coherence, Amplification and Quantum Effects in Semiconductor Lasers. John Wiley & Sons, New-York

Yamamoto Y, Slusher RE (1993) Optical processes in microcavities. Physics Today 46(6) : 66

Yang FR, Ma KP, Qian Y, Itoh T (1999a) A uniplanar compact photonic-bandgap (UC-PBG) structure and its applications for microwave circuits. IEEE Trans Microwave Theory and Tech 47 : 1509-1514

Yang FR, Ma KP, Qian Y, Itoh T (1999b) A novel TEM waveguide using uniplanar compact photonic bandgap (UC-PBG) structure. IEEE Trans Microwave Theory and Tech 47 : 2092-2098

Yanik MF, Fan S (2004a) Stopping light all optically. Phys Rev Lett 92 : 083901

Yanik MF, Fan S (2004b) Time reversal of light with linear optics and modulators. Phys Rev Lett 93 : 173903

Yanik MF, Fan S, Soljacic M (2003) High contrast all optical bistable switching in photonic crystal microcavities. Appl Phys Lett 83 : 2739

Yanik MF, Suh W, Wang Z, Fan S (2004c) Stopping light in a waveguide with an all-optical analog of electromagnetically induced transparency. Phys Rev Lett 93 : 233903

Yariv A (1989) Quantum Electronics. John Wiley & Sons, New York

Yariv A (1997) Optical Electronics in Modern Communications. Oxford University Press, 5th Edition: 76-120

Yariv A, Xu Y, Lee RK, Scherer A (1999) Coupled-resonator optical waveguide: a proposal and analysis. Optics Letters 24 : 711-713

Yee KS (1966) Numerical solution of initial boundary-value problems involving Maxwell equations in isotropic media. IEEE Trans Antennas and Propagation 14 : 302-307

Yeh P (1988) Optical Waves in Layered Media. John Wiley & Sons, New York

Yeh P, Yariv A (1976) Bragg Reflection Waveguides. Opt Commun 19 : 427-

Yeh P, Yariv A, Marom E (1978) Theory of Bragg fiber. J Opt Soc Am 68(9) : 1196–1201

Yokoyama H (1992) Physics and device applications of optical microcavities. Science 256 : 66-

Yokoyama H (1995a) Spontaneous Emission and Laser Oscillation in Microcavities. CRC Press, Boca Raton

Yokoyama H, Brorson SR (1989) Rate equation analysis of microcavity lasers. J Appl Phys 66 : 4801-

Yokoyama H, Nambu Y, Kawakami T (1995b) Controlling spontaneous emission and microcavities in : Burstein E, Weisbuch (dir.) Confined electrons and photons : New physics and applications. Plenum, New-York

Yoshie T, Scherer A, Hendrickson J, Khitrova G, Gibbs HM, Rupper G, Ell C, Shchekin OB, Deppe DG (2004) Vacuum Rabi splitting with a single quantum dot in a photonic crystal nanocavity. Nature 432 : 200-202

Yoshie T, Shchekin O, Chen H, Deppe D, Scherer A (2002) Quantum dot photonic crystal lasers. Electron Lett 38 : 967-

Yoshie T, Vuckovic J, Scherer A, Chen H, Deppe D (2001) High-quality two-dimensional photonic crystal slab cavities. Appl Phys Lett 79 : 4289-

Yoshino, K, Shimoda Y, Kawagishi Y, Nakayama K, Ozaki M (1999) Temperature tuning of the stop band in transmission spectra of liquid-crystal infiltrated synthetic opal as tunable photonic crystal. Appl Phys Lett 75 : 932-934

Young RJ, Stevenson RM, Atkinson P, Cooper K, Ritchie DA, Shields AJ (2006) Improved fidelity of triggered entangled photons from single quantum dots. New J Phys 8 : 29-

Youssif HA, Köhler S (1988) Scattering by two penetrable cylinders at oblique incidence. I. The analytical solution. J Opt Soc Am A 5 : 1085-1096

Yuan Z, Kardynal B, Stevenson R, Shields A, Lobo C, Coopper K, Beattie N, Ritchie D, Pepper M (2002) Electrically driven single photon source. Science 295 : 102-

Zaets W, Ando K (1999) Optical waveguide isolator based on nonreciprocal loss/gain of amplifier covered by ferromagnetic layer. IEEE Photon Technol Lett 11: 1012-1014

Zakhidov AA, Baughman RH. Khayrullin II, Udod IA, Kozlov M, Eradat N, Vardeny VZ, Sigalas M, Biswas R (2001) Three-dimensionally periodic conductive nanostructures: network versus cermet topologies for metallic PBG. Synthetic Metals 116 : 419-426

Zavieh L, Mayer ThS (1999) Demonstration of a three-dimensional simple-cubic infrared photonic crystal. Appl Phys Lett 75 : 2533-2535

Zhang S, Fan W, Panoiu NC, Malloy KJ, Osgood RM, Brueck SRJ (2005) Experimental Demonstration of Near-Infrared Negative-Index Metamaterials. Phys Rev Lett 95 : 137404

Zhang WY, Lei XY, Wang ZI, Zheng DG, Tam WY, Chan CT, Sheng P (2000) Robust Photonic Band Gap from Tunable Scatterers. Phys Rev Lett 84 : 2853-2856

Zhang X, Zhang ZQ, Chan CT. (2001) Absolute photonic band gaps in 12-fold symmetric photonic crystals. Phys Rev B 63 : (R)081105-

Zhou J, Shao H, Yu X, Wong KS (2005a) Storage and release of femtosecond laser pulses in a resonant photonic crystal. Opt Lett 30 : 1560-

Zhou J, Zhou Y, Ng SL, Zhang HX, Que WX, Lam YL, Chan YC, Kam CH (2000) Three-dimensional photonic band gap structure of a polymer-metal composite. Appl Phys Lett 76 : 3337-3339

Zhou L, Li H, Qin Y, Wei Z, Chan CT (2005b) Directive emissions from subwavelength metamaterial-based cavities. Appl Phys Lett 86 : 101101

Zijstra ES, Janssen T (2000) Non-spiky density of states of an icosahedral quasicrystal. Europhys Lett 52 : 578-583

Ziman JM (1972) Principles of the Theory of Solids. Cambridge University Press, Cambridge

Zimmerman J., Scherer H, Kamp M, Deubert S, Reithmaier JP, Forchel A, März R, Anand S (2004) Photonic crystal waveguides with propagation losses in the 1 dB/mm range. J Vac Sci Technol B22 : 3356-3358

Zinoni C, Alloing B, Monat C, Zwiller V, Li LH, Fiore A, Lunghi L, Gerardino A, de Riedmatten H, Zbinden H, Gisin N (2006) Time-resolved and antibunching experiments on single quantum dots at 1300 nm. Appl Phys Lett 88 : 131102-

Ziolkowski RW, Heyman E (2001) Wave propagation in media having negative permittivity and permeability. Phys Rev E 64 : 056625-

Zolla F, Felbacq D, Guizal B (1998) A remarkable diffractive property of photonic quasicrystals. Optics Commun 148 : 6-10

Zoorob ME, Charleton MD, Parker GJ, Baumberg JJ, Netti MC (2000) Complete and absolute photonic bandgaps in highly symmetric photonic quasicrystals embedded in low refractive index materials. Mater Sci Eng B 74 : 168-174

Index

A

absorption condition 86-87
add-drop filter 289, 297, 335-336
air filling factor 298-299, 378, 386
amplitude map (of fields) 333, 338,
AlOx (AlAs oxyde) 265-267, 272, 314
Anderson localisation of light 115-118
antenna 414-418, 422-424, 426-430,
antenna substrate 414-418
anti-crossing 177-180
Archimedean tilings 111-115
artificial dielectrics 121, 210, 413

B

backward wave tubes 201
band diagram (band structure, dispersion curves, dispersion relations) 21-45, 55, 73-76, 114, 131, 133, 135, 149, 154, 176, 183, 188, 192, 202, 298, 301, 353, 341, 344, 357, 380
band folding 28, 177, 180, 187–189
band-edge laser 313-316
bandgap (forbidden band), 21-43, 112, 128, 129, 131, 133, 146-148, 152, 275, 288, 334, 382, 395, 398,
Bérenger's method 87
Bessel function 19-20, 94, 451-457
birefringence 205, 263-270, 273, 277 340, 381, 388
bistability 280
black body 412
Bloch functions, Bloch modes, Bloch waves 6, 9, 11, 12, 13, 20, 43, 47, 49, 53-54, 62, 65, 76, 142, 164, 191, 300-304, 325
Bloch impedance 437
boundary, interface conditions 6, 85-87, 96, 138, 139, 203-204, 200, 214
Bragg (grating, law, mirror, multilayers, reflector) *Foreword*, 30-33, 40, 44-46, 56, 228-230, 264, 270, 276, 277, 306, 348-350, 357, 358-360, 367
Brillouin (zone) 15, 22-25, 30, 33, 37, 38, 42

C

carcinotrons 200,
centred cubic (cc) lattice 23, 25, 41
chemically-assisted ion-beam etching (CAIBE) 311, 399
chiral material, chiral structure 395-396
chromatic dispersion 378-379
cloaking 221
conduction (air) band 28-30
confinement loss 375
controllable photonic crystal 424-428
coplanar line 414, 430-433
Coulomb (interaction) 261, 262, 367, 368
coupled mode theory 182-183, 302
coupled resonator optical waveguide (CROW) 188-189, 335-336, 354
coupling of defects 49, 50-51

coupling (strong) 231-234, 256-260
coupling (weak) 234-237, 250-254
cubic lattice (simple) 41, 395

D

deep ultraviolet lithography (DUV) 304
density of states (DOS) 59-63, 174-178, 187-188
DFB/DBR laser diode 181, 193-194, 278, 303, 306, 354, 355, 357
diamond, diamond symmetry, diamond structure 21, 25, 42, 49, 131-132, 394-395, 402, 403, 404, 405
differential method (coupled wave method) 100-102
diffraction, diffraction grating, diffraction pattern 65, 66, 113, 140, 141, 148-150, 163-165
diffraction-limited 220, 441
dipole 232, 233, 235, 257, 325, 332, 419-422
dipole antenna, dipolar antenna 414, 427-428
Dirac function 60, 100, 169
Dirac's monopole 211
direct lattice 5, 7, 8, 11, 12, 13
dispersion curves, dispersion relations (see band diagram)
distributions (theory) 6, 100, 102
doped crystals 43
doped silica 288, 292, 295, 371, 383
Drude function, Drude formula 121-125, 139, 137, 396

E

Ebbesen's structure 150
effective index, effective medium 100-103, 209, 221, 294, 299, 309
effective volume (of cavity, of mode) 186, 232, 248, 249, 250, 338, 368
electron beam lithography 304-305
electromagnetically induced transparency (EIT) 390
electronic waves (electrons and photons) *Foreword*, 261-262
elementary (unit) cell 5, 11, 19, 22, 26, 72, 109-110
E-method 13-15, 18-20
end-fire method (light injection) 321-323
energy balance equation 99, 104
enhanced back-scattering 115-117
etching depth 308, 311
Ewald spheres, circles 203, 204
exciton 231-234, 256-259
extended defect 54-56
extraction (of light) 230, 297-298, 320, 342, 345-352

F, G

Fabry-Perot (cavity, condition) 44, 168-169, 186-187, 227-229, 332
face-centred-cubic (fcc) lattice 25, 41, 340, 351
Faraday (effect) 459-461
Fermi surfaces 206
fibre attenuation 378, 386
Fibonacci structure 110
finite difference time domain (FDTD) 80-90, 98, 104
finite elements, finite element method 100-102, 104, 379
Floquet-Bloch (theorem) 6-9, 141
focused ion beam (FIB) etching 401
form birefringence 264-269 273, 381
Fourier series, Fourier component, Fourier expansion 8, 9, 18-20, 21, 67, 68, 91, 92, 102
Fourier transform 18-20, 26, 54, 80, 89, 107
Fourier-Bessel function 93-95, 449-454
fractal 109, 110, 111
free photon diagram 28, 33, 34, 35
frequency conversion 261-279

frequency doubling 262-264
frequency selective surface (FSS) 152, 440
Fresnel, Fresnel coefficients 40, 205
fundamental cases of polarization 17
GaAs 230, 242, 243, 247-255, 257-259, 263-266, 269, 272, 274, 281, 305, 307-314, 318, 319, 325, 327, 331, 338, 341, 345, 347, 349, 351, 353, 359, 360-363, 366-369, 399, 402,
Galerkin's method 101
GaN 299, 318, 345, 351-352
Gibbs phenomenon 21
Graf formula 98
graphite-type lattice 38-39
Green function 21, 100, 102, 451,
group index 201, 202-203
group velocity (of light) 197-202, 204, 206, 214
guided modes 55, 90, 168-185, 188-196, 290-295, 299, 307-308, 324-328, 329-330, 350, 351-352, 352-355, 366

H, I, J, K

Hankel function 93, 94, 96, 99, 126, 449, 450, 451, 461
Heaviside function 19
Helmholtz (equation) 68, 92, 122, 126, 141, 213, 450, 451, 461
hermiticity, hermitian 10, 11
hexagonal symmetry 12, 25, 71, 150, 204-206, 406
HFSS 104, 133
high-impedance surface 153-155, 418
H method 13, 15-18
Ho method 13, 20-21
holography (non linear) 279, (laser) 403-404
hollow waveguide, hollow core photic crystal fibres (HC-PCF) 371, 372, 373, 374, 382, 383, 385, 386, 387, 388, 389, 390, 391
homogenization 102-103
honeycomb lattice 38
Huyghens ('s principle) 89
impedance matching 222, 426, 437-438
InAs (quntum dots) 242, 243, 250, 251, 252, 254, 255, 257, 258, 318, 319, 362, 363, 366, 367, 369
InGaAs 259
InP, InGaAsP 305, 306, 308, 310, 311, 312, 318, 319, 321, 324, 348, 354, 357, 359, 361, 362, 402,
integral method (integral equations) 100-101
integrated optics 287-344
invisibility 222
isofrequency curve, isofrequency surface 202, 203, 204, 206, 207, 208
isotropic bandgap 110
Kagomé structure 388, 389
KKR method 21
Kronecker delta symbol 8

L, M

Laplacian 24, 448
leaky modes (guided with leakage) 53, 155, 192-193, 226, 237, 302, 306, 307, 308, 346, 350, 351, 378, 385, 386, 387
leaky modes (field leakage) in microcavities 185-187, 226, 230, 238, 245, 248, 254, 330, 338
left-handed materials (LHM) 212
light bend *Foreword*, 309, 312, 325, 328, 329-330, 334, 340, 341
light cone (line) 139, 140, 148, 146, 147, 190-196, 293, 300, 301, 302, 303, 306, 307, 309, 314, 324, 325
light emitting diode (LED) 226, 230, 237, 297, 299, 318, 345-352
linear combination of atomic orbitals (LCAO) method 53
lithium niobate 287
Mach-Zehnder (modulator) 341
macroporous silicon 273, 313, 314-316, 324

magneto-optic materials, magneto-photonic crystals 457-459
map (of gaps) 61-62, 298-299, 339, 382-383
Maxwell equations (conditions) *Foreword*, 5-6, 70, 72, 80-84, 100, 102, 121, 138, 143, 151, 152, 210, 211, 214, 222, 231, 291
Maxwell Garnett (theory) 134, 135
Membrane (waveguide, approach) 305, 311-314, 320, 323, 326, 327, 328, 329, 330, 333, 337-341, 350, 351, 355, 357, 358, 362, 364
metamaterials 210-223, 429-430, 440
microcavity 48, 169, 185-188, 225-260, 270, 272, 313, 320, 330-333, 337- 339, 348, 360-364, 367, 368, 369
microdisk 245, 247-248, 252, 259, 331, 360-361, 363, 367,
micro(cavity)laser 237-244, 360-364
micropillar 245-247, 251, 252, 253, 254, 255, 256, 366, 367, 368, 369
microstrip line 414, 415, 416, 432, 433
microstructured fibre (MOF) 372-382
Mie (theory)134, 135
mini-stopband 181-182, 342
mode volume 186, 232, 248, 249, 338, 368
MOEMS 311
multipole method (modal method) 91-99, 449-457

N, O, P

nanocrystal 365, 367
nanophotonics 443
near-field microscopy 218
negative refraction 207-209, 212-215, 218-221
nonlinear (optics, photonic crystals, functions, devices) 261-282, 287, 297, 334, 339, 341, 344
one-dimensional crystal *Foreword*, 22, 23, 25-33
opals (artificial) 167, 170, 405-409
optical fibre modelling 91
orthogonality relations 8, 12
patch antenna 414, 415, 416, 417, 418, 422, 423, 426, 427, 429
parametrical fluorescence 269, 272, 279
Pendry method 70-78
perfect left-Handed material (PLHM) 215-217
perfect lens 210, 213, 217-218, 220
perfectly matched layer (PML) 87
phase matching 262-264, 266, 267, 268, 269, 270, 272, 273
phase velocity (of light) 197-201
phased array (PHASAR) 287, 294, 296, 343
photoelectrochemical etching 314
photoluminescence (continuous, time-resolved) 247, 248, 249, 250, 251, 252, 253, 255, 259, 317- 318, 320, 331, 350,
photon interband transition 267
photon sieve 150-151
photonic crystal fibres (PCF) 371-392
photonic crystal filter (filtering) 295, 297, 324, 331, 422, 426, 428, 431, 432, 433-434, 436
photonic crystal loss 185-186, 189, 192-196, 274, 298-299, 300-304, 307-308, 309, 312, 324-333, 336, 341
photonic crystal mirror 163-168, 418-422
plane-wave method (model) 13-21
planar integrated optics 287-344
plasmons (surface plasmons, plasmonics) 135, 137-154, 440-442
plasmon-like band 126-128, 129, 131, 132, 424, 426
point defect 44-51
polarization 17, 18, 137, 139, 141, 149, 150, 229, 231, 263, 265, 266, 267, 269, 275, 291, 294, 296, 298,

308, 309, 310, 321, 334, 339, 340, 381, 384, 418, 431
pololology 144, 148
polymer 315, 316, 399, 400, 404, 408
polymethyl-methacrylate (PMMA) 304, 305, 400
Poynting vector 201, 203, 212, 437
pseudo-periodic, pseudo-periodicity 7, 8, 9, 10, 11, 65, 75, 77
Purcell effect 234-237, 238, 239, 242, 243, 244, 245, 251-254, 254-256, 363, 366, 367, 369
Purcell factor 236, 249, 250, 252, 253

Q, R

quality factor (Q-factor) 185, 230, 233, 235, 238, 242, 243, 244, 246, 250, 253, 258, 330-333, 337-339, 362, 368, 424, 433
quantum cascade lasers 435
quantum dots 245-246, 250-254, 256-260, 318-321, 341, 362-364, 365, 366, 367, 368, 369
quantum cryptography 364, 365, 366, 445
quasi-crystals 107-119
quasi-phase matching 263, 274-276
radar equivalent surface (RES) 427, 428
radiation (outgoing wave) condition 67-69, 71, 77, 86, 87, 94
radome 422-424, 426-428, 430
Raman scattering 148
Rayleigh (expansion, scattering) 67, 91, 144, 186
reactive ion etching (RIE) 282
reciprocal lattice, reciprocal space 8, 11, 12, 13, 22, 23, 24, 25, 26, 34, 38, 40, 62
reciprocity theorem 104
reflection phase 164, 365-366
refraction (of light in photonic crystals and metamaterials) 197-223
resonator (see also microcavity) 185-190, 330-333, 335-337

S

scattering matrix 71, 91-99, 165, 194, 302, 447-455
Schrödinger (equation) *Foreword*, 21, 292
second harmonic generation (SHG) 262, 269, 270, 273, 278
self-organisation 397-399, 405-409
silicon-on-insulator (SoI) 295, 312, 330, 335, 340, 341
single photon source 364-369
single-mode emission 237-245,
single-mode fibre 375-378
single-mode waveguide 292, 293, 294, 295, 312
skin effect 124-125
slow light, slow mode 281, 328, 329, 341, 356
Snell-Descartes law 203, 208, 215
solid-core (all-solid) photonic band-gap (SC-PBG) fibres 371, 390, 392
solid-state physics *Foreword*, 9, 22
space-filling mode 383
split ring resonator (SRR) 219, 220, 440
spontaneous emission 226-237, 238, 239, 250-254, 254-256, 297, 347, 349, 351, 360, 366, 367, 412
spontaneous emission factor (beta factor) 237
square lattice, square symmetry 24, 25, 33-37, 47, 52
supercell 52-53
supercontinuum generation 323, 380, 381
superlens 217-218,
superluminal propagation 220
superprism 207-208, 295-296, 303, 343-344
surface defect 56-58
surface impedance 151, 152, 418, 421
surface roughness 115, 117, 247, 248, 295,
surface waves 137-155
symmetry operator 24

T

taper (mode-matching) 322, 323, 340
TE (or *p*) polarization 18, 137
terahertz (THz) 413, 434-436, 439-440
three-dimensional crystal *Foreword*, 11, 20, 23, 25, 41-43, 46-49, 170-172, 393-412
thresholdless laser 237-244
TM (or *s*) polarization 17-18, 137
total (internal) reflection 245, 290-295, 372, 383
transfer, transmission matrix 65-80
translation operator 6-8
triangular lattice 25, 37-38, 55, 62, 298-299, 382
two-dimensional crystal (see also planar integrated optics) *Foreword*, 12, 17-18, 22-25, 33-41, 46-47, 66, 81-84, 90, 172-174, 298-299
two-photon lithography 404-405

U, V, W

ultra-compact photonic crystals 430-434
ultra-refraction 208-209
valence (dielectric) band 28-30
Van Hove singularity 60
Vavilov-Cherenkov effect 211
vector operator 5
vertical cavity surface emitting laser (VCSEL) 167, 348-349, 358, 360, 361
Wannier functions 44
waveguide 54-56, 90, 148, 168-185, 188-196, 290-344, 352-355, 378, 379, 383, 388, 390, 433-434, 437-438, 441-442
wideband division multiplexing (WDM) 289, 294, 330, 332, 335
Wood (anomalies) 144-148
woodpile (layer-by-layer) structure, 48, 49, 50, 395, 410, 411

X, Y, Z

X-ray lithography 399-400
yablonovite *Foreword*, 25, 42, 43, 56, 57, 58, 394, 395, 399-401, 415, 416
ZnO 352
$c^{(1)}$ photonic crystal 265-273
$c^{(2)}$ photonic crystal 274-279
$c^{(3)}$ photonic crystal (third-order susceptibility) 279-282